

BULMAN HOBSON TAYLOR

TRANSFERRED ELECTRON DEVICES



# Transferred Electron Devices

by

**P. J. BULMAN**

*Royal Radar Establishment,  
Great Malvern,  
Worcs.*

**G. S. HOBSON**

*Department of Electrical Engineering,  
Sheffield University,  
Sheffield.*

and

**B. C. TAYLOR**

*Royal Radar Establishment,  
Great Malvern,  
Worcs.*

1972



ACADEMIC PRESS · London and New York

ACADEMIC PRESS INC. (LONDON) LTD.  
24/28 Oval Road,  
London NW1

*United States Edition published by*  
ACADEMIC PRESS INC.  
111 Fifth Avenue  
New York, New York 10003

Copyright © 1972 by  
ACADEMIC PRESS INC. (LONDON) LTD.

*All Rights Reserved*

No part of this book may be reproduced in any form by photostat, microfilm, or any other means, without written permission from the publishers

Library of Congress Catalog Card Number: 76-189934  
ISBN: 0-12-140850-7

PRINTED IN GREAT BRITAIN BY  
ROYSTAN PRINTERS LIMITED  
Spencer Court, 7 Chalcot Road  
London NW1

## **Preface**

We hope that this book will help all those who wish to study or use Transferred Electron Devices (Gunn Diodes), and that it will also be comprehensible to those who have no previous knowledge of the subject. We have assumed that the reader, whether he be graduate, undergraduate or school leaver, will have a basic understanding of semiconductor physics and microwave circuits.

Most aspects of Transferred Electron Devices are covered, from the basic physics to their exploitation. The different regimes of amplifier and oscillator operation provided by the velocity field characteristics are discussed; for example, transit time oscillators and amplifiers, overlength LSA, hybrid mode and quenched oscillators. We then describe in detail different types of oscillator, amplifier and logic device, and for those who wish to read further into the complexities of the subject, we have provided extensive references.



## **Acknowledgements**

We are greatly indebted to our colleagues and friends who work in the field of solid state physics and devices for their helpful ideas and advice, which have assisted us so much in the preparation of this book.

We thank the Director of the Royal Radar Establishment for permission to publish this work, and the Controller of Her Majesty's Stationery Office for those parts which are Crown Copyright.

**P. J. BULMAN**

**G. S. HOBSON**

**B. C. TAYLOR**

# Contents

Preface . . . . .	v
Acknowledgements . . . . .	vi

## CHAPTER 1. THE SEARCH FOR A BULK NEGATIVE RESISTANCE IN SOLIDS

1.1 Introduction . . . . .	1
1.2 Non-Linear Conduction in Solids . . . . .	1
1.3 Negative Effective Mass—An Alternative Approach to Negative Resistance . . . . .	3
1.4 Exploitation of Band Structure . . . . .	4
1.5 Electron Transfer in GaAs . . . . .	5
1.6 Domains—A Consequence of Negative Differential Mobility . . . . .	6
1.7 Microwave Oscillations Observed in GaAs and InP . . . . .	8
1.8 Interpretation of the Gunn Effect . . . . .	8
1.9 The Avalanche Diode—Another Microwave Semiconductor Generator . . . . .	10
References . . . . .	11

## CHAPTER 2. RELEVANT SEMICONDUCTOR PROPERTIES

2.1 Introduction . . . . .	13
2.2 The Wave Mechanical Theory of Semiconductors . . . . .	13
2.3 Carrier Statistics . . . . .	28
2.4 Conduction in Solids . . . . .	32
2.5 Lattice Vibrations . . . . .	35
2.6 Scattering Mechanisms . . . . .	41
2.7 High Field Effects . . . . .	47
2.8 Carrier Diffusion . . . . .	50
2.9 Dielectric Relaxation Time . . . . .	53
2.10 Small Signal Mobilities . . . . .	54
References . . . . .	56

## CHAPTER 3. THE VELOCITY-FIELD CHARACTERISTIC

3.1 Introduction . . . . .	57
3.2 Formulation of the Problem . . . . .	61
3.3 Band Structure of GaAs . . . . .	63
3.4 The Boltzmann Equation . . . . .	63
3.5 Important Electron Scattering Mechanisms in GaAs . . . . .	66
3.6 Solution of the Boltzmann Equation . . . . .	73

3.7	Monte Carlo Calculation of the Velocity-Field Characteristic . . . . .	85
3.8	The Importance of the Velocity-Field Characteristic and Energy Relaxation Effects . . . . .	90
3.9	Measurement of the Velocity-Field Characteristic . . . . .	93
3.10	Comparison of Theory and Experiment . . . . .	101
3.11	The Effect of Reducing the Intervalley Energy Difference . . . . .	101
3.12	Gunn Effect in Other Materials . . . . .	104
References . . . . .		105

## CHAPTER 4. DYNAMIC EFFECTS

4.1	Introduction . . . . .	108
4.2	Static Negative Resistance? . . . . .	109
4.3	Domains . . . . .	113
4.4	$N_0 l$ Product—Space Charge Growth . . . . .	113
4.5	$N_0 l^2$ Product . . . . .	115
4.6	$N_0 d$ Product . . . . .	116
4.7	Stable Dipole Domains . . . . .	116
4.8	Triggered and Multiple Domain . . . . .	126
4.9	Accumulation Layers . . . . .	126
4.10	The L.S.A. Mode . . . . .	128
4.11	Amplifiers . . . . .	132
4.12	Power and Frequency Performance Limitations . . . . .	133
4.13	Electron Energy Relaxation Effects at High Frequencies . . . . .	135
References . . . . .		135

## CHAPTER 5. TRANSIT TIME MODES

5.1	Introduction . . . . .	137
5.2	Domains . . . . .	137
5.3	Domain Nucleation . . . . .	137
5.4	Domain Capacity and Device Reactance . . . . .	139
5.5	Power Output and Efficiency . . . . .	143
5.6	Limitations on Power Output . . . . .	145
5.7	Operation with a Sine Wave of Voltage . . . . .	147
5.8	Operation with a Sine Wave of Current . . . . .	151
5.9	Numerical Analysis of a Domain Mode . . . . .	153
5.10	Continuous Wave Operation . . . . .	157
5.11	Equivalent Circuit . . . . .	159
5.12	Continuous Wave Results . . . . .	160
5.13	Pulsed Operation and Hybrid Modes . . . . .	161
5.14	Rise Time . . . . .	166
References . . . . .		168

## CHAPTER 6. L.S.A. AND NON-TRANSIT (OVERLENGTH) MODES

6.1	Introduction . . . . .	169
6.2	The Limited Space Charge Accumulation (L.S.A.) Mode . . . . .	169
6.3	The Quenched Domain Mode of Oscillation . . . . .	181
6.4	The Hybrid Mode . . . . .	186
6.5	Comparison of Modes . . . . .	187

6.6	Starting Conditions and Cavities . . . . .	190
6.7	Maximum Power Limitations . . . . .	196
6.8	C.W. Operation . . . . .	198
6.9	Maximum Frequency Limitations . . . . .	198
6.10	Useful Characteristics of Non-Transnt Modes . . . . .	200
	References . . . . .	202

## CHAPTER 7. TRANSFERRED ELECTRON AMPLIFIERS

7.1	Introduction . . . . .	203
7.2	The Bulk Negative Conductance Amplifier . . . . .	203
7.3	The Travelling Wave Amplifier . . . . .	224
7.4	The Travelling Domain Amplifier . . . . .	225
7.5	Parametric Amplification from Gunn Diodes . . . . .	228
	References . . . . .	230

## CHAPTER 8. NOISE

8.1	Introduction . . . . .	231
8.2	Noise in Gunn Oscillators . . . . .	231
8.3	Noise in L.S.A. Oscillators . . . . .	244
8.4	Noise in Transferred Electron Amplifiers . . . . .	244
8.5	Other Fluctuation Phenomena . . . . .	247
	References . . . . .	247

## CHAPTER 9. NON-UNIFORM DEVICES AND LOGIC APPLICATIONS

9.1	Introduction . . . . .	249
9.2	Domain Current Control . . . . .	249
9.3	The Influence of Non-Uniform Electric Fields on Domain Nuclea- tion and Quenching . . . . .	253
9.4	External Control of Uniform Devices . . . . .	257
9.5	Domain Transient Response . . . . .	262
9.6	Mixed Devices, and Systems . . . . .	267
	References . . . . .	275

## CHAPTER 10. ENGINEERING AND APPLICATIONS

10.1	Introduction . . . . .	276
10.2	Thermal Design for Continuous Operation . . . . .	276
10.3	Thermal Design for Pulsed Operation . . . . .	281
10.4	Cavities . . . . .	284
10.5	Small Continuous Wave Oscillators . . . . .	285
10.6	Coaxial Cavity . . . . .	286
10.7	Mechanical Tuning of a Coaxial Cavity . . . . .	288
10.8	Electronical Tuning of Coaxial Cavity . . . . .	292
10.9	Electronic Tuning with a Yig Sphere . . . . .	298
10.10	Stability, Noise and Temperature Effects . . . . .	299
10.11	Modulation . . . . .	300
10.12	Frequency Locking—Multiple Devices . . . . .	301
10.13	Operation at 1 to 8 GHz . . . . .	302
10.14	Drive Requirements . . . . .	303
10.15	Miniature Doppler Systems . . . . .	305

10.16	Precision Ranging Radars . . . . .	306
10.17	Short Pulse Radar . . . . .	307
10.18	Short Pulse Transponders . . . . .	308
10.19	Beacons . . . . .	310
10.20	SPRAT . . . . .	311
	References . . . . .	312

#### CHAPTER 11. MATERIAL GROWTH AND DEVICE FABRICATION

11.1	Introduction . . . . .	313
11.2	Growth of Bulk Gallium Arsenide . . . . .	313
11.3	Vapour Epitaxial Growth . . . . .	316
11.4	Liquid Phase Epitaxy . . . . .	321
11.5	Material Characterization . . . . .	327
11.6	Contacts . . . . .	334
11.7	Device Construction . . . . .	342
	References . . . . .	353

#### CHAPTER 12. FURTHER DEVELOPMENTS IN BULK NEGATIVE CONDUCTIVITY

12.1	Introduction . . . . .	355
12.2	Negative Mobility due to Intra-Band Scattering . . . . .	357
12.3	Other Suitable III-V Compounds . . . . .	358
12.4	The Importance of the Intervalley Coupling Constant . . . . .	362
12.5	Future Developments . . . . .	368
	References . . . . .	371

#### CHAPTER 13. CIRCUIT FUNCTIONS

13.1	Introduction . . . . .	373
13.2	Local Resonances in Waveguide Mounts . . . . .	373
13.3	Oscillator Destabilization by Transmission Line Defects . . . . .	376
	References . . . . .	378

APPENDIX 1.	Scattering Term for the One Phonon Process . . . . .	380
-------------	--	-----

APPENDIX 2.	The Relaxation Time Approximation . . . . .	382
-------------	---	-----

APPENDIX 3.	Finite Difference Computation of Transferred Electron Problems in One Dimension . . . . .	387
-------------	---	-----

	References for Computer Simulation . . . . .	391
--	--	-----

	Author Index . . . . .	393
--	------------------------	-----

	Subject Index . . . . .	399
--	-------------------------	-----

## *Chapter 1*

# **The Search for a Bulk Negative Resistance in Solids**

### 1.1 INTRODUCTION

When J. B. Gunn in 1963 discovered that the current through a sample of bulk GaAs became unstable if the applied bias field exceeded a certain threshold value<sup>(1)</sup> he reached the culmination of some ten years of world-wide speculation on the possibility of obtaining negative resistance and active effects in bulk semiconductors. With this discovery a new era of development of semiconductor devices was born. Prior to this discovery the role of semiconductors at microwave frequencies was primarily a passive one, performing the functions of detection and mixing. Suddenly the possibility existed of replacing the existing microwave vacuum tube sources and their bulky, high voltage power supplies with much simpler, low voltage solid state oscillators. This possibility loomed large and provided the target for intense activity on the new effect in laboratories all over the world.

The consequence of all this activity is that today sources based on Gunn's original observation have generated new microwave applications by virtue of their simplicity, convenience and compactness, and they are making significant in-roads into the camp of the established vacuum tube sources, replacing low power microwave tubes just as the transistor replaced low frequency vacuum tubes in the 1950's.

### 1.2 NON-LINEAR CONDUCTION IN SOLIDS

In 1827 Ohm established his famous law which states that the current through a solid is directly proportional to the voltage applied to it. Metals obey the law remarkably well; semiconductors a good deal less well. The reasons for this difference are two fold. Firstly the practical reason that the high conductivity of metals prevents the application of high fields. Secondly, and fundamentally,

the mean energy of the electrons in a metal is high, being measured in electron volts, whereas in semiconductors the mean electron energy is considerably less, (around 0.025 eV at 300°K). Thus when a high field is applied to a metal the increase in electron energy which it produces is negligible, while a high field applied to a semiconductor can significantly increase the mean electron energy (making the electrons "hot") and this can alter the electron states which the electrons occupy, or the nature or the effectiveness of the scattering mechanisms to which the electrons are subject. As a result we cannot expect Ohm's law to be obeyed in semiconductors, except at low fields. It is this complexity in the electrical behaviour of semiconductors which makes their behaviour so much more interesting than that of metals.

It was a fascinating possibility that the deviation from linearity of the current-voltage relationship of a piece of bulk semiconductor might be sufficiently drastic to produce a negative slope at high fields. Shockley<sup>(2)</sup> in 1948 was the first to speculate along these lines. He saw in such an effect the possibility of a means of generating power at high frequencies. The theory which he put forward was based on the fact that the main mechanism for energy dissipation in semiconductors, namely scattering by thermal lattice vibrations, does not allow the removal of more than a small amount of energy from the electrons per collision and there is a maximum rate  $P_{\max}$  at which energy can be removed from the electrons. At high electric fields the rate of energy input to an electron ( $eEv$ ) must not exceed the rate of removal  $P_{\max}$  so that we have

$$eEv \leq P_{\max}$$

where  $E$  is the applied field and  $v$  the electron drift velocity. Hence we have that

$$v \leq \frac{P_{\max}}{eE}$$

and the electron drift velocity must fall with increasing field at sufficiently high values of the applied field. The slope mobility  $dv/dE$  and the differential resistance will then be negative. A more detailed theory of this effect has been given by Kroemer.<sup>(3)</sup>

This prediction<sup>(2,4)</sup> led to a search for negative differential mobility in high fields,<sup>(5,6)</sup> but without success.

Subsequently Shockley showed<sup>(2)</sup> that even if a bulk negative differential mobility had been present at high fields, its existence would not have been detected. This is because in a material biased into a negative (differential) mobility region an increase in terminal voltage leads to the injection of additional carriers into the device, setting up a non-uniform field distribution through the device and producing an increase in the carrier level which more

than compensates for the reduction in carrier mobility. A positive terminal conductance therefore results.

However, it takes time for this injection to occur and a steady state to be reached. The time involved is the order of the carrier transit time, so that if the terminal current voltage relationship could be measured in a time short compared to this, such a measurement could be interpreted directly in terms of the velocity field relationship of the carriers themselves.

The pulsed measurement called for required considerable sophistication, and it was eventually carried out in 1956 by J. B. Gunn himself.<sup>(7)</sup> Unfortunately the conclusion was that no negative differential mobility region existed in Germanium so the first determined quest for a bulk negative resistance was unsuccessful.

### 1.3 NEGATIVE EFFECTIVE MASS—AN ALTERNATIVE APPROACH TO NEGATIVE RESISTANCE

It was recognized that if an electron could be given sufficient energy by the applied field to populate the upper reaches of the conduction band, then its effective mass would be negative (Fig. 1.1). (A similar effect will occur for holes in the valence band). Under a steady field electrons at the bottom of the conduction band will be accelerated in the direction of the field and increase in energy until, above a certain energy, the effective mass becomes negative and the electron will be accelerated in a direction opposite to the field. Thus they will slow down, stop and move in the opposite direction, giving up energy to the field until they find themselves once more in the region of positive mass and their motion reverses. The electrons therefore oscillate to and fro and we have a current oscillation produced by the steady applied field. In practice however, scattering and avalanche multiplication act to limit the electron energy and prevent electrons from reaching negative mass regions of the conduction band. It is worth pointing out though that ideas for negative differential resistance based on the oscillation of conduction band electrons are still around.<sup>(8)</sup>

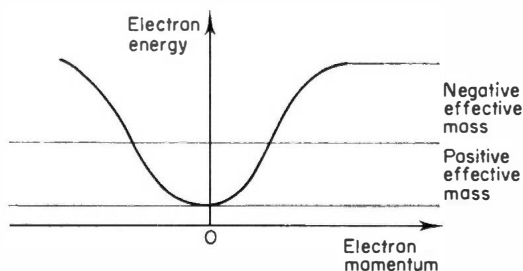


FIG. 1.1. Electron energy-momentum diagram for a simple energy band, showing the regions in which electrons have positive and negative effective mass.



Kroemer pointed out in 1959<sup>(9)</sup> that the complex valence band structures of Ge and Si were such that negative mass states could be attained in practice by the holes since these states were available at quite low energies. The negative mass states occur only for holes travelling in certain directions through the crystal and the negative mass will only be presented to fields in a *perpendicular* direction. Kroemer thus proposed that if enough holes could be induced to move in these directions by applying a bias field in the correct crystallographic direction, then a differential negative resistance would be available in a direction perpendicular to the bias field.

The major problem attending the observation of such a negative mass effect is that of maintaining sufficient holes travelling in the right crystal directions while the scattering mechanisms in general act to destroy such streaming of the holes. The experiment was performed, but once again a negative conductivity was not observed.

#### 1.4 EXPLOITATION OF BAND STRUCTURE

Although failing in its particular objective, Kroemer's ideas focussed attention on the possibilities which might be offered by seemingly esoteric band structure effects. Ridley and Watkins<sup>(10)</sup> and Hilsum<sup>(11)</sup> recognised that a negative differential conductivity could arise due to the field induced transfer of carriers from a set of high mobility states to a set of low mobility states into which the carriers would be accelerated at high fields (Fig. 1.2). The transfer would occur over a range of fields and if transfer took place over a sufficiently small range (Fig. 1.3a) then a region of negative differential mobility must ensue.

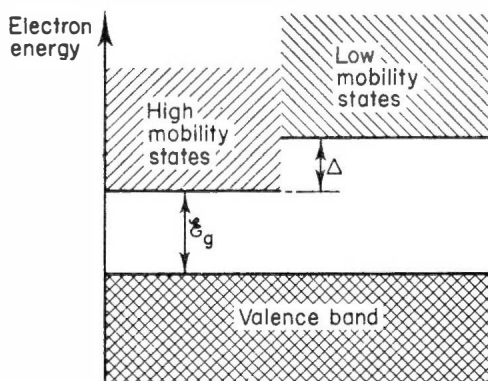


FIG. 1.2. Energy band structures required.  $E_g$  is the familiar energy gap of the semiconductor.  $\Delta$  is the energy separation between the two sets of conduction band states.

For a material to exhibit negative conductivity it had to have a band structure which satisfied certain well defined requirements. Firstly there must exist the two sets of electronic states, with the low mobility set at a higher energy than the high mobility set (Fig. 1.2). Secondly the energy separation  $\Delta$  must be less than the energy gap  $\mathcal{E}_g$ , or the energy input to the electrons from the field will lead to impact ionization of the lattice before the energy is reached at which transfer can begin. Thirdly, the transfer of electrons must occur rapidly with increasing field.

Means of realizing the appropriate band structure with the familiar elemental semiconductors Ge and Si by alloying and strain were considered by Ridley and Watkins. However, as they note, such artificial means are not required since the band structure called for occurs quite naturally in many of the III-V compound semiconductors, and the work of Hilsum<sup>(11)</sup> is concerned exclusively with the possibility of negative resistance due to electron transfer in GaAs.

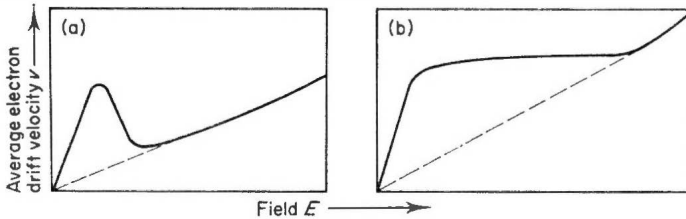
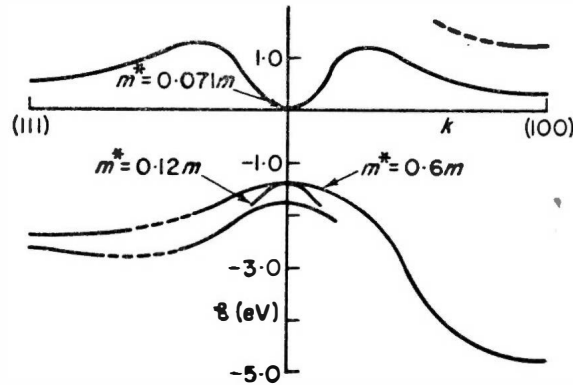


FIG. 1.3. Average drift velocity versus applied field for (a) electron transfer occurring over a small range of field. (b) electron transfer occurring slowly with applied field.

### 1.5 ELECTRON TRANSFER IN GaAs

Figure 1.4 shows the shape of the conduction band edge in GaAs. There is a central valley at (000) and at higher energy subsidiary minima which occur along the (100) crystallographic directions. The latter we will refer to as the satellite valleys. At still higher energy further minima occur which lie along the (111) directions, but these will not concern us.

At room temperature and for low electric fields almost all the electrons are near the bottom of the central valley. Because of their low effective mass the electrons in the central valley have high mobility ( $7\text{--}8000\text{ cm}^2/\text{V sec}$  typically) and this high mobility means that it is comparatively easy for a strong electric field to accelerate the electrons, that is, to heat them up, to high energies of the order of the satellite valley energy. When this happens, the electrons can scatter into the satellite valleys and there they have a much higher effective mass and a much lower mobility, and they therefore contribute much less to the current. If this inter-valley transfer were to take place only gradually

FIG. 1.4. The band structure of GaAs.<sup>(31)</sup>

with increasing field it would merely lead to a slow decrease of the conductivity and the current would continue to rise with increasing field. However, the transfer sets in rapidly with increasing field, and the current decrease due to electron transfer into the satellite valleys is stronger than the current increase due to the velocity increase of those electrons that remain in the central valley. As a result, the overall current drops as shown in Fig. 1.5 and the crystal exhibits a bulk negative differential conductivity. The threshold for the onset of the negative conductivity is about 3 kV/cm. When most of the electrons have been transferred into the satellite valleys, the current voltage relationship will be dictated solely by the mobility in the satellite valleys.

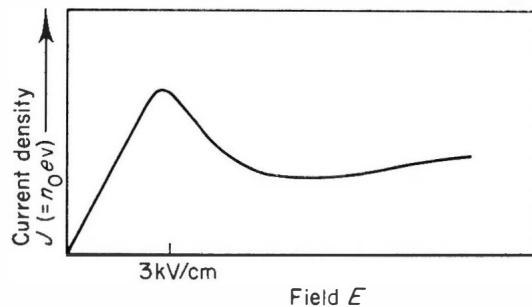


FIG. 1.5. Static current density—field characteristic for bulk *n*-type GaAs (schematic). The threshold for negative differential conductivity occurs at around 3 kV/cm.  $n_0$  is the carrier density,  $v$  the electron drift velocity.

## 1.6 DOMAINS—A CONSEQUENCE OF NEGATIVE DIFFERENTIAL MOBILITY

It was pointed out by Reik that a crystal whose velocity field characteristic has a region of negative slope (Fig. 1.6(a)) will be electrically unstable, and

this aspect was taken up and analyzed in late 1963 by Ridley.<sup>(12)</sup> The basic ideas can be outlined as follows. Consider a voltage applied to the crystal such that the field everywhere in the crystal  $E_{AV}$  lies just above the threshold value for negative differential mobility. Now consider what happens when a random fluctuation of carrier density occurs at some point in the crystal, of the form shown in Fig. 1.6(b). There will be an increase in the field locally at this space charge region and because we are in a region of negative slope mobility, this will lead to a *reduction* in electron velocity. Hence the electrons ahead of the fluctuation will travel faster and move away from the fluctuation while those behind will pile into the back of it. In consequence the dipolar fluctuation will grow in amplitude until the crystal stabilizes itself. The field in the crystal corresponding to the stable state is shown in Fig. 1.6(c).  $E_H$  is the field in the large amplitude dipole “domain” to which the fluctuation has grown and  $E_L$  the field elsewhere in the crystal. Prior to the growth of the domain the current flowing will be given by  $J = n_0 e v_m$  while after domain formation it will be given by  $J = n_0 e v_d$ . Since  $v_m > v_d$  it is clear that there is a fall in sample current associated with the growth of a domain.

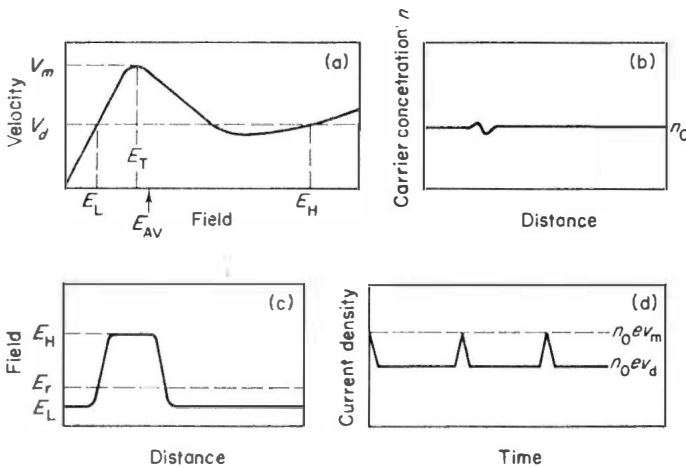


FIG. 1.6. (a) A velocity-field curve with a region of negative slope. (b) A local dipolar fluctuation in carrier density. (c) Steady state form of field distribution after growth of the dipolar fluctuation. (d) Time dependence of current density in the crystal. The rapid rise and fall of current are associated with the exit of a domain at the anode, and re-nucleation of a new domain in the crystal.

Since the domain consists of mobile electrons it moves along with the electrons from the negative to the positive electrode. As the high field domain disappears into the positive electrode, the field  $E_L$  outside the domain, and therefore the current through the sample, increase towards their threshold

values. As these threshold values are reached, a new high field domain will grow and the current decreases again. In this way periodic current oscillations (Fig. 1.6(d)) and periodically propagating space charge layers are generated.

### 1.7 MICROWAVE OSCILLATIONS OBSERVED IN GaAs AND InP

At this point in time (late 1963) all the main contributions to the theory of electron transfer effects had been made, negative slope mobilities had been postulated to exist in some semiconductors, Hilsum had worked out detailed figures relating to GaAs, and Ridley had presented a picture of how such negative mobilities would manifest themselves to the external world. All that was required was an experiment to clinch the theoretical predictions. Curiously enough the experiment had been performed already, a few months prior to the publication of Ridley's work on domains. It was unwittingly carried out by J. B. Gunn.<sup>(1)</sup> He had been examining the behaviour of bulk GaAs and InP samples in high fields when he found that above a certain threshold field, the current flowing through his samples became unstable and oscillated with a frequency related to the sample thickness. Figure 1.7 shows a typical current wave shape as observed by Gunn.<sup>(13)</sup> The measurements are pulsed and the steady current trace is for an applied voltage just below the threshold value. At a voltage above threshold the current is observed to oscillate with a maximum value equal to the current at threshold.

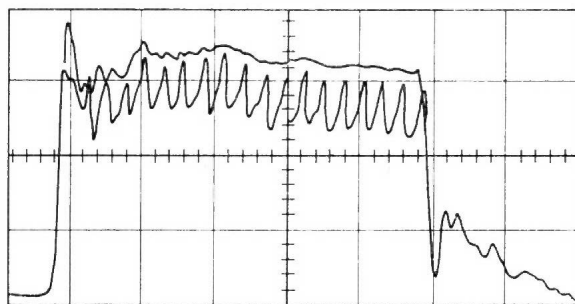


FIG. 1.7. Typical current oscillation as observed by Gunn.<sup>(13)</sup> The non-oscillating current pulse is for a bias field just below threshold, the oscillating curve is for a bias just above threshold. The scales are 45 mA and 2 nsec per division.

### 1.8 INTERPRETATION OF THE GUNN EFFECT

Although in retrospect the electron transfer effect was a clear candidate to provide the explanation for Gunn's observations, this effect suffered from the disadvantage that it was only hypothetical, and that other active effects in solids were in existence and were proven; in particular amplification of acoustic waves in piezoelectric semiconductors by an electron stream travell-

ing at a velocity slightly higher than the velocity of sound.<sup>(14)</sup> Gunn considered such an interaction and rejected it on the grounds that the electron velocity in GaAs at the oscillation threshold was orders of magnitude greater than the velocity of sound. Instead he proposed a mechanism involving the amplification of optical phonons by the drifting electrons.<sup>(13)</sup>

Among other active effects considered by Gunn were the two stream instability which is well known in vacuum tubes,<sup>(15)</sup> and a possible mechanism which necessitated energy dependent scattering of the electrons such that at high electron energies the increasing effectiveness of the scattering would actually lead to a drift velocity which decreased with increasing field.<sup>(13)</sup>

Gunn did in fact consider the electron transfer mechanism as a possible explanation and dismissed it on the grounds that the electron temperature required for transfer, as estimated by Ridley and Watkins,<sup>(10)</sup> was of the order of 4000°K while his measurements indicated considerably lower temperatures. In fact this estimate contained an over simplified approximation and the more accurate calculations of electron temperature by Hilsun<sup>(11)</sup> were overlooked by Gunn. Kroemer pointed this out in a letter published in late 1964<sup>(16)</sup> in which he examined in detail all the facts then known about the Gunn Effect and concluded that the most likely explanation for Gunn's observations was electron transfer to satellite minima. He further suggested that domains should be present in accordance with Ridley's predictions,<sup>(12)</sup> not knowing that Gunn had in fact already observed and reported on such domains.<sup>(17)</sup>

The feeling grew that electron transfer was responsible for the oscillations and all reasonable doubts were removed in early 1965 by the experiment of Hutson *et al.*<sup>(18)</sup> This showed that with increasing hydrostatic pressure the threshold field for oscillations would first decrease, and then at pressures above 26 kbar the oscillations would disappear altogether. This behaviour was consistent with the known movement of the satellite minima in GaAs relative to the central minimum, namely that the energy separation reduces with increasing pressure and goes to zero at around 30 kbar. Thus we would expect just such a reduction in the threshold field for transfer, with no transfer effect at all occurring when the minima were at approximately the same energy.

In the months following the weight of evidence for electron transfer continued to increase. Allen *et al.*<sup>(19)</sup> partially substituted Phosphorus for Arsenic in GaAs, modifying the band structure in a similar way to that of the pressure experiment, and confirmed the disappearance of oscillation for a sufficient proportion of Phosphorus in the alloy. The effect had already been observed in InP as well<sup>(1)</sup> and now it was observed in CdTe too,<sup>(20)</sup> both semiconductors being known to have the appropriate conduction band structure.

The effect was not found in any *p*-type semiconductor, consistent with the absence of satellite minima in the valence band of semiconductors with a Zinc

Blende type of lattice. Nor was it found in any semiconductor with low mobility valleys *below* a high mobility valley (e.g. Ge, Si, GaP). Nor in a semiconductor where low mobility valleys lie at an energy above a high mobility valley but where this separation is greater than the energy gap (e.g. InSb, InAs). In the latter case avalanching will occur which prevents the field for transfer being attained.

By the end of 1965 it was abundantly clear that a true bulk negative resistance effect in solid had at last been found, that it was due to the mechanism of electron transfer between high and low mobility states in the conduction band of a few semiconductors with the appropriate band structure (notably GaAs, InP, CdTe), and that it was capable of being exploited to provide a simple semiconductor source for the generation of pulsed<sup>(21)</sup> and C.W. power<sup>(22,23)</sup> at microwave frequencies. It was also known by then that under certain conditions the devices could also be stabilized and used to amplify microwave signals.<sup>(24)</sup>

### 1.9 THE AVALANCHE DIODE—ANOTHER MICROWAVE SEMICONDUCTOR GENERATOR

At the same time another candidate for direct generation from semiconductors at microwave frequencies had arrived on the scene.<sup>(25)</sup> This was the Avalanche Diode or Impatt Diode (IMPact Avalanche and Transit Time) which also depended on the properties of hot electrons in solids.<sup>(25)</sup> This device however could in principle be fabricated in any semiconductor, since it does not rely on any property peculiar to a particular group of semiconductors as does the transferred electron effect.

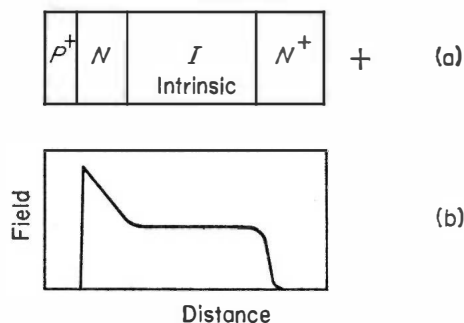


FIG. 1.8.(a) Structure for Avalanche Diode Oscillator proposed by Read.<sup>(26)</sup> (b) Field distribution for reverse bias.

It utilises a semiconductor in which a junction formed at one end is reverse biased into avalanche breakdown and the carriers produced in the avalanche drift across the crystal to the collecting electrode. The structure

originally proposed for such a device<sup>(26)</sup> is shown in Fig. 1.8(a), with the field distribution being as shown in Fig. 1.8(b). The high field at the junction is sufficient to cause an avalanche at this point and the field in the intrinsic zone is high enough for all the carriers to drift across it with a constant "saturated" velocity (see Section 2.6.1) which is independent of the field magnitude. In effect we have a situation analogous to that in a vacuum tube where an electrode at one end injects carriers into a drift space. The device oscillates by virtue of a phase lag (of  $180^\circ$  ideally) between the applied voltage and the resulting current. The phase lag is due partly to the inductive nature of the avalanche process and partly to the time taken by the carriers produced in the avalanche to drift across the intrinsic zone to the collecting electrode. A more detailed description of the operation of this device can be found in Ref. 27.

Thus by late 1965 the curtain had been well and truly raised on the era of microwave generation by bulk effects in semiconductors. From that time our understanding of the effects has considerably improved and new ways of using the devices have been discovered.<sup>(28,29)</sup> The pace has been fast and furious<sup>(30)</sup> as we have sought to improve device performance by better understanding and better control of material and device technologies. The stage has now been reached where the pace of research has steadied and much of the emphasis is on development of devices for applications, many of which are novel, taking advantage of the unique properties of the new microwave sources.

In this Book we set out in detail all aspects of the Transferred Electron Effect, from the fundamentals of the velocity-field relationship (Chapter 3) to the applications which the devices are now finding (Chapter 10), with due attention paid to the basic technologies of material growth and device fabrication (Chapter 11). By far the most important transferred electron material is GaAs and it is on GaAs that we have concentrated throughout. In Chapter 12 we try to indicate future developments in the field and what new transferred electron materials might be involved.

## REFERENCES

1. Gunn, J. B. (1963). *Solid State Commun.* **1**, 88.
2. Shockley, W. (1954). *Bell System Tech. J.* **33**, 799.
3. Kroemer, H. (1953). *Zeits. f. Physik*, **134**, 435.
4. Shockley, W., Mason, W. P. (1954). *J. Appl. Phys.* **25**, 677.
5. Ryder, E. J., Shockley, W. (1951). *Phys. Rev.* **81**, 139.
6. Ryder, E. J. (1953). *Phys. Rev.* **90**, 766.
7. Gunn, J. B. (1956). *Journ. Electronics*, **2**, 87.
8. Esaki, L., Tsu, R. (1970). *I.B.M. J. Res. and Develop.* **14**, 61.
9. Kroemer, H. (1959). *Proc. IRE*, **47**, 397.



10. Ridley, B. K., Watkins, T. B. (1961). *Proc. Phys. Soc.* **78**, 293.
11. Hilsun, C. (1962). *Proc. I.R.E.* **50**, 185.
12. Ridley, B. K. (1963). *Proc. Phys. Soc.* **82**, 954.
13. Gunn, J. B. (1964). *I.B.M. J. Res. and Develop.* **8**, 141.
14. Hutson, A. R. *et al.* (1961). *Phys. Rev. Lett.* **7**, 237.
15. Beck, A. H. W. (1958). "Space Charge Waves". Pergamon Press, New York.
16. Kroemer, H. (1964). *Proc. I.E.E.E.* **52**, 1736.
17. Gunn, J. B. (1965). Paper presented at 1964 Conf. on Physics of Semiconductors published in *Plasma Effect in Solids*, Dunod, Paris. p. 199.
18. Hutson, A. R. *et al.* (1965). *Phys. Rev. Lett.* **14**, 639.
19. Allen, J. W. *et al.* (1965). *Appl. Phys. Lett.* **7**, 78.
20. Foyt, A. G. *et al.* (1965). Paper presented at Solid State Device Res. Conf. Princeton, N. J. and *I.E.E.E. Trans.* **ED-13**, **1**, 79, 1966.
21. Dow, D. G. *et al.* (1966). *I.E.E.E. Trans.* **ED-13**, **1**, 105.
22. Hakki, B. W., Irvin, J. C. (1965). *Proc. I.E.E.E. Corres.* **53**, 80.
23. Hilsun, C. *et al.* (1965). *Electroc. Lett.* **1**, 178.
24. Thim, H. W. *et al.* (1965). *Appl. Phys. Lett.* **7**, 167.
25. Johnston, R. L. *et al.* (1965). *Bell System Tech. J.* **44**, 369.
26. Read, W. T. (1968). *Bell System Tech. J.* **37**, 401.
27. Carroll, J. E. (1970). "Hot Electron Microwave Generators", Edward Arnold, London.
28. Copeland, J. A. (1966). *Proc. I.E.E.E. Corres.* **54**, 1479.
29. Prager, H. J., Chang, K. K. N. (1967). "Proc. of Conf. on High Freq. Generation and Amplification". Cornell University, p. 266. and Prager, H. J. *et al.* (1967). *Proc. I.E.E.E.* **55**, 586.
30. *Special Issue*, (1966). *I.E.E.E. ED-13*, No. 1.  
*Special Issue* (1967). *I.E.E.E. ED-14*, No. 9.  
*Special Issue*, (1970). *I.E.E.E. MTT-18*, No. 11.
31. Herman, F. (1955). *Proc. I.R.E.* **43**, 1703.

## Chapter 2

# Relevant Semiconductor Properties

### 2.1 INTRODUCTION

In this chapter we introduce the basic ideas of semiconductor physics which are relevant to the electron transfer effect. In the first part of the chapter the object is to indicate the fundamentals without going into more detail than is sufficient to give the reader an appreciation of the origin of the band structure of semiconductors and of the basis for the semi classical model of electron motion. The processes which determine electron motion in a semiconductor are then examined, and particular attention is paid to effects which arise when applied fields are high and electrons “hot”. Aspects such as carrier diffusion and dielectric relaxation which are important in non-uniform situations are examined towards the end of the chapter. The behaviour of electron density fluctuations in a moving electron system is analysed in detail because of its particular relevance to the transferred electron effect.

### 2.2 THE WAVE MECHANICAL THEORY OF SEMICONDUCTORS

#### 2.2.1 THE WAVE FUNCTION AND OBSERVABLES

A number of physical experiments, the most notable being the phenomenon of electron diffraction, force us to abandon a concept of the electron as a simple particle obeying the laws of classical mechanics. The electron is seen to have properties which imply a wave-like character and in seeking to explain our observations we naturally attempt to describe the electron in a manner which accords it such a wave-like character. We find that our observations can be explained if we describe the electron by a wave-function  $\psi$  which is a solution of the Schrödinger wave equation. The one-dimensional, time dependent, form of the equation is

$$-\frac{\hbar^2}{2m} \frac{\partial^2 \psi}{\partial x^2} + V\psi = j\hbar \frac{\partial \psi}{\partial t}. \quad (2.1)$$

where  $V(x)$  is the potential energy,  $\hbar$  is Planck's constant and  $m$  the electron mass.

It is instructive to examine the form of the wave function  $\psi$  for an electron in a simple system having constant potential energy  $V$ . As is customary in the solution of wave equations, we look for a simple solution of the type

$$\psi = \exp j(kx - \omega t) \quad (2.2)$$

representing a wave of frequency  $\omega$  and wavelength  $2\pi/k$ . Putting this into Eqn (2.1) we find that

$$\frac{\hbar^2 k^2}{2m} = [\hbar\omega - V]. \quad (2.3)$$

From Planck's relation we identify  $\hbar\omega$  as the electron energy  $\mathcal{E}$  and since  $V$  is the potential energy,  $\hbar^2 k^2/2m$  represents the kinetic energy of the electron. Thus  $\hbar k$  can be identified as a parameter equivalent to the classical quantity momentum. The electron momentum  $p$  is thus given by  $p = \hbar k = h/\lambda$  where  $\lambda$  is the electron wavelength, and this is the relationship between electron momentum and wavelength which emerges from experiments on electron diffraction. In a simple, constant potential system the electron wave function is thus

$$\psi = \exp j(kx - \omega t) = \exp \frac{j}{\hbar} (px - \mathcal{E}t). \quad (2.4)$$

The wave function itself has no physical significance. It cannot be measured experimentally. Its value lies in the fact that a knowledge of it allows all the quantities in a system which are physically observable to be calculated, and after all it is only the physical observables which are of interest to us. The approach to any problem in wave mechanics is to solve the Schrödinger equation for the system, subject to whatever boundary conditions are imposed, and then to deduce all that needs to be known about the system from a knowledge of  $\psi$ .

Knowledge of the wave function enables us to calculate the probability  $P(x)$  that a given electron is in an interval  $dx$ . The probability is given by<sup>(1,2)</sup>

$$P(x) = \psi^* \psi dx \quad (2.5)$$

and since the electron must exist somewhere it follows that  $\int_{\text{All space}} \psi^* \psi dx$  is unity.

Once the wave function  $\psi$  is known, the average or expectation value of any physical parameter is calculable. Thus the expectation value of the

position  $x$  is given by

$$\langle x \rangle = \int \psi^* x \psi \, dx. \quad (2.6)$$

Likewise the expectation value for the electron momentum  $p$  can be determined by evaluating

$$\langle p \rangle = \int \psi^* p \psi \, dx. \quad (2.7)$$

From Eqn (2.4) we can deduce that  $p = \hbar/j \cdot \partial/\partial x$ , and if we assume that this also holds for varying potentials, then Eqn (2.7) can be re-written

$$\langle p \rangle = \int \psi^* \left[ \frac{\hbar}{j} \frac{\partial}{\partial x} \right] \psi \, dx. \quad (2.8)$$

In a similar manner the average value of all the physical observables  $q$  can be determined from a knowledge of the wave function by evaluating

$$\langle q \rangle = \int \psi^* Q \psi \, dx \quad (2.9)$$

where  $Q$  is some operator associated with the observable  $q$  just as  $[\hbar/j \cdot \partial/\partial x]$  is the operator associated with the observable momentum.

### 2.2.2 ELECTRON IN A CONSTANT POTENTIAL

The problem which we want to solve is that of electron motion in a crystal. However it will be instructive first to determine the electron wave functions for the simplest systems.

The elementary case of an electron moving in a region of constant potential has been solved already. There it was shown that the electron wave function has the simple form given in Eqn (2.4), and that there is also a simple relationship between electron energy and wave vector  $k$  viz.  $\mathcal{E} = V + (\hbar^2 k^2)/2m$ . So if we plot Energy against wave vector we obtain a simple parabola as shown in Fig. 2.1. For the free electron case ( $V = 0$ ) the parabola will pass through the origin.

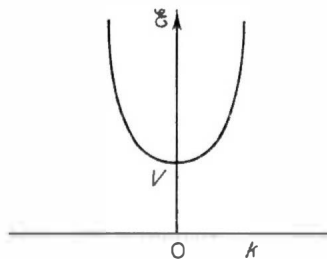


FIG. 2.1. Energy versus wave number for an electron wave in a system with constant potential  $V$ .

If the region in which the electron moves is unbounded then the electron wave number, and thus the electron energy, can take up any value. If however the region is bounded, we can readily show that only certain values of  $\mathcal{E}$  and  $k$  become permissible. For example we take the system illustrated in Fig. 2.2(a) where the electron can move in a well which is bounded at  $x = 0, L$  by infinite potential barriers. We look for solutions of the form

$$\psi = \psi(x) \exp -j\omega t = \psi(x) \exp -j \frac{\mathcal{E} t}{\hbar} \quad (2.10)$$

so that Eqn (2.1) becomes

$$-\frac{\hbar^2}{2m} \frac{\partial^2 \psi(x)}{\partial x^2} + V(x) \psi(x) = \mathcal{E} \psi(x) \quad (2.11)$$

which is the time independent form of the Schrödinger equation. For  $0 \geq x \geq L$ ,  $\psi(x) = 0$  and if we choose  $V(x) = 0$  for  $0 < x < L$ , as we are at liberty to do, then Eqn (2.11) becomes

$$\frac{\partial^2 \psi(x)}{\partial x^2} = -\frac{2m\mathcal{E}}{\hbar^2} \psi(x) = -k^2 \psi(x) \quad (2.12)$$

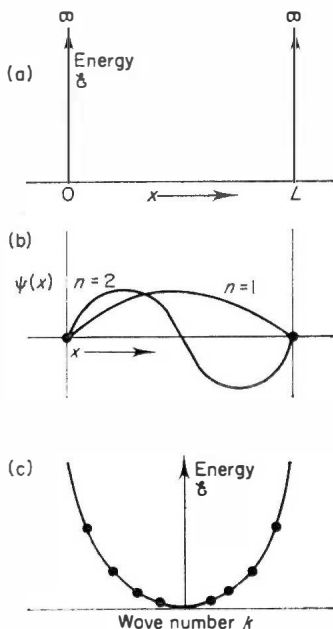


FIG. 2.2. (a) Model for electron in confined region. (b) Form of the electron wave functions corresponding to the two lowest order solutions. (c) The discrete  $\mathcal{E}$ - $k$  solutions for electron waves in a confined region.

where

$$k^2 = \frac{2m\mathcal{E}}{\hbar^2}. \quad (2.13)$$

The required solutions for  $\psi(x)$  are then  $\psi(x) = A \sin kx$  where the boundary conditions at  $x = 0, L$  dictate that  $kL = n\pi$  where  $n$  is an integer. The electron wave number thus takes on discrete values in this case. The two lowest order wave functions are shown in Fig. 2.2(b). From Eqn (2.13) we have that  $\mathcal{E} = \hbar^2 k^2 / 2m$  so that the allowable energy states and corresponding wave numbers for electrons in the potential well are illustrated in Fig. 2.2(c).

The problem can be readily extended to three dimensions and by assuming that the wave function takes the form

$$\psi = \psi(x) \psi(y) \psi(z) \exp -j \frac{\mathcal{E}}{\hbar} t.$$

We find that the electron energy is given by

$$\mathcal{E} = \frac{\hbar^2}{2m} [k_x^2 + k_y^2 + k_z^2] \quad (2.14)$$

where  $k_x, k_y, k_z$  are the components of the electron wave vector along the  $x, y$  and  $z$  directions in space. If the region is bounded in all three directions then the solutions for  $k_x, k_y$  and  $k_z$  will all take discrete values.

From Eqn (2.14) it is evident that if the surfaces of constant electron energy are plotted in  $k$ -space they will have a spherical form, as shown in Fig. 3.

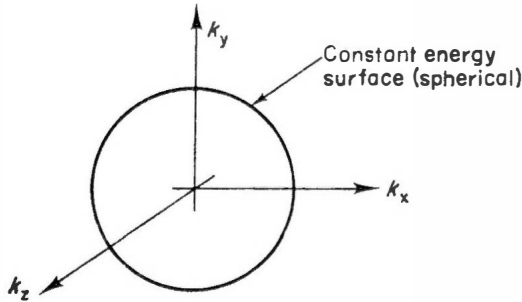


FIG. 2.3. Constant energy surface in  $k$ -space.

### 2.2.3 ELECTRON IN A CRYSTAL

An electron moving through a crystal will be subject to a periodic variation of potential, the periodicity being that of the crystal lattice, i.e.  $V(x) = V(x) \mp 1$  where  $1$  is the lattice spacing. In principle knowledge of the  $V(x+l)$

potential distribution allows us to solve for the behaviour of the electrons in the crystal, in particular for the allowed energy states. However in practice the real problem is very complex since each electron in the crystal moves in a potential which is due to the potential of the nuclei *and* to the potential of all the other electrons in the system. Thus to solve for the wave function of a given electron we must know all the other electron wave functions first! For a simple system, such as the Helium atom, the solution can be arrived at by a process of guessing the wave functions for the first electron, calculating the wave function of the second, using it to calculate the wave function of the first, and a process of iterations is entered into until a self consistent solution is arrived at.

The problem of determining the electron states in a semiconducting crystal, however, where electrons are present in numbers of around  $10^{24}$  per cc, is impossibly complex and in practice we content ourselves by assuming a periodic potential  $V(x)$  to describe the effect of the nuclei and all the other electrons in a system, and examine the wave function which describes a single electron in that system. This is the so-called "one electron approximation" and it leads to a satisfactory description of the electron system in solids.

#### 2.2.4 THE ONE DIMENSIONAL RECTANGULAR POTENTIAL MODEL

A number of the essential characteristics of electrons in crystals emerge by considering our single electron in a one-dimensional potential. This potential will have the periodicity of the crystal and will take a form as shown in Fig. 2.4(a). For our qualitative picture of the electron characteristics we approximate this with the simple rectangular (Kronig-

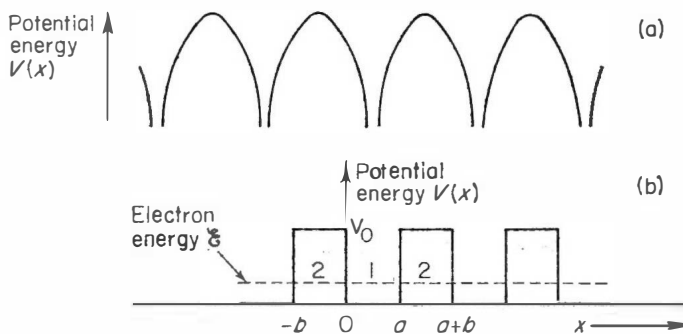


FIG. 2.4. Realistic (a) and Approximate (b) forms for the potential variation through the crystal. The lattice spacing is  $(a + b)$ .

Penney) model shown in Fig. 2.4(b).  $\mathcal{E}$  is the electron energy and  $V_0$  the maximum potential energy. As before we look for solutions of the form

$$\psi = \psi(x) \exp -j \frac{\mathcal{E}}{\hbar} t$$

and we find that once again we have to solve Eqn (2.11), the time independent Schrödinger equation, but this time  $V(x)$  is no longer constant but periodic, with period  $a + b$ .

The rectangular potential can be regarded as a series of uniform potential regions, and we are required to solve Eqn (2.11) in each region, subject to the appropriate boundary conditions. Solution of the equation in region 1 will yield two unknown coefficients, likewise region 2. The four unknowns are determined by applying the conditions that

(i)  $\psi, \frac{d\psi}{dx}$  must be continuous

(ii)  $\psi(x) = u(x) e^{jkx}$  where  $u(x)$  is periodic with the same period as the potential function.

The latter result is a statement of Bloch's Theorem.

Solving Eqn (2.11) in the two regions

$$\frac{d^2 u_1(x)}{dx^2} + 2jk \frac{du_1(x)}{dx} - (k^2 - \alpha^2) u_1(x) = 0 \quad 0 < x < a$$

$$\frac{d^2 u_2(x)}{dx^2} + 2jk \frac{du_2(x)}{dx} - (k^2 - \beta^2) u_2(x) = 0 \quad -b < x < 0$$

where

$$\alpha^2 = \frac{2m\mathcal{E}}{\hbar^2} \quad (2.15)$$

$$\beta^2 = \frac{2m(\mathcal{E} - V_0)}{\hbar^2} . \quad (2.16)$$

The solution takes the form

$$u_1(x) = A \exp j(\alpha - k)x + B \exp -j(\alpha + k)x \quad (2.17)$$

$$u_2(x) = C \exp j(\beta - k)x + D \exp -j(\beta + k)x. \quad (2.18)$$



Applying the boundary conditions deduced from (i) and (ii) above, namely,

$$\begin{aligned} u_1(0) &= u_2(0) \\ \left. \frac{du_1}{dx} \right|_{x=0} &= \left. \frac{du_2}{dx} \right|_{x=0} \\ u_1(a) &= u_2(-b) \\ \left. \frac{du_1}{dx} \right|_{x=a} &= \left. \frac{du_2}{dx} \right|_{x=-b} \end{aligned}$$

gives four simultaneous equations for  $A$ ,  $B$ ,  $C$  and  $D$ . This leads to a determinantal equation which can be written in the form

$$-\frac{\alpha^2 + \beta^2}{2\alpha\beta} \sin \alpha a \sin \beta b + \cos \alpha a \cos \beta b = \cos k(a + b) \quad (2.19)$$

In a real crystal we would have  $\mathcal{E} < V_0$  so that the quantity  $\beta$  is purely imaginary and we can write  $\beta = j\gamma$  so that Eqn (2.19) becomes

$$\frac{\gamma^2 - \alpha^2}{2\alpha\gamma} \sinh \gamma b \sin \alpha a + \cosh \gamma b \cos \alpha a = \cos k(a + b) \quad (2.20)$$

Equation (2.16) becomes

$$\gamma^2 = \frac{2m(V_0 - \mathcal{E})}{\hbar^2} \quad (2.21)$$

and putting the expressions for  $\alpha$  and  $\gamma$  (from Eqn (2.15) and (2.21)) into Eqn (2.20) gives the relationship between the electron energy  $\mathcal{E}$  and wave number  $k$ . Since the energy  $\mathcal{E}$  only appears on the L.H.S. of this equation and wave number  $k$  only on the R.H.S. we can represent it by writing

$$f_1(\mathcal{E}) = f_2(k).$$

Examination of this equation reveals that the R.H.S. can only take on values between  $\pm 1$ , while the L.H.S. does not have this restriction. Thus for real values of  $k$  there will be solutions only for restricted ranges of energy  $\mathcal{E}$ . Furthermore, the solutions of the equation remain unchanged if we add any integral number of  $2\pi/(a + b)$  to  $k$  i.e. the solutions are periodic in  $k$ , with period  $2\pi/(a + b)$ .

The general form of the solution to Eqn (2.20) is shown in Fig. 2.5. The allowed energy states of the electron are divided into bands which are separated by forbidden regions. By way of comparison the continuous  $\mathcal{E}$ - $k$  relationship for the free electron is also shown.

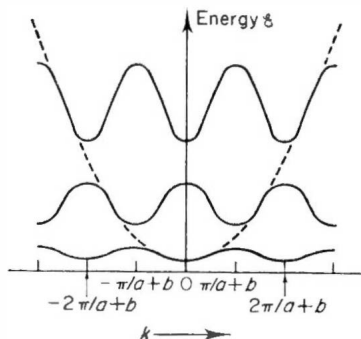


FIG. 2.5. General relationship between energy  $\mathcal{E}$  and wave number  $k$  for electrons in a crystal.

There is a direct analogy here between the behaviour of electrons in a crystal and electromagnetic wave propagation on a transmission line with a periodic variation of impedance. In the latter case we obtain the familiar pass and stop bands, and the allowed and forbidden bands in the crystal are directly analogous to these. In the pass bands of the periodic line and the allowed bands of the crystal the propagation constant (wave number)  $k$  is real, while the stop bands and forbidden bands are characterised by purely imaginary values of  $k$ .

We lose no information if we confine our interest in the  $\mathcal{E}$ - $k$  diagram to the region between  $\pm(\pi/a + b)$ . Although the wave function alters when  $n\pi/(a + b)$  ( $n$  integer) is added to the restricted zone value of  $k$ , the

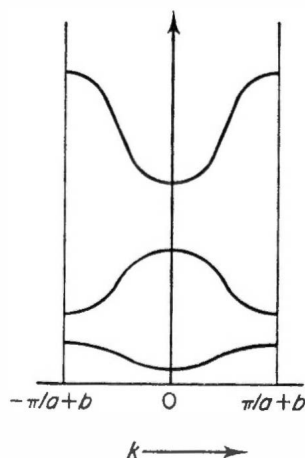


FIG. 2.6. The reduced zone representation.

observables energy, position, momentum etc. do not. Thus in future discussion we will only be concerned with the reduced zone representation shown in Fig. 2.6. This  $\mathcal{E}$ - $k$  diagram then represents the allowed energy states for electrons in the crystal. For an infinite crystal  $k$  may take any value, but as noted previously, for a crystal of finite length  $L$ ,  $k$  will take on discrete values separated by  $2\pi/L$ .

### 2.2.5 INSULATORS, SEMICONDUCTORS AND METALS

We have deduced the allowable electronic states in a crystal and these states will be filled up to a certain level by all the electrons in the crystal. We can distinguish two main types of solid—those in which there are, in ascending energy, a number of completely filled bands followed by a number of completely empty bands, and those in which the completely filled bands are followed by a band which is only partially filled. A filled band cannot contribute to electronic conduction because there are no free states in the band for an electron to move to. A completely empty band clearly makes no contribution to conduction so that the first type of solid is an insulator. The second type, where a great many electrons in the partially filled band are free to move under an applied field, is of course a metal.

A semiconductor belongs to the insulator type and is an insulator at  $0^\circ\text{K}$ . However at room temperature due to thermal excitation, the uppermost filled band (valence band) has a few unoccupied states near the top of the band, and the first empty band (conduction band) has a few occupied states near to the bottom of the band. It is these states in the valence and conduction bands which are involved in the process of conduction in semiconductors. Thus, our interest in the electronic band structure is generally confined to its form at the top of the valence band and bottom of the conduction band.

### 2.2.6 CRYSTAL MOMENTUM AND EFFECTIVE MASS

From the previous section we have the solution to the Schrödinger wave equation

$$\psi = u(x) \exp j \left( kx - \frac{\mathcal{E}}{\hbar} t \right)$$

where  $u(x)$  is a periodic function with the period of the lattice. From this wave function we can determine the momentum by applying Eqn (2.8). We find that the crystal momentum is

$$p = \hbar k \quad (2.22)$$

so that

$$\psi = u(x) \exp \frac{j}{\hbar} (px - \mathcal{E}t). \quad (2.23)$$

The Heisenberg Uncertainty Principle tells us that

$$\Delta x \Delta p \sim h \quad (2.24)$$

where  $\Delta x$ ,  $\Delta p$  are the uncertainties in position and momentum of an electron. Thus to enable us to localise the position of an electron we have to construct a wave packet made up of a number of wave functions having a range of values of momentum about some central value  $p$ . Such a wave packet will travel with a velocity which is the group velocity  $V_g$  that we deduce from Eqn (2.23). Thus

$$V_g = \frac{d\mathcal{E}}{dp}. \quad (2.25)$$

This is therefore the velocity with which an electron of energy  $\mathcal{E}$  will move through the lattice.

If we assume that Newton's law is applicable to the electron motion, then when an electric field  $E$  is applied the crystal momentum  $p$  will alter in accordance with

$$\frac{dp}{dt} = eE. \quad (2.26)$$

If we examine the rate of change of the electron velocity  $V_g$  we have

$$\frac{dV_g}{dt} = \frac{d}{dt} \left( \frac{d\mathcal{E}}{dp} \right) = \frac{d}{dp} \left( \frac{d\mathcal{E}}{dp} \right) \frac{dp}{dt} = \frac{d^2\mathcal{E}}{dp^2} \cdot eE \quad (2.27)$$

where Eqn (2.26) has been used.

By analogy with classical mechanics we see that the quantity  $1/(d^2\mathcal{E}/dp^2)$  has the character of a mass. We call it the effective mass  $m^*$  of the electron in the crystal.

$$m^* = 1 \left/ \frac{d^2\mathcal{E}}{dp^2} \right. \quad (2.28)$$

Using this effective mass we can ignore the effect of the periodic lattice potential and describe the motion of an electron by the familiar laws of classical mechanics. This description will be equivalent to that which would obtain from a direct application of wave mechanics.

From a knowledge of the  $\mathcal{E}$ - $k$  diagram we can now calculate the electron velocity ( $1/\hbar \cdot d\mathcal{E}/dk$ ) and the effective electron mass ( $1/\hbar^2 \cdot d^2\mathcal{E}/dk^2$ ). For a typical band these are shown in Fig. 2.7. In many cases the  $\mathcal{E}$  -  $k$  relation at the centre of the zone ( $k = 0$ ) and at the zone edge will have a parabolic form. The effective mass will then be constant near to the centre

and near to the zone edge, though its value may be very different from the mass of the free electron ( $m$ ).

However, we note from Fig. 2.7 that our wish to use simple classical mechanics to describe the electron motion leads us to require that the effective mass increases to infinity away from the zone centre and even becomes negative at the extremities of the zone.

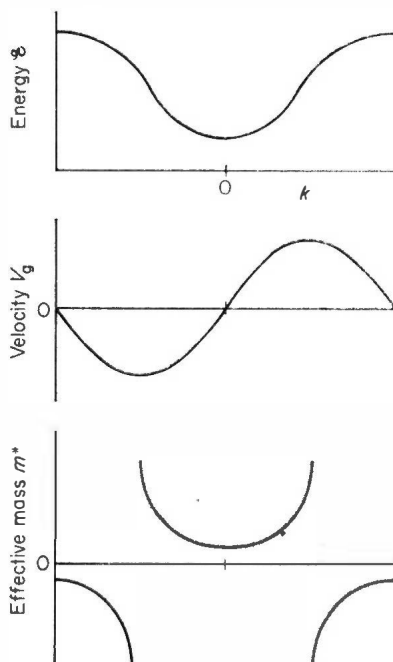


FIG. 2.7. Electron energy, velocity and effective mass as functions of wave number.

When the simple treatment above is extended to three dimensions, we must introduce the components  $k_x$ ,  $k_y$  and  $k_z$  of the electron wave vector. The reduced zone of Fig. 2.6 then becomes a three-dimensional Brillouin zone in  $k$ -space, and for a simple cubic lattice the Brillouin zone will be cubic. Effective masses  $m_x$ ,  $m_y$ ,  $m_z$  have now to be specified for the three directions in  $k$ -space and for the simple cubic lattice  $m_x = m_y = m_z$ .

The electron energy can now be expanded as

$$\mathcal{E} = Ak_x^2 + Bk_y^2 + Ck_z^2 + \text{higher powers} \quad (2.29)$$

where the energy has been taken to be measured from an extremum. The expansion must be in even powers since energy takes the same value for positive and negative values of  $k_x$ ,  $k_y$ ,  $k_z$ . Once again for a cubic lattice,  $A = B = C$  and if higher powers of  $k_x^2$ ,  $k_y^2$ ,  $k_z^2$  can be neglected, then the surfaces of constant energy will be spherical.

## 2.2.7 REAL CRYSTALS

For the simple one-dimensional Kronig-Penney model we find that the allowed bands are separated by forbidden regions and further, that all the energy maxima and minima occurred at the centre of the zone. Real crystals however, being three-dimensional and often with a complex lattice structure, yield  $\mathcal{E}$ - $k$  diagrams which are in general much more complex. We find that band extrema may no longer be at the zone centre or zone edge and that a given band may possess a number of maxima or minima. In addition

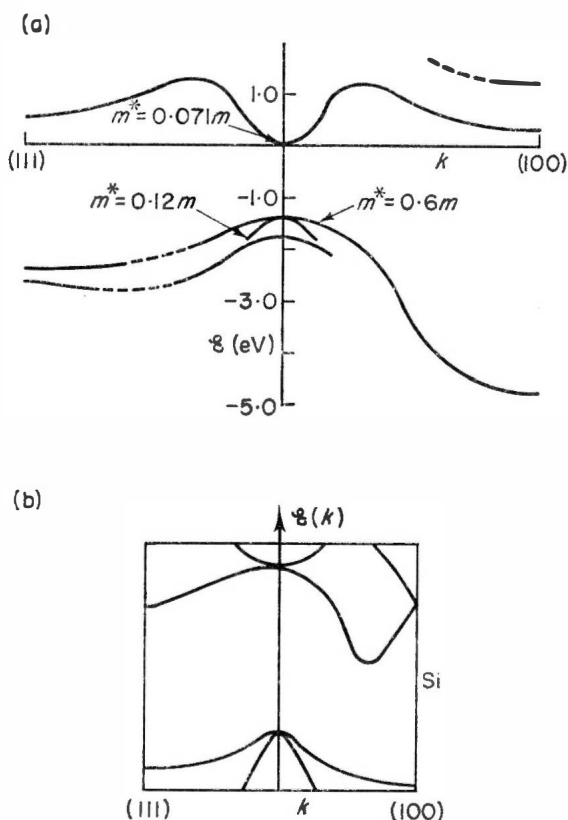


FIG. 2.8. (a) The band structure of GaAs. The lowest conduction band minimum is at the centre of the zone ( $k = 0$ ). The next lowest is in the  $(100)$  crystallographic direction and at the zone edge. The valence band consists of three bands, two being degenerate at  $k = 0$ .<sup>(3)</sup> (b) The band structure of Si. The lowest minimum is located along the  $(100)$  direction and is approximately half way to the zone edge. The next lowest lies along the  $(111)$  direction. Again the valence band consists of three separate bands, of which two are degenerate at  $k = 0$ .<sup>(4)</sup>

the shape of the band may depend on the direction in the crystal. Energy bands may overlap or they may be degenerate. Not only will effective mass in general take up different values in different directions, but it may become a tensor, implying that an electric field in a given direction through a crystal will produce an acceleration which is not parallel to the field.

In general we are only interested in the extrema of the bands in semiconductors and Fig. 2.8 shows the bottom of the conduction band and top of the valence band for GaAs<sup>(3)</sup> and Si.<sup>(4)</sup> For GaAs we see that the conduction band minimum lies at  $k = 0$ , but a subsidiary minimum exists along the (100) crystallographic direction and lies at the edge of the zone. The conduction band minimum in Si does not occur at  $k = 0$  but is approximately half way to the zone edge, along the (100) direction. The next lowest minimum lies along the (111) direction. In both semiconductors the valence band structure is seen to be rather complex, with several bands of different effective masses, two of which are degenerate at  $k = 0$ .

In the conduction band of GaAs at room temperature, only the central minimum ( $k = 0$ ) will be occupied by electrons. However application of high electric fields can increase the energy of the electrons so that they are able to transfer to the subsidiary (or "satellite") minimum along the (100) direction (in fact since there are six equivalent (100) directions in the crystal there will be six equivalent minima). It is this process and the marked difference in effective electron mass in the central and satellite minima which is the origin of transferred electron effects. The electron effective mass  $m^*$  ( $\propto 1/(d^2\mathcal{E}/dk^2)$ ) is low at the zone centre and high in the satellite minima.

In the central minimum of GaAs the energy dependence on  $k$  is

$$\mathcal{E} = A(k_x^2 + k_y^2 + k_z^2) \quad (2.30)$$

where  $\mathcal{E}$  is measured relative to the conduction band minimum. The energy surfaces are spherical and the effective masses equal in all directions.

### 2.2.8 THE HOLE

It has been mentioned earlier that the existence of a few empty states at the top of the valence band allows the band to contribute to electric conduction. Instead of examining the motion of the many electrons in the nearly full band, we can similarly obtain the necessary information about conduction by examining how the empty states "move" in an applied field. We find that these states behave as if they had a positive charge,  $+e$ , and a positive effective mass  $|\hbar^2/(d^2\mathcal{E}/dk^2)|$ . This gives rise to the concept of the positive hole.

### 2.2.9 IMPURITIES

In a pure semiconductor the number of electrons in the conduction band will be equal to the number of holes in the valence band, and for a given semiconductor both will be dependent only on temperature. When this is the case the semi-conductor is said to be intrinsic. At normal temperatures the number of intrinsic electrons and holes present is very small ( $\sim 10^6$  per  $\text{cm}^3$  in GaAs at 300°K), and the numbers present in a real piece of semiconductor will often be dictated instead by the amount of impurity atoms which are inevitably present.

These impurity atoms may contribute additional electrons to take part in conduction processes, in which case the impurity is a donor. Alternatively the impurity atoms may act to capture electrons from the valence band, in which case the impurity is an acceptor. In either case, if each impurity donates or accepts one electron and the impurity level is say 1 ppm then the number of electrons involved is  $\sim 10^{17}$  per  $\text{cm}^3$ , which is considerably more than the number intrinsically present. Hence the considerable importance of impurities in semiconductors.

An appreciation of how donor impurity atoms contribute additional electrons may be gained from the following simple picture. It is well known that in the hydrogen atom there are only certain allowed states the electron can occupy, and thus only certain allowed energies it can have. In particular there is a state of lowest energy—the ground state; this is 13.5 eV lower than the energy of the electron at rest well away from the proton of charge  $+e$ . The situation of an electron in the conduction band of a semiconductor under the influence of the excess charge  $+e$  of a donor ion is closely analogous; however, the electrostatic forces are reduced by the dielectric constant of the crystal and the mobile charge now has effective mass  $m^*$ . Consequently the ground state of an electron attracted by a donor may be such that only a small amount of energy is required to free it for conduction. The amount required—the donor ionisation energy—may be as little as 0.01 eV. Thermal energy will often be sufficient to ionise the donor ( $kT = 0.025$  eV at 300°K) and create a free electron to take part in conduction.

For acceptor impurities the situation is analogous but we are dealing instead with a positively charged hole attracted to the negative charge of the acceptor ion.

We can represent the effects of the impurities by introducing levels on our energy level diagrams. The donor impurity levels will then be situated just below the minimum of the conduction band and acceptor levels just above the maximum of the valence band. Donor impurities give a crystal which is *n*-type where the carriers making the majority contribution to conduction



are electrons. Acceptor impurities dope the crystal  $p$ -type and the majority carriers are positive holes. Typically the amount of impurities present is controlled so that the majority carrier has a concentration of around  $10^{14}$ – $10^{18}$  per  $\text{cm}^3$ .

## 2.3 CARRIER STATISTICS

### 2.3.1 DENSITY OF AVAILABLE STATES

It was pointed out previously (section 2.1.4) that in the one dimensional diagram of Fig. 2.6, the wave number takes on discrete values of separation  $2\pi/L$  for a length  $L$  of crystal. Thus the number of states between  $k_x$  and  $k_x + dk_x$  will be  $Ldk_x/2\pi$ . Now taking the three-dimensional case, we have that the number of states for which the vector  $k$  has a value in the element  $dk_x dk_y dk_z$  of  $k$ -space is given by

$$N(k) dk_x dk_y dk_z = \frac{L^3}{8\pi^3} dk_x dk_y dk_z, \quad (2.31)$$

per unit volume of crystal this becomes  $(1/8\pi^3) dk_x dk_y dk_z$ . Thus there is one allowed state per volume  $8\pi^3$  of  $k$ -space. If we are concerned with bands having spherical energy surfaces, then

$$\mathcal{E} = \frac{\hbar^2}{2m^*} k^2 \quad \text{where} \quad k^2 = k_x^2 + k_y^2 + k_z^2 \quad (2.32)$$

as can be deduced from Eqn (2.29) and the definition of effective mass.

The number of allowed states between energies  $\mathcal{E}$  and  $\mathcal{E} + d\mathcal{E}$  will then be the number between the two spherical energy surfaces corresponding to  $\mathcal{E}$  and  $\mathcal{E} + d\mathcal{E}$ .

The volume of  $k$ -space enclosed  $= 4\pi k^2 dk$

$$\therefore \text{Number of allowed states } N(\mathcal{E}) d\mathcal{E} = \frac{4\pi k^2 dk}{8\pi^3}.$$

Using Eqn (2.32) we can write this as

$$N(\mathcal{E}) d\mathcal{E} = \frac{2\pi}{h^3} (2m^*)^{3/2} \mathcal{E}^{1/2} d\mathcal{E}. \quad (2.33)$$

We note that the density of states is proportional to  $m^{*3/2}$ . Since in the conduction band of GaAs the satellite minimum has an effective mass approximately 16 times that of the central minimum, we see that each satellite minimum has  $16^{3/2}$  (64) more available states. Since there are three such satellite minima due to equivalent directions through the crystal,

the total availability of states in the satellite minimum is around 200 times greater than in the central valley—a fact which is very relevant to the transferred electron effect.

### 2.3.2 THE FERMI-DIRAC DISTRIBUTION FUNCTION

Having calculated the density of states available to the electrons as a function of electron energy, we must consider how the available electrons occupy these states. We must in effect determine the probability of occupancy of the states.

In thermal equilibrium the occupation of a state is continually changing in a random way, and we can only speak of an occupation probability. A very general result of thermodynamics gives this probability in terms of the energy  $\mathcal{E}$  of the state:

$$f(\mathcal{E}) = \frac{1}{1 + \exp(\mathcal{E} - \mathcal{E}_F/kT)} \quad (2.34)$$

where  $\mathcal{E}_F$  is an arbitrary constant called the Fermi Energy. The shape of the Fermi function  $f(\mathcal{E})$  is shown in Fig. 2.9. When  $\mathcal{E} = \mathcal{E}_F$ ,  $f(\mathcal{E}) = 0.5$ . At zero temperature all the available states are filled up to the level  $\mathcal{E}_F$ .

When  $\mathcal{E} - \mathcal{E}_F \gg kT$ , Eqn (2.34) becomes approximately

$$f(\mathcal{E}) = \exp - \left( \frac{\mathcal{E} - \mathcal{E}_F}{kT} \right) \quad (2.35)$$

which is known as the Maxwell-Boltzmann approximation. It is a valid approximation for all but the most heavily doped semiconductors and is certainly valid at the doping levels employed in transferred electron devices.

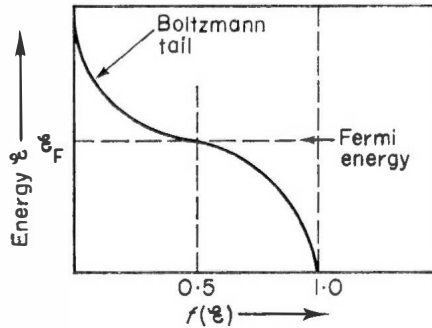


FIG. 2.9 The Fermi function  $f(\mathcal{E})$ .

### 2.3.3 ELECTRON AND HOLE CONCENTRATIONS

We can now use our expression for the density of states (Eqn (2.33)) and the occupation probability of states (Eqn (2.35)) to determine the concentrations of electrons occupying states in the conduction band. In Fig. 2.10 we show the density of states function  $N(\mathcal{E})$  and the Maxwell-Boltzmann tail of the Fermi function, plotted against the electron energy.  $\mathcal{E}_c$  is the energy at the conduction band minimum and  $\mathcal{E}_F$  is the Fermi Energy.

The total number of electrons in the conduction band will be given by

$$n = \int_{\mathcal{E}_c}^{\infty} f(\mathcal{E}) N(\mathcal{E}) d\mathcal{E}.$$

The upper limit of integration should strictly be the energy at the top of the conduction band, but the exponential fall off of the Fermi function allows the limit to be safely taken as infinity.

From Eqns (2.33) and (2.35) we then have

$$n = 2M \cdot \frac{2\pi}{h^3} (2m^*)^{3/2} \int_{\mathcal{E}_c}^{\infty} \mathcal{E}^{\frac{1}{2}} \exp - \left( \frac{\mathcal{E} - \mathcal{E}_F}{kT} \right) d\mathcal{E}$$

where an additional factor  $2M$  is included. The factor 2 accounts for the fact that because of electron spin two electrons may occupy a given energy state, and  $M$  is the number of equivalent minima which may exist.

Evaluating the expression for  $n$  we arrive at

$$n = N_c \exp - \left( \frac{\mathcal{E}_c - \mathcal{E}_F}{kT} \right) \quad (2.36)$$

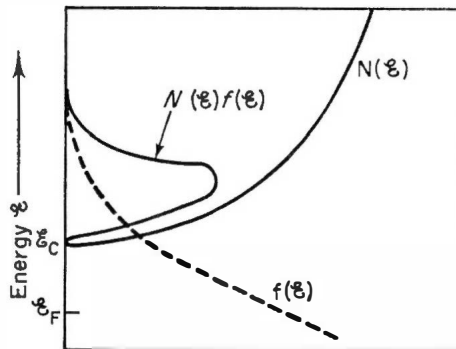


FIG. 2.10. Energy distribution of electrons in the conduction band.  $N(\mathcal{E})$  is the conduction band density of states function. For a non-degenerate semiconductor the electrons have a Maxwellian distribution.

where

$$N_c = 2M \left( \frac{2\pi m^* kT}{h^2} \right)^{3/2}. \quad (2.37)$$

The quantity  $N_c$  is known as the effective density of states in the conduction band and at 300°K its value for GaAs is  $4.7 \times 10^{17}$  per  $\text{cm}^3$ . When the electron density in the conduction band approaches this value, the semiconductor is said to be degenerate and the Maxwell-Boltzmann approximation breaks down.

The calculation for the hole concentration proceeds in an exactly analogous way. The probability that a certain state is vacant will be given by  $1 - f(\mathcal{E})$  so that the total number of holes in the valence band is

$$p = \int_{-\infty}^{\mathcal{E}_v} [1 - f(\mathcal{E})] N(\mathcal{E}) d\mathcal{E}$$

where  $\mathcal{E}_v$  is the energy at the maximum of the valence band. From which we can calculate that

$$p = N_v \exp \frac{\mathcal{E}_v - \mathcal{E}_F}{kT} \quad (2.38)$$

$N_v$  being the effective density of states in the valence band.

For GaAs,  $N_v = 8.0 \times 10^{18} \text{ cm}^{-3}$  at 300°K.

In a pure crystal we must have  $n = p (=n_i = p_i)$  so that the product of  $n$  and  $p$  in the intrinsic case can be written

$$n_i p_i = N_c N_v \exp - \frac{\mathcal{E}_g}{kT} \quad (2.39)$$

where  $\mathcal{E}_g = \mathcal{E}_c - \mathcal{E}_v$  is the width of the energy gap. For GaAs this is approximately 1.4 eV. The intrinsic electron and hole densities calculated at 300°K turn out to be around  $10^6 \text{ cm}^{-3}$ .

If the semiconductor contains impurities then the carrier concentrations will differ significantly from  $n_i$  and  $p_i$  (as discussed in Section 2.1.9). However we note from multiplying Eqns (2.36) and (2.38) that

$$np = N_c N_v \exp - \frac{\mathcal{E}_g}{kT}, \quad (2.40)$$

i.e., the product of the electron and hole concentrations still has the same value. This is because doping the crystal with impurities only alters the Fermi energy  $\mathcal{E}_F$  and this does not appear in the  $np$  product. Thus we have

$$np = n_i p_i = n_i^2.$$

For an  $n$ -type semiconductor ( $n \gg n_i$ ) we have  $p \ll p_i \ll n$ .

## 2.4 CONDUCTION IN SOLIDS

No contribution to conduction can be made by a band which is full. This can be appreciated by considering what happens when an external field  $E$  is applied to the electrons in such a band. Each of the electrons is accelerated and changes its momentum by an amount

$$dk = \frac{1}{\hbar} eE dt \quad (2.41)$$

where  $dt$  is the length of time for which the field is applied. Hence those electrons at one extremity of the Brillouin zone will move out of the first zone and into the second, while a similar shift at the other extremity will vacate states at the zone edge. But it has already been pointed out that those outside the first Brillouin zone have equivalent positions within the first zone, in fact just those states in the first zone which have been vacated. No net change of electron distribution has therefore occurred, and hence no current can be flowing.

If we consider now a partially filled band, with zero field applied the distribution of electrons must be symmetrical about the band minimum. This must be so since the current flowing in one direction through the crystal due to electrons with positive velocities (positive  $1/\hbar \cdot \partial \mathcal{E} / \partial k$ ), say, must be balanced by that flowing in the opposite direction due to electrons with negative velocities (negative  $1/\hbar \cdot \partial \mathcal{E} / \partial k$ ).

When a field is applied the centre of gravity of the electron distribution can, and does, shift by the amount given in Eqn (2.41). This shift means a slight bias in the electron velocities in the direction of the applied field i.e., a small drift velocity is superimposed on the random motion of the electrons around the crystal lattice. A net current is therefore flowing in the direction of the field.

$$\text{Net drift velocity } \frac{\hbar dk}{m^*} = \frac{eE}{m^*} dt$$

$$\therefore \text{Net current density } dJ = \frac{ne^2 E}{m^*} dt \quad (2.42)$$

where  $n$  is the total number of electrons in the band.

As we have formulated the problem, when we remove the applied field the current will continue to flow since we have provided no means whereby the electrons can randomise their velocities again. In fact this is achieved by the electrons colliding with the lattice, or being deflected by ionised impurities in the lattice etc. It is important to note that scattering by the

crystal lattice is not due to the smooth, periodic variations in electric potential for these have been taken account of in ascribing an *effective* mass to the electron, which differs from its real mass. The scattering referred to is due to deviations from this periodicity, and may be due to mechanical vibration of the lattice (phonons) or localised impurities or defects in the lattice.

Due to such scattering the current flowing will decay when the applied force is removed. We assume the current to decay at a constant rate

$$\therefore \frac{dJ}{dt} = -\frac{J}{\tau} \quad (2.43)$$

where  $\tau$  is the time constant of decay known as the carrier relaxation time and is a value averaged over all the electrons in the band.

When a field  $E$  is applied continuously, the steady state condition will then occur when the rate of increase of current is balanced by the rate of decrease due to scattering events. From Eqns (2.42) and (2.43) we have

$$\frac{J}{\tau} = \frac{ne^2 E}{m^*}$$

i.e.,

$$J = \left( \frac{ne^2 \tau}{m^*} \right) E. \quad (2.44)$$

The quantity in brackets is the conductivity  $\sigma$  of the crystal. The average drift velocity of the electrons in the direction of the field is given by

$$v = \mu E \quad (2.45)$$

where  $\mu$  is defined as the electron mobility. Since the current flowing is  $nev$  we have

$$\mu = \frac{e\tau}{m^*} \quad (2.46)$$

as the relationship between electron mobility and relaxation time.

In an analogous way, when we consider a band which is almost filled, we can show that

$$\left. \begin{aligned} J_p &= \frac{pe^2 \tau_p}{m_p^*} E \\ \sigma_p &= \frac{pe^2 \tau_p}{m_p^*} v = \mu_p E \quad \mu_p = \frac{e\tau_p}{m_p^*} \end{aligned} \right\} \quad (2.47)$$

where  $p$  is the number of holes,  $m_p^*$  the effective mass of the holes,  $\mu_p$  their mobility etc.

Any semiconductor must contain both electrons and holes, so that under the driving force of an applied field  $E$ , current will flow due to the drift of conduction band electrons in one direction and of valence band holes in the other. The total current will be

$$J_{\text{tot}} = J_n + J_p = (ne\mu_n + pe\mu_p) E \quad (2.48)$$

where subscript  $n$  refers to the electrons.

For an  $n$ -type semiconductor, say,  $n \gg p$  and we will have a current carried almost entirely by electrons. This will be the case for the GaAs devices to be examined later. When this  $n$ -type semiconductor has two separate conduction band minima each of which contain electrons, as in GaAs at high fields or high temperatures, then we must describe the total current flow as a summation of contributions from the two minima. Thus

$$J = (n_1 e\mu_1 + n_2 e\mu_2) E \quad (2.49)$$

where  $n_1, n_2$  are the numbers of electrons in the two bands and  $\mu_1, \mu_2$  are the corresponding electron mobilities in the two bands.

#### 2.4.1 MAGNITUDES

Values for the electron and hole effective masses and mobilities are indicated in the table below for the three common semiconductors GaAs, Ge and Si. Whereas the conduction band minima in GaAs are spherical

		GaAs	Ge	Si
Effective mass $m^*/m$	electron	0.066	1.6	0.97
			0.08	0.19
			0.12	0.26
	hole	0.6	0.3	0.5
		0.12	0.04	0.16
Drift mobility $\text{cm}^2/\text{V sec}$	electron	8000	3800	1900
	hole	400	3400	400

and the electrons can be described by a single value of effective mass, the minima in Si and Ge are ellipsoidal corresponding to different effective masses in the three directions in  $k$ -space ( $A \neq B \neq C$  in Eqn (2.29)). It is believed that the effective electron masses in the subsidiary  $\langle 100 \rangle$  conduction band minimum of GaAs will be similar to those in the  $\langle 100 \rangle$  mini-

num of Silicon (given above). The two values quoted for the hole mass in each case reflect the fact that the valence band is degenerate in all three semiconductors i.e., two bands have the same energy maximum as shown for example in Fig. 2.8.

The mobility values above apply at room temperature. The values are proportional to the scattering time and this is sensitive to temperature in a manner which depends on the scattering mechanism—this we will comment upon further in Section 2.5. At room temperature scattering times are of the order  $10^{-12}$ – $10^{-13}$  sec. This is approximately the time between successive collisions, assuming that the electron velocity is randomized after each collision.

#### 2.4.2 THERMAL AND DRIFT VELOCITIES

Electrons populating the conduction band will in general have an energy distribution which is of Maxwell Boltzmann form (this will not be the case for degenerate semiconductors or for semiconductors in very high fields). The mean square velocity for electrons moving randomly about the lattice will therefore be given by

$$\frac{1}{2}m^* \overline{v^2} = \frac{3}{2}kT. \quad (2.50)$$

Since the average electron velocity is not significantly different from  $[\overline{v^2}]^{\frac{1}{2}}$  we have

$$\bar{v} \approx \left[ \frac{3kT}{m^*} \right]^{\frac{1}{2}}$$

This gives a value of around  $10^7$  cm/sec for the average thermal velocity of electrons at a temperature of  $300^\circ\text{K}$ .

Under low field bias conditions (up to 100 V/cm, say) we can calculate from the mobility data earlier that the vector velocities super-imposed on the random thermal motion will have magnitudes up to  $10^6$  cm/sec. Thus, in low fields the effect of the applied field is to give the electron system an average drift velocity in the direction of the field, which is much smaller than the random velocities with which the electrons move around the lattice.

#### 2.5 LATTICE VIBRATIONS

Atoms in a crystalline lattice are not fixed in position. They vibrate about their equilibrium positions and these vibrations, representing as they do variations of the lattice periodicity, act to scatter electrons in motion around the crystal. This electron-lattice interaction is one of the important mechanisms whereby the electron distribution randomises itself after the removal of an applied field.



Each atom in the lattice is coupled to its neighbours by the bonding forces and we can liken the lattice to a three-dimensional array of identical particles each of mass  $m$ , where neighbouring particles are connected together by springs of stiffness  $K$ . In examining the mechanical vibrations of the lattice one approach is to consider the lattice as an identical set of coupled harmonic oscillators, whose natural frequency is determined by the particle mass and the stiffness  $K$  of the spring.  $K$  is of course proportional to the bonding force in the actual crystal. The alternative approach, which we shall adopt here, is to consider the lattice as a single entity and to examine its normal modes of vibration. Any lattice vibration can then be described as a combination of normal modes.

### 2.5.1 MONATOMIC LATTICE

Taking a one-dimensional lattice for simplicity we have the simple model of Fig. 2.11(a).  $a$  is the atomic spacing. We expect that the restoring force on a particular particle will be proportional to the relative displacements of that particle and its neighbours. Considering only immediate neighbours, the restoring force  $F_n$  acting on the  $n$ th particle will therefore be given by

$$F_n = m \frac{d^2 y_n}{dt^2} = K(y_{n+1} + y_{n-1} - 2y_n) \quad (2.51)$$

where  $y_n$  is the displacement of the  $n$ th particle.

Looking for solutions of the type

$$y_n = A \exp j(qx - \omega t) = A \exp j(qna - \omega t) \quad (2.52)$$

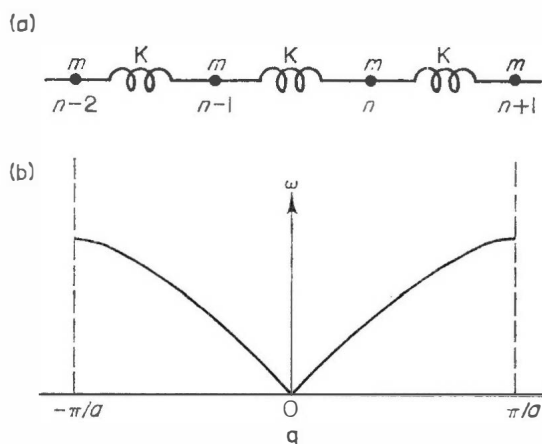


FIG. 2.11. (a) One-dimensional monatomic lattice model. (b) Dispersion diagram for monatomic lattice (reduced representation).

we have

$y_{n+1} + y_{n-1} - 2y_n = A \exp j(qna - \omega t) [\exp jna + \exp -jna - 2]$ . Putting this into Eqn (2.51) yields the relationship

$$\omega^2 = 2 \frac{K}{m} (1 - \cos qa). \quad (2.53)$$

This equation is clearly periodic with period  $2\pi/a$  and the reduced zone representation for the frequency-propagation constant diagram is shown in Fig. 2.11(b). The velocity of propagation of a mechanical disturbance through the lattice is as usual given by the group velocity  $d\omega/dq$  and at low frequencies, where the propagation constant is proportional to frequency, this is a constant which is the velocity of sound waves through the lattice ( $v = 105$  cm/sec). As the frequency is raised  $d\omega/dq$  decreases steadily to zero. Note that the lattice will not support vibrations above a certain frequency.

For a linear lattice comprising  $N$  particles, there will be  $N$  normal modes of vibration described by

$$q_p a = \frac{p\pi}{N} \quad p = 1, 2, \dots, N \quad (2.54)$$

and the corresponding frequency of vibration  $\omega_p$  follows from Eqn (2.53).

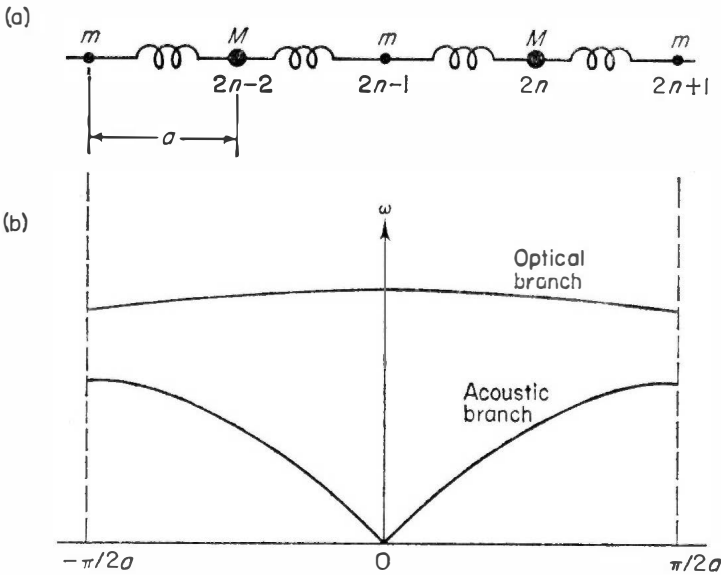


FIG. 2.12. (a) One-dimensional diatomic lattice model (b). Dispersion diagram for diatomic lattice.

Eqn (2.54) can also be expressed as

$$p \frac{\lambda_p}{2} = Na \quad p = 1, 2, \dots N \quad (2.55)$$

where  $\lambda_p$  is the wavelength of the  $p$ th order mode of mechanical vibration.

### 2.5.2 DIATOMIC LATTICE

We now examine the natural modes of vibration of a linear lattice comprising particles of masses  $m$  and  $M$  as shown in Fig. 2.12(a). Again assuming only interactions between nearest neighbours, the equations of motion for the particles  $M$  (the even numbered particles) and  $n$  (the odd numbered particles) are:

$$F_{2n} = M \frac{d^2 y_{2n}}{dt^2} = K(y_{2n+1} + y_{2n-1} - 2y_{2n}) \quad (2.56)$$

$$F_{2n+1} = m \frac{d^2 y_{2n+1}}{dt^2} = K(y_{2n+2} + y_{2n} - 2y_{2n+1})$$

We assume that the solutions of Eqn (2.56) take the form

$$y_{2n} = A \exp j(2naq - \omega t)$$

$$y_{2n+1} = B \exp j(2n+1)aq - \omega t)$$

Substituting these into Eqn (2.56) we obtain

$$\omega^2 A = \frac{2K}{M} (A - B \cos aq)$$

$$\omega^2 B = \frac{2K}{m} (B - A \cos aq)$$
(2.57)

This equation has a non-trivial solution only if

$$\begin{vmatrix} \omega^2 - \frac{2K}{M} & \frac{2K}{M} \cos aq \\ \frac{2K}{m} \cos aq & \omega^2 - \frac{2K}{m} \end{vmatrix} = 0 \quad (2.58)$$

Solving the determinant we find

$$\omega^2 = K \frac{M+m}{Mm} \pm \sqrt{K^2 \left( \frac{M+m}{Mm} \right)^2 - \frac{4K^2}{Mm} \sin^2 aq} \quad (2.59)$$

Hence for a given value of propagation constant there are two frequencies which satisfy the equation. For small values of  $k$  the low frequency solution is characterized by all neighbouring particles moving in the same direction. Whereas for the high frequency solution all the neighbouring particles with the same mass move in the same direction, neighbours of different mass move in opposite directions i.e. they oscillate in anti-phase.

The  $\omega$ - $q$  diagram for the normal modes of the one-dimensional diatomic lattice is shown in Fig. 2.12(b). The lower branch where adjacent masses  $M, m$  move in phase is known as the Acoustic branch, while the upper branch where adjacent masses  $M, m$  move in antiphase, is known as the Optical branch. The latter branch is so-called because in the case of a polar crystal (GaAs, for example) the masses  $M, m$  will carry opposite charges so that this mode of oscillation of the lattice is coupled strongly to by an electro-magnetic wave and the electromagnetic wave required is in the infra red because of the very high natural frequencies of the vibrations (around  $10^{13}$  Hz).

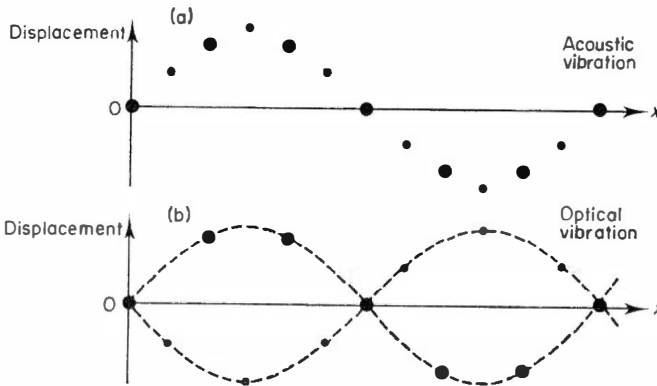


FIG. 2.13. Particle displacements for (a) acoustic mode of low  $k$  (b) Optical mode of low  $k$ .

Fig. 2.13 shows the vibration of a linear diatomic lattice in acoustic and optic modes of the same wavelength. In fact the displacements shown may be either transverse or longitudinal to the axis, so that we can have a total of six different modes of lattice vibration—a Longitudinal Acoustic (LA) and two orthogonal Transverse Acoustic (TA) modes, and a Longitudinal Optic (LO) and two orthogonal Transverse Optic (TO) modes. In general the

orthogonal transverse modes are degenerate and there are just four branches on the  $\omega$ - $q$  diagram. The set appropriate to GaAs is indicated in Fig. 2.14.

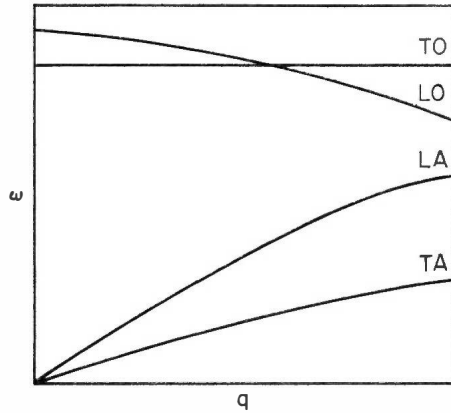


FIG. 2.14. Phonon Dispersion diagram for GaAs (schematic). TO, LO—transverse and longitudinal optic phonons TA, LA—transverse and longitudinal acoustic phonons.

### 2.5.3 PHONONS

A phonon is a quantum of lattice vibration. The occupancy of the available phonon states is determined by the application of Bose-Einstein statistics. Thus at temperature  $T$  the probability of occupancy of a given state of energy  $\hbar\omega$  will be

$$P(\omega) = \frac{1}{\exp \frac{\hbar\omega}{kT} - 1} \quad (2.60)$$

and the average total energy in a mode of frequency  $\omega$  will therefore be

$$\mathcal{E}(\omega) = \frac{\hbar\omega}{\exp \frac{\hbar\omega}{kT} - 1} \quad (2.61)$$

The frequencies corresponding to the optical branches of the phonon  $\omega$ - $q$  diagram are in the vicinity of  $2\pi \times 10^{13} \text{ sec}^{-1}$ . Thus the optical phonon quantum has an energy which is much in excess of  $kT$  (at 300°K). In consequence the probability of occupancy  $P(\omega)$  of the optical phonon states is low and the optical phonons are only weakly excited at room temperature. For a low frequency acoustic phonon  $\hbar\omega \ll kT$ , and hence these low  $q$  states

are well filled. From Eqn (2.61) the average energy in a mode of frequency  $\omega$  is  $kT$ , in agreement with the classical description.

## 2.6 SCATTERING MECHANISMS

### 2.6.1 LATTICE SCATTERING BY ACOUSTIC MODES

Electron scattering from the mechanical vibration of the lattice is important in many semiconductors. The scattering can be most easily appreciated by considering an electron wave in a lattice which is supporting a single longitudinal acoustic mode of vibration. The latter will give rise to periodic compression and rarefactions in the lattice spacing and it is the fluctuations in potential energy due to these which are effective in scattering (reflecting) the electron wave. In common with other problems of wave reflection, the scattering is most effective when the electron wave length is half the wavelength of the acoustic vibration of the lattice. If the electron wavelength is much greater than the acoustic wavelength the effect of the vibrations average out to zero over an electron wavelength. Similarly electrons of wavelength much less than the acoustic wavelength will suffer only weak scattering since the potential gradient due to the vibrations will be small.

Since at room temperature the electron wavelength ( $\lambda = h/m^*v$ ) has an averaged value which is an order of magnitude or, more, greater than the lattice spacing (which is around  $2\text{--}3 \times 10^{-8}$  cm), we can conclude that the vibrations which scatter electrons most effectively are those which lie well down the acoustic branch of the vibrational spectrum i.e. the long wavelength

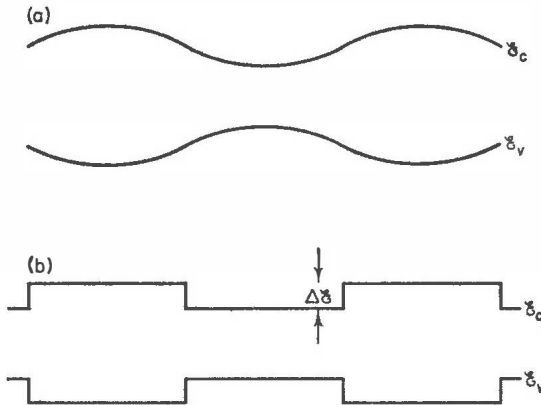


FIG. 2.15. (a) Variation of the energies of the band edges due to lattice vibration at a single frequency. (b) Simple square wave approximation to (a).  $\mathcal{E}_c$ ,  $\mathcal{E}_v$  are the energies at the conduction band minimum and valence band maximum, respectively.

acoustic modes. In Si and Ge electron scattering is due principally to interactions with these long wavelength phonons.

We shall consider here a simple qualitative treatment of such scattering (2.1). In the regions where the crystal is compressed due to the vibrations the positions of the energy bands are altered in such a manner that the width of the forbidden gap is reduced—in regions of extension the gap width increases. The effect causes a local variation in the energy associated with the conduction band edge. For a simple vibration this will result in the variation shown in Fig. 2.15(a). For simplicity, we take a step-wise variation as shown in Fig. 2.15(b). The height of each step is taken to be  $\Delta\mathcal{E}$  in energy.

Since the averaged electron velocity is around  $10^7$  cm/sec and the acoustic wave velocity is  $10^5$  cm/sec, we can take the lattice to be at rest for the purpose of our calculation. The wave function of the incident electron wave is

$$\psi_0(x) = A \exp jk_0 x$$

where  $k_0 = m^*v/\hbar$ . And that of the transmitted wave

$$\psi_1(x) = B \exp jk_1 x.$$

Equating energies we have

$$\frac{\hbar^2}{2m^*} (k_1^2 - k_0^2) = -\Delta\mathcal{E}. \quad (2.62)$$

It can be shown that the probability of reflection ( $R$ ) of the electron wave at the step is given by

$$R = \frac{(k_0 - k_1)^2}{(k_0 + k_1)^2} \quad (2.63)$$

Since the energy step is small and therefore  $k_0 \simeq k_1$ , we can simplify  $R$  to

$$R = \left( \frac{m^* \Delta\mathcal{E}}{2\hbar^2 k_0^2} \right)^2 \quad (2.64)$$

The quantity  $\Delta\mathcal{E}$  can be related to the strain in the lattice. Assuming a linear relationship

$$\Delta\mathcal{E} = -\Xi \frac{\delta V}{V_0} \quad (2.65)$$

where  $\delta V/V_0$  is the fractional change in volume of the lattice and  $\Xi$  is the deformation potential and represents the shift of the conduction band edge per unit dilational strain.

For effective scattering the wavelength of the acoustic vibration must be comparable with that of the electron wave. Thus the length of each compression or extension which we are concerned with will be approximately  $\pi/k_0$ .

The volume element  $V_0 (= \pi/k_0)^3$  of this linear extent is subject to some maximum pressure  $\delta P$  to cause a volume change  $\delta V$ . The stored strain energy is then  $\delta P \delta V/2$  and this must be proportional to  $kT$  since the origin of the vibrations is thermal. Thus

$$\Delta \mathcal{E} = \frac{1}{2} \delta P \delta V = ckT \quad (2.66)$$

where  $c$  is a constant whose value is close to unity.

If we define the compressibility  $\beta$  of the lattice as

$$\beta = \frac{\delta V}{V_0 \delta P} \quad (2.67)$$

then using Eqns (2.67), (2.66), (2.65) in Eqn (2.64) we obtain

$$R = \frac{m^{*2} c \beta k T}{2 \hbar^4 k_0^4 V_0} \Xi^2. \quad (2.68)$$

In travelling a distance equal to the linear dimension of the volume  $V_0$ , i.e.  $\pi/k_0$ , the probability of reflection is  $R$ . Thus the mean free path  $\bar{L}$  is given by

$$\begin{aligned} \bar{L} &= \frac{\pi}{k_0 R} \\ &= \frac{h^4}{8 m^{*2} c \beta k T \Xi^2} \end{aligned} \quad (2.69)$$

and the mean relaxation time  $\langle \tau \rangle$  is given by

$$\langle \tau \rangle = \frac{h^4}{3 \sqrt{8\pi} m^{*3/2} c \beta (kT)^{3/2} \Xi^2}. \quad (2.70)$$

Since  $\mu = e \langle \tau \rangle / m^*$  the electron mobility due to scattering by acoustic vibrations should vary as  $T^{-3/2} / m^{*5/2}$ . In practice a stronger temperature dependence is usually observed due to the presence of additional scattering processes between equivalent valleys (see Section 2.5.3).

A similar treatment to the above can be given for the hole mobility limit due to acoustic scattering.



### 2.6.2 LATTICE SCATTERING BY OPTICAL MODES

Because of their high energy, optical phonons are only weakly excited at normal temperatures (Section 2.4.3). In consequence they do not play a significant role in limiting the low field mobility of carriers in the elemental semiconductors. However, despite their low excitation they represent the dominant scattering mechanism in the compound semiconductors such as GaAs. This is because the latter have an ionic compound in their bonding which means that associated with optical vibrations there will be a strong polarization of the lattice, and this is very effective in scattering the electrons.

At room temperature the electron mobility in GaAs is limited to around  $9000 \text{ cm}^2/\text{V sec}$  by polar scattering due to the longitudinal optic modes. As the temperature is raised the increasing excitation of optical phonons will contribute to the reduction in carrier mobility. For crystals with a zinc blende structure, such as GaAs, the mobility limit due to polar optical scattering has been given as<sup>(6)</sup>

$$\mu = 3 \times 10^{31} \left( \frac{e}{e^*} \right)^2 \left( \frac{m}{m^*} \right)^{3/2} F \bar{M} a^3 \nu \left[ \exp \frac{h\nu}{kT} - 1 \right] \text{ cm}^2/\text{V sec} \quad (2.71)$$

where  $e^*$  is an effective charge,  $\bar{M}$  the reduced mass of the atoms ( $Mm/M+m$ ),  $a$  the lattice constant and  $\nu$  the longitudinal fundamental optical frequency.  $F$  is a slowly varying function of  $h\nu/kT$  which at  $300^\circ\text{K}$  is approx. 0.7.

### 2.6.3 INTRAVALLEY AND INTERVALLEY LATTICE SCATTERING

Interactions between the electron system and the lattice must be such that energy and momentum are conserved. Thus if we consider an electron wave of energy  $\hbar\omega_0$  and momentum  $\hbar k_0$  being scattered such that its energy and momentum are altered to  $\hbar\omega_1$ ,  $\hbar k_1$  then we can deduce the quantum of lattice vibration involved in the exchange is such that

$$\begin{aligned} \hbar\omega_0 - \hbar\omega_1 &= \hbar\omega_s \\ \hbar k_0 - \hbar k_1 &= \hbar q_s \end{aligned} \quad (2.72)$$

$\hbar\omega_s$ ,  $\hbar q_s$  are the energy and momentum of the phonon involved.

Intravalley scattering processes are ones where the electron is scattered between states in the same minimum, the change in wave number is small so that  $k_s$  is small and only long wavelength phonons are involved. The long wavelength phonons may be acoustic in which case the amount of energy exchanged is small (electron scattering is highly elastic), or they may be optical in which the energy exchanged is high (scattering inelastic).

However in semiconductors with multiple valleys there is also the possibility of scattering between different conduction band minima. This is known

as intervalley scattering. In many cases the two minima between which the electron is scattered are equivalent, corresponding to equivalent crystallographic directions. In these events a large change in wave-number will be necessarily involved so that phonons of high wave number and high energy will be required. These processes account for the discrepancies referred to at the end of Section 2.5.1.

#### 2.6.4 IMPURITY SCATTERING

Scattering by ionized impurities in the lattice is simply due to the Coulomb field of the impurity atom. It can readily be appreciated that the deflection or scattering of the electron will be most effective when the electron is travelling at low velocities. Hence ionized impurity scattering is most effective at low temperatures.

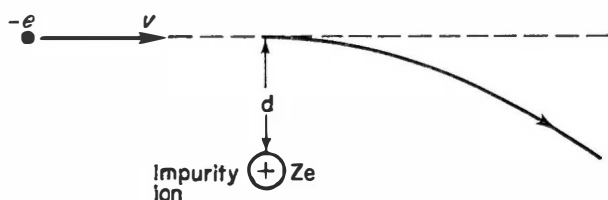


FIG. 2.16. Simple model for scattering by an impurity ion.

We can deduce the approximate dependence of the carrier mobility on impurity scattering in the following simple analysis.<sup>(5)</sup> Fig. 2.16 shows an electron of velocity  $v$  approaching the ion of charge  $+Ze$ . Assuming no deviation of the electron, its nearest approach would be  $d$ . The force on it  $F$  will be

$$F = \frac{Ze^2}{4\pi\epsilon\epsilon_0 d^2} = m^* a_{\perp} \quad (2.73)$$

where  $a_{\perp}$  is the perpendicular acceleration. The interaction time is approximately  $d/v$  so that the electron is given a transverse velocity component

$$V_{\perp} = \frac{a_{\perp} d}{v} = \frac{Ze^2}{4\pi\epsilon\epsilon_0 m^* v d} \quad (2.74)$$

The electron is deflected through  $45^\circ$  if  $V_{\perp} = v$ . Thus if  $V_{\perp} \geq v$  we will consider that a collision has taken place which has randomized the electron velocity. This will be the case if  $d$  is less than a value

$$d_c = \frac{Ze^2}{4\pi\epsilon\epsilon_0 m^* v^2} \quad (2.75)$$

The collision cross section of this ionized impurity is thus  $\pi d_c^2$ . If  $N$  is the number of ionized impurities per unit volume, then the relaxation time will be given by

$$\begin{aligned}\langle\tau\rangle &= \frac{1}{\pi d^2 N v} \\ &= \frac{16\pi\epsilon^2\epsilon_0^2 m^{*2} V^3}{N\pi Z^2 e^4} \\ &= \frac{16\pi\epsilon^2\epsilon_0^2 (m^*)^{1/2} (m^* v^2)^{3/2}}{N Z^2 e^4}\end{aligned}\quad (2.76)$$

where  $v$ ,  $\langle\tau\rangle$  are averaged values.

Using Eqn (2.50) to remove  $v$ , we then have

$$\langle\tau\rangle = \frac{16\pi\epsilon^2\epsilon_0^2 (m^*)^{1/2} (3kT)^{3/2}}{N Z^2 e^4} . \quad (2.77)$$

The simple expression deduced differs only slightly from the correct Conwell-Weisskopf formula<sup>(7)</sup> for mobility as limited by impurity scattering.

We note from the  $T^{3/2}$  dependence in Eqn (2.77) that, in contrast to lattice scattering, impurity scattering is most effective at low temperatures—as we anticipated. It is also most important in heavily doped semiconductors ( $N$  large), again, as we would expect.

### 2.6.5 COMBINATION OF SCATTERING TIMES

The probability of a collision taking place per unit time is  $1/\langle\tau\rangle$ . Thus when several scattering mechanisms are operative we must have

$$\frac{1}{\langle\tau\rangle_{\text{total}}} = \frac{1}{\langle\tau_1\rangle} + \frac{1}{\langle\tau_2\rangle} + \dots$$

and similarly for mobilities

$$\frac{1}{\mu_{\text{total}}} = \frac{1}{\mu_1} + \frac{1}{\mu_2} + \dots \quad (2.78)$$

### 2.6.6 TEMPERATURE DEPENDENCE OF MOBILITY

We have seen previously that scattering by lattice vibrations results in a carrier mobility which decreases with temperature, whereas scattering by ionized impurities results in a mobility which increases with temperature.

When these are the two most important mechanisms we thus expect the actual electron mobility to be dominated by impurity scattering at low temperatures and by lattice scattering at high temperatures. Hence we expect the value of the carrier mobility to exhibit a maximum at some intermediate temperature.

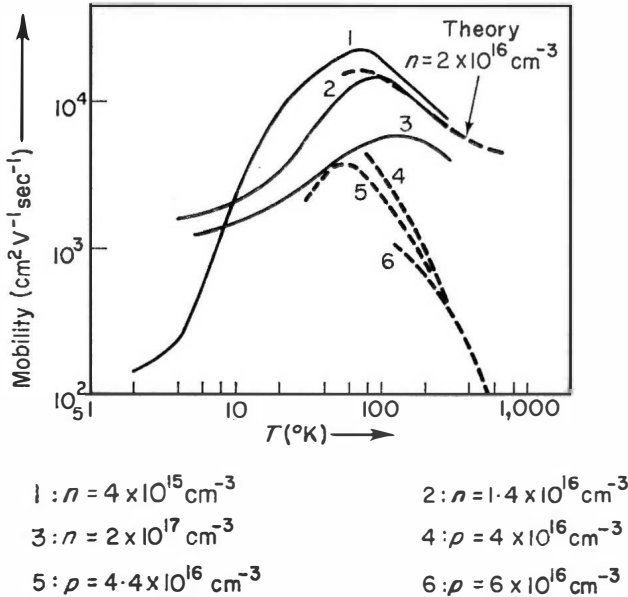


FIG. 2.17. The temperature dependence electron and hole mobilities in GaAs.<sup>(3)</sup>

Figure 2.17 shows how the electron and hole mobilities<sup>(3)</sup> vary in practice in a range of samples of GaAs of differing impurity concentrations. It is evident that the general form is as expected. The temperature at which maximum mobility occurs will largely depend on the number of impurities, as indeed will the maximum value of mobility. It is to be noted that at 300°K and above, impurity scattering will not be important in GaAs unless the doping level is extremely high.

Figure 2.18 presents similar information for electrons and holes in Si<sup>(8)</sup> and Ge.<sup>(9)</sup>

## 2.7 HIGH FIELD EFFECTS

In all that we have considered so far we have assumed that the applied field produces only a small perturbation of the electron distribution so that the velocities imparted to carriers by the applied field are very small compared to their random thermal velocities. Under these conditions the electron tem-

perature, as defined by Eqn (2.50), is always that of the lattice,  $T_0$  (room-temperature).

If the applied field is high, however, it will impart a significant velocity to the electron as it travels between successive collisions. Referring to Section 2.3.2, for example, we see that if the applied field exceeds  $10^3$  V/cm, the electron drift velocity calculated will have a magnitude close to the average thermal velocity! The electron distribution must then be significantly different from that in the absence of an applied field, and the concept of a small drift velocity superimposed on the thermal velocity, which had formed the basis of many of our assumptions, is no longer valid. The mean energy of the electrons is increased by the field and, defining a new electron temperature  $T_e$  according to Eqn (2.50) we now have  $T_e > T_0$ , the lattice temperature, and the electrons are said to be "hot".

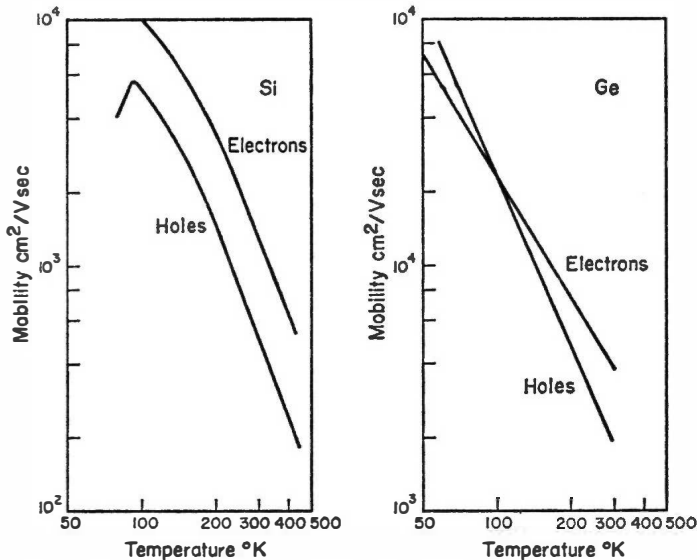


FIG. 2.18. The temperature dependence of electron and hole mobilities in Si and Ge.<sup>(8), (9)</sup>

There are important differences between the "hot" electron problem and the "cold" electron case considered hitherto. Thus as the average electron velocity is increased the rate of collisions with the lattice will increase so that simple lattice scattering will become more effective. Conversely, scattering due to ionized impurities or to optical polar lattice modes will become less effective. Other scattering mechanisms, unimportant for the "cold" electrons, may become important due to the much increased electron energy. Thus it is evident that when the electrons are heated the scattering becomes field dependent, and the whole problem of the electron-lattice

interaction becomes much more complex than in the low field case. The formulation of the hot electron problem and its solution form the basis of the following Chapter. However it will be instructive to consider here one aspect of the hot electron problem which is of importance in the elemental semiconductors Si and Ge.

### 2.7.1 VELOCITY SATURATION

In high fields the electrons can attain sufficient energy to excite optical mode vibrations of the lattice. From Fig. 2.14 it is clear that a minimum energy is required to do so, and this energy is very high, around 0.06 eV, more than double that of carriers at lattice temperature (300°K). A hot carrier, whose energy is sufficiently high, can lose this energy by colliding with the lattice and exciting an optical phonon. This emission of an optical phonon becomes an increasingly important means of removing energy from the electron system as the applied field is increased. Thus whereas optical mode interactions are of little importance at low fields because of their low thermal excitation, at the highest fields they are of prime importance because of the ineffectiveness of the low energy acoustic phonons in removing energy from the electrons. They act to limit the energies which the electrons can attain, and do it so effectively that the carrier drift velocities tend to a saturated value at very high fields.

We can determine this saturation value by analysing the steady state condition where the rate of energy input to the carriers from the field ( $R_1$ ) is balanced by the rate at which they give up their energy by emission of optical phonons ( $R_2$ ). If  $\tau_0$  is the relaxation time for this process we have that

$$R_1 = \frac{e^2 \tau_0 E}{m^*} \quad (2.79)$$

and

$$R_2 = \frac{h\nu_0}{\tau_0} \quad (2.80)$$

where  $h\nu_0$  is the optical phonon energy.

Equating  $R_1$  and  $R_2$  we have

$$\tau_0 = \frac{(h\nu_0 m^*)^{\frac{1}{2}}}{eE} \quad (2.81)$$

so that the saturated drift velocity of the carrier is given by

$$V_{\text{sat}} = \frac{e\tau_0}{m^*} E = \left( \frac{h\nu_0}{m^*} \right)^{\frac{1}{2}}. \quad (2.82)$$

The carrier saturation sets in at fields of around  $10^4$ – $10^5$  V/cm and the saturated velocities are around  $10^7$  cm/sec in all cases. Figure 2.19 shows<sup>(10)</sup> the high field region of interest for both types of carrier in Si.

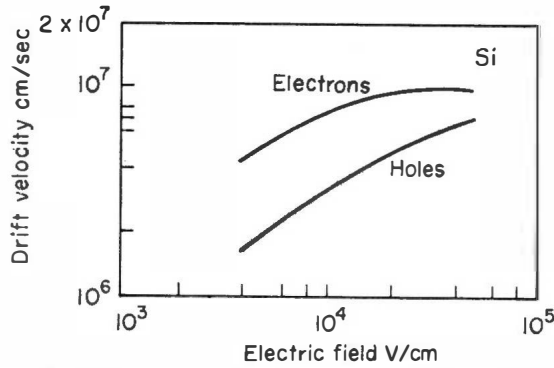


FIG. 2.19. Velocity field characteristic for electrons and holes in Si showing onset of velocity saturation.<sup>(10)</sup>

## 2.8 CARRIER DIFFUSION

When a non-uniform distribution of carriers exists in a material then a current will flow in the absence of any applied field which is due to diffusion of carriers from one region to another.

The non-uniformity referred to may simply be in carrier concentration, or it may be a non-uniformity in carrier temperature.

Carrier diffusion is analogous to the diffusion which occurs in gases. If we consider the simple one-dimensional case shown in Fig. 2.20 where a pressure gradient exists along the  $X$ -direction, then the total force on all carriers in the length  $\delta x$  is

$$-\frac{dp}{dx} \cdot \delta x \cdot A$$

where  $A$  is the cross-sectional area.

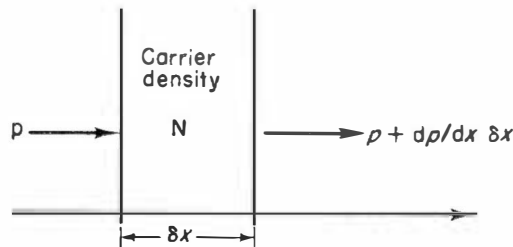


FIG. 2.20. Simple model for carrier diffusion.

In the volume considered there are  $nA\delta x$  carriers, where  $n$  is the carrier density. Hence the force per carrier is  $1/n \cdot dp/dx$  and this force will produce a drift velocity

$$V = -\frac{\mu}{e} \frac{1}{n} \frac{dp}{dx}. \quad (2.83)$$

In thermal equilibrium the relationship between pressure, temperature and carrier density in our carrier “gas” is simply

$$p = nkT \quad (2.84)$$

$$\therefore V = -\frac{\mu}{e} \frac{1}{n} \frac{d}{dx} (nkT). \quad (2.85)$$

Defining a diffusion coefficient

$$D = \frac{\mu}{e} kT \quad (2.86)$$

we have

$$V = -\frac{1}{n} \frac{d}{dx} (nD) \quad (2.87)$$

and the current density due to diffusion will be

$$J_{\text{diff}} = -e \frac{d}{dx} (nD). \quad (2.88)$$

When carrier temperature, and therefore diffusion coefficient, are independent of position the drift velocity due to diffusion becomes

$$V = -\frac{D}{n} \frac{dn}{dx}. \quad (2.89)$$

The values of the diffusion coefficient at 300°K for electrons and holes in GaAs are 200 cm<sup>2</sup>/V sec and 6 cm<sup>2</sup>/V sec respectively.

## 2.8.1 DEBYE LENGTH

In a semiconductor in the steady state, the total current flowing will be the sum of the current due to diffusion and that due to the applied field (Eqn (2.44))

$$J_{\text{tot}} = J_{\text{diff}} + J_c = -e \frac{d}{dx} (nD) + \sigma E. \quad (2.90)$$



If a non-uniform carrier distribution exists in a material in the steady state and under zero applied bias (as at an  $n^+ - n$  boundary for example), then  $J_{\text{tot}} = 0$  since no net current can flow in the absence of an applied field. If we take for example an  $n$ -type semiconductor, and assume that the carrier temperature is uniform everywhere, we can then write

$$eD \frac{dn}{dx} = n e \mu E \quad (2.91)$$

where  $E$  is a built-in internal electric field which must be set up to produce a force on the electrons to balance the natural force of diffusion.

If the background ionised impurity density is  $n_0$  we have from Poisson's law

$$\frac{dE}{dx} = \frac{e}{\epsilon \epsilon_0} (n - n_0). \quad (2.92)$$

If  $(n - n_0) = \Delta n \ll n_0$  we have

$$\frac{dE}{dx} = \frac{e}{\epsilon \epsilon_0} \Delta n. \quad (2.93)$$

Hence from Eqns (2.91) and (2.93) we can write

$$\frac{d^2 \Delta n}{dx^2} = \frac{e \mu n_0}{\epsilon \epsilon_0 D} \Delta n \quad (2.94)$$

for which the solution is

$$\Delta n = n - n_0 = A \exp - x/L_D \quad (2.95)$$

where

$$L_D = \sqrt{(D \epsilon \epsilon_0 / e \mu n_0)}$$

or, alternatively,

$$L_D = \sqrt{(kT \epsilon \epsilon_0 / n_0 e^2)}. \quad (2.96)$$

Thus if a localized non-uniform carrier concentration is set up in a material its influence will mainly be restricted to a length  $L_D$ , known as the Debye length. Putting in values appropriate to GaAs with  $10^{15}$  electrons/cm<sup>3</sup> and at 300°K, we find that  $L_D \sim 10^{-5}$  cm. Although the derivation of Debye length given here applies strictly only to the case of zero net current, it is still applicable to the situation where net current flows, provided that the current is much less than the two opposing currents of which it is the resultant.

The Debye length can also be written in the form

$$L_D = \sqrt{(D\epsilon\epsilon_0/\sigma)} = \sqrt{D\tau_r} \quad (2.97)$$

where  $\tau_r$  is the dielectric relaxation time.

## 2.9 DIELECTRIC RELAXATION TIME

We will consider an  $n$ -type semiconductor with electron density  $n_0$  to which a field is applied and the resulting electron drift velocity is  $v_0$ . Suppose that for some reason a small excess electron bunch builds up in the semiconductor. This will necessitate adjustments in the field distribution and electron velocity, and the situation is depicted in Fig. 2.21, as can readily be verified by applying Poisson's equation. Thus the electrons at the front of the perturbation travel faster than  $v_0$  and those at the rear travel slower than  $v_0$ . The result is that the excess charge begins to spread itself out and eventually it disappears.  $\tau_r$  is a measure of the time it takes to do so.

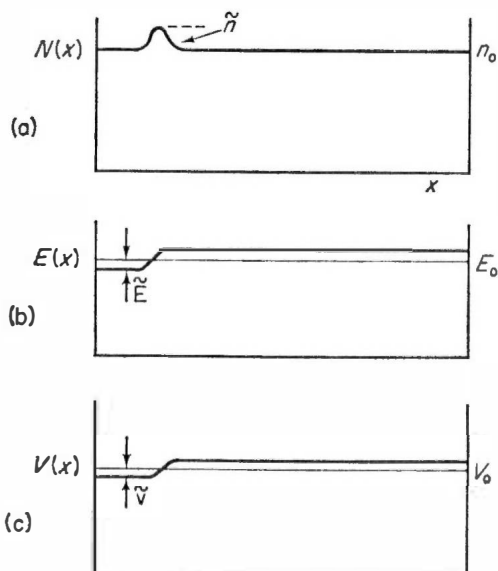


FIG. 2.21. Electric field (b) and electron velocity (c) distributions in an  $n$ -type semiconductor due to a localised perturbation in the electron density (a).  $E_0$ ,  $v_0$ ,  $n_0$  are the unperturbed values and  $\tilde{E}$ ,  $\tilde{v}$ ,  $\tilde{n}$  represent the fluctuations.

The current density in the material will be

$$J_0 + \tilde{J} = e(n_0 + \tilde{n})(v_0 + \tilde{v}) \quad (2.98)$$

where  $J_0$ ,  $n_0$ ,  $v_0$  are steady state values and  $\tilde{J}$ ,  $\tilde{n}$ ,  $\tilde{v}$  the small signal fluctuations.

From Poisson's equation we have

$$\frac{\partial \tilde{E}}{\partial x} = \frac{\tilde{n}e}{\epsilon\epsilon_0} \quad (2.99)$$

and from the continuity equation

$$e \frac{\partial \tilde{n}}{\partial t} + \frac{\partial \tilde{J}}{\partial x} = 0. \quad (2.100)$$

Eliminating  $\tilde{J}$  and  $\tilde{n}$  from Eqns (2.98)–(2.100) we obtain

$$v_0\epsilon\epsilon_0 \frac{\partial^2 \tilde{E}}{\partial x^2} + \epsilon\epsilon_0 \frac{\partial^2 \tilde{E}}{\partial x \partial t} + en_0 \frac{\partial \tilde{v}}{\partial x} = 0. \quad (2.101)$$

Writing

$$\tilde{v} = \mu \tilde{E} \quad (2.102)$$

we have

$$v_0\epsilon\epsilon_0 \frac{\partial^2 \tilde{E}}{\partial x^2} + \epsilon\epsilon_0 \frac{\partial^2 \tilde{E}}{\partial x \partial t} + en_0\mu \frac{\partial \tilde{E}}{\partial x} = 0. \quad (2.103)$$

If at time  $t = 0$  the field distribution is  $f(x)$ , then it can readily be seen from Eqn (2.103) that at time  $t$

$$\tilde{E}_t = f(x - v_0t) \exp - \frac{t}{\tau_r} \quad (2.104)$$

where

$$\tau_r = \epsilon\epsilon_0/en_0\mu. \quad (2.105)$$

Thus the perturbation travels with the same velocity as the electrons and decays at a rate  $1/\tau_r$ .  $\tau_r$  is known as the dielectric relaxation time. Taking again as our example, GaAs with  $10^{15}$  electrons/cm<sup>3</sup> and at 300°K,  $\tau = 10^{-12}$  sec.

It is important to point out that the analysis given here, applying as it does to small changes in all the quantities, does not presuppose a completely linear  $v - E$  relationship for the electron. The mobility defined in Eqn (2.102) applied to small signal values and we have only required linearity over a small excursion about  $E = E_0$ . The mobility as defined is in fact the differential mobility  $dv/dE$  and says nothing about the  $v - E$  relationship at fields other than  $E_0$ .

## 2.10 SMALL SIGNAL MOBILITIES

### *Longitudinal Mobility $\mu_L$*

Consider a semiconductor subject to a bias field  $E_0$  in a certain direction

which produces an electron drift velocity  $v_0$  in the same direction. If the field is increased by an amount  $dE$  as shown in Fig. 2.22(a), this leads to an increase  $dv$  in drift velocity. The semiconductor mobility appropriate to small changes in the field is  $dv/dE$  and in this case it is simply given by the slope of the velocity field curve at the field  $E = E_0$  (Fig. 2.22(c)).

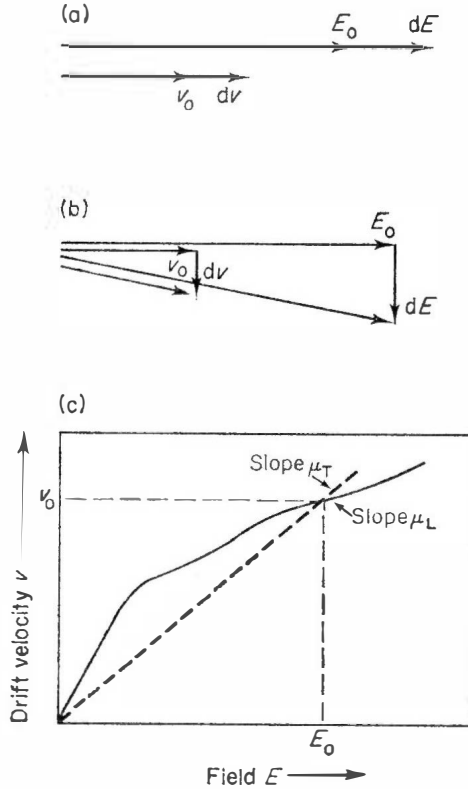


FIG. 2.22. Field and velocity vectors relating to field perturbations (a) in the longitudinal direction (b) in the transverse direction,  $E_0$  is a steady bias field and  $v_0$  the corresponding velocity. A general velocity field characteristic for the electrons is indicated in (c). The longitudinal and transverse small signal mobilities are given by the tangential and d.c. ( $v_0/E_0$ ) values respectively.

### Transverse Mobility $\mu_T$

We now examine the mobility which is appropriate when the perturbing field is transverse to the bias field. The situation is described in Fig. 2.22(b). The effect is to rotate the field vector slightly, leading to a corresponding rotation in the velocity vector. To a first order the magnitude of the field vector, and therefore also the velocity vector, will remain unchanged, so that

the field and velocity triangles are similar. Hence we can deduce that

$$\frac{dE}{E_0} = \frac{dv}{v_0}. \quad (2.106)$$

where  $dv$  is the component of the electron drift velocity in the direction of the perturbing field. The semiconductor mobility  $\mu_T$  appropriate to small transverse perturbations is again  $dv/dE$  and it is seen from Eqn (2.106) to be given in this case by

$$\mu_T = \frac{v_0}{E_0}. \quad (2.107)$$

Thus whereas the small longitudinal mobility  $\mu_L$  is given by the slope of the velocity field curve at  $E = E_0$ , the small signal transverse mobility is given by the slope of the line connecting the working point to the origin (Fig. 2.22(c)).

The longitudinal mobility  $\mu_L$  may become negative in some semiconductors over certain ranges of  $E$ , and it is this property which provides the basis for the active devices discussed in this book.

#### REFERENCES

1. McKelvey, J. P. (1966). "Solid State and Semiconductor Physics". Harper and Row, New York.
2. Schiff, L. I. (1955). "Quantum Mechanics". McGraw-Hill, New York.
3. Hilsum, C. (1965). "Gallium Arsenide", *Progress in Semiconductors*, **9**, 144.
4. Herman, F. (1955). *Proc. I.R.E.* **43**, 1703.
5. Robson, P. N. Private Communication.
6. Hilsum, C. (1960). *Proc. Phys. Soc.* **76**, 414.
7. Conwell, E. M., Weisskopf, V. F. (1950). *Phys. Rev.* **77**, 388.
8. Ludwig, G. W., Watters, R. L. (1956). *Phys. Rev.* **101**, 1699–1701.
9. Morin, F. J. (1954). *Phys. Rev.* **93**, 62–63.
10. Norris, C. B., Gibbons, J. F. (1967). *I.E.E.E. Trans.* **ED-14**, 38–43.

## Chapter 3

# The Velocity-Field Characteristic

### 3.1 INTRODUCTION

A general introduction to semiconductor conduction processes was given in Chapter 2. In this chapter a more detailed description will be given of the processes relevant to materials exhibiting the transferred electron effect. At low electric fields the relationship between the drift velocity and electric field of gallium arsenide is ohmic. As the electric field is increased a point is reached where the drift velocity no longer increases but begins to decrease. The drift velocity-electric field characteristic has a region of negative differential mobility (Fig. 3.1). The electric field at the turning point is called the threshold field,  $E_T$ . The negative differential mobility will be shown in Chapter 4 to cause a rapid readjustment of space charge within the material resulting in a non-uniform electric field. For this reason it is extremely difficult to make the observation described above. The techniques required will be described towards the end of this chapter. Initially we will be concerned

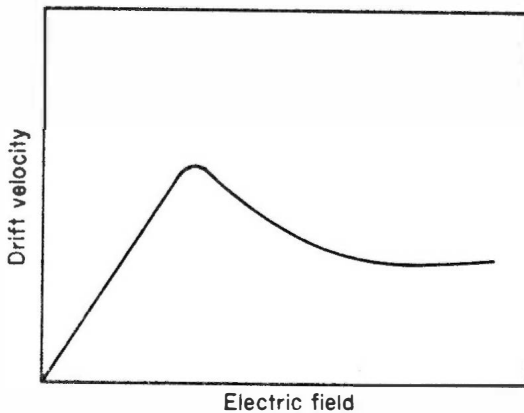


FIG. 3.1. The form of the velocity-field characteristic of electrons in GaAs.

with the description and calculation of the relationship between the mean electric field under assumed steady conditions and the drift velocity.

The negative differential mobility arises from the particular form of the conduction band structure of gallium arsenide (Fig. 3.2). At low electric field and room temperature the conduction electrons occupy the central conduction band valley over the thermal energy range (about 0.025 eV). The electrons are accelerated by the electric field and they collide with crystal lattice imperfections (predominantly thermal vibrations in pure material). On collision, they lose a component of their momentum directed along the electric field and lose some of their increased kinetic energy to the lattice as Joule heating. The latter energy appears as Joule heating. For the polar scattering mechanism predominant in the central valley of pure GaAs not all of the directed momentum is randomised, nor is all the excess kinetic energy delivered to the lattice at each collision. After application of an electric field some of the kinetic energy gained from the field is effectively shared between all the electrons as their momentum is redirected, so that their mean energy or temperature rises. This causes an increase in the scattering rate until equality again exists between the energy delivered by the electric field to the electrons and the energy delivered by the electrons to the lattice. As the electric field is increased the equilibrium state exists at a higher electron temperature, and there is a directed component or "streaming" of the electron velocities (Fig. 3.3) because momentum is not randomised at each collision. It might be expected that the change in scattering rate arising from the increased electron temperature would cause deviations from Ohms law as the electric field is increased. However, the polar scattering mechanism becomes progressively weaker at the generally higher electron velocities associated with the increasing electric field, and this compensates the increased scattering rate to give a rate of momentum redistribution which is almost field independent. Therefore electronic conduction in the

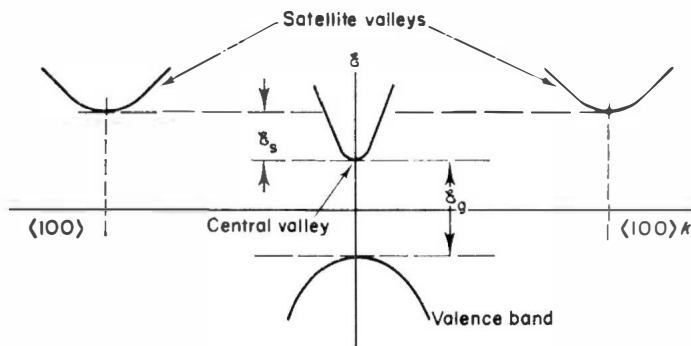


FIG. 3.2. The band structure of GaAs on either side of the forbidden energy gap.

central valley is approximately ohmic for fields below threshold even though the electrons have a temperature in excess of that of the lattice.

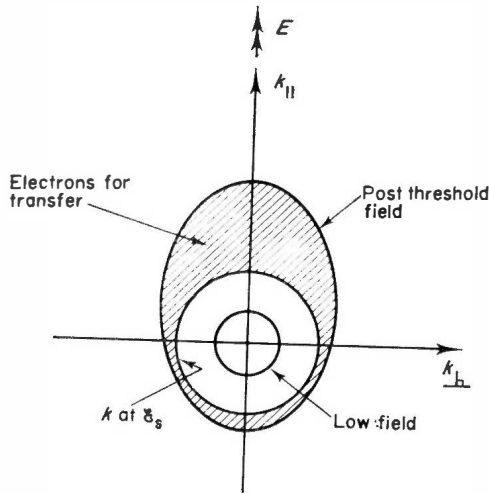


FIG. 3.3. Schematic cross-section of a surface of constant  $f(k)$  in  $k$  space for a low and a high electric field. It illustrates the streaming and temperature increase of the electrons at high fields in the central valley if intervalley transfer did not occur. Electrons with  $k$  greater than the value corresponding to  $\mathcal{E}_s$  have the possibility of intervalley transfer.

The electron temperature increase continues until the thermal and drift energy is comparable with the energy spacing of the central valley of the conduction band and the next highest energy band (Figs 3.2 and 3.3). The latter band is known as the satellite valley of which there are three equivalents in gallium arsenide. These satellites lie 0.36 eV above the central valley minimum and have an electronic effective mass of  $0.4 m_0$  (about six times the central valley electron effective mass). As a result of the higher effective mass the density of available electron states in unit energy interval is much higher in the satellite valleys than in the central valley. Electrons whose energy is greater than the satellite valley minimum have the possibility of scattering to this valley from the central valley. When equilibrium is achieved in this so-called intervalley transfer process the greater proportion of electrons with the energetic capability lie in the satellite valleys. As the electric field is further increased more electrons have sufficient energy for intervalley transfer and so more of them occupy the satellite valleys. The electron mobility in the satellite valleys is much smaller than in the central valley (about a factor of 70) owing to the higher effective mass of the electrons and the stronger scattering processes which are operative in the satellite valleys. There is now the possibility of a differential negative resistance existing in the velocity-field characteristic.



The steepness of this negative differential resistance depends on the rate of change of the valley populations with electric field (Fig. 3.4). If this is small there may be no negative resistance and only a saturation effect.

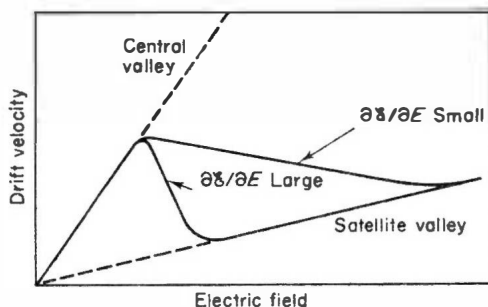


FIG. 3.4. The variation of the negative slope for field sensitive and field insensitive distribution functions in the central valley.

The characteristics of the polar scattering mechanism in the central valley now become important. It was mentioned earlier that this form of scattering becomes weaker as the electron kinetic energy increases. At a critical electric field (peculiar to the material) the polar scattering can no longer transfer electronic kinetic energy to the crystal lattice as rapidly as it is supplied by the electric field. Therefore the electron temperature “runs away”. This phenomenon has been related to dielectric breakdown in other materials. For gallium arsenide the critical field is about 5 kV/cm. At electric fields a little below the critical one the electron temperature (mean energy) in the central valley rises considerably for small electric field increases, and the predominant energy electron temperature increases occur in this region. The threshold electron for intervalley transfer occurs at an applied field of about 3.5 kV/cm and the high sensitivity of electron energy in the central valley to electric field causes a rapid intervalley transfer of electrons so that a negative differential resistance occurs.

It is the purpose of this chapter to describe quantitatively this transferred electron effect. Most of the calculations will refer to GaAs because this material has received far more practical attention than any other which exhibits the transferred electron effect. Where appropriate, the properties of other materials will be considered.

We now turn briefly to the experimental evidence that the above mechanism is indeed the one occurring in the Gunn effect and related devices. All materials that have exhibited the effect (gallium arsenide, indium phosphide, cadmium telluride, zinc selenide and indium arsenide under pressure) have the same band structure as described above. Other materials with the same conduction band structure which do not exhibit the effect

have their valence band to conduction band energy gap smaller than the central valley (lowest conduction band) to satellite valley energy gap. As a result the electron temperature runaway, described above, causes impact ionisation of electrons across the fundamental energy gap, before intervalley transfer can occur.<sup>(1)</sup> Indium arsenide is a material whose behaviour may be changed from the exhibition of impact ionisation to the Gunn effect by application of uniaxial stress along the  $\langle 111 \rangle$  direction.<sup>(2)</sup> Such a stress modifies the band structure by lowering the satellite valley energy with respect to the central valley and increasing the fundamental energy gap. After the attainment of a critical pressure, intervalley transfer occurs before impact ionisation.

The crucial experiment which first demonstrated that the two valley transfer model was correct was performed on gallium arsenide under hydrostatic pressure.<sup>(3)</sup> As the pressure was increased it was found that the threshold field for the Gunn effect decreased in accordance with the reduction of the energy separation of the satellite and the central valleys. At a pressure of 26 kilobars the Gunn effect oscillations disappeared. This pressure is in good agreement with that theoretically required to cause the satellite valley minima to fall to the same energy as the central valley minimum. Under this condition the satellite valleys would be occupied at room temperature in the absence of an electric field. Therefore no field induced transfer could take place and no differential negative resistance could be observed.

All other explanations of the Gunn effect required only one conduction band valley for the electrons. The importance of the above evidence is the demonstration of the necessity of a two valley model to explain the behaviour of the threshold field and the absence of effects when intervalley transfer cannot occur.

The following sections consider quantitatively the form of the velocity-field relationship in gallium arsenide that is derived from the intervalley transfer mechanism. This involves the quantitative formulation of the calculation, together with consideration of the relevant properties of gallium arsenide and the approximations required to carry the calculation to completion.

### 3.2 FORMULATION OF THE PROBLEM

Calculation of the velocity-field characteristic involves knowledge of the electron band structure of the material under consideration and the distribution of electrons over it. In this section it is shown how these two features may be separately considered.

A conductor in an electric field,  $E$ , carries a current density,  $J(E)$ , which is related to the sum over unit volume of material of the individual electron

velocities,  $\mathbf{v}$ :—

$$J(\mathbf{E}) = e \left( \sum_{\text{unit vol.}} \mathbf{v} \right). \quad (3.1)$$

The number distribution of the electrons over the available velocities is required to perform the summation. In order to incorporate the results of the wave mechanical calculation of the electronic distribution function in (3.1) it is convenient to use the wave vector  $\mathbf{k}$ , of the electronic wave function. The velocity of the electron is the group velocity of the electronic wave function given by:—

$$\mathbf{v}(\mathbf{k}) = \frac{1}{\hbar} \left( \frac{\partial \mathcal{E}}{\partial \mathbf{k}} \right) \quad (3.2)$$

where  $\mathcal{E}$  is the electron energy. For a parabolic band, labelled  $i$ , with effective mass  $m_i^*$  and energy minimum at  $\mathbf{k}_i$ , (3.2) simplifies to:—

$$\mathbf{v}(\mathbf{k}) = \frac{\hbar}{m_i^*} (\mathbf{k} - \mathbf{k}_i) \quad (3.2a)$$

$\mathbf{k}$  can only take discrete values which have a constant spacing in a three-dimensional representation of this vector quantity known as “ $\mathbf{k}$  space”. These individual values are known as “ $\mathbf{k}$  states”. The electron distribution function  $f(\mathbf{k})$  is now defined as the probability for each electron that the state  $\mathbf{k}$  is occupied, so that  $f(\mathbf{k})$  is normalised by the condition:—

$$\sum_{\mathbf{k}} f(\mathbf{k}) = 1 \quad (3.3)$$

which simply states that the electron exists somewhere in  $\mathbf{k}$ -space.

The current summation of (3.1) can be rewritten using (3.2) as:—

$$J(\mathbf{E}) = \frac{ne}{\hbar} \sum_{\mathbf{k}} \frac{\partial \mathcal{E}}{\partial \mathbf{k}} f(\mathbf{k}). \quad (3.4)$$

A frequently used alternative to  $J(\mathbf{E})$  is the mean electron drift velocity

$$\bar{\mathbf{v}}(\mathbf{E}) = \frac{J(\mathbf{E})}{ne} = \frac{1}{\hbar} \sum_{\mathbf{k}} \frac{\partial \mathcal{E}}{\partial \mathbf{k}} f(\mathbf{k}) \quad (3.5)$$

which for a parabolic band structure simplifies to:—

$$\bar{\mathbf{v}}(\mathbf{E}) = \frac{\hbar}{m_i^*} \sum_{\mathbf{k}} (\mathbf{k} - \mathbf{k}_i) f(\mathbf{k}). \quad (3.5a)$$

The dependence of mean drift velocity on applied electric field may be calculated once the field dependence of the distribution function  $f(\mathbf{k})$  and

the band structure of the material (giving  $(\partial \mathcal{E}/\partial \mathbf{k})$ ) have been determined. Determination of the former is carried out by solution of the Boltzmann equation which is formulated in Section 3.4.

### 3.3 BAND STRUCTURE OF GAAS

The lower part of the conduction band structure of GaAs<sup>(4,8)</sup> within which transferred electron effects occur is illustrated in Fig. 3.2. The valence band edge is also included for comparison.

The single valley conduction band edge ("central valley") lies at the centre of the Brillouin zone. It is spherically symmetric with respect to the electron wave vector but is non-parabolic. 0.36 eV above the conduction band edge the effective mass is about 2.8 times that at the band edge, where the minimum effective mass ratio is approximately 0.07. The conduction electrons occupy this valley at room temperature with low electric fields.

The next valleys at higher energy lie along the  $\langle 100 \rangle$  directions 0.36 eV ( $\mathcal{E}_s$ ) above the central valley minimum. Much less is known about these "satellite" valleys. Theory indicates that they lie at the Brillouin zone boundary<sup>(5,6)</sup> so that there are three equivalent valleys and they have ellipsoidal constant energy surfaces. By comparison of known values for  $\langle 100 \rangle$  valleys in Si and GaP ( $\langle 100 \rangle$  valleys at the conduction band edge) with a calculation of the transverse effective mass ratio in GaAs<sup>(5)</sup> Conwell and Vassell<sup>(4)</sup> estimated that the transverse effective mass ratio (perpendicular to  $\langle 100 \rangle$ ) is 0.23 and the longitudinal effective mass (parallel to  $\langle 100 \rangle$ ) is 1.3. These values can only be regarded as tentative.

Information on the higher valleys of the conduction band is even more sketchy than that of the  $\langle 100 \rangle$  satellite valleys. No reason has yet been found to include effects from them and they will therefore be neglected.

### 3.4 THE BOLTZMANN EQUATION†

The electron distribution function depends upon external forces due to fields and diffusion which cause it to alter from its unperturbed equilibrium state, and the scattering effects of lattice imperfections which tend to restore this equilibrium. The Boltzmann equation describes these processes: the net rate of change of  $f(\mathbf{k})$  is equal to the algebraic sum of the rate of electron redistribution. i.e.

$$\frac{d}{dt}f(\mathbf{k}) = \left( \frac{\partial}{\partial t}f(\mathbf{k}) \right)_{\text{diffusion}} + \left( \frac{\partial}{\partial t}f(\mathbf{k}) \right)_{\text{fields}} + \left( \frac{\partial}{\partial t}f(\mathbf{k}) \right)_{\text{scatt.}} \quad (3.6)$$

† For a full discussion see J. M. Ziman, "Electrons and Phonons", Oxford University Press, 1963, and E. M. Conwell, 'High Field Transport in Semiconductors', "Solid State Physics", suppl. 9, Academic Press, 1967.

The following development of the Boltzmann equation includes effects which are not required for the present chapter but will be needed for reference in subsequent chapters.

(i) *Diffusion effects*

The first term on the right hand side of 3.6 arises when spatial gradients of electron density or temperature exist so that the number of electrons with a particular value of  $\mathbf{k}$  (classically with a particular velocity) entering a region of the material does not equal the number leaving.

$$\left( \frac{\partial}{\partial t} f(\mathbf{k}) \right)_{\text{diffusion}} = -\mathbf{v}(\mathbf{k}) \cdot \left( \nabla_{\mathbf{r}} f(\mathbf{k}) \right). \quad (3.7)$$

$\mathbf{v}(\mathbf{k})$  indicates the electron velocity as a function of  $\mathbf{k}$ , and  $\nabla_{\mathbf{r}}$  is the spatial gradient.  $f(\mathbf{k})$  also has an implicit spatial dependence when 3.7 is non-zero.

(ii) *Electric and magnetic field effects*

When an electron is accelerated by the effect of an external field it changes its  $\mathbf{k}$ -state. The second term on the right hand side of 3.6 arises from such effects and is the  $\mathbf{k}$  space analogue of the real space equation 3.7

$$\left( \frac{\partial}{\partial t} f(\mathbf{k}) \right)_{\text{fields}} = - \frac{\partial \mathbf{k}}{\partial t} \cdot \left( \nabla_{\mathbf{k}} f(\mathbf{k}) \right). \quad (3.8)$$

$\nabla_{\mathbf{k}}$  indicates that the gradient is to be taken in  $\mathbf{k}$  space.

The electron acceleration is caused by external electric and magnetic fields:—

$$\frac{\partial \mathbf{k}}{\partial t} = \frac{e}{\hbar} (\mathbf{E} + \mathbf{v}(\mathbf{k}) \wedge \mathbf{H}). \quad (3.9)$$

In this chapter  $f(\mathbf{k})$  is required from the solution 3.6 under the following conditions:—

- (a) steady state i.e.  $(d/dt) f(\mathbf{k}) = 0$
- (b) spatial uniformity i.e.  $((\partial/\partial t) f(\mathbf{k}))_{\text{diffusion}} = 0$
- (c) magnetic field absent i.e.  $\mathbf{H} = 0$ .

Equations (3.6), (3.7), (3.8), and (3.9) simplify to:—

$$\frac{e}{\hbar} \mathbf{E} \cdot \nabla_{\mathbf{k}} f(\mathbf{k}) = \left( \frac{\partial}{\partial t} f(\mathbf{k}) \right)_{\text{scatt.}} \quad (3.10)$$

(iii) *Scattering effects*

The objective of this section is to show how the scattering term on the right hand side of Eqn (3.10) may be “broken down” into the separate effects of

the number of scattering imperfections (regarded generally) and their individual scattering power.

The scattering term in (3.10) may be written as:—

$$\left( \frac{\partial f(\mathbf{k})}{\partial t} \right)_{\text{scatt.}} = \sum_{\mathbf{k}'} \{ S(\mathbf{k}', \mathbf{k}) f(\mathbf{k}') (1 - f(\mathbf{k})) - S(\mathbf{k}, \mathbf{k}') f(\mathbf{k}) (1 - f(\mathbf{k}')) \}. \quad (3.11)$$

$S(\mathbf{k}', \mathbf{k})$  is the scattering probability from a state  $\mathbf{k}'$  to state  $\mathbf{k}$  in unit time, and is weighted by the necessary transition conditions that an electron occupies the initial state (probability  $f(\mathbf{k}')$ ) and the final state is empty (probability  $1 - f(\mathbf{k})$ ). It would be possible to write Eqn (3.10) as a differential equation, but for the presence of  $f(\mathbf{k}')$  in Eqn (3.11) and it is this term which causes the complexity in solving the Boltzmann equation.

For the non-degenerate materials used in transferred electron devices  $f(\mathbf{k}) \ll 1$  and (3.11) simplifies to:—

$$\left( \frac{\partial f(\mathbf{k})}{\partial t} \right)_{\text{scatt.}} = \sum_{\mathbf{k}'} \{ S(\mathbf{k}', \mathbf{k}) f(\mathbf{k}') - S(\mathbf{k}, \mathbf{k}') f(\mathbf{k}) \}. \quad (3.12)$$

The summation of (3.12) is conveniently transformed to an integral over  $\mathbf{k}$ -space because of the quasi-continuous spacing of allowed  $\mathbf{k}$  states. Each of these states occupies a volume of  $(8\pi^3/V)$  of  $\mathbf{k}$ -space<sup>(7)</sup> throughout which they are uniformly spaced.  $V$  is the crystal volume. Therefore the transformation of the summation of (3.12) to the equivalent integral is:—

$$\sum_{\mathbf{k}'} (\text{R.H.S of 3.12}) = \int_{\mathbf{k}'} (\text{R.H.S. of 3.12}) \frac{V}{8\pi^3} d\mathbf{k}'$$

where  $d\mathbf{k}'$  is an elementary volume of  $\mathbf{k}$ -space. In general  $S(\mathbf{k}', \mathbf{k}) \neq S(\mathbf{k}, \mathbf{k}')$  but (3.12) may be developed to the following more convenient form for one phonon scattering processes, which requires only one coupling coefficient,  $P(\mathbf{k}, \mathbf{k}')$  between the states  $\mathbf{k}$  and  $\mathbf{k}'$ . (see Appendix 1.)

$$\begin{aligned} \left( \frac{\partial f(\mathbf{k})}{\partial t} \right)_{\text{scatt.}} &= \sum_{\mathbf{k}'} P(\mathbf{k}, \mathbf{k}') [ \{ N_{(\mathbf{q})} f(\mathbf{k}') - (N_{(\mathbf{q})} + 1) f(\mathbf{k}) \} \delta(\mathcal{E}(\mathbf{k}) \\ &\quad - \mathcal{E}(\mathbf{k}') - \hbar\omega_{(\mathbf{q})}) - \{ N_{(\mathbf{q})} f(\mathbf{k}) - (N_{(\mathbf{q})} + 1) f(\mathbf{k}') \} \\ &\quad \times \delta(\mathcal{E}(\mathbf{k}') - \mathcal{E}(\mathbf{k}) - \hbar\omega_{(\mathbf{q})}) ] \end{aligned} \quad (3.13)$$

where the thermal equilibrium phonon population  $N_{(\mathbf{q})}$  per unit volume at temperature  $T$ , phonon frequency  $\omega$  and wave-vector  $\mathbf{q}$  is given by:—

$$N_{(\mathbf{q})} = \{ \exp(\hbar\omega(\mathbf{q})/k_B T) - 1 \}^{-1} \quad (3.14)$$

$k_B$  is Boltzmann's constant and the  $\delta$ -function is included in Eqn (3.13) to

indicate that the scattering probability is only non-zero if the overall energy is conserved.

For many scattering processes in an isotropic semiconductor the scattering rate is approximately proportional to the deviation of the distribution function from its equilibrium value and an alternative development of Eqn 3.10 can be made. i.e.

$$\left( \frac{\partial f(\mathbf{k})}{\partial t} \right)_{\text{scatt.}} \propto [f(\mathbf{k}) - f_0(\mathbf{k})] \quad (3.15)$$

where the subscript 0 indicates the thermal equilibrium distribution function. The constant of proportionality has the dimensions of  $(\text{time})^{-1}$  and (3.15) is usually referred to as the relaxation time approximation. It was used in Chapter 2. The conditions for its validity are considered in Appendix 2. If the relaxation time is  $\tau$ :—

$$\left( \frac{\partial f(\mathbf{k})}{\partial t} \right)_{\text{scatt.}} = \frac{[f(\mathbf{k}) - f_0(\mathbf{k})]}{\tau}. \quad (3.16)$$

Great difficulty is generally encountered in solving Eqn (3.10) owing to the complexity of the scattering terms of (3.12) and simplifications such as (3.16) have to be introduced. Before considering the methods of solution the important scattering processes will be presented. The semiconductor band structure places restrictions on the type of scattering processes allowed and on the possible values of  $\mathbf{k}$  and  $\mathbf{k}'$ . The relative strength of the allowed processes will determine the important mechanisms to be included in (3.12).

### 3.5 IMPORTANT ELECTRON SCATTERING MECHANISMS IN GaAs

In the following sections the important electron scattering mechanisms are summarised and references to detailed treatments are made. Wherever phonons have been involved in the calculation of scattering probabilities they will have been assumed to be in thermal equilibrium with the lattice. Their distribution over energy (or frequency) is described by the Bose-Einstein Eqn (3.14).

The weak dependence of  $\omega_{(\mathbf{q})}$ , and so of  $N_{(\mathbf{q})}$  on  $\mathbf{q}$  for optical phonons near the centre or a boundary of the Brillouin zone, will be neglected.

#### (i) Intravalley scattering in the central valley

For scattering events between initial and final states in the same valley (intravalley scattering) the electron wave vector is always close to the wave vector of minimum energy ( $\mathbf{k} = 0$  for central valley). Therefore, conservation of wave vector requires that scattering interactions only take place with large wavelength phonons.

(a) *Polar scattering by longitudinal optical phonons.* The crystal binding of GaAs is partially ionic<sup>(8)</sup> so that an electron introduced into such a material will induce an electrical polarisation of the lattice. In turn, the dipolar electric field arising from the opposite displacement of negatively and positively charged atoms provides a coupling force between the electron and lattice, which is most powerful when the maximum number of induced dipoles are in parallel alignment. Motion of the electron will result in a sympathetic movement of the lattice in response to the dynamical coupling forces. This description is indicative of the interaction between electrons and longitudinal optical phonons which is strongest for long wavelength phonons. By comparison the interaction with transverse optical phonons is negligible because the relative displacements of nearest neighbour atoms produces no first order polarisation.

The polar scattering mechanism is dominant in the central valley of GaAs for low electron energies and its coupling coefficient (see Section 3.4.iii) is given<sup>(9)</sup> by:—

$$P(\mathbf{k}, \mathbf{k}')_{\text{polar}} = \frac{4\pi^2 e^2 \omega_0}{V \epsilon_0} \left( \frac{1}{\epsilon_\infty} - \frac{1}{\epsilon_s} \right) \frac{1}{|\mathbf{k} - \mathbf{k}'|^2}. \quad (3.17)$$

$\omega_0$  is the longitudinal optical phonon frequency at the centre of the Brillouin zone,  $V$  is the crystal volume and  $\epsilon_\infty$  and  $\epsilon_s$  are the high frequency and static dielectric constants respectively. The latter quantities are a measure of the effective ionic charge of the Ga and As atoms.<sup>(8)</sup>

The existence of  $|\mathbf{k} - \mathbf{k}'|^2$  in the denominator of (3.17) is a consequence of two effects. The shorter wavelength (large  $\mathbf{k} - \mathbf{k}'$ ) phonons have a smaller scattering effect on the electrons and the scattering experienced by high velocity electrons is weak, as is expected of all coulomb scattering processes. As the electron energy (and consequently its  $\mathbf{k}$ -vector) increases, the rate of energy loss of electrons in a parabolic band to polar optical phonons reduces.<sup>(10)</sup> Frohlich<sup>(11)</sup> has shown that the electron distribution in a parabolic band subject *only* to polar scattering is unstable and “runs away” under the influence of an electric field of any magnitude. However, there are always other scattering mechanisms operative at high electron energies. For example, electron–electron collisions which conserve total momentum and energy in the electron system, but tend to share the energy between all electrons, increase the mean scattering probability by involving the low energy electrons. The result of these additional scattering mechanisms is to stabilize the electron energy distribution for applied electric fields below a maximum  $E_c$ . At  $E_c$  the distribution becomes unstable and runs away.<sup>(12)</sup> This effect has been associated with dielectric breakdown of polar crystals<sup>(2)</sup> and is referred to as “polar breakdown”.



Non-parabolicity of the energy bands can also stabilize the distribution.<sup>(13,14)</sup> This arises from the increased number of states to which an electron can be scattered owing to the decreased slope of the  $\mathcal{E}$ - $\mathbf{k}$  relationship that is implied by non-parabolicity. Providing that there is a sufficient deviation from a parabolic  $\mathcal{E}$ - $\mathbf{k}$  relation the electron distribution function resulting from the polar mode scattering is not unstable under any electric field.

(b) *Acoustic intravalley scattering.* Deformation potential scattering by acoustic phonons is far weaker than polar scattering at low electron energies but they become comparable at higher energies when polar scattering becomes weaker. This is particularly so if non-parabolicity of the central valley is neglected. The deformation potential scattering process is caused by dilation of the lattice by long wavelength longitudinal acoustic phonons. Electrons travelling through the lattice experience a long wavelength modulation of the lattice periodic potential so changing their propagation characteristics. The effect is similar to the passage of light through a medium of slowly varying refractive index. The reflection coefficient (i.e. scattering) of the electron waves from this spatial modulation is dictated by the change in propagation characteristics. Bardeen and Shockley<sup>(39)</sup> analysed this model and characterised the scattering probability in terms of a deformation potential,  $\Xi_{ac}$ , which is the mean change in potential energy of the lattice periodic potential per unit strain, and also the energy change of that part of the electron band structure under consideration.

The deformation potentials differ for each valley of the overall band structure but are of the order of 10 eV for most materials. The explicit form of the coupling coefficient,  $P(\mathbf{k}, \mathbf{k}')_{ac}$ , for longitudinal acoustic phonons is:<sup>(15)</sup>

$$P(\mathbf{k}, \mathbf{k}')_{ac} = \frac{\pi \Xi_{ac}^2}{\rho s V} |\mathbf{k} - \mathbf{k}'| \quad (3.18)$$

where  $\rho$  is the density of the material and  $s$  the sound velocity. For energy bands with spherical constant energy surfaces there is no contribution to scattering from transverse acoustic phonons because to a first order they do not dilate the lattice.

(c) *Electron-Electron Scattering.* Collisions between electrons conserve both the total momentum (wave vector) and the energy of the electron distribution. For this reason they are only of secondary importance in the calculation of a mean electron drift velocity. Their importance lies in the "mixing" of the distribution function that such collisions cause, and so they modify the effect of other scattering mechanisms owing to the energy dependence of the latter. In practice the electron-electron collision rate (which increases as the electron density increases) is compared with other

energy and momentum loss processes in order to decide the appropriate approximation to use in solving the Boltzmann equation.<sup>(16)</sup> If the carrier concentration is high enough for energy and momentum redistribution to occur more rapidly with electron–electron collisions than with other scattering mechanisms the distribution function is forced to be Maxwellian, and the drift motion induced by an electric field is equally shared by all electrons. This “drifted Maxwellian” approximation was first introduced by Frohlich and Paranjape<sup>(17)</sup>, and the distribution function is of the form:—

$$f(\mathbf{k}) = \left( \frac{\hbar^2}{2\pi m^* k_B T} \right)^2 \exp \left\{ \frac{-\hbar^2}{2m^* k_B T} (\mathbf{k} - \mathbf{d})^2 \right\} \quad (3.19)$$

where  $\mathbf{d}$  is the drift motion written as a displacement in  $\mathbf{k}$ -space.

At intermediate concentrations the energy distribution is Maxwellian, but the drift motion is not equally shared by all electrons. This distinction between the importance of electron–electron collisions in determining the drift motion (momentum) and energy distribution arises because of the generally longer time required for energy relaxation, compared with momentum relaxation. In the case of collisions with phonons, each collision redirects the momentum, but the probability that a phonon will be emitted is proportional to  $(N(\mathbf{q}) + 1)$  while the probability that a phonon will be absorbed is proportional to  $N(\mathbf{q})$  (3.39). ( $N(\mathbf{q})$  is the number of phonons available for scattering—see Eqn (3.14)). Therefore on average the electron will only lose one phonon’s “worth” of energy every  $(2N(\mathbf{q}) + 1)$  collisions.

For very low electron densities, electron–electron collisions are negligible and the distribution function is generally non-Maxwellian under the influence of an external field. In the central valley of GaAs the rate of energy loss of electrons in electron–electron collisions can only exceed their rate of energy loss in polar optical phonon collisions if the electron density is greater than  $3 \times 10^{17} \text{ cm}^{-3}$ .<sup>(10)</sup> Practical transferred electron devices have an electron density between  $10^{14} \text{ cm}^{-3}$  and  $10^{16} \text{ cm}^{-3}$ , so that electron–electron collisions are not significant.

(d) *Impurity Scattering*. In addition to the electron scattering by dynamic lattice imperfections discussed in the previous sections, scattering is also caused by static imperfections. Except at low temperatures scattering by electrically charged ionized impurities is the most important of these phenomena. This mechanism is the same as Rutherford scattering of  $\alpha$ -particles by nuclei. The change of electron trajectory on passing a charged impurity is illustrated in Fig. 3.5. The scattering is strongest for small impact parameters (distance of closest approach of electron and impurity if no scattering occurred) and for low electron velocities. As the impact parameter is increased the effect of all the other electrons in the material is to “screen”

out the electric field of the charged impurity. Calculation of the scattering strength by Conwell and Weisskopf<sup>(18)</sup> neglected impact parameters greater than half the mean separation of impurity atoms, while the calculations of Brooks and Herring<sup>(19)</sup> applied a Debye screening term to limit the scattering at large impact parameters. Fuller details are given by Paige.<sup>(15)</sup> Both calculations give similar results differing only by a small factor. For isotropic constant energy surfaces in  $\mathbf{k}$  space the energy dependent relaxation time,  $\tau_I(\mathcal{E})$ , for electrons is given by Conwell and Weisskopf as:—

$$\frac{1}{\tau_I(\mathcal{E})} = \frac{Z^2 e^4}{16\pi \epsilon^2 \epsilon_0^2 (2m^*)^{\frac{1}{2}}} \mathcal{E}^{-\frac{3}{2}} n_I \cdot \ln \left[ 1 + \left( \frac{4\pi\epsilon\epsilon_0 \mathcal{E}}{Ze^2 n^{1/3}} \right)^2 \right] \quad (3.20)$$

$Z$  is the number of electronic charges on the impurity which has a number density  $n_I$  per unit volume.  $\epsilon\epsilon_0$  is the dielectric constant of the material. No energy is exchanged in ionized impurity scattering which becomes progressively weaker at high electron energies. As noted previously, the weakening of the interaction is a characteristic of all coulomb scattering process. Scattering of electrons by neutral impurity atoms also occurs but is negligible except at very low temperatures and will not be considered further

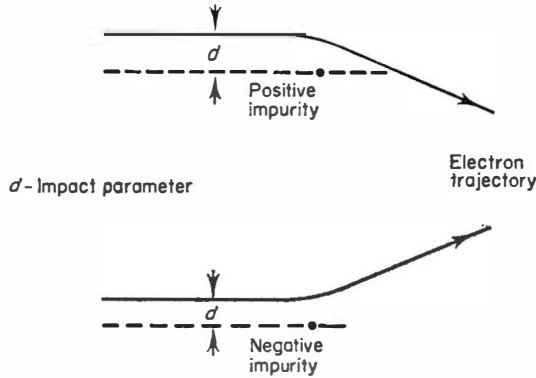


FIG. 3.5. Scattering by ionized impurities.

Two other scattering mechanisms occur under the general heading of impurity scattering. In these the scattering centre is not a single atom but a multiplicity of atoms, and is caused by a material growth defect. In order to explain anomalies in the low field mobility of  $n$ -type GaAs Weisberg<sup>(20)</sup> suggested that intrinsic regions occur in the material due to local compensation of the donors. This intrinsic region will be surrounded by space-charge owing to the difference in Fermi level of the bulk of the material and the intrinsic region. For a carrier concentration of  $10^{15} \text{ cm}^{-3}$  or greater (typical for Gunn effect material) the potential difference is about one half the

energy gap, and is effectively an infinite wall for all conduction band electrons concerned in transferred electron action. Conwell<sup>(4)</sup> estimates their diameter as 200 Å for a free carrier concentration of  $10^{15} \text{ cm}^{-3}$ . Treating these scattering centres as large impenetrable spheres she estimates the relaxation time for the process as:—

$$\begin{aligned} \frac{1}{\tau_s} &= n_s Q v \\ &= \frac{\sqrt{2} n_s Q (\mathcal{E} - \mathcal{E}_0)^{\frac{1}{2}}}{(m^*)^{\frac{1}{2}}} \end{aligned} \quad (3.21)$$

$n_s$  is the number density of the impenetrable spheres of cross-sectional area  $Q$ .  $v$  is the electron velocity in a valley with energy minimum  $\mathcal{E}_0$ . Space charge effects may also occur at dislocations causing a similar type of scattering.<sup>(21)</sup>

(e) *Resonant Scattering.* The scattering processes discussed so far are first order processes. They are weak perturbation interactions of one phonon or one impurity with an electron. Second order processes in which two scattering agencies simultaneously participate are usually neglected because of their much smaller probability. In the case of weak polar coupling it has been shown that two phonon processes may cause scattering rates which are comparable with the single phonon scattering rates.<sup>(65)</sup> These processes take two forms. In the elastic process one phonon is absorbed and one emitted so that the electronic momentum may be randomized without a change in kinetic energy. In the inelastic processes two phonons are simultaneously absorbed or emitted. Calculation of the scattering rates of these two phonon processes shows that it is proportional, not to the square of the polar coupling constant as may be expected, but is linearly proportional to it. The elastic scattering will tend to drive the electron distribution function towards a near spherically symmetric form in  $\mathbf{k}$ -space, so giving a little extra support to the later use of a drifted Maxwellian form of the distribution function by Butcher and Fawcett.

(ii) *Intervalley scattering from the central valley.*

Electrons with an energy greater than 0.36 eV above the conduction band minimum have the possibility of transfer to the heavy mass, low mobility,  $\langle 100 \rangle$  satellite valleys at the edge of the Brillouin zone. This scattering process requires a phonon with a large wave vector, and group theoretical selection rules<sup>(22)</sup> show that the longitudinal optical phonon is the only one allowed if the satellite valley minimum lies on the edge of the Brillouin zone. Because the initial and final electron states are always close to the centre or edge of the

Brillouin zone the phonon wave vector lies close to the zone edge and its energy dependence on wave vector may be neglected. By convention the scattering probability is written in the deformation potential formalism and is of the form

$$P(\mathbf{k}, \mathbf{k}')_{12} = \frac{\pi}{\rho \omega V} \cdot D_{12}^2 \quad (3.22)$$

$\omega$  is the zone edge frequency of the scattering phonon and  $D_{12}$  is the coupling constant or deformation potential field of the interaction. The formalism is slightly different from the case of acoustic phonons (Eqn (3.18)) because phase velocity is not a convenient description of the dispersion relation of a zone edge phonon. The sound velocity,  $s$ , is replaced by  $\omega/q$  where the phonon wave vector  $q$  (equal to  $k - k'$  for the electron) is close to the zone edge value  $\pi/a$ .  $a$  is the lattice spacing.  $D_{12}$  is equivalent to  $\Xi\pi/a$  and so has the form of a deformation potential field with expected values of  $10^8$  eV/cm to  $10^9$  eV/cm. At the time of writing  $D_{12}$  had not been calculated or measured and had to be treated as an arbitrary parameter. If the value chosen is too low, the intervalley scattering probability will be small. Consequently, the predicted upper frequency limit for transferred electron oscillations will be low and there will be too many high energy electrons in the central valley. Copeland<sup>(23)</sup> has shown that these high energy electrons will cause a low field avalanche at an electric field of about 4 kV/cm. Such an effect does not occur in good quality material.<sup>(24)</sup> Both of the above observations may be used to set a lower limit to  $D_{12}$  of about  $10^8$  eV/cm.

(iii) *Intravalley scattering in the satellite valleys.*

As in the central valley both polar optical and acoustic deformation potential scattering must be considered. There is generally a poor knowledge of the electron transport parameters in the satellite valleys because they are not appreciably occupied by electrons under normal conditions. Their ellipsoidal constant energy surfaces in  $k$ -space must be taken into account in summing their contributions to the conduction process. By comparison with the similar band structures of silicon and gallium phosphide and calculations for gallium arsenide Conwell and Vassell<sup>(4)</sup> assume that the effective mass parallel to  $\langle 100 \rangle$  is  $1.3 m_0$  and perpendicular to  $\langle 100 \rangle$  is  $0.23 m_0$ . ( $m_0$  is the free electron mass.) They find that the satellite valley mobility due to acoustic scattering is  $1400 \text{ cm}^2/\text{Vsec}$  by following the technique of Herring and Vogt.<sup>(25)</sup> The mobility due to polar scattering in the satellite valley is  $900 \text{ cm}^2/\text{Vsec}$ .<sup>(4)</sup> Measurements of the combined mobility can be made if the conduction electrons occupy these valleys. This has been achieved either by alloying gallium arsenide with gallium phosphide,<sup>(27)</sup> or applying pressure to gallium arsenide.<sup>(26)</sup> Both processes can cause the satellite valleys

to assume the lowest conduction band energy and the measured low field mobilities may be extrapolated to the pure or undisturbed conditions. Values lying between  $100 \text{ cm}^2/\text{Vsec}$  and  $200 \text{ cm}^2/\text{Vsec}$  are obtained. The next section will give the explanation of these low mobilities. Impurity scattering in the satellite valleys is neglected owing to the already low mobility caused by intrinsic processes.

(iv) *Intervalley scattering in the satellite valleys.*

Scattering occurs between satellite valleys (equivalent intervalley scattering) or between satellite and central valleys (non-equivalent intervalley scattering). The low density of states in the central valley cause non-equivalent intervalley scattering from the satellite valleys to have a negligible effect on the satellite valley mobility. The equivalent intervalley scattering coupling coefficient is of the same form as (3.22), i.e.

$$P(\mathbf{k}, \mathbf{k}')_{22} = \frac{\pi}{\rho \omega V} D_{22}^2 \quad (3.23)$$

$D_{22}$  is estimated as  $10^9 \text{ eV/cm}$  by comparison with results for the similar band structure of silicon.<sup>(4)</sup> Quantitatively this scattering process is dominant and when added to the previous intravalley processes the low field satellite valley mobility becomes  $145 \text{ cm}^2/\text{Vsec}$ , in substantial agreement with experiment. At high electric fields this value decreases owing to the increasing effectiveness of the scattering mechanisms as the electrons are heated.

### 3.6 SOLUTION OF THE BOLTZMANN EQUATION

Having developed the Boltzmann equation and considered the relevant electron scattering processes we should be in a position to solve the intervalley transfer transport problem in GaAs. In general, such a solution is impossible without approximation. Initially two approximate approaches will be described and this will be followed by a discussion of more satisfying computer techniques.

(i) *The method of Butcher and Fawcett*<sup>(28,29)</sup>

The approach of these authors followed that of Frohlich and Paranjape.<sup>(17)</sup> The difficulty of solving the Boltzmann equation is avoided by assuming the form of the answer. If the electron density is sufficiently high, electron-electron collisions are predominant in "mixing" the electron energies and momenta. Under these conditions each electron can be considered to have the same drift velocity and the distribution function is described by a displaced Maxwellian distribution function in  $\mathbf{k}$  space<sup>(17)</sup>:—

$$f_i(\mathbf{k}) = \left( \frac{\hbar^2}{2\pi m_i^* k_B T_i} \right)^{\frac{3}{2}} \exp \left\{ - \frac{\hbar^2}{2m_i^* k_B T_i} [\mathbf{k} - \mathbf{k}_i - \mathbf{d}_i]^2 \right\} \quad (3.24)$$

The subscript  $i$  refers to the  $i$ th valley which has an energy minimum at  $\mathbf{k}_i$ , an electron density  $n_i$ , electron temperature  $T_i$  and displacement in  $\mathbf{k}$ -space of  $\mathbf{d}_i$ . It is difficult to justify this approach. However, no dependence of the velocity field characteristic on electron density was known at the time of these calculations and their convenience has much to recommend them.

Butcher and Fawcett assumed that the distribution function had the above form in the central valley and in the satellite valleys with different values of the parameters for each valley. The calculation was further simplified by assuming that the satellite valleys were spherically symmetrical and parabolic so that only one valley need be considered in the calculation. Its contribution was multiplied by three to account for all the satellite valleys and a suitably averaged effective mass ( $0.4 m_0$ ) was used. Justification for this procedure is found in the absence of crystal orientation effects in experimental results.

Having assumed the form of the distribution function, it is relatively simple to calculate its parameters  $n_i$ ,  $\mathbf{d}_i$  and  $T_i$  from the conservation equations of electron density, wave vector and energy for the two valley system. In equilibrium the total rate of change of each of these quantities in each valley must be zero, i.e.

$$\int_i \frac{\partial}{\partial t} \{f(\mathbf{k}) \phi(\mathbf{k})\} d\mathbf{k} = \int_i \frac{\partial f(\mathbf{k})}{\partial t} \cdot \phi(\mathbf{k}) \cdot d\mathbf{k} = 0 \quad (3.25)$$

where  $\phi(\mathbf{k})$  is a function of  $\mathbf{k}$  only, taking, in turn, the values 1,  $(\mathbf{k} - \mathbf{k}_i)$ , and  $(\mathcal{E}_i(\mathbf{k}) - \Delta_i)$ . The subscript  $i$  indicates that the integral is taken over valley  $i$ , and  $\mathbf{k}_i$  and  $\Delta_i$  are respectively the electron wave vector and energy at the valley minimum. This technique is referred to as taking moments of the Boltzmann equation. For each valley one equation results for each of the two scalar integrals of (3.25) and three equations from the vector integral making a total of ten for central and satellite valleys. These equations and the equation

$$\sum n_i = n$$

are just sufficient to determine the ten values of the adjustable parameters  $n_i$ ,  $\mathbf{d}_i$ ,  $T_i$ .

$\partial f(\mathbf{k})/\partial t$  in (3.25) is the sum of the rates of change of  $f(\mathbf{k})$  due to fields and scattering, so that both valleys are coupled through the intervalley scattering term. Intravalley electron-electron scattering does not appear in the calculation because it conserves the values of the three adjustable parameters in each valley. The scattering mechanisms considered by Butcher and Fawcett were polar and acoustic scattering in the central valley, intervalley scattering from the central to satellite valleys, and polar, acoustic and equivalent intervalley scattering in the satellite valleys.

The determination of the parameters of the drifted Maxwellian distribution function allows a simple calculation of the field dependence of the electron drift velocity from:—

$$\bar{v} \left( \frac{E}{\tau} \right) = \frac{hV}{8\pi^3 m_i^*} \int (\mathbf{k} - \mathbf{k}_i) f(\mathbf{k}) d\mathbf{k} \quad (3.5a)$$

Further details of these calculations may be found in the original papers<sup>(30,31)</sup> and the later review articles.<sup>(28,29)</sup> The results of the calculations are shown in Figs (3.6–3.10). They are independent of electron concentration except as a scaling factor because the scattering processes are weak enough for each process to proceed independently of any other, so allowing a simple addition of their effects.

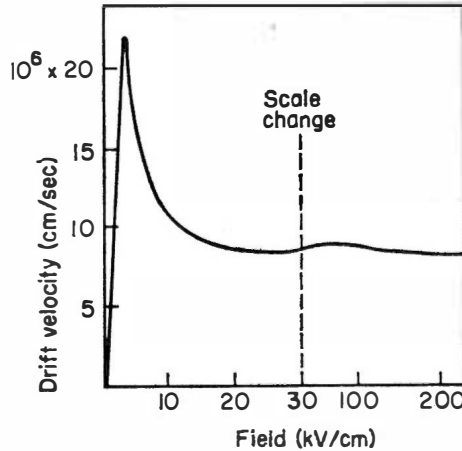


FIG. 3.6. The velocity–field characteristic of *n*-type GaAs calculated by Butcher and Fawcett at 300°K.<sup>(29–31)</sup> (Crown Copyright, reproduced by permission of the controller of Her Majesty's Stationery Office.)

The velocity–field curve is substantially linear to threshold with a mobility of 8100 cm<sup>2</sup>/Vsec which is typical of good quality GaAs. This linearity is a consequence of the small number of electrons transferred to the satellite valleys below threshold (6% at threshold). Above threshold the transfer proceeds rapidly with increasing electric field owing to the considerable temperature rise of the central valley electrons which is caused by the decreasing effectiveness of the polar scattering. The steep negative slope has a minimum value of about –3000 cm<sup>2</sup>/Vsec. Above 25 kV/cm the characteristic is substantially saturated owing to the decrease of electron mobility in both the central and satellite valleys as the electron temperature increases. The electron temperature rise and high electron drift velocity allows the



electrons to occupy a greater energy range of the conduction band structure and this is associated with a stronger intervalley scattering from the central valley and stronger scattering in the satellite valleys.

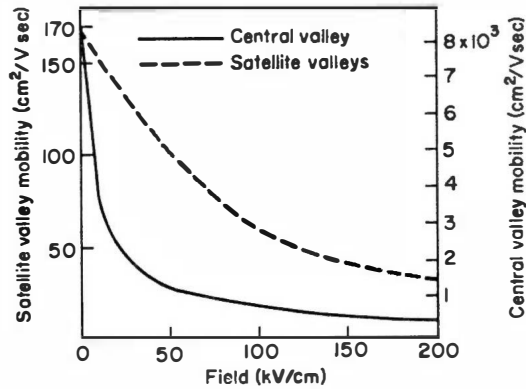


FIG. 3.7. The electric field dependence of the mobility of electrons in the central and satellite valleys of gallium arsenide calculated by Butcher and Fawcett.<sup>(29-31)</sup> (Crown Copyright, reproduced by permission of the controller of Her Majesty's Stationery Office.)

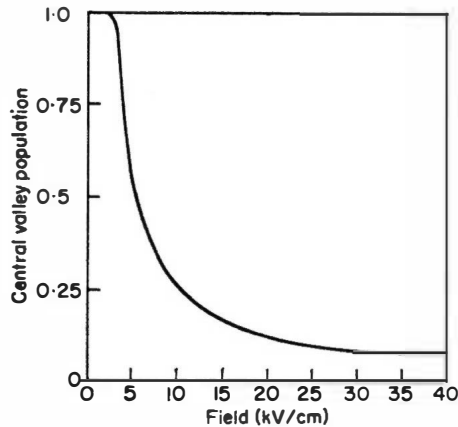


FIG. 3.8. The fraction of the total number of electrons in the central valley as a function of electric field (Butcher and Fawcett<sup>(29-31)</sup>). (Crown Copyright, reproduced by permission of the controller of Her Majesty's Stationery Office.)

The rapid increase of electron temperature in the central valley (Fig. 3.9) above threshold is a consequence of the decreasing effectiveness of the polar scattering mechanism at high electron velocities. At high electric fields the number of electrons in the central valley becomes very small but their temperature is extremely high and is communicated to the satellite valley

electrons after intervalley scattering so causing their high field temperature increase. Otherwise the satellite valley electron temperature is substantially constant because of the dominance of equivalent intervalley scattering and the absence of the breakdown behaviour of polar scattering.

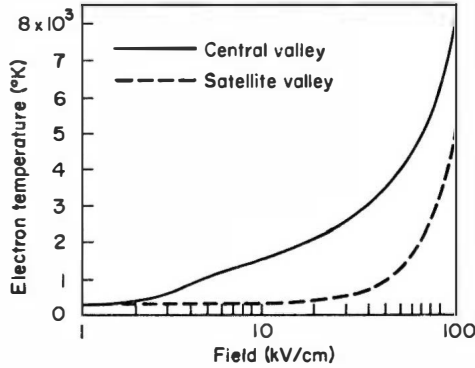


FIG. 3.9. Electron temperatures in the central and satellite valleys as functions of electric field (Butcher and Fawcett<sup>(29-31)</sup>). (Crown Copyright, reproduced by permission of the controller of Her Majesty's Stationery Office.)

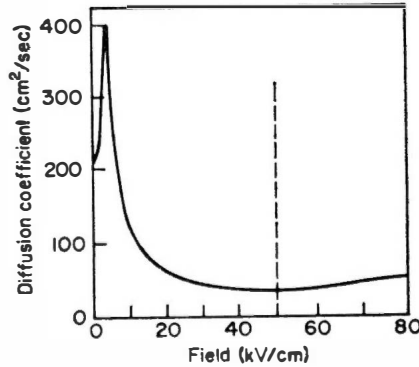


FIG. 3.10. Variation of the diffusion coefficient with electric field (Butcher and Fawcett<sup>(29-31)</sup>). (Crown Copyright, reproduced by permission of the controller of Her Majesty's Stationery Office.)

The behaviour of the diffusion coefficient obtained from an electron density weighting of the Einstein relationship in each valley is also illustrated (Fig. 3.10) and will be used later in calculations of device behaviour,

$$D(E) = \left( \frac{n_1 \mu_1 T_1 + n_2 \mu_2 T_2}{n_1 + n_2} \right) \frac{k_B}{e}. \quad (3.26)$$

The subscripts <sub>1</sub> and <sub>2</sub> refer respectively to the central and satellite valleys.  $n$  is electron density,  $\mu$  is mobility,  $T$  is temperature,  $k_B$  is the Boltzmann constant.

(ii) *The technique of Conwell and Vassell.*

In the material used for Gunn effect devices the electron density is typically  $10^{14} \text{ cm}^{-3}$  to  $10^{16} \text{ cm}^{-3}$ . This is insufficient for electron-electron collisions to be the predominant momentum scattering mechanism and the assumption of a drifted Maxwellian distribution function is highly suspect. In order to circumvent this difficulty Conwell and Vassell<sup>(4)</sup> solved the Boltzmann equation neglecting electron-electron collisions, to calculate the distribution function of the electrons and from this the other transport properties. In order to obtain a solution they assumed that the distribution function was almost symmetrical in  $\mathbf{k}$  space and its Legendre polynomial expansion may be truncated after the first two terms, i.e.

$$f(\mathbf{k}) = f + g \cdot \cos \theta + (0) \cdot (3 \cos^2 \theta - 1). \quad (3.27)$$

Here  $f$  and  $g$  are spherically symmetrical in  $\mathbf{k}$ -space and therefore are functions only of electron energy.  $\theta$  is the angle between  $\mathbf{k}$  and the applied electric field causing the disturbance of the distribution function. Equation (3.27) is a good approximation for small applied electric fields when the disturbance of the distribution function is small, or in high electric fields when the scattering process is nearly elastic and does not have pronounced anisotropy. In the latter case the scattering redistributes electrons around a constant energy surface so tending to preserve the near spherical symmetry of the distribution function. Unfortunately, polar optical scattering, which is predominant for the central valley electrons of GaAs in good quality material, does not satisfy these conditions for the electron energy range of greatest interest. This arises because the polar optical phonon has an energy about 10% of the energy difference of satellite and central valleys in GaAs, and this energy is interchanged with an electron upon scattering. There is also a considerable forward scattering (Eqn (3.17)). Any calculations of transferred electron effects must be regarded with suspicion if the approximation of (3.27) is used.<sup>(32)</sup>

The solution of the Boltzmann equation proceeds as follows. Under steady conditions Eqn (3.10) holds:

$$\frac{e}{\hbar} \mathbf{E} \cdot \nabla_{\mathbf{k}} f(\mathbf{k}) = \left( \frac{\partial}{\partial t} f(\mathbf{k}) \right)_{\text{scatt}} \quad (3.10)$$

Recognizing the symmetry in  $\mathbf{k}$  space about the axis defined by  $\mathbf{E}$ , the left

hand side of (3.10) becomes:—

$$\frac{e\mathbf{E}}{\hbar} \cdot \nabla_{\mathbf{k}} f(\mathbf{k}) = \frac{e}{\hbar} |\mathbf{E}| \left\{ \left( \frac{\partial f}{\partial \mathcal{E}} + \frac{\partial g}{\partial \mathcal{E}} \cos \theta \right) \frac{\partial \mathcal{E}}{\partial |\mathbf{k}|} \cos \theta - \frac{g \sin \theta}{|\mathbf{k}|} (-\sin \theta) \right\}.$$

The terms on the right-hand side are now rearranged into a Legendre polynomial series which extends to three terms owing to the above differentiation:

$$\begin{aligned} \frac{e\mathbf{E}}{\hbar} \cdot \nabla_{\mathbf{k}} f(\mathbf{k}) = & \frac{e|\mathbf{E}|}{\hbar} \left\{ \frac{g}{|\mathbf{k}|} + \frac{1}{3} \left( \frac{\partial g(\mathcal{E})}{\partial \mathcal{E}} \frac{\partial \mathcal{E}}{\partial |\mathbf{k}|} - \frac{g}{|\mathbf{k}|} \right) \right. \\ & \left. + \frac{\partial f}{\partial \mathcal{E}} \frac{\partial \mathcal{E}}{\partial |\mathbf{k}|} \cos \theta + \frac{1}{3} \left( \frac{\partial g}{\partial \mathcal{E}} \frac{\partial \mathcal{E}}{\partial |\mathbf{k}|} - \frac{g}{|\mathbf{k}|} \right) (3 \cos \theta - 1) \right\}. \end{aligned}$$

Only the first two terms of the series are retained:—

$$\therefore \frac{e\mathbf{E}}{\hbar} \cdot \nabla_{\mathbf{k}} f(\mathbf{k}) = \frac{e|\mathbf{E}|}{\hbar} \left\{ \frac{1}{3} \left[ \frac{2g}{|\mathbf{k}|} + \frac{\partial g}{\partial \mathcal{E}} \cdot \frac{\partial \mathcal{E}}{\partial |\mathbf{k}|} \right] + \frac{\partial f}{\partial \mathcal{E}} \frac{\partial \mathcal{E}}{\partial |\mathbf{k}|} \cdot \cos \theta \right\} \quad (3.28)$$

$|\mathbf{k}|$  and  $\partial \mathcal{E} / \partial |\mathbf{k}|$  are expressed in terms of the electron energy  $\mathcal{E}$  after the explicit form of the band structure has been determined.

The scattering term on the right-hand side of (3.10) takes the following form:—

$$\left[ \frac{\partial f(\mathbf{k})}{\partial t} \right]_{\text{scatt}} = \left( \frac{\partial f}{\partial t} \right)_s + \left( \frac{\partial g}{\partial t} \right)_s \cos \theta \quad (3.29)$$

Equations (3.28) and (3.29) are substituted in (3.10) and it is evident that the coefficients of the symmetrical and drift terms must separately sum to zero, i.e.

$$\left( \frac{\partial f}{\partial t} \right)_s = \frac{e|\mathbf{E}|}{3\hbar} \frac{1}{|\mathbf{k}|^2} \frac{\partial}{\partial \mathcal{E}} \left[ g |\mathbf{k}|^2 \right] \cdot \frac{\partial \mathcal{E}}{\partial |\mathbf{k}|} \quad (3.30)$$

and

$$\left( \frac{\partial g}{\partial t} \right)_s = \frac{e|\mathbf{E}|}{\hbar} \cdot \frac{\partial f}{\partial \mathcal{E}} \frac{\partial \mathcal{E}}{\partial |\mathbf{k}|}. \quad (3.31)$$

In order to solve the coupled Eqns (3.30) and (3.31) it is necessary to make a further assumption. If the scattering mechanism satisfies the relaxation time conditions (see Appendix 2) (3.31) may be written as:

$$- \frac{g}{\tau} = \frac{e|\mathbf{E}|}{\hbar} \cdot \frac{\partial f}{\partial \mathcal{E}} \cdot \frac{\partial \mathcal{E}}{\partial |\mathbf{k}|}. \quad (3.32)$$

$\tau$  is the overall (energy dependent) relaxation time of all the scattering processes operative. (3.32) may now be inserted in (3.30) to give the differential

equation to be solved for the energy dependence of the distribution function:—

$$\left(\frac{\partial f}{\partial t}\right)_s = -\frac{e^2 |\mathbf{E}|^2}{3\hbar^2} \frac{1}{|\mathbf{k}|^2} \frac{\partial}{\partial \mathcal{E}} \left[ \tau \frac{\partial f}{\partial \mathcal{E}} \cdot \frac{\partial \mathcal{E}}{\partial |\mathbf{k}|} \cdot |\mathbf{k}|^2 \right] \frac{\partial \mathcal{E}}{\partial |\mathbf{k}|}. \quad (3.33)$$

$(\partial f / \partial t)_s$  may be calculated from the sum of expressions obtained from (3.10) for all the relevant scattering processes.

Those processes involving phonons of appreciable energy connect  $\mathbf{k}$  states with energy of  $\mathcal{E}$  and  $\mathcal{E} \pm \hbar\omega$  where  $\hbar\omega$  is the phonon energy. In order to allow for the different values of  $f$  at these energies it is assumed that the distribution function is a slowly varying function of energy and  $f(\mathcal{E} + \hbar\omega)$  may be related to  $f(\mathcal{E})$  by a Taylor expression to second order, i.e.

$$f(\mathcal{E} \pm \hbar\omega) = f(\mathcal{E}) \pm \hbar\omega \frac{\partial f}{\partial \mathcal{E}} + \frac{(\hbar\omega)^2}{2} \frac{\partial^2 f}{\partial \mathcal{E}^2}. \quad (3.34)$$

A similar approximation is made in the calculation of the relaxation time, and in this way a second order differential equation in  $f(\mathcal{E})$  is obtained from Eqn (3.33). One such differential equation exists for both the central valley and for the satellite valleys. These equations are not independent however because:—

$$\left(\frac{\partial f}{\partial t}\right)_s = \sum_{\text{all processes}} \left(\frac{\partial f}{\partial t}\right)_{\text{scatt}} \quad \text{and} \quad \frac{1}{\tau} = \sum_{\text{all processes}} \frac{1}{\tau}$$

and each of these terms involves intervalley scattering. In this way the differential equation of each valley type contains the distribution function of both valleys at the implied electron energy. The resulting two coupled linear second order differential equations are solved by numerical integration. The scattering mechanisms invoked by Conwell and Vassell were polar and space charge scattering within the central valley which was non-parabolic, intervalley scattering between the central and satellite valleys, and polar, acoustic and equivalent intervalley scattering within the satellite valleys. For full details of the calculation the reader is referred to the excellent summary article by Conwell and Vassell.<sup>(4)</sup>

The form of the distribution functions obtained from the calculation are shown in Fig. (3.11). The log-linear plot chosen results in a straight line for a Maxwellian form of distribution function with the slope determined by the electron temperature of the distribution. It is seen that the distribution in the central valley is strongly non-Maxwellian below the threshold energy and it shows a strong streaming effect which rises from the decreasing

effectiveness of polar optical scattering at high fields. At higher electron energies in the central valley the distribution function becomes Maxwellian. The satellite valley electrons have a Maxwellian distribution at all energies with a temperature which follows that of the high energy central valley electrons. This arises from the scattering of the hot electrons from central to satellite valleys. The velocity-field curve is calculated from the following expression:—

$$|\mathbf{v}| = \frac{1}{\hbar} \sum_{\mathbf{k}} g \cos \theta \cdot \frac{\partial \mathcal{E}}{\partial |\mathbf{k}|}, \quad (3.35)$$

$g$  is obtained from the symmetrical part of the distribution function, discussed above, with the aid of Eqn (3.31). These calculations were sensitive to the assumed value of  $D_{12}$ , the intervalley coupling coefficient. Comparison of the number of electrons in the satellite valleys with the results of Gunn and Zilberstein<sup>(33)</sup> under pre-threshold conditions, the non-occurrence of a low field avalanche at approximately 4 kV/cm and the low threshold electric field predicted for low  $D_{12}$  all suggested that the most reasonable value of  $D_{12}$  is about  $5 \times 10^8$  eV/cm.

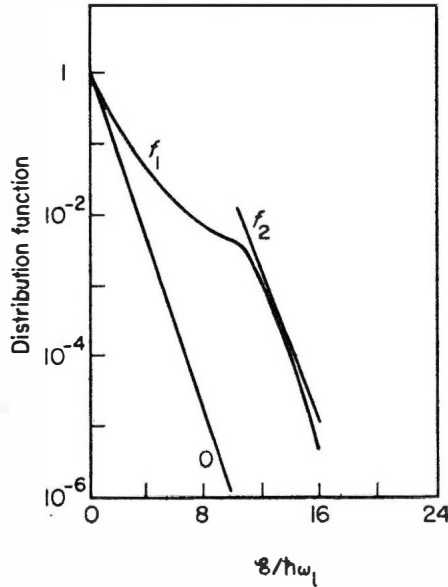


FIG. 3.11. Distribution functions for electrons in the central valley ( $f_1$ ) and in the satellite valleys ( $f_2$ ) for an electric field of 2.4 kV/cm (Conwell and Vassell<sup>(4)</sup>).  $D_{12} = 5 \times 10^8$  eV/cm,  $D_{22} = 10^9$  eV/cm and non-parabolicity of the central valley is included. 0 is the Maxwell-Boltzmann distribution in zero field.  $\hbar\omega$  is the longitudinal optical phonon energy.

The threshold electric field of these calculations is generally low compared with experiment. Attempts were made to explain this by introducing the

Table 3.1

	Butcher and Fawcett	Conwell and Vassell
$m_1^*$ light electron mass	$0.067 m_0$	$0.072 m_0$
$m_2^*$ heavy electron mass. (Geometric mean) (Density of states)	$0.4 m_0$ not required	$0.36 m_0$ $1.2 m_0$
$\frac{\epsilon_s}{\epsilon_0}$ low frequency relative permittivity	12.53	13.5
$\frac{\epsilon_\infty}{\epsilon_0}$ high frequency relative permittivity	10.82	11.6
$\hbar\omega_l$ longitudinal optical phonon energy at $k = 0$	0.0354 eV or 410°K	0.036 eV or 418°K
$\hbar\omega_i$ longitudinal optical phonon energy for inter-valley transfer	0.03 eV or 348°K	0.029 eV or 336°K
$\hbar\omega_s$ satellite inter- valley phonon energy	0.03 eV or 348°K	0.025 eV or 290°K
$\Xi_1$ deformation potential for central valley	7 eV	neglected
$\Xi_2$ deformation potential for satellite valleys	7 eV	10.3 eV longitudinal 8.8 eV transverse
$D_{12}$ coupling constant for central to satellite scattering	$5.35 \times 10^8$ eV/cm	$5 \times 10^8$ eV/cm
$D_{22}$ coupling constant for satellite intervalley scattering	$10^9$ eV/cm	$10^9$ eV/cm
$s$ sound velocity	$5.22 \times 10^5$ cm/sec.	$5.22 \times 10^5$ cm/sec
$\rho$ density	$5.37$ g/cm <sup>3</sup>	$5.31$ g/cm <sup>3</sup>

effects of a non-parabolic central valley and space charge scattering. Figure 3.12 shows the results for  $D_{12}$  with a parabolic central valley, with a non-parabolic central valley and with sufficient space charge scattering to reduce the low field mobility to 5500 (typical of bulk grown material).

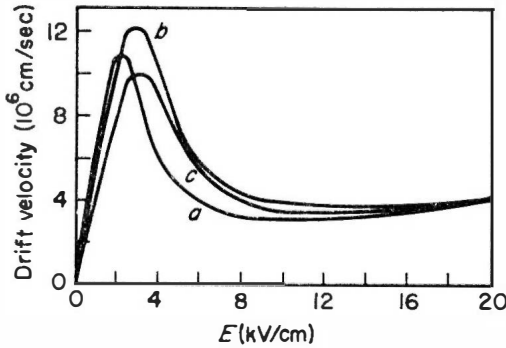


FIG. 3.12. Velocity-field curves (Conwell and Vassell<sup>(4)</sup>) at room temperature with  $D_{12} = 5 \times 10^8$  eV/cm. (a) for parabolic central valley; (b) for non-parabolic central valley; (c) with space-charge scattering and parabolic central valley.

### (iii) Comparison of the approximate solutions of the Boltzmann equation

The comparison of the velocity-field curves derived by Butcher and Fawcett and by Conwell and Vassell is facilitated by the almost identical values of the transport coefficients they each used. These are summarised in Table 3.1.

The velocity-field curves of both calculations are qualitatively very similar, but the Conwell and Vassell treatment gives threshold and post-threshold velocities which are about half that of the Butcher and Fawcett treatment. Also the threshold field for the onset of negative differential resistance is somewhat lower for the former treatment. It is impossible at this stage to decide which treatment, if any, gives the more reliable result. An appeal to experiment would appear to provide the answer to this question and this shows good agreement with the velocities of Butcher and Fawcett.

The approach of Butcher and Fawcett is certainly not justified for the range of electron densities occurring in real devices. Conwell and Vassell start from much firmer ground but the approximations necessary to obtain a solution considerably reduces this strength. In particular the assumption of a nearly isotropic distribution function is only true for scattering processes which provide a vanishingly small energy change when the electron momentum is randomised. The polar scattering predominant in the central valley certainly does not fulfil the conditions assumed in either theory, and will lead to a pronounced "streaming" of the electron velocities. This led Stenflo<sup>(32)</sup> to attempt a solution by assuming the "maximum anisotropy" distribution



function for the electrons.<sup>(34)</sup> Again however the approximations necessary to attempt a solution are overwhelming.

Crudely, the true velocity-field curve may be expected to lie between the results of Butcher and Fawcett and of Conwell and Vassell. The enforced Maxwellian form assumed in the former case will underestimate the number of high energy electrons present in the actual case of a "streaming" distribution function. The poor approximation of small energy exchange in electron scattering necessary to use the nearly isotropic distribution function results in an overestimate of the number of high energy electrons by Conwell and Vassell. Because the high energy electrons are the ones predominantly concerned with intervalley transfer near the threshold electric field we may expect this quantity to be overestimated by Butcher and Fawcett and underestimated by Conwell and Vassell.

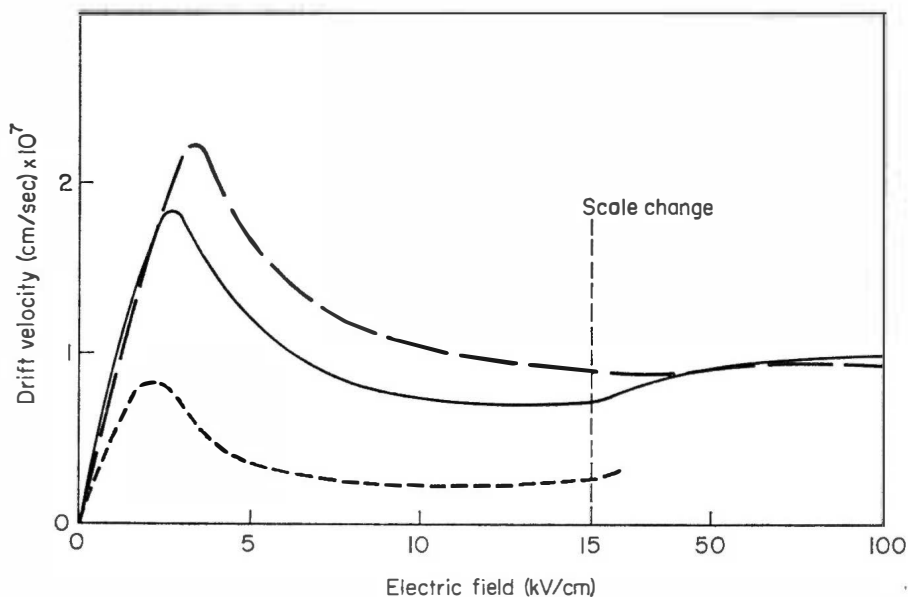


FIG. 3.13. Comparison of the calculated velocity-field relationship for *n*-type gallium arsenide using the Monte Carlo method (full curve), the Butcher and Fawcett displaced Maxwellian distribution function (broken curve) and a Conwell and Vassell calculation. The parameters for each calculation are essentially the same as given earlier.

A difficulty inherent in both calculations is that it is impossible to estimate the magnitude of the errors introduced by the respective assumptions. In order to overcome all the above difficulties another approach to the problem has been taken and is described in the next section.

### 3.7 MONTE CARLO CALCULATION OF THE VELOCITY-FIELD CHARACTERISTIC

The previous calculations have attempted to determine the electron distribution function by calculating the dynamic equilibrium properties of all electrons at one fixed time. In the treatment of this section the behaviour of one electron over a long time is studied in order to obtain its distribution function over all allowable  $\mathbf{k}$ -states. The equivalence of these two approaches has been dealt with in the theory of noise processes.<sup>(36)</sup> The approach to be described derives its strength from its natural suitability for computer calculation through Monte Carlo techniques. The basic idea is to follow the random motion of an electron through  $\mathbf{k}$ -space and log the time that the electron spends in each  $\mathbf{k}$ -state. The distribution function is directly proportional to this "visiting" time. The technique was first applied by Kurosawa<sup>(37)</sup> to studies of  $p$ -type germanium and has been adapted to the electron transport problem in GaAs by Boardman, Fawcett and Rees.<sup>(38)</sup> Both problems encounter similar difficulties in the conventional Boltzmann approach. A detailed description of the technique was later given by Fawcett, Boardman and Swain.<sup>(72)</sup> This paper also gives a good review of the transport properties and their uncertainties in gallium arsenide.

The time of free flight of an electron between scattering events and the scattering it undergoes are determined by the following procedure:—

- (i) An electron which has just been scattered to an initial  $\mathbf{k}$ -state  $\mathbf{k}_{in}$  is accelerated through  $\mathbf{k}$ -space by the applied electric field  $\mathbf{E}$ , according to the relation:—

$$\mathbf{k} = \mathbf{k}_{in} + \frac{e \mathbf{E} t'}{\hbar} \quad (3.36)$$

where  $\mathbf{k}$  is the  $\mathbf{k}$ -state after time  $t'$ .

- (ii) The time of free flight,  $t$ , is determined by a computer-generated random number whose probability distribution is that of the time of free flight. This distribution is calculated from the summation of the scattering probabilities of all processes (as described in Sections 3.4 and 3.5) and is as follows:—

$$P(t) = \sum_i \lambda_i[\mathcal{E}(t)] \exp \left\{ - \sum_i \int_0^t \lambda_i[\mathcal{E}(t')] dt' \right\} \quad (3.37)$$

$\lambda_i(\mathcal{E})$  is the total scattering rate due to mechanism  $i$  at energy  $\mathcal{E}$  and is a function of energy alone for bands with spherical constant energy surfaces.

$$\lambda_i(\mathcal{E}) = \sum_{\mathbf{k}'} S_i(\mathbf{k}, \mathbf{k}') \quad (3.38)$$

where  $S_i(\mathbf{k}, \mathbf{k}')$  is the scattering rate from  $\mathbf{k}$  to  $\mathbf{k}'$  as defined in Section 3.4.

- (iii) After the time of free flight has been determined another random number is generated to decide the state to which the electron is scattered. This state becomes the initial state of the next free flight and the process is repeated. The probability distribution of this random number follows that for the scattering to the final state due to all scattering processes.

In order to maintain computer time for the calculation within reasonable bounds it is convenient if the integral in the exponent of equation 3.37 can be evaluated analytically. Otherwise the integration has to be performed for each free flight, or the numerical values of the integral have to be tabulated. The former involves a considerable waste of computer time and can make the problem impractical, and the latter involves considerable storage space within the computer to make a fine enough mesh of points in  $\mathbf{k}$ -space for accurate computation. Most scattering processes allow analytic solution of the integral but the important polar scattering does not. To overcome this difficulty a physically insignificant scattering process is introduced which makes the integral soluble. This process has a scattering rate which does not change  $\mathbf{k}$  and is given by:—

$$S(\mathbf{k}, \mathbf{k}') = \left[ \Gamma - \sum_i \lambda_i(\mathcal{E}) \right] \delta(\mathbf{k} - \mathbf{k}') \quad (3.39)$$

The  $\delta$ -function is zero for  $\mathbf{k} \neq \mathbf{k}'$  and unity for  $\mathbf{k} = \mathbf{k}'$ .  $\Gamma$  is an arbitrary positive number and under this condition (3.37) becomes:

$$P(t) = \Gamma e^{-\Gamma t}. \quad (3.40)$$

This simplification appears very attractive for general use. However, there is one disadvantage introduced. The internal scattering events add to the visiting time of each  $\mathbf{k}$ -state in direct proportion to the visiting time due to all real scattering processes and so do not alter the distribution function. They do consume computational time and the advantage over direct numerical integration in equation 3.37 could be lost and the calculation rendered impractical if they were used indiscriminantly.

$\mathbf{k}$  space is divided into a finite mesh in the computer and the visiting times to each point are accumulated throughout the calculation. The histogram (distribution function) so obtained converged to an invariant form after about 50,000 real scattering events. The drift velocity is calculated by accumulating the velocities during each flight. This continuous accumulation principal can be applied to the estimate of any physical variable depending on an integration over the distribution function.

The calculated velocity-field curve is shown in Fig. 3.14. It was obtained with the same parameters that were used in the previous displaced Maxwellian calculation of Butcher and Fawcett with which it is compared. The curves show close similarity of form, but the Monte Carlo calculation predicts a lower threshold voltage and lower post-threshold current than the Butcher and Fawcett calculation. Both these quantities are significantly higher than those from the calculations of Conwell and Vassell. These discrepancies are consistent with the underestimate of the number of high energy electrons in the Butcher and Fawcett calculation, and the overestimate by Conwell and Vassell as discussed in Section 3.6(iii). The distribution function is found to be non-Maxwellian below threshold and assymetric in  $k$ -space, with a drift velocity which approaches the thermal velocity at electric fields below and above the threshold field. Both the previous approximations are therefore invalid. Many of the later calculations of device properties will, for historical reasons, use the results of the earlier approximations, and due account of their accuracy will have to be taken. For many purposes the errors involved will be insignificant.

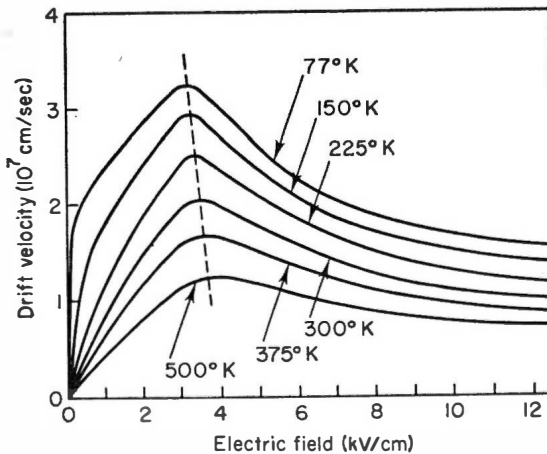


FIG. 3.14. Calculated temperature dependence of the electron velocity-field characteristic in intrinsic gallium arsenide (Ruch and Fawcett<sup>(68)</sup>).

Further calculations of the temperature and impurity dependence of the velocity-field characteristic have been carried out by Ruch and Fawcett<sup>(37)</sup> using the Monte Carlo technique. The parameters were essentially the same as those given in Table 3.1. In intrinsic material it was found that the threshold field only changed from 3.1 kV/cm at 77°K to 3.7 kV/cm at 500°K, while the maximum negative differential mobility reduced from 4200

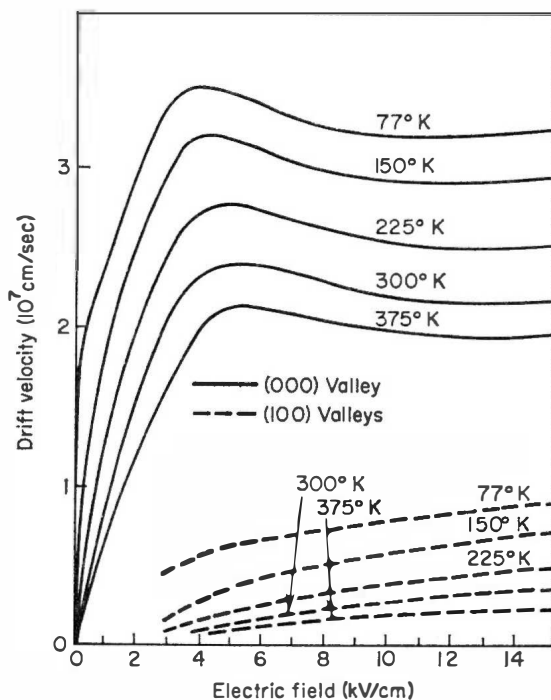


FIG. 3.15. Temperature dependence of the drift velocity in the  $\langle 000 \rangle$  and  $\langle 100 \rangle$  valleys as functions of field strength (Ruch and Fawcett<sup>(68)</sup>).

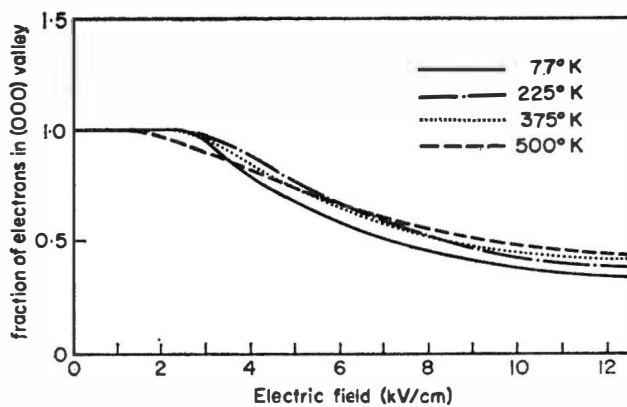


FIG. 3.16. Fraction of electrons in the  $\langle 000 \rangle$  valley as a function of field strength at various temperatures (Ruch and Fawcett<sup>(68)</sup>).

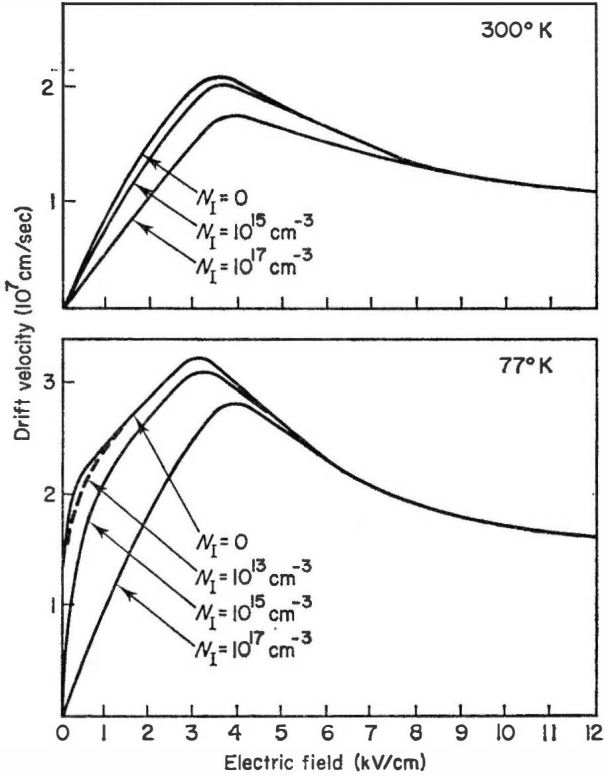


FIG. 3.17. The influence of ionized impurity scattering on the velocity-field characteristic (Ruch and Fawcett<sup>(68)</sup>).

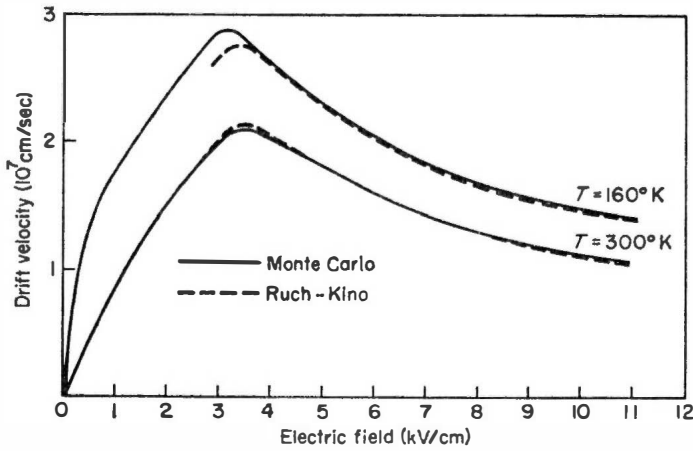


FIG. 3.18. Comparison of the measured and calculated velocity-field characteristics at 150°K and 300°K (Ruch and Fawcett<sup>(68)</sup>).

to  $1000 \text{ cm}^2/\text{Vsec}$  over the same temperature range. The velocity-field characteristics are shown in Fig. 3.14. Variation of drift velocity within the separate valleys and the population ratio of central and satellite valleys is shown in Figs 3.15 and 3.16, respectively, for various temperatures. (Compare Fig. 3.16 with Fig. 3.8). The effect of impurity scattering on the velocity-field characteristic at  $77^\circ\text{K}$  and  $300^\circ\text{K}$  is illustrated in Figure 3.17. The excellent agreement between theory and the experiments of Ruch and Kino<sup>(64)</sup> is clear from Fig. 3.18. The calculations were carried out for pure material and the divergence of theory and experiment near threshold for  $T = 160^\circ\text{K}$  is probably an indication of the unknown impurity concentration in the devices. An empirical relationship which fits the velocity-field characteristic within 5% from  $300^\circ\text{K}$  to  $600^\circ\text{K}$  (relevant to practical device operation) is:—

$$v = \frac{2.25 \times 10^9 E}{T} \frac{\left\{ 1 + \frac{0.265(E/E_0)^3}{1 - 5.3 \times 10^{-4} T} \right\}}{\left\{ 1 + \left( \frac{E}{E_0} \right)^4 \right\}}$$

$E$  is in units of  $\text{kV/cm}$  and  $E_0$  is  $4 \text{ kV/cm}$  giving a threshold field of  $3.5 \text{ kV/cm}$ .

### 3.8 THE IMPORTANCE OF THE VELOCITY-FIELD CHARACTERISTIC AND ENERGY RELAXATION EFFECTS

The treatment so far has considered the electron equilibrium dynamics in a temporally and spatially invariant electric field. For the device applications of later chapters it is necessary to know the electron behaviour in electric fields without these restrictions. The correct approach to this problem is to start from fundamentals as we did with the Boltzmann equation or with the Monte Carlo approach and calculate directly the electron transport properties for the appropriate conditions. This would involve the treatment of a distribution function with temporal and spatial variation and, as will be seen later, the necessity for accurate treatment of these variations as large signal quantities. In view of the difficulties experienced with the relatively simple uniform field conditions the problem is formidable. The usual approach is to bypass the problem and assume that the mean electron drift velocity and other transport properties are single valued functions of the electric field with the former given by the velocity-field curve which we have derived for uniform conditions. Under what conditions is this an accurate approximation?

Let us apply a step function increase of electric field (otherwise uniform) to a sample of GaAs. Momentarily there is an imbalance in Eqn (3.10) between the acceleration of electrons through  $\mathbf{k}$ -space and the redistribution of electrons in  $\mathbf{k}$ -space by collisions. This situation persists for about the time it takes to randomize the electron velocity (the momentum relaxation time). This time,  $\tau_m$ , may be estimated from the mobility of electrons,  $\mu$ , their effective mass,  $m^*$ , and their charge,  $e$ , :—

$$\mu = \frac{e \tau_m}{m^*}.$$

For the electrons in the central valley  $\tau_m$  is approximately  $10^{-13}$  sec and is less for electrons in the satellite valleys. The time for transfer of electrons (with the energetic capability) between the central and satellite valleys is also in this momentum scattering category. It has been estimated from the intervalley coupling constants to be  $10^{-11}$  sec to  $10^{-13}$  sec.<sup>(4)</sup> For events whose time scale is shorter than these momentum scattering processes electrons cannot change their state and no transferred electron effects would be observed. When the time scale is longer the equilibrium balance of the scattering and accelerative forces described by Eqn (3.10) is maintained. However, this is only a quasi-static balance. It has been mentioned earlier that many more collisions are usually required to deliver the electronic kinetic energy to the lattice than to randomize the momentum. The electron velocity is predominantly redirected with, on average, only a small decrease in its magnitude. This redirection causes a general increase of the kinetic energy, or a heating, of the electron system until the mean collision rate with the lattice has risen sufficiently to balance the increased supply of energy to the electrons from the increased electric field. The characteristic time for this thermal readjustment is known as the energy relaxation time,  $\tau_\epsilon$ . At this point it should be noted that the thermal effects are in the electron system only and the lattice temperature is unaltered. If the time scale of any device effect is shorter than  $\tau_\epsilon$  then the transport properties (drift velocity, diffusion etc.) will not be single valued functions of the applied electric field, and must be related to the instantaneous value of the distribution function. If this is Maxwellian, so that a temperature can be assigned to the electrons, then the transport properties become single valued functions of the electron temperature. In this case a full solution of the Boltzmann equation is required. These effects have been considered by Stratton<sup>(40)</sup> in some detail for junction devices. If the time scale of the effects is longer than  $\tau_\epsilon$  then the transport properties are single valued functions of the electric field, and the velocity-field characteristic is a valid representation of the drift velocity.



The above considerations have shown that processes must take place more slowly than the energy relaxation time for a relatively simple treatment of the transport properties. The energy relaxation time has a more fundamental significance than this. For intervalley transfer to take place the electrons in the central valley must have a greater energy, relative to the band edge, than the energy separation of central and satellite valleys. After application of the step increase of electric field the additional electrons to be transferred to the satellite valleys cannot make the transition until their energy has increased sufficiently to allow the transfer. Therefore energy relaxation could be the limiting process for the upper frequency limit of transferred electron devices.  $\tau_e$  has been estimated by Das and Bharat<sup>(41)</sup> to be about  $10^{-12}$  seconds. They used a small signal approach in a displaced Maxwellian approximation. Rees<sup>(42, 69)</sup> has given a more accurate treatment which requires no *a priori* knowledge of the distribution function. The response of the electron distribution to a step change in electric field was Fourier analysed to give the frequency response. Heating processes in the central valley, where polar scattering gives slow velocity randomisation, control the response of the negative differential conductivity. The negative differential mobility is illustrated as a function of electric field for D.C., 35 GHz and 140 GHz in Fig. 3.19.<sup>(71)</sup> The same parameters were used in this calculation as in the Monte Carlo calculation of the velocity-field characteristic.

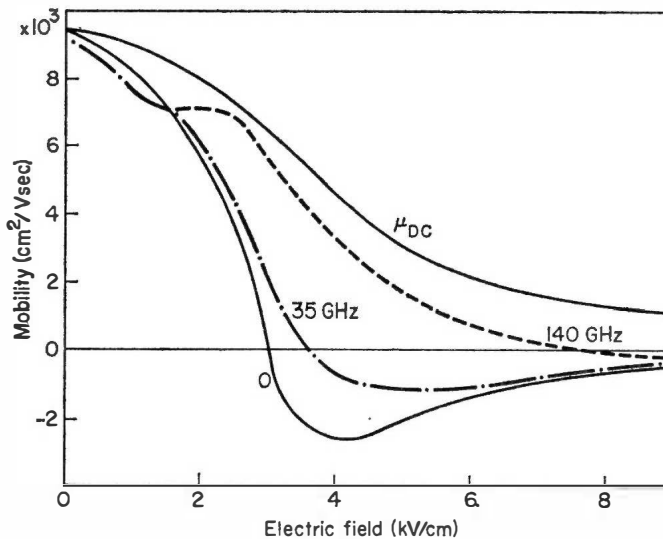


FIG. 3.19. Field dependence of the differential mobility at zero frequency, 35 GHz, and 140 GHz. The D.C. mobility is included for comparison (Rees<sup>(71)</sup>). (Crown Copyright, reproduced by permission of the controller of Her Majesty's Stationery Office.)

The calculational technique used by Rees was an alternative computer technique to the Monte Carlo method which also avoided solution of the Boltzmann equation. It exploited the stability of the steady state distribution function in the following manner.  $\mathbf{k}$ -space was divided into cells as in the Monte Carlo technique. Any arbitrary distribution of electrons over these cells was introduced at the start of the calculation. From each cell in turn the electrons were "scattered" to all other cells according to  $S(\mathbf{k}, \mathbf{k}')$  and a chosen time step (small enough to avoid finite element inaccuracies). The process was then iterated until (for constant electric field) the form of the distribution became invariant. A great advantage of this process is that it allows calculation of the time variation of the distribution function and its physical observables when there is a time-varying external influence.

An instructive estimate of the minimum time required to heat the electron distribution in the central valley under large signal conditions can be obtained from a very crude model. The fraction of the electron energy lost at each collision has been shown to be a small fraction<sup>(4)</sup> of the total kinetic energy in the central valley. We simply neglect all the electronic collisions and calculate the time taken to accelerate an electron from the bottom of the central valley until its energy is sufficient for intervalley transfer. The electric field is taken as the threshold field. This simple calculation is directly relevant to the limiting characteristic time taken to make electrons "climb" up the central valley and become available for intervalley transfer. The time variation of the kinetic energy,  $\mathcal{E}_v$ , of an electron accelerated from rest in an electric field  $E$  is:—

$$\mathcal{E}_v = \frac{e^2 E^2}{2m^*} \cdot t^2$$

for

$$\mathcal{E}_v = 0.36 \text{ eV} \quad \text{and} \quad E = 3.5 \text{ kV/cm.}$$

then

$$t = 1.5 \times 10^{-12} \text{ sec.}$$

This time is of the same order as that obtained from rigorous calculation where collisions increase its value.

### 3.9 MEASUREMENT OF THE VELOCITY-FIELD CHARACTERISTIC

When a sample of gallium arsenide is biased into the negative differential resistance region of the velocity-field curve the spatial distribution of the electric field becomes unstable. This subject will be dealt with in Chapter 4 where two broad categories of behaviour emerge. If the product of electron density,  $n$ , and device length,  $l$ , is greater than a critical value lying between

$10^{11} \text{ cm}^{-2}$  and  $10^{12} \text{ cm}^{-2}$  the electric field assumes a highly non-uniform shape (the domain) which travels towards the anode of the device. A further condition on the value of  $nl^2$ , treated in Chapter 4, is satisfied for all practical devices which exceed the critical “ $nl$ ” product. If the “ $nl$ ” product is less than the critical value the travelling non-uniformity does not form, but the electric field exhibits a large static distortion.

Both of these effects cause considerable difficulty in the measurement of the velocity-field curve owing to the simultaneous involvement of a large range of both quantities. Measurement techniques take account of the above considerations and fall into three categories. (i) Sub-threshold measurements which do not encounter the above difficulties. (ii) High speed measurements made in a time shorter than the formation time of the non-uniformities. (iii) Measurements on sub-critically doped devices.

#### (i) *Sub-threshold measurements*

In long samples of GaAs the sub-threshold current-voltage characteristic is substantially linear. If the formation of electric field instabilities is used as a gauge of the onset of negative differential resistance we have a simple method of measuring the threshold field, providing that the device is uniform. In order to check the last point it is necessary to probe the electric field distribution along the sample. Careful measurements of these quantities have been carried out by Gunn<sup>(43)</sup> who found that some samples exhibited a stationary non-uniformity close to the cathode which is known as the “cathode drop”. The electric field in this region can be five times the field in the rest of the device, and it is unwise to trust simple current-voltage measurements to determine the threshold field. The origin of the cathode drop is not clear but appears to be related to impurities or imperfect contact technology. It has been suggested that it may be the type of stationary “domain” considered by Boer<sup>(44)</sup> for impure materials. After eliminating results which were untrustworthy due to electrical non-uniformity Gunn estimated that the true threshold field lay between 3.6 kV/cm and 3.8 kV/cm and was independent of the sample length.

In shorter samples the non-uniform fields at contacts play a proportionally greater part in the determination of the sub-threshold current-voltage relation. However devices less than a few tens of microns long may be prepared with epitaxial techniques which are capable of producing material which is much purer than the bulk material of the long devices. The sub-threshold current-voltage relation of these devices usually shows a greater curvature than that of the long devices, and the threshold field apparently increases as the device length decreases. After correction for voltage drop in the substrate, doping tails and contact resistance, Brady *et al.*<sup>(45)</sup> found that the threshold field for all samples was  $(3.2 \pm 0.2) \text{ kV/cm}$ . The peak

velocities in both long and short samples is estimated to be about  $2 \times 10^7$  cm/sec. This latter measurement is complicated by the necessity of accurate knowledge of device electron density in the above techniques.

The fraction of electrons which have transferred to the satellite valley below threshold can be estimated with Hall effect measurements. Zylbersztejn and Gunn<sup>(45)</sup> concluded from such measurements that only a small fraction of electrons (about 1% at 2 kV/cm) are in the satellite valleys below threshold. This result is in good agreement with the displaced Maxwellian calculations of Butcher and Fawcett.

#### (ii) *High speed measurements above threshold*

The characteristic rate for the formation of electric field non-uniformities is the negative differential dielectric relaxation time,  $\tau_n$ , of the material. This depends inversely on electron density and the negative slope at the bias point of the velocity-field curve and is treated in Chapter 4. The maximum slope of all the theoretical velocity-field curves is about the same and can be used to indicate the minimum value of  $\tau_n$  to be expected. A typical value of  $\tau_n$  is  $30 \times 10^{-12}$  sec for an electron density of  $10^{14}$  cm<sup>-3</sup> (corresponding to good quality 10  $\Omega$  cm GaAs at room temperature). If measurements of device current (for electron drift velocity) can be made in a time shorter than  $\tau_n$  the distortion of the internal electric field should be negligible. Fast pulse and high field microwave techniques have been used to satisfy this condition.

Gunn and Elliot<sup>(47)</sup> have generated fast pulses of 250 picoseconds duration by discharging a superconducting transmission line with a bouncing ball switch through the sample gallium arsenide under test. The switch was chosen for its extremely high speed of operation, and the transmission line was fabricated in superconducting material to reduce frequency dispersive effects associated with resistive loss. By these means rise times of about 40 picoseconds were obtained. Because measurements must be made in a time comparable with the dielectric relaxation time the flow of displacement current through the sample is of the same order as the required drift component. In order to measure the latter alone readings are taken when the rate of change of voltage across the device is zero. The current flow is then the drift component only, providing that there is no appreciable space charge injection and the large signal readjustment of the internal electric field has not commenced. Initial measurements were inaccurate owing to the latter effect, and it is necessary to check that  $\tau_n$  calculated from the measured velocity-field characteristic is appreciably longer than the period of measurement. Results are shown in Fig. 3.20.

An alternative way of generating high speed excursions into the negative differential mobility region is through the use of high power microwave

signals. The sample under investigation is placed across the centre, between the broad walls, of a waveguide. The relation between the small A.C. current and voltage applied to the device is measured for a range of microwave electric fields whose amplitude is great enough to exceed threshold in each cycle. The D.C. or mean current,  $J$ , through the sample in a large microwave field,  $E_i \sin \omega t$ , and a small D.C. field  $E_0$  is:—

$$J = \frac{1}{2\pi} \int_0^{2\pi} J(E_0 + E_i \sin \omega t) d(\omega t).$$

By Taylor expansion:—

$$J = \frac{1}{2\pi} \int_0^{2\pi} \{J(E_i \sin \omega t) + (dJ/dE) E_0\} d(\omega t) \quad (3.41)$$

The first term of the right-hand side will only be zero if the sample has an ideal antisymmetrical  $J$ - $E$  characteristic. Otherwise it will contribute a rectified D.C. current which is independent of  $E_0$ , providing  $E_i$  is independent of  $E_0$ . The velocity-field characteristic is the curve which, after use in the evaluation of the time variation of  $dJ/dE$  in the second term of the right hand side of (3.41), generates the best fit to the experimental relationship of  $J$  and  $E_0$ .  $E_i$  is determined from the power transmitted past or reflected from the sample.

Some care is required with the mounting of the sample in the waveguide. If it is short and its contacts are within the microwave field there is a danger of rectified currents from non ideal contacts adding to  $J$ . If the sample is long and is mounted through two holes in the broad walls of the waveguide, the contact regions are outside the microwave field. The effect of non-uniform fields at the mounting holes in the waveguide can be reduced by making these holes, and the lateral device dimensions, small compared with the sample height in the waveguide.

We have already pointed out the importance of making these high speed measurements in a time shorter than  $\tau_n$ . In addition the measurements must not be made in a time shorter than is necessary for the electron distribution function to reach equilibrium. The discussion of Section 3.8 has shown that this time is the energy relaxation time which is having appreciable effect above approximately 10 GHz rates. These two conflicting conditions can only be accurately met in material with a low field resistivity of somewhat greater than  $10 \Omega \text{ cm}$ . Otherwise the internal readjustment of the electrical field in the sample will be well advanced before the mean velocity for the applied electric field has reached an equilibrium state. The results reported by Acket<sup>(48)</sup> and Hamagachi *et al.*<sup>(49)</sup> would appear to involve some energy relaxation effects from these considerations. The measurements by Braslau<sup>(50)</sup>

and Kalashnikov *et al.*<sup>(51)</sup> were made on higher resistivity material (10 to 20  $\Omega$  cm) but the purity of that of the latter was poor.

After imposing the above restrictions it is also necessary that a non-uniform electric field distribution does not build up over many R.F. cycles. If the non-uniformity arising in each cycle can be treated as a small signal the growth of the non-uniformity during the time that the mean field exceeds threshold must be less than the damping during the time below threshold. If  $t^+$  is the time below and  $t^-$  the time above threshold the condition is:—

$$\frac{t^+}{\tau_p} > \frac{t^-}{\tau_n}$$

where  $\tau_p$  is the low field dielectric relaxation time. Some representative results of the microwave measurement of the velocity-field characteristic are shown in Fig. 3.20.

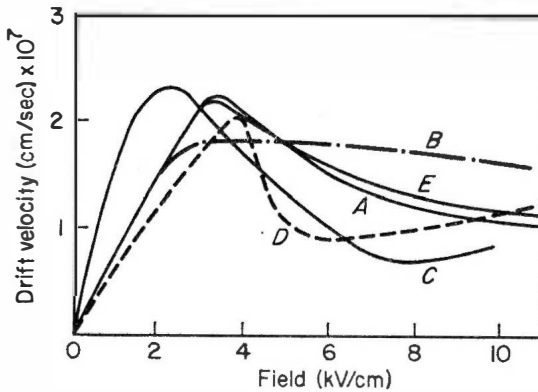


FIG. 3.20. Velocity-field characteristics for gallium arsenide. A, calculated by Butcher and Fawcett; B, measured by Gunn and Elliot; C, measured by Chang and Moll; D, measured by Thim; E, measured by Ruch and Kino.

### (iii) Measurements in sub-critically doped material

There are two basic techniques in this section. The first group involves measurements in semi-insulating gallium arsenide with a resistivity of  $10^6$ – $10^8$   $\Omega$  cm in which the electric field distribution is essentially uniform. The second group of techniques applies to materials in which there is an appreciable static distortion of the electric field by space charge.

Chang and Moll<sup>(52)</sup> have measured the photo current induced in a Schottky barrier photo diode. The diode consisted of an intrinsic piece of GaAs with a reversed biased, evaporated gold contact. The other contact

was an  $n^+$  ohmic contact. Only a very small reverse bias was required to completely deplete the intrinsic region, indicating that the higher bias used in the subsequent experiments produced an electric field which was not rendered non-uniform by depletion. A 50 nanosecond pulse of light from a GaAs laser was transmitted by the thin (150 Å) gold contact and produced electron-hole pairs at the junction interface. The holes were immediately swept into the gold contact and the electrons drifted through the intrinsic gallium arsenide under the influence of the applied bias until they were trapped at some impurity site. The trapping rate was too high to allow the electrons to drift through the entire intrinsic region. Under the assumption of a field independent time of flight before trapping the photo-current is directly proportional to the electron velocity. Chang and Moll measured this current as a function of reverse bias and obtained a velocity-field relation with an arbitrary velocity scale. The measurements were limited to 50 nanoseconds duration in order to avoid appreciable distortion of the bias electric field by the accumulating trapped electron space charge and to avoid the possibility of electron re-emission from the trapping sites. The intensity of the laser light was also maintained low enough to avoid the build up of appreciable trapped space charge. The results of this measurement scaled to the Butcher and Fawcett peak velocity are shown in Fig. 3.20.

Ruch and Kino<sup>(53)</sup> have also carried out measurements on the intrinsic region of reverse biased diodes but were fortunate in obtaining better quality material whose trapping time was long enough to allow a large fraction of the electrons to drift straight through the semi-insulating region. Their diodes had a junction consisting of a thin (less than 1000 Å) evaporated silicon dioxide film on the intrinsic gallium arsenide with a thin (again less than 1000 Å) evaporated gold contact on the silicon dioxide. This construction avoided any electron injection. The reverse contact was  $n^+$  and ohmic. A very short pulse of electrons (0.1 nanoseconds) was directed onto the gold contact of the sample by rapidly sweeping an electron beam past a small aperture in line with the sample. This injected pulse of electrons penetrated to the gallium arsenide and then drifted under the influence of the reverse electric field towards the  $n^+$  contact. As in the previous technique the injected charge must be small enough to avoid appreciable space charge distortion of the electric field. Current flow is observed in the external circuit for the duration of the electron flight across the intrinsic region. The rise time of this current pulse is determined by the width of the injected space charge bunch. The fall time is increased by spreading of the injected bunch of electrons during transit. This difference of rise and fall times may be used to estimate the diffusion constant (and its electric field dependence). A typical current pulse is shown in Fig. 3.21. The current decrease through the pulse arises from some electron trapping. The time of flight is quite well

defined by the rise and fall of the current pulse so allowing a direct determination of the electron drift velocity as a function of electric field. The results, which show excellent agreement with the Butcher and Fawcett theoretical characteristic, are illustrated in Fig. 3.20. A comparison of the temperature variation of the characteristic with the better calculations of Ruch and Fawcett has already been given in Fig. 3.18.



FIG. 3.21. Induced current in the experiment of Ruch and Kino. The difference of rise and fall times arises partly from diffusion within the injected charge pulse. The current decay through the pulse arises from trapping effects.

In anticipation of later requirements, the electric field dependence of the diffusion coefficient as determined from the difference of the fall time and rise time of the injected current pulse is illustrated in Fig. 3.22.<sup>(64)</sup> This is compared with the results predicted by Butcher and Fawcett using a two term Einstein relation between the electron mobility in each valley and the diffusion coefficient:—

$$D(E) = \left( \frac{n_1 \mu_1 T_1 + n_2 \mu_2 T_2}{n_1 + n_2} \right) \frac{k_B}{e}. \quad (3.26)$$

The discrepancy between the measured and predicted results may be, in part at least, ascribed to the neglect in (3.26) of the interchange of an

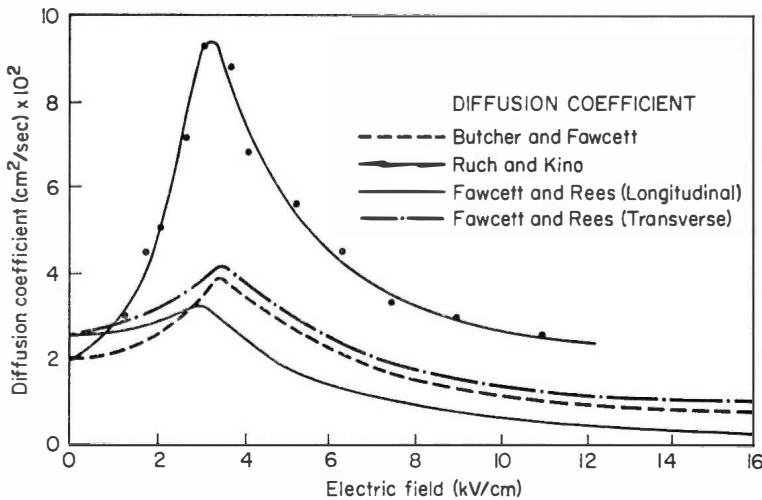


FIG. 3.22. Comparison of measured and calculated diffusion coefficients.



electron between the light and heavy mass state as well as to experimental inaccuracies. An additional term must be included in (3.26) to account for the continuous fluctuations of electrons between each state, because the light electrons drift more rapidly than the mean drift velocity, whereas the heavy electrons drift more slowly. The width of a "pulse" of charge is then related to the mean time between transfer of electrons from the light to heavy state, and vice versa. However, a Monte Carlo calculation<sup>(70)</sup> of the diffusion coefficient indicates lower values than are measured, as shown in Fig. 3.22, and it includes the intervalley effects.

The second type of measurement on subcritically doped diodes has been made by Thim<sup>(54)</sup> on amplifier diodes (see Chapter 6). In these diodes the electric field distribution is highly non-uniform when the mean bias field exceeds threshold. Neglecting diffusion the relevant one-dimensional equations describing the static field non-uniformity are Poisson's equation and the current continuity equation:—

$$\epsilon\epsilon_0 \frac{dE(x)}{dx} = e\{n(x) - N_D(x)\}$$

and

$$J = n(x) e v\{E(x)\}.$$

$\epsilon\epsilon_0$  is the dielectric constant,  $J$  is the device current density,  $v$  the electron velocity, and  $n(x)$  and  $N_D(x)$  are respectively the spatially dependent electron and donor distribution. Upon elimination of  $n(x)$  these equations give:—

$$v\{E(x)\} = \frac{J}{eN_D(x) + \epsilon\epsilon_0 [dE(x)/dx]}.$$

In order to calculate the velocity as a function of electric field the spatial dependence of  $N_D(x)$  and  $E(x)$  was required. These were obtained by resistively probing the electric field distribution along the sample with a tungsten probe of 2 micron point diameter.  $N_D(x)$  was obtained from the electric field distribution below threshold and  $E(x)$  from the above threshold measurements. The measurements were complicated by ionization of electrons in the high field regions of the sample for mean electric fields above threshold. This caused  $N_D(x)$  to be altered from its value in low fields and it was not possible to obtain results for an electric field in excess of 10 kV/cm. In order to obtain sufficiently pure material to take results to this field it was necessary to use a sample which was doped above the critical value for domain formation. The sample became subcritically doped upon cooling to about  $-50^\circ\text{C}$  because a substantial number of carriers were "frozen out" onto donor sites. The velocity-field curve obtained from these measurements

is shown in Fig. 3.20. Its accuracy is limited by the difficulty of accurate interpolation of the electric field distribution, it refers to material not at room temperature and shows strong ionization characteristics above 10 kV/cm.

### 3.10 COMPARISON OF THEORY AND EXPERIMENT

The measurements of Ruch and Kino in the previous section appear to suffer the least experimental objection and are also the most direct in their measurement of electron velocity. The generally good agreement of this measurement with the displaced Maxwellian calculations of Butcher and Fawcett and with Monte Carlo calculations have lead to the acceptance of this velocity-field curve as the one relevant to gallium arsenide of all resistivities, despite the fact that the measurements were made in semi-insulating material. Further developments in material uniformity and the microwave experimental technique have produced results<sup>(73,67)</sup> in good agreement with curves A and E in Fig. 3.20. Measurements of the wavelength of growing space charge waves<sup>(74)</sup> propagating in semi-insulating gallium arsenide biased above threshold are also in excellent agreement with these two curves.

### 3.11 THE EFFECT OF REDUCING THE INTERVALLEY ENERGY DIFFERENCE

On the basis of the intervalley transfer mechanism it would be expected that a reduction of threshold field would arise from a reduction of the central to satellite valley energy difference. Indeed, it was just this effect which gave the first direct experimental verification that the intervalley transfer mechanism was the basis of the Gunn effect.<sup>(3)</sup> The required energy reduction can be brought about with a reduction of the lattice inter-atomic spacing, either by pressure or by alloying gallium arsenide with gallium phosphide. In each case the threshold field has been determined experimentally as the electric field at which the device current was a maximum before the onset of Gunn oscillations.

Hydrostatic experiments have been carried out by Hutson *et al.*<sup>(3)</sup> and Wasse *et al.*<sup>(26)</sup> and the results are shown in Fig. 3.23. The threshold field is normalized to its value at zero pressure. Also shown in Fig. 3.23 are theoretical calculations of the threshold field.<sup>(58)</sup> These calculations were made for different intervalley energy separations which were related to the pressure from earlier electron transport experiments<sup>(55)</sup> with a pressure coefficient of  $-1.1 \times 10^{-2}$  eV/kbar. On the basis of this pressure coefficient good agreement is obtained for the critical pressure of 26 kbars, beyond which a differential negative resistance is not obtained. The calculations were an early version of the displaced Maxwellian approximation which did

not include all the relevant scattering mechanisms. However this will have little effect on the velocity-field characteristic up to and including the threshold field owing to the predominance of the polar scattering over this range.

There is an increase of threshold field with pressure in the theoretical results and the experimental results of Wasse *et al.* at high pressures. This arises when the intervalley energy separation has become small and some thermal population of the satellite valleys has occurred. The differential negative resistance occurring beyond threshold arises from a strong decrease of the central valley electron population with increasing electric field. When the satellite valleys are partially populated by thermal excitations of electrons a sufficiently strong decrease of the central valley population with electric field is delayed to higher fields. Beyond this region when the central and satellite valleys are closer in energy, the thermal population of the satellite valleys is sufficient to inhibit the differential negative resistance.

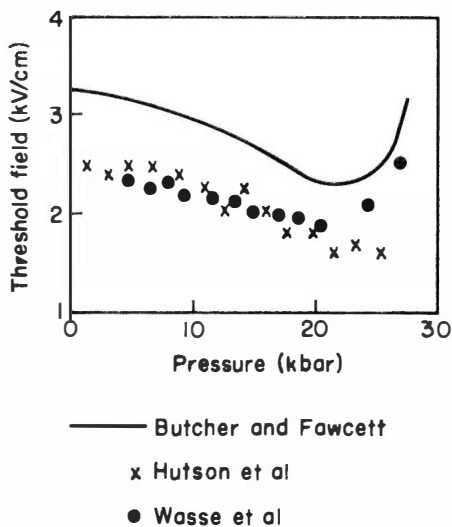


FIG. 3.23. The effect of hydrostatic pressure on the threshold field.

Experiments using uniaxial stress<sup>(56)</sup> show similar threshold field behaviour. It was found that the variation of threshold field with stress was most rapid for stress along the  $\langle 100 \rangle$  direction, giving additional confirmation that the satellite valleys are along the  $\langle 100 \rangle$  directions.

In the interpretation of these pressure effects it has been assumed that the variation of the threshold field is predominantly determined by the intervalley energy separation. Previous studies of high mobility semiconductors<sup>(15)</sup> have shown that the stress dependence of electron mobility

is weak in any one valley of the band structure. In all of the pressure experiments care has to be taken in the choice of material. If it has impurity levels whose energy separation from one of the occupied conduction band valleys is ever within the thermal energy range, "freeze out" of carriers onto the impurity or trapping site may occur. A variation of carrier concentration with stress will occur in the experiment and increase the complexity of interpretation.<sup>(57)</sup>

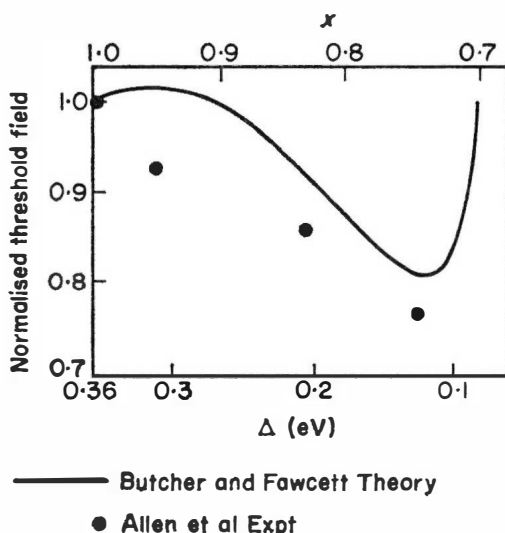


FIG. 3.24. The variation of threshold field in  $\text{GaAs}_x\text{P}_{1-x}$  alloys.

Gallium arsenide and gallium phosphide form a continuous range of solid solutions  $\text{GaAs}_x\text{P}_{1-x}$  ( $x$  is the arsenic proportion). Both of the pure materials have a similar band structure except that the central valley is the conduction band edge in gallium arsenide and the  $\langle 100 \rangle$  valleys are at the conduction band edge in gallium phosphide. An alloy of the two materials shows a decrease of the intervalley energy separation as the phosphide content increases. It may be expected that the threshold field for Gunn oscillations in  $\text{GaAs}_x\text{P}_{1-x}$  alloys would decrease with increasing phosphide content. Such behaviour has been observed<sup>(58)</sup> for a phosphide content of less than 0.34. Theoretical calculations of the threshold field<sup>(59)</sup> in this alloy system have been made assuming that the intervalley separation decreases linearly with decreasing arsenic content, and becomes zero at  $x = 0.6$ . The experimental and theoretical results are compared in Fig. 3.24. The initial theoretical increase of threshold field arises from the expected increased strength of the polar scattering which is due to the stronger ionic character of the phosphide atoms. It is not observed in practice.

Both the pressure and alloying experiments allow population of the satellite valleys at low electric fields. This permits measurement of the electronic transport properties in these valleys for use in calculations of the high field velocity-field characteristic.

### 3.12 GUNN EFFECT IN OTHER MATERIALS

The Gunn effect has been observed in several other materials, all of which have the same conduction band structure as gallium arsenide. We have already dealt with gallium arsenide/phosphide alloys in the previous section. Indium phosphide has measured values of the threshold field between 5 kV/cm and 7.2 kV/cm<sup>(1,60)</sup> and Butcher and Fawcett<sup>(30)</sup> have predicted a threshold field of 6.65 kV/cm. using their early displaced Maxwellian calculation with the relevant indium phosphide parameters. Cadmium telluride has a measured threshold field of about 13 kV/cm<sup>(1,61)</sup> compared with a predicted value of 14.25 kV/cm.<sup>(39)</sup> Zinc selenide may also exhibit the effect with a threshold field of 45 kV/cm but this is not clear.<sup>(61)</sup>

An interesting situation arises with indium arsenide because its conduction band is of the correct form but its intervalley energy separation is greater than its fundamental energy gap. Normally, at high electric fields, it exhibits avalanche breakdown as the mean carrier energy approaches that of the fundamental energy gap. Uniaxial stress along the  $\langle 111 \rangle$  direction increases the fundamental energy gap but decreases the energy difference of the central and satellite valleys. At a pressure of 14 kbars the avalanche breakdown gives way to Gunn effect oscillations<sup>(2)</sup> with a threshold field of 1.7 kV/cm. For higher pressures the behaviour is analogous to that of gallium arsenide under stress.

The effects in these materials do not have practical significance at present because the material technology is much less advanced than that of gallium arsenide. Any alloy materials also suffer from the disadvantage of a reduced thermal conductivity due to the increased lattice disorder. This will reduce their mean power handling capacity when used as practical devices.

Finally in this section, effects observed in germanium deserve mention. All materials considered so far have polar scattering as the predominant low field scattering mechanism. The "breakdown" nature of the scattering is responsible for the very rapid intervalley repopulation with increasing electric field which causes a differential negative resistance. In non-polar semiconductors such a "breakdown" effect should not be so pronounced, if it is present at all, and it is of interest to know whether a differential negative resistance can occur in such materials. Observations of oscillations and weak differential negative resistance effects have been made in germanium at low temperature<sup>(62)</sup> and at room temperature under pressure<sup>(63)</sup>, and a

modified intervalley transfer mechanism appears to be a possible explanation. The conduction band edge of germanium consists of four equivalent valleys at the  $\langle 111 \rangle$  Brillouin zone boundary. The valleys have ellipsoidal constant energy surfaces in  $k$ -space with a principal effective mass ratio of 19. The next higher valleys lie in  $\langle 100 \rangle$  directions 0.21 eV above the  $\langle 111 \rangle$  valleys. The intervalley explanation of the effects has postulated an electric field induced transfer of electrons from light mass states of the  $\langle 111 \rangle$  valleys to heavier mass states in the  $\langle 100 \rangle$  valleys for the low temperature effects in unstressed germanium. The effects at room temperature appear to be related to an electric field induced redistribution of electrons from light mass to heavy mass states of the anisotropic  $\langle 111 \rangle$  valleys. The uniaxial stress is required to reveal the anisotropy of the  $\langle 111 \rangle$  valleys by changing their relative energy and this allows the preferential population of suitable  $k$ -states by the electric field.

## REFERENCES

1. Foyt, A. G. and McWhorter, A. L. (1966). *I.E.E.E. Trans. Electron Devices* ED-13, 79-87.
3. Allen, J. W., Shyam, M., and Pearson, G. L. (1966). *Appl. Phys. Lett.* 9, 39-41.
3. Hutson, A. R., Jayaramam, A., Chynoweth, A. G., Coriell, A. S., and Feldman, W. L. (1965) *Phys. Rev. Lett.* 14, 639-641.
4. Conwell, E. M., and Vassell, M. O. (1968). *Phys. Rev.* 166, 797-821.
5. Cohen, M. L. and Bergstresser, T. K. (1966). *Phys. Rev.* 141, 798.
6. Pollak, F. H., Higginbotham, C. W. and Cardona, M. (1966). *J. Phys. Soc., Japan, Suppl.* 21, 20.
7. McKelvey, J. P. (1966). "Solid State and Semiconductor Physics". p. 133, Harper and Row, London.
8. Hilsum, C. (1964). Proc. 7th Intern. Conf. Phys. Semicond., Paris, 1964, pp. 1127-1139. Dunod, Paris.
9. Ehrenreich, H. (1957). *Phys. Chem. Solids* 2, 131-150.
10. Conwell, E. M., and Vassell, M. O. (1966). *I.E.E.E. Trans. Electron Devices*, ED-13, 22-27.
11. Frohlich, H. (1947). *Proc. Roy. Soc.* A188, 532-541.
12. Frohlich, H. (1947). *Proc. Roy. Soc.* A188, 521-532.
13. Matz, D. (1967). *J. Phys. Chem. Solids* 28, 373.
14. Dykman, I. M. and Tomchuk, P. M. (1966). *Soviet Phys. Solid State* 8, 1075.
15. Paige, E. G. S. (1964). *Progr. Semicond.* 8, 62.
16. Stratton, R. (1957). *Proc. Roy. Soc.* 245, 242.
17. Frohlich, H. and Paranjape, B. V. (1957). *Proc. Phys. Soc. (London)*, B69, 21-32.
18. Conwell, E. M. and Weisskopf, V. F. (1950). *Phys. Rev.* 77, 388.
19. Brooks, H. (1955). *Advanc. Electron.* 7, 87.
20. Weisberg, L. R. (1962). *J. Appl. Phys.* 33, 1817.
21. Read, W. T. (1954). *Phil. Mag.* 45, 775.
22. Birman, J. L., Lax, M., and Loudon, R. (1966). *Phys. Rev.* 145, 620-622.
23. Copeland, J. A. (1966). *Appl. Phys. Lett.* 9, 140-142.

24. Thim, H. W. and Knight, S. (1967). *App. Phys. Letts.* **11**, 83.
25. Herring, C. and Vogt, E. (1956). *Phys. Rev.* **101**, 944.
26. Wasse, M. P., Lees, J. and King, G. (1966). *Solid-State Electron*, **9**, 601–604.
27. Allen, J. W., Shyam, M., Chen, Y. S. and Pearson, G. L. (1965). *Appl. Phys. Lett.* **7**, 78–80.
28. Butcher, P. N. (1967). “Reports on Progress in Physics”, **30**, p. 97.
29. Bott, I. B. and Fawcett, W. (1968). *Advances in Microwaves* **3**, 223.
30. Butcher, P. N. and Fawcett, W. (1965). *Proc. Phys. Soc. (London)* **86**, 1205–1219.
31. Butcher, P. N. and Fawcett, W. (1966). *Phys. Letters* **21**, 489–490.
32. Stenflo, L. (1967). *Proc. I.E.E.E.* **55**, 1088.
33. Zylbersztejn, A. and Gunn, J. B. (1967). *Phys. Rev.* **157**, 668.
34. Baraff, G. (1964). *Phys. Rev.* **133**, A26.
35. Yamashita, J. and Inoue, K. (1959). *Phys. Chem. Solids*, **12**, 1.
36. Bell, D. A. (1960). “Electrical Noise”. Van Nostrand, p. 39.
37. Kurosawa, T. (1966). *Proc. Int. Conf. Phys. Semiconductors, Kyoto, 1966, J. Phys. Soc. Japan (Supplement)* **21**, 424–426.
38. Boardman, A. D., Fawcett, W. and Rees, H. D. (1968). *Solid State Communications* **6**, 305.
39. Bardeen, J. and Shockley, W. (1950). *Phys. Rev.* **80**, 72.
40. Stratton, R. (1962). *Phys. Rev.* **126**, 2002–2014.
41. Das, P. and Bharat, R. (1967). *App. Phys. Letts.* **11**, 386.
42. Rees, H. D. (1969). *I.B.M. J. Res. Develop.* **13**, 527–542.
43. Gunn, J. B. (1966). *I.B.M. J. Res. Develop.* **10**, 300–309.
44. Boer, K. W. (1965). *Phys. Rev.* **139**, A1949–1959.
45. Brady, D. P., Knight, S., Lawley, K. L. and Uenohara, M. (1966). *Proc. Symp. Gallium Arsenide, Reading, England*, pp. 162–167.
46. Zylbersztejn, A. and Gunn, J. B. (1967). *Phys. Rev.* **157**, 668.
47. Gunn, J. B. and Elliot, B. (1966). *J. Phys. Letts.* **22**, 369, and IPPS. Conference Manchester 1967, unpublished.
48. Acket, G. A. (1967). *Phys. Letts.* **24A**, 200.
49. Hamaguchi, C., Kono, T. and Imishi, Y. (1967). *Phys. Letts.* **24A**, 500.
50. Braslau, N. (1967). *Phys. Letts.* **24A**, 531.
51. Kalashnikov, S. G., Lyubchenko, V. E. and Skvortsova, N. E. (1967). *Soviet Physics-Semiconductors*, **1**, 1206.
52. Chang, D. M. and Moll, J. L., (1966). *Applied Phys. Letts.* **9**, 283.
53. Ruch, J. G. and Kino, G. S. (1967). *Applied Phys. Letts.* **10**, 40.
54. Thim, H. W. (1966). *Electronics Letters* **2**, 403.
55. Ehrenreich, H. (1960). *Phys. Rev.* **120**, 1951–1963.
56. Shyam, M., Allen, J. W. and Pearson, G. L. (1966). *I.E.E.E. Trans. Electron Devices ED-13*, 63–67.
57. Hutson, A. R., Jayaraman, A., and Coriell, A. S. (1967). *Phys. Rev.* **155**, 786–796.
58. Allen, J. W., Shyam, M., Chen, Y. S. and Pearson, G. L. (1965). *Appl. Phys. Letts.* **7**, 78–80.
59. Butcher, P. N., Fawcett, W. and Hilsum, C. (1966). *I.E.E.E. Trans. Electron Devices ED-13*, 192–193.
60. Gunn, J. B. *I.B.M. J. Res. Develop.* **8**, 141–159.
61. Ludwig, G. W., Halsted, R. E. and Aven, M. (1966). *I.E.E.E. Trans. Electron Devices ED-13*, 671.

62. Elliot, B. J., Gunn, J. B. and McGroddy, J. C. (1967). *Appl. Phys. Letts.* **11**, 253.
63. Smith, J. E. (1968). *Appl. Phys. Letts.* **12**, 233.
64. Ruch, J. G. and Kino, G. S. (1968). *Phys. Rev.* **174**, 921-931.
65. Sher, A. and Thornber, K. K. (1967). *Appl. Phys. Letts.* **11**, 3-5.
66. Fawcett, W. and Paige, E. G. S. (1967). *Electronics Letters* **3**, 505.
67. Acket, G., A. (1969) *Phys. Letts.* **29A**, 596.
68. Ruch, J. G. and Fawcett, W. (1970). *J. Appl. Phys.* **41**, 3843-3850.
69. Rees, H. D. (1969). *J. Phys. Chem. Solids.* **30**, 643-655.
70. Fawcett, W. and Rees, H. D. (1969). *Phys. Letts.* **29A**, 578-579.
71. Rees, H. D. (1969). *Solid State Communications* **7**, 267.
72. Fawcett, W., Boardman, A. D. and Swain, S. (1970). *J. Phys. Chem. Solids* **31**, 1963-1990,
73. Braslau, N. and Hauge, P. S. (1970). *I.E.E.E. Trans. on Electron Devices* **ED-17**, 616-622.
74. Fay, B. and Kino, G. S. (1969). *Appl. Phys. Letts.* **15**, 337-339.



## *Chapter 4*

# **Dynamic Effects**

### **4.1 INTRODUCTION**

The exploitation of the potentialities of the negative resistance characteristic discussed in the last chapter hinges upon an understanding of various dynamic effects. The negative resistance produces distortions in the internal electric fields and charge distributions, which are harnessed or suppressed to differing extents in the several modes of operation. In this chapter the basic mechanisms are described, and more detailed discussion follows later.

To set the scene, we first see what would happen if there were no dynamic effects at all. We find that there would then be no negative resistance at the device's terminals and it would be useless. The next section deals with the domain mode which was the effect first observed by Gunn and since has been exploited to the greatest extent. This mode is, in a sense, the most uncontrolled where dynamic effects are very prominent. We conclude the section with a brief mention of accumulation layers.

Sections 4.9 and 4.10 cover two methods of domain control. In the L.S.A. mode control is essentially by time, for under suitable conditions a mature domain may not have time to form; whereas in the amplifier mode it is the low conductivity which stabilises and controls space charge distortion. This mode approaches the static situation of Section 4.2 in the limiting case of zero conductivity.

Finally we try to assess the relative merits of the modes in terms of their capacities for generating power at microwave frequencies.

This is an appropriate point at which to mention the slightly confused nomenclature surrounding the L.S.A. and hybrid modes. The distinction we seek to make in this and the two following chapters is between transit length and longer devices. Accordingly, transit length devices are generally covered under "domain modes" and over-length devices, be they L.S.A.,

multiple quenched domain or hybrids, are all classified under "L.S.A. modes", except where logical presentation of the subject dictates otherwise.

## 4.2 STATIC NEGATIVE RESISTANCE?

In the last chapter we concluded that some materials exhibit static bulk negative resistance, and now we consider some dynamic effects which follow from this.

To emphasize the importance of dynamic effects, we first examine the general proposition that *no bulk negative resistance diode can exhibit negative resistance at its terminals if the internal electric field distribution is static*. By "static" we do not exclude time variation in response to a varying applied voltage, we mean that a given applied voltage defines the spatial variation of electric field within the device, and that the applied voltage varies sufficiently slowly that  $\partial q/\partial t$  may be neglected in Eqn (4.2) below.

Consider Poisson's equation in one dimension

$$\frac{\partial E}{\partial x} = \frac{e}{\epsilon\epsilon_0} (n - N_0) = \frac{q}{\epsilon\epsilon_0} \quad (4.1)$$

and the current continuity equation, neglecting diffusion,

$$\frac{\partial(env)}{\partial x} + \frac{\partial q}{\partial t} = 0. \quad (4.2)$$

where  $E$  is the electric field,  $e$  the electronic charge,  $\epsilon\epsilon_e$  the permittivity,  $n$  the carrier concentration, and  $N_0$  the donor concentration.

Since we are seeking a static solution  $\partial q/\partial t = 0$  we may integrate Eqn (4.2) to obtain:

$$env(E) = I = \text{constant}. \quad (4.3)$$

Here  $v(E)$  is the effective electron drift velocity given by a static velocity field characteristic such as shown in Fig. 4.1 for GaAs.

We do not need to be specific however, and make only the following assumptions here:

$$\begin{aligned} \frac{dv}{dE} &> 0 \quad \text{for} \quad 0 < E < E_T \\ \frac{dv}{dE} &< 0 \quad \text{for} \quad E_T < E < E_V \\ \frac{dv}{dE} &> 0 \quad \text{for} \quad E_V < E. \end{aligned} \quad (4.4)$$

It is tempting to look at Eqns (4.1) and (4.3) and select the solution  $n = N_0$ . This implies that  $F$  and  $n$  are spatially uniform and the static characteristic of Fig. 4.1 may be measured at the terminals of a device. Shockley<sup>(1)</sup> and Kroemer<sup>(2)</sup> have pointed out, however, that this solution violates the boundary conditions and is incorrect in the time independent case.

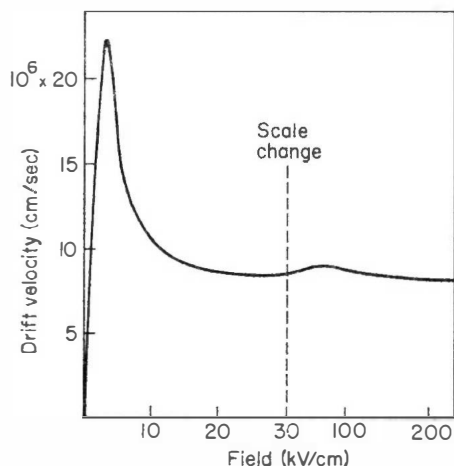


FIG. 4.1. Static velocity-field characteristic. (Butcher and Fawcett<sup>(1,5)</sup>). (Crown Copyright, reproduced by permission of the controller of Her Majesty's Stationery Office).

The active bulk material must be terminated in contacts which are heavily doped and support only very small electric fields, except near the active material where there may exist substantial fields which decay rapidly with distance into the contact region.

An idealised doping profile for an  $n$ -type crystal of length  $l$  is shown in Fig. 4.2. Here  $N_0$  is very large for  $x < 0$  and  $x > l$  and there are sharp transitions at  $x = 0$  to the active region which is moderately doped (e.g.  $N_0 \sim 10^{15} \text{ cm}^{-3}$  for  $1\Omega \text{ cm GaAs}$ ). In practice the transitions would not be perfectly sharp but the argument which follows is not altered if diffuse transitions are included.

From Eqns (4.1) and (4.3) we deduce that

$$\frac{\partial E}{\partial x} = \frac{eN_0}{\epsilon\epsilon_0} \left( \frac{I}{eN_0 v(E)} - 1 \right) \quad (4.5)$$

where all the quantities on the right-hand side of Eqn (4.5) are constant throughout  $0 < x < l$  except  $v(E)$ .

Suppose we apply a voltage to the device such that

$$\frac{V}{l} > E_T. \quad (4.6)$$

For  $x < 0$  we have the boundary conditions that  $E$  is small and  $n = N_0$ . From Eqn (4.5) we see near  $x = 0$ , where  $E$  is small and  $v(E)$  is small (from Fig. 4.1), that  $\partial E/\partial x$  is large and  $n > N_0$  (Eqn (4.3)).

As  $x$  increases,  $E$  increases,  $v$  increases,  $\partial E/\partial x$  decreases and  $n$  decreases. These changes continue monotonically until  $E = E_T$ .

At this point it must be the case that  $\partial E/\partial x > 0$ , for if  $\partial E/\partial x = 0$  we should have the stable solution of  $E = E_T$  throughout the rest of the crystal and the condition  $V/l > E_T$  could not be met. *A fortiori*  $\partial E/\partial x < 0$  is excluded.

As  $x$  increases from the point at which  $E = E_T$ , then,  $E$  increases,  $v$  decreases,  $\partial E/\partial x$  increases and  $n$  increases.

These changes continue monotonically up to the point where  $E = E_V$ , and as  $x$  increases further;  $E$  increases,  $v$  increases,  $\partial E/\partial x$  decreases and  $n$  decreases.  $\partial E/\partial x$  remains  $> 0$  unless there exists a value of  $E$  such that

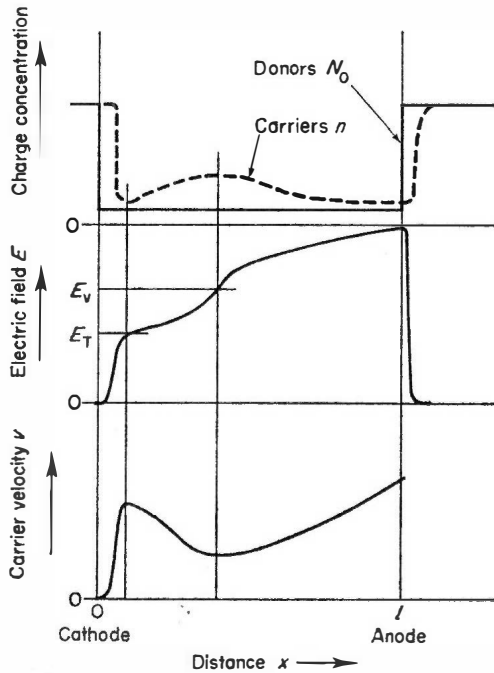


FIG. 4.2. Profile of donor and free carrier concentrations, electric field and carrier velocity for the time independent solution of a bulk negative resistance device.

$v(E) > v(E_T)$ . This situation is not shown in Fig. 4.2 as it merely adds a series positive resistance.

The next change occurs at  $x = l$  where  $N_0$  becomes very large,  $\partial E/\partial x < 0$ , and  $E$  decays rapidly to a small value.

The position at which  $E = E_T$  is very close to  $x = 0$ , and almost independent of  $V$ , provided  $V/l > E_T$ , because  $E$  in the contact region is very small. It is sometimes called a virtual cathode.

The quantity which changes most directly in response to changes in  $V$  is  $\partial E/\partial x$  at  $E = E_T$ . This determines the field, and by integration, the voltage in the remainder of the sample. An increase of total voltage must be accompanied by an increase of  $\partial E/\partial x$  at that point, and by an increase in  $n$ , since  $v(E_T)$  is a maximum value of  $v(E)$ .

Any increase of  $V$  therefore implies an increase in  $I$ , which constitutes positive resistance.

This treatment neglects the effects of diffusion, energy transport and variations in  $N_0$ . McCumber and Chynoweth<sup>(3)</sup> have verified by numerical integration that inclusion of these effects does not alter the argument.

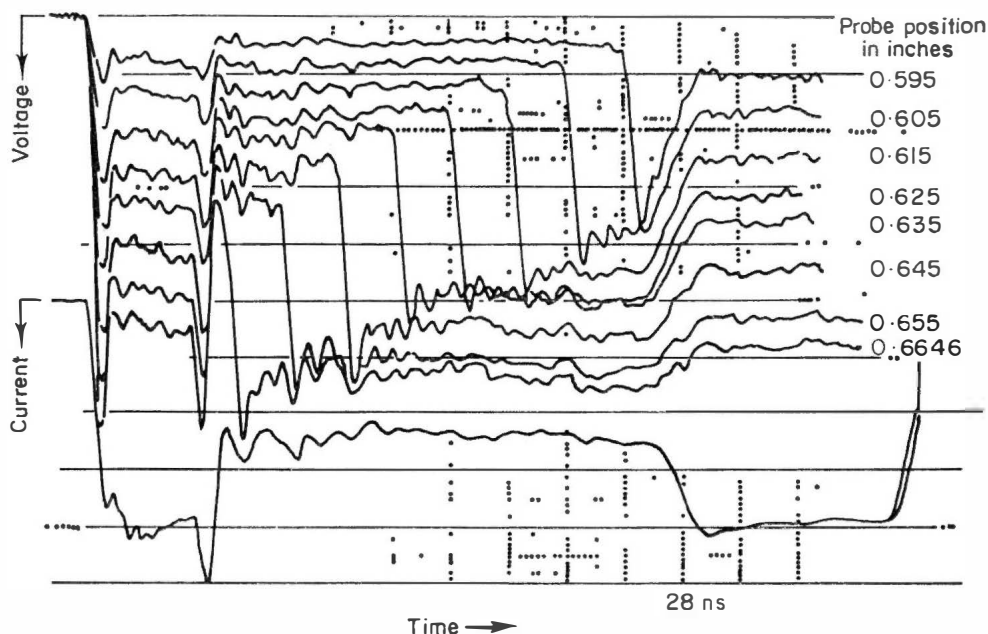


FIG. 4.3. Transit of a high field domain observed by Heeks<sup>(5)</sup> with a capacitively coupled probe. The lower trace is the current through the 0.25 cm Gunn diode and the upper traces are the probe voltages measured at successive probe positions. The device was operated with a triggered domain and a negative applied voltage.

## 4.3 DOMAINS

We study domains first because they show dramatically the importance of dynamic effects and it was these which were first observed by Gunn.<sup>(4)</sup> Gunn carried out two main experiments. In the first he observed oscillations in the current through some III-V compounds (notably GaAs) when the electric field in an oscillating sample was probed, and it was observed that high field regions or domains propagated through the sample from cathode to anode. The domain disappeared into the anode coincidentally with a maximum in the current waveform, and a new domain was nucleated at the cathode. The probe experiment was repeated by Heeks<sup>(5)</sup> using a triggered domain technique and Fig. 4.3 is a sequence showing domain propagation very clearly.

The experiments showed that the domains reached a stable amplitude and shape very rapidly (the product of doping and length,  $N_0l$ , was high) and then travelled at about  $10^7$  cm/sec.

4.4  $N_0l$  PRODUCT—SPACE CHARGE GROWTH

The essential assumption which led to the result of positive resistance at all frequencies in Section 4.2 was

$$\frac{\partial q}{\partial t} = 0 \quad \text{in Eqn (4.2).}$$

If time variation is included, negative resistance may be observed at certain frequencies even in D.C. stable devices; this is known as the amplifier mode of Thim<sup>(6)</sup> and occurs when the product of carrier concentration and length ( $N_0l$ ) is less than about  $10^{11}$  cm<sup>-2</sup>. At much higher values of  $N_0$  devices are unstable and the travelling high field domains are formed, as seen by Gunn.

Calculation of the critical  $N_0$  value involves a complete numerical analysis of the stability of the amplifier mode against small fluctuations. This was first done by McCumber and Chynoweth<sup>(3)</sup>, and when that calculation is updated to include the effects of energy transport, diffusion and more sharply negative velocity-field characteristics, a value of  $N_0l = 0.76 \times 10^{11}$  cm<sup>-2</sup> is obtained.<sup>(7)</sup>

Various simpler arguments had been advanced predicting a critical  $N_0$  value<sup>(8)</sup>, and a very straightforward one by Kroemer<sup>(9)</sup> is based on Poisson's equation. Any domains must most certainly be no longer than the sample, so the difference  $\Delta E$  between the peak domain field and the field elsewhere must satisfy

$$\Delta E < \frac{N_0 l e}{\epsilon \epsilon_0} = N_0 l \times 1.6 \times 10^{-7}$$

hence

$$N_0 l > \Delta E \frac{\times 10^7}{1.6} \text{ cm}^{-2} \quad \text{if domains are to form.}$$

The threshold field in GaAs is  $3 \times 10^3 \text{ V/cm}$  and a domain must presumably have a field at least twice as large. More important, a domain must be considerably shorter than the sample if it is to propagate. These two considerations amount to (say) a factor of 4 to give a critical value near the  $0.76 \times 10^{11} \text{ cm}^{-2}$  required by rigorous calculation, and this seems reasonable.

Experimental evidence confirms the value of  $10^{11} \text{ cm}^{-2}$  only rather imprecisely since so far the determination of carrier concentration and uniformity has not been good enough. The increasingly widespread use of  $C$ - $V$  plotters for the measurement of charge carrier profiles however should yield interesting evidence on this point.

An analytical approach gives useful insight into domain growth, although the small signal approximation can take us only as far as an embryo domain.

The relations governing space charge growth are the continuity, particle current and Poisson's equation:

$$\frac{\partial J}{\partial x} + e \frac{\partial n}{\partial t} = 0$$

$$J = nev - e \frac{\partial}{\partial x} (Dn)$$

$$\frac{\partial E}{\partial x} = \frac{(n - N_0) e}{\epsilon \epsilon_0}$$

where  $J$  is the particle current density and  $D$  the diffusion coefficient.

To discover the conditions for initial growth from equilibrium a small signal approximation is valid. We express the quantities as the sums of their static parts (suffix 0) and small signal components:

$$J = J_0 + J_x$$

$$n = n_0 + n_1$$

$$v = v_0 + \mu E_x$$

$$D = D_0 + \left( \frac{\partial D}{\partial E} \right)_0 E_x$$

$$E = E_0 + E_x$$

where  $\mu$  is the slope (negative) mobility  $\partial v / \partial E$ .

Substitution in the governing equations and elimination of  $E_x$  and  $J_x$  leads to

$$D_0 \frac{\partial^2 n_1}{\partial x^2} - \left\{ v_0 - \frac{e n_0}{\epsilon \epsilon_0} \left( \frac{\partial D}{\partial E} \right)_0 \right\} \frac{\partial n_1}{\partial x} + \frac{n_0 e \mu}{\epsilon \epsilon_0} n_1 = \frac{\partial n_1}{\partial t}.$$

Now  $\epsilon \epsilon_0 / (n_0 e \mu)$  is the negative dielectric relaxation time  $\tau_n$ ; writing the expression in the brackets as  $v_x$  we have

$$D_0 \frac{\partial^2 n_1}{\partial x^2} - v_x \frac{\partial n_1}{\partial x} + \frac{n_1}{\tau_n} = \frac{\partial n_1}{\partial t}$$

which may be recognised as a wave equation.

It has solutions of the form

$$n_1 \propto \exp \left\{ \left( \frac{1}{\tau_n} - D_0 k^2 \right) t \right\} \exp \{ jk(x - v_x t) \}$$

which is a growing wave if  $1/\tau_n > D_0 k^2$ , where  $k$  is the wave number.

In most Gunn devices  $1/\tau_n \gg D_0 k^2$  so that the small signal growth is dominated by  $\tau_n$ .

The significance of the  $nl$  product lies in the magnitude of this growth exponent in one transit.

A transit time is  $t = l/v_x$  so the exponent is

$$\frac{l}{\tau_n v_x} = \frac{l n e \mu}{\epsilon \epsilon_0 v_x}.$$

The velocity may be appreciably altered by  $\partial D/\partial E$ , but if we take its value as  $10^7$  cm/sec, then for  $N_0 l = 10^{11}$  cm<sup>-2</sup> ( $N \sim n_0$ ) the exponent is 3. This is stretching the validity of a small signal argument, but a large exponent of growth in one transit must be necessary if a domain is to form.

#### 4.5 $N_0 l^2$ PRODUCT

Thermal diffusion not only modifies the velocity, as shown in the last section, but gives also the overriding requirement

$$\frac{1}{\tau_n} > D_0 k^2$$

if space charge waves are to grow.<sup>(8)</sup>

This inequality states that a very short device cannot generate domains, even if the  $N_0 l$  product would allow it, because diffusion would smooth out any such charge non-uniformities.



The limiting condition is

$$D_0 k^2 = D_0 \left( \frac{\pi}{l} \right)^2 = \frac{N_0 e \mu}{\epsilon \epsilon_0}$$

so

$$N_0 l^2 = \frac{\epsilon \epsilon_0 D_0 \pi^2}{e \mu}$$

taking  $D = 200 \text{ cm}^2 \text{ sec}^{-1}$  and the slope negative mobility  $\mu$  as  $2000 \text{ cm}^2 \text{ V}^{-1} \text{ sec}^{-1}$  we obtain  $N_0 l^2 = 0.69 \times 10^7 \text{ cm}^{-1}$ .

We may readily see that the  $N_0 l^2$  limit does not affect practical domain devices, for if

$$N_0 l > 0.7 \times 10^{11} \text{ cm}^{-2}$$

then for

$$l > 10^{-4} \text{ cm } (= 1 \mu\text{m})$$

$$N_0 l^2 > 0.69 \times 10^7 \text{ cm}^{-1}.$$

$$\sim 10^{11} \text{ cm}^{-2}$$

$$= 10^{11} \times 10^{-4} \text{ cm} = 10^7 \text{ cm}^{-1}$$

$$1 \mu$$

As far as is known, no Gunn devices as short as  $1 \mu\text{m}$  have yet been made.

#### 4.6 $N_0 d$ PRODUCT

Domains may also be stabilized, or inhibited from forming, if the thickness of the active material in a direction perpendicular to the electric field is small enough. If this dimension is  $d$  then the critical value is given approximately by

$$N_0 d = 10^{11} \text{ cm}^{-2}.$$

The electric field outside the device, produced by a domain or incipient domain inside, acts in such a sense as to restore the charge distribution to a uniform state, opposing the formation of the domain. With sufficiently thin geometry the effect is important. It can be enhanced by placing high permittivity material against the active device so that the depolarizing field has greater effect.<sup>(24,25)</sup>

The technique can be used to stabilize comparatively high current devices for use as amplifiers, which would form domains and oscillate if the  $N_0 l$  factor were the only controlling influence.<sup>(26)</sup>

#### 4.7 STABLE DIPOLE DOMAINS

When the conditions for rapid space charge growth or accumulation are satisfied, then it is the dipole domain which is found in real samples. It traverses the sample at nearly constant speed, and for a given applied voltage its amplitude is nearly independent of time.

The precise nature of these conditions we will discuss in Section 4.9 on the L.S.A. mode. For the moment, let us simply say that the charge accumulation time is much less than the time that the average voltage is above threshold, and the  $N_0 l$  product is large.

We consider Poisson's equation in one dimension

$$\frac{\partial E}{\partial x} = \frac{e}{\epsilon \epsilon_0} (n - N_0) = \frac{q}{\epsilon \epsilon_0} \quad (4.6)$$

and the current continuity equation

$$\frac{\partial}{\partial x} \left[ env(E) - e \frac{\partial}{\partial x} (D(E) n) \right] + \frac{\partial q}{\partial t} = 0 \quad (4.7)$$

where  $D(E)$  is a field dependent thermal diffusion term.

We substitute for  $q$  from Eqn (4.6) and integrate with respect to  $x$ :

$$env(E) - e \frac{\partial}{\partial x} (D(E) n) + \epsilon \epsilon_0 \frac{\partial E}{\partial t} = I(t). \quad (4.9)$$

Here we must remember that  $\partial I / \partial x = 0$ . Equations (4.8) and (4.9) simply represent the conservation of electrons in one dimension. Conduction is by electrons only, and we exclude hole-electron pair creation or annihilation.

We wish to show that a high field domain propagating without change of shape at a velocity  $v_D$  (say) is a solution of these equations.

We transform to the moving coordinate system  $x' = x - v_D t$  in which  $n$  and  $E$  have unchanging shapes. Outside the domain the field is uniform, hence by Poisson's equation  $n = N_0$ . In this region displacement current is zero.

Now

$$\frac{\partial E}{\partial x} = \frac{\partial E}{\partial x'} \quad \text{and} \quad \frac{\partial E}{\partial t} = -v_D \frac{\partial E}{\partial x'}$$

so Eqn (4.6) becomes:

$$\frac{E}{dx'} = \frac{e}{\epsilon \epsilon_0} (n - N_0)$$

and Eqn (4.9) becomes:

$$env(E) - e \frac{d}{dx'} (D(E) n) - e(n - N_0) v_D = e N_0 v_R$$

or

$$\frac{d}{dx'} (D(E) n) = n(v(E) - v_D) - N_0(v_R - v_D). \quad (4.10)$$

Now

$$\frac{d}{dx'} = \frac{dE}{dx'} \frac{d}{dE}$$

so, Eqn (4.10) becomes:

$$\frac{e}{\epsilon\epsilon_0} \frac{d}{dE} (D(E)n) = \frac{n(v(E) - v_D) - N_0(v_R - v_D)}{n - N_0}. \quad (4.11)$$

In Fig. 4.4 we show typical carrier concentration and field profiles for a domain, and in Fig. 4.5 carrier concentration is shown as a function of field. It is clear that  $n$  is a double valued function of  $E$ , the upper branch corresponding to the accumulation layer and the lower branch to the depletion layer.

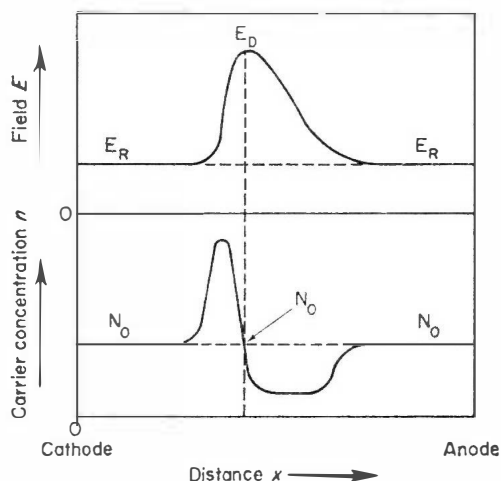


FIG. 4.4. Field  $E$  and carrier concentration,  $n$ , profiles for a fully developed domain. (Crown Copyright, reproduced by permission of the controller of Her Majesty's Stationery Office).

Numerical methods must be employed to obtain a general solution of Eqn (4.11) as has been done by Copeland<sup>(10)</sup> and Butcher *et al.*<sup>(11)</sup> However, a very instructive approximate solution has been obtained analytically by Butcher.<sup>(12)</sup>

If we assume that  $D(E)$  has a constant value  $D$  then Eqn (4.11) may be integrated to give:

$$\frac{n}{N_0} - \log \left( \frac{n}{N_0} \right) - 1 = \frac{\epsilon\epsilon_0}{D e N_0} \int_{E_R}^E \left[ (v(E') - v_D) - \frac{N_0}{n(E')} (v_R - v_D) \right] dE' \quad (4.12)$$

where  $n = N_0$  at  $E = E_R$  from Fig. 4.5.

The boundary conditions are that  $n = N_0$  at  $E = E_R$  and  $E = E_D$ . The left-hand side of Eqn (4.12) vanishes when  $n = N_0$  so the right-hand side must vanish at  $E = E_D$  whether the integration is performed along either the upper or the lower branch in Fig. 4.6. However, the second term of the integrand takes different values for the two branches, unless  $v_R = v_D$ , while the first does not. Clearly then,

$$v_R = v_D.$$

Equation (4.12) also enables us to deduce a dynamic characteristic. Since the integral vanishes we can determine the peak domain field  $E_D$  from the condition that the two shaded areas in Fig. 4.6 are equal. This construction gives the dotted curve—which is a plot of  $v_R$  against  $E_D$ .

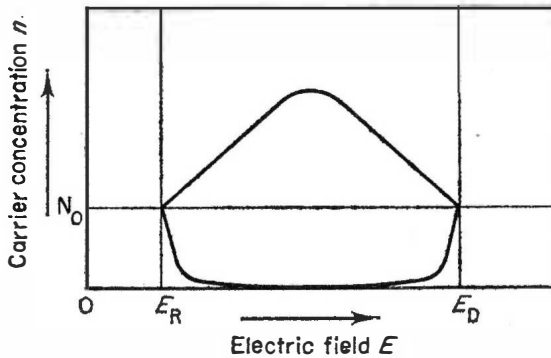


FIG. 4.5. Carrier concentration,  $n$ , as a function of field  $E$ . (Butcher *et al.*<sup>(12)</sup>). Crown Copyright, reproduced by permission of the controller of Her Majesty's Stationery Office).

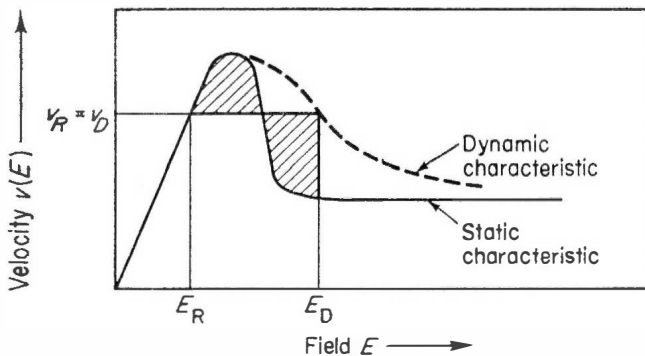


FIG. 4.6. Geometric construction of the dynamic characteristic by Butcher's equal areas rule. (Crown Copyright, reproduced by permission of the controller of Her Majesty's Stationery Office).

For high electric fields, the shape of the dynamic characteristic and indeed the domain itself may have very different shapes depending on the static curve. If the static curve saturates at a velocity not much greater than the valley velocity, it is possible to satisfy the equal areas rule, for domain fields which tend to infinity, as in Fig. 4.7. On the other hand, if the static curve continues to rise steadily beyond the valley, we eventually must reach the situation in Fig. 4.8 in which  $v_D = v(E_D)$  and the peak domain field is bounded. In this case if the average bias field is further increased, the domain becomes flat topped, rather than triangular, and there is a uniform high field region between the depletion and accumulation layers in which  $n = N_0$ . This situation has not been observed experimentally, as the static characteristic remains nearly saturated up to the impact ionization potential of about 200 kv/cm, and above this observations have not been made (Heeks<sup>(5)</sup>).

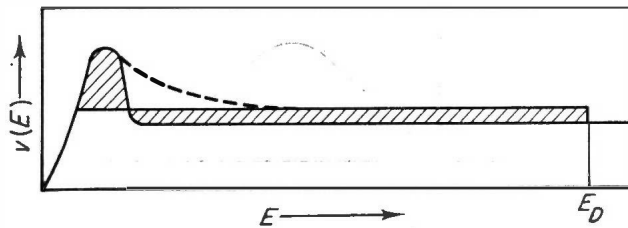


FIG. 4.7. Dynamic characteristic for a saturating static characteristic.  $E_D \rightarrow \infty$  for sufficiently high bias fields.

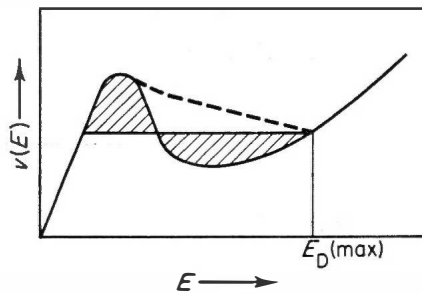


FIG. 4.8. Dynamic characteristic for a non-saturating static characteristic. There exists a maximum value for  $E_D$ .

This treatment may be refined in various ways, generally by numerical analysis. The assumption which most needs modification is that  $D$  is constant. Allen *et al.*<sup>(13)</sup> used an approximation to field dependent diffusion  $D = D(E)$  and obtained a modified equal areas rule

$$\int_{E_R}^{E_D} \frac{v(E) - v_R}{D(E)} dE = 0.$$

However, we will here consider the further simplifications of zero diffusion  $D = 0$ . This has the advantage of providing an analytic solution to the domain shape, although it is somewhat unrealistic as it predicts an infinite carrier concentration in the accumulation layer, and total depletion in the depletion layer, even in short samples, which is not found experimentally.

We see from Eqn (4.12) that as  $D \rightarrow 0$ ,  $n \rightarrow \infty$  in the accumulation layer and  $n \rightarrow 0$  in the depletion layer.

The width of the accumulation layer is zero and the field changes abruptly from  $E_R$  to  $E_D$ . In the depletion layer there is a linear change of field in a distance  $d$  given by Poisson's equation

$$\frac{E_D - E_R}{d} = \frac{n_D}{\epsilon\epsilon_0}.$$

The total excess voltage across the domain therefore is

$$\Phi_D = \frac{1}{2}(E_D - E_R)d = \frac{\epsilon\epsilon_0}{2N_0}(E_D - E_R)^2,$$

in addition to that due to  $E_R$ .

The total bias across the device is:

$$\Phi = \Phi_D + E_R l \quad (4.13)$$

so all the parameters of a domain may be calculated once  $E_D/E_R$  is determined from the equal areas rule.

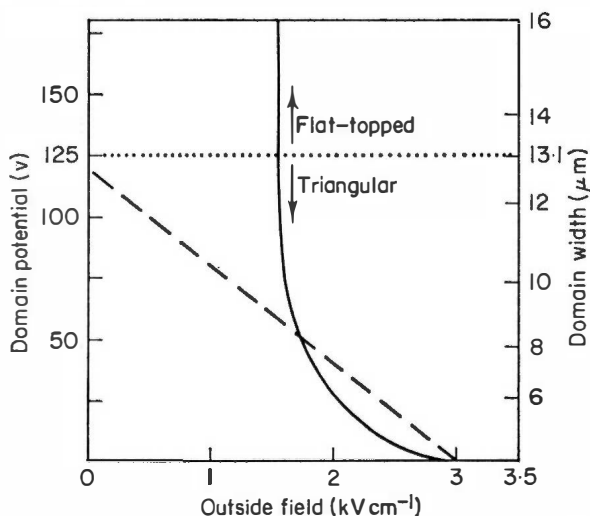


FIG. 4.9. Domain potential as a function of field outside the domain in the zero diffusion limit for 1 Ohm cm resistivity (full curve). The broken straight line is the load line for a 400  $\mu\text{m}$  long sample subject to 120 V bias (Butcher *et al.*<sup>(12)</sup>). (Crown Copyright, reproduced by permission of the controller of Her Majesty's Stationery Office).

The foregoing treatment is that of Butcher *et al.*<sup>(12)</sup>, and in Fig. 4.9 we reproduce their final diagram from which may be deduced the peak domain field, domain width and velocity for any sample, in the approximation of zero diffusion.

An improvement on this calculation was made by Butcher and Fawcett<sup>(14)</sup> using an analytic approximation to their velocity field curve<sup>(15)</sup> and constant diffusion,  $D = 178 \text{ cm}^2/\text{V sec}$ . The inclusion of diffusion smooths out the perfect sharpness of the domain shapes calculated above.

The calculated domain shapes for several values of peak domain field in 1 cm GaAs are shown in Fig. 4.10.

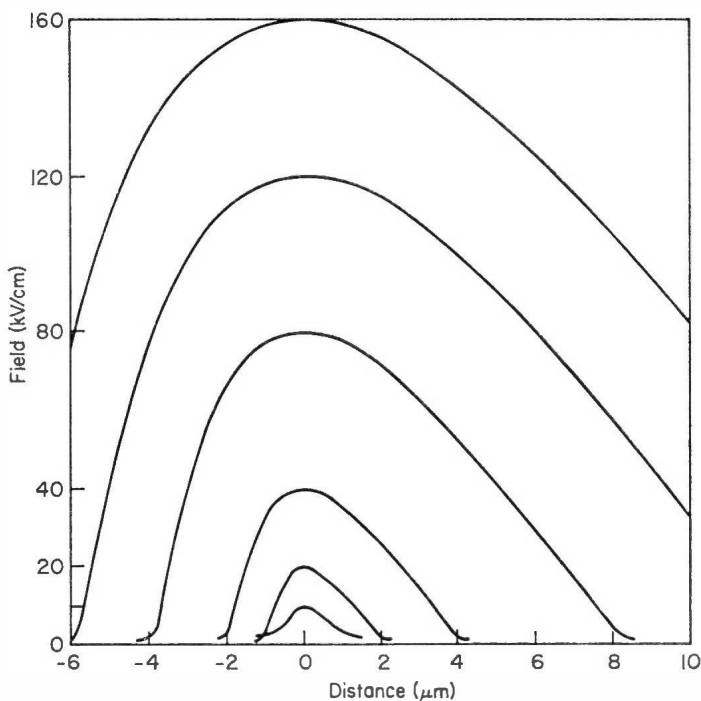


FIG. 4.10. Calculated domain shapes in 1 Ohm cm GaAs for various peak domain fields. (Butcher and Fawcett<sup>(14)</sup>). (Crown Copyright, reproduced by permission of the controller of Her Majesty's Stationery Office).

Full calculations of domain behavior from Poisson's equation and the current continuity Eqns (4.9) and (4.10) have been made by Copeland<sup>(10)</sup> and Butcher *et al.*<sup>(11)</sup> The important differences between these results and the more approximate analysis are that the domain velocity differs from that of the electrons outside the domain to an extent dependent on the resistivity, and that the peak domain field is also resistivity dependent.

The results of these full calculations, using field dependent diffusion, are given in Figs. 4.11 to 4.15 for 1, 5 and 10 Ohm cm GaAs<sup>(11)</sup>. In Fig. 4.11 we show the dependence of domain and electron velocity on the field outside the domain for various values of resistivity. The domain velocity is greater than that of the electrons outside except near threshold, and the difference decreases as the resistivity is increased. The dependence of the peak domain field on the field outside is shown in Fig. 4.12, and in Fig. 4.13 that of the extreme values of electron population in the domain. Figure 4.14 shows the domain widths, and may be compared with Fig. 4.10. Figure 4.15 is the most important of the set. It is a plot of domain potential,

$$\Phi_D = \int (E - E_R) dx, \text{ as a function of the field outside, } E_R.$$

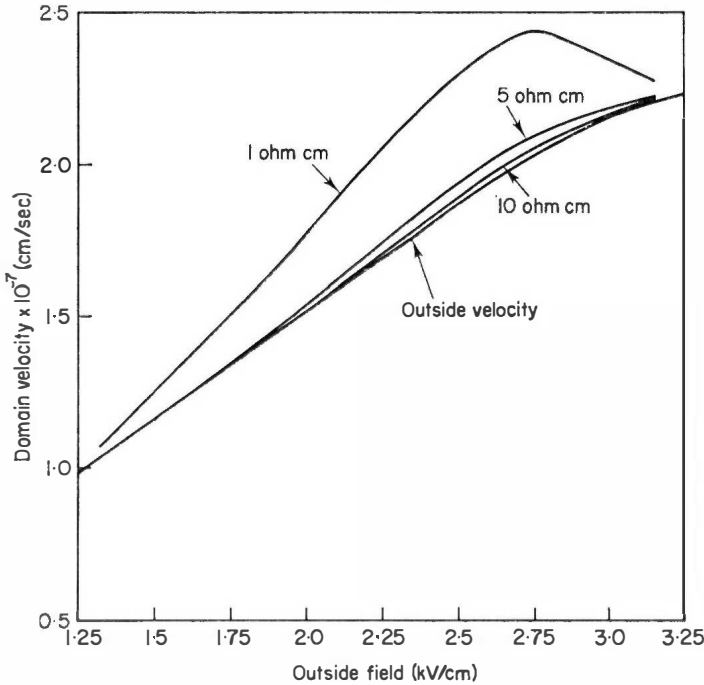


FIG. 4.11. Electron drift velocity and domain velocity against field outside the domain.

If we plot on this graph the boundary condition, Eqn (4.13), representing the applied bias, we have a straight line with slope  $-1$ . The intersection with the characteristic curve gives  $\Phi_D$  and  $E_R$  and the remaining parameters may then be read off from Figs. 4.11 to 4.14.



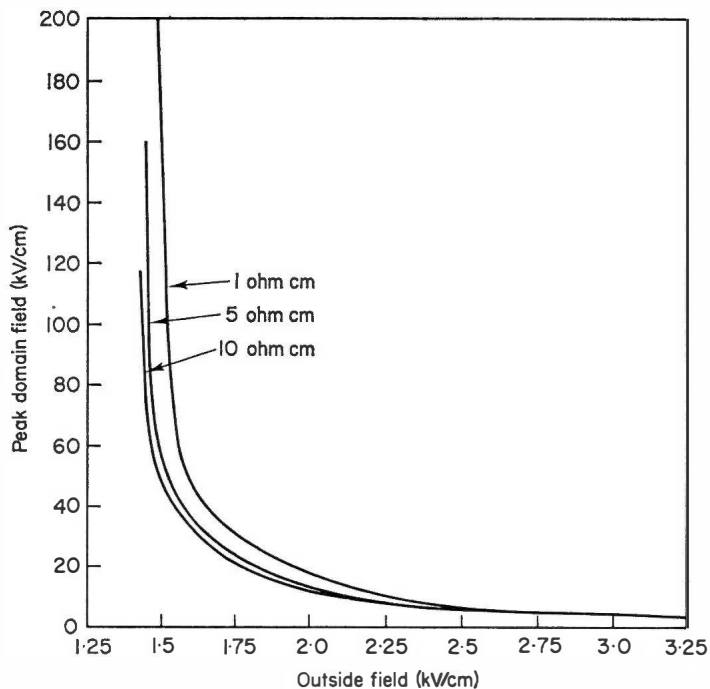


FIG. 4.12. Peak domain field against field outside the domain. (Crown Copyright, reproduced by Permission of the controller of Her Majesty's Stationery Office).

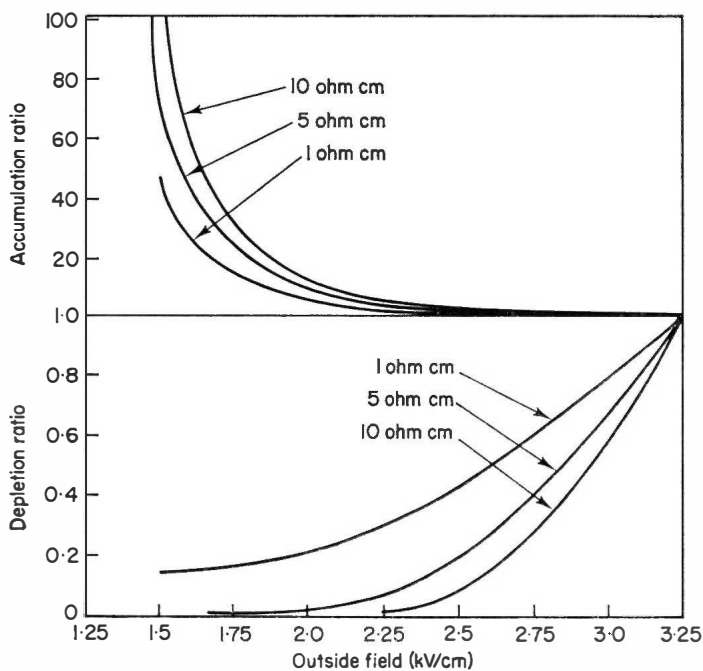


FIG. 4.13. Maximum and minimum values of electron population in the domain against field outside the domain. (Crown Copyright, reproduced by permission of the controller of Her Majesty's Stationery Office).

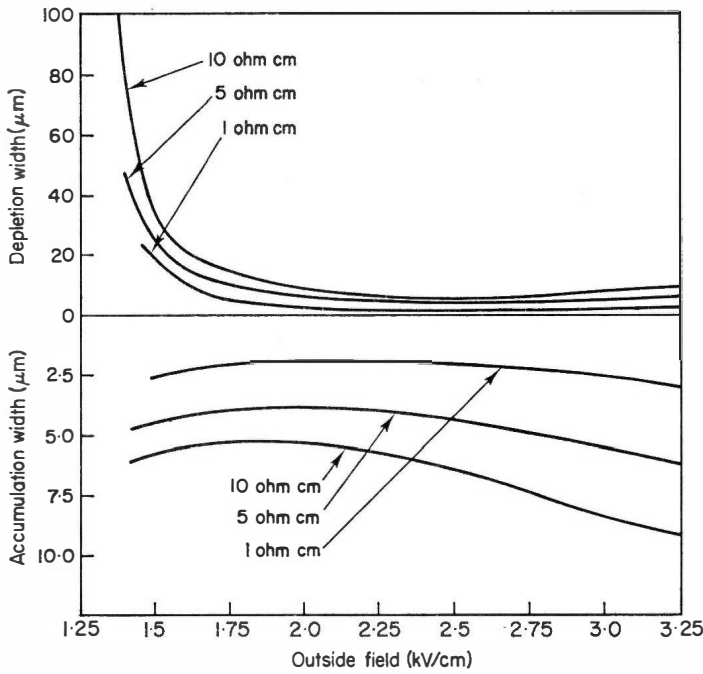


FIG. 4.14. Depletion and accumulation layer widths against field outside the domain. (Crown Copyright, reproduced by permission of the controller of Her Majesty's Stationery Office).

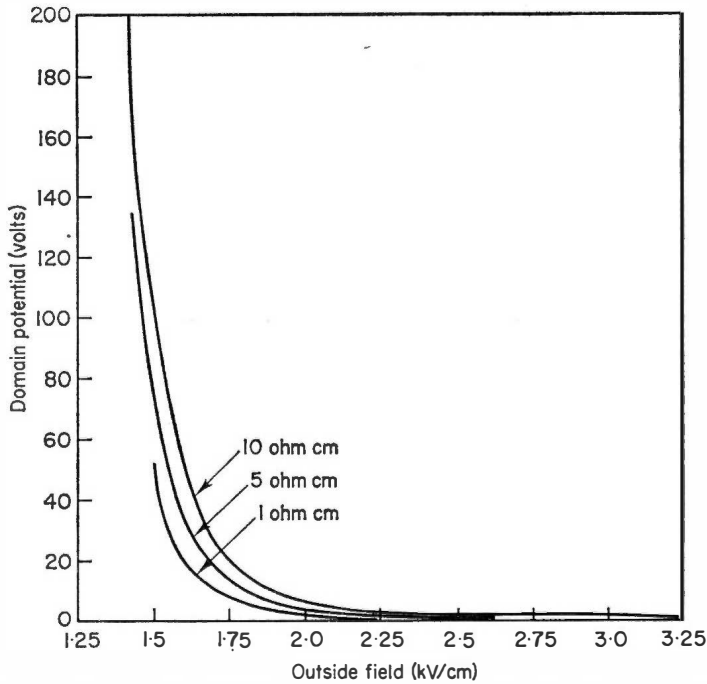


FIG. 4.15. Domain potential plotted against the field outside the domain. A "load line" representing Eqn 4.13 may be drawn on this graph, and the domain potential and outside field read-off. Figures 4.11 to 4.14 can then be used to find all the domain parameters. (Crown Copyright, reproduced by permission of the controller of Her Majesty's Stationery Office).

#### 4.8 TRIGGERED AND MULTIPLE DOMAIN

Triggered domains are best understood by considering a Gunn device in a resistive circuit.

To initiate a domain the average field  $V/l$  must rise above threshold. Once it is formed, however, it will survive as long as the average field remains above the (lower) sustaining value. This can be calculated from the equal areas rule and for long samples it is not much greater than half the threshold field.

This situation has been exploited (Heeks<sup>(5)</sup>) in the generation single triggered domains. A bias field was applied, and a short pulse sufficient to take the device over threshold, and initiate a domain, was superimposed.

The domain then made one transit and did not repeat until another trigger pulse was applied. This technique was used primarily as a diagnostic tool as it was very valuable in studying domain motion. It is also important however, in digital applications such as the Dofic (Chapter 9).

It is occasionally possible to initiate a second domain while the first one is still transversing the specimen. If this occurs one domain grows at the expense of the other which decays to zero. This is a consequence of the essentially unstable nature of space charge growth. The only stable situation is that in which there is a single domain with the electric field elsewhere below threshold. Multiple domains may be significant however, if there is too little time for the stable situation to be achieved. The multiple quenched domain mode, which is a hybrid of L.S.A. and domain modes, is discussed in Chapter 6.

#### 4.9 ACCUMULATION LAYERS

The accumulation layer is a form of domain studied by Kroemer.<sup>(9)</sup> Consider a velocity field characteristic such as that of Fig. 4.16, and apply constant voltage to a sample in which  $E = 0$  and  $n = N_0$  at each end. Poisson's

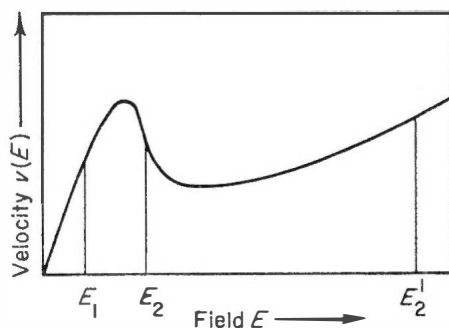


FIG. 4.16. Accumulation layer mode working points.

equation and the charge continuity equation predict an excess of carriers at the cathode just as we had in Fig. 4.2. This is an accumulation layer and as the field rises through threshold ( $N_0 l > 10^{11} \text{ cm}^{-2}$ ), most of the layer detaches from the cathode and drifts through the sample (Fig. 4.17). The field between the cathode and the accumulation layer is below threshold and that nearer the anode is above threshold. By current continuity the two fields  $E_1$ ,  $E_2$  are related by the displacement current of the travelling and growing accumulation layer; so that in general  $v(E_1) \neq v(E_2)$  and the velocity of the layer is not constant. The layer travels to the right, with the electron flow, and grows so that  $E_1$  decreases and  $E_2$  increases. When  $E_2$  reaches the valley field it then increases on the high field positive resistance branch,  $E_2'$ , and  $E_1$  goes up with it. This continues until the accumulation layer reaches the anode or  $E_1$  reaches threshold, when a further layer detaches itself.

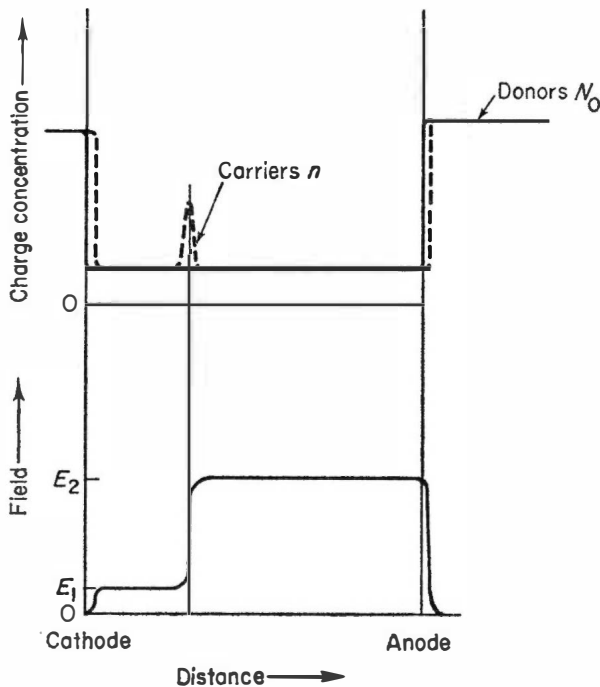


FIG. 4.17. Carrier concentration, doping profile and electric field for the accumulation layer mode.

This behaviour is not that observed by Gunn or Heeks although it has some relevance to the L.S.A. mode as we shall see later. The reason is that the doping profile was assumed to be perfectly uniform which it can never be in practice.

Doping non-uniformities have been considered by Kroemer<sup>(16)</sup> and McCumber and Chyoweth<sup>(3)</sup> showed that a fluctuation as small as  $10^{-5}$  over a distance of  $1\mu\text{m}$  initiated a depletion layer which merged and grew with the accumulation layer to form the dipole domains observed experimentally.

This is a consequence of the basic instability of bulk negative resistance material characterized by a high  $N_0l$  value.

#### 4.10 THE L.S.A. MODE

The limited space charge accumulation (L.S.A.) mode was first predicted by Copeland in a computer simulation of Gunn diode behaviour.<sup>(17)</sup> There followed experimental evidence<sup>(18)</sup> and there is no doubt that the mode exists, although it is much more difficult to observe in its pure form than was thought as first.

It was the first of the "overlength" modes (i.e. longer than transit length). These modes are important because they are free of the impedance limitation which restricts the transit length modes. Other overlength modes, multiple quenched domain and hybrid, occur under less ideal conditions and are included under the same head.

The sequence of events approaches very closely that which one might hope for from a bulk negative resistance device. The major portion of the L.S.A. diode is in the high field, negative resistance region, and there are no transit time effects, so there is no limit in theory to the active length.

The circuit and diode are arranged so that the average applied field,  $V/l$ , dips below threshold every cycle of the R.F. and the accumulation layer breaks away from the cathode as the field rises through threshold (Fig. 4.18). It then travels to the right at a speed presumably close to the peak electron velocity. The region on the left of the layer is then in the low field state and that on the right in the high field state.

The average field  $V/l$  remains above threshold for less than a cycle and when it is once more in the ohmic region any accumulation space charge disperses.

Let us return to the current continuity and Poisson's equations

$$\frac{\partial E}{\partial x} = \frac{e}{\epsilon\epsilon_0} (n - N_0) \quad (4.14)$$

$$\frac{\partial}{\partial x} (env) = \frac{e}{\partial t} \frac{\partial n}{\partial t} = 0 \quad (4.15)$$

and see why the problem is different from that of Section 4.1.

This time  $e \partial n / \partial t (= \partial q / \partial t)$  is non-zero and plays a vital part in the negative resistance mechanism.

Instead of Eqn (4.3), we have

$$env(E) + e \int_0^x \frac{\partial n}{\partial t} dx' = I = \text{const.} \quad (4.16)$$

and for Eqn (4.5), we have

$$\frac{\partial E}{\partial x} = \frac{eN_0}{\epsilon\epsilon_0} \left( \frac{I - e \int_0^x \frac{\partial n}{\partial t} dx'}{eN_0 v(E)} - 1 \right). \quad (4.17)$$

In Fig. 4.18 we show the field and charge profiles for an average field at that moment above threshold. On the left the field ( $E_L$ ) is in the ohmic

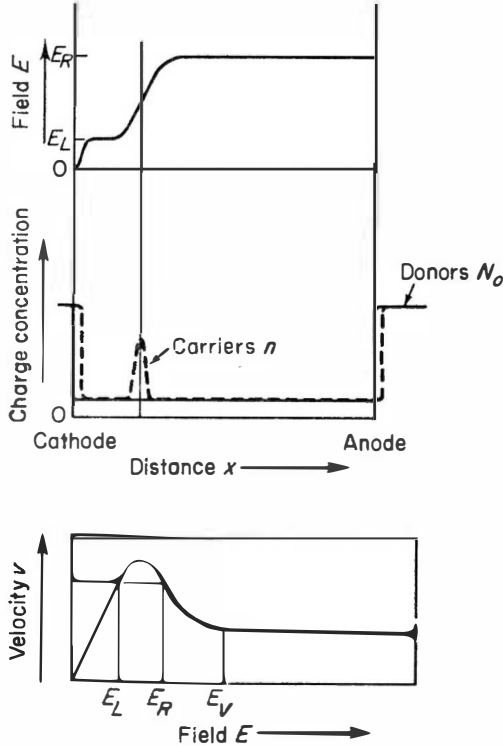


FIG. 4.18. Field, charge, and donor profiles for an L.S.A. diode. The average field is above threshold in the figure. The  $v$ - $E$  curve shows the field to the left,  $E_L$ , and right  $E_R$ , of the accumulation layer, when the average field is at a turning value.

region, on the right ( $E_R$ ) in the negative resistance region (possibly even  $E > E_V$ ), both fields correspond to nearly the same velocity, and  $n = N_0$ .

As  $V/l$  decreases the process is reversed, except that the quadrature component has now swung negative and the carrier velocity and field to the left of the accumulation layer are slightly lower than those on the right.

In this way, in sufficiently long samples the true negative resistance of the bulk material is exhibited at the terminals, or very nearly so. We now turn to examine the conditions under which the mode may be observed and why dipole domains do not form.

A basic requirement for this mode is that the field must lie in the negative differential mobility region of the velocity-field curve only for very short times compared with the average "negative dielectric relaxation time"†, so that the charges have very little time in which to accumulate. The particular shape of the velocity field curve for GaAs is rather helpful in achieving this end in practice.

As we see in Fig. 4.19, the steep negative slope is confined approximately to the region  $E_T < E < 3E_T$  and for larger fields the differential mobility is nearly zero. For sine waves then, one can envisage a rapid change of field from  $E_T$  to  $3E_T$  with the slow maximum occurring out on the flat part of the curve, and the minimum in the ohmic region.

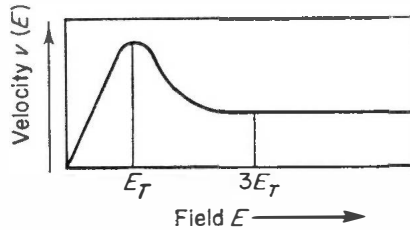


FIG. 4.19. Velocity-field curve for GaAs showing that the negative slope region is largely confined to field values  $E_T < E < 3E_T$ .

This brings us to the second condition, that the field must remain in the ohmic region long enough to disperse the accumulation layer and any charge accumulated when the field was above threshold. We can express these two requirements as:

$$\frac{1}{f} < \frac{2\epsilon\epsilon_0}{N_0\mu_N e}$$

and

$$\frac{1}{f} \gg \frac{\epsilon\epsilon_0}{N_0\mu_p e} \quad (4.18)$$

† If a bunch of carriers is introduced into a conductor it will disperse and smooth out exponentially to equilibrium in a characteristic time  $\epsilon\epsilon_0/\sigma$  which is the dielectric relaxation time.  $\sigma$  is the differential conductivity, and if this is negative charge accumulates rather than disperses, and the dielectric relaxation time is said to be negative.

where  $f$  is the frequency,  $n$  the carrier concentration,  $e$  the electronic charge,  $\epsilon\epsilon_0$  the permittivity and  $\mu_N, \mu_p$  the notional negative and positive dielectric relaxation times. The choice of the constant 2 and the factor represented by  $\gg$  are somewhat arbitrary (or inspired) and 10 is usually taken for the latter. With the physical constants appropriate to GaAs, we then arrive at the condition:

$$2 \times 10^5 > \frac{N_0}{f} > 2 \times 10^4 \text{ cm}^{-3} \text{ sec.} \quad (4.19)$$

We stress the existence of a lower limit,  $N_0 > 2 \times 10^4$ . If  $N_0$  were very low both growth and decay would be equally affected and we should not expect growth. However the requirement is not only that net growth over a cycle should not occur, but also that the accumulation layer which detaches from the cathode every cycle should decay when the field is below threshold. This requires an adequately fast dielectric relaxation time and hence  $N_0 > 2 \times 10^4$ .

We will look more fully at the conditions for space charge growth and circuit control in Chapter 6, and we will see then that these approximately derived bounds for  $N_0$  are a good working guide.

The contact regions are similar to the D.C. case (Section 4.2) but the accumulation layer is very different. The layer is moving to the right with a velocity  $v_D$ , so at its left-hand edge at any time  $\partial n / \partial t$  is large and negative, and to obey current continuity (Eqn (4.16)) there is an increase in  $n$  and  $v$ . In Eqn (4.17)  $\partial E / \partial x$  is  $> 0$ , for  $v$  can only increase by about a factor of two, whereas  $\partial n / \partial t$  is large, so  $E$  increases throughout the accumulation layer.

$\partial n / \partial t$  passes through zero and becomes negative at the peak of the charge distribution if  $d/dt (V/l)$  is temporarily zero, and in this case

$$\int_0^x \frac{\partial n}{\partial t} dx'$$

is zero at points to the right of the layer, as it is to the left.

However, if  $V$  is increasing

$$\int_0^x \frac{\partial n}{\partial t} dx' > 0$$

at points to the right of the layer, so that conduction current, hence  $v$ , must be greater to the left of the layer. This represents a capacitive current in quadrature with the conduction current. The "plates" of the capacitor are the accumulation layer, and the right hand contact.



The accumulation layer travels into the diode until it is quenched when the average field  $V/l$  drops below threshold again. There are no transit time effects, and usually the region on the right of the layer is much longer than that on the left. In that case the average voltage  $V$  must be dominantly related to the field on the right, as that on the left occupies only a small distance.

As  $V/l$  increases, then the high field (on the right) increases, and the current there falls (provided  $V/l < E_v$ ). By current continuity the current on the left must fall equally, except for the effect of the quadrature component, and the accumulation layer grows, so providing greater values of displacement current to satisfy the requirement for larger values of  $E$  integrated from Eqn (4.17).

#### 4.11 AMPLIFIERS

An oscillator is usually regarded as an amplifier with feedback. Because of the essentially unstable nature of the bulk negative resistance in GaAs this is not a useful approach to the examination of either domain of L.S.A. modes. The amplifier mode we are about to discuss is manifest in GaAs with different parameters (length and doping) from those appropriate to the oscillator modes.

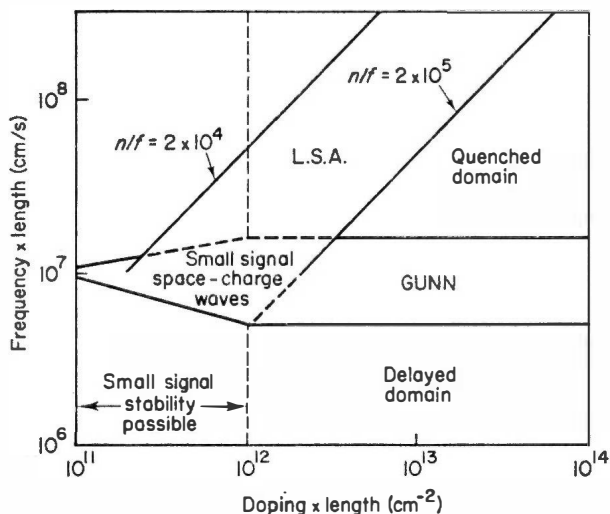


FIG. 4.20. The frequency  $\times$  length and doping  $\times$  length products are plotted to show the values appropriate to various modes in GaAs. The positions of the lines vary with material quality, temperature and circuit conditions, and represent diffuse rather than hard boundaries. (Copeland<sup>(19)</sup>).

Figure 4.20 is a very useful chart of the various modes possible in GaAs (Copeland<sup>(9)</sup>). The ordinate and abscissa are the frequency  $\times$  length and doping  $\times$  length products respectively and a locus of constant doping/frequency ratio is a straight line at  $45^\circ$  to the axes.

We see for  $N_0 l < \sim 10^{11}$  (Section 4.3) domains are not normally formed, although if the device is near transit length some space charge waves may be generated. The magnitude of the  $N_0 l$  product determines whether these waves grow into domains. At higher  $N_0 l$  products the sample would generate transit time Gunn domains.

For high  $N_0 l$  values we also see the two circuit controlled domain modes; delayed domains, which are most frequently exploited in practice and give reasonable efficiencies (Chapter 5), and quenched domains. A quenched domain is a dipole domain which is able to travel only part way across a specimen before the average field swings below the sustaining level, and so the domain dies.

The L.S.A. conditions are fulfilled above the line  $N_0 = 2 \times 10^5$  approximately and this mode, or a hybrid, is usually exploited for high frequency high power operation.

Below  $N_0 l \simeq 10^{11}$  then, we see that domains are not normally formed. There is a still bulk negative resistance however, and this can be used to make an amplifier. As we would expect from the discussion at the beginning of the chapter, negative resistance can only be observed over certain frequency ranges, and is absent at low frequencies.

#### 4.12 POWER AND FREQUENCY PERFORMANCE LIMITATIONS

We turn now to consider the ultimate performance that might be obtained from Gunn Effect Devices. The approach was suggested by Early<sup>(20)</sup> and Johnson<sup>(21)</sup> for transistors and applies to any transit time generator. Clearly it is always possible in principle to increase output by using many devices in parallel, or by increasing the cross-sectional area of one, so to make the discussion meaningful we must include the impedance,  $Z$ , at which the system works.

In practice  $Z$  cannot be made arbitrarily small. The problem of matching the impedance so that the power may be delivered usefully to a load is difficult below about 10 ohm, and below 1 ohm it is extremely so.

A semiconductor material has a breakdown field  $E_B$  and a maximum or saturation carrier velocity  $v_s$ . The maximum voltage which can exist across a transit time device of frequency  $f$  is:

$$V = \frac{E_B v_s}{f}, \quad \text{since the length is } \frac{v_s}{f},$$

and the maximum rapidly switchable current at the impedance  $Z$  is

$$I = \frac{V}{Z} = \frac{E_R v_s}{Z f}.$$

The greatest power obtainable at this frequency from such a device is then:

$$P = VI = \frac{E_B^2 v_s^2}{f^2 Z} \quad \text{for square waves.}$$

To achieve this power would involve reversing the current and voltage in perfect antiphase at that frequency. In a perfect unidirectional device the maximum power is a quarter of that given above.

So

$$P f^2 Z = \frac{E_B^2 v_s^2}{4}.$$

The product  $P f^2 Z$  is then a good means of comparing different devices and for a particular device it is a measure of how closely the fundamental limitations have been approached. In practical devices it is likely that the ultimate achievement would be nearer a tenth of  $E_B^2 v_s^2 / 4$  than perfection itself.

In this way the advantage of the L.S.A. mode can be strikingly illustrated. There is no transit length restriction and so the limitation

$$V = E_B \cdot \frac{v}{f} \text{ is absent.}$$

There is then no limitation on  $PZf^2$  on fundamental grounds; one has to examine restrictions in crystal technology, skin depth or cavity size in order to find any limitation. In units of Watts . Ohms . (GHz)<sup>2</sup> values of over  $10^6$  have already been achieved<sup>(22)</sup> and there is no reason why  $10^8$  should not be reached in a year or two.

All these arguments apply to pulsed operation and at the moment thermal considerations are much more restrictive for continuous generation. In principle however, geometries are possible which would enable heat to be removed sufficiently fast. It is in this direction that the most valuable progress will be made in the near future, rather than in simply increasing peak power values, important though that is.

It is clear, however, that for high peak powers and high frequencies the overlength modes have substantial advantages over transit length limited modes.

## 4.13 ELECTRON ENERGY RELAXATION EFFECTS AT HIGH FREQUENCIES

The high frequency performance of Gunn devices is limited by the frequency dependence of the negative differential mobility. Rees<sup>(23)</sup> has shown that due to the weak scattering of electrons with energies between 0.1 and 0.36 eV in the central valley, the threshold electric field rises and the differential mobility falls as the frequency increases. Below 10 GHz the effects are small but become important above 30 GHz. At 100 GHz the threshold is 6.5 KV/cm and by 140 GHz the negative conductivity is negligible.

Contrary to earlier expectations Rees shows that neither intervalley scattering times nor relaxation within the upper valley are important at microwave frequencies.

It is to be expected that relaxation time effects would have a profound influence on domain behaviour, especially at the sharp trailing edge. Here the electric field gradient is very large, and as the domain velocity and electron velocity are not in general equal, the electrons are required to change energy extremely rapidly as the domain propagates. The effect of a limited energy relaxation time must presumably be to smooth out the otherwise sharp transition, but as far as is known this extremely difficult calculation has received little study.

## REFERENCES

1. Shockley, W. (1954). *Bell System Tech. J.* **33**, 799–825.
2. Kroemer, H. (1965). *Proc. I.E.E.E.* **53**, 1246.
3. McCumber, D. E. and Chynoweth, A. G. (1966). *I.E.E.E. Trans.* **ED-13**, 4–21.
4. Gunn, J. B. (1964). *I.B.M. J. Res. Develop* **8**, 141–159.
5. Heeks, J. S. (1966). *I.E.E.E. Trans.* **ED-13**, 68–78.
6. Thim, H. W. *et al.* (1965). *Appl. Phys. Letters* **7**, 167.
7. Bott, I. B. and Fawcett, W. (1968). *Advances in Microwave* **3**, 223–299.
8. Ridley, B. K. (1966). *I.E.E.E. Trans.* **ED-13**, 41–43.
9. Kroemer, H. (1964). *Proc. I.E.E.E.* **52**, 1736.
10. Copeland, J. A. (1966). *J. Appl. Phys.* **37**, 3602–3609.
11. Butcher, P. N. *et al.* (1967). *Brit J. Appl. Phys.* **18**, 755–759.
12. Butcher, P. N. *et al.* (1966). *Brit. J. Appl. Phys.* **17**, 841–850.
13. Allen, J. W. *et al.* (1966). *J. Appl. Phys.* **37**, 3191–3195.
14. Butcher, P. N. and Fawcett, W. (1966). *Brit. J. Appl. Phys.* **17**, 1425–1432.
15. Butcher, P. N. and Fawcett, W. (1966). *Phys. Letters* **21**, 489–490.
16. Kroemer, H. (1966). *I.E.E.E. Trans.* **ED-13**, 27–40.
17. Copeland, J. A. (1966, 1967). *Proc. I.E.E.E.* **54**, 1479; *I.E.E.E. Trans.* **ED-14**, 55–58.
18. Copeland, J. A. (1967). *Bell System Tech. J.* **46**, 284–287.
19. Copeland, J. A. (1967). *J. Appl. Phys.* **38**, 3096.
20. Early, J. M. (1959). *I.R.E. Trans.* **ED-6**, 322–325.
21. Johnson, E. O. (1965). *I.E.E.E. Internat. Conv. Record* **pt.5**, 27–34, 1965; *R.C.A. Review*, 163–177, June 1965.

22. Kennedy, W. K. *et al.* (1967). Proc. Cornell Conf. High Frequency Generation and Amplification, 94–108.
23. Rees, H. D. (1969). *Sol. St. Comms.* **7**.
24. Kataoka, *et al.* (1969). *Electron. Lett.* **5**, 48.
25. Kataoka, *et al.* (1970). *Electron. Lett.* **6**, 169.
26. Robson, P. N. *et al.* (1967). *I.E.E.E.* ED-14, 612–5.

## *Chapter 5*

# **Transit Time Modes**

### **5.1 INTRODUCTION**

In the previous chapter we obtained the dynamic current–voltage characteristic for the stable domain propagation. We now go on to consider domain modes in detail and see how an oscillating circuit reacts on the generator which is sustaining it. We must bear in mind that the dynamic characteristic was derived for constant applied voltage, and allowance must be made for the domain's response to an oscillating applied voltage.

This chapter includes only transit modes, in which the domain transit time is roughly within a factor or two of an oscillation half period. Quenched domains, in which the sample is much longer, are left to Chapter 6 which covers all the “long sample” modes.

We start by considering domain properties in more detail to see how they will affect performance, and then proceed to examine the limiting cases under favourable assumptions. Three approaches to calculating device performance are then given, and the remainder of the chapter deals with practical operation and some experimental results achieved up to mid-1969.

### **5.2 DOMAINS**

Transit time operation is confined to domain modes and some hybrids in which domains are only partly formed. The distinction is made partly by the  $nI$  product of the diode and partly by the circuit frequency, bias and r.f. swing. High power transit time devices are particularly likely to have incompletely formed domains because of the high bias voltages usually employed, whereas small C.W. devices operate more nearly in a conventional domain mode.

### **5.3 DOMAIN NUCLEATION**

The nucleation of domains is not fully understood, even though working rules are known.

It is expected that a domain will nucleate where the electric field first exceeds threshold as the applied voltage is increased. In general, this will be the highest resistance layer in the device; highest either because of a doping variation, or a geometric constriction. While this is found to be broadly true, there are some exceptions.

Devices have been made in which the electric field is in the plane of the epitaxial layer rather than normal to it. In some of these transverse devices it was found that a heavily doped  $n^+$  GaAs cathode would not nucleate domains even though the geometry was favourable, and metal cathodes had to be used.<sup>(1)</sup> Again, in some longitudinal devices, even with a high resistance layer near the substrate, domains would not nucleate when the substrate was the cathode; high field regions seemed to form at the metal top contact whether this was anode or cathode. Symmetrical devices can be made with  $n^+$  GaAs contacts in the longitudinal geometry however.

Simple longitudinal devices with metal top contacts are geometrically asymmetrical and it is not surprising that these have usually been found to operate only if the metal contact is the cathode. When the bias was reversed most devices were destroyed after a few hundred nanoseconds. A current-voltage characteristic taken with short pulses usually showed a very limited saturation region, or even only a slight point of inflection, followed by avalanche or injection (Fig. 5.1).

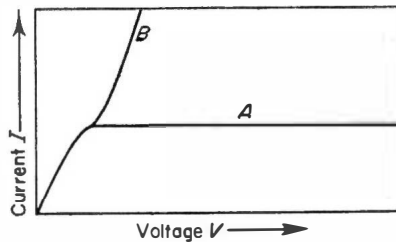


FIG. 5.1. Pulsed I-V characteristics for epitaxial metal contact longitudinal devices. Curve A—metal as cathode, Curve B—metal as anode.

Recent work at S.T.L.<sup>(21)</sup> has shown that some non-reciprocal behaviour is due to the loss of arsenic from the GaAs during the contacting procedure, which leaves a high resistivity layer adjacent to the contact. Metal contact deposition in an atmosphere containing arsenic has yielded devices whose current-voltage characteristics are nearly as symmetrical as those of devices with  $n^+$  GaAs contacts.

If a high field domain does form in a position where it does not propagate, such as against the anode, the device is likely to be destroyed. The power density in that region could be 10 to 100 times (depending on the  $nI$  product and the bias) the mean values for a device operating normally. The high

electric field at the anode may lead to hole injection from that contact, or there may simply be avalanche generation. Either mechanism would lead to the non-saturating curve B in Fig. 5.1. Curve A is the residual characteristic which is observed when the measurement is slow compared to domain formation, and should not be confused with the true instantaneous characteristic, such as Fig. 4.1, which may be observed directly only with difficulty. The residual characteristic usually either saturates or has a slightly negative slope, with one or more abrupt negative jumps in current when the device breaks into oscillation or changes its mode. In some, presumably good, devices the jump occurs immediately after the peak current is reached, and may amount to a drop in current of up to about 60%.

#### 5.4 DOMAIN CAPACITY AND DEVICE REACTANCE

In order to calculate the capacity of a domain, we return to develop further the domain properties discussed in Chapter 4. We are concerned for the moment with stable domain propagation following the treatment of Butcher *et al.*<sup>(2)</sup> with zero diffusion.

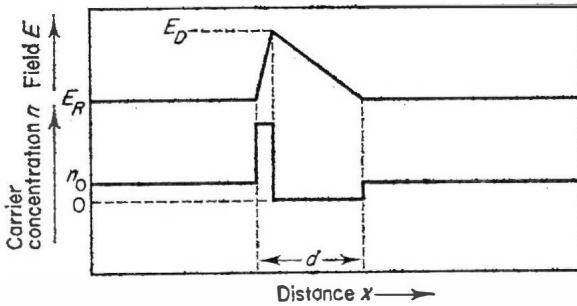


FIG. 5.2. Field and carrier concentration in a simple domain. The domain propagates to the right.

Figure 5.2 shows the field and carrier concentration profiles for a fully depleted domain with a sharp concentration in the trailing edge. We saw in Chapter 4 that such a domain is stable and moves at the speed of the electrons in the remainder of the sample.

The excess domain voltage is

$$\phi_D = \left\{ \frac{(E_D - E_R)}{2} \right\} d,$$

and the peak field is related to the donor concentration by Poissons equation

$$\epsilon \epsilon_0 \left( \frac{E_D - E_R}{d} \right) = N_0 e,$$

where  $e$  is the electronic charge, if the accumulation layer is very narrow.



So 
$$E_D - E_R = \frac{1}{\epsilon\epsilon_0} N_0 ed.$$

and 
$$\phi_D = \frac{1}{\epsilon\epsilon_0} \frac{N_0 ed^2}{2}.$$

The total charge redistributed in the domain

$$Q = N_0 ed \quad (\text{per unit cross-section})$$

so the static capacity

$$C = \frac{Q}{\phi_D} = \frac{2\epsilon\epsilon_0}{d} \quad (\text{per unit cross-section}).$$

Due to the shape of the charge distribution the incremental capacity per unit cross-section  $C_{r.f.}$  is half this figure, for

$$\phi_D = \frac{N_0 ed^2}{2\epsilon\epsilon_0}$$

so 
$$\frac{d\phi_D}{dd} = \frac{N_0 ed}{\epsilon\epsilon_0}$$

and 
$$\frac{dQ}{dd} = N_0 e$$

so 
$$\frac{dQ}{d\phi} = \frac{\epsilon\epsilon_0}{d} = C_{r.f.}$$

The energy stored in the domain

$$\begin{aligned} &= \int_0^d \phi \frac{dQ}{dx} dx \\ &= \int_0^d \frac{N_0 ex^2}{2\epsilon\epsilon_0} N_0 e dx \\ &= \frac{1}{6\epsilon\epsilon_0} (N_0 e)^2 d^3 \\ &= \frac{\epsilon\epsilon_0}{6} (E_D - E_R)^2 d \quad (\text{per unit cross-sectional area}). \end{aligned}$$

Fully depleted domains do not, of course occur in all samples—a large  $nl$  product is required for full depletion. The inclusion of diffusion affects these results mainly through  $d$ , the effective domain width. If this parameter is read from Figs. 4.11 to 4.15 the above expressions may still be used with reasonable accuracy. The experiments of Kuru *et al.*<sup>(3)</sup> largely confirm the validity of these calculations.

It is instructive to consider the magnitudes of the quantities derived above. A Gunn device is commonly used as C.W. generator near 10 GHz in the form of an active layer of GaAs 10  $\mu\text{m}$  thick with  $10^{15}$  carriers/ $\text{cm}^3$  and a mobility of  $6200 \text{ cm}^2 \text{ V}^{-1} \text{ sec}^{-1}$ . The resistivity is  $1 \Omega \text{ cm}$  which implies a low field resistance of  $20 \Omega$  for a cross-section,  $A = 30 \times 10^{-6} \text{ cm}^2$ . The threshold voltage corresponding to  $3 \text{ kV/cm}$  is  $3 \text{ V}$  and the saturation current is thus  $0.1 \text{ A}$ , giving  $1 \text{ W}$  dissipation at a typical working point of  $10 \text{ V}$ .

These figures represent a very familiar “standard model” Gunn generator such as has been marketed since 1966. It is not a very good example to choose as a stable domain can hardly form, but nevertheless it is useful as an illustration.

Reading from Fig. 4.15 we see that the “load line” for  $10 \text{ kV/cm}$  and  $10 \text{ V}$  is almost a horizontal straight line giving an outside field of  $1.75 \text{ kV/cm}$  and a domain potential of nearly  $10 \text{ V}$ . Figure 4.14 gives the accumulation layer width as  $2.5 \mu\text{m}$  and the depletion layer width as about  $6 \mu\text{m}$ . Figure 4.13 indicates accumulation of about 15 times, and depletion down to less than 20% where it is rather insensitive to changes in outside field and hence applied voltage. The static capacity  $2\epsilon\epsilon_0 A/d$  is approximately  $0.1 \text{ pF}$  which has a reactance at  $10 \text{ GHz}$  of  $160 \Omega$ . We should expect that, since depletion is considerable and insensitive to field changes,  $C_{r.f.}$  would be about half this value. Unfortunately this leaves aside the question of the formation time of an  $8 \mu\text{m}$  domain in a  $10 \mu\text{m}$  layer. The experimental results in Section 5.5 suggest that  $C_{r.f.}$  is nearer  $0.1 \text{ pF}$  in fact. The energy stored in this capacity would be about  $5 \times 10^{-12} \text{ Joules}$  and if this were released usefully every cycle at  $10 \text{ GHz}$  the power developed would be  $50 \text{ mW}$ . This would not be a trivial power if it were usefully available, but it is unlikely to be so, as can be seen from the following two extreme cases.

If the domain runs into the anode during a turning value in current, then the domain voltage  $V$  runs to zero and the capacity  $C$  to infinity, preserving the product  $Q = CV$  constant, because the charge on the trailing edge cannot escape until it comes into coincidence with the sharp depletion region at the anode contact on the final extinction of the domain (see Fig. 5.3).

On the other hand, in the more realistic situation of the domain reaching the anode near a turning value in voltage when the current is free to vary, then the capacity, of course, still runs to infinity and the voltage to zero, but as the voltage drops in the domain so it must rise in the remainder

of the sample which is in an ohmic condition. The current therefore rises and the charge increases as the domain runs out, until it is extinguished when the accumulation region reaches the depleted region in the heavily doped anode. In this case the voltage goes to zero more slowly than in the steady current case.

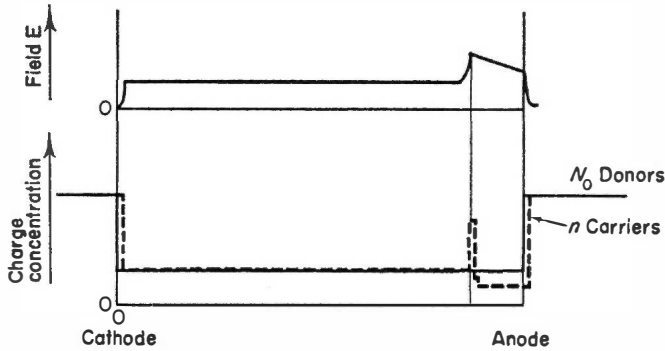


FIG. 5.3. Field distribution and donor and carrier concentration in a Gunn device whose current varies little while the domain runs into the anode.

In neither of these extreme cases is the domain discharge accompanied by reverse flow or diminution of flow of current in the circuit. It is not a capacitive discharge in the normal sense, which implies constant or slowly varying capacitance, and is in sharp contrast to domain formation, modulation, or extinction, in the interior of the device such as occurs in the quenched domain mode.

Another major contribution to the reactance of a device is the non-linearity of the current-voltage characteristic. In Fig. 5.6 the current and voltage are shown in their optimum relation,  $180^\circ$  out of phase. In this special case the reactance is assumed to be negligible. However, since the domain sustaining voltage is lower than the threshold voltage, the current in general is not symmetrical about the voltage minimum and a large quadrature component may flow.

### 5.5 POWER OUTPUT AND EFFICIENCY

It is clearly most important in any generator to examine the power output and efficiency that can be obtained. We also need to consider other properties such as noise, frequency stability etc., depending on the application envisaged. For a local oscillator, for example, the latter properties would be very important, whereas the power output would simply have to be

above minimum (say 5 mW), and the efficiency would matter hardly at all. In a radar transmitter, on the other hand, power output is paramount. Due to thermal considerations it might be limited by efficiency, and noise is sometimes unimportant.

The highest efficiency that can be obtained from a generator is that corresponding to square wave operation with current and voltage perfectly out of phase, and the extremes of the waveforms at the most favourable points on the characteristic. Transistor circuits operating in this way can achieve conversion efficiencies of over 90% since advantage can be taken of the low saturation voltage in the "on" condition and the low leakage current in the "off" condition.

Most analyses of realisable situations for Gunn devices cannot be carried out analytically so we can do no more, in such cases, than state the results of numerical calculations. It is instructive, however, to start with the ideal square wave case and then study analytical treatments of sine wave operation before dealing with the more exact computed results.

In the idealized situation of Fig. 5.4, the power output is:

$$P_{\text{out}} = \left[ \frac{I_1 - I_2}{2} \right] \cdot \left[ \frac{V_1 + V_2}{2} \right]$$

for square wave generation. The sine wave power content at the fundamental frequency is

$$P_{\text{r.f.}} = P_{\text{out}} \cdot \left( \frac{8}{\pi^2} \right).$$

The power input is

$$P_{\text{in}} = \left[ \frac{I_1 + I_2}{2} \right] \cdot \left[ \frac{V_1 + V_2}{2} \right],$$

so the efficiency

$$\eta = \left[ \frac{I_1 - I_2}{I_1 + I_2} \right] \cdot \left[ \frac{V_1 - V_2}{V_1 + V_2} \right] \left( \frac{8}{\pi^2} \right).$$

Clearly it is desirable to have  $I_1$  and  $V_1$  as large as possible and  $I_2$  and  $V_2$  as small as possible.

For Gunn effect devices  $I_1/I_2$  and  $V_2$  are fixed by the properties of the active material used.  $V_1$  is less restrained, being determined by the circuit and bias conditions and only limited by the breakdown field. For GaAs a value of about 2 for  $I_1/I_2$  is typical, and  $V_2$  is determined by the threshold field of 3 kV/cm.

For these values, then, as  $V_1 \rightarrow \infty$  the efficiency  $\eta \rightarrow 27\%$  if the fundamental sine wave component is filtered, or if the whole square wave is regarded as the output

$$\eta \rightarrow 33.3\%.$$

This is the absolute maximum efficiency for a device with  $I_1/I_2 = 2$ , and, of course, for finite values of voltage, the efficiency is lower.

While square wave operation is the most efficient way of generating some sort of a.c. power it is not the best way to produce fundamental power.

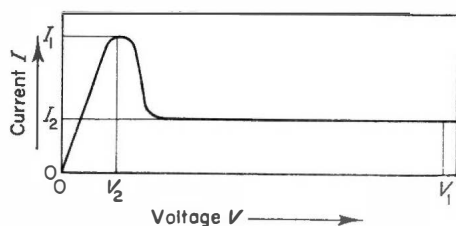


FIG. 5.4. Simple current-voltage relation and idealized square waveforms in a Gunn device.

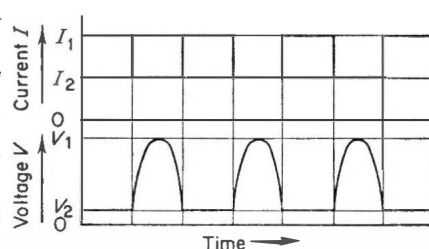


FIG. 5.5. A square current waveform and half sinusoidal voltage as suggested by Day *et al.*<sup>(4)</sup>

The square current and voltage waveforms contain odd harmonic components which are in phase and so waste power. For maximum efficiency in the fundamental the voltage waveform should not contain any odd harmonic components in phase with those of the current waveform. Such a voltage waveform is the half sinusoid<sup>(4)</sup> of Fig. 5.5. This has only the fundamental and even harmonic components and has exactly the same conversion efficiency to the fundamental as the square waveform has to square-wave power for

Peak-valley ratio $I_1/I_2$	Maximum efficiency %	Efficiency % Square wave filtered fundamental				Efficiency % Half sinusoid			
		$V_1/V_2 = \infty$	$V_{dc}/V_2 = \infty$	20	10	$V_1/V_2 = \infty$	$V_{dc}/V_2 = \infty$	20	10
2	33	27	25	22	9	33	29	25	7.7
2.5	43	35	32	29	12	43	37	32	10
3	50	41	37	33	14	50	43	37	12
4	60	49	44	40	16	60	51.5	45	14

the same bias voltage,  $V_{dc}$ . The peak voltage is higher however. For square waves the peak voltage is  $V_1 = 2V_{dc} - V_2$ , whereas for the half sinusoid  $V_1 = \pi V_{dc} - (\pi - 1)V_2$ . If the breakdown field is low, this factor would mean that filtered square wave operation would give higher efficiency, but in good material with high breakdown fields the half sinusoid would be superior.

The above table shows the efficiencies corresponding to the two modes of operation under various peak to valley ratios ( $I_1/I_2$ ).

The half sinusoid waveform requires a short circuit load at all odd harmonics and an open circuit load at all even harmonics—an exacting design problem to say the least. However, a waveform which contains only a second harmonic component in the appropriate phase is a reasonable approximation to a half sinusoid, and can give efficiencies up to about 20% for  $V_1/I_2$  up to about 8.<sup>(20)</sup>

It would clearly be desirable to discover a material with as high a peak-to-valley ratio ( $I_1/I_2$ ), and as high a breakdown field, as possible. The peak-to-valley ratio of GaAs seems to be rather more than 2 : 1, perhaps 2.5 : 1 from the best results so far, and the purity of the material still leaves much to be desired.

## 5.6 LIMITATIONS ON POWER OUTPUT

As discussed in Chapter 4, a device cannot be scaled indefinitely to give any desired output power. A transit time device has a limited thickness and therefore a limited voltage, so the power handling capacity of a single device, or of devices in parallel, can only be increased by raising the total current and thereby lowering the impedance.

As we saw in Section 4.12,

$$PZf^2 = \frac{E_B^2 V_s^2}{4}.$$

The limitation on transit time devices is absolutely fundamental and cannot be exceeded for a single device or a parallel combination of devices. Indeed, it cannot even be approached by quite a large factor since the analysis assumes 100% efficiency and square wave operation. As we saw in Section 5.5, the efficiency  $\eta$  can never exceed  $(I_1 - I_2)/(I_1 + I_2)$ .

It is instructive to put in some figures for GaAs. The values are  $E_B = 200$  kV/cm and  $V_s = 10^7$  cm/sec, typically.

So

$$PZF^2 = \frac{E_B^2 V_s^2}{4} \eta$$

$$\approx 10^6 \eta \text{ Watt} \cdot \text{Ohm} (\text{GHz})^2.$$

We have seen that the efficiency is unlikely much to exceed 30%, so at 10 GHz a  $PZ$  of 3000 Watt Ohms must be about the limit for a transit time device. The best result known so far (1968) is 34 Watts at about 9 GHz at an impedance probably between 10 and 20 Ohms (5.5). This gives an equivalent  $PZ$  at 10 GHz of about 500 Watt Ohms which is remarkably good.

### *Skin depth*

The limitation imposed by skin depth is mechanically annoying, but does not impose an absolute limit since it is in principle possible to arrange the geometry of the device to give large surface area.

The field distribution due to the skin effect in a generating conductor or semi-conductor is exactly the same as in an absorbing one, surprising though this may seem at first sight.<sup>(6,7)</sup> The general electromagnetic wave equation in a medium of conductivity  $\sigma$  and permeability  $\mu$  is:

$$\nabla^2 E = \mu\sigma \frac{\partial E}{\partial t} + \mu\epsilon_0 \frac{\partial^2 E}{\partial t^2}$$

where  $\epsilon_0$  is the permittivity.

If we consider propagation perpendicular to the plane of the surface of the semi-conductor, then this equation has four solutions representing decaying and growing waves† travelling in both directions.

A decaying wave travelling into the material is the familiar solution for positive conductivity which gives the normal skin effect. Where the conductivity is negative, we expect a growing wave, and since it is a generator it must be propagating outwards, so that the energy may be available to the outside world rather than disappearing into the centre of the conductor. A decaying wave going in has exactly the same envelope as a growing wave coming out, so the skin depth may be calculated in the usual way as

$$\delta = (\frac{1}{2}\omega\mu\sigma)^{-\frac{1}{2}}.$$

In the presence of large space charge currents the skin depth is greater than this, by up to about five times when the displacement current is ten times the conduction current.<sup>(6)</sup>

In 1Ω-cm material of unit relative permeability the skin depth is approximately 0.5 mm at 10 GHz. When designing a generator with one dimension small, then that dimension should be rather less than twice the skin depth in order that the field within the specimen be reasonably uniform. If the dimension is too large, any perturbations at the centre will grow so large

† The term 'wave' is used here to include also very strong growth or decay which may show no periodicity.

before they reach the surface that the field excursions will be running well off the negative resistance part of the  $I - V$  curve, and so no advantage will be gained.

### 5.7 OPERATION WITH A SINE WAVE OF VOLTAGE

We now turn to the simple analytical treatment of the power output and efficiency of Gunn diodes given by Warner.<sup>(8)</sup> This section and the next are included since these analytical studies clarify some of the ways in which the circuits and devices interact. They cannot be regarded as rigorous as a full numerical treatment may be, and some of the assumptions have since been shown to be incorrect. They give, nevertheless, a useful insight into device operation.

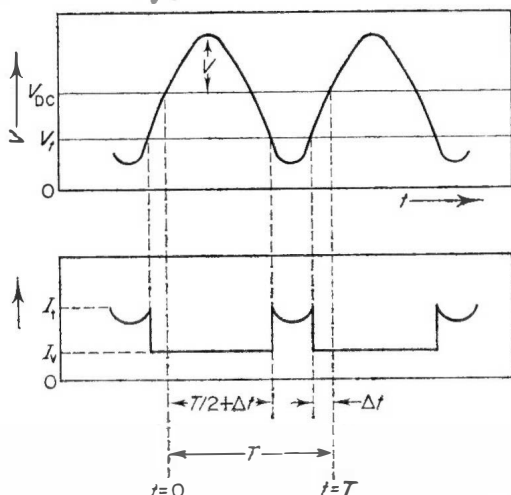


FIG. 5.6. Voltage and current waveform for Gunn device. Warner.<sup>(8)</sup> (Crown Copyright, reproduced by permission of the Controller of Her Majesty's Stationery Office).

Figure 5.6 shows the voltage and current waveforms assumed. The device is in a high  $Q$  circuit or cavity which constrains the voltage to be a sine wave at the desired frequency. The voltage has a mean value  $V_{dc}$  and swings below threshold,  $V_t$ , once each cycle. The current, following an  $I - V$  characteristic such as that of Fig. 5.4, is substantially constant,  $I_v$ , while the voltage is well above threshold and obeys Ohm's law before threshold. It is assumed that domain formation is instantaneous and that the relation between the frequency of oscillation and the transit time of the sample is such that the domain reaches the anode at the instant when the voltage swings back through the threshold value. This is the time relation giving maximum efficiency. The effects of the domain capacity are assumed to make no contribution to the power output and the capacitive component of current is omitted in Fig. 5.6.



Following the notation of Fig. 5.6 it is clear that

$$V_{dc} + V \sin \{2\pi(-\Delta t/T)\} = V_t$$

and so

$$\Delta t = \frac{T}{2\pi} \sin^{-1} \left( \frac{V_{dc} - V_t}{V} \right).$$

Using Fourier analysis, the peak amplitude of the fundamental inphase component in the current through the device is

$$\begin{aligned} I &= \frac{2}{T} \int_0^{(T/2)+\Delta t} I_v \sin \frac{2\pi t}{T} dt + \frac{2}{T} \int_{(T/2)+\Delta t}^{T-\Delta t} \frac{V_{dc} + V \sin (2\pi t/T)}{r} \sin \frac{2\pi t}{T} dt \\ &\quad + \frac{2}{T} \int_{T-\Delta t}^T I_v \sin \frac{2\pi t}{T} dt \\ &= - \left\{ \frac{2}{\pi} \left( \frac{V_{dc}}{r} - I_v \right) \cos \frac{2\pi \Delta t}{T} - \frac{V}{r} \left( \frac{1}{2} - \frac{2\Delta t}{T} + \frac{1}{2\pi} \sin \frac{4\pi \Delta t}{T} \right) \right\} \end{aligned}$$

where  $r$  is the low-field resistance of the device.

The output power is

$$P_{out} = V(-I)/2$$

so

$$\begin{aligned} P_{out} &= \frac{V}{2} \left[ \left\{ 1 - \left( \frac{V_{dc} - V_t}{V} \right)^2 \right\}^{\frac{1}{2}} \left( \frac{V_{dc} + V_t - 2I_v r}{\pi r} \right) \right. \\ &\quad \left. - \frac{V}{2r} + \frac{V}{\pi r} \sin^{-1} \left( \frac{V_{dc} - V_t}{V} \right) \right]. \end{aligned}$$

On differentiating with respect to  $V$ , and equating the result to zero,  $P_{out}$  is found to be greatest when  $V = V_{opt}$ , where

$$\frac{V_{opt}}{2} = \frac{V_t - I_v r}{\pi} \frac{1}{\left\{ 1 - \left( \frac{V_{dc} - V_t}{V_{opt}} \right)^2 \right\}^{\frac{1}{2}}} + \frac{V_{opt}}{\pi} \sin^{-1} \left( \frac{V_{dc} - V_t}{V_{opt}} \right).$$

To simplify this equation, let  $\sin^{-1} \{(V_{dc} - V_t)/V_{opt}\} = \theta$ .

$$\text{Hence } \frac{\tan \theta}{2\{(V_{dc}/V_t) - 1\}} + \theta = \frac{\pi}{2}$$

for  $I_t = 2I_v$ . Fig. 5.7 shows how  $\theta$  varies with  $V_{dc}/V_t$ .

It follows that

$$P_{\text{out max}} = \frac{V_t^2}{r} \frac{1}{2\pi \sin \theta} \left( \frac{V_{\text{dc}}}{V_t} - 1 \right) \left( \frac{V_{\text{dc}}}{V_t} \cos \theta - \frac{1}{2 \cos \theta} \right).$$

$$V_{\text{opt}} = V_t \frac{(V_{\text{dc}}/V_t) - 1}{\sin \theta}$$

and

$$I_{\text{opt}} = -\frac{V_t}{r} \frac{1}{\pi} \left( \frac{V_{\text{dc}}}{V_t} \cos \theta - \frac{1}{2 \cos \theta} \right).$$

The average value of the supply current is

$$\begin{aligned} I_{\text{av}} &= \frac{1}{T} \left( \int_0^{(T/2)+\Delta t} I_v dt + \int_{(T/2)+\Delta t}^{T-\Delta t} \frac{V_{\text{dc}} + V \sin(2\pi t/T)}{r} dt + \int_{T-\Delta t}^T I_v dt \right) \\ &= \frac{1}{T} \left\{ I_v \left( \frac{T}{2} + 2\Delta t \right) + \frac{V_{\text{dc}}}{r} \left( \frac{T}{2} - 2\Delta t \right) - \frac{VT}{\pi r} \cos \frac{2\pi \Delta t}{T} \right\} \end{aligned}$$

which simplifies to

$$I_{\text{av}} = \frac{V_t}{r} \left( \frac{1}{4} + \frac{\theta}{2\pi} + \frac{1}{2} \frac{V_{\text{dc}}}{V_t} - \frac{\theta}{\pi} \frac{V_{\text{dc}}}{V_t} - \frac{1}{\pi} \frac{V_{\text{opt}}}{V_t} \cos \theta \right).$$

The efficiency  $\eta$  is  $P_{\text{out}}/V_{\text{dc}}I_{\text{av}}$ , and it follows that

$$\begin{aligned} \eta &= \frac{\frac{1}{2\pi \sin \theta} \left( \frac{V_{\text{dc}}}{V_t} - 1 \right) \left( \frac{V_{\text{dc}}}{V_t} \cos \theta - \frac{1}{2 \cos \theta} \right)}{\frac{V_{\text{dc}}}{V_t} \left\{ \frac{1}{4} + \frac{\theta}{2\pi} + \frac{1}{2} \frac{V_{\text{dc}}}{V_t} - \frac{\theta}{\pi} \frac{V_{\text{dc}}}{V_t} - \frac{1}{\pi} \left( \frac{V_{\text{dc}}}{V_t} - 1 \right) \cot \theta \right\}} \end{aligned}$$

Figure 5.7 shows how  $\eta$  varies with  $V_{\text{dc}}/V_t$ . It is seen that the efficiency reaches a maximum value of 7.2% when  $V_{\text{dc}}/V_t = 1.9$ .

The circuit oscillation frequency

$$f_{\text{osc}} = 1/T$$

and the domain transit time frequency

$$f_d = \frac{1}{\tau}$$

so it is clear that

$$\tau = T/2 + 2Vt$$

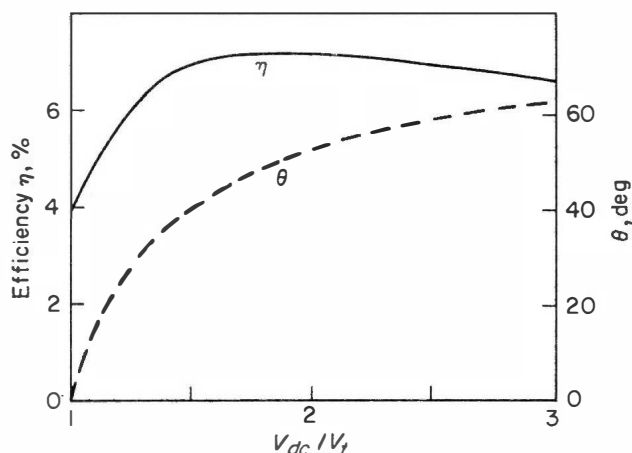


FIG. 5.7. Efficiency and  $\theta$  as functions of  $V_{dc}/V_t$ .<sup>(8)</sup> (Crown Copyright, reproduced by permission of the controller of Her Majesty's Stationery Office).

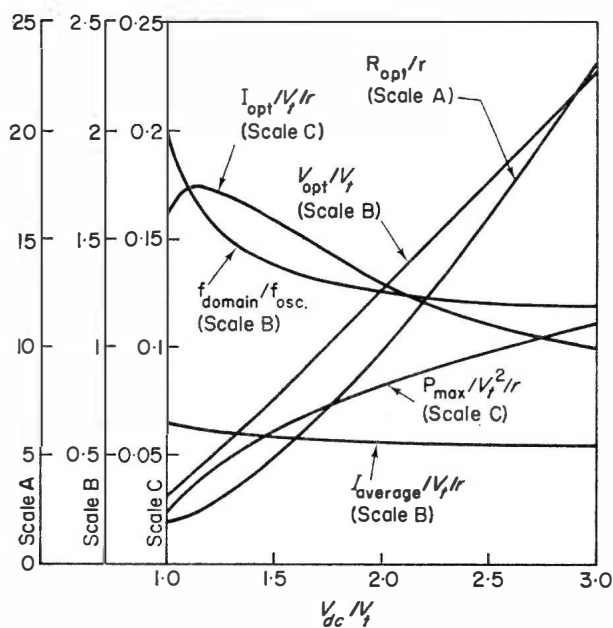


FIG. 5.8. Theoretical results as functions of  $V_{dc}/V_t$ .<sup>(8)</sup> (Crown Copyright, reproduced by permission of the Controller of Her Majesty's Stationery Office).

and hence

$$f_{\text{domain}} = \frac{2\pi}{\pi + 2\theta} f_{\text{osc}}.$$

The results of the analysis are shown in Fig. 5.8. For the optimum efficiency of 7.2% we have  $V_{\text{dc}} = 1.9V_t$

$$R_{\text{opt}} = 8.6r$$

$$\text{and } f_{\text{domain}} = 1.28f_{\text{osc}}.$$

The main weaknesses of this simple treatment are that instantaneous domain formation followed by uniform current is only likely in long samples at low frequency ( $\sim 1$  GHz) under high bias. At 10 GHz or so the domain formation time is likely to be appreciable and should improve the efficiency. Some experiments with domain modes since the paper was written indicate that the field does not always swing below threshold.

Nevertheless the analysis remains an excellent illustration of the working of a Gunn device in a circuit and emphasizes that low efficiency must be expected unless special steps are taken to shape the waveforms.

## 5.8 OPERATION WITH A SINE WAVE OF CURRENT

One approach which has been suggested by Carroll<sup>(9)</sup> is interesting because he suggests a current drive rather than the voltage drive favoured by most authors.

If the circuit presents high impedance at all harmonic frequencies the current through the device must be approximately sinusoidal. The analysis is based on this assumption.

Figure 5.9 illustrates a steady sine wave of current through the device and the corresponding voltage waveforms. Clearly the voltage which has greatest out-of-phase magnitude (corresponding to maximum power generation) and gives least mean power input, is one which is zero everywhere, except for a delta function at the time when the current is minimum. This, of course, is not realisable. There must be a background voltage  $V_p$  greater than threshold to hold the device in its negative resistance region and an infinite spike of voltage is impossible. However a large hump of voltage occupying rather less than half the cycle ( $\pi - 0.4$ ) can be realizable and should give good results.

A domain is initiated at time  $t = 0$  ( $\therefore \omega t = 0$ ) when the current is maximum and starts to grow and propagate through the device. The growth however, is inhibited so that the domain voltage remains at the low level  $V_p$ . The inhibition results from the shape of the device which fans out rapidly from the cathode contact and then tapers gently in, and ensures that the

current  $I_s$  defined as the product of domain drift velocity, carrier concentration and cross-sectional area exactly follows the sinusoidal driving current  $I$  so that the domain cannot accumulate charge. (see Fig. 5.10).

At a time given by  $\omega t = \theta_D$  the domain reaches the point on the device where the cross-section is abruptly reduced.  $I - I_s$  is thus abruptly increased and the domain charges up rapidly, generating the hump of voltage in Fig. 5.9.

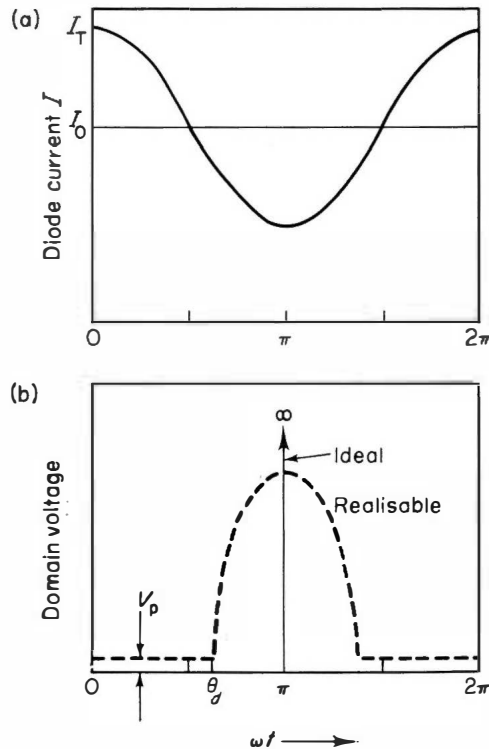


FIG. 5.9. Current and voltage waveforms for high efficiency operation of a current driven Gunn device. Carroll.<sup>(9)</sup>

At time  $\omega t = 2\pi - \theta_D$  the domain reaches the point where the device cross-section begins to increase rapidly so that  $I - I_s$  becomes large and negative, discharging the domain by the time the device current  $I$  again reaches threshold at the cathode. The restriction on the magnitude of the voltage hump is dictated by the necessity to make the cross-section at the cathode the smallest in the device, so that the current density there is greatest, and the domain initiates infallibly at the cathode and not at the constriction.

This analysis predicts for a peak to valley ratio of 2, an efficiency for fundamental sine wave power of 25% for  $\theta_D = \pi/2$  and 27% for  $\theta_D = \pi/2 - 0.2$  which is exactly the value given by the  $8/\pi^2 (2 - 1)/(2 + 1)$  of the square wave analysis.

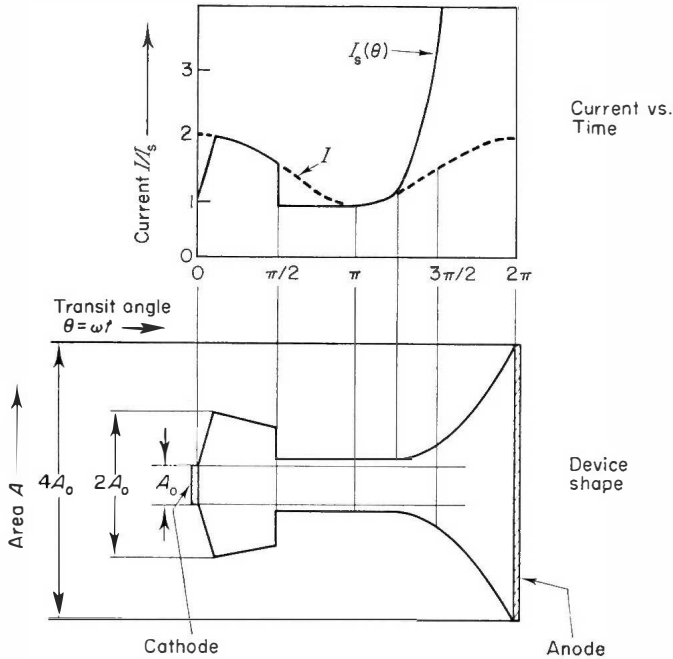


FIG. 5.10. "Domain" current  $I_s = pAv_s$  and device current  $I$  as a function of time resulting from the shape of the device shown. The domain charging current is  $I - I_s$ . The cross-sectional area at the cathode is the smallest on the device. Carroll.<sup>(9)</sup>

This analysis is approximate in a number of ways, particularly as regards domain readjustment, but serves to illustrate an alternative approach to the problem, and highlights the importance of geometrical, or more commonly electrical, non-uniformities in a device. The shaping has been discussed in terms of the geometrical shape of a uniform conductivity device. It could as well have been a profile of doping in a uniform geometry. Doping non-uniformities are all too common in presently available GaAs and it is clearly important that they should be correct rather than random or systematically wrong.

## 5.9 NUMERICAL ANALYSIS OF A DOMAIN MODE

We now turn to an "exact" study of the operation of a domain mode generator necessarily made by computer, by Copeland.<sup>(10)</sup> The word "exact"

is placed in inverted commas, partly because the circuit used in the analysis is very difficult to realise at microwave frequencies, due to the effects of stray capacity and inductance, and more fundamentally because experiments with short samples, such as  $10\text{ }\mu\text{m}$  appropriate to  $10\text{ GHz}$ , show qualitative as well as quantitative differences from the theory.

Figure 5.11 shows the L.C.R. circuit and the Gunn diode as treated by the program. The circuit equations and those for current continuity, Poisson's equation, and a velocity/field characteristic in the device, form a set of partial differential equations with two independent variables, time and distance. The device is assumed to be one dimensional, and field dependent diffusion is given by Fig. 5.12. The velocity-field characteristic used in the original work was similar to that of McCumber and Chynoweth.<sup>(11)</sup>

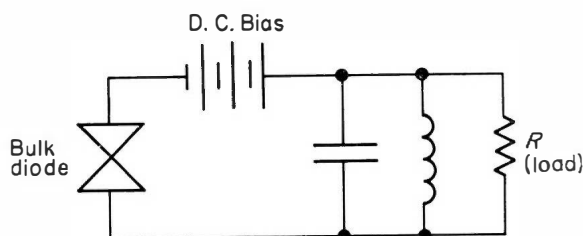


FIG. 5.11. Circuit used for computer study of Gunn diode. Copeland.<sup>(10)</sup>

The analysis is performed by dividing the sample into small cells of distance and calculating in small steps the time variation in each cell of the various quantities. It is a long calculation and precautions must be taken to ensure that it is mathematically stable. The technique is fully described in the appendix on computer simulation.

Figure 5.14 shows the efficiency and output power as a function of bias voltage for three values of load resistance, expressed as a multiples of the ohmic low field resistance of the diode  $R_0$ . This figure is from the original

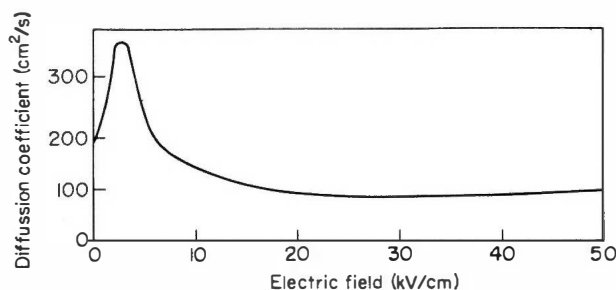


FIG. 5.12. Diffusion coefficient as a function of electric field. Copeland.<sup>(10)</sup>

work and is based on the velocity-field characteristic of McCumber and Chynoweth. Results based on Butcher and Fawcett's characteristic<sup>(12)</sup> would be slightly different.

The optimum efficiency was calculated as a function of doping  $\times$  length product  $N_0 l$  (Fig. 5.15) and a mode chart was drawn which describes the LSA mode and the Gunn mode (Fig. 5.15). It was an admirable illustration of the power of computer techniques that the L.S.A. mode was predicted in this way before its existence was suspected experimentally (see Chapter 6). The predicted power as a function of frequency is shown in Fig. 5.17.

It is significant in these results that the efficiency peaks at quite low values of bias voltage (two and three times threshold at 10 GHz) and power output

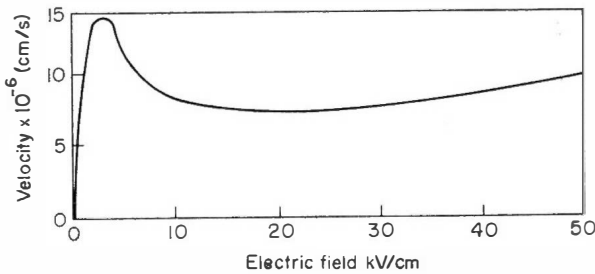


FIG. 5.13. Velocity field characteristics as used by Copeland.<sup>(10)</sup>

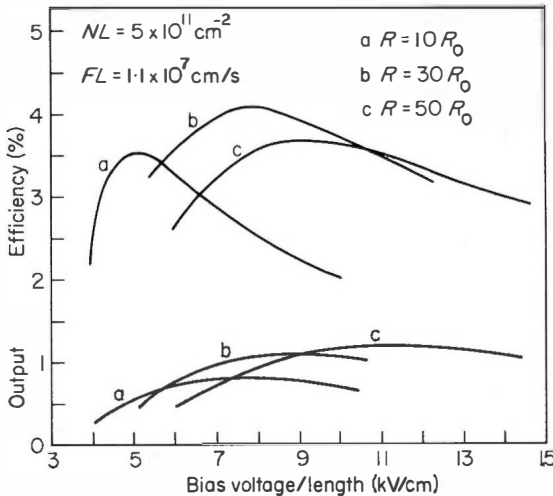


FIG. 5.14. Output power and efficiency as functions of bias voltage Copeland.<sup>(10)</sup> Based on the McCumber and Chynoweth characteristic.



either peaks or saturates at only slightly higher values. It is found experimentally in pulsed work, however, that both power output and efficiency generally increase monotonically with bias voltage up to breakdown which can be 10 to 12 times threshold. Certainly, the circuit used in practice will not approximate to a parallel L.C.R. combination, but will be a complicated network of stray reactances; probably most nearly represented by an L.C.R. circuit connected to the device by a series inductance. Such a circuit has been described<sup>(4)</sup> at frequencies around 1 GHz as giving nearly 20% efficiency.

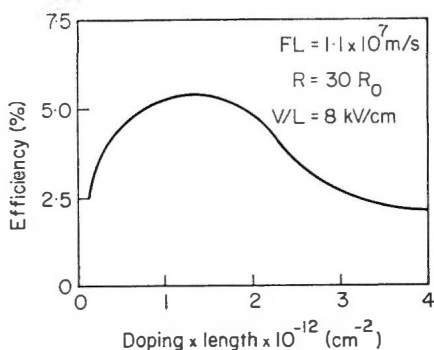


FIG. 5.15. Efficiency as a function of  $NI$  product. Copeland.<sup>(10)</sup>

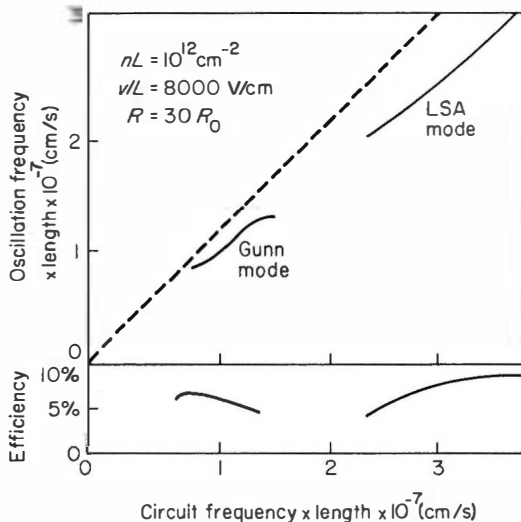


FIG. 5.16. Mode chart showing the first prediction of the LSA mode. Copeland.<sup>(10)</sup>

Apart from the difficulty of realising a parallel L.C.R. circuit in practice it must also be borne in mind that the results at frequencies above about 8 GHz are taken from samples in which, usually, the domain is an appreciable fraction of the transit length. This fact certainly was not taken into account in the treatments of Warner and Carroll, although in the computer programs it presents no problems.

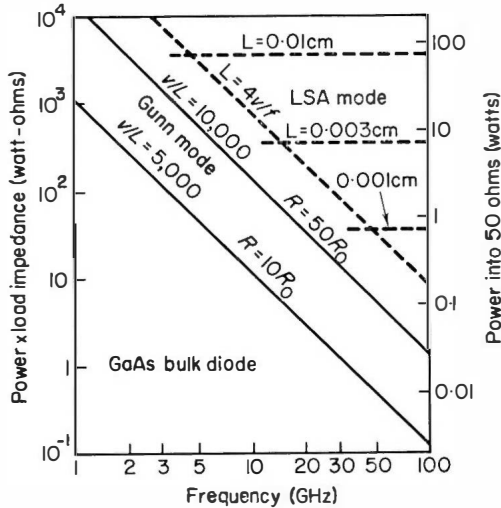


FIG. 5.17. Power and frequency prediction. Copeland.<sup>(10)</sup>

### 5.10 CONTINUOUS WAVE OPERATION

Low power continuous wave operation of domain transit mode Gunn devices is the most thoroughly exploited and strikingly successful application of solid state microwave generation so far. Devices suitable for local oscillator use from 8–12 GHz were first marketed by the Mullard organization in 1966, and all the major firms now produce several types in quantity.

A suitable specification for such a local oscillator is discussed fully in Chapter 10. Here we simply note the power requirement of 5 to 20 mW. This was the target of many of the early workers in the field because the thickness required at this frequency (10  $\mu\text{m}$ ) allowed reasonable heat conduction from the centre of a device, and was available by epitaxial growth techniques, which also yielded purer GaAs than bulk methods. Most important, of course, was the comparatively large development potential for compact local oscillators for portable and airborne equipment.

The choice of material parameters is given first by the transit length requirement of approximately 10  $\mu\text{m}$  at 10 GHz. The resistivity should be

as high as possible so that the heat dissipation can be spread through a large volume, but must not violate the limitation on  $Nl$  product of about  $10^{11} \text{ cm}^{-2}$ , so one arrives at about one ohm-cm for GaAs with a mobility  $6000 \text{ cm}^2 \text{ V}^{-1} \text{ sec}^{-1}$  or greater. There remains the device area, which depends largely on the adequacy of the heat transmission path. Most devices rely on heat flow diverging radially from the contact into the much larger cross-section of the adjacent heat sink.

Early laboratory devices had heat sinks applied to both sides of the active layer as shown in Fig. 5.18. The GaAs die was soldered to a molybdenum header, which most nearly matches the thermal expansion, and contact was made to the  $10 \mu\text{m}$  epitaxial layer by an alloyed tin dot or blob against which, in turn, was pressed a spring loaded copper plunger. The heat was generated in the active region which was almost entirely surrounded by heat sink paths. Such a structure dissipated 2–3 watts without exceeding  $200^\circ\text{C}$ , which is near the limit for reliable operation. This structure, however, is very difficult to encapsulate hermetically and the tin dot contact had a short life. Modern devices have an evaporated silver tin contact to which a thin ( $50 \mu\text{m}$  diameter) gold wire is bonded. This removes almost no heat and such structures can safely dissipate little more than 1 watt, through the substrate. More recently, techniques for bonding the device with its epitaxial layer adjacent to a copper heat sink have been devised. This greatly improves the heat dissipation as described in Chapter 10.

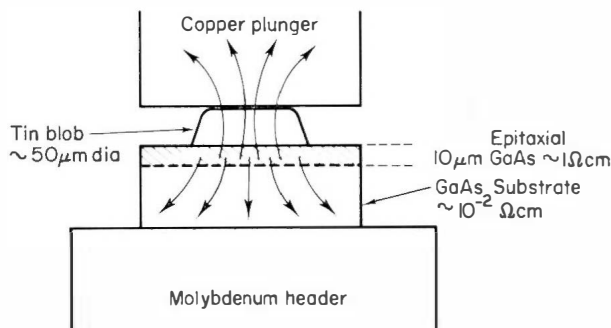


FIG. 5.18. Early design of a C. W. Gunn diode for operation near 10 GHz. The arrows indicate the heat flow paths. The heat is generated in the active region, shown shaded.

These considerations, then, determine the power input and for a given operating voltage the design is completely specified. There is some freedom in the choice of operating voltage. It must be reasonably well above threshold (ideally 3 to 4 volts) but too high a value would imply a high power

dissipation, due to the difficulty in making GaAs much above  $1\ \Omega\text{-cm}$ . After making allowance for contact resistance, most devices have terminal operating points at between 7 and 17 volts.

These devices, operating in small coaxial (or other) cavities, typically give outputs of 5 to 40 mW from about 8 to 12 GHz, and comparable powers up to about 18 GHz are obtained from rather thinner layers. Hobson<sup>(13)</sup> found that the bias voltage  $V_B$ , at which maximum power was obtained, was frequently dependent and that approximately

$$fV_B = \text{constant} \sim 70 \text{ to } 120 \text{ GHz V.}$$

The constant is different for different devices, in the range stated. The most likely explanation of the Hobson peak is the temperature dependence of domain velocity, which is expected to decrease with increasing temperature, so that a reduced bias voltage would give a reduced temperature and a higher velocity, appropriate to a higher frequency. The peak is not observed under pulsed low duty cycle operation.

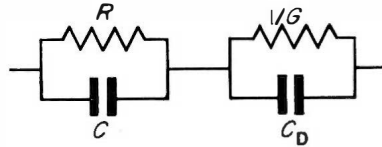


FIG. 5.19. Equivalent circuit of C. W. Gunn diode. Hobson.<sup>(14)</sup> (Crown Copyright, reproduced by permission of the controller of Her Majesty's Stationery Office).

### 5.11 EQUIVALENT CIRCUIT

The equivalent circuit of C. W. Gunn diodes has been established by Hobson<sup>(14)</sup> using standing wave techniques under both small and large signal conditions at frequencies from 10 to 15 GHz.

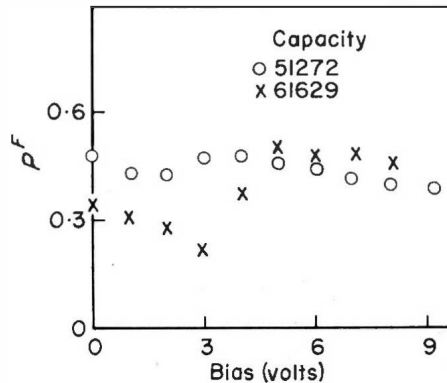


FIG. 5.20. Variation of domain capacity  $C_D$  with bias voltage. Hobson.<sup>(14)</sup> (Crown Copyright, reproduced by permission of the controller of Her Majesty's Stationery Office).

Figure 5.19 shows the equivalent circuit for an unencapsulated device and Figs 5.20 and 5.21 show the variation of the parameters with bias voltage for 10  $\mu\text{m}$  samples of about 1-cm GaAs and area 100  $\mu\text{m}$  square.

$C_D$  and  $1/G$  are the active components in the circuit.  $C_D$  is the domain capacity, typically 0.3 pF or so at the operating point, and  $G$  the negative conductance or power generating part of the circuit. Usually  $1/G \sim -500$  ohms. The components  $C$  and  $R$  represent the dielectric relaxation time and low field resistance of the major part of the sample which is ohmic.  $R$  is about 10 ohms and  $C$  about 0.1 pF.

The domain capacity, which is the average over an R.F. cycle, should not be identical to the steady state values calculated in Section 2. They should of course be of the same order and indeed the agreement is not unreasonable.

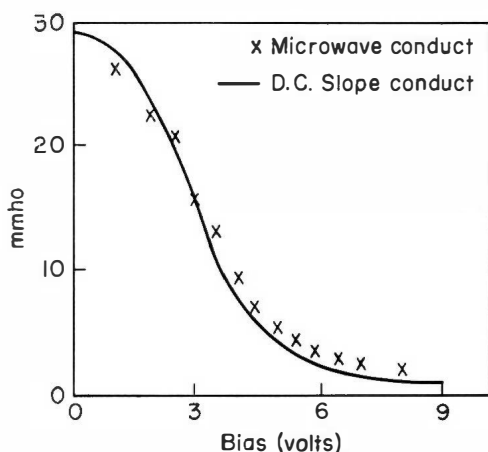


FIG. 5.21. Variation of Microwave conductance and D.C. slope conductance with bias voltage. Hobson.<sup>(14)</sup> (Crown Copyright, reproduced by permission of the controller of Her Majesty's Stationery Office).

## 5.12 CONTINUOUS WAVE RESULTS

We have discussed above the operation of the oscillators mainly for the frequency band 8–12 GHz where most development has been carried out.

The performance has been successfully extended to about 18 GHz by appropriate scaling and such devices were also soon on the market. Higher frequencies still, up to say 40 GHz are less easily obtained from transit mode devices due to the difficulty of making and operating very thin (2–3  $\mu\text{m}$ ) samples. However, the stringent requirements which the L.S.A. mode places on uniformity of material are even more difficult to meet and greater production success has so far attended transit mode devices even at these frequencies.

While at frequencies below 8 GHz the thickness of the sample begins to make heat dissipation from its centre difficult, C.W. operation as low as 2 GHz has been observed.

Figure 5.22 shows some of the production results from C. W. devices.

Frequency GHz	Power mW (up to)	Efficiency % (up to)
3 - 8	200	5
8 - 12	300	4
12 - 18	80	6
26 - 40	10	1

FIG. 5.22. Typical continuous wave performance. Transit length Gunn devices listed in the table were in production or development at several firms in U.K. and U.S.A. in 1969. Laboratory records are, of course, higher.

### 5.13 PULSED OPERATION AND HYBRID MODES

The design of small pulsed transit mode devices, from 1 to 18 GHz, is in some ways simpler than that of C.W. devices due to the absence of thermal restrictions at low duty cycles. We centre our discussion around 10–15 GHz and bear in mind that the parameters may be scaled to cover the wider frequency range.

The designer is generally concerned to achieve the highest output power possible, with good efficiency.

The thickness again is decided by the transit time requirement and the area and resistivity together determine the impedance, which will usually be as low as can be handled by the microwave circuit and driving pulse generator. A low field resistance of  $1 \Omega$  is acceptable, which implies a working point value of about  $15 \Omega$ . The area and resistivity can be traded against each other to some extent, but of course, the  $nI$  product must still be larger than  $10^{11}$ , whereas if it is much greater than about  $3 \times 10^{13}$  the domains may generate such large electric fields that avalanche will occur. At 10 GHz then, we arrive at a device  $10 \mu\text{m}$  thick of  $0.32 \Omega\text{-cm}$  GaAs and a contact area of about  $200 \mu\text{m}$  diameter, typically.

It is difficult to ascertain the equivalent circuit of such devices because pulsed operation places restrictions on the type of measurement made in the C.W. case.

It is clear, moreover, that the stable domain theory cannot apply, Fig. 6 to  $10 \mu\text{m}$  devices are commonly biased to 30 to 70 kV/cm, 10 to 20 times threshold, and a glance at the stable domain curves (Figs 4.10 to 4.15) shows

that a stable domain with a potential of 30 V or so would be about twice as wide as the device. A similar argument can be based on domain formation time as calculated by Copeland.<sup>(6)</sup> The mode chart (Fig. 4.20) shows that the device we have described is in the overlap region between L.S.A. and domain modes, so that the choice made is determined by the circuit and bias conditions. It is to be expected that a hybrid model should be appropriate.

No Hobson peak has been observed for pulsed operation, and power and efficiency are usually observed to increase monotonically with bias voltage until breakdown occurs. This behaviour can be readily studied using a charge limited pulse generator, such as a switched delay line and Fig. 5.23 shows a current-voltage characteristic taken right through into the avalanche region.<sup>(15)</sup>

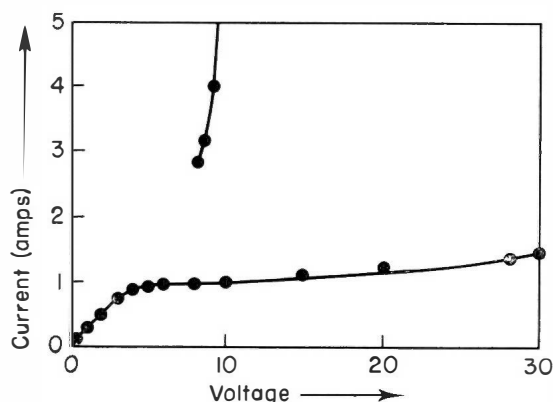


FIG. 5.23. Characteristic for a 10  $\mu\text{m}$  Gunn device under pulsed operation, extended into the breakdown region.<sup>(15)</sup> (Crown Copyright, reproduced by permission of the Controller of Her Majesty's Stationery Office).

The absence of a peak in output as predicted by Warner and Copeland is some further evidence of a different mode, but it may also be important that practical circuits probably approximate to that of Fig. 5.24 with a series inductance, rather than the parallel L.C.R. circuits of these theories. The circuits cannot be transformed from one to the other since it is known that the waveforms are harmonically rich and do not approximate to single frequency sine waves.

Thorough analysis of such a circuit must be made under large signal conditions by computer. We can here attempt some qualitative remarks illustrated by Fig. 5.25. The upper waveform is the voltage  $V_1$  of Fig. 5.24, the second is the voltage  $V_2$  and the third is the current.

The voltage  $V_1$  is assumed to be nearly sinusoidal as determined by the L.C.R. combination. The effect of the series inductance is to apply a sharp

step of voltage whenever the current changes rapidly, and in conjunction with a negative resistance this does not have a stabilizing effect, but rather speeds up the transition through the threshold of the Gunn device. The addition of these sharp steps will lead to the rather sawtooth waveform  $V_2$  and double humping is possible. The current will be very nearly a square wave as the positive going transition will be very rapid, due to the voltage step, and there will be little time for domain formation before the zero differential conductivity part of the Gunn characteristic is reached. As the voltage drops once more through the high differential conductivity region domain formation will again be inhibited since it would require a rise in current to charge the domain capacity. This will react on the series inductance producing a rapid collapse of voltage across the Gunn device, stabilizing once the positive resistance below threshold is reached.

These qualitative arguments imply that a greater degree of domain control may be achieved than would be expected from predictions based solely on

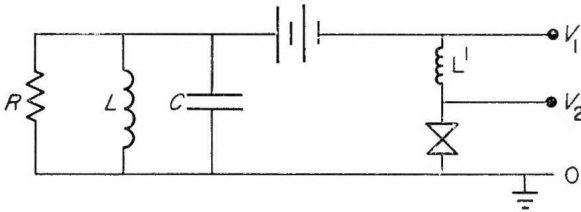


FIG. 5.24. Parallel L.C.R. circuit connected to Gunn diode by a series inductance.

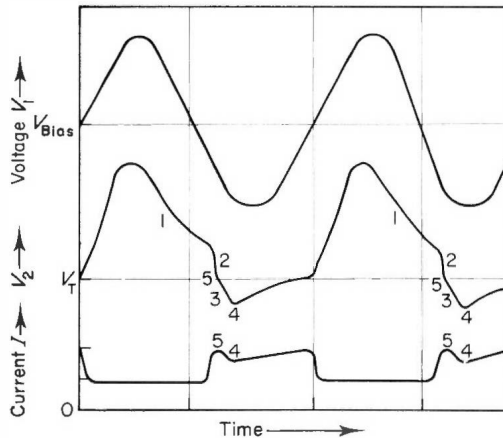


FIG. 5.25. Voltage and current waveforms suggested for the circuit of Fig. 2.24. (1) Smooth falling curve until current starts to rise; (2) Sharper drop to  $V_T$  while current rises; (3) Change to gentler fall below  $V_T$ ; (4) Lowest point above lowest current point; (5) Crosses  $V_T$  at same time as current is greatest.



fundamental  $n/f$  values, since the transitions are governed by the harmonic frequencies introduced by the series inductance. The detailed behaviour has not been studied experimentally but Day<sup>(4)</sup> has used a series inductance to reach an efficiency of 20% at 1 GHz. The method leads to the generation of very high voltages, and places more severe demands on the material than simple sine wave operation. In these cases domain control has not been as complete as in L.S.A., and the frequency is still related to the transit time. Presumably, however, a series inductance could be used to extend the range of L.S.A. operation.

Bott and Fawcett<sup>(16)</sup> have made an analysis of Gunn diode behaviour at  $n/f$  values in the border region between L.S.A. and domain modes, and found

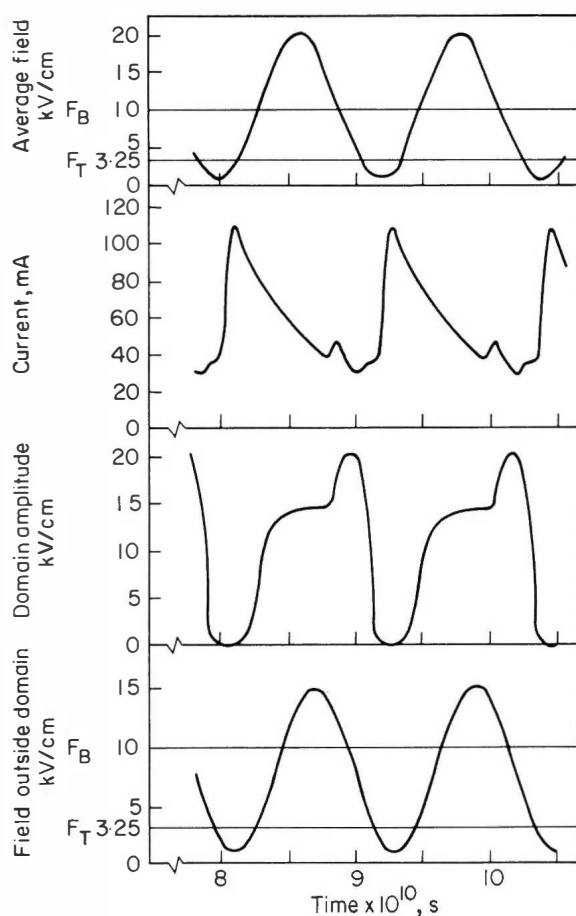


FIG. 5.26. Theoretical time dependence of current and electric field in a hybrid mode. Bott and Fawcett.<sup>(16)</sup>

that a hybrid operation was possible under large bias and r.f. voltages. The domain grows only while the voltage passes through the steep negative resistance region of the  $I$ - $V$  characteristic and does not grow at the peak of the r.f. cycle. This is shown in Fig. 5.25 where the two rapid increases in domain field are clearly separated. The dependance of this behaviour on r.f. swing is shown dramatically in Fig. 5.27 which shows the build up of the r.f. oscillation from zero, first as a large amplitude domain mode, and followed by a transition to the immature domains of a hybrid. It is seen that the field outside the domain is above threshold for most of each cycle after the transition, but is mostly below threshold initially.

It is striking, however, that neither this analysis nor a similar model of Huang and Mackenzie<sup>(5)</sup> predict the monotonic rise of power and efficiency

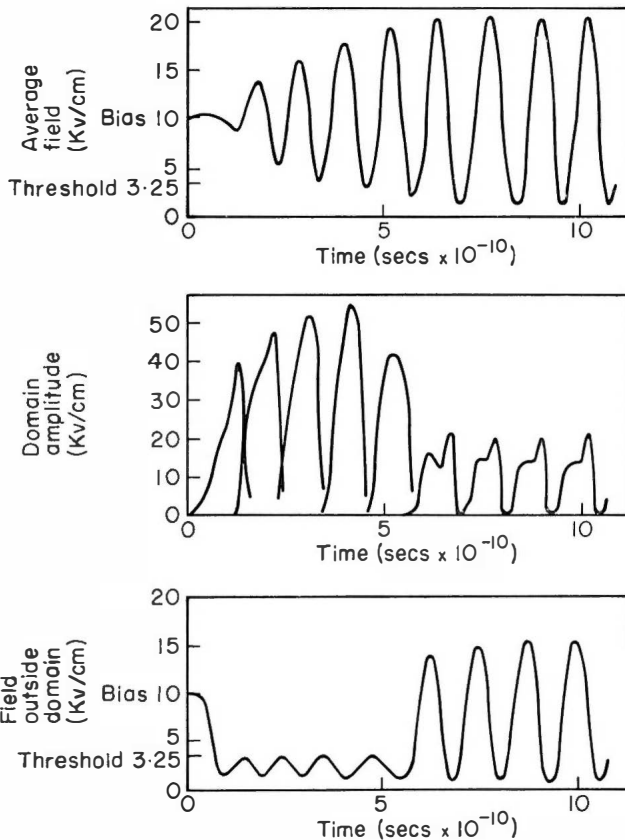


FIG. 5.27. Theoretical growth of microwave output showing a sharp transition from a domain to a hybrid mode. Bott and Fawcett.<sup>(16)</sup> (Crown Copyright, reproduced by permission of the controller of Her Majesty's Stationery Office).

with bias field up to  $20 E_r$  which is the experience of Bass and Edridge<sup>(17)</sup>, Califano<sup>(18)</sup> and the authors. It may also be noted that these comparatively high power results, including that of Huang and Mackenzie, were obtained in transit time samples. The effect of  $nI$  control on domain formation (a stable domain would be larger than the device at these bias levels) is one possibility which was neglected. The analysis did not include field dependent diffusion, which would enlarge domains to about  $20\text{ }\mu\text{m}$  from the  $7\text{ }\mu\text{m}$  or so of a simple domain theory.

The use of simplified circuits in the models may also be important as most experimental circuits have appreciable series inductance. These suggestions are, of course, speculative at the moment as the problem is not fully understood.

#### 5.14 RISE TIME

One of the appealing features of pulsed operation is the remarkably rapid rise times which can be achieved. Figure 5.28 is a photograph of a sampling oscilloscope display of the build-up of microwave power at 14 GHz from a  $6\text{ }\mu\text{m}$  Gunn diode in a waveguide mount. The rise time is about 1 ns, or some 14 cycles at the microwave frequency.<sup>(19)</sup> This performance is in sharp contrast to most vacuum tube devices where the oscillation must

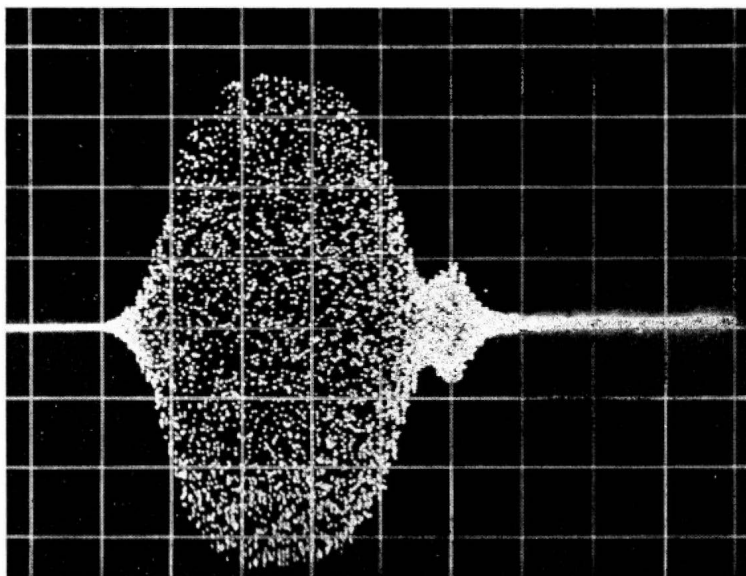


FIG. 5.28. Sampling oscilloscope display of a sharp 14 GHz pulse of 1.6 watts peak power from a  $6\text{ }\mu\text{m}$  Gunn diode. The time graticule is 1 ns per division. (*Crown Copyright, reproduced by permission of the Controller of Her Majesty's Stationery Office*).

not be made to build too rapidly if the correct mode is to be generated. The essential reasons for this difference is that the Gunn devices are much smaller than the wavelength, they do not rely on setting up an internal travelling wave synchronism in order to generate power, and they are low impedance devices which work well in low  $Q$  circuits. Hence the stored energy in the r.f. field is not large.

Sometimes, however, a delay may be observed between the rise of the driving pulse and the rise of the microwave power, which can be some tens of nanoseconds, and exceptionally even seconds. Experimentally it is observed that at least two time constants are involved, as the actual rise, when it does occur, is still only a few nanoseconds. This may be interpreted in terms of a weak small signal instability which has to build up to some threshold before the stronger large signal instability is obtained. In good samples either the large signal instability extends down to low level or the small signal instability is strong enough to give a rapid transition. The very long delays of up to a second or so, which may be observed, for example, as a delay in the switching on of some C.W. samples, can only be explained by suggesting that the above instabilities are temperature dependent, as the delay is unreasonably long to be solely an electrical effect.

The cause of the difference between "good" samples and those which show a delay is not definitely known, but is presumable related to the effective slope of the negative resistance characteristic in relation to the microwave circuit impedance. This is influenced by material quality and series contact resistance.

To summarize this section, the table of Fig. 5.29 shows the production performance of some pulsed transit mode Gunn Diodes.

Frequency (GHz)	Power W (up to)	Efficiency % (up to)
1-2	200	20
3-8	50	10
8-12	30	8
12-18	15	8
26-40	2.0	2

FIG. 5.29. Typical pulsed performance. Transit length Gunn devices listed in the table were in production or development at several firms in U.K. and U.S.A. in 1969. Laboratory records are, of course, higher.

## REFERENCES

1. Newton, C. O. Private communication.
2. Butcher, P. N. *et al.* (1966). *Brit. J. Appl. Phys.* **17**, 841–850.
3. Kuru, I. *et al.* (1968). *I.E.E.E. Trans.* **ED-15**, 21–29.
4. Day, G. F. *et al.* (1966). “Proc. Symp. GaAs”. Reading, England pp. 189–162.
5. Huang, H. C. and McKenzie, L. E. (1968). *Proc. I.E.E.E.* **56**, 1232–1233.
6. Copeland, J. A. (1967). *J. Appl. Phys.* **38**, 3096.
7. Au, H. K. Private communication.
8. Warner, F. L. (1966). *Electron. Letts.* **2**, 260–261.
9. Ladbrooke, P. H. and Carroll, J. E. (1968). *Electron. Letts.* **4**, 83–85.
10. Copeland, J. A. (1967). *I.E.E.E. Trans.* **ED-14**, 55–58.
11. McCumber, D. E. and Chynoweth, A. G. (1966). *I.E.E.E. Trans.* **ED-13**, 4–21.
12. Butcher, P. N. and Fawcett, W. (1966). *Phys. Letters* **21**, 489–490.
13. Hobson, G. S. (1967). *Electron. Letts.* **3**, 110–111.
14. Hobson, G. S. (1966). “Proc. Int. Conf. Microwave and Optical Generation and Amplification”, pp. 314–318. I.E.E. Conf. Publ. 27.
15. Bulman, P. J. and Talbot, J. A. A. (1967). “Proc. Cornell Conf. Microwave Generation and Amplification”. Cornell University. pp. 218–227.
16. Bott, I. B. and Fawcett, W. (1968). *Electron. Letts.* **4**, 207–209.
17. Edridge, A. L. *et al.* (1969). *Electron. Letts.* **5**, 103–104.
18. Califano, F. P. (1969). *Proc. I.E.E.E.* **57**, 251–252.
19. Bulman, P. J. Private communication.
20. Kino, G. S. and Kuru, I. (1968). Stanford University. Microwave Report No. 1689.
21. King G. Private Communication.

## Chapter 6

# L.S.A. and Non-Transit (Overlength) Modes

### 6.1 INTRODUCTION

Chapter 5 describes modes of operation of transferred electron devices involving the transit time of space charge through the entire device. Modes in which this time is not the frequency controller are described in the following sections. The three modes in which different degrees of space charge control are exercised are the Limited Space Charge Accumulation mode, the Quenched Domain mode and an intermediate mode, the Hybrid mode.

### 6.2 THE LIMITED SPACE CHARGE ACCUMULATION (L.S.A.) MODE

The objective with the L.S.A. mode of operation is to directly utilize the negative differential resistance of the velocity-field characteristic in order to convert d.c. power to r.f. oscillatory power. This process is in direct contrast to the "switching" mode of power conversion utilized in domain oscillators.

Initially it will be assumed that we have a gallium arsenide device which remains electrically uniform so that its current-voltage relationship is given directly by the velocity-field characteristic. The device is mounted within a resonant circuit which causes the impression of a sinusoidal voltage waveform on the d.c. bias (Fig. 6.1). The current waveform which results for a biasing voltage greater than threshold is illustrated in Fig. 6.2 for four values of the amplitude of the r.f. voltage. The current waveform is clearly in anti-phase with the r.f. voltage waveform for the smaller amplitudes of the latter, but the larger current dip, coincident with the voltage minimum in the positive resistance part of the current-voltage relationship, causes the fundamental frequency component of the current to be in phase with the voltage for the latter's largest value. The negative resistance of the device for small r.f. voltage amplitudes has become a positive resistance.

Fourier analysis of the current waveform using the analytic version of the velocity-field characteristic of Fig. 6.1 shows that the dynamic resistance

of the device at the fundamental frequency has the form of Fig. 6.3. This dynamic negative resistance should not be confused with the negative differential resistance of the velocity-field characteristic. The dashed section of this curve will subsequently be shown to be unattainable. It can be seen that  $R$  becomes positive when the r.f. voltage amplitude becomes comparable with the steady biasing voltage. In order that the device can operate under steady conditions the positive resistance reflected to the device terminals through the tuned circuit must be equal to  $R$ . If the tuned circuit is represented by the simple parallel form of Fig. 6.4 with a parallel load resistance  $R_L$

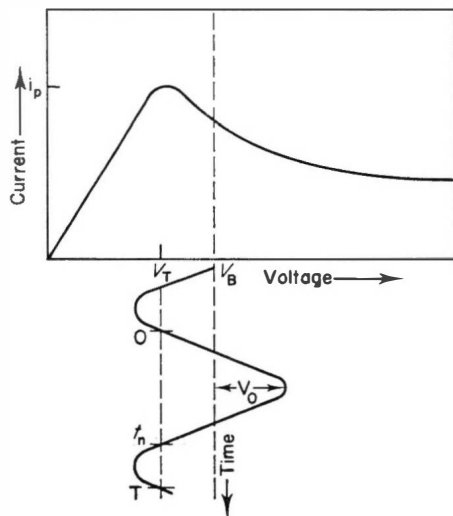


FIG. 6.1. Current-voltage characteristic for an ideally uniform L.S.A. device; and the d.c. plus r.f. voltages superimposed upon the device.

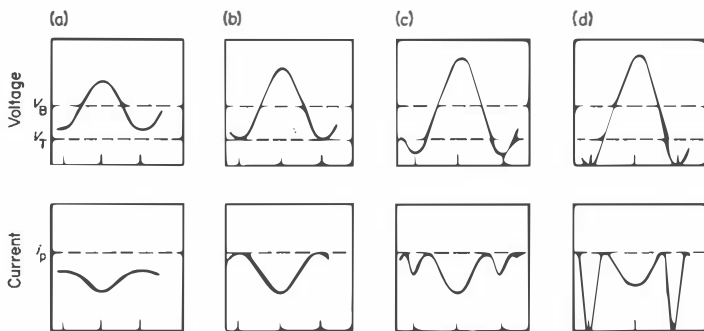


FIG. 6.2. Current and voltage waveforms for idealized L.S.A. oscillation. Abscissa is time.

then

$$R_L = -R.$$

If this resistance match does not exist, and the operation is on that part of the negative resistance characteristic of Fig. 6.3 where the modulus of  $R$  increases with increasing r.f. voltage amplitude, then the r.f. voltage amplitude will grow or decay, as required, until the resistance match occurs providing that the load resistance is not less than  $R_{\min}$ . This is a stabilising action that must occur in all useful oscillators. The power generated by the device,  $P_{r.f.}$ , is  $V_0^2/2R_L$ . This can be calculated from the results of Fig. 6.3 or directly from the product of the fundamental Fourier antiphase components of current and voltage from the waveforms of Fig. 6.2. The d.c. power,  $P_{d.c.}$ , dissipated in the device may also be obtained from the product of the mean values of the current and voltage, and the form of the resulting power conversion efficiency,  $P_{r.f.}/P_{d.c.}$ , is illustrated in Fig. 6.5. As the r.f. voltage amplitude increases, the efficiency initially increases owing to the increase of r.f. current and voltage amplitudes. It reaches a maximum when the minimum voltage,  $V_B - V_0$ , across the device is a little less than the threshold

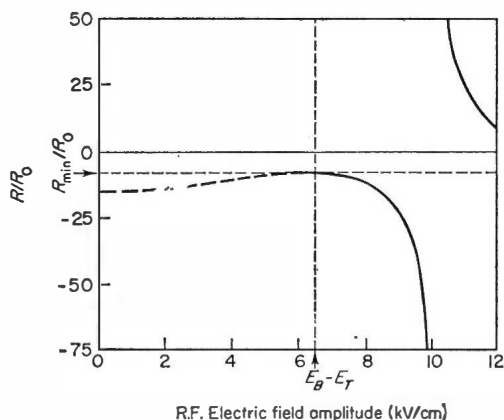


FIG. 6.3. Device resistance,  $R$ , at the fundamental frequency<sup>(1)</sup> normalized by the low field positive resistance,  $R_0$ , versus r.f. electric field amplitude. The bias electric field is 10 kV/cm.

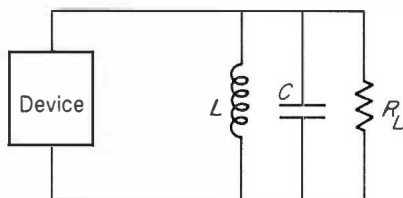


FIG. 6.4. Equivalent lumped circuit of the resonant circuit containing the oscillating device.



voltage and then decreases as the r.f. current amplitude decreases due to the effect illustrated in Fig. 6.2. (iv). The minimum value of  $R$  occurs when the r.f. voltage amplitude is slightly less than that required for the efficiency optimization. The maximum value of the efficiency depends directly on the peak/valley ratio of the static characteristic because this sets the limit to the peak-peak r.f. current. This point will be referred to in later discussions of the optimum form of the static characteristic for L.S.A. operation. The maximum efficiency in Fig. 6.5. depends on the bias voltage. It's variation is shown in Fig. 6.6 where the initial optimized efficiency increase arises from the larger r.f. voltage amplitude accompanying the increased bias voltage. The decrease of optimized efficiency at the highest bias arises from a decrease of the fundamental r.f. current owing to the more rapid voltage change through the region just above threshold. This effect is illustrated in Fig. 6.7.

The above introductory treatment assumed electrical uniformity within the device. However, when the electric field is within the negative differential

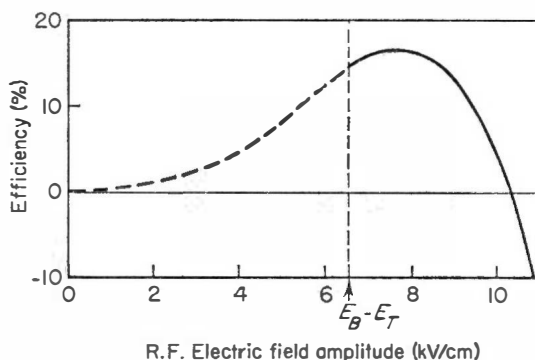


FIG. 6.5. Efficiency as a function of r.f. electric field amplitude<sup>(1)</sup> Bias field = 10 kV/cm. There is an implicit assumption that space charge is controlled so that the optimum efficiency is achieved for any given set of conditions.

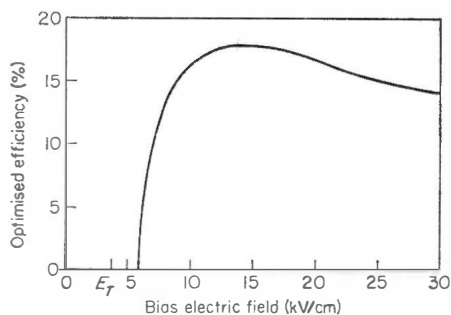


FIG 6.6. Optimized efficiency (the maximum in Fig. 6.5) versus biasing electric field<sup>(1)</sup>.

resistance region, space charge growth occurs (see Chapter 4) with the formation of electric field non-uniformities and, ultimately, domains. In these circumstances the device current-voltage characteristic is time varying; it does not follow the form of the static velocity-field characteristic and transit time effects may be important. A treatment such as that given for the domain modes of Chapter 5 or later in this Chapter may be more appropriate than the above discussion.

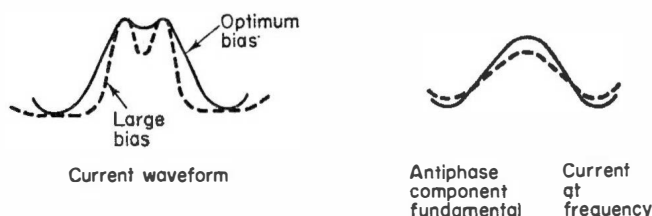


FIG. 6.7. Illustration of decrease of fundamental r.f. current amplitude at high bias due to larger rate of change of electric field near threshold.

In order to control the space charge accumulation and utilize the L.S.A. mode it is necessary for the r.f. voltage across the device to “swing” below threshold into the positive resistance region of the current-voltage characteristic. The frequency of operation and the amplitude of the r.f. voltage must be such that the following conditions are met:

(i) There must not be any appreciable accumulation of space charge during that part of the oscillation when the voltage across the device is greater than threshold. This is necessary to preserve the electrical uniformity and thereby the required current-voltage characteristic.

(ii) Any incipient space charge non-uniformities must be completely damped out when the voltage across the device is less than threshold. This is necessary to avoid space charge accumulation over many cycles of oscillation. The small signal growth of space charge is described by (Chapter 4)

$$\rho = \rho_0 \exp \left\{ - \left( \frac{ne \frac{\partial v}{\partial E}}{\epsilon \epsilon_0} \right) t \right\} \quad (6.1)$$

$\rho$  is the net space charge density with value  $\rho_0$  at time  $t = 0$ .  $\partial v / \partial E$  is the slope of the velocity-field characteristic at the existing electric field. Below threshold  $\partial v / \partial E$  is positive so that the space charge exponentially decays but above threshold  $\partial v / \partial E$  is negative so that exponential space charge growth occurs. In the earlier discussion of this section the electric field was time

varying so that the instantaneous value of  $\partial v/\partial E$  must be used in Eqn (6.1). The space charge,  $\rho_n$ , existing in the device after time  $t_n$  spent in the negative differential mobility region (see Fig. 6.1) is the infinite product of infinitesimal amounts of growth with varying growth rates (depending on the time variation of the electric field as implied by Eqn (6.1)). Because of the exponential form of the growth this simplifies to:

$$\frac{\rho_n}{\rho_0} = \exp \left\{ - \frac{ne}{\epsilon \epsilon_0} \int_0^{t_n} \left( \frac{\partial v}{\partial E} \right)_t dt \right\} \quad (6.2)$$

$(\partial v/\partial E)_t$  indicates that this quantity is time varying through the time dependence of the electric field in the device.

Applying the same considerations to the space charge damping during the positive differential resistance excursion from  $t_n$  to  $T$  ( $T$  is the period of oscillation), the final space charge  $\rho_T$  is given by:

$$\frac{\rho_T}{\rho_n} = \exp \left\{ - \frac{ne}{\epsilon \epsilon_0} \int_{t_n}^T \left( \frac{\partial v}{\partial E} \right)_t dt \right\}. \quad (6.3)$$

The exponent,  $g$ , of Eqns (6.2) and (6.3) may be expressed in one of two more convenient forms:

$$g = \frac{T}{T_p} \cdot \frac{1}{\mu_p} \cdot \frac{1}{T} \int_{0,t_n}^{t_n,T} \left( \frac{\partial v}{\partial E} \right)_t dt \quad (6.4)$$

$$\text{or} \quad g = \frac{n}{f} \cdot \frac{e}{\epsilon \epsilon_0} \cdot \frac{1}{T} \int_{0,t_n}^{t_n,T} \left( \frac{\partial v}{\partial E} \right)_t dt \quad (6.5)$$

$T_p$  and  $\mu_p$  are, respectively, the low field dielectric relaxation time and mobility and  $n/f = 1000 \times T/T_p \text{ sec cm}^{-3}$  for  $\mu_p = 6875 \text{ cm}^2/\text{V sec}$ . 6.4 is a more convenient form for later considerations of the optimum form of the velocity-field characteristic, while (6.5) is more convenient for practical considerations owing to the direct use of the practical device quantities  $n$  and  $f$ .

In either case the growth or decay exponent depends on the product of a term involving electron density and frequency with an averaged mobility (averaging performed by the electric field excursion). The form of the variation of  $g$  with electric field amplitude using the same parameters as in Figs 6.3 and 6.5 is illustrated in Fig. 6.8. The static characteristic<sup>(1)</sup> to determine  $(\partial v/\partial E)_t$  is similar to the Butcher and Fawcett form with a low field mobility of  $6875 \text{ cm}^2/\text{V sec}$   $n/f = 5 \times 10^4 \text{ sec cm}^{-3}$  ( $T/T_p \approx 50$ ).  $n/f$  or  $T/T_p$  may be treated as scaling factors on the curves of Fig. 6.8. The important point to note from these curves is the strong influence of the steep negative slope of the velocity-field characteristic just above threshold. In order to hold the

space charge growth as small as possible it is necessary for the electric field to pass through this "critical" region as rapidly as possible. This is achieved with an r.f. electric field whose amplitude is large enough to place the turning point of the waveform as far below the critical region as possible and a biasing electric field which is large so that the rate of change of electric field is as large as possible in the critical region. Unfortunately both of these effects are limited by the reduction of efficiency that they can cause.

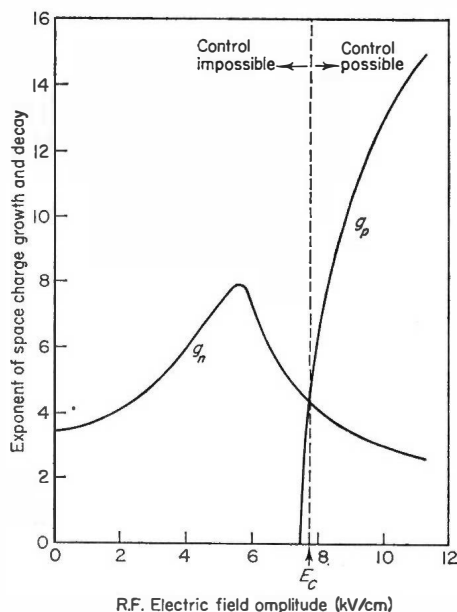


FIG. 6.8. Exponents of space charge growth,  $g_n$ , and decay,  $g_p$ , versus r.f. electric field amplitude  $n/f = 5 \times 10^4 \text{ sec cm}^{-3}$  ( $T/T_p = 50$ ) Bias field =  $10 \text{ kV/cm}^{(1)}$ .

Apparently, the space charge growth limitation (ii) is met for an r.f. amplitude greater than  $E_c$ . Limitation (i) will then be met simply by reducing the electron density (increasing  $T_p$ ) until the growth of space charge per cycle is less than the ratio of the upper limit for the onset of large signal distortions of the electric field (order of magnitude about 10% space charge non-uniformity over a few Debye lengths) to the initial space charge non-uniformities. In ideally pure and uniform material the starting point of growth is the random thermal fluctuations of the electron density and the random static fluctuations in the donor density. In this case a growth of  $e^5$  to  $e^7$  is allowable.<sup>(2)</sup> In real materials the bulk doping inhomogeneities will set a lower limit to the allowable growth by providing a starting point<sup>(8)</sup> as is illustrated in Fig. 6.9. The solid line illustrates the non-uniform doping density. If the

random motion of electrons is neglected and they are considered as a continuous "sea" of charge, then, in the absence of an electric field, the electron density profile would be the same as the doping profile to ensure charge neutrality. On application of an electric field the electrons would drift from cathode to anode and shift their profile, as shown by the dotted line. In a positive resistance medium the resulting space charge would be readjusted towards neutrality. In a negative differential resistance medium, this space charge grows so that the doping inhomogeneity forms the effective space charge profile from which growth occurs.

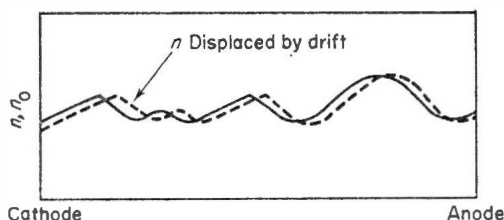


FIG. 6.9. Illustration of space charge arising from inhomogeneity.

The simple considerations of the last paragraph have neglected the layer of accumulated charge that is injected into the device at the electric field peak of each cycle (see Chapter 4). This is a mature large signal non-uniformity at the time of injection with peak space charge,  $\rho_{acc}$ , given approximately by<sup>(1)</sup>:

$$\rho_{acc} = \epsilon \epsilon_0 (E_B + E_0) \quad (6.6)$$

The process of accumulation layer formation is illustrated in Fig. 6.10. A particularly simple example is chosen, A step function of voltage greater than threshold is applied to a device which is uniformly doped except for a highly doped contact. Only the cathode region is considered. Just after the field is applied the electron and donor densities and the electric field distribution are as shown in Fig. 6.10a. Bearing in mind the velocity-field characteristic shown in Fig. 6.10c the maximum electron drift velocity will occur at point A. These faster electrons "overtake" electrons drifting away from the cathode and on the anode side of A, so that an increased accumulation occurs at a point somewhere in front of A. However, this accumulation runs into a higher field, lower velocity region towards the maximum value of  $E$ . In order to maintain current continuity and simultaneously satisfy Poisson's equation the following events occur. The electric field at B (Fig. 6.10b) falls, so contributing a negative displacement current (in a region of high electron velocity). Additionally the space charge,  $(n - n_0)$ , falls at B so that the particle current is also reduced. At point C the electric field rises to maintain the total device

voltage constant, and causes a positive displacement current which partly compensates the reducing particle current as the accumulation layer runs into the high field region. The result is that the accumulation layer “breaks away” from the cathode leaving an electric field less than threshold between it and the cathode. The electric field difference between  $B$  and  $C$  is related to the total charge in the accumulation layer, by integration of Poisson’s equation.

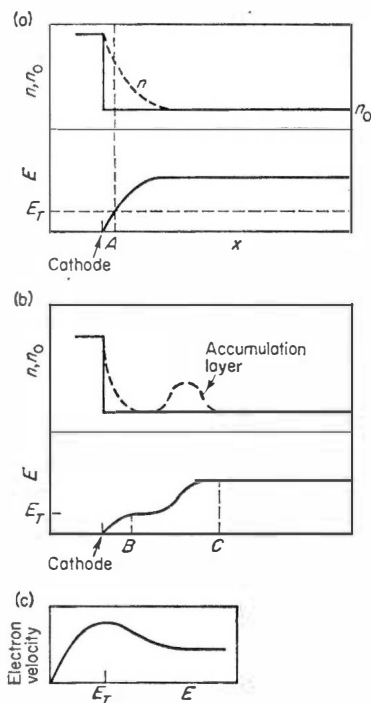


FIG. 6.10. Development of an accumulation layer.

In order that this layer does not destroy L.S.A. operation it is necessary for its transit through the device in one cycle to be only a small fraction of the device length and it must be completely damped to the starting point of internal space charge growth at the end of each cycle. The space charge damping factor must be greater than the growth factor for this damping to occur. A requirement now exists for a large electron density in order that the necessary damping can occur, otherwise for a large fraction of each cycle the electric field must be below threshold so reducing the efficiency. Fortunately the modulus of the average negative mobility is much smaller than the positive mobility. This allows the simultaneous satisfaction of the low  $n/f$  (or  $T/T_p$ ) requirement for the control of space charge growth and the high

$n/f$  (or  $T/T_p$ ) requirement for the space charge decay, with the following values:

$$2 \times 10^4 \text{ sec. cm}^{-3} < \frac{n}{f} < 2 \times 10^5 \text{ sec cm}^{-3}. \quad (6.7)$$

This description of L.S.A. operation has used two assumptions which are:

(i) the velocity-field curve of gallium arsenide represents the device current-voltage characteristic if (6.7) is satisfied.

(ii) the interaction between circuit and device superimposes a "clean" sine wave voltage on the device which causes the harmonic rich current waveform as shown in Fig. 6.2. It is not immediately obvious that these assumptions are correct. Their justification is found in the detailed treatment of L.S.A. operation by Copeland.<sup>(1)</sup> This involves the computer calculation of the device-cavity interaction by the method described in Appendix 3. Providing that a space charge growth of  $e^5$  was allowed the current and voltage waveforms were much as assumed earlier in this chapter with only slight modifications at the end of each space charge growth period when space charge non-uniformities were just significant. The efficiencies calculated by this technique agree closely with those calculated with analytical techniques<sup>(3,10)</sup> using the earlier assumptions of this chapter.

The decay of the accumulation layer may appear at first sight to set a major limitation on the control of space charge. However, an accumulation layer decays for almost the entire time that the terminal voltage is decreasing with time as shown by the following calculation. This calculation is only valid for devices whose length is much greater than the accumulation layer transit length so that the terminal current-voltage characteristic is determined by the uniform electric field between the accumulation layer and the anode. The electric field distribution is illustrated in Fig. 6.1 la. The relevant equations to be satisfied by the accumulation layer are current continuity and Poisson's equation. Also the integral of electric field across the device must be equal to the terminal voltage. The current  $J$  is given by:

$$J = nev(E) + \epsilon\epsilon_0 \frac{\partial E}{\partial t} - eD \frac{\partial n}{\partial x}. \quad (6.8)$$

Far away from the accumulation layer,  $\partial n/\partial x = 0$ , the electric fields are  $E_1$  and  $E_2$  on either side, and the corresponding drift velocities are  $v_1$  and  $v_2$ . From Eqn 6.8:

$$nev_1 + \epsilon\epsilon_0 \frac{\partial E_1}{\partial t} = nev_2 + \epsilon\epsilon_0 \frac{\partial E_2}{\partial t}$$

i.e.

$$\frac{\partial(E_2 - E_1)}{\partial t} = \frac{ne}{\epsilon\epsilon_0} (v_1 - v_2). \quad (6.9)$$

This equation describes the growth or decay of the accumulation layer electric field non-uniformity. If  $v_1 = v_2$  then the layer is in equilibrium. Growth occurs if  $v_1 > v_2$  and decay if  $v_2 > v_1$ .

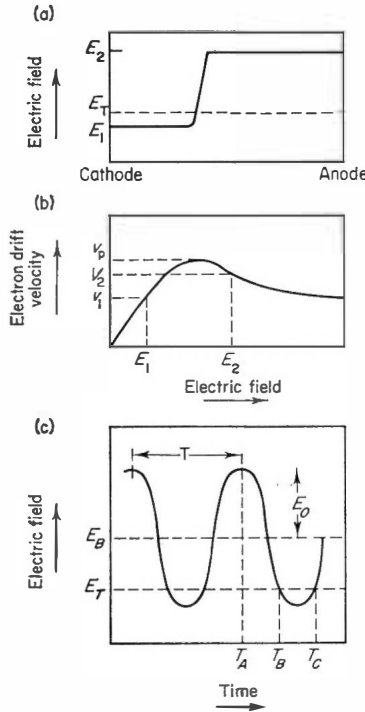


FIG. 6.11. Accumulation layer dynamics.

The largest possible value of  $E_2 - E_1$  at the peak of the r.f. cycle (at  $T_A$  in Fig. 6.11c) is approximately  $E_B + E_0$ . As the mean field decreases with time  $E_2$  and  $E_1$  fall to smaller values causing  $v_1$  to decrease and  $v_2$  to increase. Decay of  $E_2 - E_1$  occurs as soon as  $v_1 < v_2$ . By making some simple approximations which underestimate the decay rate it is simple to show that the magnitude of  $E_2 - E_1$  will be less than  $E_T$  when the mean field falls below threshold for all the optimum L.S.A. conditions. In Eqn (6.9),  $v_2$  is taken as a constant equal to the valley velocity,  $v_v$ , and it is assumed that  $-E_T < E_1 < E_T$  so that

$$v_1 = \mu_p E_1$$



where  $\mu_p$  is the low field mobility.  $E_2$  is assumed to be equal to the mean field.

i.e.

$$E_2 = E_B + E_0 \cos\left(\frac{2\pi t}{T}\right).$$

Therefore Eqn 6.9 may be rewritten as:

$$\frac{\partial E_1}{\partial t} + \frac{E_1}{T_p} = \frac{v_v}{\mu_p T_p} - E_0 \frac{2\pi}{T} \sin\left(\frac{2\pi t}{T}\right). \quad (6.10)$$

The solution of Eqn (6.10) when the mean field has its peak value and  $E_1 = v_v/\mu_p$  at  $t = 0$  (i.e. maximum possible magnitude of the accumulation layer) is:

$$\frac{E_1 - \frac{v_v}{\mu_p}}{E_0} = \frac{\left[ \exp\left(\frac{t}{T_p}\right) - \cos\left(\frac{2\pi t}{T}\right) + \frac{T}{2\pi T_p} + \sin\left(\frac{2\pi t}{T}\right) \right]}{\left[ 1 + \frac{1}{4\pi^2} \left(\frac{T}{T_p}\right)^2 \right]}. \quad (6.11)$$

The right-hand side of Eqn (6.11) is plotted as a function of time in Fig. (6.12) and the time is indicated at which the terminal voltage falls below threshold. In order that  $E_1$  is never less than  $-E_T$  the maximum value of  $E_0$  as a function of the ratio  $T/T_p$  must not be greater than shown in Fig. (6.13). This curve also indicates the maximum bias voltage (because  $E_0 \approx E_B$ ) for the field difference across the accumulation layer to be less than  $E_T$  when the terminal voltage falls below threshold. Fortunately these conditions will be met for the optimum L.S.A. conditions. In practice this approximation should be well met in view of the generous nature of the earlier worst case

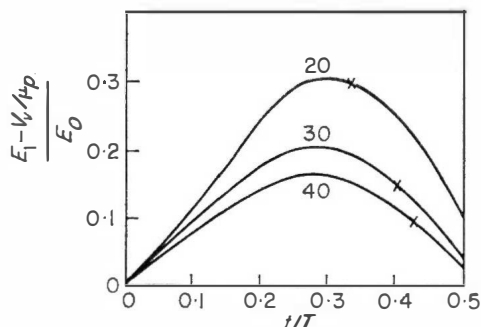


FIG. 6.12. Time variation of the electric field between the cathode and the accumulation layer.

approximations. An important point to emphasise is the rapid decay of an accumulation layer which occurs even when the mean field is greater than the threshold field. This is to be contrasted with the case of a dipole domain, where the approximate relaxation time is  $\sqrt{T_p \cdot T_D}$ .<sup>(7)</sup>  $T_D$  is the transit time of space charge through the entire device and can make dipole relaxation slow compared with a cycle of operation. Additionally the domain peak field will usually be much greater than that when there is only an accumulation layer present, so that the required overall decay factor for the domain will be much greater than for an accumulation layer.

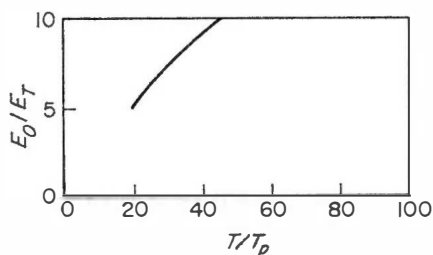


FIG. 6.13. Limiting values of the r.f. electric field amplitude.

If the material has bulk inhomogeneities which are much larger than the inherent fluctuations, a smaller space charge growth is required to form large signal non-uniformities. A discussion of the difficulties in obtaining L.S.A. operation under these conditions will be deferred until after the description of the other non-transit modes.

### 6.3 THE QUENCHED DOMAIN MODE OF OSCILLATION

For material with  $n/f \gg 10^5 \text{ sec cm}^{-3}$  space charge distortion of the internal device electric field becomes important and high electric field domains may be formed. In the limit of infinite  $n/f$  the domain would be in quasi-static equilibrium with the electric field. This assumption is made for the description of the quenched mode so that the current-voltage relationship of the device under a time varying electric field (cavity control) is given by the stable domain dynamics of Chapter 4. Accordingly the current-voltage characteristic of Fig. 6.14 will be used. It is linear to threshold and its form follows the stable domain dynamics curve for post-threshold voltages. This has a current which decreases towards an asymptote for devices of finite length and the entire post-threshold characteristic tends towards the asymptote as the device length increases. As the voltage is reduced below threshold along the post-threshold characteristic the sustaining voltage below which domains cannot exist is reached. For devices of finite length there is a

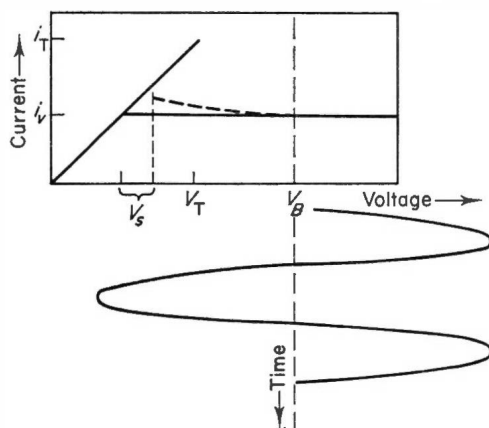


FIG. 6.14. Current-voltage characteristic for quenched mode of oscillation neglecting capacitive effects. Two post-threshold characteristics are shown, the dashed line shows a device of finite length and the solid line shows a device of infinite length.

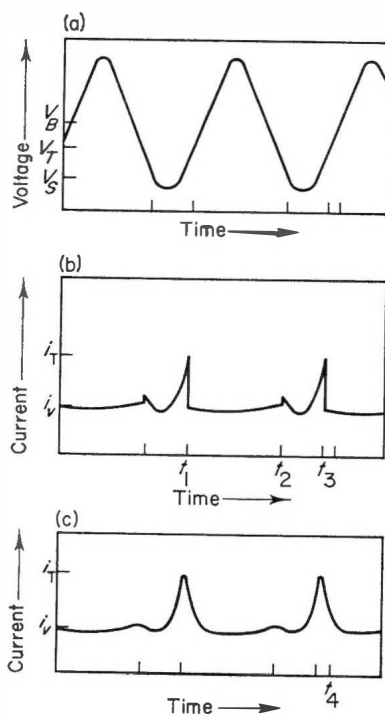


FIG. 6.15. Current waveform arising from a sinusoidal voltage in quenched mode. (a) Voltage waveform. (b) Current neglecting domain space charge. (c) Current including flow to and from domain space charge.

small current discontinuity at this voltage as the current assumes the value of the uniform field sub-threshold characteristic.

The current and voltage waveforms of the quenched mode are shown in Fig. 6.15 and are impressed upon the device by a cavity as in Fig. 6.4. The r.f. voltage must cause the total device voltage to fall below the domain sustaining voltage for part of each cycle and the time required for domain transit over the entire device length must be greater than the domain "existence" time  $T_d$ . As the total voltage across the device rises above threshold at time  $t_1$  a domain forms and causes a rapid current drop from the ohmic to the post-threshold current characteristic. This domain drifts through the device until at time  $t_2$  it is quenched by the falling voltage. The current shows a small discontinuous upward jump and the device remains ohmic to  $t_3$  when the cycle of operations is repeated.

The calculation of dynamic negative resistance and efficiency of the oscillator follows that described for L.S.A. calculations. The r.f. power,  $P_{r.f.}$ , generated by the device is the product of the fundamental antiphase components of current through and voltage across the device. These are obtained by Fourier analysis which reduces to

$$P_{r.f.} = \frac{\omega}{2\pi} \int_0^{2\pi/\omega} i(t) \cdot V_0 \cos \omega t \cdot dt \quad (6.12)$$

for the waveforms depicted in Fig. 6.15.  $i(t)$  is the current waveform and is related to the total voltage applied to the device through the chosen form of the device current-voltage characteristic. Because the electron drift velocity at threshold and the threshold electric field are quantities independent of sample length and carrier concentration,  $i(t)$  may be rewritten as a function of voltage in the following form which is true for all samples when the frequency is low enough to allow the current to follow the voltage instantaneously:

$$\frac{i(t)}{i_p} = f\left(\frac{V}{V_T}\right) \quad (6.13)$$

where  $V = V_B + V_0 \cos \omega t$ .

$i_p$  is the peak current at threshold for the particular device under consideration,  $V_T$  is its threshold voltage,  $V_B$  is the bias voltage and  $f(V/V_T)$  is the current-voltage characteristic. Eqn (6.12) may now be rewritten as:

$$P_{r.f.} = V_T i_p \left[ \left( \frac{V_0}{V_T} \right) \frac{\omega}{2\pi} \int_0^{2\pi/\omega} f\left(\frac{V_B + V_0 \cos \omega t}{V_T}\right) \cos \omega t \cdot dt \right]. \quad (6.14)$$

The term in the square brackets has all voltage terms normalized to the threshold voltage so that for fixed values of these normalized terms the power

output is proportional to the sample volume ( $V_T$  proportional to length,  $i_p$  to area for fixed doping density) as is the case for L.S.A. and all non-transit time devices. The biasing power input,  $P_B$ , is given by:

$$P_B = \left( \frac{\omega}{2\pi} \right) \int_0^{2\pi/\omega} i(t) V_B dt$$

$$= V_T i_p \left[ \left( \frac{V_B}{V_T} \right) \frac{\omega}{2\pi} \int_0^{2\pi/\omega} f \left( \frac{V_B + V_0 \cos \omega t}{V_T} \right) dt \right]. \quad (6.15)$$

The efficiency,  $\eta$ , of bias to r.f. power conversion is given by:

$$\eta = \frac{P_{r.f.}}{P_B}$$

i.e.

$$\eta = \frac{\left[ \left( \frac{V_0}{V_T} \right) \int_0^{2\pi/\omega} f \left( \frac{V_B + V_0 \cos \omega t}{V_T} \right) \cos \omega t \cdot dt \right]}{\left[ \left( \frac{V_B}{V_T} \right) \int_0^{2\pi/\omega} f \left( \frac{V_B + V_0 \cos \omega t}{V_T} \right) dt \right]}. \quad (6.16)$$

In this equation the volume terms have disappeared and the efficiency does not fall as the sample length is increased at constant frequency, providing that the voltages normalized to the threshold voltage are kept constant. The optimum efficiency and negative resistance as a function of bias voltage are shown in Fig. 6.16.

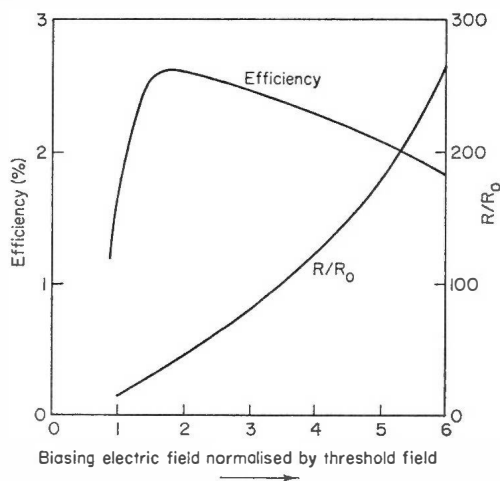


FIG. 6.16. Variation with biasing field of optimum efficiency and negative resistance  $R$  (normalized by low field resistance) for the quenched mode.

This result is contrary to some opinion. It has been stated that the anode region of quenched mode devices contributes nothing to power generation and is a source of r.f. power absorption. Such an idea would be directly applicable to a linear negative resistance region. In this case a sine wave current through both regions would produce two antiphase voltages in series so that the terminal voltage amplitude would be less than that across the negative resistance (power generator), and power output and efficiency would be lost. The quenched mode device is not in this category as it has a time and spatial variation of its internal impedance. (The domain may be thought of as a voltage sensitive switch which controls the device current). A negative differential resistance characteristic is not primarily responsible for power output and efficiency. These last two factors are directly determined by the antiphase amplitudes of current and voltage, and a negative differential resistance is only an indicator that r.f. power may be generated. If we consider removing an anode section of an efficiency optimized quenched mode device in order to improve its efficiency still further, this will in fact cause a degradation of performance by altering the current waveform in time  $t_2$  to  $t_3$  of Fig. 6.15 so that the fundamental antiphase current amplitude is reduced.

In this simple model of the quenched mode the domain formation and decay times were assumed instantaneous. However, the characteristic time of formation and decay of these space charge double layers may be much longer than the characteristic times for L.S.A. operation. This arises because the operation may be represented by a capacitor which is in series with the resistance of the rest of the sample (field below threshold field). Particularly in a long sample the domain charging and discharging time constant (approximately the square root of domain transit time and low field dielectric relaxation time<sup>(7)</sup>) of these equivalent circuit elements can be much longer than the relevant dielectric relaxation time of the L.S.A. mode. It may cause further limitations in achieving L.S.A. operation because a dipolar space charge layer will not disperse as rapidly as expected from the simple small signal theory of Section 6.2.

Even though the space charge flow to the domain has not been taken into account in the simple quenched mode model a source of device susceptance does exist in it. In general the fundamental current component (Fig. 6.15) is not exactly in antiphase with the voltage waveform. Quadrature components of current and voltage exist and their magnitude depends on the working conditions of the device. In this way a susceptance is generated and is in parallel with the effective device negative resistance and varies with the loading and biasing of the device. This consideration is important for the frequency stability of the oscillator. It is important to note that this susceptance has arisen entirely from the non-linearities of a resistive current-voltage characteristic.

Two additional effects arise from the space charge flow to and from the domain. The flow will contribute to the mean device capacity which may be calculated for a quasi-stable domain<sup>(4)</sup> from the stable dynamics (Chapter 4). This capacity in turn will depend on the bias voltage and load impedance (through the r.f. voltage amplitude) and will cause an inherent electronic tuning in the device. The second effect of the space charge flow concerns the efficiency of r.f. power generation. For the half cycle of operation where the voltage is decreasing the domain discharges its space charge, causing a current reduction compared with the purely resistive conditions described above. When the domain sustaining voltage is reached the domain is almost entirely discharged. These effects are illustrated by the current waveform of Fig. 6.15. As the voltage increases the device initially remains ohmic and no space charge flow occurs. When the threshold voltage is reached a large space charge current must flow to charge the domain, and the modification to the current waveform is illustrated at time  $t_1$  and  $t_3$  in Fig. 6.15. If the domain formation time is an appreciable fraction of a cycle the area under the current waveform may be increased at the time when it is antiphase with the voltage waveform. This effect will be a maximum when the current waveform is extended to time  $t_4$  when the r.f. component of the voltage is zero. Such a time extension arises when  $n/f \approx 4 \times 10^4 \text{ sec cm}^{-3}$ .<sup>(5)</sup> This effect may well be important in devices with a sufficiently large doping inhomogeneity to preclude L.S.A. operation. A satisfactory calculation of these effects can only be made with the computer simulation of Appendix 3.

#### 6.4 THE HYBRID MODE

This mode arises if  $n/f \gtrsim 5 \times 10^4 \text{ sec cm}^{-3}$  and is midway between the L.S.A. mode and a quenched mode. The space charge growth proceeds to appreciable large signal non-linearity during each cycle of oscillation, but does not reach the quasistable domain condition of the quenched mode. Multiple domains (not mature) may exist in the device, separated spatially by the transit distance per cycle of oscillation. This behaviour is to be contrasted with the single domain propagation only part of the way through the device in the quenched mode. Some degree of the space charge control in the hybrid mode is provided by the partially formed domains running out of the anode of the device. The electric field outside the space charge dipole layers remains above threshold for a large part of the time that the mean device voltage is above threshold. As a result the device current when the voltage is closed to threshold is larger than that of the quenched mode, so that a larger fundamental r.f. current amplitude is generated and operation in the hybrid mode is more efficient. The waveform lies midway between that of the L.S.A. mode and the quenched mode and will be discussed later. The strong time variation of the

current-voltage characteristic inherent in this mode causes difficulties in its analytic description. An attempt has been made<sup>(6)</sup> by splitting the time variation of the device conditions into two parts. For the domain formation time (this is defined as the time until the minimum internal electric field has fallen to threshold when the mean electric field is greater than threshold) the external resistive current-voltage characteristic is taken directly from the velocity-field characteristic. After this time the characteristic is assumed to be described by the stable domain dynamics of Butcher and Fawcett (Chapter 4). The calculation shows that the efficiency is comparable with L.S.A. efficiency for  $n/f \sim 5 \times 10^4 \text{ sec cm}^{-3}$  and it is maintained to much higher  $n/f$  values ( $\sim 20 \times 10^4 \text{ sec cm}^{-3}$ ) than for the L.S.A. mode. More satisfactory results are obtained from computer simulation of the device-circuit interaction.

### 6.5 COMPARISON OF MODES

The L.S.A. mode is the most efficient convertor of d.c. to r.f. power for single frequency operation. For a given r.f. amplitude the antiphase current component at the fundamental frequency decreases from L.S.A. through the hybrid to the quenched mode (Fig. 6.17). In addition the optimised L.S.A. conditions do not require the device voltage to fall as far below threshold as for the other modes. This allows an even larger fundamental antiphase

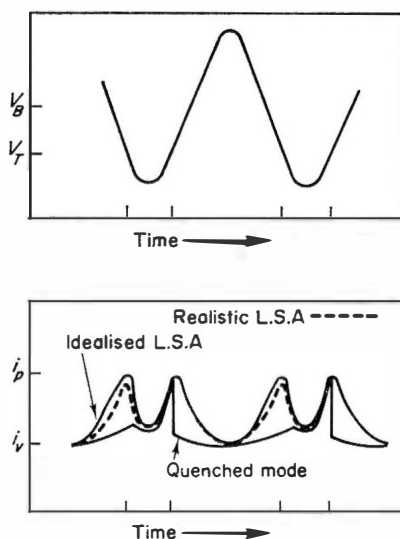


FIG. 6.17. Illustration of the decrease in efficiency from L.S.A. to quenched mode due to different current waveforms for the same r.f. voltage. The hybrid mode current waveform is intermediate between these two.



component of current. It has been assumed that the cavity impresses a sinusoidal voltage across the device. The ideal L.S.A. current waveform is symmetrical about the voltage minimum but some deviation from this condition occurs due to a small but finite space charge growth in the device. The presence of space charge causes the instantaneous current through the device to be smaller than for a uniform device and this effect causes the reduction in the peak-peak r.f. current at the fundamental frequency from L.S.A. through the hybrid mode to the quenched modes as space charge becomes greater.

Even though the L.S.A. mode is the most efficient it also presents the greatest difficulties for space charge control. The previous discussion of Section 6.2 assumed an ideal device in which the inherent electrical non-uniformities only arose as a result of the discrete nature of the electronic charge (thermal fluctuations of electron density and random static doping non-uniformities). In all practical devices there will be larger amplitude and larger scale inherent non-uniformities owing to imperfect crystal growth. These "nucleation regions" for space charge growth only require smaller growth before they cause appreciable electrical non-uniformity and the "death" of L.S.A. operation. Therefore the r.f. voltage amplitude across the device must increase from the optimum of Fig. 6.5 in order to decrease the growth rate when the voltage is greater than threshold and to increase the time available for positive resistance space charge damping (see Fig. 6.8). This increase dictated by space charge control requirements can only be obtained with a reduction of efficiency (see Fig. 6.5). Copeland<sup>(8)</sup> has shown that the efficiency falls off as in Fig. 6.18 with increased device non-uniformity which causes dipolar space charge. The calculation included the full details of the interaction between the device and circuit and assumed a linear doping gradient whose sign changed at regular intervals through the

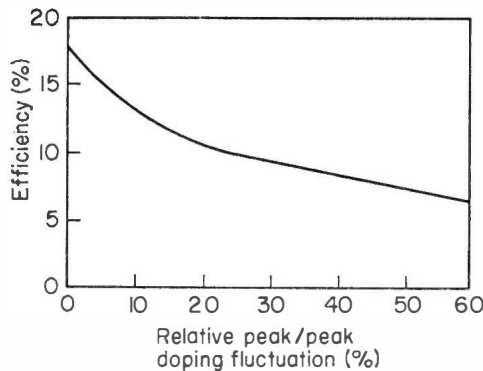


FIG. 6.18. Reduction of maximum efficiency in L.S.A. operation<sup>(8)</sup> due to doping non-uniformities.

device. A similar conclusion was reached by Thim<sup>(9)</sup> and also by Hobson<sup>(10)</sup> in attempting to derive the optimum form of the velocity-field characteristic. This latter calculation showed that the efficiency of L.S.A. operation would be maintained for sample non-uniformity up to 5% (over a distance of about 25 Debye lengths) providing no dipolar space charge was injected from the cathode. The Butcher and Fawcett velocity-field characteristic was found to be close to the optimum for single tuned circuit operation if this stringent technological limitation could be met.

The lower limit to the magnitude of space charge non-uniformity for the nucleation of space charge growth is provided by random fluctuations in the electron density (dynamic) and random variation in the donor density (static).<sup>(2)</sup> They have equal r.m.s. deviation and the same statistical distribution in ideal material. The r.m.s. deviation is large for small dimensions so that a small growth is required to cause large signal non-uniformities. However the growth rate is drastically reduced by diffusion for dimensions of the order of a Debye length. Also the lateral dimensions of the nucleating region must not be too small otherwise divergence of the quasi-one dimensional electric field also reduces the growth rate. These effects result in there being an optimum extent of the nucleating region which has the fastest achievement of large signal distortion of the electric field.<sup>(2)</sup> Quantitatively such considerations indicate that nucleating regions for space charge non-uniformities have a length of about 25 Debye lengths and a diameter of about 200 Debye lengths, and the maximum allowable space charge growth varies from  $e^7$  for material with  $10^{14}$  donors per  $\text{cm}^3$  to  $e^5$  for  $10^{16}$  donors per  $\text{cm}^3$ . In general these limiting fluctuations will be masked by bulk doping inhomogeneities or space charge injection from the cathode.

The quenched mode has lower efficiency than the L.S.A. mode but the same difficulties are not experienced with space charge control—it is utilized in the operation. In order to obtain the maximum power output from all these modes a high peak electric field must be applied to the device. In the quenched mode the domain is in quasi-static equilibrium with the instantaneous device voltage, and extremely high domain voltages (see Chapter 4) may be built up in long devices which would be used for maximum power output. When the domain electric field exceeds about 150 kV/cm impact ionization occurs and the runaway current that results rapidly destroys the sample. This difficulty is avoided in L.S.A. operation because the maximum electric field in the device is only the maximum mean field.

The L.S.A. and quenched modes of oscillation have been compared and contrasted in the above paragraph. The hybrid mode appears to be a good compromise between them. The efficiency is lower than that of the L.S.A. but is higher than that of the quenched mode. Space charge growth causes appreciable electrical non-uniformity which is not damped out completely

in each cycle because of the long decay time constant of large signal non-uniformities (Section 6.3). As a result there is a succession of domains<sup>(9)</sup> in a long sample which are separated by the product of mean domain velocity and period of oscillation. These share the voltage in excess of that required to maintain the electric field outside the domains so that electrical breakdown of the device is less likely to occur than with single domain quenched mode operation. A theoretical best operating efficiency of 13% has been predicted<sup>(9)</sup> for this mode if the sample has a random 11% doping inhomogeneity and it is controlled by a single frequency resonant cavity.

Improvements in efficiency to all of these modes may be made, in principle at least, by designing a cavity which is also resonant at some harmonics of the fundamental frequency. The objective is to “square” the current and voltage waveforms which in the limit take the same form as those for the similar case of domain oscillators in Chapter 5. The efficiencies obtained from simple calculation improve in the same way as for non-transit modes. Space charge control should be made easier for squared waveforms because of the rapid excursion of the electric field through the critical region above threshold. In order to quench the domain in the quenched mode it would be necessary to momentarily “underswing” the voltage below the sustaining voltage before the voltage could rise to its quasi-steady value just below the threshold voltage.

## 6.6 STARTING CONDITIONS AND CAVITIES

The previous description of non-transit modes has only treated the oscillator steady state. The oscillator period must undergo drastic modification during the “start-up” of oscillations<sup>(1,11,12,20)</sup> (see Fig. 6.19). Presumably the initial oscillations will have the transit time period or be dictated by local “ringing”

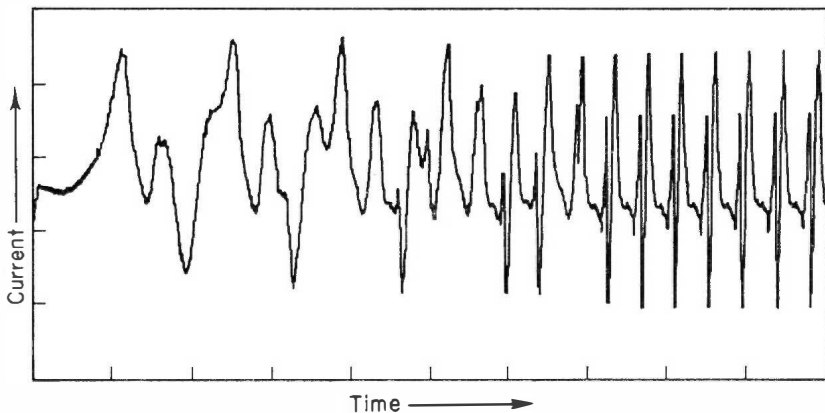


FIG. 6.19. Illustration of transient mode during start of non-transit oscillations.

conditions at the device mount. There will be considerable harmonic content if the  $nI$  product of the device is much greater than  $10^{12} \text{ cm}^{-2}$ . There are two ways in which these initial oscillations may grow to steady state maturity.

The cavity electromagnetic field which is present in the steady state may be built up from the power generated at the harmonic frequency which is closest to the natural resonant frequency of device susceptance and cavity. This process can only occur if the electromagnetic field reflected by the circuit to the device in a non-synchronous fashion causes a modification of the fundamental device frequency (due to modification of domain properties) in such a way that the relevant harmonic moves towards synchronism with the circuit. In this way there will be a device frequency shift which depends on the stored electromagnetic energy in the cavity and both will change smoothly until the steady state is achieved.

The second growth process requires the broadband negative conductance that may occur at the device terminals when it is oscillating in a different mode (see Chapter 7). This conductance may amplify any signals occurring at the cavity resonant frequency until they become large signals which may take over the frequency control. The initial oscillatory mode may arise in various ways. It may be the simple sample controlled transit mode or it may be a different cavity resonant mode from the one required. In a waveguide cavity, for example, the device susceptance may resonate with the evanescent mode inductance of the waveguide below its cut-off frequency. If the resonant frequency of such a cavity is close to the domain transit frequency, or a low harmonic, then a cavity controlled mode may be set up in a similar fashion to the modes of Chapter 5.

In general both effects in the above paragraphs will participate in the build up of the steady state electromagnetic field in the cavity. It is not apparent that there will be any qualitative difference between these conditions for any of the non-transit modes of the Chapter. Experiments attempting to use this change of oscillation<sup>(11)</sup> period, or the temporal extinction of existing cavity modes of oscillation to determine the oscillatory mode will not be able to distinguish between the non-transit modes.

In order that the oscillations can grow by the above process it is necessary that there is not too great a power loss either to the external circuit or internally by cavity wall losses at the L.S.A. frequency. The cavity should have a small stored energy to allow rapid achievement of stable operation. This feature may be desirable for systems use and is a necessity for long devices as discussed in the next paragraph. A further necessary feature of the cavity design is the avoidance of stable operation in domain modes at lower frequencies than those required for L.S.A. operation. Otherwise a "latching" of oscillations onto the domain mode may occur and prevent the attainment of L.S.A. action.

The most serious limitation to setting up the L.S.A. and Hybrid modes of oscillation, particularly in long samples, is the avalanche breakdown that may occur due to the high domain fields present in transient domain modes immediately after switching the bias onto the device. In order to avoid this trouble the time required to establish these modes must be as short as possible (usually only a few cycles of domain oscillation are required to permanently damage the device). This "establishment" time may be neatly minimized<sup>(14)</sup> by inserting a suitable inductance in the video bias lead of the devices, so that the current fall of the device when it exceeds threshold causes the device voltage to rise much more rapidly than the externally applied voltage. In this way the optimum bias voltage for the mode of operation was achieved in a time comparable with the domain formation time. An additional bonus from this technique may be the excitation in the cavity of frequency components which are close to the required resonant frequency of device and cavity.

Some of the cavities used to excite these modes are shown in Fig. 6.20.

A circuit realization of multiple harmonic operation which also removes some of the difficulties encountered in single frequency L.S.A. operation has been called the "relaxation" mode and has been extensively studied by Jeppsson and Jeppesen.<sup>(25)</sup> The operation is essentially the same as discussed in Section 9.5 and has the voltage and current waveforms shown in Fig. 6.21. The circuit is a series combination of an inductance and the device, which are in parallel with a zero impedance bias source. When the terminal voltage is below threshold the voltage and current rise exponentially towards the bias level with the  $L/R$  time constant which approximates to that of the circuit and the device low field resistance. As the voltage passes through threshold the current drops sharply causing the voltage to rise rapidly and then fall again in a time dictated by the circuit inductance and device capacity (the instantaneous resistive impedance in parallel with the capacity is high because of the near constant current nature of the diode). After the voltage falls below threshold the cycle of events is repeated. The period of oscillation is strongly dependent on the bias voltage (Fig. 6.22) because this controls the time at which the device terminal voltage passes through threshold. This feature may be a disadvantage in some applications and an advantage in others.

From an efficiency point of view the current achieves the desirable condition of switching rapidly and periodically between the highest current, lowest voltage and the lowest current, highest voltage states. At first sight the relaxation mode should be possible for the uniform field condition of L.S.A. operation or the highly non-uniform domain operation because both schemes essentially require switching between the peak and valley of the velocity-field characteristic. The domain modes carry several disadvantages and may even destroy the mode. The high field domain is undesirable in the long

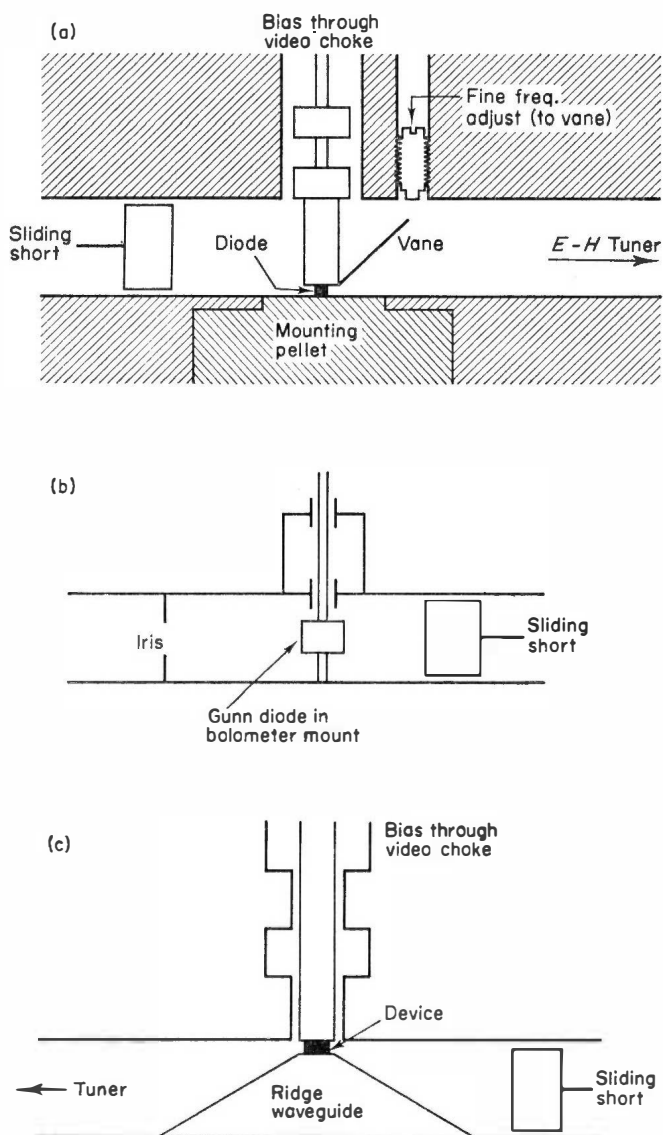


FIG. 6.20. A selection of L.S.A. cavities. (a) Copeland and Spiwak;<sup>(13)</sup> (b) Kennedy;<sup>(22)</sup> (c) Gibbs.<sup>(21)</sup> (Crown Copyright, reproduced by permission of the controller of Her Majesty's Stationery Office).

devices usually used because of the possibility of avalanche breakdown. A further disadvantage is the relatively slow decay of a high field domain which will require the voltage to fall further below threshold than for L.S.A. operation in order to dissipate the dipolar space charge. Efficiency would then be reduced. In some cases the decay time may be longer than the required period so the mode would be unattainable. Even though large doping non-uniformities such as deep notches must be avoided to prevent dipole domain injection, the similarity of the current and voltage waveforms for L.S.A. or domain operation make the mode much less sensitive to doping non-uniformities than single frequency L.S.A. operation. Computer simulations which

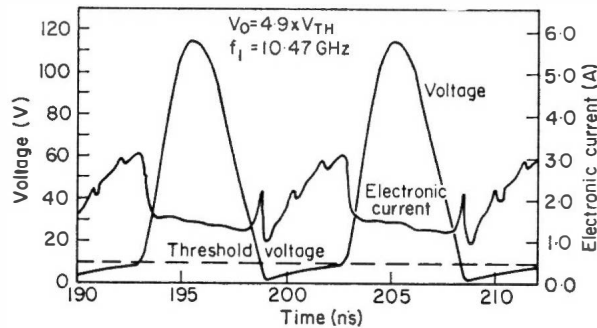


FIG. 6.21. Voltage and electronic current versus time from computer simulation of *X*-band waveguide iris circuit.<sup>(25)</sup>

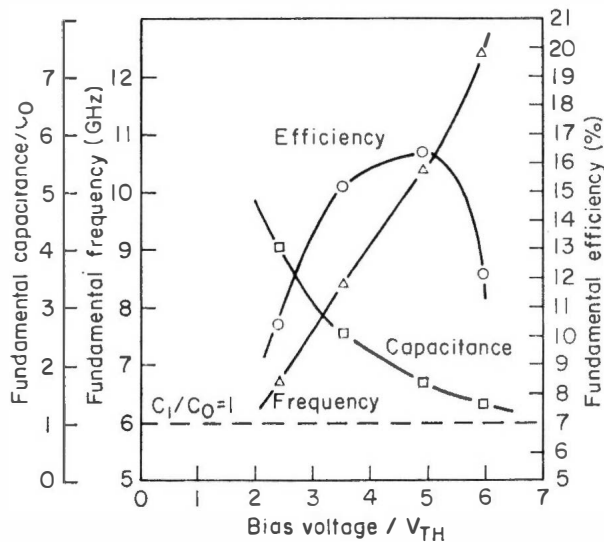


FIG. 6.22. Fundamental frequency, efficiency, and capacitance, the latter normalized to the dielectric capacitance  $C_0$ , versus normalized bias voltage.<sup>(25)</sup>

gave a 22.8% efficiency for a flat doping profile gave 10% efficiency for a 60% variation sloping up to the anode.

The most efficient operation is obtained at an  $n/f$  ratio between  $1 \times 10^5$  and  $5 \times 10^5 \text{ sec cm}^{-3}$ . This higher value arises because the time that the voltage is greater than threshold occupies a much smaller fraction of a cycle than in single frequency operation. Furthermore, the higher doping density allows more rapid electric field readjustment within the diode so that the voltage can change quickly between its extreme values.

The low stored energy nature of the mode and its circuit appears advantageous for rapid start up of oscillation (Fig. 6.23), both for systems use, and to avoid initial destructive domain formation. A possible disadvantage is the low relative value of the rate of change of voltage at the threshold crossing time. The device may be susceptible to noise and temperature instability but this is not clear at the time of writing.

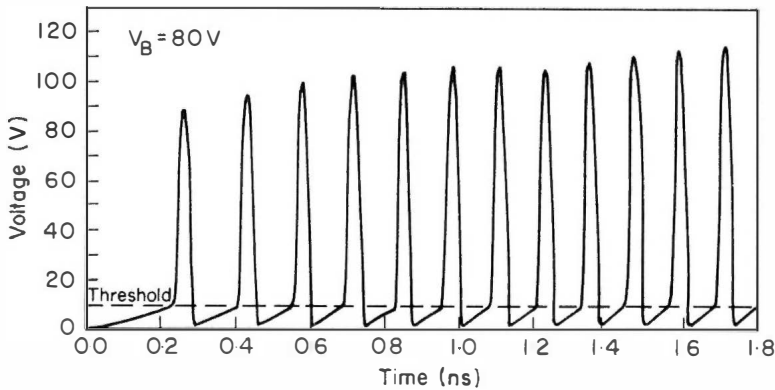


FIG. 6.23. Buildup of device voltage versus time.<sup>(25)</sup>

A circuit realization is shown in Fig. 6.24. The thick iris provides the essentially lumped inductance in the transverse parallel plate mounting. The matching transformers are required to present the correct resistive load impedance to the diode to obtain maximum efficiency. Figure 6.22 illustrates the simulated oscillator performance for the following parameters. The thick iris inductance was equivalent to a quarter wavelength short-circuited line at 36 GHz and characteristic impedance of  $100\Omega$ . The diode doping density was  $1.8 \cdot 10^{15} \text{ cm}^{-3}$  giving an  $n/f$  ratio of  $10^5 \text{ sec cm}^{-3}$  at 9 GHz. It had a low field mobility of  $8000 \text{ cm}^2/\text{V sec}$ , a length of 30 microns and a peak/valley ratio of 2.5. The ridge waveguide transformers were a quarter wavelength long at 9 GHz and had characteristic impedances of  $200\Omega$  and  $400\Omega$ . The waveguide had a characteristic impedance of  $500\Omega$ . The wavetrapped



was a quarter wavelength long at 11.6 GHz and had a characteristic impedance of  $1\Omega$ . It was fed from a bias supply with  $25\Omega$  output impedance. Owing to the large number of parameters involved in the simulation it was not possible to carry out a complete optimization, but a maximum efficiency of 26.5% was calculated for an  $n/f$  ratio of  $2.6 \times 10^5 \text{ sec cm}^{-3}$ . This is approaching the maximum predicted in Chapter 4. The best practical efficiencies achieved in this type of circuit are 15% at 1.75 GHz with 6 kW output, at the time of writing.

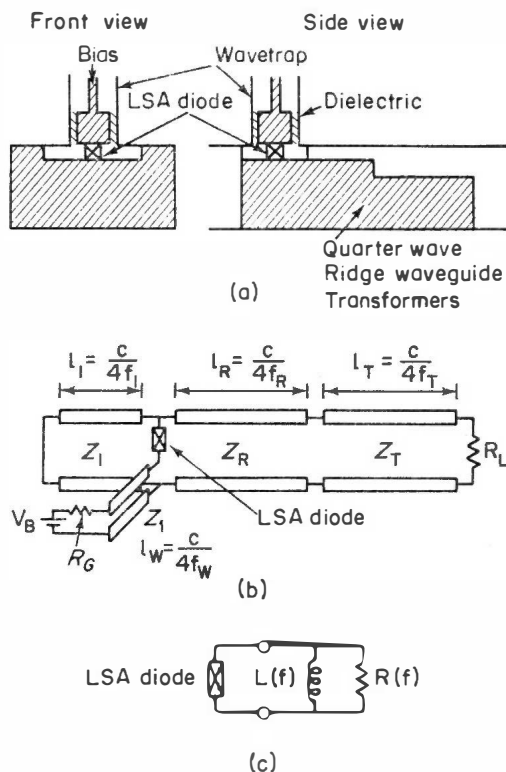


FIG. 6.24. (a) Sketch of X-band waveguide iris circuit. (b) Equivalent diagram of iris circuit. (c) Representation of overall load impedance.

## 6.7 MAXIMUM POWER LIMITATIONS

The non-transit modes have a d.c. to r.f. conversion efficiency which is independent of the device volume. Providing that material preparation problems of uniformity can be overcome the maximum power output is only limited by the volume of the device. In turn the volume is limited by the necessity of maintaining a substantially uniform distribution of r.f. and d.c.

electric fields at points transverse to the electron drift. Otherwise one part of the device may be operating under optimum efficiency conditions whereas another part of the device could be operating at very low or even negative efficiency. There are two sources of r.f. electric field non-uniformity which limit the device dimensions. No account of the required cavity will be given in the following discussion. It simply has to be designed to "fit around" the optimum device. The standing wave electromagnetic fields in a cavity vary from maximum to minimum over a quarter-wavelength, and the penetration of electrical fields into a conducting device are limited by skin effect considerations. The first non-uniformity is inherent in any standing wave circuit and the device can only occupy a fraction of a wavelength *within the device*.

The skin depth in a negative conductivity medium has been the subject of much confusion. Solution of Maxwell's equations in a uniform negative differential conductivity medium show that the electric and magnetic field amplitudes grow in the direction of propagation. The solutions have the same apparent decay with distance for both positive and negative conductivity<sup>(15)</sup> but closer inspection shows that the direction of propagation is reversed in the negative conductivity medium. A wave incident upon the medium is partially reflected at the interface owing to the mismatch of the characteristic impedances of the electromagnetic wave circuit and the negative conductivity medium. That part of the wave which enters the medium grows as it propagates until it is incident on the second surface. Here it is again partially reflected and partially transmitted.

Chawla and Coleman<sup>(19)</sup> have predicted that samples which are sufficiently long can act as their own resonators. If the signal gain in transit between the faces is greater than the transmission loss through a face then coherent oscillations may be generated providing that the material remains electrically uniform. There is no experimental evidence of this effect at the time of writing.

In an L.S.A. device the frequency of operation is of necessity close to the negative dielectric relaxation frequency. This implies that the displacement current and conduction current associated with the electromagnetic wave have similar magnitudes and account must be taken of this in calculating the skin depth. The simple skin effect formula for a metal in which the displacement current is negligible is not sufficient. The effect of the displacement current is to increase the skin depth.

The effects of the non-uniform standing wave field and skin effect have been discussed by Copeland<sup>(8)</sup> for a device that is transverse to the direction of propagation of the electromagnetic waves. The skin effect limitations arise from the interference of two waves propagating and growing from each side of the device. He shows that a gallium arsenide device must not be longer than one thirtieth of a free space wavelength in the direction of propagation

for  $n/f = 5 \times 10^4 \text{ sec cm}^{-3}$ . The r.f. electric field would then be constant to better than 10%. Copeland's calculations assumed uniformity transverse to the electromagnetic wave. This will be true for plane wave circuits (i.e. no sidewalls) but in waveguide the transverse field variation will set a limit to this dimension.

The longitudinal dimension of a 10 GHz. L.S.A. device with  $n/f = 5 \times 10^4 \text{ sec cm}^{-3}$  is limited to about 1 mm for an electric field uniformity better than 10%. If practical limitations for the height and width of the device are taken as 1 cm when it is inserted into plane wave circuitry the bias power dissipation will be approximately 1 megawatt for a biasing electric field of  $10^4 \text{ volts/cm}$ . Assuming 10% efficiency, a power output of 100 kilowatts r.f. may be obtained. The low field device resistance would be about 20 ohms for good quality gallium arsenide so that the device impedance should not be difficult to drive or match to the r.f. circuit. Eastman and Kennedy<sup>(16)</sup> have used similar device dimensions to predict similar r.f. powers from 10 GHz to 100 GHz.

## 6.8 C.W. OPERATION

Electrical non-uniformities due to dimensional limitations and material imperfections cause considerable difficulty in the achievement of L.S.A. operation. These difficulties are increased when c.w. operation is attempted because of thermally induced non-uniformities. The earliest practical forms of transferred electron devices (longitudinal orientation) had the same path for heat and electrical conduction. This causes the centre of the device to work at a higher temperature than the contact regions. The mobility of the electrons depends upon temperature so that there is an additional thermally induced, electrical non-uniformity in the device.

In order to avoid this non-uniformity heat should be removed from the sides of the device. This can be achieved with epitaxial layers of GaAs grown on a high resistivity substrate. More details of this "surface orientated" or "lateral" device will be given in a later Chapter.

C.w. operation also carries another disadvantage. The temperature dependence of the velocity-field characteristic<sup>(23)</sup> causes a reduction of the peak/valley ratio and the negative slope, with less reduction of the valley velocity. The reduction of peak/valley ratio will reduce the current amplitude of L.S.A. oscillation and also the efficiency of d.c. to r.f. conversion.

## 6.9 MAXIMUM FREQUENCY LIMITATIONS

The calculation of all oscillator properties in this chapter have, at least implicitly, assumed that there is a time invariant velocity-field characteristic from which the current-voltage device characteristics have been obtained.

When the frequency is sufficiently high this is incorrect (see Chapter 3). The redistribution of the internal electronic momenta after an electric field alteration takes approximately  $10^{-11}$  sec to  $10^{-12}$  sec so that there is lag in the attainment of a steady mean electron velocity for about this time. A device operating in the L.S.A. mode with an oscillation period which is comparable with this relaxation time conducts a higher current than expected from the static velocity-field curve when the electric field is increasing but the current is lower than expected when the electric field is decreasing (see Fig. 6.25). The resulting phase lead of current with respect to voltage appears as an additional device susceptance which increases with increasing frequency. The in phase current component decreases with increasing frequency because the mean current-voltage characteristic tends towards a positive resistance in the high frequency limit when there is no r.f. component of intervalley transfer.

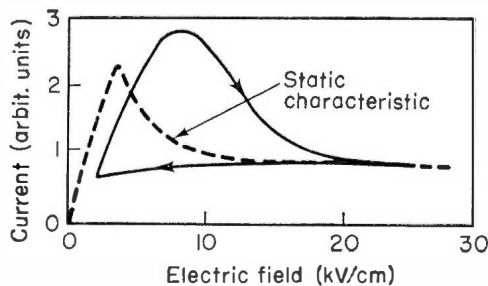


FIG. 6.25. Current-electric field relation of an L.S.A. oscillator when the inverse frequency approaches the electronic distribution function relaxation time.<sup>(17)</sup> Frequency = 60 GHz; r.f. field amplitude = 13.1 kV/cm. Bias field = 15 kV/cm.

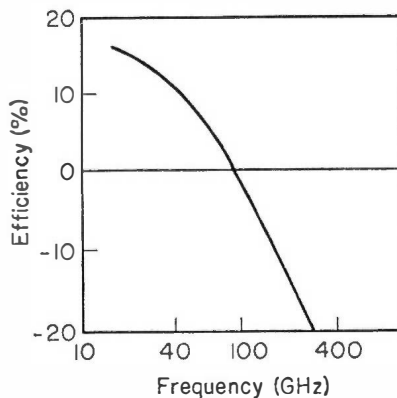


FIG. 6.26. Decrease of L.S.A. efficiency at high frequencies due to energy and intervalley relaxation processes<sup>(17)</sup> r.f. field amplitude 13.1 kV/cm; Bias field = 15 kV/cm.

The effects of energy relaxation and intervalley transfer rate appear to have almost equal significance in limiting the high frequency performance. The former does not allow electrons to reach the energy necessary for intervalley transfer and the latter limits the transfer rate after achievement of required energy. The dependence of d.c. to r.f. conversion efficiency on frequency for L.S.A. operation is illustrated in Fig. 6.26 as calculated by Butcher and Hearn.<sup>(17)</sup> Energy relaxation modifications to the velocity-field characteristic have been discussed in Chapter 3.

The relaxation of the electronic momentum distribution may carry a bonus for the control of space charge. As the upper frequency limit for L.S.A. operation is approached the negative slope of the "dynamic" velocity-field characteristic will be decreased and the space charge accumulation rate should decrease. Conversely, the velocity reduction of electrons in front of the accumulation layer may cause additional difficulties in damping this layer<sup>(24)</sup> (see Section 6.2).

#### 6.10 USEFUL CHARACTERISTICS OF NON-TRANSIT MODES

The principle advantage of the non-transit modes is the direct dependence of output power on material volume. The state of the art at the time of writing is illustrated in Fig. 6.27.

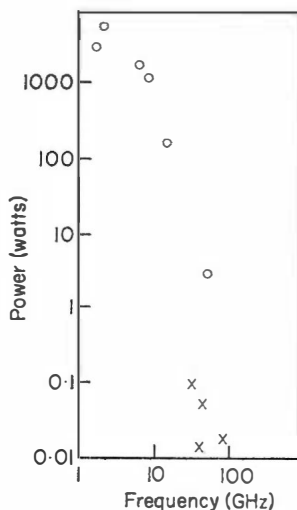


FIG. 6.27. State of the art performance of overlength devices, June 1971.

It may be expected that the lack of frequency dependence on a transit time may allow wide range mechanical tuning (i.e. by variation of cavity dimensions). This feature appears to be shown in the results of Taylor and

Howes<sup>(18)</sup> but there is very little information on this aspect at present. Most high power results have been obtained in cavities which will not allow the mechanical tuning feature to be exploited because they contain many parasitic elements which give frequency controlling resonances.

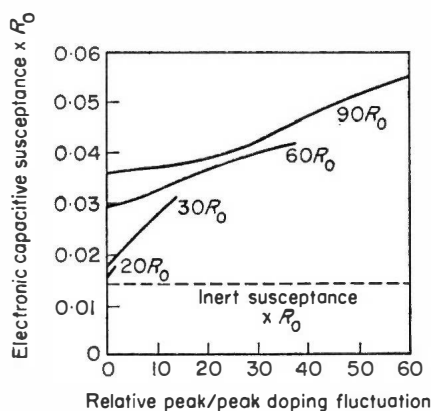


FIG. 6.28. The capacitive susceptance of an L.S.A. diode<sup>(8)</sup> whose length is 5 transit lengths. The parameters are load resistance,  $R_0$  is the low field device resistance.

The inherent electronic tuning (i.e. frequency dependence on bias) characteristics of non-transit oscillators should depend on the particular details of the mode. Those modes which exhibit large space charge non-uniformities also have a large capacitive component due to the space charge and a large assymetry of the current waveform with respect to the r.f. voltage minimum. This assymetry arises from the modification of the instantaneous device current-voltage characteristic by space charge formation. A small space charge exists immediately after the device voltage rises through threshold and a large space charge is in existence just before the voltage passes below threshold. Both effects cause a susceptance component in the equivalent circuit of the device. Because the space charge non-uniformities depend on the oscillator working conditions this susceptance may be altered by a change of bias voltage or external r.f. loading so that the resonant frequency of cavity and device may be changed. L.S.A. operation in which there is ideally no space charge growth may be expected to show the weakest dependence of frequency on external working conditions and therefore the greatest frequency stability. The dependence of this susceptance on the working conditions and material inhomogeneity is shown in Fig. 6.28.<sup>(8)</sup> The calculation was made by computer simulation. Operation was essentially L.S.A. and even larger variations may be expected in quenched mode oscillators.

## REFERENCES

1. Copeland, J. A. (1967). *J. Appl. Phys.* **38**, 3096-3101.
2. Hobson, G. S. (1969). *Brit. Journ. Appl. Phys.* **2**, 1203-13.
3. Bott, I. B. and Hilsun, C. (1967). *I.E.E.E. Trans. on Electron Devices* **ED-14**, 492-497.
4. Hobson, G. S. (1966). "Proc. International Conf. on Microwave and Optical Generation and Amplification". Cambridge, England, I.E.E.E. Conf. Publication 27, 314-318.
5. Barber, M. R. (1968). *Proc. I.E.E.E.* **56**, 752-3.
6. Huang, H. C. and Mackenzie, L. A. *Proc. I.E.E.E.* **56**, 1232-3. (1968)
7. Kuru, I., Robson, P. N. and Kino, G. S. (1968). *I.E.E.E. Trans on Electron Devices* **ED-15**, 21-29.
8. Copeland, J. A. (1967). *I.E.E.E. Trans. on Electron Devices* **ED-14**, 497-500.
9. Thim, H. W. (1968). *J. Appl. Phys.* **39**, 3897-3904.
10. Hobson, G. S. (1968). *Electron. Lett.* **4**, 230-232.
11. Higgins, J. A., Grande, V. J. and Pearson, G. L. (1967). *I.E.E.E. Trans. on Electron Devices* **ED-14**, 719-720.
12. Chilton, R. A. and Kennedy, W. K. (1968). *Proc. I.E.E.E.* **56**, 1124-5.
13. Copeland, J. A. and Spiwak, R. R. (1967). "Digest of 1967 International Solid State Circuits Conference". I.E.E.E., New York. pp. 26-27.
14. Eastman, L. P. (1968). IPPS, Conference on Solid State Devices, Manchester, Unpublished.
15. Lewin, L. (1968). *Electron. Lett.* **4**, 145-7
16. Kennedy, W. K. and Eastman, L. F. (1967). *Proc. I.E.E.E.* **55**, 434-5.
17. Butcher, P. N. and Hearn, C. J. (1968). *Electron. Lett.* **4**, 459-463.
18. Taylor, B. C. and Howes, M. J. (1969). *I.E.E.E. Trans. on Electron Devices* **ED-16**, 928-34.
19. Chawla, B. R. and Coleman, D. J. (1969). *Electron. Lett.* **5**, 31-33.
20. Shaw, M. P. and Shuskas, A. J. (1966). *Proc. I.E.E.E.* **54**, 1580-1.
21. Gibbs, S. E. (1969). "P.G.M.T.T. Symposium". Dallas.
22. Kennedy, W. K. (1966). "Proc. of 6th International Conf. on Microwave and Optical Generation and Amplification". Cambridge, pp. 286-271, I.E.E. Conf. publication No. 27.
23. Ruch, J. G. and Fawcett, W. (1970). *J. App. Phys.* **41**, 3843-50.
24. Curtice, W. R. and Purcell, J. J. (1970). *Proc. M.O.G.A.* 70, pp. 20-23, Kluwer-Deventer, Amsterdam.
25. Jeppsson, B. I. and Jeppesen, P. (1971). *I.E.E.E. Trans. on Electron Devices* **ED-18**, 432-449.

## Chapter 7

# Transferred Electron Amplifiers

### 7.1 INTRODUCTION

In Chapter 4 it was shown, not surprisingly, that the negative differential resistance present in transferred electron materials provides us with devices capable of either oscillation or amplification, depending upon certain device parameters. The previous two chapters have examined in detail the characteristics of the oscillators. In this chapter we set out to examine in detail the mechanisms, directly and indirectly due to electron transfer, whereby amplification can be obtained, and to consider the performance of such amplifiers.

### 7.2 THE BULK NEGATIVE CONDUCTANCE AMPLIFIER

It has already been pointed out (Chapter 4) that there is a lower limit on the value of the  $nl$  product, below which no travelling high field domain can form. Such devices are stable against domain formation and it might be thought that, in consequence, such a device would have a terminal I-V characteristic similar to the  $v$ - $E$  characteristic, thereby presenting us with a very broad band differential negative resistance. In fact we do not obtain this and instead, as we exceed the threshold voltage, electrons are injected into the material from the cathode thereby raising the total charge and over compensating for the reduction in electron mobility at fields above threshold. Thus the terminal current continues to rise as we exceed threshold and no d.c. negative resistance is obtained. Figure 7.1 shows some typical terminal I-V characteristics calculated by Holmstrom<sup>(1)</sup> for a range of values of the  $nl$  product.

Space charge effects prevent us from obtaining a static negative resistance. Equally no negative resistance will be seen at any frequency where this space charge readjustment has time to take place. This means that no negative resistance can be obtained when the period of the applied signal is much greater than the transit time of a carrier through the crystal. At higher



frequencies however the possibility arises of negative resistance effects in these d.c. stable devices, and it is the conditions surrounding these effects that we now want to examine. It is to be emphasized that we are here concerned with small negative resistance effects.

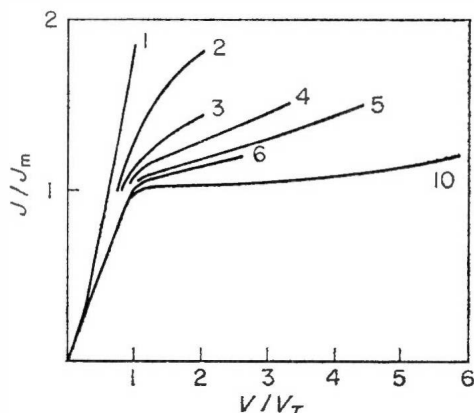


FIG. 7.1. Normalized current density-voltage characteristics for Gunn diodes having different values of the  $nl$  product.  $V_T = E_T L$ , where  $E_T$  is the threshold field (3.3 kV/cm) and  $L$  the sample length,  $J_m = n_0 e \bar{v}_m$  where  $\bar{v}_m$  is the maximum electron drift velocity. The parameter is

$$L^1 \left( = \frac{e}{\epsilon \epsilon_0 E_T} n_0 L \right). \quad (\text{Ref. 1})$$

For any reasonable analysis of the time-space dynamics of negative conductance devices, we are forced to simpler approximate models for the description of the electron system than those described in Chapter 3. A very useful model has been presented by McCumber and Chynoweth,<sup>(2)</sup> and using it they have made computer calculations of the behaviour of devices with low  $nl$  products. This model, and the results it yields, will form the basis of our considerations of these devices.

### 7.2.1 THE MCCUMBER CHYNOWETH MODEL

Here it is assumed that the electrons have a Boltzmann distribution, with a common temperature, and that they possess a common temperature relaxation time. The electron temperature is then determined by the energy transport equation.

$$\frac{\partial}{\partial t} \mathcal{E} = - \frac{\partial}{\partial x} (\bar{v} \mathcal{E}) - \frac{3}{2} \frac{T - T_0}{\tau_T} + E \bar{v}, \quad (7.1)$$

where  $\tau_T$  is the temperature relaxation time, to which the estimated value of  $2 \times 10^{-12}$  sec is assigned in the calculations and  $\bar{v}$  is the average carrier velocity.

The populations of the upper and lower valleys,  $n_U$  and  $n_L$  are determined by the application of Maxwell-Boltzmann statistics and the remaining equations to describe the system are Poisson's equation

$$\frac{\partial E}{\partial x} = \frac{e}{\epsilon\epsilon_0} (n_L + n_U - n_0) \quad (7.2)$$

the continuity equation

$$\frac{\partial}{\partial t} (n_L + n_U) = - \frac{\partial}{\partial x} [\bar{v}(n_L + n_U)], \quad (7.3)$$

and the expression for the average electron velocity

$$\bar{v} = \left\{ (\mu_L n_L + \mu_U n_U) E - \frac{\partial}{\partial x} [T(\mu_L n_L + \mu_U n_U)] \right\} / (n_L + n_U). \quad (7.4)$$

where the Einstein relation has been used to convert diffusion constants to mobilities. Setting time derivatives in the above equation to zero we have the general steady state equations

$$T(x) = T_0(x) + \frac{2}{3} \tau_T \left\{ \bar{v}(x) E(x) - \frac{\partial}{\partial x} [\bar{v}(x) T(x)] \right\} \quad (7.5)$$

$$\frac{\partial E(x)}{\partial x} = \frac{e}{\epsilon\epsilon_0} [n(x) - n_0(x)], \quad (7.6)$$

$$j = e \bar{v}(x) n(x) \quad (7.7)$$

$$\bar{v}(x) = \bar{\mu}(x) E(x) - \frac{1}{n(x)} \frac{\partial}{\partial x} [T(x) \bar{\mu}(x) n(x)] \quad (7.8)$$

where  $j$  is the steady state current density and  $\bar{\mu}$  is the average electron mobility, defined as  $\bar{v}/E$ .

The last (energy transport) term in Eqn 7.5, and the last (diffusion) term in Eqn (7.8) are only important in the vicinity of rapid changes in material properties, and may therefore be neglected in a first approximation. In this case the equations can be combined to yield

$$\frac{dE(x)}{dx} = \frac{en_0(x)}{\epsilon\epsilon_0} \left[ 1 - \frac{j/en_0(x)}{\bar{v}(E(x))} \right]. \quad (7.9)$$

The importance of the boundary conditions in this problem has previously been noted. McCumber and Chynoweth separate their mathematical boundaries ( $E = 0$ ,  $T = T_0$ ,  $n_U = 0$ ) from the region of real interest by short

heavily doped end regions. With these boundaries, solution of Eqn (7.9) yields the internal field distributions shown in Fig. 7.2. The parameter here is  $j/n_0 e \bar{v}_m$  where  $\bar{v}_m$  is the maximum value of  $\bar{v}$ , so that  $n_0 e \bar{v}_m$  corresponds approximately to the saturation current in a sample with uniform internal fields. Thus it is seen that as  $j/n_0 e \bar{v}_m$  exceeds unity (approximately) the field distribution becomes very non-uniform, indicating the presence of excess charge in the layer which has come from the cathode contact. The anode contact is not shown in the figure but there the field must fall rapidly to zero through the heavily doped anode region.

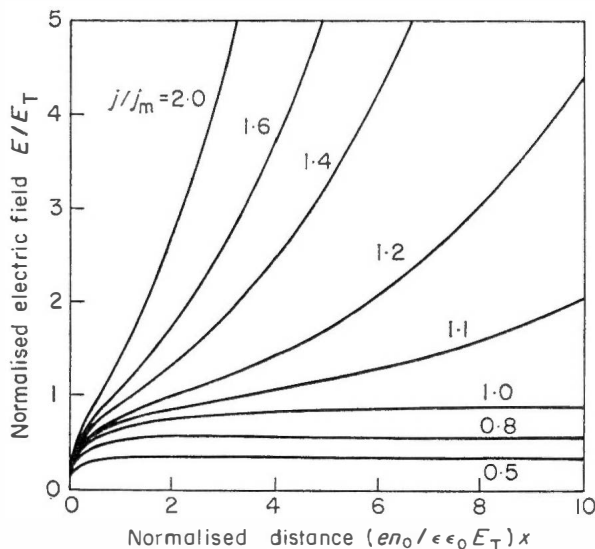


FIG. 7.2. Electric field  $E(x)$  versus distance  $x$  from  $x = 0$  where  $E(0) = 0$ . The current density  $j$  for the different curves is measured in units of  $j_m = n_0 e \bar{v}_m$  and the electric field in units of  $E_T$ . Distance is measured in units of

$$\frac{\epsilon \epsilon_0 E_T}{en_0}. \quad (\text{Ref. 2})$$

At any point in the crystal the electric field  $E(x)$  is seen from Fig. 7.2 to be a monotonically increasing function of the current density. A corollary of this is that the voltage across the whole device  $\int_0^L E dx$  is also a monotonically increasing function of the current density  $j$ . In other words the terminal  $I$ - $V$  characteristic has everywhere a positive slope, as shown in Fig. 7.1.

### 7.2.2 THE SMALL SIGNAL IMPEDANCE OF D.C. STABLE DIODES

In a first approximation of the small signal behaviour, we can again neglect diffusion and energy transport. This means that the average velocity  $\bar{v}(x, t)$  and the electron temperature  $T(x, t)$  are instantaneous functions of the

electric field  $E(x, t)$  so that we can relate small changes in velocity and field according to

$$\delta \bar{v}(x, t) = \zeta(x) \delta E(x, t) \quad (7.10)$$

where  $\zeta(x) = \partial \bar{v} / \partial E$ , the slope of the drift velocity-field characteristic.

The small signal fluctuations are also governed by Poisson's equation

$$\frac{\partial}{\partial x} \delta E(x, t) = \frac{e}{\epsilon \epsilon_0} \delta n(x, t) \quad (7.11)$$

and the continuity equation

$$\frac{\partial}{\partial t} \delta n(x, t) = - \frac{\partial}{\partial x} [n(x) \delta \bar{v}(x) + \bar{v}(x) \delta n(x, t)]. \quad (7.12)$$

Combining these equations and introducing Fourier transforms such that

$$\delta n(x, t) = \frac{1}{2\pi} \int_{-\infty}^{\infty} \delta n(x, \omega) e^{-j\omega t} d\omega \quad (7.13)$$

etc., we arrive at the following differential equation for  $\delta E(x, \omega)$

$$\bar{v}(x) \frac{\partial}{\partial x} \delta E(x, \omega) + [\zeta(x) - j\omega] \delta E(x, \omega) = \frac{1}{\epsilon \epsilon_0} \delta C(x) \quad (7.14)$$

where

$$\zeta(x) = \frac{e}{\epsilon \epsilon_0} n(x) \zeta(x) \quad (7.15)$$

and  $\delta C(\omega)$  is the Fourier transform of the small signal current (including displacement current).

The Fourier transform of the small signal voltage across the sample length,  $L$ , is

$$\delta W(\omega) = \int_0^L \delta E(x, \omega) dx. \quad (7.16)$$

Using this together with Eqn (7.14) and applying the boundary conditions  $\delta E(0^-, \omega) = 0$ , we obtain the following expression for the small signal impedance:

$$Z(\omega) = \frac{\delta W(\omega)}{\delta C(\omega)} = \int_0^L dx_1 \int_0^{x_1} dx_2 \frac{1}{\bar{v}(x_2)} \exp \left\{ - \int_{x_2}^{x_1} dx [\zeta(x) - j\omega] / \bar{v}(x) \right\} \quad (7.17)$$

Since the integrals of (7.17) are well behaved for all admissible functions  $\bar{v}(x)$ ,  $\zeta(x)$  and for all finite values of  $\omega$ , it can be concluded that  $Z(\omega)$  has no

singularities for finite  $\omega$ . A corollary is that the device is always stable against small signals when operated under constant current conditions.

The very complex expression for the small signal impedance can be considerably simplified if the assumption is made that  $\bar{v}(x)$ ,  $\bar{\zeta}(x)$  can be approximated by constant average values  $\bar{v}$ ,  $\bar{\zeta}$  between  $x = 0, L$ . In this case Eqn (7.17) can be integrated to give

$$Z(\omega) = \frac{L^2}{\epsilon \epsilon_0 \bar{v}} \frac{e^{-s} + s - 1}{s^2} \bigg|_{s=L(\bar{\zeta}-i\omega)/\bar{v}} \quad (7.18)$$

This simple expression can readily be examined to give an approximate insight into the stability of the diode against small fluctuations when driven from a constant voltage source. Because it has a denumerable number of zeros, it can be unstable when at least one zero of the impedance function crosses over into the upper half of the  $\omega$  plane, or into the right half of the  $s$  plane.

With the exception of  $S = 0$ , the zeros of  $Z(\omega)$  correspond to zeros of

$$f(s) = e^{-s} + s - 1. \quad (7.19)$$

Putting  $s = \alpha \pm j\beta$  and separating  $f(s)$  into real and imaginary parts, we see that the zeros  $S_n$  satisfy

$$e^{-\alpha_n} \cos \beta_n = 1 - \alpha_n \quad (7.20)$$

$$e^{-\alpha_n} \sin \beta_n = \beta_n. \quad (7.21)$$

From which it follows that

$$\alpha_n = -\frac{1}{2} \log [\beta_n^2 + (1 - \alpha_n^2)] \quad (7.22)$$

$$\beta_n = \frac{4n+1}{2} \pi - \sin^{-1} [(1 - \alpha_n) e^{\alpha_n}] \quad (7.23)$$

which can be readily solved iteratively for  $\alpha_n$ ,  $\beta_n$ . In the  $\omega$  plane the zeros of  $Z(\omega)$  occur at

$$\omega_n = -j\bar{\zeta} + j \frac{\bar{v} S_n}{L} = \pm \frac{\bar{v}}{L} \beta_n - j(\bar{\zeta} - \bar{v} \alpha_n/L). \quad (7.24)$$

When the bias voltage is well below threshold,  $\bar{\zeta}$  has its positive, low field, value and all zeros of  $\omega_n$  lie in the lower half plane.

As the bias is increased  $\bar{\zeta}$  steadily decreases and the first zero of  $\omega$  to cross

into the upper half plane is  $\omega_1$  and this occurs when

$$\bar{\zeta} < \frac{\bar{v}}{L} \alpha_1 \quad (7.25)$$

$\alpha_1 = -2.09$  so that

$$\frac{d}{dE} \log \bar{v}(E) < -\frac{2.09 \epsilon \epsilon_0}{en_0 L}. \quad (7.26)$$

Now  $(d/dE) \log \bar{v}(E)$  will be a negative quantity in the region of interest, so that Eqn (7.26) can be rewritten

$$n_0 L > \frac{2.09}{e |(d/dE) \log \bar{v}(E)|}. \quad (7.27)$$

Thus we see again the importance of the  $nl$  product in determining device behaviour. Evaluation of the maximum modulus of the differential for typical GaAs material at room temperature yields a value of around  $5 \times 10^{11} \text{ cm}^{-2}$ . This means that, when this simplified analysis is applicable, devices with  $nl$  products much less than  $5 \times 10^{11} \text{ cm}^{-2}$  will always be stable. Equally, devices with very high  $nl$  products will be unstable immediately  $d\bar{v}/dE$  becomes negative. A more detailed and exact description of stability will be left until Section 7.2.4.

### 7.2.3 THE FREQUENCY DEPENDENCE OF THE SMALL SIGNAL IMPEDANCE

Referring back to our simple expression for the impedance, Eqn 7.18, we can separate  $Z(\omega)$  into its resistive and reactive components. Thus:

$$R(\omega) = \frac{\bar{v}}{\epsilon \epsilon_0} \left\{ (\omega^2 - \bar{\zeta}^2) \left[ 1 - \frac{L\bar{\zeta}}{\bar{v}} - e^{-L\bar{\zeta}/\bar{v}} \cos \frac{L\omega}{\bar{v}} \right] + 2\bar{\zeta}\omega \left[ \frac{L\omega}{\bar{v}} - e^{-L\bar{\zeta}/\bar{v}} \sin \frac{L\omega}{\bar{v}} \right] \right\} / [(\bar{\zeta}^2 - \omega^2)^2 + 4\bar{\zeta}^2\omega^2] \quad (7.28)$$

$$X(\omega) = \frac{\bar{v}}{\epsilon \epsilon_0} \left\{ -2\bar{\zeta}\omega \left[ 1 - \frac{L\bar{\zeta}}{\bar{v}} - e^{-L\bar{\zeta}/\bar{v}} \cos \frac{L\omega}{\bar{v}} \right] + (\omega^2 - \bar{\zeta}^2) \left[ \frac{L\omega}{\bar{v}} - e^{-L\bar{\zeta}/\bar{v}} \sin \frac{L\omega}{\bar{v}} \right] \right\} / [(\bar{\zeta}^2 - \omega^2)^2 + 4\bar{\zeta}^2\omega^2]. \quad (7.29)$$

For  $\bar{\zeta} > 0$ ,  $R(\omega)$  is positive for all real  $\omega$ .

For  $\xi = 0$

$$R(\omega) = \frac{\bar{v}}{\epsilon\epsilon_0\omega^2} \left( 1 - \cos \frac{L\omega}{\bar{v}} \right) \quad (7.30)$$

which is never negative, but does go to zero at the carrier transit frequency  $\bar{v}/L$  and at all harmonics of it. If  $\xi < 0$  then  $R(\omega)$  is negative near to the transit frequency and harmonics.

From the above, and Eqn (7.25), we can see that there will always be a range of negative resistance, without instability, defined by

$$\frac{\alpha_n \epsilon \epsilon_0 \bar{v}}{en_0 L} < \frac{\partial \bar{v}}{\partial E} < 0. \quad (7.31)$$

However with increasing  $nl$  product the range of bias fields for which this condition can be met decreases rapidly.

From Eqns (7.28) and (7.29) the conductance

$$\frac{R(\omega)}{R^2(\omega) + X^2(\omega)} \quad \text{and capacitance} \quad \frac{1}{\omega} \frac{X(\omega)}{R^2(\omega) + X^2(\omega)}$$

have been computed by McCumber and Chynoweth (Figs 7.3, 7.4) for several

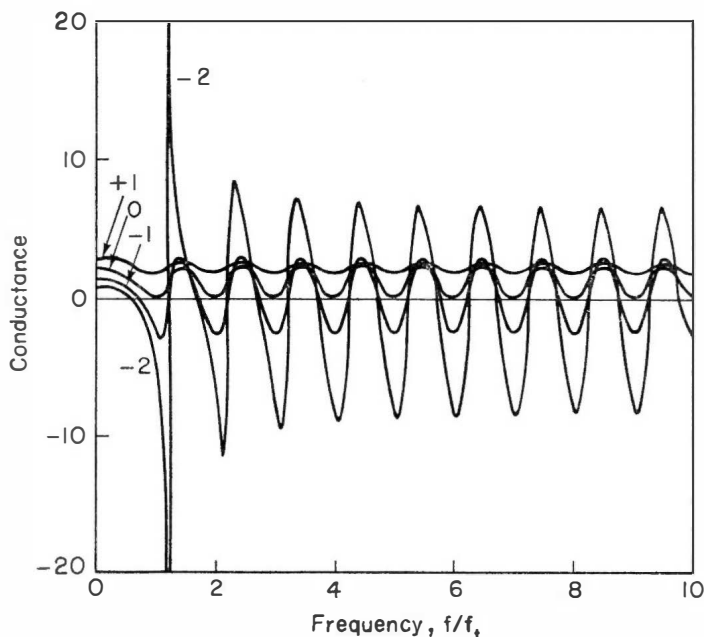


FIG. 7.3. Conductance  $G(\omega)$  versus frequency normalized to the transit frequency

$$f_t \left( = \frac{\bar{v}(E)}{L} \right).$$

The parameter is  $\alpha_n^{(2)}$

values of the dimensionless parameter  $\alpha = L\bar{\zeta}/\bar{v}$ . In all cases  $G(\omega)$  is seen to be periodic in frequency with the period of the transit frequency.

For  $\alpha = 0$  i.e.  $\bar{\zeta} = 0$ , the conductance is seen to be on the verge of becoming negative. For negative  $\alpha$ ,  $\bar{\zeta} < 0$ , the negative conductance bands appear. The greatest value of the negative conductance is obtained near to the transit frequency. Clearly the maximum conductance available will increase steadily as  $\alpha$  approaches the value  $\alpha_1 = -2.09$  when the device will have reached the limit for stability. On this very approximate model note that ranges of negative conductance exist up to the highest frequencies. From Fig. 7.4 the effective capacitance is also seen to vary considerably with frequency for values of  $\alpha$  approaching  $-2.09$ .

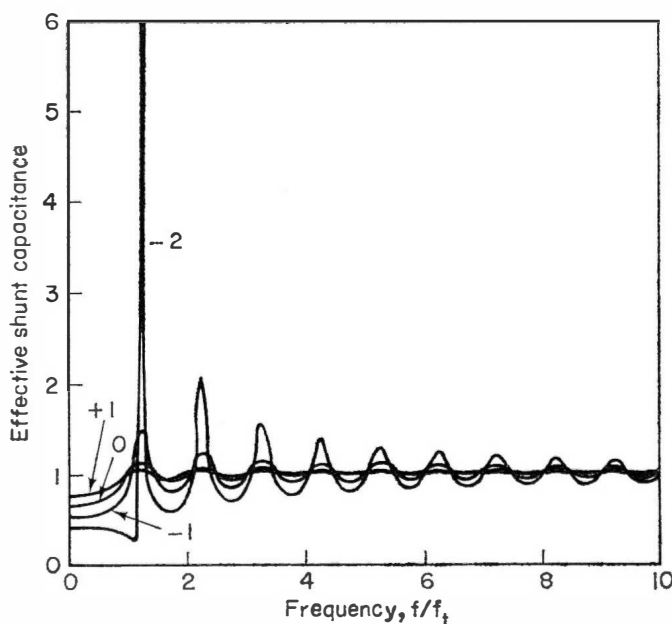


FIG. 7.4. The effective shunt capacitance versus normalized frequency. Parameter  $\alpha$ .<sup>(2)</sup>

A more exact numerical computation has also been carried out by McCumber and Chynoweth based on their model, outlined in Section 7.2.1, and thus including the effects of energy transport, diffusion and the non-uniformity of the field in the samples. The computation was for two samples, each  $200\text{ }\mu\text{m}$  long, having carrier concentrations of  $10^{13}\text{ cm}^{-3}$  and  $10^{14}\text{ cm}^{-3}$  i.e.  $nl$  values of  $2 \times 10^{11}$  and  $2 \times 10^{12}\text{ cm}^{-2}$ . The results are shown in Figs. 7.5–7.8. Several points are worth noting. Firstly, the sample with  $nl = 2 \times 10^{12}$  became unstable at an average field in excess of  $3100\text{ V/cm}$ , consistent with the indications given by Eqn (7.31). Secondly, the negative



conductance ranges are seen to be damped out as we go to higher frequencies—the same calculations, but neglecting diffusion, yield almost identical curves to Figs 7.5–7.8, so that it appears that for these samples diffusion does not account for this damping. However, calculations by Kroemer<sup>(3)</sup> for samples with zero doping show the importance of diffusion in that case in damping out the high frequency negative conductance ranges. Thirdly, the field distribution in the sample with  $nl = 2 \times 10^{12}$  was essentially uniform while for the  $nl = 2 \times 10^{11}$  case it was very non-uniform—thus the carrier transit frequencies in the two cases were quite different, accounting for the different frequency ranges for which negative conductances are obtained.

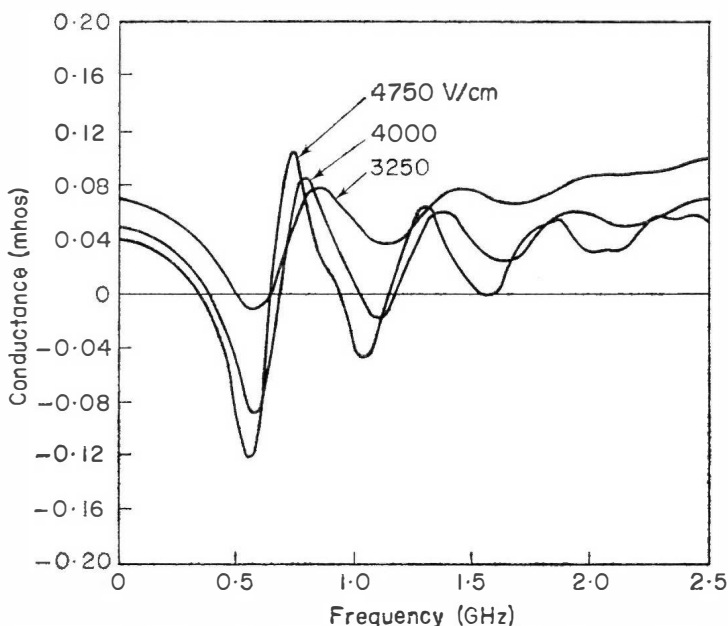


FIG. 7.5. Conductance  $G(\omega)$  in  $\text{mhos}/\text{cm}^2$  of sample cross-sectional area for  $200\text{-}\mu\text{m}$  sample of GaAs with  $n_0 = 10^{13}\text{ cm}^{-3}$ . Three curves are shown corresponding to average bias fields of 3250, 4000 and 4750  $\text{V}/\text{cm}$ .<sup>(2)</sup>

While detailed numerical computations, such as those giving the results first described, provide the most accurate description of the small signal behaviour, it is nevertheless extremely valuable to have analytic approximations for the impedance. Such analytic forms allow a more ready insight into device behaviour. Equation (7.18) is one such form which followed from rather severe approximations. A number of authors<sup>(4–6)</sup> have made various less severe approximations and arrived at impedance descriptions of consequently increased complexity. Most have neglected the effects of diffusion, which appears reasonable when we note that its inclusion by

McCumber and Chynoweth (for higher  $nl$  samples) made little difference, and that for undoped samples Kroemer<sup>(3)</sup> has found it made little difference at least up to the first, and most significant, negative conductance region. It will be instructive to consider the simple analytic expression which has been derived by Kroemer for the case of zero doping. In this case all carriers present in the crystal are there by injection from the cathode. The model takes the inhomogeneous fields into account and neglects diffusion. It provides a simple impedance expression which has almost quantitative validity for samples with  $nl$  values well below critical. Since the approximations leading to Eqn (7.18) are almost reasonable for samples with  $nl$  products near to and above the critical value (since for this range the injected space charge is small relative to the donor density, thereby leading to relatively uniform internal fields) these two expressions together bound the  $nl$  range of interest.

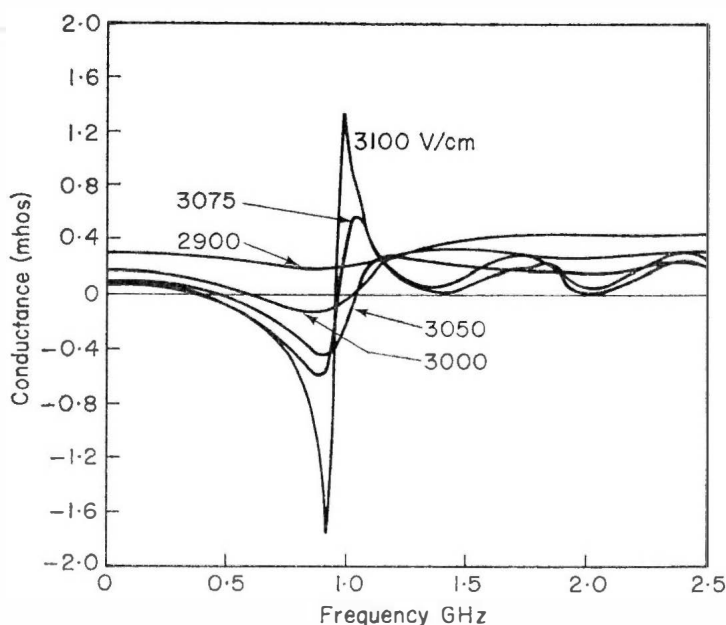


FIG. 7.6. Conductance  $G(\omega)$  in mhos/cm<sup>2</sup> of sample cross-sectional area for 200  $\mu\text{m}$  sample of GaAs with  $n_0 = 10^{14} \text{ cm}^{-3}$ . Five curves are shown corresponding to average bias fields of 2900, 3000, 3050, 3075, 3100 V/cm. The sample is unstable for average bias fields slightly above 3100 V/cm.<sup>(2)</sup>

From Poisson's and the current continuity equations, Kroemer has evaluated the small signal impedance  $Z(\omega)$  by expressing quantities in terms of static and small signal terms in  $e^{j\omega t}$ . The assumption was made that  $v$  is

an instantaneous function of  $E$ . He obtained the following simple expressions for  $R(\omega)$  and  $X(\omega)$ .

$$R(\omega) = \frac{1}{\omega} \int_0^\tau v \sin \omega (\tau - \xi) d\xi \quad (7.32)$$

$$X(\omega) = \frac{1}{\omega \epsilon \epsilon_0} \int_0^\tau v \cos \omega (\tau - \xi) d\xi - \frac{1}{\omega C} \quad (7.33)$$

where  $\xi = \int_0^x \frac{dx}{v}$  is a partial transit time.  $\tau$  is the total transit time,  $\xi(\omega)$  and

$C$  is the cold capacitance of the diode.

Note that

$$\xi = \int_0^x \frac{dx}{v} = \int_0^x \frac{nedx}{nev} = \frac{\epsilon \epsilon_0}{J} \int_0^E dE = \frac{\epsilon \epsilon_0 E}{J} \quad (7.34)$$

where Poisson's equation has been used, and  $J$  is the d.c. current in the diode.

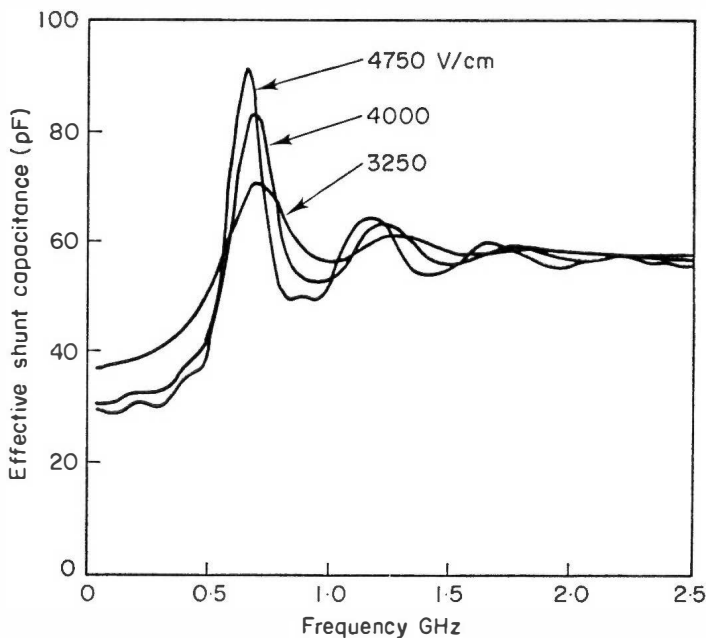


FIG. 7.7. Effective shunt capacitance in pF/cm<sup>2</sup> of sample cross-sectional area for 200  $\mu\text{m}$  sample of GaAs with  $n_0 = 10^{13} \text{ cm}^{-3}$ , and for three values of the average bias field.<sup>(2)</sup>

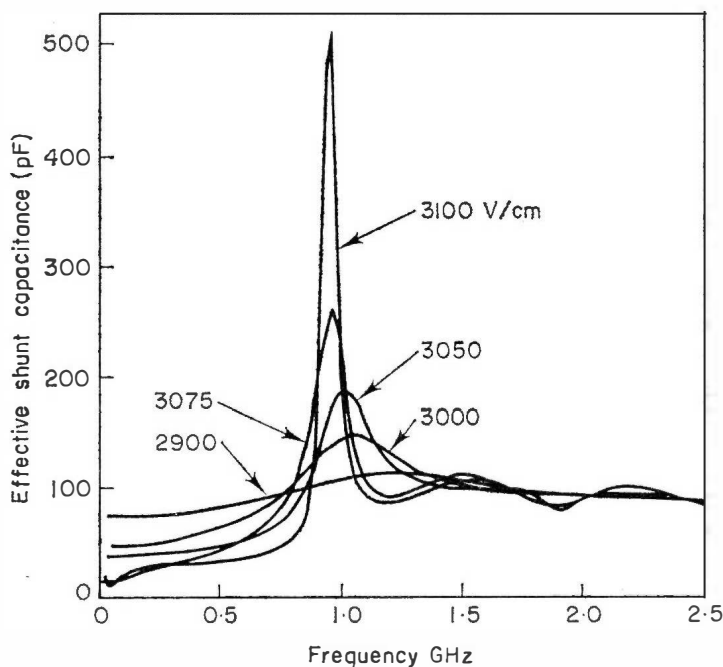


FIG. 7.8. Effective shunt capacitance in pF/cm<sup>2</sup> of sample cross-sectional area for 200  $\mu$ m sample of GaAs with  $n_0 = 10^{14}$  cm<sup>-3</sup>, and for five values of the average bias field.<sup>(2)</sup>

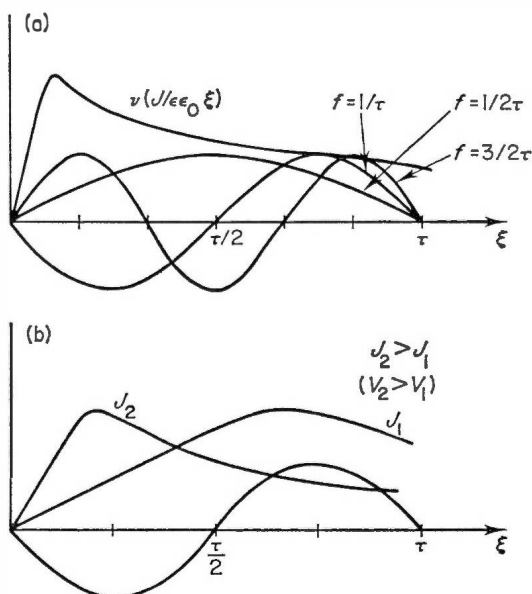


FIG. 7.9. The  $v(F)$  characteristic and the frequency dependent periodic weighting factor that determines the terminal device resistance  $R(\omega)$  according to Eqn (7.32).<sup>(3)</sup>

Figure 7.9(a) shows how ranges of negative resistance in the undoped sample can be examined. It shows the two factors contributing to the integrand in Eqn (7.32). Equation (7.34) has shown that  $v(E)$  can be plotted as a function of  $\zeta$ , for a given d.c. current. The sign of  $R(\omega)$  is thus determined by the product of the two functions integrated up to  $\zeta = \tau$ . It is clear that  $R(\omega)$  can only be negative for frequencies above half the transit frequency  $1/2\tau$ . For all lower frequencies the sine term is always positive, leading to a positive value of  $R(\omega)$ . Only as the frequency exceeds  $1/2\tau$  does the sine term become negative, beginning at low values of  $\zeta$ . If we consider behaviour at the transit frequency  $1/\tau$  we see that exactly the first half of the integration makes a negative contribution. By varying the bias voltage on the device, and thereby the current density  $J$ , the velocity-field curve can be made to lie in any position relative to the sine curve (Fig. 7.9(b)). From the approximately known form of the  $v$ - $E$  characteristic (Chapter 3) we can deduce that if the velocity reaches its maximum value sufficiently far inside the first half cycle (i.e. for sufficiently high bias), then the negative contribution to  $R(\omega)$  can exceed the positive, and a negative conductance will exist at the transit frequency  $1/\tau$  for the range of bias values thus determined. Hence even an undoped diode will exhibit negative conductance at the transit frequency.

From Fig. 7.9(a) we see that at a frequency of  $3/2\tau$  the situation is unfavourable for negative conductance, as will also be the case at  $5/2\tau$  etc. while at even multiples of  $1/2\tau$  the situation will be favourable. This is very much the same sort of result as was obtained in a first approximation, for the behaviour of a doped diode (Fig. 7.3). Figure 7.9 makes possible simple and ready evaluation of the approximate ranges of bias values and frequencies over which negative conductance can be expected in samples with  $nl$  products well below critical. Note also that it allows ready evaluation of the effects of peak to valley ratio and the magnitude of the negative slope on the device behaviour.

## 7.2.4 STABILITY

Thus far we have noted that all diodes are stable against small signals when driven from a constant current supply, and have obtained the approximate condition that all are also stable when driven from a constant voltage supply as long as the  $nl$  product does not exceed about  $5 \times 10^{11} \text{ cm}^{-2}$ . A detailed analysis of the small signal stability has been carried out by Holmstrom<sup>(1)</sup> on a model neglecting diffusion but taking into account field non-uniformities.

Figure 7.10 shows Nyquist diagrams of  $R(\omega)$  and  $X(\omega)$  obtained for several values of  $nl$  and bias current, and for a piecewise linear approximation of the  $v$ - $E$  characteristic. The stability of the impedance function

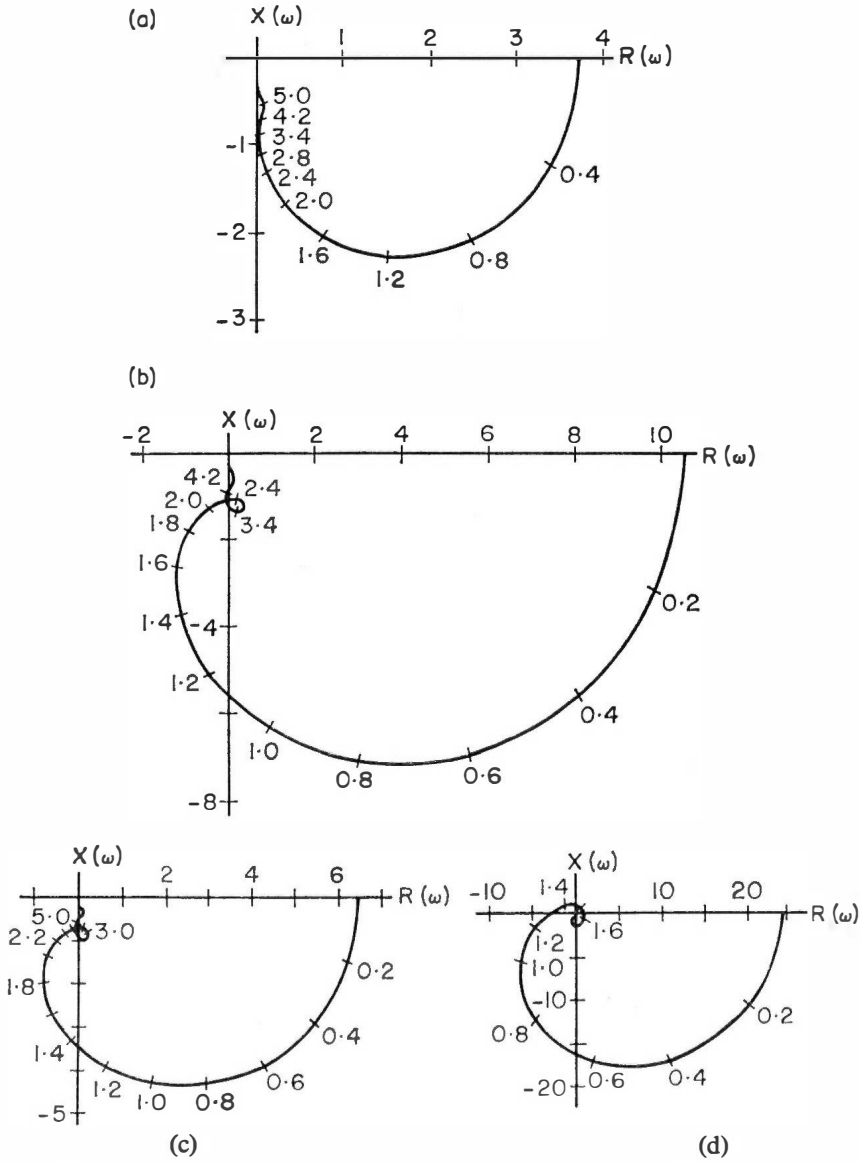


FIG. 7.10. Nyquist diagrams of resistance and reactance as a function of frequency for Gunn diodes. Values are normalized to the low field d.c. resistance  $R_0$ , and frequency is in units of  $1/\tau_d$  where  $\tau_d$  is the dielectric relaxation time. Plots are shown for differing values of the parameter

$$L^1 \left( = \frac{e}{\epsilon \epsilon_0 E_T} n_0 L \right)$$

and the normalized current density  $J^1 (= J/n_0 e \bar{v}_m)$ . (a)  $L^1 = 3.0$ ,  $J^1 = 1.1$ ; (b)  $L^1 = 4.0$ ,  $J^1 = 1.1$ ; (c)  $L^1 = 3.0$ ,  $J^1 = 1.2$ ; (d)  $L^1 = 4.0$ ,  $J^1 = 1.2$ .<sup>(1)</sup>

can be examined by calculating impedance along the real  $\omega$  axis from  $\omega = -\infty$  to  $\omega = +\infty$  and then closing the path with an infinite semicircle in a clockwise direction; since the diodes are capacitive at very high frequencies, the infinite semicircle maps into an infinitesimal semicircle about the origin in the right half of the  $Z(\omega)$  plane. Completing the  $Z(\omega)$  curve in Fig. 7.10d in this way, for example, leads to the impedance function encircling the origin twice  $R(-\omega) = R(\omega)$ ;  $X(-\omega) = -X(\omega)$ . From Nyquist's theorem the device will thus be unstable, when operated from a zero impedance source. It will still oscillate if operated in series with another (load) impedance if the Nyquist diagram for total impedance still circles the origin. It is clear from Fig. 7.10d that too large a series resistance or series reactance will prevent oscillation. By the same token, if we operate a device with  $Z(\omega)$  diagram as in Fig. 7.10(b, c) in series with appropriate reactances this can lead to the total impedance encircling the origin and consequent instability. In theory any diode which has a range of negative resistance can be so tuned that it will oscillate (we refer here of course to small signal oscillations).

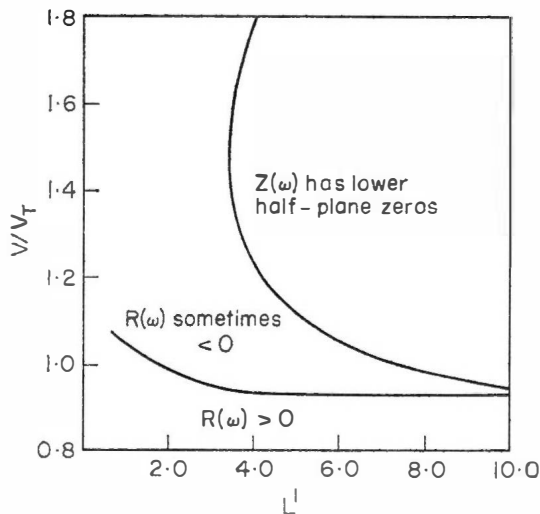


FIG. 7.11. Diagram summarizing the impedance behaviour of diodes with products from  $2 \times 10^{10} \text{ cm}^{-2}$  to  $2 \times 10^{11} \text{ cm}^{-2}$ , corresponding to values of  $L^1$  (as defined in Figs 7.1, 7.10) from 1 to 10 approx.<sup>(1)</sup>

Figure 7.11 summarises the impedance behaviour of diodes with  $nl$  values from  $2 \times 10^{10}$  to  $2 \times 10^{11} \text{ cm}^{-2}$ . Reference to Fig. 7.1 earlier will allow an equivalent description of device behaviour in terms of normalized current rather than normalized voltage. Operation has to be above the lower curve in Fig. 7.11 to obtain a negative resistance over some frequency range or ranges. Operation above the upper curve will lead to instability. The figure

gives us a clear indication of how the allowable bias range for stable amplification decreases rapidly as  $nl$  increases. For  $nl$  approximately less than  $8 \times 10^{10}$  we see that all devices are stable for all bias values (unless reactively tuned). Note also that for the higher  $nl$  values, the range of bias voltages over which stable amplification is possible can be greatly increased by the inclusion of a series resistor. In this way we can even stabilize samples with high  $nl$  products against small signal fluctuations. They may not however be stable against large fluctuations and a domain oscillation may occur.

### 7.2.5 GAIN CHARACTERISTICS OF THE LOW $nl$ NEGATIVE CONDUCTANCE AMPLIFIER

So far we have concentrated on the basic aspects of the small signal negative resistance. We now wish to make the overall picture more complete by examining the type of gain characteristics such amplifiers will provide and the factors which influence them.

Firstly we consider how the negative conductance varies with bias voltage. We can expect that the magnitude of the negative conductance will depend upon the relative lengths of the region of positive and negative differential mobility. Clearly for a given sample this will vary with bias. For a sample which remains stable for all bias levels ( $nl < 8 \times 10^{10}$ , from Fig. 7.11) when at high bias values the low slope mobility at high fields will result in a small value for the terminal negative conductance, if indeed any negative conductance exists. The negative conductance versus voltage characteristic will therefore pass through a maximum as the bias is increased beyond the voltage at which it first appears. This behaviour is indicated in Fig. 7.12. Consider-

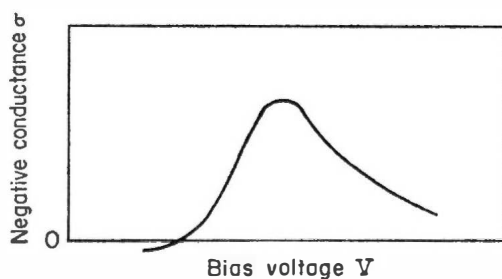


FIG. 7.12. Typical negative conductance versus bias voltage dependence.

ation of Fig. 7.9 for the special case of zero doping will confirm the form of the  $\sigma_- - V$  relationship. The actual  $\sigma_- - V$  curve will of course depend on the particular value of  $nl^{(6)}$  since this controls the internal field profile. If we consider operation at higher values of  $nl$  than  $8 \times 10^{10}$  (Fig. 7.11) then the maximum negative conductance obtainable is limited only by how close



we choose to operate to the bias at which the sample becomes unstable and oscillates.

We have already seen that the important negative conductance range occurs around the carrier transit frequency. This quantity is very dependent upon bias voltage and internal field profile (determined by the  $nl$  product), so that its actual value for a given sample length can vary widely as shown for example in Figs 7.5 and 7.6. The frequency at which the maximum negative conductance is observed in a given diode will fall somewhat with increasing bias voltage.<sup>(7)</sup>

### *Gain versus Frequency*

This is the quantity of real interest to us. The diodes are most commonly used as reflection amplifiers in transmission line circuits<sup>(8,9)</sup> as shown in Fig. 7.13. The circulation serves to isolate input and output circuits. If the transmission line admittance is  $Y_0$  and the diode admittance  $Y(\omega)$  then the amplifier gain is

$$\text{Reflection gain} = \frac{Y_0 - Y(\omega)}{Y_0 + Y(\omega)}. \quad (7.35)$$

Since the transmission line is usually matched,  $Y_0$  is purely real and can be replaced by its conductance component  $G_0$ . Then

$$\text{Power gain} = \left| \frac{G_0 - Y(\omega)}{G_0 + Y(\omega)} \right|^2. \quad (7.36)$$

The actual magnitude of the gain is thus critically dependent upon the susceptive component of the diode admittance and the transmission line conductance, as well as on the magnitude of the negative conductance. The bandwidth of the amplifier also depends critically on the relative magnitudes of these quantities as well as on their frequency dependence.

Figure 7.14 shows a typical experimental gain-frequency characteristic for frequencies in the first negative resistance range of the particular diode used. It can be seen that as the bias voltage is raised above threshold

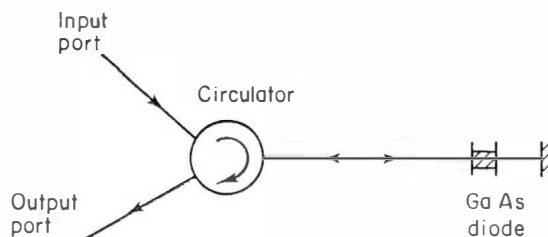


FIG. 7.13. Schematic of reflection amplifier.

amplification is obtained in accordance with the forms of the  $G(\omega)$  and  $B(\omega)$  characteristics described earlier and Eqn (7.36). With increase of bias field above 3600 V/cm this device became unstable and broke into oscillation. Note the rapid decrease in amplifier bandwidth as the maximum gain increased.

An important question which arises is what value of  $nl$  should be chosen for a practical amplifier. For an  $nl$  value which is too low, the ratio  $R(\omega)/R_0$  falls, since less and less of the sample is in the negative slope region due to the considerable internal field inhomogeneity. Hence operation becomes very inefficient. Secondly the currents flowing through these devices at the transit frequency are largely capacitance so that even small parasitic series resistances in the device will have a large effect and may even prevent negative resistance being obtained.

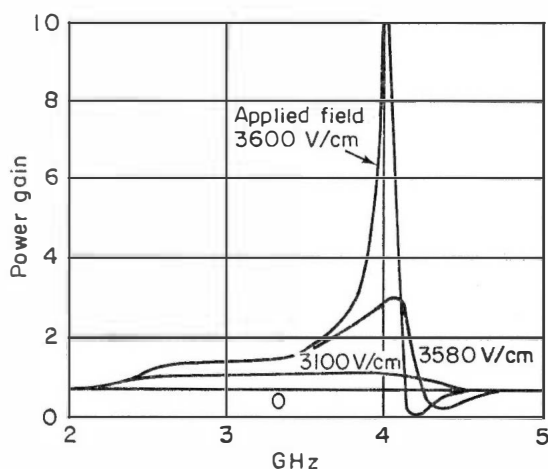


FIG. 7.14. Gain versus frequency characteristics for different values of the average bias field.<sup>(8)</sup>

The larger  $nl$  values are thus to be preferred, subject to the stability requirements being met, and the power per unit area of device not being excessive. Typically power gains of around 40 db have been obtained to date with saturation power levels equal to the power which the devices can deliver when operated as optimally tuned negative resistance oscillators.<sup>(10)</sup> Conversion efficiencies are still only at the few percent level and much room for improvement remains. At the moment the amplifier is hampered by the material and device problems of producing uniform layers of high resistivity material and making good ohmic contacts to it. Thus if we take  $5 \times 10^{11} \text{ cm}^{-2}$  as a desirable  $nl$  value and we want amplifiers to operate from, say 2–20 GHz then we are involved with materials from 50  $\mu\text{m}$  thick, 10  $\Omega \text{ cm}$

through to  $5\text{ }\mu\text{m}$  thick,  $1\text{ }\Omega\text{ cm}$ . At the moment only the latter requirement can consistently be met.

For maximum gain at a given frequency, the device area is chosen to suit the impedance level of the system. The  $nl$  product will be determined according to previous considerations. Thus in going to higher operating frequencies, the carrier concentrations must increase to maintain  $nl$ , and device area must fall to maintain the impedance level. In consequence there is once again a  $PZf^2 = \text{constant}$  limitation imposed, where  $Z$  is determined by the impedance level of the system.

### 7.2.6 THE HIGH $nl$ NEGATIVE CONDUCTANCE AMPLIFIER<sup>(11,12)</sup>

By far the most impressive results from a negative conductance amplifier (indeed from any transferred electron amplifier) have been obtained with devices whose  $nl$  products ( $1\text{--}2 \times 10^{12}\text{ cm}^{-2}$ ) considerably exceed the maximum value of  $5 \times 10^{11}\text{ cm}^{-2}$  deduced for a stable device from the simple analysis in Section 7.2.2.

It has been shown possible to stabilize such high  $nl$  devices by operating them at bias levels well beyond the threshold value. Just above threshold the devices exhibit the usual instability associated with devices having high  $nl$  products. However by raising the voltage further to exceed some critical value it is possible to stabilize the devices and operate them as amplifiers over a very wide bandwidth. The critical voltage is typically 2.5 times threshold for continuous operation, and much higher for a pulsed device at low duty cycle. It thus appears that operating temperature plays an important role in determining the threshold for stabilization.

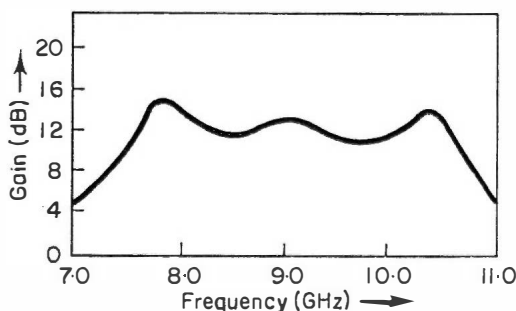


FIG. 7.15. Typical gain response of a high  $nl$  negative conductance amplifier.<sup>(11)</sup>

The devices used to make this amplifier have so far had thicknesses less than 20 microns and the wide-band amplifications has been obtained at frequencies approximately centred on the transit frequency. The devices are used in circulator coupled circuits as shown in Fig. 7.13 and present results

cover the frequency range 4–16 GHz. Amplification is linear with a dynamic range in excess of 90 dB and single stage small signals gains are typically 6–8 dB with instantaneous bandwidths of over 4 GHz. Saturation power outputs of individual devices in C.W. operation have exceeded 0.5 watt.<sup>(11)</sup>

Figures 7.15 and 7.16 show typical gain–frequency and input power–output power characteristics for the high  $nl$  negative conductance amplifier.

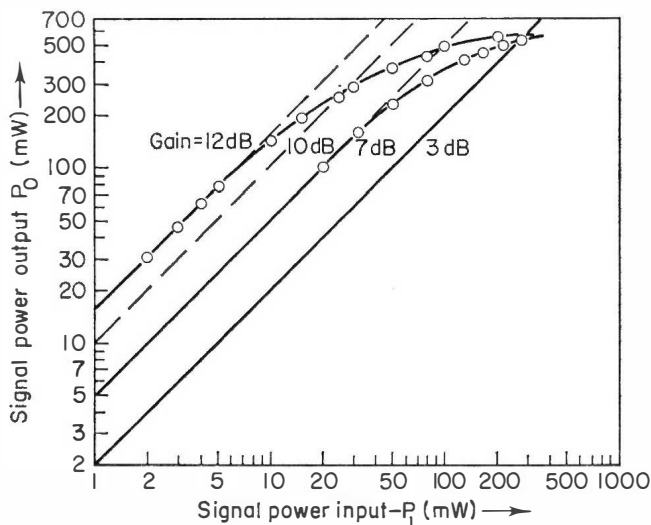


FIG. 7.16. Input power–output power characteristics for a single X-band C.W. negative conductance amplifier.<sup>(11)</sup>

The conditions for stability in this amplifier, and the amplifier performance are notably different from the low  $nl$  devices discussed in the previous section. The low  $nl$  amplifier has been operated at voltages close to threshold (hence the power output of these devices is limited) whereas to achieve stability with the high  $nl$  device much higher bias levels are required. The low  $nl$  device has also had narrow bandwidth whereas the high  $nl$  device has exhibited very broad band operation. At this point in time a theory has not been developed to explain the stability and wide bandwidth of the high  $nl$  amplifier, but there is no reason to believe that its performance will not be understood on the basis of an analysis similar to that presented in the previous sections, but taking into account additional features as noted below.

Firstly the simple stability condition derived earlier ( $nl < 5 \times 10^{11} \text{ cm}^{-2}$ ) was based on the assumption that the internal field distribution was uniform and the applied bias level just above threshold—in fact the internal field can be highly non-uniform, and new stability criteria need to be developed for bias levels beyond threshold where the  $(d/dE) \log \bar{v}(E)$  term in Eqn (7.27)

can take on very different values. Secondly the calculation assumed that the device was operating at room temperature and calculations for different device temperatures are required (100–200°C are typical operating temperatures for a C.W. device) to take account of the temperature variation of the velocity field curves for the material.<sup>(13)</sup> Thirdly the simple stability criterion was based on the assumption of zero load impedance whereas we know that it is possible to make a device having any  $nl$  value small signal stable by choosing the load impedance to preclude an oscillating condition,<sup>(14)</sup> as was indicated in Section 7.2.4. Finally, it may be that in the short devices used to construct this amplifier, diffusion may play an important role in determining stability.

The criteria for stability in transferred electron devices are thus more complex than the simple rule  $nl < 5 \times 10^{11} \text{ cm}^{-2}$  implies, and a detailed understanding of the high  $nl$  amplifier may well follow from considerations of the field and load dependence of the stability criterion, and the inclusion of temperature and diffusion effects.

The high C.W. powers, wide bandwidths and moderate noise figures (15 dB at C- and X-bands) obtained with those amplifiers represent a considerable potential for application in broad band systems, for example, as solid state replacements for travelling wave tubes.

### 7.3 THE TRAVELLING WAVE AMPLIFIER

An early estimate of the critical  $nl$  product (Chapter 4) was based on limiting the growth of small signal fluctuations as they traverse the crystal, being convectively amplified by the negative slope characteristic. In this Chapter we have so far examined the small signal impedance of stable diodes and have seen that narrow band amplification can be produced by using the negative real parts of the impedances of the diodes. These same diodes can be used to produce broad band amplification by coupling the input directly to the drifting electrons.<sup>(15)</sup> This method of using the diodes is indicated schematically in Fig. 7.17. The input signal injects a space charge wave on the electron stream which is convectively amplified as long as the local electric field is in the negative slope range. This mode of amplification is clearly broadband, and the space charge growth factor  $G$  is given by

$$G = \exp \int_{x_1}^{x_2} - \frac{ne}{\epsilon\epsilon_0} \left| \frac{dv}{dE} \right| dx$$

where  $x_1$ ,  $x_2$ , are the positions of the input and output ports respectively. The growth available is clearly limited since the small fluctuations which may grow to domains are also being amplified by a corresponding factor. Assuming that the fluctuations which grow to become domains originate

at the cathode, we have the advantage that they must traverse the whole crystal, whereas the signal ports can be arranged to straddle only the region where space charge growth occurs. The maximum gain will occur as we approach the condition for instability. At this gain level the maximum power input to the amplifier will probably be limited to a value which will preclude the formation of a domain from the injected signal. This amplifier will therefore have to operate at low signal levels. For lower  $nl$  (and therefore lower gain) values, larger input signals can clearly be accepted.

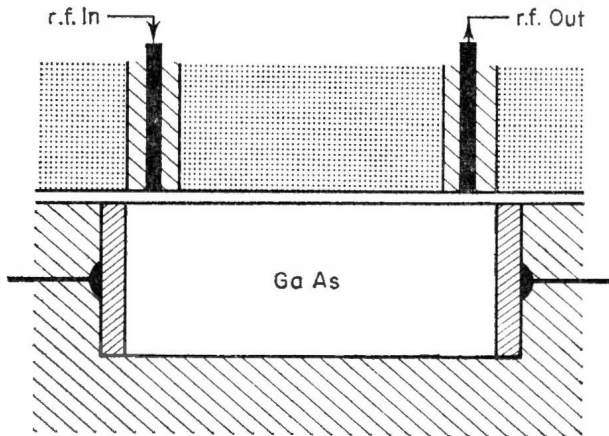


FIG. 7.17. A typical configuration for the space charge wave amplifier.

One of the main problems with this type of amplifier is matching at the input and output ports. Present results include a *net* gain of 28 dB at 9.2 GHz with a saturation power level of 0.2 mW and a noise figure of 25 dB.<sup>(16)</sup> Net gains have also been observed up to 20 GHz.

#### 7.4 THE TRAVELLING DOMAIN AMPLIFIER

In both amplifiers discussed so far, an essential requirement for operation was the stability of the diode. The types of amplifier to be discussed in the next two sections involve diodes which are simultaneously oscillating. If we consider the terminal voltage and current for a diode oscillating in a stable domain mode, as outlined in Chapter 4, then we see that as the terminal voltage is increased, there is a reduction in current through the device. We have therefore a terminal negative resistance in the presence of the travelling domain. The negative resistance appears for frequencies from d.c. up to the highest frequency at which the domain can respond to the applied voltage, so that we have a very broad band amplifier. Furthermore, since with this amplifier we are dealing with domains, signal amplitudes and saturation

power levels can be much greater than those for the low  $nl$  amplifiers. However in view of the need for a simultaneous oscillation, circuit requirements are much more stringent in this case.

#### 7.4.1 SMALL SIGNAL IMPEDANCE

The equivalent circuit for an oscillating diode has been indicated previously (Fig. 5.19). Using this equivalent circuit we can write the total device impedance (per unit area) as<sup>(17)</sup>

$$Z(\omega) = \frac{L}{n_0 e \mu + j \omega \epsilon \epsilon_0} + \left( n_0 e \mu \frac{\Delta E_R}{\Delta V_D} + j \omega \epsilon \epsilon_0 \frac{\Delta(E_D - E_R)}{\Delta V_D} \right)^{-1}.$$

The upper frequency limit for this amplifier can be determined by evaluating the frequency at which the real part of  $Z(\omega)$  ceases to be negative. Thim has evaluated this approximately as

$$f_{\max} L = \frac{\mu}{4\pi} (E_D - E_0).$$

The maximum value for  $E_D$  is the breakdown field, approx.  $2 \times 10^5$  V/cm. Taking  $\mu$  as typically  $6000 \text{ cm}^2/\text{Vsec}$ , then

$$f_{\max} L = 10^8 \text{ cm/sec}$$

i.e.

$$f_{\max}/f_t \doteq 10.$$

Thus the maximum frequency at which this amplifier can operate is about ten times the transit frequency  $f_t$ .

#### 7.4.2 POWER AND EFFICIENCY

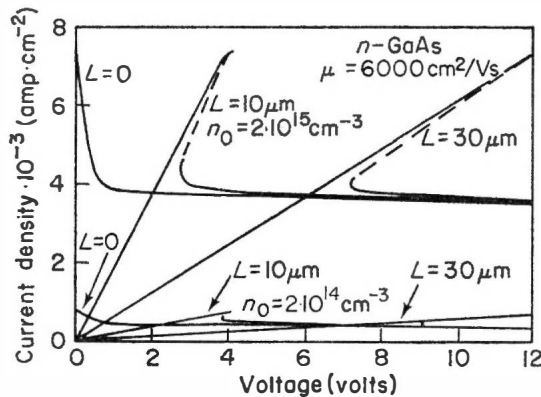


FIG. 7.18. Theoretical I-V characteristics for Gunn oscillators with a range of lengths and doping densities.<sup>(17)</sup>

Terminal I-V characteristics are shown plotted in Fig. 7.18 for a range of values of sample length and donor density. The dotted portions correspond to non-stable domain solutions. It is seen from these curves that the efficiency of operation is increasing as the diode length decreases, since as  $L \rightarrow 0$  a large linear negative conductance range is obtained for low d.c. drive power. In going to the lowest values of  $L$  we must increase  $n_0$  correspondingly so that  $n_0 L \gg 10^{12}$ , as required by the domain oscillation. A practical limit will be imposed on the maximum value of  $n_0$  by impedance and thermal considerations. The former is likely to be the more important so that the maximum power obtained from the oscillator will be determined by the minimum attainable circuit impedance level, and will to a first approximation be frequency independent.

### 7.4.3 CIRCUIT ASPECTS

The amplification principle here is based on the propagation of a stable domain whose amplitude is affected only by the signal applied at the device terminals. However, the domain amplitude must vary during formation and collapse. Furthermore in the general case there will be an interaction with the circuit which will modulate the domain in transit. These factors will generate undesirable parametric effects. From the device viewpoint these can be minimized by going to high  $nl$  products, thereby reducing the ratio of domain size to sample length. From the circuit viewpoint this entails operating the device so that it is near a voltage minimum at the frequency of Gunn oscillation. This places a constraint on the circuit design which results in a reduction of the amplifier bandwidth. In addition in order to maintain stability in the signal circuit, the source admittance presented to the diode must have a real part which is greater than the negative conductance of the diode. Ideally the oscillator and signal circuits should be decoupled. A simple circuit which has been used for this amplifier is shown in Fig. 7.19.

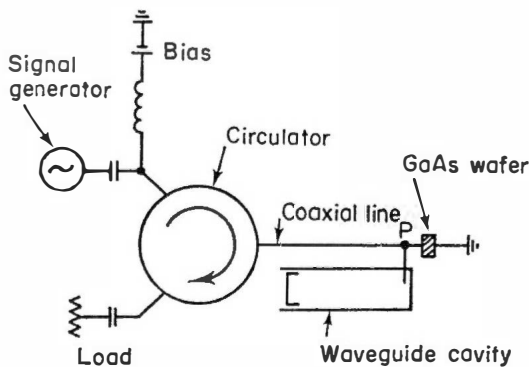


FIG. 7.19. A simple amplifier circuit.<sup>(17)</sup>



By arranging for the point  $P$  to be at a voltage minimum, parametric effects are minimized. However in this circuit we are restricted to frequencies below the waveguide cut-off to avoid undesirable susceptances in the signal circuit.

#### 7.4.4 PRESENT PERFORMANCE FIGURES

To date relatively little work has been carried out to indicate the ultimate potential of these amplifiers in terms of maximum gain, saturation level and bandwidth. Thim<sup>(17)</sup> has studied Gunn diodes with d.c. input powers at the several watt level in the simple circuit of Fig. 7.19, and obtained bandwidths of around 1 GHz in C-band. He has also indicated that these diodes have saturation levels which approach their maximum power outputs as oscillators, indicating their potential as high power amplifiers. His results for several typical diodes are shown in Fig. 7.20.

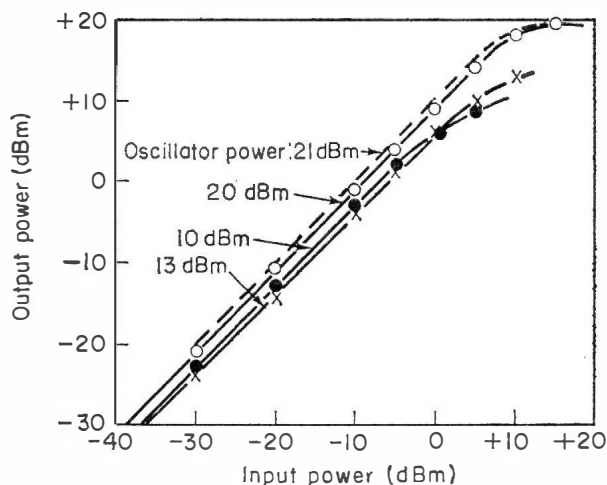


FIG. 7.20. Gain characteristics obtained from a number of Gunn oscillators.<sup>(17)</sup>

#### 7.5 PARAMETRIC AMPLIFICATION FROM GUNN DIODES

It has already been established that the dipole layers of a domain constitute a capacitance within a sample. In an oscillating sample this capacitance is time varying so long as the domain does not reach a stable amplitude. In samples with low values of the  $nl$  product a mature domain can never be formed and the domain capacitance varies continuously throughout the cycle. In samples with high  $nl$  products ( $\geq 10^{12} \text{ cm}^{-2}$ ) the capacitance may only vary as the domain is formed and as it is extinguished. In either

case, by virtue of the Gunn oscillation, a self pumped capacitance appears at the device terminals, and this may form the basis of a very simple parametric amplifier.

This has been shown experimentally.<sup>(18,19)</sup> Figure 7.21(a) shows the circuit which has been used to produce a maximum gain of 30 dB for signal frequencies in X-band.<sup>(18)</sup> The  $6\text{ }\mu\text{m}$  sandwich device used in this experiment generated a Gunn or pump frequency of about 17 GHz. The separate pump, idler and signal circuits are all coupled through the diode as shown in the equivalent circuit representation of Fig. 7.21(b). The gain bandwidth product of the amplifier was 50 MHz and a minimum single sideband noise figure of 18 dB was measured. Gain compression of 1 dB occurred at an output of 5 dBm which is to be compared with the figure of 13 dBm for the output of the device operating as an optimally tuned Gunn oscillator. Other workers<sup>(19)</sup> have constructed a degenerate parametric amplifier using an X-band Gunn diode and have operated it with gains in excess of 20 dB at C-band signal frequencies.

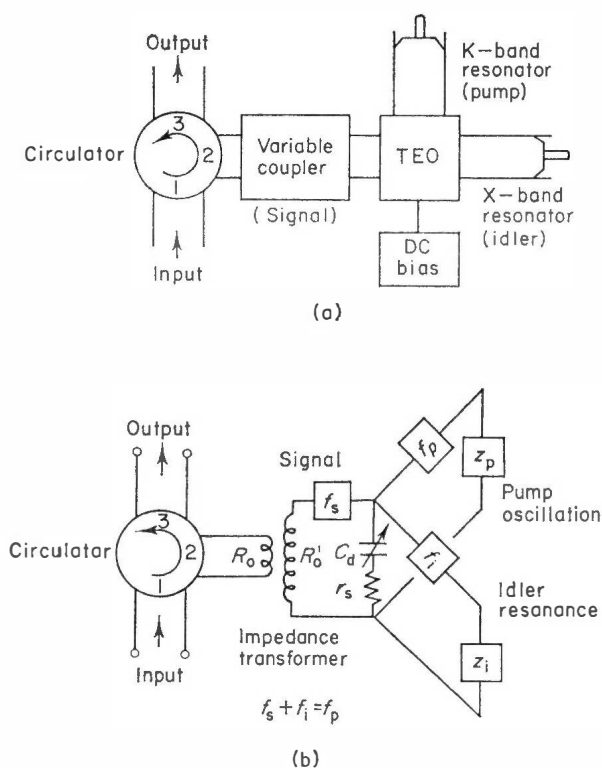


FIG. 7.21. (a) Microwave circuit for an X-band Gunn parametric amplifier; (b) An equivalent circuit of the transferred electron, self-pumped paramp.<sup>(18)</sup>

The capacitance time characteristic depends strongly on such features as the  $nl$  product of the device, the bias voltage and the tuning of the microwave circuit. A proper optimization of these quantities has not yet been attempted and should lead to much improved gain bandwidth figures for the Gunn parametric amplifier. Noise performance will certainly improve by going to higher frequencies than those mentioned above. Saturation power levels will inevitably lie somewhat, but not appreciably, below the maximum power levels for operation as an oscillator—the limits on these have been outlined already in Chapter 4.

## REFERENCES

1. Holmstrom, D. (1967). *I.E.E.E. Trans.* ED-14, 644.
2. McCumber, D. E., Chynoweth, A. G. (1966). *I.E.E.E. Trans.* ED-13, 4.
3. Kroemer, H. (1967). *I.E.E.E. Trans.* ED-14, 476.
4. Mahrous, S., Robson, P. N. (1966). *Electron Lett.* 2, 107.
5. McWhorter, A. L., Foyt, A. G. (1966). *Appl. Phys. Lett.* 9, 300.
6. Hakki, B. W. (1967). *J. Appl. Phys.* 38, 808.
7. Thim, H. W. (1967). *I.E.E.E. Trans.* ED-14.
8. Thim, H. W. *et al.* (1965). *Appl. Phys. Lett.* 7, 167.
9. Hakki, B. W., Knight, S. (1966). *I.E.E.E. Trans.* ED-13, 94.
10. Hayes, R. E. (1968). *I.E.E.E. Trans.* ED-15, 183.
11. Perlman, B. S. *et al.*, (1970). *I.E.E.E. Trans.* MTT-18, 911; (1971), *Proc. I.E.E.E.* 59, 1229.
12. Magarshack, J., Mircea, A. (1970). I.S.S.C. Conf. Dig. Tech. Papers (Philadelphia, Pa.) p. 132.
13. Ruch, J. G., Fawcett, W. (1979). *J. Appl. Phys.* 41, 3843.
14. Stertzer, F. (1969). *Proc. I.E.E.E.* 57, 1781.
15. Robson, P, N. *et al.* (1967). *I.E.E.E. Trans.* ED-14, 612.
16. *Microwaves* p. 10, April 1971.
17. Thim, H. W. (1967). *I.E.E.E. Trans.* ED-14, 517.
18. Kuno, H. J. (1969). *Electron. Lett.* 5, 232.
19. Aitchison, *et al.* (1969). *Electron. Lett.* 5, 36.

## Chapter 8

# Noise

### 8.1 INTRODUCTION

The noise performance of transferred electron devices has received brief attention which is sufficient to allow assessment of their performance in practical systems applications. Very little investigation of the fundamental origin of the noise has been carried out. The following sections will point out the large proportion of frequency modulation noise in Gunn oscillators and the practical solution for its reduction, the poor noise figures for transferred electron amplifiers and will finally give brief consideration to electron density fluctuations in the bulk of gallium arsenide.

### 8.2 NOISE IN GUNN OSCILLATORS

A consistent feature of all measurements<sup>(1,2)</sup> of Gunn oscillator noise is the much greater magnitude of the frequency modulation component compared with the amplitude modulation. The power variation of the latter component with modulation frequency is illustrated in Fig. 8.1. It is comparable with a good quality local oscillator klystron and has not caused difficulty in the performance of systems using the device. Indeed, some results have been given<sup>(29)</sup> where system performance has been improved. The noise power in Fig. 8.1 is the sum of that occurring in a 1 Hz bandwidth in both sidebands at a frequency  $f_m$  from the centre or carrier frequency. Various different presentations of the noise power are currently in use. The specification may be for one sideband only when the noise power will be half that in Fig. 8.1. Different noise power bandwidths are used by different authors. The scaling factor for the noise power is directly proportional to this bandwidth.

Before discussing the f.m. noise performance it is necessary to identify two different modes of presentation. The first one is the same as for a.m. noise where the noise to carrier power ratio is presented as a function of modulation frequency. In this case the integral of the noise power over all frequencies is the total power output of the oscillator. This presentation

may seem to have a good physical basis but it is not usual to directly measure it to describe the performance of devices in systems such as doppler radar. The second mode of presentation is based on the definition of the depth of modulation in a frequency modulated signal. The noise power in a given band width is equivalent to the sideband power produced by a pure modulating sine wave at the same modulating frequency. The noise power measure is taken as the depth of modulation of the carrier (the frequency deviation) that

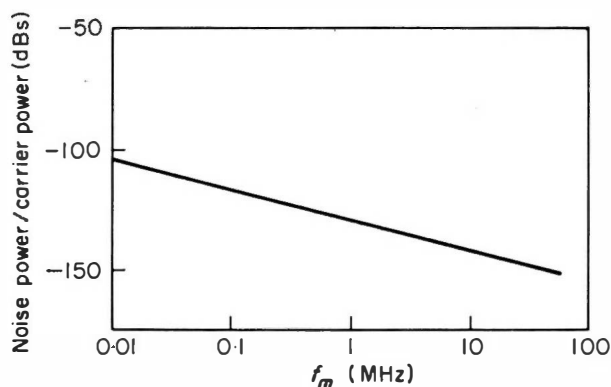


FIG. 8.1. Amplitude modulation noise to carrier power ratio in sidebands in a 1 kHz bandwidth as a function of modulating frequency.<sup>(24)</sup>

is necessary to produce this equivalent amount of power. When the depths of modulation by *all* noise components is small a simple relationship exists between the two modes of presentation as shown below. The small signal approximation is one where only the first f.m. sidebands caused by any modulating signal contain a significant power. The voltage  $V$  of a carrier wave frequency modulated by a single frequency is:

$$V = A \cos \left\{ 2\pi f t + \frac{\Delta f_p}{f_m} \cos (2\pi f_m t + \phi) \right\} \quad (8.1)$$

where  $A$  is the amplitude,  $f$  is the carrier frequency,  $\Delta f_p$  is the peak frequency deviation,  $f_m$  is the modulating frequency and  $\phi$  is a phase constant. When  $\Delta f_p/f_m \ll 1$  Eqn (8.1) may be expanded to give:-

$$V = A \left\{ \cos 2\pi f t - \frac{\Delta f_p}{2f_m} \cdot \sin [2\pi(f + f_m)t + \phi] \right. \\ \left. - \frac{\Delta f_p}{2f_m} \cdot \sin [2\pi(f - f_m)t - \phi] \right\}. \quad (8.2)$$

The single sideband to carrier power ratio is  $(\Delta f_p/2f_m)^2$  from Eqn (8.2) so that the equivalent noise,  $N$ , to carrier,  $C$ , power ratio in decibels is:

$$\left(\frac{N}{C}\right)_{\text{dB}} = 10 \log_{10} \left(\frac{\Delta f_p}{2f_m}\right)^2$$

It is more usual to specify the r.m.s. frequency deviation  $\Delta f_{\text{r.m.s.}}$  ( $= \Delta f_p/\sqrt{2}$ )

$$\therefore \frac{N}{C} = -20 \log_{10} \left(\frac{\sqrt{2}f_m}{\Delta f_{\text{r.m.s.}}}\right) \quad (8.3)$$

Equation (8.3) shows that the  $N/C$  power ratio is proportional to the square of the ratio of the frequency deviation and modulating frequency. This causes the two presentations to have different graphical slopes. In particular, the simple case of a “white” noise modulating spectrum causes  $\Delta f_{\text{r.m.s.}}$  to be independent of  $f_m$  in the frequency deviation mode of presentation, while the noise to carrier power ratio decreases at 6 dB/octave with increasing modulation frequency. The two presentations are illustrated in Fig. 8.2. A further point can be drawn from the above analysis. The frequency deviation is proportional to the square root of the noise power. In comparing f.m. noise results in the frequency deviation presentation it is necessary to scale the frequency deviation with the square root of the ratio of the noise measurement bandwidths.

The frequency deviation presentation of f.m. noise data is usually the most suitable for Gunn oscillators. Most measurements are carried out with a microwave discriminator which detects the frequency deviations by converting them to amplitude deviations so that demodulation can be carried out with diode detectors. This process then allows a measurement of the noise power in a narrow bandwidth at a variety of modulating frequencies by a low frequency (audio and video range) spectrum analyser. Without any further consideration of the detection system or the noise properties the results may be expressed as an equivalent frequency deviation caused by a single modulating frequency. If it is wished to convert the results to the noise to carrier power ratio it is necessary to know further details about the noise spectrum. If any noise modulation frequencies exist at which the small signal criterion given above is not met, then the noise power which has been measured may contain a contribution from higher order sidebands of other (lower) modulating frequencies. Until this possibility has been eliminated it is not justifiable to use the transformation of Eqn (8.3), and the required transformation is unknown until further noise details have been determined. We will use the frequency deviation presentation throughout because Gunn oscillators have a large proportion of their noise power at modulating frequencies close to the carrier. The noise power increases with decreasing modulation frequency

more rapidly than is the case for a white noise spectrum.<sup>(3)</sup> In this situation it is not immediately obvious that  $\Delta f_{r.m.s.}/f_m$  is much smaller than unity for the lower modulating frequencies.

Typical measurements of the f.m. noise are illustrated in Fig. 8.3 and 8.4. If the noise originated from a white noise source (such as Johnson noise<sup>(4)</sup>) the frequency deviation would be independent of the modulating frequency. The preponderance of noise at frequencies close to the carrier frequency without any clear reproducibility from device to device (as may be verified from the results in references 1 and 2) suggest that a flicker noise modulation process may be operating. Flicker noise is characteristic of imperfections of device technology<sup>(5)</sup> such as electron trapping at impurities within the bulk of a material or surface and contact effects which cause a correlation of an individual electron's behaviour over an appreciably longer period of time than the time scale of desired effects in the device under consideration.

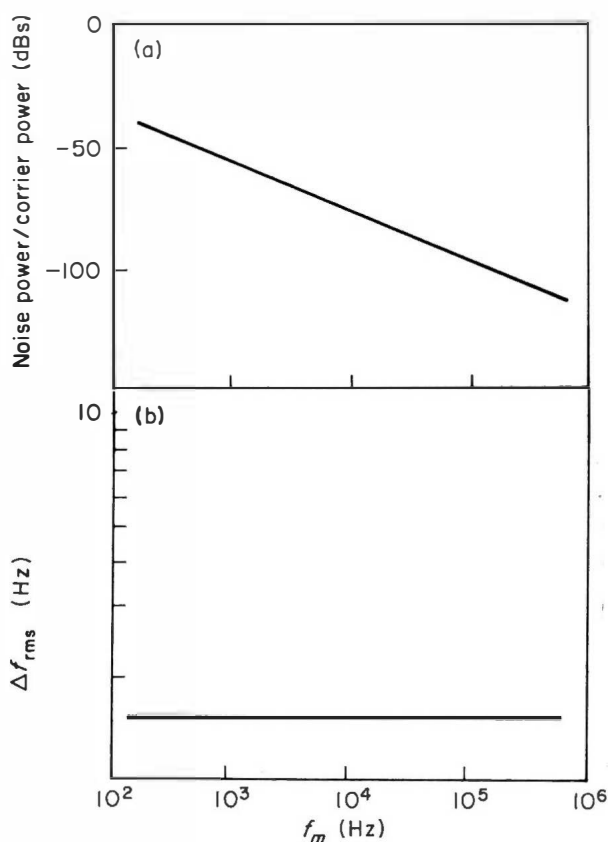


FIG. 8.2. Comparison of the two frequency modulation noise representations for a hypothetical "white" noise source.

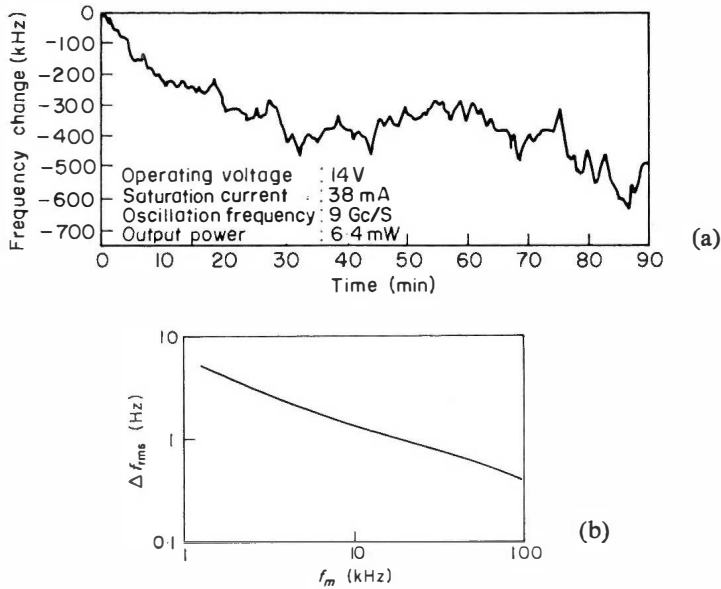


FIG. 8.3. (a) Long term frequency stability of a coaxial cavity Gunn oscillator.<sup>(22)</sup> (b) F.m. noise in both sidebands in a 1 Hz bandwidth for a coaxial cavity Gunn oscillator.<sup>(22)</sup> (Crown Copyright, reproduced by permission of the Controller of Her Majesty's Stationery Office).

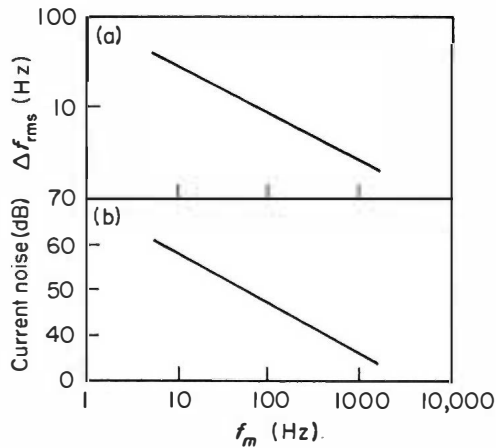


FIG. 8.4. Comparison of (a) f.m. noise and (b) current noise of a Gunn oscillator (A.S.M. 106CXY).  $\Delta f_{r.m.s.}$  is measured in unit bandwidth of  $f_m$  and the current noise power is expressed relative to the current shot noise power in a  $p-n$  junction carrying the same d.c. current.<sup>(4)</sup>



It is usually characterised by a noise power which decreases with an inverse low power of the frequency (often referred to as  $1/f$  noise). In addition to low frequency fluctuations introduced by the above correlation effects another mechanism may arise from flicker noise in Gunn diodes. The slow local electric field variations associated with the noise may cause the domain nucleating site to "jump" between various sites. The variation of domain transit time which would result would cause a frequency fluctuation.

If a flicker noise source is operative it is a reasonable hope that the f.m. noise power will be reduced as the material technology of GaAs is improved. Results indicating such a trend in the surface preparation have been obtained by Kuhn.<sup>(25)</sup> He found a considerable decrease of current noise and f.m. noise when the surface of the devices was etched. The improvement was reversed by treating the surface with  $H_2O_2$ . The ultimate material ideal is one where the total electron population suffers no appreciable fluctuations in total number due to recombination of electrons with donors, holes or impurities. The bandgap of GaAs is sufficient to ensure the second condition at room temperature and the material technology is required to satisfy the first and third conditions. When such a state of the material art is achieved the statistical fluctuations of electrons in ideal material are left as fundamental limitations.<sup>(4)</sup> These do not appear to have been achieved at the time of writing and are considered later.

Attempts have been made to correlate the low frequency current fluctuations through a device with the frequency fluctuations<sup>(3)</sup> in order to verify the presence of  $1/f$  current noise as the origin of the f.m. noise. A strong correlation was observed as illustrated in Figs. 8.4 and 8.5. It is possible that the current fluctuations are caused by the frequency fluctuations themselves and are simply a different manifestation of the f.m. noise. This possibility has been checked by frequency modulating a cavity controlled Gunn oscillator with a varactor and observing the resulting current fluctuations.<sup>(20)</sup> In general this current modulation effect is too small to account for the quantitative correlation of f.m. and current fluctuations, but in some cases may cause an appreciable perturbation of the observations. The coupling coefficient between frequency and current fluctuations is typically  $10^4$  MHz/A in a coaxial cavity with small stored r.f. energy but may be as small as  $10^2$  MHz/A in a waveguide cavity with a larger stored r.f. energy. Two coupling mechanisms have been proposed to explain the magnitude of this coefficient. Meade<sup>(26)</sup> suggested that carrier density fluctuations would cause both a current fluctuation and a frequency fluctuation. The latter arose from capacity variations of the dipole domain assumed to exist in the device as its width varied in sympathy with the carrier density. Good agreement was obtained between the experimental and theoretical results considering the simplicity of the model.

Hobson and Latham<sup>(27)</sup> examined the possibility that the current fluctuations would cause temperature fluctuations in the active region of the diode which would alter the frequency through its temperature dependence. This model should show considerable differences in the correlation of current and frequency fluctuations for modulation frequencies above and below the inverse of the thermal relaxation time of the diode. This is typically 200 microseconds<sup>(28)</sup> in a diode which is not "flip-chipped". The measurements showed that there was not a large difference of the coefficient for these two conditions and at most there was a 20% contribution from such effects. The diodes with the largest rate of change of frequency with temperature ( $df/dT$ ) were expected to show the largest differences in their low and high modulation frequency coefficients, but their spectral dependence was much more complex and not reproducible from diode to diode. It is now thought that the large  $df/dT$  is related to imperfect contact technology so that other "pathological" effects not considered may have been occurring in such diodes. The absence of a strong modulation frequency dependence of the coupling coefficient is consistent with Meades model and it would appear that space charge fluctuations are the responsible agency.

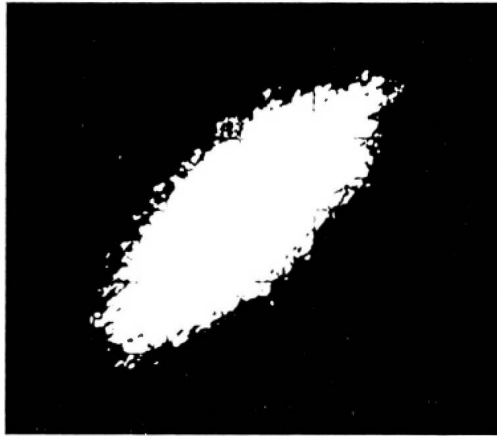


FIG. 8.5. Correlation of current noise and f.m. noise.<sup>(3)</sup> Voltages proportional to the instantaneous frequency and current are applied to the  $X$  and  $Y$  axes respectively of the oscilloscope.

An effect which may play an important part in the f.m. noise fluctuations is the decreasing ease with which a Gunn oscillator may be frequency modulated by external bias voltage variations as the modulation frequency increases<sup>(6)</sup> (Fig. 8.6). This frequency dependence appears to be linked to thermal relaxation effects, as mentioned in the previous paragraph. It was such

effects which suggested the thermal coupling mechanism. The effect of this frequency dependence is not clear but any spurious internal current or voltage fluctuations in a device may be excited most strongly at the low frequencies where thermal variations may occur. It should be pointed out that even though the frequency to current coupling coefficient is substantially frequency independent, both of the fluctuations show a reduction at the higher modulation frequencies.

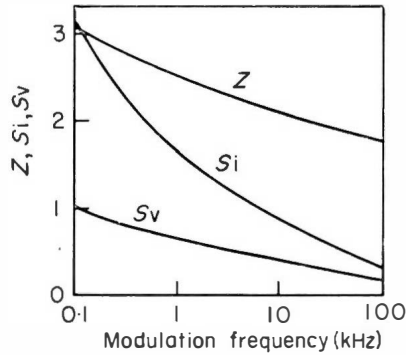


FIG. 8.6. Typical bias circuit modulation properties of a Gunn oscillator<sup>(6)</sup>

$$Z = \frac{\Delta V}{\Delta I} \text{ (k}\Omega\text{)}; \quad S_I = \frac{\Delta f}{\Delta I} \text{ (kHz}/\mu\text{A}\text{)}; \quad S_V = \frac{\Delta f}{\Delta V} \text{ (kHz/V)}$$

where  $\Delta V$ ,  $\Delta I$  and  $\Delta f$  are a change of bias voltage, bias current and frequency respectively.

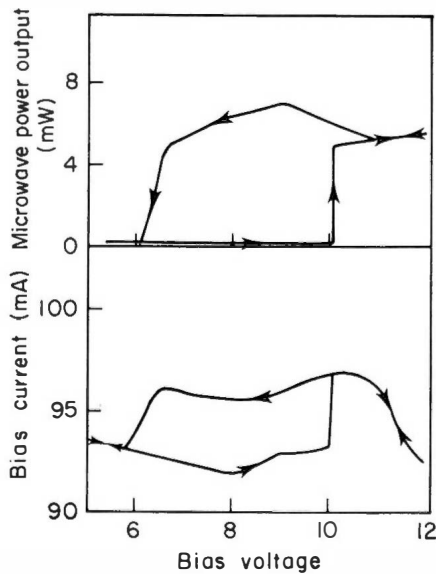


FIG. 8.7. Bias hysteresis of current and power output.<sup>(7)</sup>

If the noise source was predominantly a current fluctuation a low noise constant current bias supply may be expected to reduce the frequency fluctuations. Experiments with constant voltage and constant current bias supplies have given similar f.m. noise performance<sup>(7)</sup> so that the more convenient constant voltage supply is preferable.

Most measurements have been made with devices operating close to their optimum power output conditions. These are not necessarily the optimum conditions for low noise. Most cavity controlled Gunn oscillators exhibit a hysteresis in the relationship between power output and bias voltage (Fig.8.7) This is particularly so for full height waveguide cavities with a diode mounted on a post across the waveguide and the power output coupling adjusted to give near to maximum output power. In the region which is only achievable with decreasing bias voltage (this is an unstable region which requires care in cavity adjustment for its achievement) the f.m. noise output is often smaller<sup>(7,8)</sup> than that when the device is biased to give optimum power output at higher voltage. The power output is also lower but not substantially so. As can be seen in Fig. 8.8 the current noise through the device does change by a small amount during these adjustments but the predominant effect is a weakening of the ratio of f.m. noise output to device current noise. The reason for this improvement is obscure.

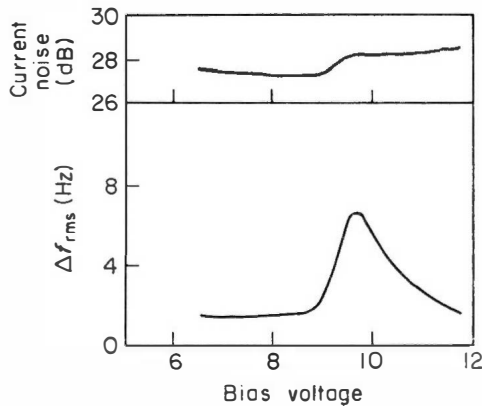


FIG. 8.8. Variation of f.m. noise and current noise as bias voltage is decreased for the diode used in the results of Fig. 8.7.

The cavity design also plays an important part in f.m. noise reduction because of the frequency control which it exerts upon the diode. The phase of the voltage and current waveforms generated by the device have a random fluctuation with respect to the device controlling waveforms associated with the r.f. energy stored in the cavity. This phase fluctuation arises from the

internal noise source (unspecified here) within the device. As a result of these phase fluctuations the phase of the cavity control waveform suffers a sequential random fluctuation as some energy is delivered to it by the device, and the equivalent amount is delivered to the load. These sequential phase deviations are small if the energy stored in the cavity is much greater than the energy delivered to the cavity during one cycle of oscillation.<sup>(4)</sup> Therefore the loaded  $Q$  factor of the cavity must be as large as possible for low noise

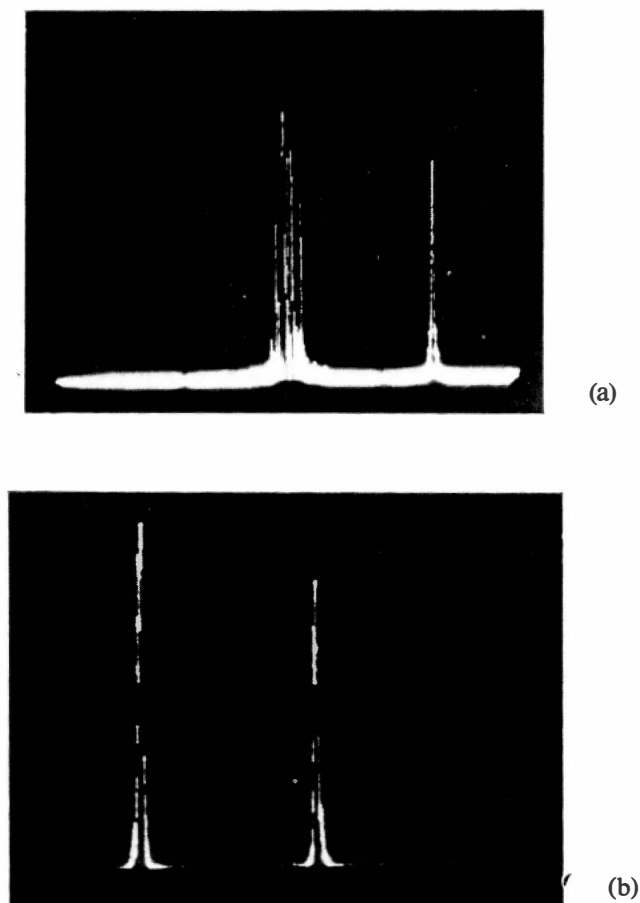


FIG. 8.9. (a) Output spectra of a coaxial miniature Gunn oscillator (in centre) and a CV2346 klystron (on right) displayed on a Hewlett Packard 851A/6551A spectrum analyser. The total width of the trace corresponds to 100 kHz.<sup>(22)</sup> (b) Similar comparison in waveguide circuit. (Crown Copyright, reproduced by permission of the Controller of Her Majesty's Stationery Office).

operation. It should be noted that a high  $Q$  alone is not sufficient to ensure low noise. The loaded  $Q$  factor is

$$Q_L = \frac{2\pi \times (\text{energy stored in cavity})}{(\text{total energy dissipation per cycle})}$$

and is ambiguous. It contains both the stored energy (which is the fluctuation smoother) and the energy dissipation. The latter is related to the operating conditions of the device and its instability mechanism. High stability will not necessarily be obtained if  $Q_L$  is made large by reducing the power dissipation without increasing the stored energy.

An alternative way to arrive at the same conclusion is from the rate of change of cavity susceptance with frequency,  $\partial B/\partial\omega$ . If  $\partial B/\partial\omega$  is large then a small impedance fluctuation by the oscillator diode is compensated for by a small change of frequency to maintain the resonance condition. For a simple cavity in which the susceptance is separately identifiable from loss (or generation) components the high  $Q_L$  condition is consistent with a large  $\partial B/\partial\omega$ .<sup>(21)</sup> For such a cavity  $Q_L$  is given by

$$Q_L = \frac{\omega_0}{G} \left( \frac{\partial B}{\partial \omega} \right)_{\omega = \omega_0} \quad (8.4)$$

where  $\omega_0$  is the oscillation frequency and  $G$  the equivalent loss conductance in parallel with the cavity susceptance  $B$ .

TABLE 8.1.

r.m.s. freq. deviation in Hz in a 70 Hz band 10 kHz away from the carrier.			
GUNN DIODE	$\lambda/2$ coaxial cavity	$\lambda/2$ waveguide cavity	$2\lambda$ waveguide cavity
1	70	6.3	1.6
2	70	6.3	2.5
3	70	7.1	—
4	70	1.4	4.5
5	70	1.6	5.0

This high- $Q$  design technique has been used to reduce the f.m. noise of an X-band Gunn oscillator to a level comparable with a good quality oscillator klystron.<sup>(9)</sup> The reduction of the r.m.s. frequency deviation for several diodes operating in different cavities is illustrated in Table 8.1. The half-wavelength coaxial cavity had the lowest loaded  $Q$ -factor. The half-wave-

length waveguide cavity had a larger  $Q$ -factor (or stored energy) because of the increase of characteristic impedance<sup>(9)</sup> as shown below. A further increase of stored energy occurred in the 2-wavelength waveguide cavity owing to the volume increase. The increase of stored energy with  $Z_0$  or lumped susceptive elements may be simply illustrated. If the cavity susceptance,  $B_L$ , is represented by a parallel  $L$ - $C$  circuit we have:

$$B_L = \omega C - \frac{1}{\omega L}.$$

This must resonate with the device susceptance,  $B$ . Then:

$$\frac{\partial B_L}{\partial \omega} = 2C + \frac{B}{\omega}$$

$B$  and  $\omega$  are constants for a particular frequency so that a large capacity is required for large  $\partial B_L/\partial \omega$  and high stability.

Another simple circuit realization is the short circuited transmission line where:

$$B_L = -\frac{1}{Z_0 \tan(\omega l/v)}$$

$l$  is the short circuited line length and  $v$  is the phase velocity of the electromagnetic waves on the line. In this case:

$$\frac{\partial B_L}{\partial \omega} = \frac{1}{Z_0 v} (1 + Z_0^2 B^2)$$

In a cavity where  $l$  is several half wavelengths so that its relative change with  $Z_0$  at constant frequency becomes small,  $\partial B_L/\partial \omega$  tends to infinity when  $Z_0$  equals zero or infinity and has a minimum when  $Z_0 = 1/B$ . An  $X$ -band C.W. device with substrate mounted on the heat sink has  $1/B \approx 50\Omega$ . In this case high stability is most conveniently achieved by working with large  $Z_0$ . The disadvantage of the high  $Q$  cavities is their poor electronic tunability (which requires low stored energy) and the mode jumping that occurs in multiple wavelength cavities. A coaxial cavity is usually used for electronic tuning applications and a multiple wavelength cavity for low noise applications such as Doppler radars. A comparison of a typical line width of a coaxial cavity oscillator is made with the linewidth of a good quality klystron in Fig. 8.9.<sup>(22)</sup>

If the large proportion of f.m. noise close to the carrier is caused by material defects it is possible that developments in materials and device technology will eventually reduce its magnitude. The ultimate limitation of the noise performance will be set by the finite number of electrons present in a

device. This fact is responsible for Johnson noise and shot noise in all devices. The ways in which the statistics of this finite number may limit the f.m. noise performance have been suggested. A simple model of the cavity control of Gunn oscillations is used to describe both mechanisms. The r.f. cavity voltage is supposed to trigger a domain (assumed to form instantaneously) when the device terminal voltage rises through threshold (see Chapter 5). In the delay mode of operation the domain travels at constant velocity until it enters the anode. The two noise limiting mechanisms arise from "jitter" in the domain triggering time<sup>(4)</sup> and velocity fluctuations of the domain.<sup>(10)</sup>

In the first mechanism electric field fluctuations at the domain nucleating region advance or retard the time at which the local electric field passes through threshold. The r.m.s. electric field fluctuation due to Johnson noise over a region 3 microns long in GaAs containing  $10^{15}$  electrons per  $\text{cm}^3$  and having a diameter of 30 microns is 15 V/cm. These dimensions have been estimated as those of the effective nucleating region for domain growth<sup>(11)</sup> in a uniform device. The number of electrons in the nucleating region is  $2 \times 10^6$ . For a device of given cross-sectional area the field fluctuation is scaled by the inverse square root of the ratio of the area of the device and of the area of the nucleating region. The time jitter of the domain nucleation is random in successive cycles so that the current waveform has a random (white noise) phase fluctuation, which, after filtering by the cavity as described earlier, appears as the f.m. noise output. It should have a  $\Delta f_{\text{r.m.s.}}$  which is independent of  $f_m$  except for a region very close to the carrier. The "turnover" frequency was estimated as  $133/Q$  Hz from the carrier frequency of  $10^{10}$  Hz.

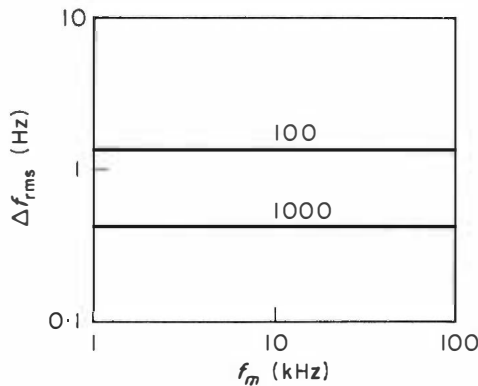


FIG. 8.10. Theoretical frequency deviation in 1 Hz bandwidth due to Johnson noise at the domain nucleating region in a sample with a cross-sectional area of  $10^{-8} \text{ m}^2$  in  $1\Omega \text{ cm}$  GaAs. The curve parameters are the cavity  $Q$ -factor.



The original calculation<sup>(4)</sup> overestimated the r.m.s. frequency deviation owing to neglect of some details of space charge growth in the device. Figure 8.10 illustrates the calculated frequency deviation.

The second fundamental limitation that has been proposed is in the domain transit time owing to fluctuations of domain velocity. These velocity fluctuations arise from fluctuations in the electronic velocity distribution function during successive scattering of the electrons by the lattice vibrations in the material. Owing to the short time between collisions of electrons and the crystal lattice ( $\sim 10^{-12}$  sec, see Chapter 3) the velocity fluctuations which result should also have an essentially white noise spectrum and give a frequency deviation,  $\Delta f_{\text{r.m.s.}}$ , which is independent of  $f_m$ . No numerical estimates of the f.m. noise are given.

Both of the above fundamental limitations are only simple semi-quantitative ideas. The operational details of C.W. oscillators at frequencies of 10 GHz and above cause a considerable complication of their effect. This arises largely through the comparable times of domain growth and transit through such devices. The only devices which might exhibit a behaviour close to that predicted would have large  $nl$  products and operate in lower frequency circuitry ( $\sim 1$  GHz). However C.W. operation has not been seen in such devices at the time of writing.

### 8.3 NOISE IN L.S.A. OSCILLATORS

The measurement of L.S.A. oscillator noise has received little attention owing to difficulty of construction of such devices. A noise to carrier power ratio of  $-134$  dBm has been measured in a 1 kHz bandwidth, 30 MHz from the carrier frequency of 50 GHz.<sup>(23)</sup>

One anticipated form of noise in an idealized L.S.A. oscillator<sup>(12)</sup> may arise from current fluctuations generated by fluctuations in the relative number of carriers in the satellite and central valleys of the conduction band structure of gallium arsenide. The effect again arises from the finite number of electrons in a device and the finite fluctuations in the number in any one state will always occur. Unfortunately no numerical estimates are given.

### 8.4 NOISE IN TRANSFERRED ELECTRON AMPLIFIERS

Subcritically doped negative resistance reflection amplifiers ( $nl \leq 10^{11}$ —see Chapter 6) have noise figures

$$\left( \text{noise figure is the ratio } \frac{\text{signal to noise ratio at output}}{\text{signal to noise ratio at input}} \right)$$

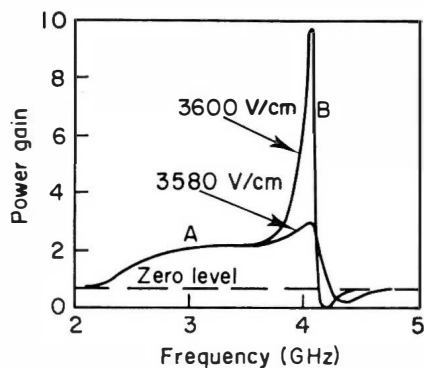


FIG. 8.11. Power gain versus frequency characteristic of a subcritically doped transferred electron amplifier.<sup>(13)</sup>

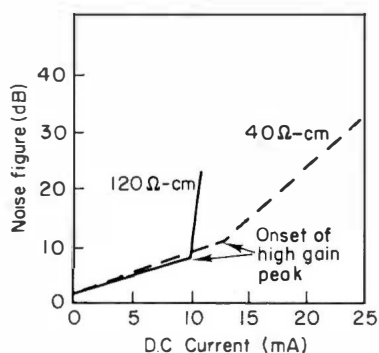


FIG. 8.12. Illustration of the rapid increase of noise figure at the onset of the gain peaking condition<sup>(13)</sup> in the amplifier of Fig. 8.11.

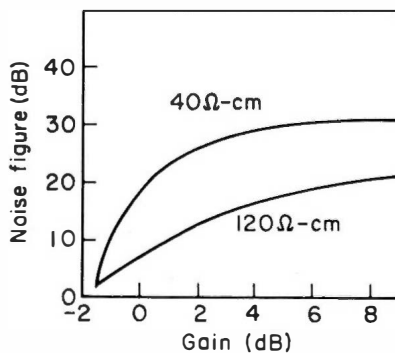


FIG. 8.13. Noise figure as a function of power gain for two devices made from GaAs with different resistivities.<sup>(13)</sup>

typically in the range 10 dB to 30 dB. This feature together with their low saturated power output does not offer much promise for their useful exploitation. As a result only a limited investigation of their noise properties has been conducted so that an empirical description is all that is possible.

The noise figure generally increases with increasing bias voltage and current (they are monotonically related in the subcritical amplifier) and also depends on the frequency of operation.<sup>(13,14)</sup> The gain characteristics have a region where the gain is low but substantially independent of frequency and a high gain region with peaks at one frequency. These regions are indicated as *A* and *B* respectively in Fig. 8.11. In region *B* the noise figure variation with bias is illustrated in Fig. 8.12. The noise figure increases steadily with bias until the high gain region is achieved. The noise figure then deteriorates rapidly with increasing bias and gain. The relationship of noise figure to power gain is illustrated in 8.13 where there is an apparently better noise performance in the higher resistivity sample. The dependence of these results on the characteristic impedance on the transmission line environment of the devices is not clear.

There does not appear to be much published work which attempts to relate the theory and experiment of these poor noise figures. The theoretical approach to the noise figure calculation is complicated by the correlation of noise signals in different regions of the amplifying device. This correlation is caused by the growth of noise signals as they propagate in the direction from cathode to anode. One method of solution<sup>(15)</sup> relates the local noise fluctuations to the local diffusion constant and treats the correlation of different regions through an "impedance field" concept. This latter quantity is the frequency and spatially dependent gradient of the diode impedance. The power spectral density of the open circuit noise voltage fluctuations,  $S(\omega)$  is given by:

$$S(\omega) = \int_{\text{VOLUME}} |\nabla Z|^2 \cdot 4e^2 Dn \cdot d(\text{VOLUME}). \quad (8.4)$$

$\nabla Z$  is the impedance field,  $D$  the local diffusion constant and  $n$  the local carrier concentration. Thim<sup>(30)</sup> has shown that the best noise figures would be obtained if the electric field was uniform throughout the device. In order to achieve such a condition it would be necessary for the cathode contact to be a low height Schottky barrier so that the electric field may rise to its uniform value in a very short distance to avoid non-uniformities. A minimum noise figure of 8 dB was estimated for GaAs devices.

The noise properties of two-port sub-critically doped amplifiers<sup>(16)</sup> are not clear at the time of writing but may be expected to be similar to those of the reflection amplifiers described above<sup>(17)</sup>. Amplifiers based on oscillating

Gunn devices<sup>(18)</sup> have only recieved limited attention. Typical noise figures are poor being of the order of 20 dB.

### 8.5 OTHER FLUCTUATION PHENOMENA

All the devices described in other Chapters have their properties modified by inhomogeneous material properties. In the ideal devices there will still be a limiting form of inhomogeneity owing to fluctuations in the finite electron population. This form of fluctuation appears as a random time variation of electron density and electric field about their mean values and is the source of Johnson noise in resistors. One possible device limitation due to these statistical properties has been described with the f.m. noise properties of Gunn oscillators. Additional limitations include the allowable space charge growth in L.S.A. oscillators and the maximum gain of Gunn effect pulse regenerators.<sup>(11)</sup> In the former case the dynamic electron density fluctuations and static donor density fluctuations will form the smallest possible space charge density from which growth will occur and so set limitations on the r.f. voltage in order to maintain space charge neutrality. The maximum gain of Gunn effect pulse regenerators is limited by the minimum difference between the bias and threshold voltages that can be used without the generation of random pulses. This difference is set by the electric field fluctuations at the domain nucleating region which may cause the local electric field to exceed the threshold for domain nucleation. At the time of writing this mechanism was the only one capable of direct experimental observation. A good correlation of the theoretical and experimental variation of the random domain triggering probability with bias voltage was obtained, but it was only possible to make measurements with a limited range of device parameters.<sup>(19)</sup>

### REFERENCES

1. Draysey, D. W., Court, W. P. N. and Bott, I. B. (1966). *Electron. Lett.* **2**, 125–126. and private communication.
2. Josenhans, J. (1966). *Proc. I.E.E.E.* **54**, 1478.
3. Faulkner, E. A. and Meade, M. L. (1968). *Electron. Lett.* **4**, 226.
4. Hobson, G. S. (1967). *Electron. Lett.* **3**, 63–64 and corrections in ref. 11.
5. Bell, D. A. (1960). "Electrical Noise". van Nostrand, New York.
6. Faulkner, E. A. and Meade, M. L., (1969). *Electron. Lett.* **5**, 217–218.
7. Meade, M. L. (1968). "Conference on physical aspects of noise in electronic devices". Proc. IPPS, Nottingham, pp. 217–218.
8. Court, W. P. N. private communication.
9. Court, W. P. N., Herman, P., Hilsum, C., Holliday, H. R. and Warner, F. L. (1967). *Electron. Lett.* **3**, 567.
10. Matsuno, K. (1968). *Proc. I.E.E.E.* **56**, 108–109.
11. Hobson, G. S. (1969). *Brit. Journ. App. Phys.* **2**, 1203–12.

12. Matsuno, K. (1968). *Proc. I.E.E.E.* **56**, 75-77.
13. Thim, H. W. and Barber, M. R. (1966). *I.E.E.E. Trans. on Electron Devices* **ED-13**, 110-114.
14. Hakki, B. W. (1967). *Journal of App. Phys.* **38**, 808-818.
15. Shockley, W., Copeland, J. A. and James, R. P. (1966). "Quantum Theory of Atoms, Molecules and the Solid State". (Editor P. O. Lowdin) Academic Press, New York, pp. 537-563.
16. Robson, P. N., Kino, G. S. and Fay, B. (1967). *I.E.E.E. Trans. on Electron Devices* **ED-14**, 612-615.
17. Kozdon, P. and Robson, P. N. (1970). "Proc. MOGA 70", pp. 16-17, Kluwer-Deventer, Amsterdam.
18. Thim, H. W. (1967). *I.E.E.E. Trans. on Electron Devices* **ED-14**, 517-522.
19. Hobson, G. S. and Izadpanah, S. H. (1970). *Solid State Electronics* **13**, 937-942.
20. Hobson, G. S. (1970). *Electron. Lett.* **6**, 118-9.
21. Montgomery, C. S., Dicke, R. H., and Purcell, E. M. (1948). "Principles of Microwave Circuits". McGraw-Hill, New York. p. 130.
22. Warner, F. L. and Herman, P. (1967). "Proc. 1st. Cornell biennial conference on engineering applications of electronic phenomena". Cornell University, New York. pp. 206-217.
23. Spiwak, R. R. (1968). *I.E.E.E. Trans. on Electron Devices* **ED-15**, 614-5.
24. Wilson, K. (1969). *Mullard Technical Communications* **10**, 286-293.
25. Kuhn, P. (1970). *Electron. Lett.* **6**, 845-7.
26. Meade, M. L. (1971). *Radio and Electronic Engineer* **41**, 126-132.
27. Hobson, G. S. and Latham, C. B. (1971). "Proc. Conf. on Noise in Active Semiconductor Devices, Toulouse".
28. De Sa, B. A. E. and Hobson, G. S. (1971). *I.E.E.E. Trans. on Electron Devices*.
29. Goldwasser, R. E., Berenz, J., Lee, C. A. and Dalman, G. C. (1970). "Proc. MOGA 70", pp. 12-19, Kluwer-Deventer, Amsterdam.
30. Thim, H. W. (1971). *Electron. Lett.* **7**, 106-108.

## Chapter 9

# Non-Uniform Devices and Logic Applications

### 9.1 INTRODUCTION

The effects of spatial non-uniformities and external circuitry on Gunn effect devices containing a travelling domain offer exciting prospects in the development of electronics. They have potential importance in signal processing for data transmission and logic applications. An understanding of these effects is necessary to appreciate possible defects or ways of improvement of the oscillators described in the previous chapters. The following descriptions may give the impression that little work is proceeding in the latter case. This only appears to be so because of the intimate involvement of advanced oscillator development with the planar technology of gallium arsenide, whereas many of the logic devices are little more than interesting first ideas. The realization of devices with planar technology is advantageous for thermal efficiency and for close matching of multiple devices (in series-parallel arrays for example). It will sometimes require non-uniform geometry for practical reasons so that understanding of the following effects is necessary.

Initially, descriptions will be given of devices with a good "pedigree". These fall into three broad groups: domain current control, the influence of non-uniform electric fields on domain nucleation and quenching and modifications introduced externally. Many devices utilize a combination of these properties and they will be described finally.

### 9.2 DOMAIN CURRENT CONTROL

Current controlled operation occurs when a mature domain travels from cathode to anode of a non-uniform device. A simple quantitative description is possible when the non-uniformities are gradual compared with the domain width. In a uniform device there is a relationship between the sub-threshold electric field,  $E_R$ , outside the domain and the excess domain voltage,  $\phi_D$  ( $\phi_D = \int_{-\infty}^{+\infty} (E - E_R) dx$ ) of the form shown in Fig. 9.1 (see Chapter 4). The current-voltage characteristic of a uniform device containing a stable

travelling domain may be calculated from this relationship. For a device with large  $nl$  product the current is substantially independent of voltage (if this is greater than threshold (Fig. 9.2)) because of the weak dependence of  $\phi_D$  on  $E_R$  when the former is large. For the gradual variations of uniformity envisaged in this section the uniform device dynamics may be taken as a good description for the relationship of excess domain voltage, and the electric field (for convenience referred to as  $E_u$ ) immediately outside the domain. The electric field in other ohmic parts of the device will be related to  $E_u$  by current continuity. The value of  $\phi_D$  at any position is determined from the simultaneous satisfaction of the relationship between  $\phi_D$  and  $E_u$  and from the integral of electric field through the device which must equal the biasing voltage. For devices with large  $nl$  product the variation of  $\phi_D$  as the domain propagates does not appreciably alter  $E_u$ . The current through the device is then

$$i = n(x) e \cdot \mu E_u \cdot A(x) \quad (9.1)$$

$n(x)$  is the local electron density,  $A(x)$  the device cross-sectional area and

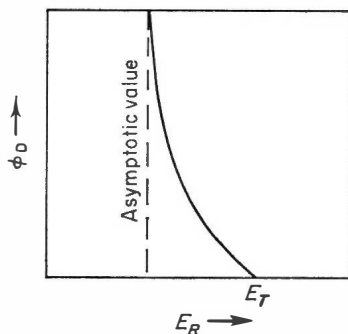


FIG. 9.1. Relationship of excess domain voltage,  $\phi_D$ , and electric field outside domain,  $E_R$ , for a stable uniform Gunn oscillator.

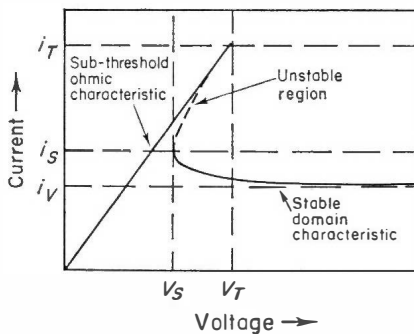


FIG. 9.2. Current-voltage characteristic of a long uniform Gunn effect device.

$\mu E_u$  in GaAs is equal to the valley velocity  $v_v$  as the device length tends to infinity.  $v_v$  is a constant of the material so that the current waveform of the device for a domain in flight is a representation of the product  $n(x) \cdot A(x)$  (also proportional to the low field resistance per unit length of the device) at the domain position.

This simple quasi-static treatment of the domain dynamics in a non-uniform medium is complicated by various effects. If the device is sufficiently short the variations of  $\phi_D$  also produce variations of  $E_u$  (see Chapter 4). The current waveform is appreciably dependent on this additional factor when  $\phi_D \leq 10$  V for  $1\Omega$  cm material. Gradual variations of uniformity on a scale comparable with the domain length will require  $E_u$  to be different on each side of the domain. It has been suggested that a modified quasi-static domain dynamics<sup>(1)</sup> may apply in this situation by taking account of the variation of current density across the domain width so that a balance between the field driven and diffusion currents is maintained. In more extreme non-uniformities the only satisfactory approach is to solve the partial differential equations of the domain dynamics in the non-uniform medium. Variations of cross-sectional area require a knowledge of the lateral spreading rate of the domains. No details of any of these modifications are available at the time of writing but some of the attractiveness of simple devices using domain current control disappears when the simple description given above is incorrect. In these more complex cases there may be an appreciable contribution to the external current waveform from the displacement current required for charging and discharging of the domain.<sup>(18)</sup> A limitation on the amplitude of the current fluctuations will be set by the effects of domain quenching and nucleation when appropriate local electric fields are reached. These effects will be discussed in the next section.

Various techniques may be employed to introduce the non-uniformity into the device.<sup>(3)</sup> Permanent profiles may be built in by introduction of suitable donor impurities or by modification of the cross-sectional area of the device. Controlled variations of non-uniformity may be introduced by selective illumination, localized impact ionization and alteration of field profiles in the device by external electrodes.

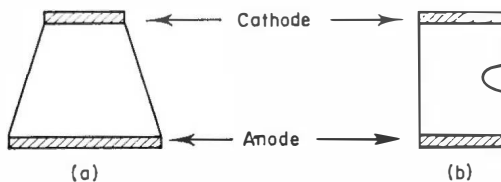


FIG. 9.3. Non-uniform samples used by Shoji<sup>(2)</sup> to demonstrate current waveform generation. The electron density is nominally uniform.



Examples of the waveforms that may be produced by domain current control are given in Figs 9.4 and 9.5. Those of Fig. 9.4<sup>(2)</sup> were produced with the laterally non-uniform devices of Fig. 9.3 when they were biased above threshold.

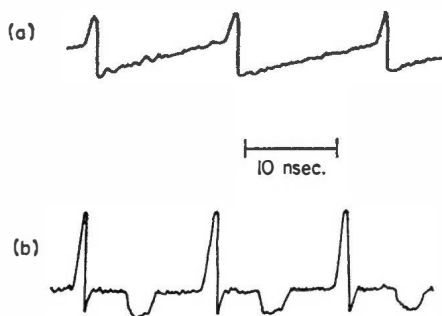


FIG. 9.4. Waveforms obtained with the samples of Figs. 9.3a and b respectively.

A device with memory properties<sup>(3, 4, 5)</sup> derived from spatial electron density variations produced the waveform of Fig. 9.5 by using the impact ionization that is induced by high domain electric fields. During the first domain transit after application of bias the waveform of Fig 9.5a. was superimposed on the steady bias voltage. The additional voltage was sufficient to cause impact ionization from trapping centres in the material to give an additional local concentration which was monotonically related to the "writing" voltage. In subsequent domain transits the pattern was reproduced in the current waveform (Fig. 9.5b) owing to the persistence of the ionized carriers caused by the long trapping time. Storage times of  $1 \mu\text{sec.}$  have been reported.<sup>(7)</sup>

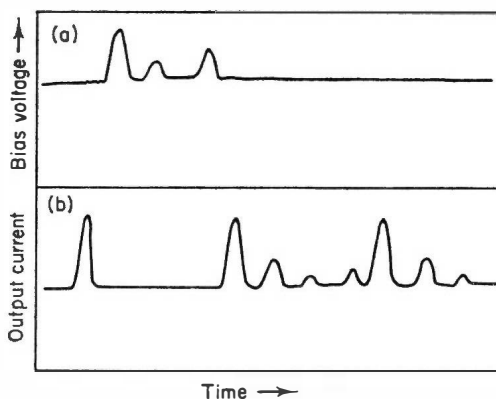


FIG. 9.5. (a) Avalanche memory<sup>(3)</sup> write in voltage, superimposed on steady bias and (b) subsequent current waveform.

In all these experiments the domain velocity is close to  $10^7$  cm/sec. The profiles usable for clear reproduction in the current waveform do not appear to alter the domain velocity.<sup>(6)</sup>

### 9.3 THE INFLUENCE OF NON-UNIFORM ELECTRIC FIELDS ON DOMAIN NUCLEATION AND QUENCHING

The current waveforms caused by domain current control are repeated at the regular intervals of the domain transit time. If the non-uniformity is large enough it is possible to control the time and position of domain nucleation and quenching. Using the quasi-stable assumptions of the previous section, domain nucleation will occur when the local electric field exceeds threshold and quenching will occur when the domain runs into a region where it is not possible to satisfy the relationship of  $\phi_D$  and  $E_u$  that is demanded by the stable domain dynamics. The quenching conditions may be calculated in a way similar to that for uniform devices.

At any point in a non-uniform device containing a domain the electric field,  $E(x)$ , is related to the electron density,  $n(x)$ , and cross-sectional area,  $A(x)$ , by:

$$E(x) = E_u \left\{ \frac{n_u A_u}{n(x) \cdot A(x)} \right\}. \quad (9.2)$$

The subscript  $u$  refers to the domain position and there is an implicit assumption that the electron mobility below threshold is constant. The total voltage,  $V$ , across the device of length  $l$  is:

$$V = \phi_D + E_u \cdot n_u A_u \int_0^l \frac{dx}{n(x) \cdot A(x)}. \quad (9.3)$$

The integral is independent of field and can be evaluated once the device profile is known. Equation (9.3) is the relationship between  $\phi_D$  and  $E_u$  that is dictated by the device boundary conditions. It varies with domain position in the device through the terms  $n_u$  and  $A_u$ . The other relationship between  $\phi_D$  and  $E_u$  that must be simultaneously satisfied is dictated by the domain dynamics illustrated in Fig. 9.1. This is substantially independent of domain position and uniformity. The position of domain quenching is found by drawing a straight (load) line from  $\phi_D = V, E_2 = 0$ , tangential to the  $\phi_D - E_R$  curve. The slope of this line enables  $n_u A_u$  and the point of quenching to be found. This construction is illustrated in Fig. 9.6 together with other load lines for different domain positions (i.e. different values of  $n_u A_u$ ).

In operation involving quenching, the current waveform of the device is not as closely related to the doping and cross-sectional profile as it was

in the devices of the previous section. This occurs because  $E_u$  has a stronger dependence on  $\phi_D$  as the quenching point is reached. The larger non-uniformity will also cause a larger contribution from domain discharging currents.

As the bias voltage is increased, the tangent to the  $\phi_D$ - $E_R$  curve (Fig. 9.6) which passes through  $\phi_D = V$ ,  $E_R = 0$  becomes steeper so that a domain will be quenched at a point with a greater  $n(x) \cdot A(x)$  product. This effect has been used to provide frequency tunability in wedge shaped devices<sup>(2)</sup> and in annular devices.<sup>(1,7,8)</sup>

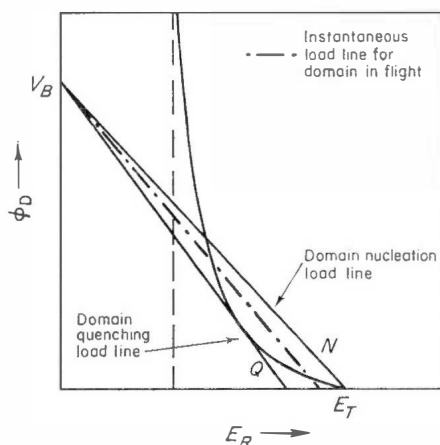


FIG. 9.6. Time varying load lines in a non-uniform device showing the domain nucleation load line  $N$ , and the quenching load line  $Q$ .

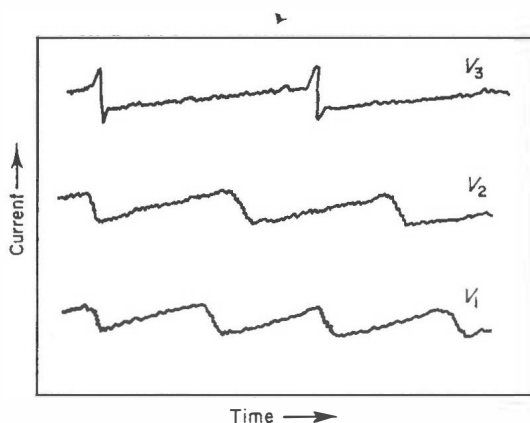


FIG. 9.7. Waveform of gradual taper giving tunability to the spiky waveform characteristic of a domain travelling to the anode<sup>(2)</sup>. Bias voltages are  $V_1 < V_2 < V_3$ .

If the non-uniformity of the sample shown in Fig. 9.3a is sufficient then a voltage tunability of about one octave is possible.<sup>(2)</sup> The current spike which occurs when a domain runs into the anode of a device does not occur in this type of operation and a smoother output waveform occurs (Figs 9.7 and 9.8). For domain nucleation at the cathode and quenching of domains in the bulk of the device it is necessary that the extreme values of  $n(x) \cdot A(x)$  within the device and the bias voltage give load lines which overlap the range from  $Q$  to  $N$  in Fig. 9.6. This mode of tunability can be extended to include voltage controlled frequency switching with a device illustrated in Fig. 9.9a. At the lower voltages the propagating domain is quenched before it reaches the largest  $nA$  product near the centre of the device. When the voltage is sufficiently high quenching does not occur in the first half of the sample, so the domain travels to the anode, with a consequent reduction of frequency (Fig. 9.9b).

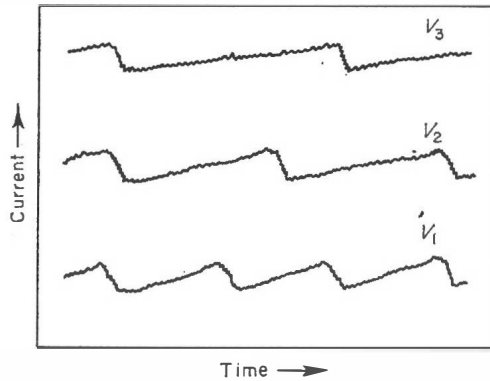


FIG. 9.8. Sawtooth waveform of a steeply tapered oscillator. The domain cannot reach the anode<sup>(2)</sup>. Bias voltages are  $V_1 < V_2 < V_3$ .

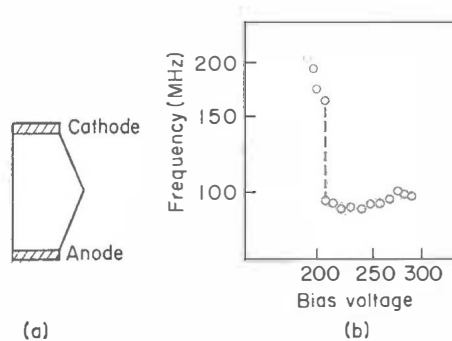


FIG. 9.9. (a) Double tapered device which causes the continuous, followed by switched, voltage tunability<sup>(2)</sup> shown in (b).

The samples in the above experiments were made with a tapered cross-section. The same results would be achieved with a tapered doping profile and these effects should be relevant to the performance of the supposedly uniform oscillators, described in previous chapters, if the starting material is non-uniform. Bulk grown GaAs has a large number of traps from which electrons can be thermally excited. This property has been used to generate an electron concentration gradient with a thermal gradient in an otherwise uniform device.<sup>(9)</sup> Similar tunability to the tapered oscillators was obtained. These results indicate the care that is necessary in the design of uniform C.W. oscillators.

Similar tunability occurs in annular devices with the centre contact as the cathode. The domain is expected to propagate as an expanding ring until it is quenched (at the lower operating voltages) or runs into the anode. A tuning range in resistive circuitry from 1.6 GHz to 5.45 GHz has been observed.<sup>(8)</sup>

Electric field non-uniformities caused by suitable contact configurations may be used to control domain nucleation as well as extinction. Two devices employing dual cathode structures<sup>(10,11)</sup> will be described as examples of this technique.

A dual cathode comparator<sup>(10)</sup> may be constructed with two small area cathodes ( $\sim 70$  microns diameter) which are separated by a distance approximately equal to their diameter (see Fig. 9.10a). The anode has a much larger area. If a bias voltage is applied between an anode and one cathode (with the other cathode floating, Fig. (9.10a)) a domain is nucleated when the electric field at the cathode exceeds the threshold field for domain nucleation. Just before domain nucleation the electric field elsewhere in the device will be below threshold because of the device non-uniformity. If the second cathode is also connected to the bias the threshold voltage for domain nucleation will be increased owing to the reduced non-uniformity of the electric field (Fig. 9.10b).<sup>(13,17)</sup> The device may be used as a comparator for two voltages whose values lie between the two threshold voltages. A

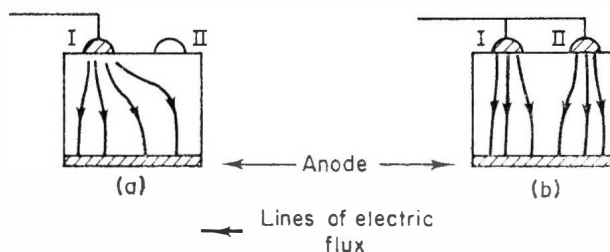


FIG. 9.10. Dual cathode comparator showing electrical non-uniformity below threshold (a) one cathode biased (b) both cathodes biased.

domain is nucleated only when one voltage is applied to either cathode. The comparator operation is summarized in the binary truth Table 9.1 where the output is the domain pulses arising from domain nucleation.

TABLE 9.1. Truth table of "exclusive or" (comparator)

Input 1	Input 2	Output
0	0	0
1	0	1
0	1	1
1	1	0

Control of the transit frequency of uniform devices with a large  $nl$  product may be achieved by splitting the cathode into two equal parts.<sup>(11)</sup> A control voltage was applied to one segment of the cathode while the other was biased normally. Frequency tunability of 15–25% was achieved with a d.c. voltage to alter the relative voltages of the cathodes. The origin of this effect is not clear but is presumably related to an alteration of the electric field pattern in the vicinity of the cathodes. When the control voltage was a C.W. r.f. signal operating close to the free running device transit frequency, frequency locking was possible. 20 dB locking gain was achieved over the frequency range from 348–360 MHz.

In order to complete this section it is necessary to mention wedge shaped devices having a laterally varying cathode-anode separation.<sup>(8)</sup> Unfortunately the properties of these devices are not clear owing to difficulties with the planar technology.

#### 9.4 EXTERNAL CONTROL OF UNIFORM DEVICES

A large variety of effects may be obtained with a simple uniform device with an  $nl$  product sufficiently large to allow stable domain propagation. One type of control is exercised by the external voltage and the other by suitable placing of external circuit components.

Series<sup>(14)</sup> and parallel<sup>(15)</sup> pulse regenerators and reshapers (Fig. 9.11) are biased just below threshold. A small additional pulse will cause the device voltage momentarily to exceed threshold and trigger a domain.<sup>(12)</sup> The fall of device current which results lasts for one domain transit time and can be much larger than the triggering pulse (Fig. 9.12). In each type of regenerator the current change also occurs in  $R_L$  and so the output appears as the corresponding voltage pulse. The smallest input pulse to produce

reliable domain triggering is limited by the minimum difference between biasing and threshold voltages,  $\Delta V_n$ , before unwanted domain triggering occurs. One possible noise source to limit this gain is discussed in Chapter 8. The maximum pulse gain is limited by this effect and the maximum possible value of  $R_L$ . If  $R_D$  is the device low field resistance and the parallel loading of the bias circuit in Fig. 9.11a is negligible the minimum input voltage to cause reliable domain triggering in the series regenerator is  $\Delta V_n(R_D + R_L)/R_D$  and for the parallel regenerator is  $\Delta V_n$ . In both cases the output voltage is  $R_L \cdot I_v$  if there is a 50% current drop after domain triggering ( $I_v$  is the valley current).

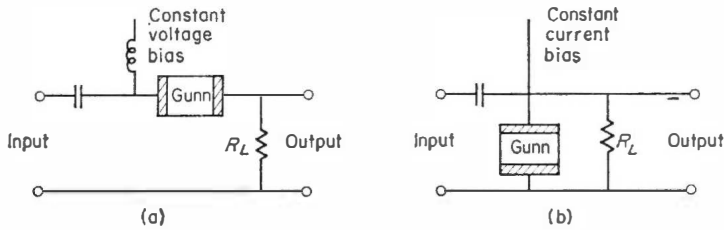


FIG. 9.11. (a) series regenerator (b) parallel regenerator.

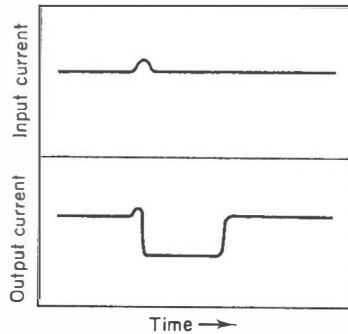


FIG. 9.12. Current waveforms of pulse regenerator.

The maximum gain for both configurations occurs as  $R_L \rightarrow \infty$  and is:

$$\frac{I_v R_D}{\Delta V_n} \left( = \frac{V_T}{2\Delta V_n} \right) \quad \text{for the series regenerator}$$

$\infty$  for the parallel regenerator.

The advantage of high gain in the parallel regenerator is offset by the disadvantage of poor isolation between stages because input and output terminals are common. There are limitations on  $R_L$  due to practical considerations and due to the slow response time that accompanies large  $R_L$ .

(see Section 9.5), which restrict the above gain figures. Detailed practical information on the operation of these devices is not available at the time of writing but a voltage gain of approximately 100 has been reported for each type. The use of regenerators in a memory loop and variable repetition rate pulse generator will be described later.

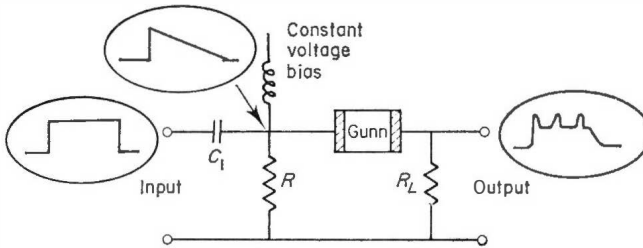


FIG. 9.13. Simple analogue to digital convertor showing waveforms (circled) at input, intermediate and output points.

Izadpanah<sup>(14)</sup> achieved analogue to digital conversion with a triangular bias pulse in the circuit of Fig. 9.13. The analogue signal is the pulse input (or step function) and is differentiated to give a step followed by an exponential decay superimposed on the steady bias voltage,  $V_B$ . The amplitude of the initial step for a fixed differentiator time constant determined the time that the bias was greater than threshold and the number of domain pulses that occurred at the output. The effect is illustrated in Fig. 9.14. An improved version has been proposed to process a continuously varying analogue voltage and will be described later.

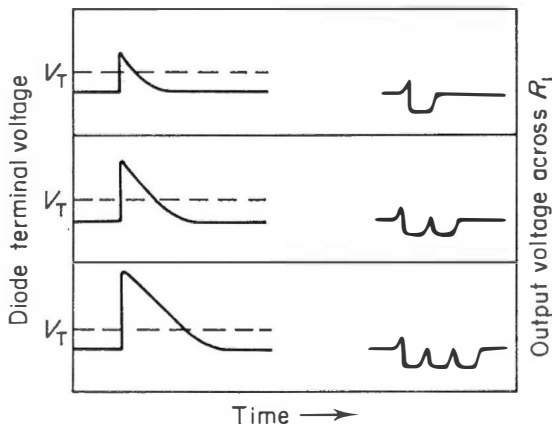


FIG. 9.14. Input and output waveforms of analogue to digital convertor for various input pulse amplitudes.



The second half of the section is concerned with the effect of external circuit components on the device operation. The effect of a series inductance and the coupling introduced by suitably placed resistors will be separately dealt with.

The first mechanism is the basis of a relaxation oscillator operating with a considerably longer period than the domain transit time.<sup>(15)</sup> In the circuit of Fig. 9.15 the diode is considered as a pure resistance,  $R_D$ , when its terminal voltage is below threshold and it does not contain a domain. Above threshold the diode acts as a constant current source,  $I_v$ .  $V_B$  is greater than the threshold voltage. Let us assume that the diode does not contain a domain. Its terminal voltage is less than the threshold voltage and must be increasing exponentially with the  $L(1/R_D + 1/R_L)$  time constant. The current and voltage waveforms through and across the device are illustrated in Fig. 9.16. When the terminal voltage reaches threshold the current drops to  $I_v$  (about half its threshold value). The terminal voltage rises rapidly to greater than  $V_B$  so that  $R_L$

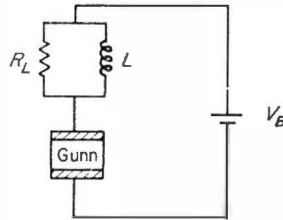


FIG. 9.15. Relaxation oscillator using series inductance.<sup>(15)</sup>

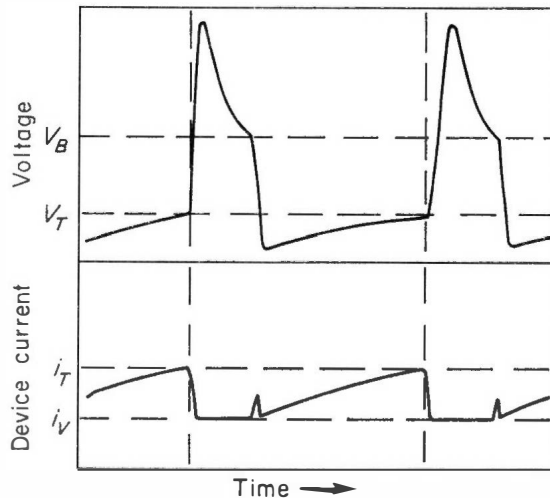


FIG. 9.16. Waveforms of relaxation oscillator.<sup>(15)</sup>

carries a current from the inductor equal to the current fall as the device switched. The device voltage now falls exponentially with time constant  $L/R_L$  as the current through  $L$  decreases until the device terminal voltage is  $V_B$ . When the domain enters the anode the device current begins to rise, the inductance causes the terminal voltage to fall and the process repeats as the current begins to build up with the device as it's low field resistance. A 100 micron diode with  $R_D = 20\Omega$ ,  $R_L = 200\Omega$ , and  $L = 10^{-6}\text{H}$  has produced 40 V pulses with a 100 MHz repetition rate.

The operation described in the last paragraph is a form of delayed domain nucleation mode of relaxation oscillation. In shorter devices where the capacity of a domain, in parallel with the current generator, becomes an important part of the circuit a quenched domain relaxation mode may occur. The difference in this mode is that the upward voltage swing caused by domain nucleation reaches a peak and then falls rapidly as half a cycle of "ringing" of the inductance and capacity occurs. This downswing can pass below the quenching voltage, quench the domain and leave the device current to build up with the low voltage time constant as before. This mode of operation is similar to one mode of operation of overlength devices described in Chapter 6.<sup>(16,29)</sup>

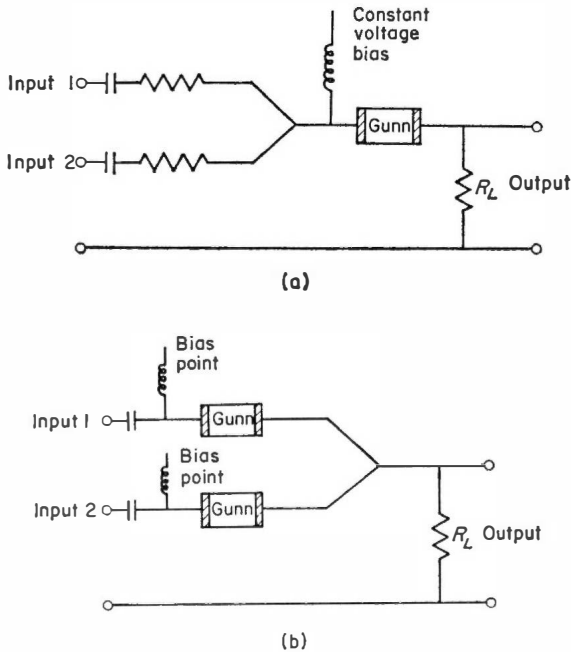


FIG. 9.17. (a) 'and' gate using a uniform diode. (b) exclusive 'or' (comparator) using uniform diodes.

Two combinations of resistors and uniform Gunn devices are illustrated in Fig. 9.17. In the circuit of 9.17a the voltage required at either input 1 or input 2 to cause domain nucleation is greater than the voltage required if inputs 1 and 2 are shorted together. This circuit is the basis of an 'and' gate<sup>(17)</sup> for two pulses whose amplitudes lie between the two critical values. The binary truth table for operation under those conditions is given in Table 9.2. Output only occurs for simultaneous application of the input voltages.

TABLE 9.2. Truth table of "and" gate.

Input 1	Input 2	Output
0	0	0
1	0	0
0	1	0
1	1	1

In the circuit of Fig. 9.17b the input voltage at either input that is required to cause domain nucleation is less than the common voltage required simultaneously at each input to cause nucleation.<sup>(13)</sup> This arises from the larger voltage drop across  $R_L$  when both diodes conduct in the latter case. The operation is that of an exclusive "or" or comparator circuit. As in the previous circuits both input voltages have to lie within prescribed limits. The binary truth table of this circuit is given in Table 9.1.

## 9.5 DOMAIN TRANSIENT RESPONSE

The response time of a domain to electric field alterations is important in estimating the maximum signal processing rate of logic devices and the current waveform resulting from bulk non-uniformities of limited extent. Very little work has been performed at the time of writing and a somewhat tentative semi-quantative account is all that is possible.

If a step function voltage is applied to a device to bias it into the negative differential conductivity region of the velocity-field characteristic the electric field distribution will initially readjust with the negative dielectric relaxation time constant at the bias point. This is a small signal process and will be considerably modified by the large signal non-linearities which occur as stable domain conditions are approached. One estimate of the relaxation time constant under large signal conditions is given by the product of low field device resistance,  $R_0$ , (essentially the device resistance outside the domain) and the domain capacity<sup>(18)</sup> (see Chapter 4). The domain capacity

is the ratio of accumulated or depleted charge,  $Q_D$ , to the domain potential,  $\phi_D$ . In the limit of zero diffusion this is:

$$\frac{Q_D}{\phi_D} = C_D = \frac{2\epsilon\epsilon_0}{d} A \quad (9.4)$$

and the differential capacity is:

$$\frac{\partial Q_D}{\partial \phi_D} = C_D' = \frac{\epsilon\epsilon_0}{d} A \quad (9.5)$$

$d$  is the domain width and  $A$  the cross-sectional area. Adopting (9.4), the relaxation time constant,  $T_R$ , is:

$$T_R = R_D C_D = \frac{l}{N_D e \mu} \cdot \frac{2\epsilon\epsilon_0}{d} \quad (9.6)$$

where  $l$  is the sample length and  $N_D$  the donor density (assumed uniform here). For a triangular domain:

$$\phi_D = \frac{N_D e d^2}{2\epsilon\epsilon_0} \quad (9.7)$$

and the device boundary conditions dictate that

$$\phi_D = (E_B - E_u)l \quad (9.8)$$

where  $E_B$  is the mean bias field. Eliminating  $\phi_D$  and  $d$  from Eqns (9.6), (9.7), and (9.8):

$$\begin{aligned} T_R &= \left\{ \frac{\epsilon\epsilon_0}{N_D e \mu} \left( \frac{E_B}{E_u} - 1 \right)^{-2} \frac{1}{E_R \mu} \right\}^{\frac{1}{2}} \\ &= \left\{ T_p \cdot T_D \left( \frac{E_B}{E_u} - 1 \right)^{-2} \right\}^{\frac{1}{2}} \end{aligned} \quad (9.9)$$

where  $T_p$  is the low field dielectric relaxation time and  $T_D$  is the domain transit time.

For a bias voltage 1.5 times threshold and  $E_u = 0.5$  times threshold:

$$T_R = \sqrt{T_p \cdot T_D} \quad (9.10)$$

For a 1 mm long device with  $10^{15}$  carriers/cm<sup>3</sup> ( $T_p = 10^{-12}$  sec),  $T_R \approx 100$  picoseconds.

At threshold,  $T_R$  is also the shortest possible time that an electron can drift across the domain.<sup>(30)</sup>  $\phi_D$  and  $l$  can be eliminated from Eqn (9.6),

(9.7), (9.8) to give:

$$T_R = \frac{d}{E_u \mu} \left( \frac{E_B}{E_u} - 1 \right)^{-1}. \quad (9.11)$$

The first group of terms on the right-hand side of Eqn (9.11) is the minimum possible time for an electron to cross the domain width,  $d$ , when the maximum electron drift velocity is twice the valley velocity (i.e. maximum velocity 'spread' is equal to the valley velocity). At threshold  $E_B = 2E_u$  so that the domain readjustment time is just this minimum transit time. If the domain runs into the anode at constant velocity the current rise time during this event will also be the same as the time constant derived above.

An extension to this approach when the Gunn device is in series with a resistor,  $R_L$ , is to consider the domain relaxation time as

$$T_R = (R_0 + R_L) C_D. \quad (9.12)$$

The dynamics of a Gunn diode in series with a resistor have not been solved rigorously at the time of writing and it is not obvious that Eqn (9.12) is the correct expression for this case.

Another approach to this problem considers the relaxation of a domain configuration from a given state to its stable state<sup>(19)</sup> in terms of the rate of change of excess domain voltage. The starting point is Poissons equation and the total current density  $J$ :

$$\frac{\partial E}{\partial Z} = \frac{e}{\epsilon \epsilon_0} (n - N_D) \quad (9.13)$$

$$J = nev(E) - e \frac{\partial(Dn)}{\partial Z} + \epsilon \epsilon_0 \frac{\partial E}{\partial t}. \quad (9.14)$$

Where the symbols have their usual meaning. The boundary conditions of the problem occur at two points  $Z_1$  and  $Z_2$  in the uniform field region on either side of the domain where

$$\frac{\partial[E(Z_1)]}{\partial Z} = \frac{\partial[E(Z_2)]}{\partial Z} = 0 \quad (9.15)$$

$$E(Z_1) = E(Z_2) = E_0. \quad (9.16)$$

At  $Z_1$  and  $Z_2$ ,  $\partial(Dn)/\partial Z = 0$  so  $J$  can be replaced by its value at these two points and  $n$  can be eliminated from Eqns (9.13) and (9.14) to give:

$$\frac{\partial(E - E_0)}{\partial t} = \frac{N_D e}{\epsilon \epsilon_0} \left\{ v(E_0) - v(E) \right\} + \frac{e}{\epsilon \epsilon_0} \frac{\partial(Dn)}{\partial Z} - v(E) \frac{\partial E}{\partial Z}. \quad (9.17)$$

Integration of Eqn (9.17) from  $Z_1$  to  $Z_2$  gives:

$$\frac{\partial}{\partial t} \int_{Z_1}^{Z_2} (E - E_0) dZ = \int_{Z_1}^{Z_2} \frac{eN_D}{\epsilon\epsilon_0} (v(E_0) - v(E)) dZ. \quad (9.18)$$

The integral on the left-hand side is the excess domain voltage  $\phi_D$ . For the zero diffusion approximation the accumulation layer has zero length and the depletion layer is fully depleted so that the integral on the right-hand side can be rewritten with the aid of Eqn (9.13):

$$\int_{Z_1}^{Z_2} \frac{N_D e}{\epsilon\epsilon_0} (v(E_0) - v(E)) dZ = \int_{E_0}^{E_d} (v(E_0) - v(E)) dE.$$

Therefore 9.18 becomes:

$$\frac{\partial \phi_D}{\partial t} \approx \int_{E_0}^{E_d} \{v(E_0) - v(E)\} dE. \quad (9.19)$$

This equation has a simple graphical interpretation. The right-hand side is the difference of the right-hand and left-hand shaded areas of Fig. 9.18. The areal difference for a given domain configuration gives the growth or decay rate to the stable configuration. For the stable domain condition,  $\partial \phi_D / \partial t = 0$ , and Eqn (9.19) reduces to the stable domain equal areas rule.

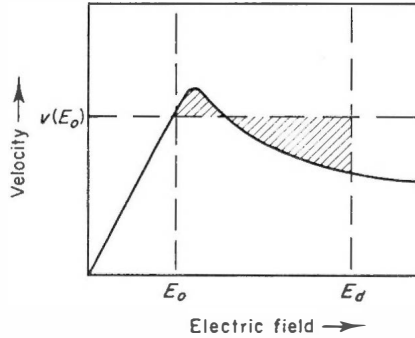


FIG. 9.18. The unequal areas rule.

No conclusive measurements of the domain readjustment rate have been made at the time of writing. Izadpanah<sup>(13)</sup> has measured the harmonic content of the current waveform of a device with large  $nl$  product in a resistive circuit with different values of series resistance. The variation of the amplitude of a high harmonic was related to the rise and fall times of the domain controlled current pulses. The rise time of a particular diode increased as the load resistance increased and the rise time of different diodes

with the same loading was longest for the lowest doping levels. Other measurements of the "in flight" domain transient response<sup>(18)</sup> have been made with a controlled step function in the bias voltage. If this decreased the terminal voltage there was a momentary current reduction as the domain discharged and vice versa (Fig. 9.19). The time integral of this current spike gave the charge removed from or added to the domain so that the differential domain capacity could be determined. It was concluded that some part of the domain discharge occurred across the domain and not through the external circuit as expected. The time resolution of the measurement system was close to the lifetime of the current discharge so that reliable measurements of this time were not possible.

Measurements with a time resolution of 28 psec have been made possible with improvement of fast sampling techniques. This has allowed a detailed examination of current waveforms during the time that a domain runs

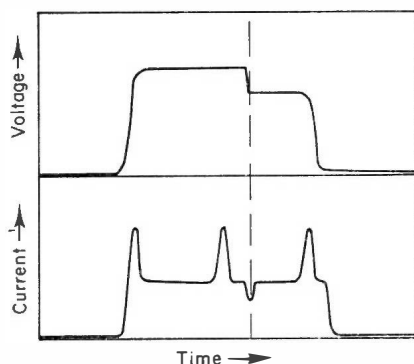


FIG. 9.19. Voltage and current waveforms for transient characteristics of domain in flight.<sup>(18)</sup>

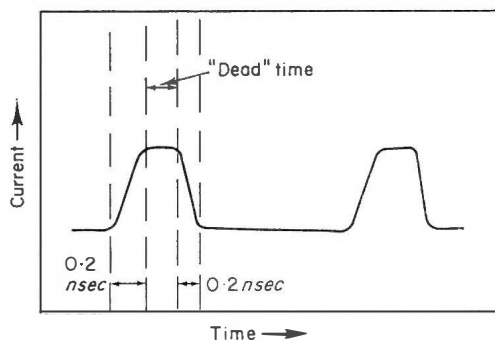


FIG. 9.20. Rise and fall times of current waveforms<sup>(20)</sup> as a domain runs into the anode and a further domain is triggered at the cathode. Sample details:  $1.14 \times 10^{15}$  electrons/cm<sup>3</sup>, 291 microns long, mobility 5565 cm<sup>2</sup>/V sec.

into the anode and another domain forms at the cathode.<sup>(20)</sup> A typical waveform is shown in Fig. 9.20. In a diode with  $1.14 \times 10^{15}$  electrons per  $\text{cm}^3$ , 291 microns long and electron mobility  $5565 \text{ cm}^2/\text{V sec}$  the rise and fall times were about 0.2 nsec. This is in good agreement with calculations using Eqn (9.19). When the bias voltage was just above threshold there was also a 'dead' time when the current was constant for about 0.2 nsec. This could be the time taken for small signal space charge growth before large signal effects become important. For a threshold bias the electric field at the cathode will not rise to threshold until the entire previous domain has passed out of the anode. This interpretation is consistent with the shortening of this dead time as the bias voltage is increased. A separate experiment in which a narrow pulse was superimposed on the main bias pulse (below threshold) also showed that domains could not be triggered if the duration of this narrow pulse was less than 0.5 nsec.

## 9.6 MIXED DEVICES, AND SYSTEMS

This final section will consider how the above processes are combined for specific applications. Many of these applications are little more than tentative at the time of writing and time will decide their role, if any. Therefore the emphasis will be placed upon a simple descriptive cataloguing of the modes of operation.

### 9.6.1 LOGIC GATES

Two "exclusive or" gates or comparators (Table 9.1) have been described in Sections 9.3 and 9.4 using respectively a dual cathode device<sup>(10)</sup> and two uniform devices with a common anode resistor.<sup>(13,17)</sup> If the former device has a series resistor in one of the cathode leads (Fig. 9.21) a domain may not

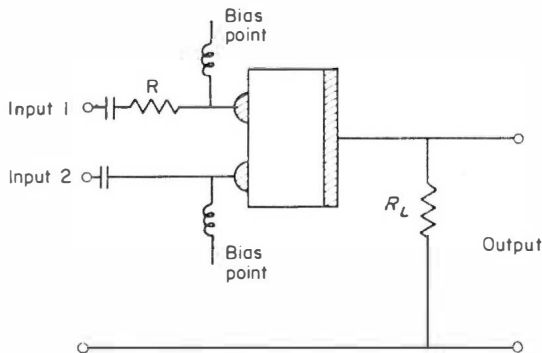


FIG. 9.21. Inhibitor, derived from the comparator<sup>(17)</sup> of Fig. 9.10.



be triggered when a pulse (whose amplitude is the same as that necessary for comparator action) is applied to this lead because of the additional voltage drop in the resistor.<sup>(17)</sup> The truth table of the action (an inhibitor) is shown in Table 9.3.

TABLE 9.3. Truth table of inhibitor.

Input 1	Input 2	Output
0	0	0
1	0	0
0	1	1
1	1	0

Also described in Section 9.4 was an ‘and’ gate which is essentially derived from the pulse regenerator of Section 9.4. The simple regenerator itself may be used as a multiple input “inclusive or” gate using the same configuration as Fig. 9.17a. and suitable adjustment of the biasing voltage. When the input voltages are unequal an ‘and’ gate may be constructed with a third contact<sup>(21)</sup> on the side of the device as illustrated in Fig. 9.22.

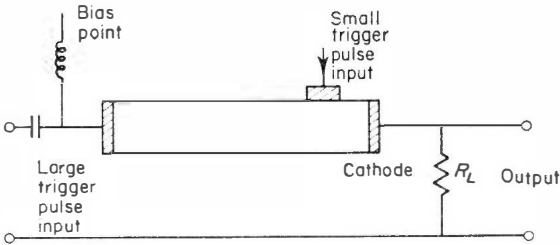


FIG. 9.22. Three terminal ‘and’ gate.<sup>(21)</sup>

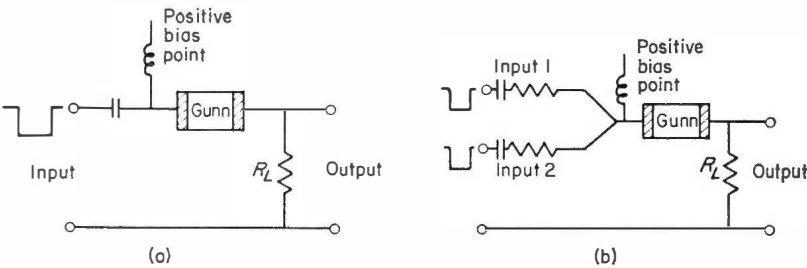


FIG. 9.23. ‘Invertor’, ‘nor’ and ‘nand’ gates.

For completeness, three other logic gate<sup>(13)</sup> proposals are included. They are all similar in construction to the previous gates but use devices biased above threshold. The continuous domain pulse output is interrupted by voltage pulses which reduce the terminal voltage and inhibit domain formation. The inverter (Fig. 9.23a) produces an output for no input and vice versa. The circuit of Fig. 9.23b acts as a 'nor' gate producing no output for a pulse at either or both input terminals or as a 'nand' gate producing no output only if there is a pulse at both inputs. The functional difference between these last two circuits is achieved by bias adjustment.

### 9.6.2 ANALOGUE TO DIGITAL CONVERTORS

Pulsed modulation telecommunications systems require devices to convert analogue voltages to digital form. The variable frequency oscillators<sup>(2)</sup> described in Section 9.3 are simple A/D convertors because the number of cycles (pulses) in a given time is proportional to the terminal voltage of the device. An A/D convertor has been demonstrated using a tapered device with additional notch non-uniformities (Fig. 9.24). The device terminal voltage determines the domain transit length which in turn determines the number of current pulses in each domain transit. The output waveform is similar to that shown in Fig. 9.13

A very neat way of accomplishing the same function has already been discussed in Section 9.4. The analogue voltage shaping required in that device may be overcome with the double device proposal illustrated in Fig. 9.25. A triangular pulse generated by a tapered waveform generator<sup>(2)</sup> is

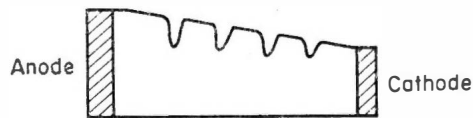


FIG. 9.24. Dofic-analogue to digital converter.<sup>(3)</sup>

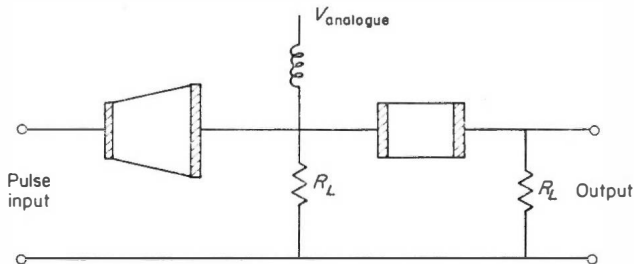


FIG. 9.25. Circuit to digitize continuous analogue voltages.<sup>(13)</sup>

superimposed on the continuously varying analogue voltage<sup>(13)</sup> so that the length of time that the device terminal voltage is above threshold is determined by the analogue voltage. This system has the additional advantage that the digital sampling time is also controlled.

In all of these A/D convertors the output is a train of pulses whose number is directly proportional to the analogue voltage. They do not provide output as a binary code. Additional circuitry has been proposed to carry out this operation (see Section 9.6.6).

### 9.6.3 MEMORIES

Two types of memory have been proposed and verified. One type using impact ionization has already been described in Section 9.2. The other type uses hysteresis effects (with respect to bias) in the continuous oscillation/no oscillation characteristics of oscillatory circuits.

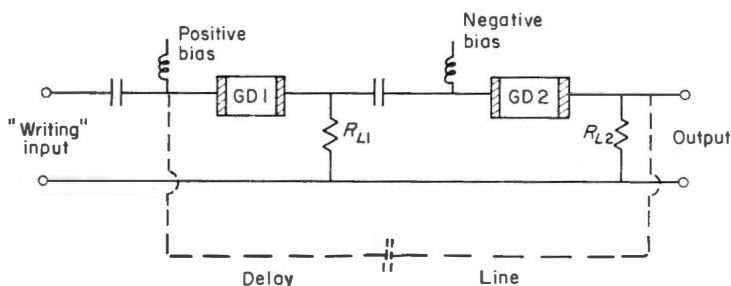


FIG. 9.26. Double regenerator memory.<sup>(22)</sup>

Two systems utilizing pulse regenerators are illustrated in Figs 9.26 and 9.27. In the former one<sup>(22)</sup> the output pulse of a triggered pulse regenerator triggers a second regenerator whose output pulse is fed back to the first regenerator through a delay line. In this way information pulses used to trigger the first regenerator are stored in a circulating memory. Writing or memory reading may possibly be accomplished with a comparator in place of one diode. A compromise has to be struck in the delay line length between access time and storage capacity.

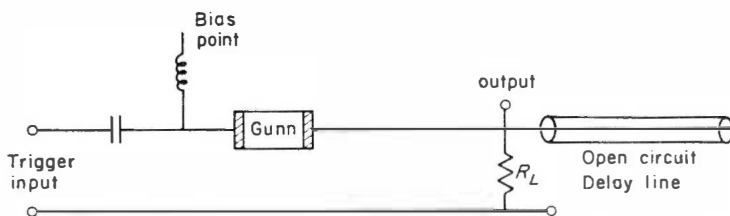


FIG. 9.27. Single regenerator memory or variable frequency pulse generator.<sup>(13)</sup>

An alternative circuit<sup>(13)</sup> using one diode is illustrated in Fig. 9.27. The output pulse of a triggered regenerator travels along an open circuited transmission line and is reflected back to the diode where it retriggers the diode, providing that the delay time is greater than the domain transit time. This process continues until a negative input pulse or bias removal stops the operation.

The memory circuit just described has some similarities with a memory element using the threshold characteristics of a cavity controlled oscillator.<sup>(21)</sup> The sustaining voltage (not to be confused with domain sustaining voltage) for cavity controlled oscillations of a C.W. Gunn diode is lower than the starting voltage. A triggering voltage which momentarily raises the device terminal voltage may be used to start the oscillations, providing that the biasing level is correctly adjusted. The oscillations will continue until stopped by a pulse of opposite polarity. The relationship between sustaining voltage and trigger voltage is illustrated in Fig. 9.28.

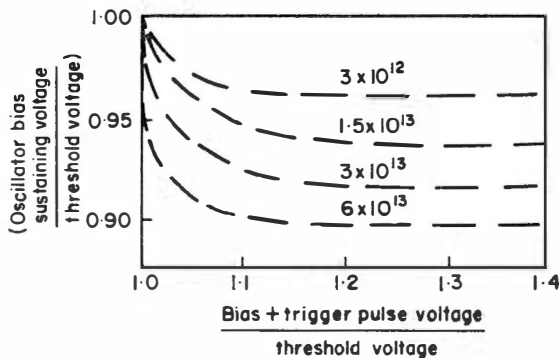


FIG. 9.28. Characteristic of threshold oscillator memory.<sup>(21)</sup>

#### 9.6.4 CLOCKS AND REPETITIVE SIGNAL GENERATORS

Many of the devices of this section have been discussed earlier. The single regenerator memory of the last section may also be used as a neat system for producing variable repetition rate pulses (with one diode) by varying the transmission line length. The waveform generators of Sections 9.2 and 9.4 and the variable frequency non-uniform oscillators of Section 9.3 all have a place in the present section. One objective in designing the variable frequency oscillators was to improve the bias voltage frequency modulation properties of the device when it operated with a circuit controlled frequency. It may also be possible to improve the efficiency of cavity controlled oscillators by shaping the device non-uniformity to give a desirable current waveform.<sup>(23)</sup> This point has been dealt with in Chapter 5. A technique for

optical control of the extinction position of a domain in a Gunn oscillator has been demonstrated.<sup>(31)</sup> The device was non-uniformly illuminated with a gallium arsenide laser so that the anode section could be shorted to give a length variation of up to 600%.

In this section on oscillators it is appropriate to consider optical frequency generation. This occurs frequently due to impact ionization within the high electric field region of the domains. By careful sample preparation (polishing the sides flat and parallel) it has been possible to obtain coherent light output from the inverted electron population produced by the impact ionization.<sup>(24)</sup>

### 9.6.5 REGENERATORS AND MODULATORS

The diode pulse regenerators have already been dealt with in Section 9.4. Improvements to sensitivity may be made with the addition of a third, triggering electrode on the side of the device and close to the cathode.<sup>(25)</sup>

A class of modulation devices is possible using a modification of the third electrode technique. In Section 9.2 it was seen that a domain could exert control over the diode current. The third electrode may be used to connect other current paths into the device, and these may be controlled by the domain over part of a domain transit only.<sup>(2)</sup> Figure 9.29a illustrates a case where a parallel current path exists between the third electrode and anode. This contributes an additional device current when the domain is travelling between the third electrode and anode. The domain controls the total device current when it lies between the cathode and the third electrode. The current waveform is illustrated in Fig. 9.29b. This technique may be used for waveform modulation if  $R_3$  is electronically controlled and may be extended to multiple terminal operation.

A further use of side electrodes is to give a current path in parallel with a domain over a central part of the domain transit as shown in Fig. 9.30a. The device current is controlled by the domain, except for the time it passes

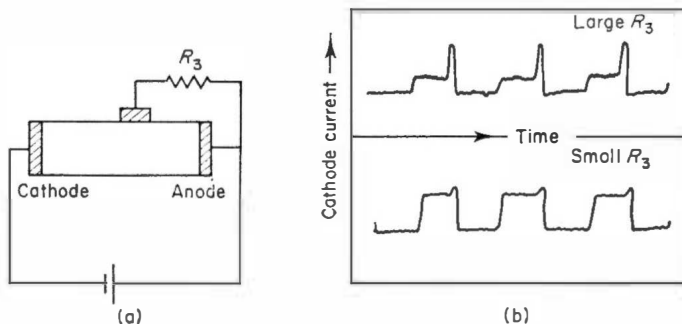


FIG. 9.29. Three terminal waveform generator.<sup>(2)</sup>

under the insulated contact. The capacitance coupling of the domain voltage through this contact causes a momentary increase of cathode current (Fig. 9.30b). No additional current is observed when the metallic part is shorted to the cathode so that the additional anode current flows to ground.

Similar waveforms may be obtained by attaching, ohmically, a resistor to cover a central part of the domain path. This may have application as a photosensor if a suitable material is used to fabricate the resistor.

If the third terminal is a rectifying junction the effective cross-sectional area of the device may be controlled by an external voltage through the width of the depletion layer.<sup>(8)</sup> This would enable effects similar to those described in Section 9.2 to be obtained. One interesting feature of the side contact devices is the relatively long time over which the resistor or voltage may have its value adjusted compared with the time occupied by the modulation which results. This may be an advantageous system feature.

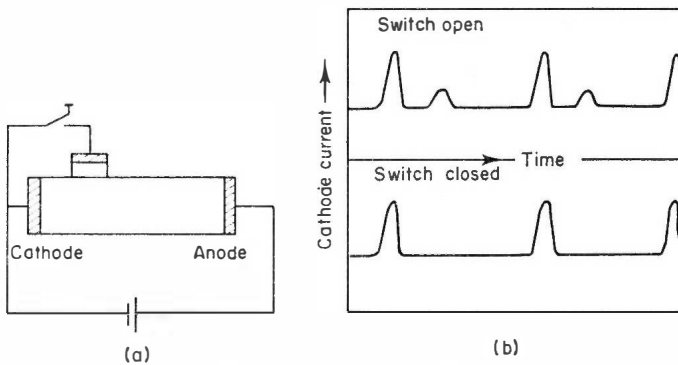


FIG. 9.30. Shunt contact modulator.<sup>(2)</sup>

This section would not be complete without mention of the non-uniform field effects caused by dielectric surface loading. As was shown in Chapter 4, devices with a small lateral dimension are stable against space charge wave growth.<sup>(32)</sup> This stabilization is caused by reduction of the electric field difference across any space charge owing to lateral flux leakage. The effect is enhanced by loading the surface with a high permittivity dielectric.<sup>(33)</sup> When the dielectric does not cover the entire surface as shown in Fig. 9.31a, electric field non-uniformities occur at its edges and can cause stabilization by reducing the field over a large part of the device below threshold.<sup>(34)</sup> Similar non-uniform effects have been observed by Kataoka *et al.*<sup>(35)</sup> and they have carried out some 2-dimensional computer simulation of such device behaviour. When the dielectric load does not cover the entire surface, and the device lateral dimensions are large enough to allow repetitive domain formation and propagation, the current waveform shown in Fig. 9.31b is observed.<sup>(36)</sup> When a domain is propagating outside the covered region

the current has its normal value. As the domain passes under the dielectric an additional capacitive current path exists in parallel with the domain. The potential across this path is just equal to the potential difference across the domain. The parallel path may be split into two series capacitive elements (Fig. 9.31c) each of which has a time varying surface area. The flow of charge to maintain the potential across the dielectric path as the surface area varies is responsible for the modification of the current waveform.<sup>(36)</sup>

Finally in this section we mention optical modulation. The high electric fields in a domain modify the refractive index of the medium through the electro-optic effect. This may be used as a modulator<sup>(26)</sup> for an optical frequency transmission system.

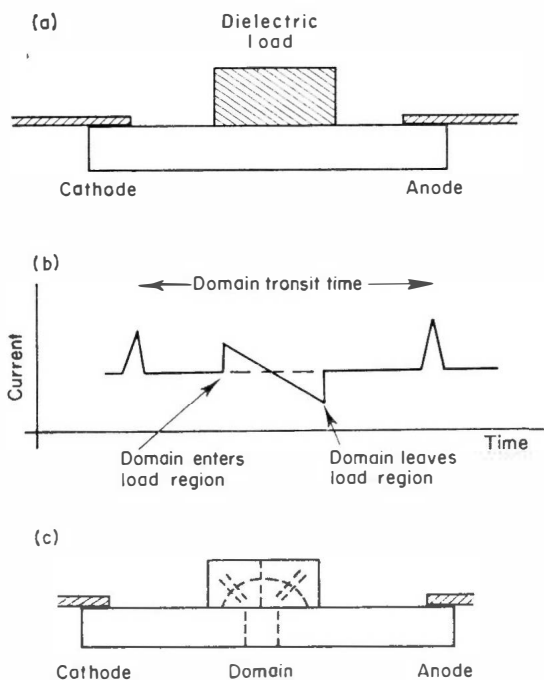


FIG. 9.31. The current waveform of an unstable diode with partial surface dielectric loading.<sup>36</sup>

### 9.6.6 SYSTEMS

The use of the fast logic and other devices which have been dealt with in this chapter has been of a very preliminary character up to the time of writing. Often the devices have operated so fast that satisfactory control of them has not been achieved. Some systems have been proposed<sup>(17, 27, 28)</sup> but time will be their judge.

## REFERENCES

1. Newton, C. O. (1969). *Britt J. App. Phys.* **2**, 341–352.
2. Shoji, M. (1967). *I.E.E.E. Trans. on Electron Devices* **ED-14**, 535–546.
3. Sandbank, C. P. (1967). *Solid State Electronics* **10**, 369–380.
4. Heeks, J. S. and Woode, A. D. (1967). *I.E.E.E. Trans. on Electron Devices* **ED-14**, 512–517.
5. Owens, J. M. and Kino, G. S. (1966). *Phys. Letts.* **23**, 453–455.
6. Guetin, P. (1967). *I.E.E.E. Trans. on Electron Devices* **ED-14**, 552–562.
7. Heeks, J. S., Woode, A. D. and Sandbank, C. P. (1967). *Electronics Letts.* **330–331**.
8. Newton, C. O. Private communication.
9. Shoji, M. (1967). *Proc. I.E.E.E.* **55**, 1646–1647.
10. Izadpanah, S. H. and Hartnagel, H. L. (1967). *Proc. I.E.E.E.* **55**, 1748.
11. Nordbotten, A. (1967). *I.E.E.E. Trans. on Electron Devices* **ED-14**, 608.
12. Heeks, J. S. (1966). *I.E.E.E. Trans. on Electron Devices* **ED-13**, 68–79.
13. Izadpanah, S. H. (1969). Ph.D. Thesis, University of Sheffield.
14. Izadpanah, S. H. and Hartnagel, H. L. (1968). *Electron. Lett.* **4**, 26.
15. Fisher, R. E. (1967). *Proc. I.E.E.E.* **55**, 2189–2190.
16. Jeppsson, B. I. and Jeppesen, P. (1971). *I.E.E.E. Trans. on Electron Devices* **ED-18** 432–449.
17. Hartnagel, H. L. and Izadpanah, S. H. (1968). *The Radio and Electronic Engineer* **36**, 247.
18. Kuru, I., Robson, P. N. and Kino, G. S. (1968). *I.E.E.E. Trans. on Electron Devices* **ED-15**, 21–29.
19. Kurokawa, K. (1967). *Proc. I.E.E.E.* **55**, 1615–1616.
20. Ohmi, T., Takeoka, Y. and Nishimaki, M. (1968). *Proc. I.E.E.E.* **56**, 2188–90.
21. Copeland, J. A., Hayashi, T. and Uenohara, M. (1967). *Proc. I.E.E.E.* **55**, 584–585.
22. Izadpanah, S. H. and Hartnagel, H. L. (1969). *Electron. Lett.* **5**, 53.
23. Ladbroke, P. H. and Carroll, J. E. (1968). *Electron. Lett.* **4**, 83.
24. Southgate, P. D. (1968). *App. Phys. Letts.* **12**, 61–63.
25. Hayashi, T. (1968). *I.E.E.E. Trans. on Electron Devices* **ED-15**, 105–110.
26. Cohen, M. G., Knight, S. and Edward, J. P. (1966). *App. Phys. Letts.* June, 269–270.
27. Hartnagel, H. L. (1969). *Solid State Electronics* **12**, 19.
28. Fisher, R. E. (1968). *I.E.E.E. Trans. on Microwave Theory and Techniques* **MTT-16**, pp. 541–547.
29. Jeppsson, B. and Jeppeson, P. (1970). “Proc. MOGA 70”, pp. 20–27, Kluwer-Deventer, Amsterdam.
30. Robson, P. N. Private communication.
31. Myers, F. A., McStay, J. and Taylor, B. C. (1968). *Electron. Lett.* **4**, 386–7.
32. Kino, G. S. and Robson, P. N. (1968). *Proc. Inst. Elect. Electron Engrs.* **56**, 2056–7.
33. Hofmann, K. R. (1969). *Electron Lett.* **5**, 289–90.
34. Hofmann, K. R. (1969). *Electron. Lett.* **5**, 227–8.
35. Kataoka, S., Kawashina, M. and Tomizawa, K. (1970). “Proc. MOGA 70”, 16–1, Kluwer-Deventer, Amsterdam.
36. Hofmann, K. R. (1969). *Electron. Lett.* **5**, 289–90.



## *Chapter 10*

# **Engineering and Applications**

### 10.1 INTRODUCTION

In this chapter some of the engineering aspects of Gunn diode operation are considered. Turning first to the device itself, the thermal design is examined and we see that there is room for considerable improvement over the early devices, and it is a topic on which research continues at the time of writing.

The detailed design of mechanical and electronic tuning systems for low power oscillators is described next, and some more general aspects of device operation are mentioned.

Finally, a number of systems which use Gunn oscillators are discussed. These are all small and portable equipments which exploit the unique convenience and other properties of these solid state generators. It is not a comprehensive list, but rather serves to illustrate the impact which these devices have already made on the design of microwave systems.

### 10.2 THERMAL DESIGN FOR CONTINUOUS OPERATION

Since Gunn oscillators are generally very small and rather inefficient it is important that the heat flow paths from the active regions to the heat sinks be as good as possible.

The electrical restraints usually impose plane parallel heat flow in the active region, and the advantages of divergent flow can only be realised in the heat sinking mount.

The temperature coefficient of resistivity in high quality epitaxial layers of GaAs is generally positive and small so that heat generation is nearly uniform in the active layers.

We therefore have to consider the problem of heat flow in a uniformly generating region, parallel flow through any contact layers, and then radial flow into a large heat sink. To illustrate this we follow the example of Knight.<sup>(1)</sup>

Figure 10.1 illustrates a parallel geometry device of  $n^+nn^{++}$  sandwich structure bonded active layer down to a large heat sinking block. The active  $n$  layer has a thickness  $l$ , the  $n^{++}$  layer a thickness  $d$ , and the metallic bond a thickness  $t$ .

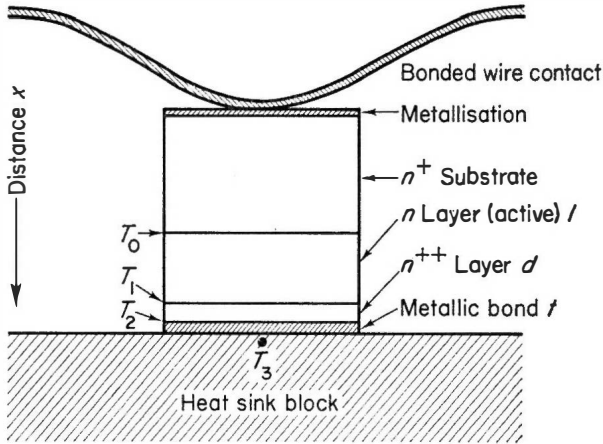


FIG. 10.1. A parallel geometry  $n^+nn^{++}$  sandwich Gunn device on a heat sink.

Measurements on the thermal conductivity,  $K$ , of GaAs, Fig. 10.2 (Carlson<sup>(2)</sup>) show that it varies approximately inversely with temperature near 300°K and can be described by  $K_1/T = 150/T$  in pure material (the  $n$  region) and  $K_2/T = 120/T$  in the heavily doped  $n^{++}$  region.

The equation for parallel heat flow in a volume in which heat is being generated uniformly at the rate  $Q$  per unit volume is

$$\frac{d}{dx} \left( K \frac{dT}{dx} \right) = -Q$$

where we take the  $n^+, n$  interface as origin, with the  $x$  direction towards the heat sink.

In this case

$$\frac{d}{dx} \left( \frac{1}{T} \frac{dT}{dx} \right) = \frac{-Q}{K_1}$$

hence

$$T_x = T_1 \exp \left( \frac{Q}{2K_1} (l^2 - x^2) \right)$$

where  $T_1$  is the temperature at the  $n^{++}, n$  interface.

The maximum temperature is

$$T_0 = T_1 \exp\left(\frac{Ql^2}{2K_1}\right). \quad (10.1)$$

In the  $n^{++}$  layer,  $Q = 0$ , so

$$\frac{1}{T} \frac{dT}{dx} = \frac{-Ql}{K_2},$$

hence

$$T_1 = T_2 \exp \frac{Qld}{K_2}$$

where  $T_2$  is the temperature of the  $n^{++}$ , metal junction.

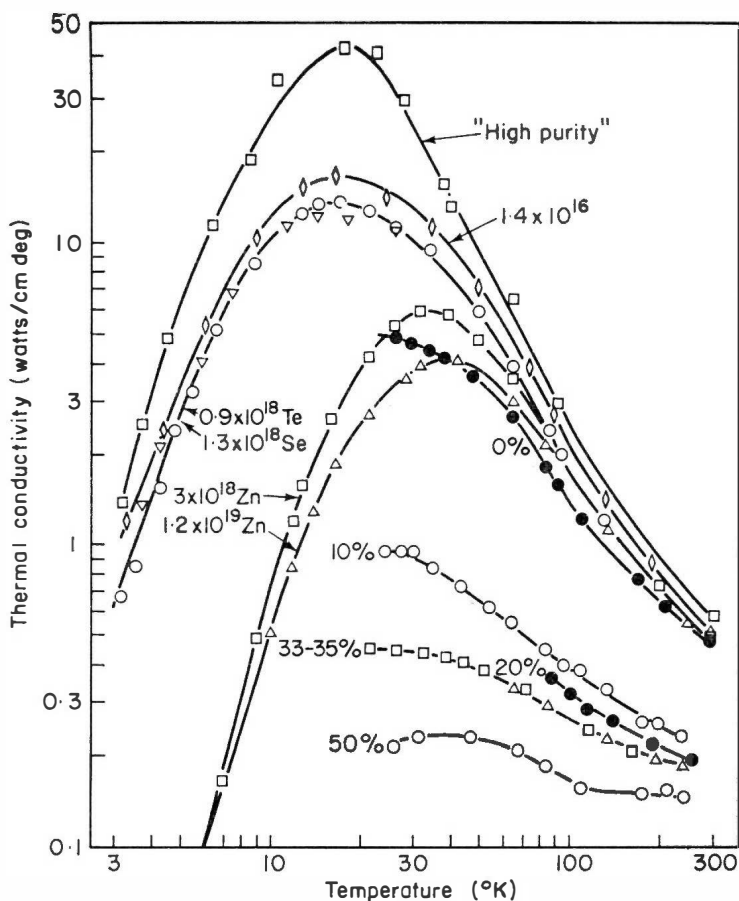


FIG. 10.2. Thermal conductivity  $K$  versus temperature for single crystal GaAs with various carrier concentrations and for GaAs P alloys (Carlson<sup>(2)</sup>).

For the metal bond

$$K_3 \frac{dT}{dx} = Ql,$$

hence

$$T_2 - T_3 = \frac{Ql}{K_3} \cdot t$$

where  $T_3$  is the temperature of the metal, heat sink junction, and  $K_3$  is the conductivity of the metal bond.

If we assume that the semiconductor is cylindrical of radius  $a$ , the temperature of the heat sink is given by the well known expression for divergent flow,

$$T_3 = T_4 + \frac{Qla}{K_4} \quad (10.2)$$

where  $T_4$  is the ambient temperature and  $K_4$  is the conductivity of the heat sink.

Thus the maximum temperature

$$T_0 = \left[ T_4 + Ql \left( \frac{a}{K_4} + \frac{t}{K_3} \right) \right] \exp \left[ Ql \left( \frac{l}{2K_1} + \frac{d}{K_2} \right) \right]. \quad (10.3)$$

It is clearly advantageous to make the  $n^{++}$  layer and the metal bond as thin as possible. In some cases it may be possible to omit the  $n^{++}$  layer altogether, and a  $1 \mu\text{m}$  layer of gold would have almost negligible effect. The  $l^2$  which appears in the exponent points to the importance of using as thin epitaxial layers as possible consistent with the desired frequency of operation, in direct conflict with the need to avoid making the microwave impedance too low.

As an example, consider a  $10 \mu\text{m}$  layer of resistivity  $\rho = 0.7 \Omega\text{-cm}$  GaAs with a  $2 \mu\text{m}$   $n^{++}$  contact layer and  $1 \mu\text{m}$  gold bond. For good efficiency the bias  $E_B$  would be  $20 \text{ kV/cm}$  ( $20 \text{ V}$ ) and the threshold field  $E_T$  on a good sample is  $3.5 \text{ kV/cm}$  ( $3.5 \text{ V}$ ). The power density  $Q = (E_T/\rho) \cdot E_B = 10^8 \text{ W/cm}^3$ , and the total power flow  $Ql = 10^5 \text{ W/cm}^2$ .

The temperature drop in the gold bond is only  $3.3^\circ\text{C}$  ( $K_3 = 3.0 \text{ W/cm}^\circ\text{C}$ ).

The magnitude of the exponent

$$Ql \left( \frac{l}{2K_1} + \frac{d}{K_2} \right) = 0.5$$

and  $e^{0.5} = 1.65$ .

The maximum allowed temperature in the GaAs depends on the life and reliability desired, but 500°K should rarely be exceeded.

Now  $500/1.65 = 303^\circ\text{K}$ , which is expected to be the ambient temperature. Hence there is no margin for any temperature drop in the heat sink block and the example is not a practical device.

On the other hand, if the  $n^{++}$  layer were omitted and the active layer bonded directly to the heat sink, the exponent is reduced to  $\frac{1}{3}$  and  $e^{1/3} = 1.4$ .

$(500/1.4) = 355$  so that at an ambient temperature of 300°K we can allow

$$Ql \left( \frac{a}{K_4} + \frac{t}{K_3} \right) = 55$$

for a device which will just work at room temperature. This gives  $a \approx 20 \mu\text{m}$  for a copper heat sink. Swan<sup>(3)</sup> has pointed out the advantages of using a type IIa diamond buffer layer to spread the heat flow to a heat sink. This material has a thermal conductivity five times that of copper at room temperature, and in a practical device an advantage of three times can perhaps be obtained. For the same conditions, then, a radius  $a = 60 \mu\text{m}$  for a diamond heat sink would be possible, which gives a total dissipation of over 10 W compared with about 1 W for copper.

If the same total power were generated in a  $6 \mu\text{m}$  layer, the exponential becomes  $e^{0.2} = 1.22$  which would allow the device to operate at an ambient temperature up to 80°C or allow a larger area device to operate at room temperature.

This example serves to illustrate the dominant importance of making the heat flow paths in the GaAs as short as possible. Applying heat sinks to both sides would bring dramatic improvements but the problem of providing mechanical stress relief is very difficult.

The heat flow problem is severe, and in large over-transit length devices particularly so, as these usually have more stringent requirements on temperature gradients (see Chapter 6). For this reason most laboratory results have been obtained under pulsed operation at low duty cycle. Various geometries have been suggested for cooling large samples, from transverse flow into a good conductivity dielectric to a set of diodes in series interleaved with heat sinks.

Liquid cooling yields no advantage at such large power flows as the slow motion in the boundary layers leads to vapourisation and the formation of hot spots. It is useful only at heat flows below about  $1000 \text{ W/cm}^2$ <sup>(25,26)</sup> and so might be employed to cool large common heat sinks for multiple devices. A liquid could not be used to improve the mean power dissipated in a single device unless cooling properties dramatically better than those of the best fluids of today can be achieved. There is little prospect of this.

### 10.3 THERMAL DESIGN FOR PULSED OPERATION

In pulsed operation, if the pulses are short enough, the peak power dissipated is limited only by electrical factors. The mean power, of course, is still limited by the same considerations as the continuous wave case except that allowance must be made for the temperature rise in the pulse. For very short pulses this may be neglected and the size of the device is not so restricted as the C.W. case.

Consider again the numerical example in the last section (Fig. 10.1). The length  $l$  could be increased if the mean power per unit area  $Ql$  were reduced in proportion, by reducing the duty cycle from C.W. This would yield an increase in peak power at the expense of mean power. Impedance limitations would allow an increase in area proportional to that in length, so that the peak power could increase as  $l^2$ . However, due to the divergent heat flow in the heat sink, this would not allow the mean power to remain unchanged as it would for parallel flow. The mean power would have to be reduced in proportion to the square root of area. Proportional increases in length and area then would give an increase in peak power as  $l^2$  and a reduction in mean power as  $l$ , for the same resistivity and drive voltage.

For intermediate pulse lengths we must consider the temperature rise within a pulse and determine at what pulse length the problem becomes essentially the C.W. one.

Consider then, low duty cycle pulsed operation so that at the start of each pulse the device and heat sink are at a comparatively low and uniform temperature.

Equation (10.1) for the temperature drop in the active region can be expressed as a heat flow equation

$$Ql = \frac{2K_1}{l} \log \left( \frac{T_0}{T_1} \right)$$

where we recognise  $Ql$  as the heat flow per unit area. The lower initial value for  $T_1$  improves the heat flow hardly at all (e.g. by only  $\log 4/3$  if  $T_1$  is reduced from 400°K to 300°K).

If the resistivity and drive field are changed from the C.W. values to increase  $Q$  by a large margin, as they frequently are for pulsed operation, then the thermal diffusion equation

$$gs \frac{\partial T}{\partial t} = K \frac{\partial^2 T}{\partial x^2} + Q \quad (10.4)$$

approximates to

$$gs \frac{\partial T}{\partial t} = Q$$

where  $s$  is the specific heat and  $g$  the density.

In other words the heat input rate so far exceeds the maximum heat sinking capacity that the GaAs may be considered as a thermally isolated mass for the duration of the pulse.

In this case the temperature rise is linear and is given by

$$\frac{\partial T}{\partial t} = \frac{Q}{gs} = \frac{E_T E_B}{\rho gs} \quad (10.5)$$

which can frequently exceed values of  $100^\circ\text{C}/\mu\text{sec}$ , virtually ruling out pulse lengths much over one microsecond.

On the other hand, if the dominant temperature drop is not in the GaAs (Eqn (10.1)) but in the heat sink (Eqn (10.2)), as would be the case in large area devices of around  $1\ \Omega\text{cm}$  resistivity, then thermal diffusion into the heat sink may lengthen the possible pulse duration.

Plane parallel thermal diffusion of a step function in temperature into a conducting medium is such that after a time  $t$  the temperature at a plane distant  $\sim (kt/gs)^{\frac{1}{2}}$  from the surface is half the temperature at the surface. Hence, very approximately, the heat sink may be said to have a transient thermal capacity

$$\sim (Kt/gs)^{\frac{1}{2}} \cdot gs = (Ktgs)^{\frac{1}{2}}.$$

Values of this quantity are given in Fig. 10.3 for various materials, and may be compared with the thermal capacity of a  $10\ \mu\text{m}$  layer of GaAs ( $1.6 \times 10^{-3}\ \text{J}^\circ\text{C}^{-1}\text{cm}^{-2}$ ). While the transient thermal capacity values must be regarded as uncertain to a factor of two due to the approximate nature of this argument, it may be seen that pulse lengths could be increased by choice of a suitable heat sink and geometry.

For example, consider a  $6\ \mu\text{m}$  layer of  $0.7\ \Omega\text{-cm}$  GaAs bonded directly to a copper heat sink. If the threshold is  $3.5\ \text{kV/cm}$  and the bias  $20\ \text{kV/cm}$  then the power density  $Q = 10^8\ \text{W/cm}$  as noted previously. For a radius  $a = 80\ \mu\text{m}$  this corresponds to  $12\ \text{W}$  total dissipation and the device would run C.W. at an ambient temperature  $T_4 = 300^\circ\text{K}$ . The interface temperature  $T_3$  would be  $420^\circ\text{K}$  and the maximum  $T_0 = 480^\circ\text{K}$  (Eqn (10.3)).

Now suppose the radius were doubled to  $a = 160\ \mu\text{m}$ . The dissipation would be  $48\ \text{W}$  and the device could not be run C.W. as the interface temperature would then be  $540^\circ\text{K}$  and  $T_0$  would be  $700^\circ\text{K}$ . If the GaAs were isolated, the rate of temperature rise within a pulse would be  $60^\circ\text{C}/\mu\text{sec}$ , so a pulse length of  $3\ \mu\text{sec}$  would be possible. If, as before, the active layer were bonded to a copper heat sink, then for a pulse of  $36\ \mu\text{sec}$  there is a transient thermal capacity of about  $22 \times 10^{-3}\ \text{J}^\circ\text{C}^{-1}\text{cm}^{-2}$  to be added to the  $1 \times 10^{-3}\ \text{J}^\circ\text{C}^{-1}\text{cm}^{-2}$  of the  $6\ \mu\text{m}$  layer of GaAs. This leaves an adequate margin in view of the approximate nature of this argument, so such a

Material	Density, $g$ , ( $gm\ cm^{-3}$ )	Specific heat, $s$ , Joules $gm^{-1}$ $^{\circ}C^{-1}$ at $300^{\circ}K$	Thermal conductivity, $K$ , Watts $cm^{-1}\ ^{\circ}C^{-1}$ at $300^{\circ}K$	Thermal diffusion constant, $K/gs$ ( $cm^2\ sec^{-1}$ )	Transient thermal capacity in a planar structure for a pulse length $t = 1\ \mu sec$ , $(Ktgs)^{\frac{1}{2}}$ , Joules $^{\circ}C^{-1}\ cm^{-2}$
GaAs	5.3	0.3	0.5 see Fig. 10.2	0.31	$0.9 \times 10^{-3}$
Diamond type IIa	3.52	0.51	20	11.1	$6.0 \times 10^{-3}$
Copper	8.89	0.39	3.85	1.1	$3.65 \times 10^{-3}$
Silver	10.5	0.234	4.07	1.65	$3.2 \times 10^{-3}$
Tin	7.3	0.226	0.65	0.39	$1.0 \times 10^{-3}$
Gold	19.3	0.125	2.93	1.21	$2.6 \times 10^{-3}$
Molybdenum	10.1	0.30	1.45	0.48	$2.1 \times 10^{-3}$

FIG. 10.3. Thermal constants for various materials.



pulse length should be safe. Clearly, a numerical analysis should be made when designing a long pulse device, but these figures illustrate the advantage that may be gained.

It remains to consider the cooling between pulses. In the example just given, where most of the heat is stored in copper adjacent to the active layer, the temperature decay is a simple exponential, since the thermal conductivity of copper (and of most likely heat sink materials except diamond) is temperature independent.

In that case then,

$$T - T_4 = (T_0 - T_4) e^{-Pt/J} \quad (10.6)$$

where  $J = Ql\pi a^2 t$ , is the total heat stored in the pulse, and  $P$  is the rate of flow of heat at the maximum allowed temperature  $T_0$ . If the heat is stored mainly in GaAs or diamond, then the tail of the exponential is shortened by the improved conductivity at lower temperatures.

The mean power dissipated under pulsed operation must always be less than under comparable C.W. operation as the temperature fluctuation prevents the maximum heat flow being obtained. Approximately, the mean power is appropriate to the mean temperature and the C.W. power is higher, corresponding to the peak,  $T_0$ . The greater the temperature rise in the pulse, the more non-linear must be the cooling between pulses and so the lower the mean temperature. In most cases it should be possible to maintain the mean temperature in excess of  $T_0/2$ , and for short pulses ( $< \sim 100$  nsec) the C.W. mean power can be approached.

## 10.4 CAVITIES

The essential negative resistance mechanism is very broad band and can generate power over at least an octave, and in favourable circumstances over several octaves. Gunn devices also operate at rather low impedance levels, especially when designed for pulsed operation.

These facts do present some difficulties in cavity design, in contrast to conventional microwave generators where single frequency transformer concepts can readily be used. The low impedance means that quite low  $Q$  circuits will support strong oscillations, so the designer must be careful to exclude from his cavity even weak resonances at unwanted frequencies. Moreover, the broad band capability implies that this must be true over a wide frequency range.

Coaxial cavities are well suited to satisfy these requirements and have been exploited with some success as described in Sections 10.5 to 10.7. A coaxial cavity in its (usual) lowest mode has a comparatively low impedance and can easily be designed to give no resonance below the design frequency

(except in the bias circuit which is readily damped). Apart from the device package resonances, it is possible to avoid other resonances at up to two to three times the design frequency, and it is comparatively exceptional for Gunn diodes to be so broad band that resonances would be preferred at frequencies higher than that.

This leaves the problems of the package resonances which are difficult above about 15 GHz and acute above 30 GHz.

Waveguide cavities have in general much higher impedances and  $Q$  values, and it is more difficult to suppress unwanted resonances which may occur even below the design frequency. The higher impedance usually results in weaker coupling between the device and the cavity, leaving more freedom to package and stray reactances to produce further unwanted resonances. More attention has to be paid to these factors when designing waveguide cavities and the tuning range is usually more limited than for coaxial cavities. Once the correct mode is reliably established, however, the higher  $Q$  leads to better stability and noise as described in Section 10.8.

The distinction made here between waveguide and coaxial cavities is based on loaded  $Q$ , or rate of change of reactance with frequency. Other circuits often used with Gunn diodes are stripline and YIG (yttrium iron garnet) sphere cavities. The stripline circuits are usually still lower  $Q$  than coaxial, and so are noisier and less stable, while YIG spheres usually provide very high  $Q$ , stable oscillators.

### 10.5 SMALL CONTINUOUS WAVE OSCILLATORS

Small C.W. Gunn oscillators are the most highly developed bulk solid state microwave source and are now well established in commercial production and military equipments.

#### General Purpose J-Band Local Oscillator

Frequency range	12.4 to 18 GHz
Continuous output power	5 mW c.w. min. when operated in a cavity controlled domain mode in a coaxial cavity.
Continuous input power	Not to exceed 3 Watts.
Noise	When driving a balanced mixer followed by a 60 MHz I.F. amplifier with a 20 MHz bandwidth the local oscillator noise must not degrade the overall noise factor by more than 0.1 dB.
Life	Over 5000 hours continuous.
Temperature range	-40 to +70°C.
Vibration and shock	To military standards.

FIG. 10.4. Specification of a typical local oscillator.

C.W. oscillators have been designed to meet two principal uses, initially at X-band (8–12 GHz) and later up to 50 GHz, as local oscillators and as transmitters for doppler equipment. They have been studied extensively by Warner and Herman<sup>(4,5)</sup> on whose work these sections are based, and by many industrial organisations.

Figure 10.4, shows the specification of a typical local oscillator, and Fig. 10.5 that of a doppler transmitter source.

Doppler Transmitter Source	
Frequency	13.3 GHz
Continuous output power	30 mW min when operated in a cavity controlled mode in a waveguide cavity.
Continuous input power	Not to exceed 3 Watts.
Noise	The F.M. noise power in a 70 Hz band 10 KHz away from the carrier shall be as low as possible but at least 50 dB down on the carrier. There must be no spurious coherent oscillations in the output.
Life	5000 hours continuous.
Temperature range	−40 to +70°C.
Vibration and shock	To military standards.

FIG. 10.5. Specification of low power doppler transmitter.

## 10.6 COAXIAL CAVITY

The coaxial cavity (Fig. 10.6) determines the mode of operation with little ambiguity and is therefore very suitable for a widely tuneable general purpose oscillator. An X-band cavity has inner and outer diameters of 0.28 and 1.0 cm respectively, or less, so that the lowest frequency waveguide mode allowed is 15 GHz, well outside the desired operating range. The

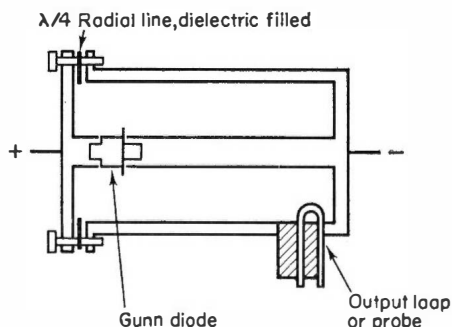


FIG. 10.6. A coaxial cavity.

length of coaxial line required to match the equivalent circuit (Fig. 5.16) is usually small and inductive, a condition which is repeated with the addition of successive half wavelengths. The cavity length chosen is just over one half wavelength and the diode position is at one eighth wavelength from one end.

A match could be found at any position in an ideal cavity, but in real cavity (with loss) the centre ( $\lambda/4$ ) is forbidden as the loss component dominates the load there presented to the diode.

Near the end of the cavity a match is also obtained at the second harmonic, but this frequency is suppressed if the diode is placed at the  $\lambda/8$  fundamental point, which is a  $\lambda/4$  second harmonic point. The lowest frequency, therefore, which may find a match is the third harmonic, and this is generally outside the favourable oscillation range of a transit time diode.

The d.c. break needed for the bias supply is provided by a quarter wavelength mica filled radial line.

The output is coupled either with a loop or a capacitive probe, and is optimised for the desired working conditions. The probe may be pushed or screwed in and out, and the loop rotated to vary the coupling. A well designed loop should permit over-coupling, that is, two peak positions should exist with the plane of the loop non-parallel to the cavity axis as shown in Fig. 10.7. The loop of internal area  $0.83 \text{ mm}^2$  was too small in this example. Equally a probe should be designed to have an optimum position which is not at one of its geometric extremes.

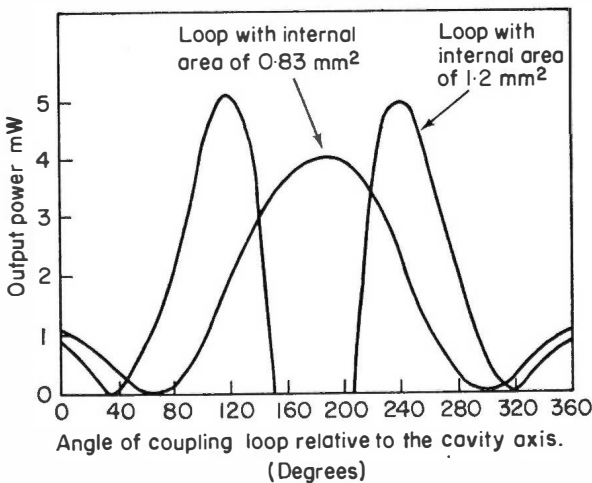


FIG. 10.7. Relative outputs from a coaxial cavity as a function of coupling loop angle for two loop sizes. The loop of area  $0.83 \text{ mm}^2$  is too small to couple optimally.<sup>(5)</sup> (Crown Copyright, published by permission of the Controller of Her Majesty's Stationery Office).

The characteristics of a diode in this cavity are shown in Fig. 10.8. The output power and efficiency jump from zero at the threshold bias level and continue to rise to the safe operating limit of this rather low power device at 7 V. The drive current shows a characteristic negative jump at the threshold for output, and a general negative trend. This is partly residual negative resistance, but mostly due to the positive temperature coefficient of resistance.

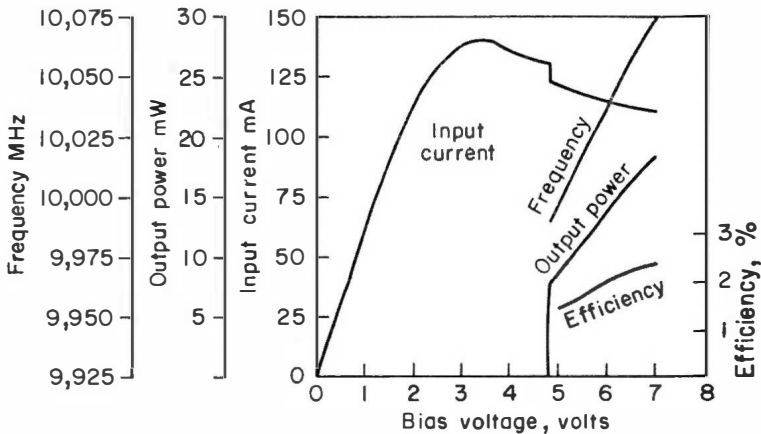


FIG. 10.8. Characteristics of a low power C. W. Gunn diode in a coaxial cavity.<sup>(5)</sup> (Crown Copyright, published by permission of the Controller of Her Majesty's Stationery Office).

The current–voltage curve for a device oscillating under pulsed drive is more nearly flat, apart from the jump.

The frequency in this case rises quite steeply with applied voltage. However, this is device and cavity dependent, and may be more nearly flat, or negative.

We remark here that modulation, either of frequency or amplitude, will not very conveniently be obtained by operating on these characteristic curves due to the severe non-linearity in the power-bias relationship, frequently much worse than Fig. 10.8, and the variability of the frequency dependence.

## 10.7 MECHANICAL TUNING OF A COAXIAL CAVITY

The cavity may be tuned by inserting a screw through the outer wall, whose inductance always lowers the frequency. This provides a rather coarse but very simple tuning mechanism and is an appropriate technique for a source with a preset frequency.

An alternative is to vary the length of the cavity by means of a choked plunger end wall. This was the technique favoured by A.S.M. Ltd., as it is very rugged, but again rather coarse.

The technique first employed, shown in Fig. 10.9, is that of sliding a dielectric washer from near one end of the cavity to its centre.<sup>(4)</sup> This gives a tuning range of up to 2 GHz for a 1 mm washer of dielectric constant 10 such as sapphire. Any desired finer range can be obtained by using lower dielectric constants and thinner washers, and the only doubt about the mechanism lies in the possible fragility of the dielectric rods which connect the washer to the tuning control. They are certainly adequate for most equipments but may be vulnerable under conditions of severe shock or vibration.

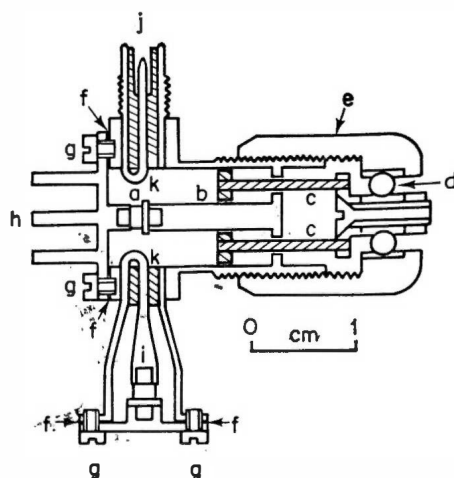


FIG. 10.9. A coaxial cavity mechanically tuned by means of a sliding dielectric washer.<sup>(5)</sup> (a) Gunn diode; (b) Alumina washer; (c) Dielectric rod; (d) Ball race; (e) Tuning knob; (f) Mica; (g) Nylon screws; (h) Copper heat sink; (i) Varactor; (j) Output connector; (k) Rotatable coupling loop. (Crown Copyright, published by permission of the Controller of H.M. Stationery Office).

The design procedure for this tuning system is as follows:

Suppose that the maximum required tuning range is from a wavelength  $\lambda_1$  to a longer wavelength  $\lambda_2$ . Let the two corresponding angular frequencies be  $\omega_1$  and  $\omega_2$ , respectively. Assume that the GaAs wafer looks like a lumped capacitance  $C$  positioned at a distance  $x$  from the left-hand end of the cavity. Let  $\epsilon$  denote the relative permittivity of the washer material and let  $Z_0$  denote the characteristic impedance of the air-filled line. First, let us consider the case when the dielectric washer is at the right-hand end, as shown in Fig. 10.10. Neglecting losses, the input reactance of the short-circuited line on the left-hand side of  $C$  is

$$jX_1 = jZ_0 \tan(2\pi x/\lambda_1) \quad (10.7)$$

and the input reactance of the short-circuited line on the right-hand side of  $C$  is

$$jX_2 = jZ_0 \frac{\varepsilon^{-\frac{1}{2}} \tan(2\pi d\varepsilon^{\frac{1}{2}}/\lambda_1) + \tan(2\pi y/\lambda_1)}{1 - \varepsilon^{-\frac{1}{2}} \tan(2\pi d\varepsilon^{\frac{1}{2}}/\lambda_1) \tan(2\pi y/\lambda_1)}. \quad (10.8)$$

The condition for resonance is that

$$jX_1 + jX_2 + (1/j\omega_1 C) = 0.$$

It follows at once from Fig. 10.10 that

$$L = x + y + d$$

From the equations above, we find, after rearrangement, that

$$L = d + x + (n\lambda_1/2) - (\lambda_1/2\pi) \tan^{-1} \{ \tan(2\pi x/\lambda_1) - (1/\omega_1 CZ_0) \} \\ - (\lambda_1/2\pi) \tan^{-1} \{ \varepsilon^{-\frac{1}{2}} \tan(2\pi d\varepsilon^{\frac{1}{2}}/\lambda_1) \} \quad (10.9)$$

where  $n$  is an integer, which is normally unity.

Let us now consider the other extreme, where the dielectric washer is centred on the voltage antinode, as shown in Fig. 10.11. It is convenient to replace capacitance  $C$  and the short-circuited line to the left of it by a straightforward short-circuited line of length  $l$ . The condition for equivalence at a wavelength  $\lambda_2$  is

$$l = (\lambda_2/2\pi) \tan^{-1} [\tan(2\pi x/\lambda_2) - (1/\omega_2 CZ_0)]. \quad (10.10)$$

The reactance at the voltage antinode, looking to the right, is

$$jZ_0 \varepsilon^{-\frac{1}{2}} \frac{\varepsilon^{\frac{1}{2}} \tan(2\pi z/\lambda_2) + \tan(\pi d\varepsilon^{\frac{1}{2}}/\lambda_2)}{1 - \varepsilon^{\frac{1}{2}} \tan(2\pi z/\lambda_2) \tan(\pi d\varepsilon^{\frac{1}{2}}/\lambda_2)} = j(\infty).$$

$$\text{Thus} \quad \varepsilon^{\frac{1}{2}} \tan(2\pi z/\lambda_2) \tan(\pi d\varepsilon^{\frac{1}{2}}/\lambda_2) = 1. \quad (10.11)$$

It follows from Fig. 10.11 and the definition of  $l$  that

$$z = \frac{L - x + l}{2} - \frac{d}{2} \quad \text{when} \quad \tan\left(\frac{2\pi x}{\lambda_2}\right) > \frac{1}{\omega_2 CZ_0} \quad (10.12)$$

and

$$z = \frac{L - x + l - (\lambda_2/2)}{2} - \frac{d}{2}$$

when

$$\tan\left(\frac{2\pi x}{\lambda_2}\right) < \frac{1}{\omega_2 CZ_0} \quad (10.13)$$

Using Eqns (10.9) and (10.10), and either (10.12) or (10.13), it is now a straightforward matter to plot a curve of  $\varepsilon^{\frac{1}{2}} \tan(2\pi z/\lambda_2) \tan(\pi d\varepsilon^{\frac{1}{2}}/\lambda_2)$  against  $d$ , for any given values of  $\lambda_1$ ,  $\lambda_2$ ,  $x$ ,  $C$ ,  $Z_0$  and  $\varepsilon$ . The two values for  $d$  at which Eqn (10.11) is satisfied are two alternative thicknesses for the dielectric washer to obtain the required tuning range. If too large a range is sought, no solutions will be found. When  $\lambda_1 = 3$  cm,  $C = 0.2$  pF,  $Z_0 = 76.9 \Omega$  and  $x = 0.4$  cm, the maximum theoretical tuning ranges are found to be 800 MHz with p.t.f.e., 1 GHz with Distrene and 2.4 GHz with sapphire.

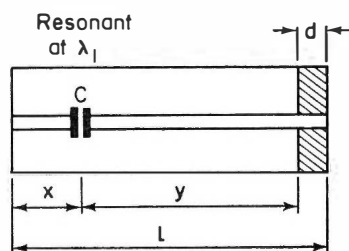


FIG. 10.10. A coaxial cavity with the dielectric tuning washer at its extreme right-hand end.<sup>(5)</sup> (Crown Copyright, published by permission of the Controller of Her Majesty's Stationery Office).

The tuning ranges obtained in practice are about 20% lower than these theoretical values. Possible reasons for this discrepancy are the finite bandwidths of the p.t.f.e.-filled choke system and the mica-filled radial lines, the omission from the theory of discontinuity reactances and over-simplifications of the equivalent circuit of the GaAs wafer.

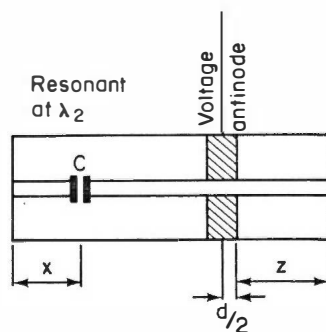


FIG. 10.11. A coaxial cavity with the dielectric tuning washer at the voltage antinode.<sup>(5)</sup> (Crown Copyright, published by permission of the Controller of Her Majesty's Stationery Office).



## 10.8 ELECTRONIC TUNING OF COAXIAL CAVITY

The cavity may conveniently be tuned electrically by means of a variable capacity diode (varactor) mounted in a separate cavity coupled to the first one. The equivalent circuit of this arrangement is shown in Fig. 10.12, and an analysis<sup>(5)</sup> is given below.

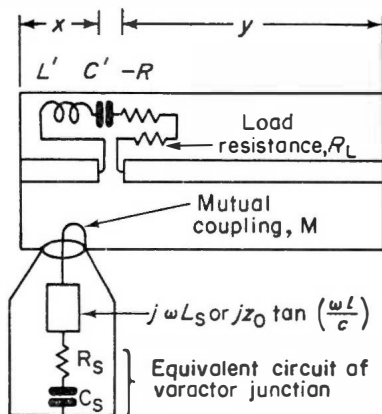


FIG. 10.12. Equivalent circuit of a Gunn diode coaxial cavity electronically tuned by means of a varactor diode.<sup>(5)</sup> (Crown Copyright, published by permission of the Controller of Her Majesty's Stationery Office).

If  $X_p$  and  $X_s$  represent the reactances of the primary and secondary circuits, the total primary impedance at an angular frequency  $\omega$  is given by:

$$Z = R_L + \frac{\omega^2 M^2 R_s}{R_s^2 + X_s^2} = R + j(X_p - X_r) \quad (10.14)$$

where

$$X_p = \omega L' - \frac{1}{\omega C'} + Z_0 \tan\left(\frac{\omega x}{c}\right) + Z_0 \tan\left(\frac{\omega y}{c}\right) \quad (10.15)$$

and

$$X_r = \frac{\omega^2 M^2 X_s}{R_s^2 + X_s^2} \quad (10.16)$$

In Eqn (10.15),  $Z_0$  denotes the characteristic impedance of the main cavity and  $c$  is the velocity of propagation. Let the cavity-controlled Gunn oscillation occur at a frequency,  $f_0$ , and angular frequency,  $\omega_0$ , at which  $X_p = X_{p0}$ ,  $X_s = X_{s0}$  and  $X_r = X_{r0}$ . Then, the condition for oscillation is seen to be:

$$X_{p0} - X_{r0} = 0. \quad (10.17)$$

Suppose now that  $C_s$  is increased to  $C_s + \Delta C_s$  and let this change cause the oscillation frequency to increase from  $f_0$  to  $f_0 + \Delta f_0$ . The condition for

oscillation now becomes:

$$X_{p0} + \left( \frac{\partial X_p}{\partial f} \right)_{f=f_0} \Delta f_0 - \left\{ X_{r0} + \left( \frac{\partial X_r}{\partial f} \right)_{f=f_0} \Delta f_0 + \left( \frac{\partial X_r}{\partial C_s} \right)_{f=f_0} \Delta C_s \right\} = 0. \quad (10.18)$$

From 10.17 and 10.18, it follows that:

$$\Delta f_0 = \frac{(\partial X_r / \partial C_s)_{f=f_0}}{(\partial X_p / \partial f)_{f=f_0} - (\partial X_r / \partial f)_{f=f_0}} \cdot \Delta C_s. \quad (10.19)$$

From (10.16) we get

$$\frac{\partial X_r}{\partial X_s} = \omega^2 M^2 \frac{(R_s^2 - X_s^2)}{(R_s^2 + X_s^2)^2}. \quad (10.20)$$

If we can assume that the inductive reactance in the secondary circuit including that of the coupling loop is provided by a lumped inductance,  $L_s$ ,

$$X_s = 2\pi f L_s - \frac{1}{2\pi f C_s} \quad \text{and} \quad \frac{\partial X_s}{\partial C_s} = \frac{1}{2\pi f C_s^2}. \quad (10.21)$$

If the side arm is large as in Fig. 10.1, we can assume that the coupling loop and the tapered line are equivalent to a shorted line of length  $l$  and characteristic impedance,  $Z_0'$ . We then have:

$$X_s = Z_0' \tan \left( \frac{2\pi f l}{c} \right) - \frac{1}{2\pi f C_s} \quad \text{and} \quad \frac{\partial X_s}{\partial C_s} = \frac{1}{2\pi f C_s^2}. \quad (10.22)$$

The loaded  $Q$  factor of the complete circuit at frequency  $f_0$  is given by:

$$Q_L = \frac{f_0 \{ (\partial X_p / \partial f)_{f=f_0} - (\partial X_r / \partial f)_{f=f_0} \}}{2(R_L + \omega_0^2 M^2 R_s / (R_s^2 + X_{s0}^2))}. \quad (10.23)$$

The fraction of the generated power which is lost in the varactor is given by:

$$\alpha = \frac{(\omega_0^2 M^2 R_s / R_s^2 + X_{s0}^2)}{R_L + \omega_0^2 M^2 R_s / (R_s^2 + X_{s0}^2)}. \quad (10.24)$$

The cut off frequency of the varactor can be defined as:

$$f_c = \frac{1}{2\pi C_s R_s}. \quad (10.25)$$

From Eqns (10.19), (10.20), (10.22), (10.23), (10.24), (10.25),

$$\Delta f_0 = \frac{\alpha f_c}{2Q_L} \cdot \frac{\Delta C_s}{C_s} \cdot \frac{R_s^2 - X_{s0}^2}{R_s^2 + X_{s0}^2}. \quad (10.26)$$

The last term in this equation is equal to +1 when  $X_{s0} = 0$  and -1 when  $|X_{s0}| \gg R_s$ . A matter of considerable interest is the variation in  $\Delta f_0$  as  $f_0$  is varied by the mechanical tuner, which changes the effective value of  $y$ . If

$$\frac{\omega_0^2 M^2 R_s}{R_s^2 + X_{s0}^2} \ll R_L,$$

eqn (10.26) can be simplified to:

$$\Delta f_0 = K \left( \frac{\omega_0}{\omega_r} \right)^2 \cdot \frac{R_s^2 - X_{s0}^2}{(R_s^2 + X_{s0}^2)^2} \quad (10.27)$$

where  $\omega_r$  is the angular frequency at which the secondary circuit is resonant and

$$K = \frac{\omega_r^2 M^2 R_s f_c}{2Q_L R_L} \cdot \frac{\Delta C_s}{C_s}. \quad (10.28)$$

Figure 10.13 shows how  $\Delta f_0$  varies with  $f_0$  for different values of  $K$  and two different side arm configurations. In order to keep  $\Delta f_0$  reasonably constant as  $f_0$  is varied, it can be seen that

- (i) a lumped circuit side arm should be used;
- (ii) resonance in the side arm should be arranged to occur at a frequency below the bottom end of the mechanical tuning range.

Experimental results obtained with a side arm, which was slightly longer than one wavelength and resonant at 9.8 GHz show that Eqn (10.26) is

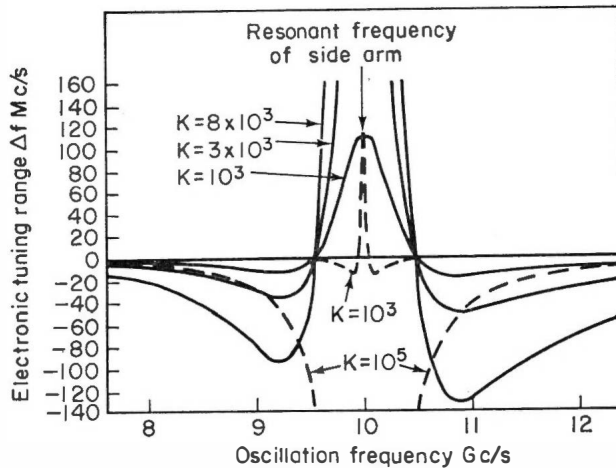


FIG. 10.13. Variation of  $\Delta f_0$  with  $f_0$  for different varactor side arm conditions.<sup>(5)</sup> (Crown Copyright, published by permission of the Controller of Her Majesty's Stationery Office).

essentially correct (see Fig. 10.14). The three different curves in this diagram were obtained by setting the varactor coupling loop at different angles to vary  $K$ .

The analysis given above is only accurate for very small changes in  $C_s$ . A lengthier treatment of this problem, for the case of special interest where  $X_s \gg R_s$ , shows that:

$$\Delta f_0 = - \frac{f_{co}}{2Q_{L0}} \frac{(C_0 - C_v)}{C_v} \frac{(P_1 - P_2)}{P_1} \quad (10.29)$$

where  $f_{co}$  is the varactor cut-off frequency with zero bias,  $Q_{L0}$  is the loaded  $Q$  factor with zero bias,  $C_0$  is the varactor capacitance with zero bias,  $C_v$  is the varactor capacitance when a reverse bias voltage,  $V$ , is applied to it,  $P_1$  is the power output with zero coupling into the varactor side arm and  $P_2$  is the power output with zero bias on the varactor and the value for  $M$  that gives the frequency change  $\Delta f_0$ .

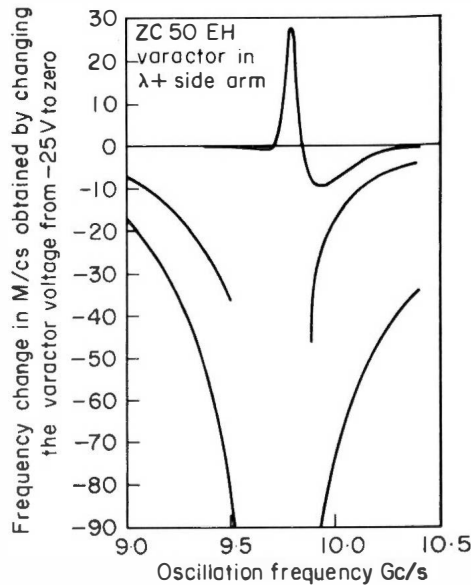


FIG. 10.14. Variation of  $\Delta f_0$  with  $f_0$  for various values of side-arm coupling.<sup>(45)</sup> (Crown Copyright, published by permission of the Controller of Her Majesty's Stationery Office).

Figures 10.15 to 10.18 show some experimental results which were obtained with ZC50EH varactor mounted in a lumped circuit side arm. With a change from  $-1$  V to zero on the varactor it can be seen from Figs. 10.15 and 10.16 that  $f = 162$  MHz,  $P_1 = 14.4$  mW and  $P_2 = 7.9$  mW. From the data for the particular varactor used in this experiment, it is estimated that:

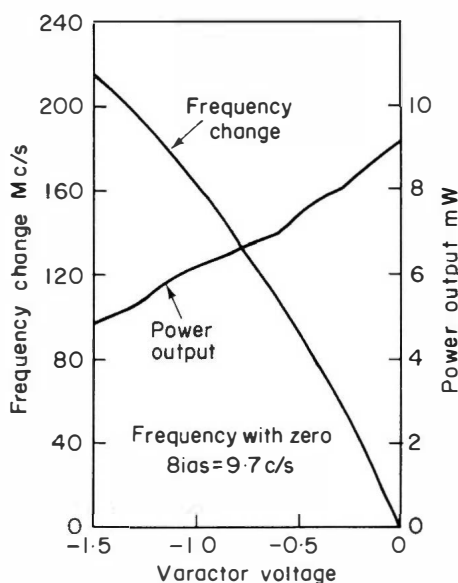


FIG. 10.15. Electronic tuning curves for a ZC50EH varactor in a lumped circuit side arm.<sup>(5)</sup> (Crown Copyright, published by permission of the Controller of Her Majesty's Stationery Office).

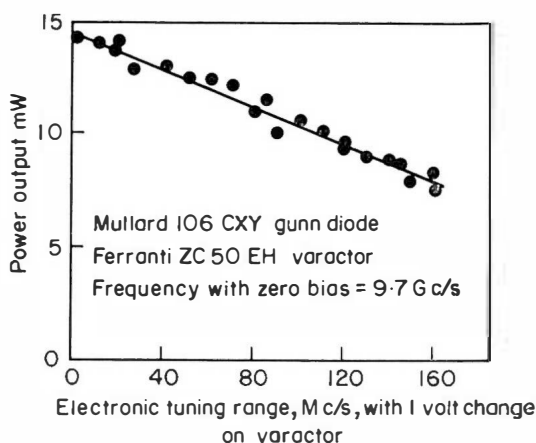


FIG. 10.16. The reduction in output power as the electronic tuning range is increased by increasing the side-arm coupling.<sup>(5)</sup> (Crown Copyright, published by permission of the Controller of Her Majesty's Stationery Office).

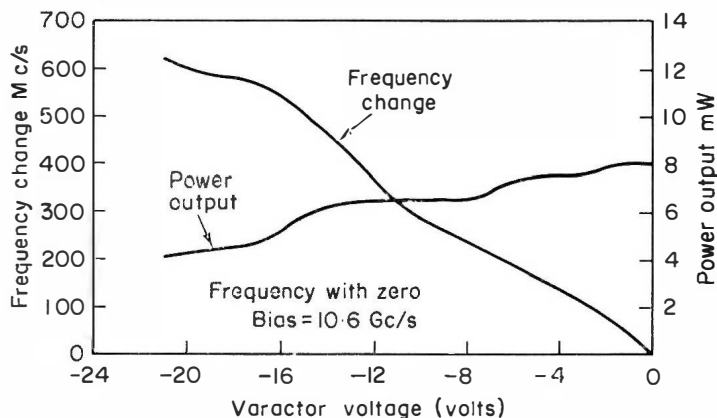


FIG. 10.17. A tuning range of over 600 MHz for a ZC50EH varactor in a lumped circuit side-arm.<sup>(5)</sup> (Crown Copyright, published by permission of the Controller of Her Majesty's Stationery Office).

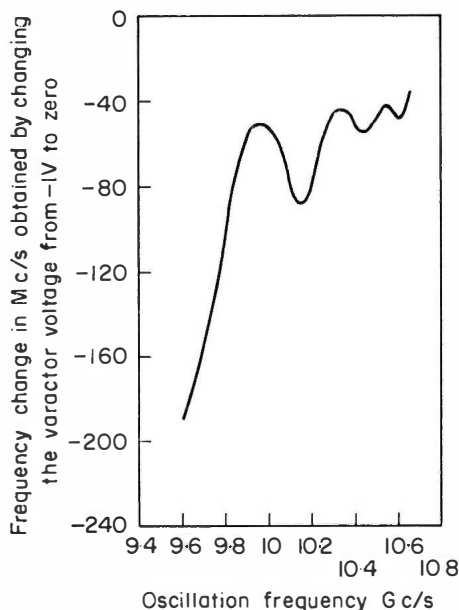


FIG. 10.18. Variation of tuning range with oscillation frequency for a ZC50EH varactor in a lumped circuit side-arm.<sup>(5)</sup> (Crown Copyright, published by permission of the Controller of Her Majesty's Stationery Office).

$f_{co} = 75 \text{ GHz}$  and  $(C_0 - C_v)/C_v = 0.37$ . With these values, a loaded  $Q$  factor of 39 is necessary for Eqn (10.29) to be satisfied. Loaded  $Q$  factors very close to this value have been deduced from pulling experiments on these miniature oscillators so the agreement between theory and practice appears to be very satisfactory.

An electronic tuning range of over 600 MHz is shown in Fig. 10.17 and the largest range obtained with this system is over 800 GHz. Tuning ranges of over 1 GHz have been obtained at 3 GHz in a stripline cavity<sup>(6)</sup>, and at 14 GHz in a waveguide cavity<sup>(7)</sup> using varactor diodes, despite the difficulty of varying the coupling in such cavities.

### 10.9 ELECTRONIC TUNING WITH A YIG SPHERE

YIG (yttrium iron garnet) sphere cavities have rather high  $Q$  values and give very stable output, but the principal reason for their use lies in the tuning that can be achieved by varying the static magnetic field in which the resonant sphere lies.

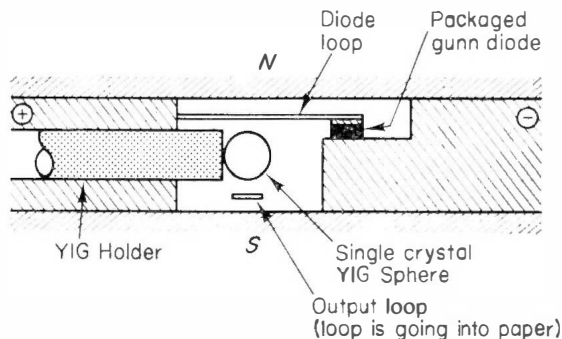


FIG. 10.19. Cross sectional view of a YIG-tuned Gunn oscillator circuit.<sup>(8)</sup>

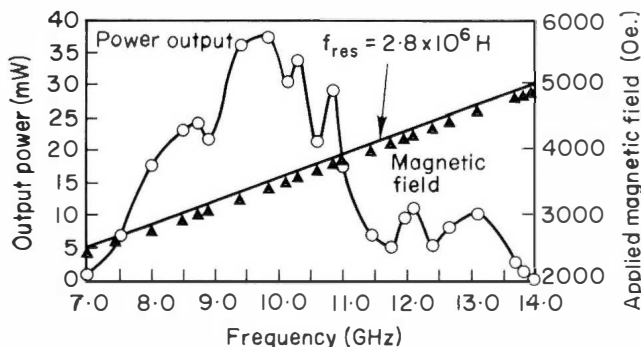


FIG. 10.20. Measured power output and applied magnetic field as functions of frequency for a YIG-tuned cavity.<sup>(8)</sup>

Figure 10.19 shows a YIG sphere cavity designed by Omori<sup>(8)</sup>. The diode loop and output loop are orthogonal so that there is zero coupling in the absence of the YIG sphere. The resonant frequency of the sphere follows the relation

$$f = 2.8 \times 10^6 H \text{ (Hz)} \quad (10.30)$$

where  $H$  is the applied magnetic field in oersteds, and Fig. 10.20 shows how closely the experimental results follow this relation. Due to stray resonances the power variation is not very smooth in this example, but Fig. 10.21 shows an excellent curve obtained when this has been remedied.

The coupling through the YIG sphere is rather weak, less than that needed for optimum power, and this of course enhances the already good stability and noise.

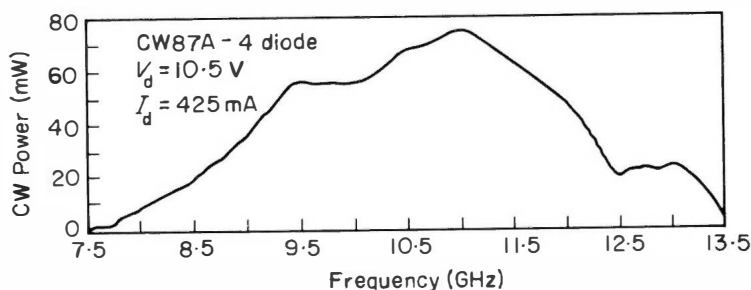


FIG. 10.21. Power output as a function of frequency for a YIG-tuned cavity.<sup>(8)</sup>

## 10.10 STABILITY, NOISE AND TEMPERATURE EFFECTS

These three properties are taken together as they are rather closely linked. The chief cause of frequency variation in a Gunn oscillator is change in the effective capacity of the diode. Random fluctuations of about one part in  $10^5$  lead to f.m. noise; its very variable temperature dependence leads to an overall frequency temperature coefficient between  $+0.5$  and  $-3.0 \text{ MHz/}^\circ\text{C}$  and a long term stability of about  $\frac{1}{2} \text{ MHz/hr}$  if there is no stabilisation (see Fig. 10.22).

These rather unsatisfactory features must be related to the cavity in which the diode operates, as they are highly dependent upon its parameters. The figures were obtained for the miniature coaxial cavity of Fig. 10.6. This cavity, although controlling very well the selection of the mode in which the diode operates, is sensitive to its capacity. If a cavity is chosen in which the rate of change of reactance with frequency is very large, then the effects of variations in the reactance of the diode are correspondingly small<sup>(9)</sup>.



As discussed in Chapter 8, the f.m. noise of a Gunn diode can in this way be reduced to a value comparable with that of a good free running klystron. A moderately long waveguide cavity, with  $2\lambda_g$  between the diode and the short-circuit, works well. For precisely the same reasons the temperature coefficient and long term stability are also greatly improved as compared with the miniature coaxial cavity. The temperature coefficient of a Gunn oscillator in a  $2\lambda_g$  waveguide cavity differs by only up to about  $50 \text{ kHz}/^\circ\text{C}$ , from that of the cavity itself, in the range  $-40$  to  $+70^\circ\text{C}$ . The long term stability in a waveguide mode cavity is shown in Fig. 10.23. This cavity was not temperature stabilised, and it may be seen that the frequency follows the temperature variations of the laboratory over two and a half days.

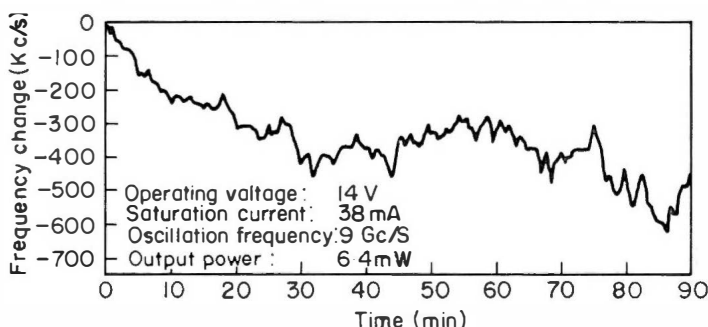


FIG. 10.22. Long term frequency stability of a Gunn oscillator in a coaxial cavity.<sup>(5)</sup> (Crown Copyright, published by permission of the Controller of Her Majesty's Stationery Office).

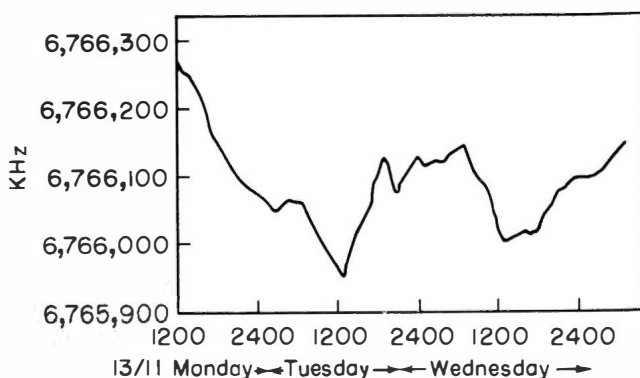


FIG. 10.23. Long term stability of a Gunn oscillator in a waveguide cavity.<sup>(9)</sup> (Crown Copyright, published by permission of the Controller of Her Majesty's Stationery Office).

### 10.11 MODULATION

Gunn oscillators may readily be modulated although good fidelity will not easily be achieved by operating on the characteristic curves themselves, due to their non-linearity and the variation from device to device.

Frequency modulation can clearly be accomplished by using the varactor tuning capability such as Fig. 10.15. This curve is reasonably linear and exceedingly high modulation frequencies are achievable as the varactor capacity presents a trivial load to a drive circuit.

Amplitude modulation is more complex as envelope feedback must generally be employed to achieve good fidelity.<sup>(10)</sup> The technique is shown in Fig. 10.24. The bias to the Gunn diode is the output of a differential amplifier, whose inputs are the desired modulating signal and an envelope feedback signal obtained from a detector diode coupled to the transmitter cavity. The degree of coupling is very small to ensure that the detector is operating in its square law regime, as does the receiver detector.

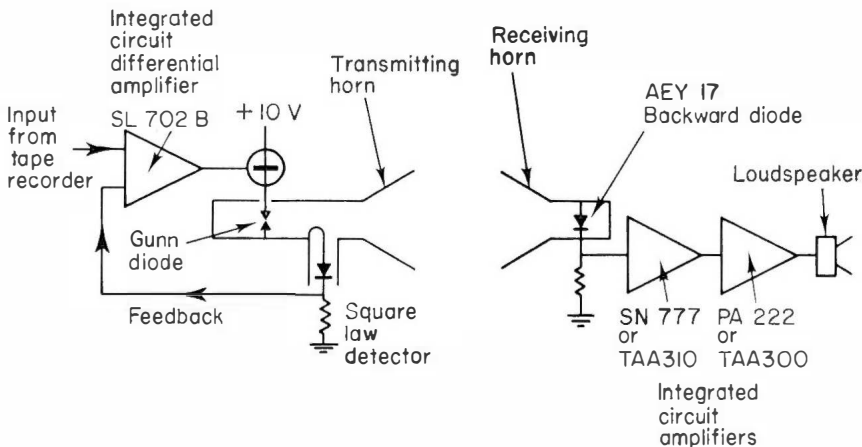


FIG. 10.24. An amplitude-modulated communication link employing envelope feedback on the transmitter.<sup>(10)</sup> (Crown Copyright, published by permission of the Controller of Her Majesty's Stationery Office).

An alternative technique is the use of pulse width or pulse code modulation. Gunn diodes can generate extremely narrow microwave pulses<sup>(11)</sup> and in Fig. 5.28 is shown a 3 nsec pulse of 1.6 W at 14 GHz. The rise time is about 1 nsec and the maximum pulse length, as determined by thermal effects in Section 10.2, would be about 1  $\mu$ sec. Thus, very precise pulse width modulation or rapid pulse code modulation (over 100 Mega bits/sec) is possible.

## 10.12 FREQUENCY LOCKING—MULTIPLE DEVICES

To meet the demands for higher powers, various attempts are being made to combine the outputs of many devices in a coherent manner. While it is difficult to define precisely what is meant by a single device, a simple convention is that one microwave package or encapsulation constitutes a

device. This has some merit in that the contents of a package, which may indeed be several parallel or series elements, usually are made from the same piece of material and phase lock together without any external aid. Devices have also been operated very successfully in series<sup>(12)</sup> but again this almost brings us back to a single source. It is in a distributed combination of many devices that the real interest lies, for in principle there is no limit to the total power that may be obtained.

Rather little has yet been achieved in this area; most of the studies have been of phase locking essential to give a coherent source.<sup>(13, 14)</sup>

The readiness with which a device can be phase locked can be characterised by a figure of merit  $\eta$  defined as

$$\eta = \frac{2\Delta_0}{\omega_0} \left( \frac{P_0}{P_L} \right)^{\frac{1}{2}} \quad (10.31)$$

where  $P_0$  is the output power of the device which would run freely at a frequency  $\Delta_0$ , and  $P_L$  is the power required to be injected to shift the frequency by  $\Delta_0$  to  $\omega_L$ .

An average value for  $\eta$  for  $X$ -band Gunn diodes is 0.016, which means that for  $P_L/P_0$  of  $-35$  dB the frequency can be shifted by about 1 MHz.<sup>(14, 15)</sup>

Unfortunately  $\omega_0$  is dependent on bias voltage and temperature to an extent which varies appreciably from device to device. This means that a distributed combination of devices would tend to break up into their component frequencies when subjected to even moderate temperature excursions unless heavy locking signals were applied. This is one of the main problems in combining devices on a large scale. The other major difficulty is to avoid breakdown of devices in the large microwave fields which could be generated.

### 10.13 OPERATION AT 1 TO 8 GHz

The operation of Gunn devices at frequencies below  $X$ -band raises a number of difficulties in obtaining the appropriate parameter values.

At 1 GHz, for example, the appropriate transit dimension is  $100 \mu\text{m}$  and the carrier concentration about  $10^{14} \text{ cm}^{-3}$ , although output can be obtained from  $50 \mu\text{m}$  samples. Until about 1968, these parameters could be achieved only in bulk material, which is usually a compensated crystal with shallow donor density ( $0.21 \text{ eV}^{(16)}$ ) and a higher defect density than epitaxially grown GaAs. The shallow donors lead to a negative temperature coefficient of resistivity, and there is some evidence that the defects promote rapid migration of contact metals (especially tin). Both these factors encourage device failure, and most experiments were carried out at very low duty cycles to avoid large temperature rises.

In 1968 a number of laboratories developed liquid epitaxy to yield uniform layers of about  $100\text{ }\mu\text{m}$  with carrier concentrations as low as  $10^{13}\text{ cm}^{-3}$  and at the same time vapour phase work was being extended to produce thicker layers with lower concentrations than the familiar X-band material.

Apart from the material, the change of scale raises more fundamental differences from X-band operation. The most important are thermal. We saw in Section 10.1 how important is the length of the heat-flow path in the active layer, and longitudinal geometry at 1 GHz brings this home acutely. For  $10\text{ }\Omega\text{cm}$  material,  $100\text{ }\mu\text{m}$  thick, working at even 1.5 times the threshold field, the upper surface temperature would be  $470^\circ\text{K}$  for a heat sink at  $300^\circ\text{K}$ . It is possible to obtain continuous operation as low as 2 GHz, and despite competition from transistors commercial success has been achieved.

If the geometry is changed to a transverse structure in which the heat flows perpendicularly to the electric field, some improvement may be obtained. This requires a good bond to a high thermal conductivity dielectric such as beryllia or diamond, and little has been achieved in this direction so far. Transverse operation in epitaxial layers on insulating GaAs is not very useful in this respect as the GaAs is such a poor thermal conductor.

The other major thermal effect is on pulse length. The appropriate resistivities at 1 GHz are ten times lower than at 10 GHz so that the power densities are lower and the possible lengths ten times greater on an adiabatic basis. The poorer heat sinking implies that little advantage will be obtained from thermal diffusion into the heat sink, as a means of increasing the pulse length.

For these reasons, the bulk of the work at 1–2 GHz has been with adiabatic pulse lengths. Under these conditions, peak powers of over 1 kW have been achieved<sup>(17)</sup> with efficiencies up to 29%.<sup>(18)</sup>

#### 10.14 DRIVE REQUIREMENTS

The input power requirements for Gunn oscillators are generally low and very convenient by conventional microwave standards.

Low power X and J(Ku) band C.W. devices usually dissipate about 1 W at 7 to 20 V, depending on the resistance. More ambitious devices may dissipate up to 20 W even on copper heat sinks<sup>(19)</sup>.

There is no difficulty in supplying these requirements from transistorised sources or from batteries for the lower powers. The only precaution that is necessary is the provision of a damping circuit to prevent bias circuit oscillations generated by the residual negative resistance which an oscillating

Gunn diode frequently presents. A capacitor or capacitor resistor chain in parallel with the active device is sufficient.

The drive requirements for pulsed devices are again readily met by transistor pulse generators. Typically a 10 W output X-band device would require a drive of up to 200 W at 20 to 50 V. The fastest rise times are achieved with avalanche transistors, or for laboratory work mercury wetted switches. Fig. 10.25 shows a 70 V 6 A pulse with a 1 nsec rise time generated by an RT.3333 avalanche transistor.<sup>(11)</sup>

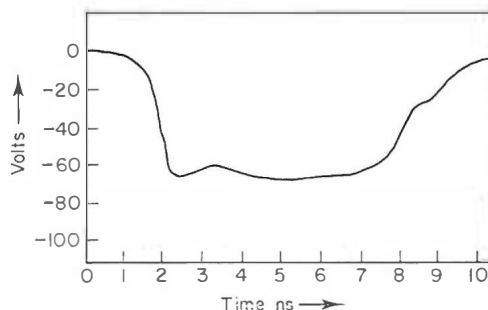


FIG. 10.25. A driving pulse of 70 V, 6 A, and a rise time of 1 nsec, generated by an RT.3333 avalanche transistor. The trace is 10 nsec long. (Crown Copyright, published by permission of the Controller of Her Majesty's Stationery Office).

There is some merit in using charge limited pulse generators such as switched delay lines, especially for laboratory work. It is comparatively easy to drive Gunn generators into avalanche breakdown during evaluation; indeed, if this is not done it is impossible to know whether maximum power has been obtained. Provided the pulse length is not too long ( $\sim < 100$  nsec) and the delay line impedance is matched to within a factor of two, the avalanche breakdown will not damage the device and the breakdown condition can be examined as a function of microwave load and driving power. This fortunate circumstance is a consequence of the fact that a perfect delay line pulse generator dissipates all its energy in the load whether matched or not. If the match is good the energy is absorbed as a single clean pulse, whereas a mismatch simply produces a train of reflections which ultimately is absorbed in the load. Any mismatch does of course imply that more energy is supplied to the device than is necessary for correct operation on the first pulse, and should be avoided under critical conditions. All this does not, nevertheless, mean that devices may be driven to avalanche with impunity, except for short pulses. The electric field distribution may be very non-uniform and lead to severe local heating, even though the average power density is no greater than when operating normally. It is clearly safer to use a delay line whose impedance is too high rather than too low, in order

to limit the current and hence the local heating under avalanche conditions.

Conventional pulse generators such as transistor power switches should again preferably be matched to the Gunn diode, rather than being voltage sources as is frequently the case, if they are used in experimental equipment or in the laboratory.

### 10.15 MINIATURE DOPPLER SYSTEMS

The simplicity of Gunn diode microwave generators has prompted the development of a new generation of miniature doppler radars. While the principles were not new and the systems could have been built with vacuum tubes in the past, as indeed speed meters were, the possibilities of miniature systems operating on low power voltage sources, such as torch batteries, have proved most attractive.

The simplest doppler system, used as a burglar alarm, is shown in Fig. 10.26. The generator and detector diodes are mounted across the same waveguide and a simple horn is used as a common transmitter and receiver aerial.<sup>(20)</sup> This arrangement is acceptable at low power levels such that the detector diode is not over-loaded by the transmitter. The detector or mixer diode is connected to a low noise low frequency amplifier capable of responding to the lowest doppler frequency of interest. At 10 GHz the doppler frequency is 33.3 Hz per knot of relative velocity, so for a burglar alarm the amplifier must respond to frequencies as low as a few Hz. Placing both transmitter and receiver in the same waveguide, while very cheap, is not the most sensitive system since under optimum conditions the detector must be adjusted to absorb half the power both for transmission and reception, hence the overall sensitivity is one quarter (6 dB down) of the ideal.

This may be improved either by using a duplexer or more commonly a separate transmitter and receiver horn. Such a system can give a detection range of fifty yards for a man and has been exploited on a large scale for burglar alarms.

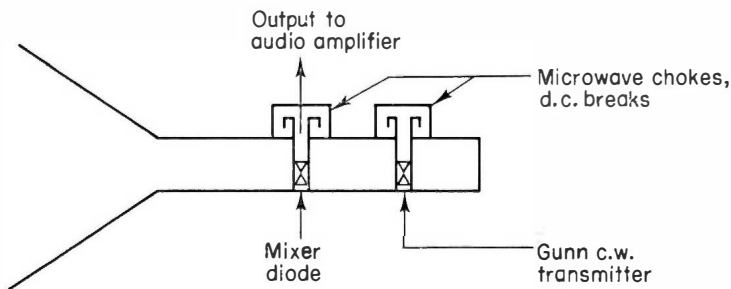


FIG. 10.26. A simple Gunn diode doppler radar, suitable for a burglar alarm or speed meter.

F.M. noise is not a serious problem with such short range equipment even though the noise is pronounced at low modulation frequencies. For a target at say fifty feet it is the frequency shift in 100 nsec that matters, so the F.M. noise suppression at low frequencies is very substantial.

There is some advantage in separating the receiver and transmitter by a large distance so that their beams overlap only in the desired protected area. This bistatic arrangement allows higher transmitter power to be used without over-loading the detector, it removes the extremely sensitive area near a common transmitter/receiver in which false alarms may be generated by birds, rodents or even insects, and it ensures that the reference signal to the receiver has much the same delay as any doppler shifted signal, and hence further reduces the effects of f.m. noise. It becomes, in fact, a clutter locked moving target indicator (M.T.I.).

A more refined doppler radar is the speed meter such as the klystron powered units which have been used for traffic control for some years. The use of Gunn generators allows a great reduction in size and some hand held "speed torches" have been made.<sup>(20)</sup>

They are basically the same as the burglar alarm except that counting circuits are included to measure the doppler frequency and display it as a speed. Targets are usually rather larger and the doppler frequencies higher than for the burglar alarm, so that the loss associated with mounting the detector in the waveguide can be tolerated.

These, and more sophisticated equipment, are used to measure speeds in industrial processes and marine pilotage as well as in traffic control.

## 10.16 PRECISION RANGING RADARS

High precision ranging has in the past usually been accomplished by phase measurement or frequency modulation techniques. Both methods are, of course, available with Gunn generators and indeed rather large frequency sweeps (1 GHz or so) have been obtained. However, the short pulse capability shown in Fig. 5.28 has improved pulsed ranging resolution to 0.5 m or less and a number of precision ranging requirements can be met with pulse techniques. This is particularly important where multiple targets are to be examined as the data processing involved in an f.m. radar is then rather costly. The chief cost in a short pulse radar is the wide band amplifier which must be used in the receiver, however, the pace of development in that field is very rapid and amplifiers with bandwidths of several hundred megahertz are now readily available.

For resolution down to about 0.5 m then, especially for multiple target evaluation, the pulsed technique is very attractive, while for better resolution down to a few inches, or where only single targets are involved, the f.m.

technique may be preferred. This broad statement is only a guide line of course and some impressive multiple target f.m. radars have been built<sup>(21, 22)</sup> using Gunn generators.

### 10.17 SHORT PULSE RADAR

As an example of the potentialities of the short pulse techniques, a high resolution pulse radar is discussed.

The block diagram shows a standard layout for a radar (Fig. 10.27). The transmitter is a Gunn diode generating 5 W at 14 GHz with a rise-time of 1 nsec and a pulse width of 3 nsec, driven by an avalanche transistor. The power passes through a circulator to the aerial and the receiver arm leads to a balanced mixer through a blanking diode switch. The blanking diode prevents transmitter break-through, which would paralyse the receiver for about 30 nsec and prevent the examination of near targets, which is one of the virtues of the system. The total energy in a pulse of 15 nJ (0.15 ergs) might damage the mixer if applied directly, but the leakage past the circular would not; the blanker is not therefore necessary if near targets are not to be examined.

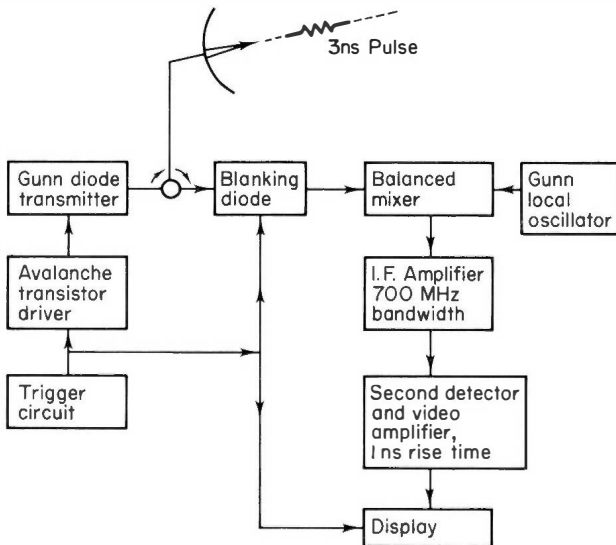


FIG. 10.27. Block diagram for a high resolution short pulse radar.

The local oscillator is another Gunn Diode and the intermediate frequency amplifier must have a pass band of 700 MHz for best resolution—although for best signal to noise 350 MHz would be appropriate. The video amplifier needs a rise time of 1 nsec and must drive 20 to 50 V to a display



if this is an intensity modulated cathode ray tube such as a P.P.I. In order to achieve adequate brightness a rather high repetition frequency is necessary in order to integrate sufficient energy per spot on the screen from the short pulses. This is acceptable as the radar would be essentially a short range device—out to about 200 m on a  $1 \text{ m}^2$  target with a 0.5 m diameter aerial.

### 10.18 SHORT PULSE TRANSPONDERS

The small size of Gunn generators enables very compact pulse transponders to be made.

Transponders usually require wide beam angles, so simple separate transmitter and receiver aerials may be used with advantage.

The receiver may have either a superheterodyne or video detector followed by a suitable amplifier the output of which triggers the avalanche transistor pulse generator. This drives the transmitter diode which feeds the second aerial.

A marine transponder generating a 5 W, 20 nsec wide transmitter pulse, for example, has a superheterodyne receiver and gives a range of over 3 km

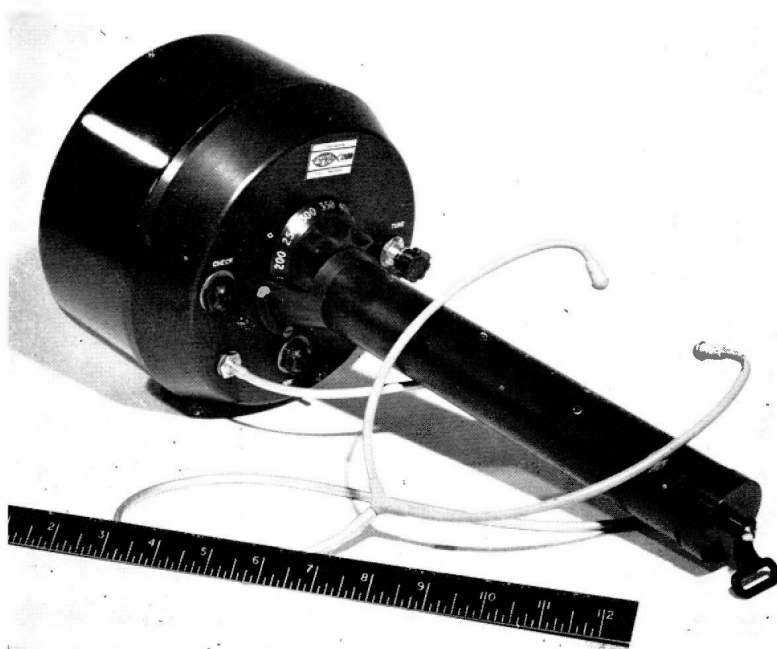


FIG. 10.28. A small portable radar torch (SPRAT) developed at the Royal Radar Establishment.<sup>(24)</sup> (Crown Copyright, published by permission of the Controller of Her Majesty's Stationery Office).

in association with a short pulse radar of similar power. The pulse separation timing circuits do, of course, need to be of adequate accuracy for such good resolution over a long range. Precision ranging with an accuracy of approximately 15 cm has in this way been extended to several kilometres. At greater ranges propagation is likely to introduce errors worse than this in many locations, but except in very special situations such accuracy at longer ranges is unlikely to be needed.



FIG. 10.29. SPRAT in use. (*Crown Copyright, published by permission of the Controller of Her Majesty's Stationery Office*).

## 10.19 BEACONS

An application to which solid state generators are well suited is that of a beacon for navigation, especially in marine use.

A particularly attractive example has been developed for placing on buoys.<sup>(23)</sup> This employs a multi-dipole aerial to restrict the beam in the vertical plane and give wide coverage in the horizontal. The whole assembly is made in microstrip using a microstrip Gunn oscillator cavity and a ferrite microstrip circulator, which results in a most compact microwave circuit. The receiver is a video detector employing integrated circuits mounted on the reverse side of the microstrip board. This type of navigational aid is required to generate 100 mW pulses 18  $\mu$ sec in duration, an exacting requirement for early Gunn diodes as the temperature rises nearly to the C.W. The frequency has to lie within a marine radar receiver bandwidth ( $\sim 5$  MHz) for the duration of an aerial rotation while being swept slowly through the entire allocated band (9.3 to 9.5 GHz) in about 1 minute.

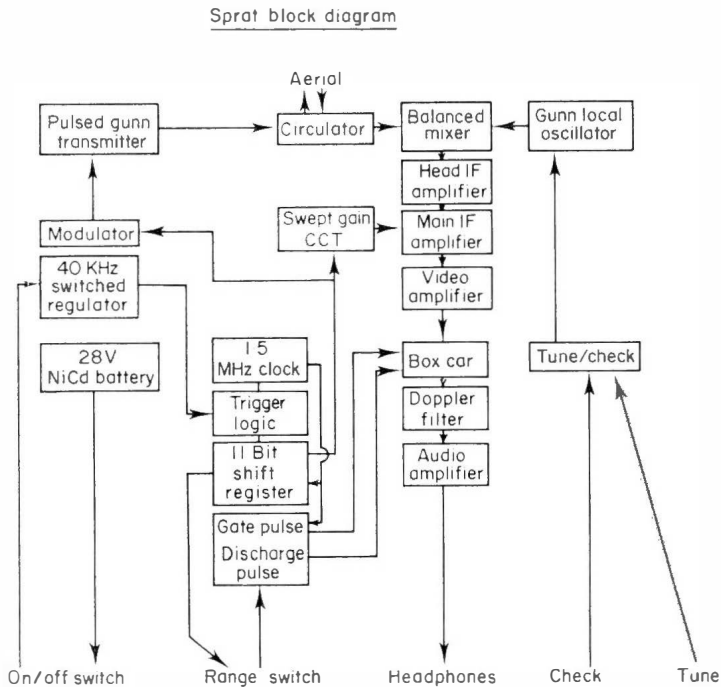


FIG. 10.30. A block diagram of SPRAT. (Crown Copyright, published by permission of the Controller of Her Majesty's Stationery Office).

## 10.20 SPRAT

A Small Portable Radar Torch (SPRAT) was developed at the Royal Radar Establishment as an experimental hand held ground surveillance radar. It is included here as an example of the way in which Gunn oscillators and careful system designs have made it possible to make a remarkably small yet high performance battery operated radar.<sup>(24)</sup>

Figure 10.28 is a general view of the equipment and it is shown in use in Fig. 10.29.

The equipment uses a Gunn diode transmitter generating about 3 W peak, 30 mW mean power in quarter microsecond pulses at a 40 kHz repetition rate. The receiver is a 60 MHz I.F. superheterodyne using a Gunn local oscillator and the whole system consumes less than 5 W from its battery.

Moving targets are detected by mixing the doppler shifted signals with echoes from fixed (clutter) targets at the same range and feeding the audible doppler signal so obtained to head-phones. The P.R.F. is sufficiently high to be above the limit of hearing and so does not interfere. Range is determined by means of a manually switched 50 m range gate which can be

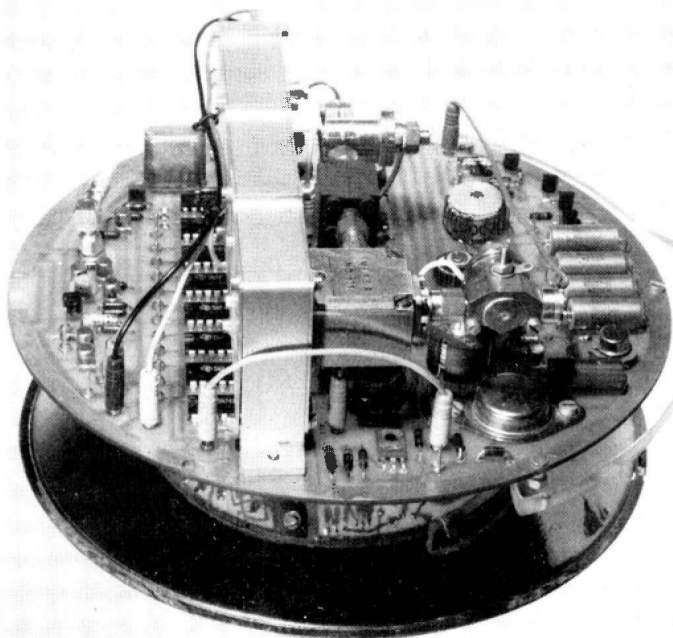


FIG. 10.31. The microwave and signal processing circuits of SPRAT. (Crown Copyright, published by permission of the Controller of Her Majesty's Stationery Office).

placed as desired in the range 25 to 625 m. Figure 10.30 shows a block diagram of the equipment and Fig. 10.31 shows that the use of integrated circuits and solid state microwave sources has yielded a most compact system.

The beamwidth is  $10^\circ$  and it is possible to locate a target with a directional accuracy of  $\pm 2^\circ$ .

Although both the local oscillator and transmitter diodes are operated in coaxial cavities, their f.m. noise is not a serious limitation. The f.m. noise suppression introduced by a 50 metre range gate is very substantial and there is only a small contribution to the system noise.

## REFERENCES

1. Knight. (1967). *Proc. I.E.E.E.* **55**, 112-3.
2. Carlson, R. O. *et al.* (1965). *J. Appl. Phys.* **36**, 505-7.
3. Swan, C. B. *et al.* *I.E.E.E. Trans.* **ED-14**, 584-9.
4. Warner, F. L. and Herman, P. (1966). *Electron. Lett.* **2**, 467-8.
5. Warner, F. L. and Herman, P. (1967). "Proc. Cornell Conf. High Frequency Generation and Amplification", pp. 206-217, RRE Memo 2394.
6. Pearson, A. Private communication.
7. Lee, B. K. and Hodgart, M. S. (1968). *Electron. Lett.* **4**, 240-2.
8. Omori, M. (1969). *Proc. I.E.E.E.* **57**, 97.
9. Court, W. P. N. *et al.* (1967). *Electron. Lett.* **12**, 567-9.
10. Warner, F. L. Private communication.
11. Bulman, P. J. Private communication.
12. Baughan, K. M. and Myers, F. A. *Electron. Lett.* **5**, 371-2. (1969)
13. Stover, H. L. (1966). *Proc. I.E.E.E.* **54**, 310-311.
14. Holliday, H. R. (1970). *I.E.E.E. Trans.* **ED-17**, 527-533.
15. Judd, S. V. and Hewitt, S. J. (1967). *Electron. Lett.* **3**, 107-8.
16. Heeks, J. S. Private communication.
17. Heeks, J. S. Private communication.
18. Stertzer, F. (1968). *Microwaves* **7**, 45-53.
19. Bass, J. C. Private communication.
20. Draysey, D. W. Private communication.
21. Edwards, J. A. and Withers, M. J. Private communication.
22. Marks, R. C. Private communication.
23. Dennison, E. and Spilling, J. S. (1969). Lab. note 69-9, Admiralty Surface Weapons Establishment, Portsmouth.
24. Skinner, J. M. *et al.* (1972/73). To be published in *Radio*.
25. Irvine, T. F. and Hartnett, J. P. (1964). *Advances in Heat Transfer* **1**, 258. Academic Press, New York.
26. Jackets, A. E., Levy, M., Rathbone, R. and Fairhurst, J. G. (1964-5). Annual Reports on CVD contract RP6-13 at A.S.M. Ltd., Wembley, England.

## *Chapter 11*

# **Material Growth and Device Fabrication**

### 11.1 INTRODUCTION

The previous Chapters have assumed the existence of a GaAs device with two terminals and characterised by a high value of low field mobility, and a peak/valley ratio of about 2·3 at room temperature. Operation of this device at a particular frequency and in a particular mode required it in addition to have particular values of carrier concentration and thickness. Given these values then (as an oscillator) the device would exhibit an efficiency around 30% when placed in a suitable circuit.

Someone has to grow the basic material and make this device, however, and somewhere along the line he goes wrong (if we are to judge by all but a few exceptional device results). Not only are high efficiencies rarely obtained in practice, but it may not always be possible to produce a device having the required carrier concentration and thickness.

This Chapter provides some insight into the difficult areas of material growth and device fabrication. In the first part we outline various methods available for the growth of the starting material, indicating what material parameters are typically available from the different methods, and how these parameters are in fact measured. In the second part of the chapter the techniques for making contact to the material and the processes involved in the mass production of devices are described.

### 11.2 GROWTH OF BULK GALLIUM ARSENIDE

Bulk GaAs is grown by freezing the molten material at 1242°C into a single crystal structure, free from chemical contaminants and structural defects. Difficulties associated with the material preparation arise largely from its high melting point and the fact that one of its constituents (arsenic) is volatile—the dissociation pressure of As at the melting point of the compound is 1·0 atm.<sup>(1)</sup> Growth from a stoichiometric melt without As loss can thus only be achieved if this external vapour pressure is provided. In practice this

is usually done by holding the system, apart from the melt, at a temperature of  $610^{\circ}\text{C}$ —the temperature at which the vapour pressure of arsenic is the 1 atm required. Two methods of growth are in common use, the Horizontal Bridgman and the Czochralski methods. Two versions of the latter method exist. The more recent one involves a technique known as liquid encapsulation and this will be described in a separate section.

### 11.2.1 THE HORIZONTAL BRIDGMAN METHOD

For this method gallium and arsenic are placed in a boat and inserted into a long silica tube which is evacuated and then sealed. The sealed tube is mounted in a furnace with three temperature zones, as shown in Fig. 11.1. The cool zone controls the pressure of As in the tube, maintaining it at one atmosphere. Synthesis of the compound takes place in the hottest zone where the boat is held for at least one hour. After this time the mullite tube is moved to the right at a speed of 2 cm/hr and the liquid GaAs solidifies as it passes into the intermediate temperature zone.

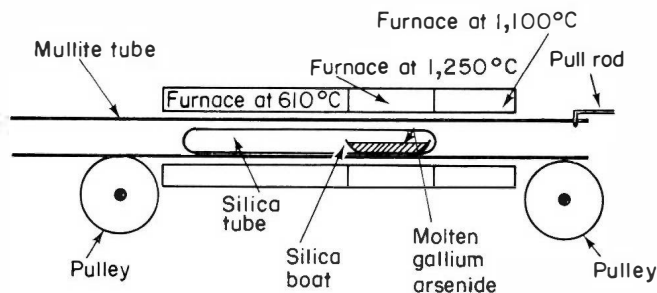


FIG. 11.1. The horizontal Bridgman method (Ref. 3 of Chapter 2).

### 11.2.2 THE CZOCHRALSKI METHOD

The Czochralski growth system is illustrated in Fig. 11.2a. A seed crystal is inserted in the melt and then slowly withdrawn so that the melt forms a meniscus and solidifies as it is raised above the molten surface, repeating the same single crystal structure as the seed. A sealed system has to be employed in order to contain the arsenic vapour, so that magnetic coupling is required to raise the crystal from the melt. An alternative arrangement uses high temperature seals and feed-throughs to pull the crystal. The r.f. coil maintains the GaAs in a molten state at a temperature of  $1242^{\circ}\text{C}$  while the remainder of the system is at  $610^{\circ}\text{C}$  to provide the correct As pressure and prevent loss of As from the melt.

### 11.2.3 LIQUID ENCAPSULATION

This technique<sup>(2)</sup> is an important extension of the above method. It avoids the presence of As in the growth system and thus also obviates the need to maintain the whole system at an elevated temperature. It achieves this object using an inert liquid on top of the melt which completely covers it and prevents the loss of the volatile arsenic. The system, shown in Fig. 11.2b contains an inert gas (argon, for example) which maintains a pressure on the surface of the liquid encapsulant in excess of the equilibrium vapour pressure of the arsenic. The features required of the liquid encapsulant are that it should be less dense than the melt, optically transparent (melt visible), and chemically stable in its environment. Furthermore, there should be no diffusion or convection of the arsenic through the layer. A widely used encapsulant which satisfies all these requirements is Boric Oxide.

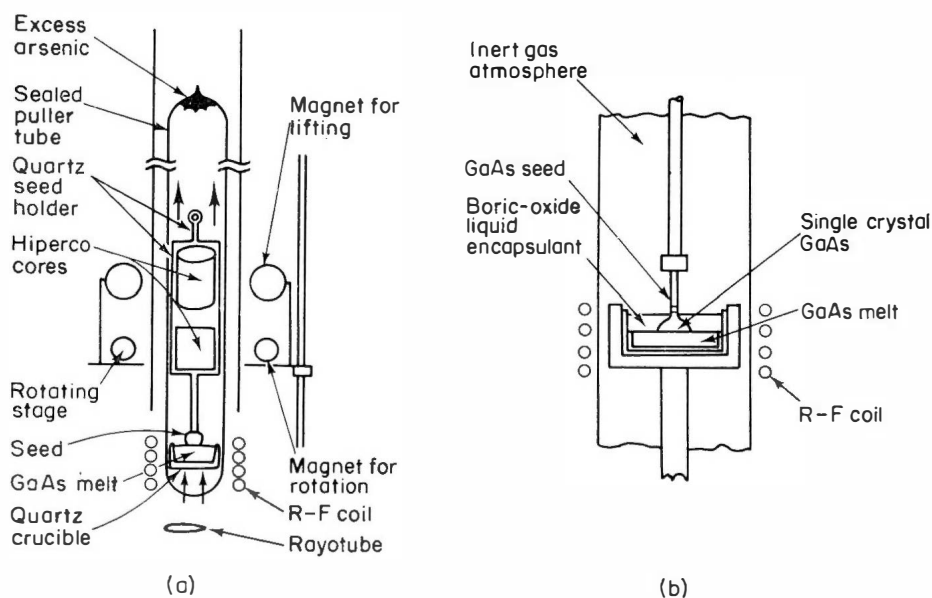


FIG. 11.2. Two versions of the Czochralski crystal growth method, (a) Sealed system with magnetic crystal pulling; (b) Pulling through boric oxide liquid encapsulant. From *Electronics*, Nov. 13, p. 111, 1967.

### 11.2.4 PURITY OF BULK MATERIAL

The purest material made by these methods contains small quantities of Silicon and Oxygen and has a total impurity content near  $10^{16} \text{ cm}^{-3}$ . Neither of these impurities is present in such amounts in the starting elements and



it is probable that a reaction between the molten GaAs and the silica in the system causes the contamination. The very high temperatures involved in the growth of bulk material assist such melt contamination by diffusion of impurities from the boat containing the melt etc.

In the growth of bulk GaAs, regions of very high resistivity sometimes occur which are believed to be due to oxygen doping. In these regions resistivities are  $10^6 \Omega \text{ cm}$  and higher with corresponding carrier concentrations below  $10^8 \text{ cm}^{-3}$ . Such material is called semi-insulating (S.I.) GaAs and its high resistivity is due to a near compensation of the appreciable number of donor and acceptor impurities which it contains.<sup>(3)</sup> This material has a number of uses. For example it is used as a passive substrate to support a semiconducting epitaxial layer in which a range of planar devices can be fabricated. It has the advantage of being able to provide isolation between such devices. S.I. GaAs is also commonly employed in the measurement of the electrical parameters of semiconducting layers. Growth of the latter on to an insulating substrate makes the electrical measurements very simple. At the present time the semi-insulating form can be grown by the addition of sufficient quantities of Chromium of the melt. However, the real breakthrough will occur when it can be deposited epitaxially in a controllable fashion.

Bulk material is not usually used for the active region of a transferred electron device, since it is unable to satisfy the stringent requirements of high purity, homogeneity and positive temperature coefficient of resistivity. The latter is required to avoid thermal runaway of devices in operation. These requirements can only be met by epitaxial growth techniques, and bulk material is usually relegated to the role of substrate material for the active epitaxial layer. The epitaxial growth can occur either from the vapour phase or from the liquid phase, and the two approaches are outlined here in turn.

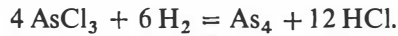
### 11.3 VAPOUR EPITAXIAL GROWTH

To achieve epitaxial growth from the vapour phase it is necessary to introduce the components of the compound into the vapour phase in a form that allows them to combine and form a single crystal at the substrate surface. As very high purity material is required the components are chosen on the basis of the purity with which they are available. Two systems are common, known as the arsenic trichloride ( $\text{AsCl}_3$ ) system and the arsine system.

#### 11.3.1 THE ARSENIC TRICHLORIDE ( $\text{AsCl}_3$ ) SYSTEM<sup>(4)</sup>

An outline of the basic growth apparatus is shown in Fig. 11.3. The furnace comprises two separate zones which can be held at separate temperatures.

The growth process occurs in two stages, saturation of the source and growth of the layer itself. For the first stage the source material, usually high purity gallium, is placed in zone 1 of the furnace. The temperature of this zone is raised to a level of around 880°C and high purity hydrogen from a palladium diffuser is bubbled in through a quantity of arsenic trichloride. The hydrogen transports the  $\text{AsCl}_3$  into zone 1 where it is reduced at the high temperature to produce hydrogen chloride vapour and arsenic vapour.



The arsenic vapour is completely absorbed by the liquid gallium source until saturation occurs at 2.25 atomic percent of arsenic. When the melt becomes saturated with arsenic a skin of GaAs forms on its surface and the arsenic vapour passes on down the furnace tube, together with gallium monochloride vapour produced by a reaction between the HCl and the gallium.

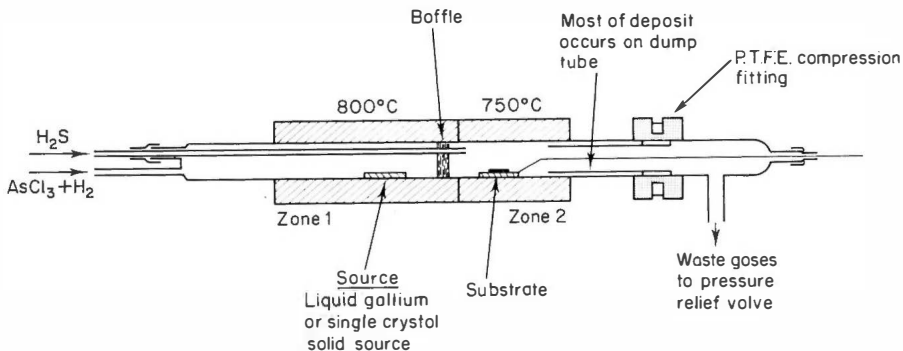
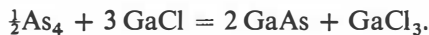


FIG. 11.3. A typical apparatus for growth from the vapour phase by the arsenic trichloride process. (By courtesy of Plessey Co. Ltd.)

At this point the flow of hydrogen is diverted to by-pass the  $\text{AsCl}_3$  bubbler and a GaAs substrate is introduced into zone 2 of the furnace and allowed to reach a steady temperature of about 750°C. The  $\text{AsCl}_3$  is then re-introduced into the gas stream and the GaCl and  $\text{As}_4$  vapours combine in zone 2, and epitaxial growth occurs on to the GaAs substrate.



During the above operations Ga and As compounds deposit beyond the furnace and a "dump tube" is commonly employed as shown in Fig. 11.3 to collect most of this deposit so that the main furnace tube can be used for many runs without significant build up of impurities in the system.

When layers are not required to have very high purity a single crystal GaAs source is often used in place of the high purity gallium.

The quality of the layers grown will depend to a large extent on the substrate surface on to which growth occurs—this should be free of chemical contaminants such as oxide layers and of damage caused by mechanical polishing or solution etching. These requirements can be readily met by a preliminary vapour etch stage for the substrate. If the substrate after insertion is held initially at a high temperature, around 900°C typically, the growth process is reversed and the substrate surface is etched in the vapour stream.

### 11.3.2 THE ARSINE ( $\text{AsH}_3$ ) SYSTEM<sup>(5,6)</sup>

Another vapour phase method has been very successful in producing high quality material for microwave devices is the Arsine process. This system is illustrated in Fig. 11.4. Hydrogen chloride and palladium diffused hydrogen

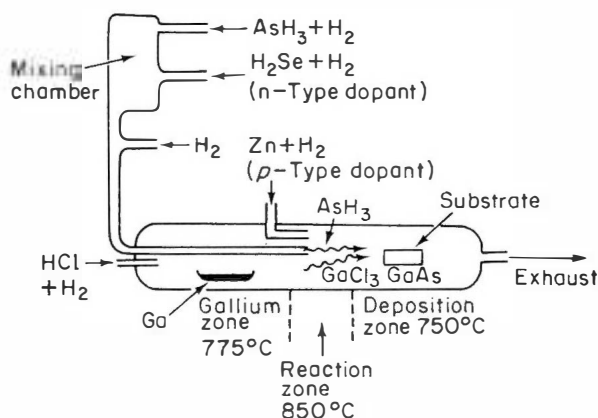


FIG. 11.4. Apparatus for growth from the vapour phase by the Arsine ( $\text{AsH}_3$ ) process.<sup>(5)</sup>

pass over a boat containing high purity gallium at about 775°C. The hydrogen chloride reacts with the gallium to produce gallium monochloride and the hydrogen transports this to the deposition zone at the other end of the tube. The temperature in the deposition zone is in the region 725–750°C. Arsine enters the same tube and dissociates in the high temperature central zone into  $\text{H}_2$  and  $\text{As}_4$ , the latter reacting in the deposition zone with the  $\text{GaCl}$  to form the epitaxial layer. Thus



### 11.3.3 THE WATER VAPOUR TRANSPORT SYSTEM

This is the simplest system and produces the least pure epitaxial material, with carrier concentrations typically well above  $10^{15} \text{ cm}^{-3}$ . Water vapour reacts with a bulk  $\text{GaAs}$  source crystal at about 1050°C to form hydrogen,

arsenic vapour and the volatile sub-oxide of gallium. This reaction is reversed at a lower temperature ( $\approx 1000^\circ\text{C}$ ) in another part of the reactor where a GaAs film is deposited.

#### 11.3.4 TYPICAL PARAMETERS OF VAPOUR EPITAXIAL MATERIAL<sup>(7)</sup>

The purity of the material produced by the last method is low mainly because of the high temperature involved leading to impurities being carried over from the source and out of the growth tube into the film. However, by purging impurities from the growth tube and from the boats in which source and substrate are mounted, the first two methods are capable of producing material with background doping levels in the region of  $10^{14}$ – $10^{15}\text{ cm}^{-3}$ , with mobilities at room temperature of  $9000\text{ cm}^2/\text{V sec}$  and liquid nitrogen mobilities exceeding  $100,000\text{ cm}^2/\text{V sec}$ . In general, material grown by the vapour phase method can not be obtained so pure as by the liquid process, although carrier concentrations approaching  $10^{13}\text{ cm}^{-3}$  have been reported with liquid nitrogen mobilities in excess of  $200,000\text{ cm}^2/\text{V sec}$ .<sup>(8)</sup>

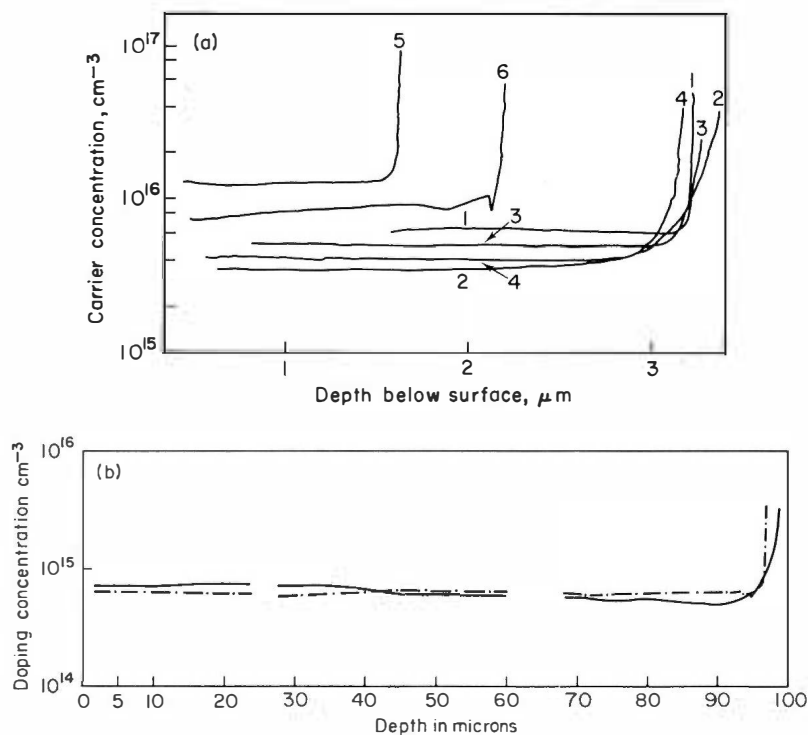


FIG. 11.5. (a) Doping profiles for thin vapour grown layers.<sup>(35)</sup>; (b) Doping profiles for thick vapour layers (by courtesy of S.T.L.). Profiles as measured by Schottky barrier capacitance method described in Section 11.5.2 with successive etching stages for the thick layers.

It will be noted that this is essentially a steady state growth process so that the production of uniform layers is favoured. The rate of growth will depend on substrate orientation and 5–15  $\mu\text{m/hr}$  is common for the usual 100 orientation. Layer uniformity will thus depend upon the control of conditions during the whole growth process. Very thin layers (1  $\mu\text{m}$ ) will suffer from the initial growth transient and very thick layers from an inability to maintain accurate control of temperatures. Nevertheless very uniform layers have been produced with thickness down to 1.5  $\mu\text{m}$  and up to 100  $\mu\text{m}$  as shown in Fig. 11.5.

#### 11.3.5 DOPING OF THE EPITAXIAL LAYER

When doping of the epitaxial layer is called for, as is often the case, this is readily achieved in the trichloride and arsine systems by using hydrogen as a carrier to introduce a compound of the required dopant to the deposition zone during the growth period.

Sulphur and selenium are two common dopants which are introduced in this manner, the compounds used being hydrogen sulphide and hydrogen selenide. Doping levels can be controlled by adjustment of flow rates.

Dopants can be more readily introduced by placing them in the boat containing the gallium source. Thus tin doping for example can easily be achieved by merely adding an appropriate amount of tin to the gallium. Selenium is often introduced in this manner by adding a suitable quantity of selenium-doped GaAs to the melt.

#### 11.3.6 BUFFER AND CONTACT LAYERS

One of the problems which can attend the growth of the high purity epitaxial layer is the diffusion of impurities from the substrate during growth. This problem can however be overcome by the growth from the vapour of a heavily doped, high purity “buffer” layer on to the substrate prior to the growth of the active region. The buffer layer effectively isolates the active layer from the impure substrate.

It is also often desirable to grow a heavily doped GaAs layer after growth of the active region. This is a technique which will receive attention in Section 11.6 but the reason for doing it is because it offers the best method of obtaining an ohmic, low resistance contact to the active region. This is to be expected since the contact itself is also GaAs.

The growth of the buffer and contact layers is best carried out by providing a separate line to the deposition zone to enable doping levels up to  $10^{18} \text{ cm}^{-3}$  or more to be attained. This is indicated in Fig. 11.3 where a separate line is provided to carry the  $\text{H}_2\text{S}$  to dope the buffer and contact layers heavily with sulphur. This line would thus be in action prior to and after the active growth run.

### 11.3.7 SUBSTRATES

The substrate can readily be purchased heavily doped with, for example, Sn, Si, Se, Te. Substrates are normally cut  $2^\circ$  off the 100 orientation in order to discourage the formation of facets during growth. They are required to be fairly dislocation free since substrate faults tend to appear in the epitaxial layers grown on to them.

When Te doped substrates are employed, autodoping of the epitaxial layer occurs. This is because of the high vapour pressure of Te so that it comes out of the substrate and is included in the layer via the gas phase. This persists until a sufficient thickness of layer is grown to prevent it. It can be a desirable feature since high resistivity regions are often seen at the substrate/grown layer interface which are possibly due to the initial growth transient. These regions can be "filled in" if Te doped substrates are used.

### 11.4 LIQUID PHASE EPITAXY

In this method, growth occurs on to the surface of a GaAs substrate due to recrystallisation of a GaAs solute at the liquid–solid interface. This method was first described by Nelson<sup>(9)</sup> as means of growing heavily doped material for tunnel diode and laser applications. However the process has been refined and controlled to the point where it can be used to produce material of high purity and uniformity such as is essential for the production of microwave oscillators.

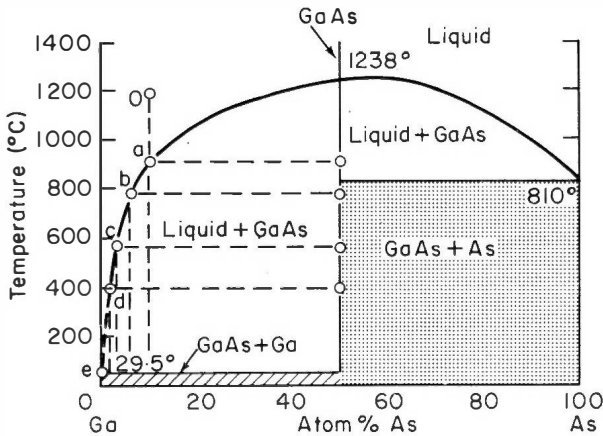


FIG. 11.6. The GaAs binary phase diagram. From K. Weiser in *Compound Semiconductors*, Vol. 1 (Ed. Willardson and Goering), Reinhold 1962.

The basic growth technique most commonly used is the transient method. Here the temperature of the liquid–solid–vapour system is uniform throughout the system and must continuously decrease in order for recrystallisation

of the solute to occur. The recrystallisation is a result of the decreasing capacity of the initially saturated solution to contain solute and remain in a near equilibrium condition as the temperature decreases. In a second method, to be discussed in Section 11.3.3, the system is in the steady state with a fixed temperature difference maintained between solution and substrate so that solute will crystallise out on to the cooler substrate.

The manner in which growth proceeds in the more common transient method can be seen by examination of the GaAs phase diagram shown in Fig. 11.6. Consider growth from a solution of composition approximately 90 atomic percent Ga, 10 atomic percent As. As the temperature decreases from the point 0, the state of the system falls vertically to intercept the liquidus curve at *a*. At this point the first solid will form, its composition being always 50% Ga, 50% As. The composition of the liquid will therefore change, becoming depleted of As. As the temperature continues to fall, the state of the system will move along the liquidus curve through point *c*, with the percentage of As in solution being given at any point by the horizontal scale. Due to the depletion of As from the melt and the changing slope of the liquidus curve, progressively less GaAs is precipitated from solution as the temperature falls. Finally growth will cease at point *e* when the entire system will be in the solid phase.

Two systems are commonly used in practice for liquid epitaxial growth. They are known as the horizontal and the vertical systems.

#### 11.4.1 HORIZONTAL SYSTEM

A typical horizontal system is shown in Fig. 11.7. The GaAs substrate *S* and melt *M* are placed in a quartz boat and positioned as shown in the furnace

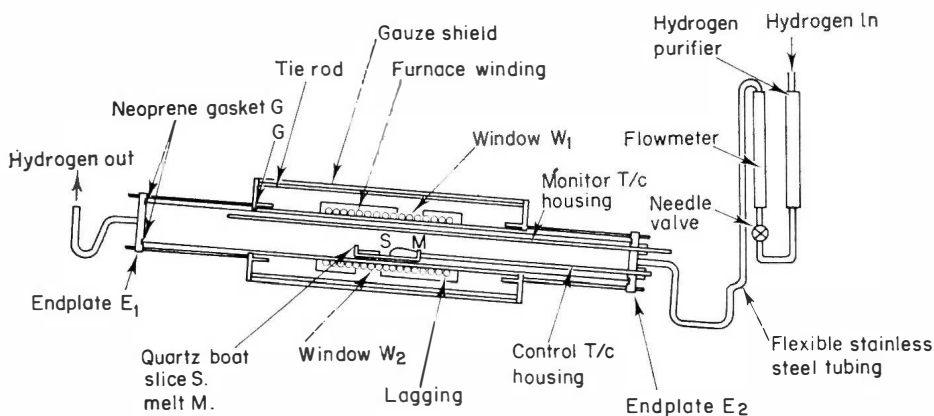


FIG. 11.7. Horizontal system for liquid epitaxial growth. S.T.L. Annual Report on RP7-43. 1967.

tube. In general the melt consists of a solvent, generally Ga, together with a piece of GaAs such that at the maximum temperature reached (point 0) the solution will be saturated. Alternatively Ga is sometimes used after saturation with As in a preliminary vapour phase reaction.<sup>(10)</sup> The reactor is then sealed and thoroughly flushed with Hydrogen to clear unwanted impurities from the system.

The procedure which follows can best be illustrated by the temperature cycle shown in Fig. 11.8. The furnace temperature is raised steadily to near the point at which the Ga melt is saturated with GaAs. The exact temperature can be determined by directly observing when all the GaAs in the melt has been dissolved. To permit the accurate determination of the saturation point, the furnace temperature is increased slowly over this range and then rapidly up to a slightly higher temperature at which a period of stabilisation is allowed before beginning the cooling cycle. When the saturation temperature  $T_s$  is reached the furnace is tilted, the melt runs on to the surface of the substrate and growth begins. Normally it is not desirable that growth takes place right down to room temperature so that after an appropriate growth period the furnace is tilted back again, the melt runs off the substrate and growth ceases.

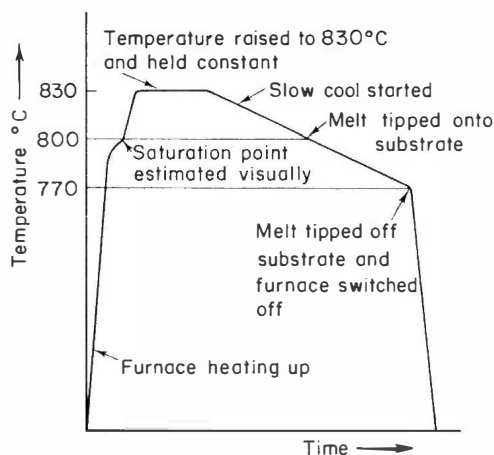


FIG. 11.8. Temperature  $N$  time cycle for layer deposition (Horizontal system) S.T.L. Annual Report on RP7-43, 1969.

Accurate determination of the saturation temperature  $T_s$  is important since if the solution is brought into contact with the substrate at a temperature above  $T_s$ , it is not completely saturated and will dissolve material from the substrate until the solution is again saturated. This removal of substrate material is known as etch-back and is in general undesirable since impurities from the substrate are subsequently incorporated into the growth layer.



## 11.4.2 VERTICAL SYSTEM

Figure 11.9 shows a typical apparatus for the growth of GaAs by the vertical method. The temperature-time cycle used is similar to that shown in Fig. 11.10. Thus the temperature of the Ga melt is raised until it is saturated with the source GaAs, the temperature again being determined accurately by visual observations. The temperature is then increased again and held constant for a stabilising period prior to the cooling cycle. Before the saturation temperature  $T_s$  is reached the substrate is lowered into a position just above the melt so that it acquires the same temperature as the melt. Then at  $T_s$  it is lowered into the melt and growth commences. After the desired growth interval the slice is lifted out of the melt and the furnace switched off.

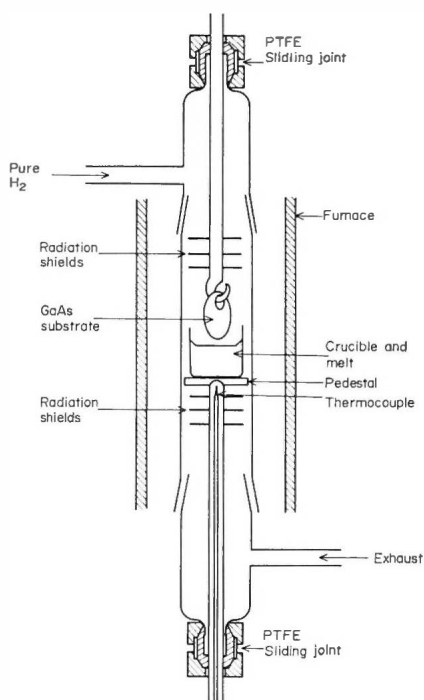


FIG. 11.9. Vertical system for liquid epitaxial growth. (By permission of Mullard Research Labs.)

In essence the vertical and horizontal methods are identical but an important advantage of the former is the ease of separating the slice from the melt at the end of the growth period. In the horizontal system this is a difficult operation since the melt tends to adhere to the slice.

### Layer Considerations

In both systems the thickness of the epitaxial layer grown will depend upon the temperature range over which growth takes place, the weight and composition of the melt etc. Typical layer thicknesses vary between 10 microns and 100 microns.

The purity of the layer will be greater than that of the source GaAs provided that the impurity contribution from the growth environment is small. This is because of the segregation from the solid phase to the liquid phase of all the important impurities in GaAs, i.e. the distribution coefficient, defined as the ratio of the impurity concentration in the solid to that in the liquid, is less than unity for all the important impurities.<sup>(11)</sup>

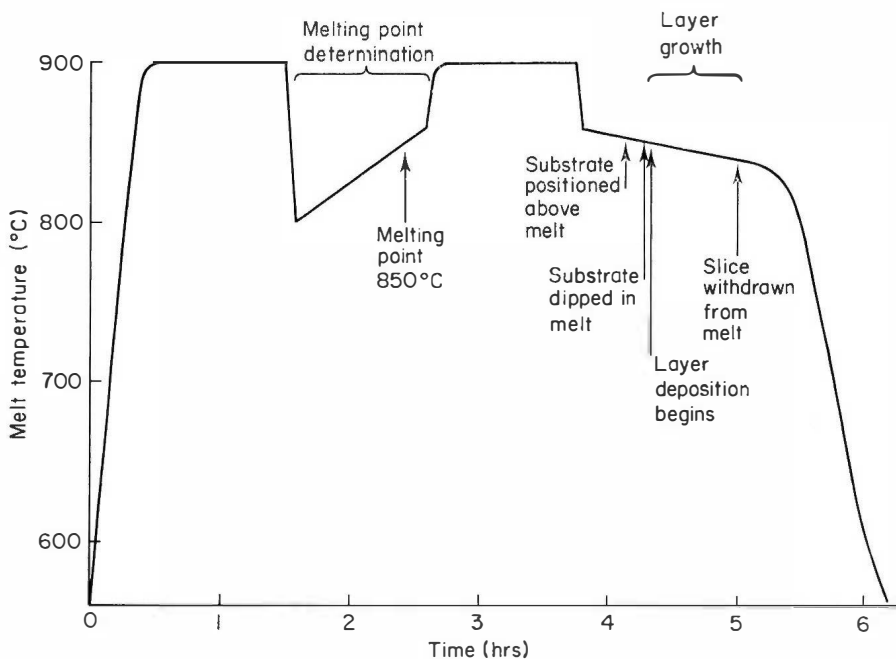


FIG. 11.10. Temperature time cycle for layer deposition (Vertical system). (By permission of Mullard Research Laboratories.)

The distribution coefficient will be temperature dependent so that as the furnace cools and the layer is deposited, the impurity concentration in each stratum of the grown layer will change. Thus the layer will be grown with a doping gradient. Even if the distribution coefficient were constant over the temperature range for growth, a doping gradient would still arise because of the increasing build up of the impurity concentration in the liquid because of the exclusion from the solid. In general both these effects will be operating

and the impurity profile in the grown layer will be the result of their combined effect. In some cases they may cancel each other out and a uniform profile will be obtained.

The above considerations are sufficient to indicate that quantities such as the growth temperature, range and cooling rate etc. have to be selected optimum for a given system in order to obtain layers of the required thickness and a good doping uniformity.

In a high purity system, it will generally be necessary to introduce into the melt controlled amounts of impurity in order to grow layers of sufficiently high electron concentration, typically  $10^{14}$ – $10^{16}$   $\text{cm}^{-3}$ , as required for transferred electron devices. The dopants commonly chosen are elemental Sn, and Se or Te in the form of Se doped or Te doped GaAs.

#### 11.4.3 STEADY STATE GROWTH

In the transient method of growth it was pointed out that the dependence of the distribution coefficient on temperature lead to a doping profile which was non-uniform. This source of non uniformity can be eliminated if growth can take place at a fixed average temperature. This, the steady state method of growth, requires that a small temperature difference be maintained between the melt and the substrate in order that the solute shall crystallise out. Such a system can be realised in a similar way to that shown in Fig. 11.7 by employing a split furnace so that the top part of the furnace can be maintained at a higher temperature than the bottom. In this way a controllable temperature gradient can be achieved across the melt and substrate and deposition will occur at a rate determined by this gradient.

#### 11.4.4 TYPICAL PARAMETERS OF LIQUID EPITAXIAL MATERIAL

Liquid phase epitaxy has been used to grow very pure material with carrier concentration levels down to  $10^{12}$ – $10^{13}$   $\text{cm}^{-3}$ <sup>(12)</sup>, liquid nitrogen mobilities of 330,000  $\text{cm}^2/\text{V sec}$ ,<sup>(12)</sup> and room temperature mobilities of over 9,000  $\text{cm}^2/\text{V sec}$ .<sup>(13)</sup> The attainment of such low background impurity levels makes it easy to dope back controllably to any desired carrier concentration.

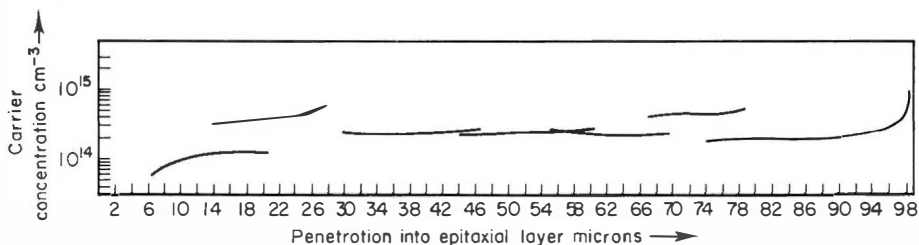


FIG. 11.11. Doping profile of a uniform thick GaAs layer grown by liquid epitaxial techniques (by courtesy of S.T.L.). Profile as measured by Schottky barrier capacitance technique (Section 11.5.2), with several stages of etching to enable a complete profile to be obtained.

Very uniform doping profiles can also be obtained as shown in Fig. 11.11 for a 100  $\mu\text{m}$  thick layer doped to a level of  $2 \times 10^{14} \text{ cm}^{-3}$ . (The doping profile was measured by the Schottky Barrier Capacitance Method and a number of separate successive measurements had to be made to penetrate the layer, hence the discontinuous nature of the profile shown). The liquid process has also been used to grow layers several times thicker than this, as well as very thin layers of 10 microns and less, again with uniform carrier concentrations.

#### 11.4.5 BUFFER AND CONTACT LAYERS

Just as for vapour grown layers, it is often desirable to grow an initial and a final heavily doped layer to provide isolation from substrate effects and good contacts to the active layer. This can be achieved in the same furnace if two melts are included, one heavily doped and one lightly doped. Thus the substrate is immersed initially in the heavily doped melt, transferred to the lightly doped for growth of the active zone, and then immersed again in the heavily doped melt for growth of the top contact. Such a system is simple but suffers from the obvious problem of cross contamination between the melts.

An alternative method is to grow the three epitaxial layers in separate consecutive runs, using one furnace for the high resistivity layer and one for the low resistivity layers. The same dopants are commonly used for the active and contact layers.

### 11.5 MATERIAL CHARACTERIZATION

Material for transferred electron devices must satisfy well defined criteria in terms of thickness, doping level and profile, mobility etc. according to the intended mode of operation and frequency of interest. A number of techniques are available to monitor the basic parameters of the grown layers, and these are briefly outlined here.

#### 11.5.1 THICKNESS

The simplest method of thickness measurement relies on the large difference between the carrier concentration in the grown layer and that in the substrate. The layer is cleaved perpendicular to the surface and a simple chemical etch or stain used to locate the interface. For example, an etch composed of HF,  $\text{HNO}_3$  and  $\text{H}_2\text{O}$  in the proportion 1 : 3 : 4 stains the more lightly doped  $n$  layer a darker colour than the  $n^+$  substrate. Layer thickness can then be measured using a calibrated microscope. Other etches operate at a rate which is dependent upon layer conductivity and these therefore reveal the interface as a step in the etched surface.

For accurate measurements on thin layers it is common practice to angle lap the wafer. That is, an edge of the wafer is polished at a small angle relative to the surface. In this way a cross section of the wafer is exposed over a much larger area than would be exposed by polishing or cleaving perpendicular to the surface.

Another approach to thickness measurement is to shine infra red obliquely on to the epitaxial surface.<sup>(14)</sup> Some radiation is reflected at the surface, some penetrates the layer and is reflected at the  $n-n^+$  interface. An interference pattern is formed between the two reflected rays. By slowly varying the wavelength of irradiation (with a spectrometer) and measuring how the interference pattern changes with wavelength, the thickness of the epitaxial layer can be deduced for a known angle of incidence.

There is a slight inaccuracy in the thickness measured by both the aforementioned techniques, which may be important if they are used to measure thin layers. This is because the metallurgical and electrical junctions between layer and substrate may not be coincident. There may be a significant region extending out from the metallurgical interface, over which the doping changes its value from that in the substrate to that in the layer. Thus for the I.R. technique there is no defined plane at which a change in reflection occurs. Similarly an etch which reveals the metallurgical interface will give the wrong thickness data. Where accurate thickness measurements are required on thin epitaxial layers ( $< 10 \mu\text{m}$ , say), a completely different technique must be employed.

### 11.5.2 DOPING PROFILE

Two methods are available for the measurement of impurity profiles of semiconducting materials. Both rely on the properties of a Schottky barrier junction<sup>(15)</sup> formed by depositing a metal contact on to the surface of the material. By varying the bias voltage applied to such a junction the region of material depleted of carriers can be altered and thereby the carrier concentration determined as a function of distance from the semiconductor surface.

Figure 11.12 shows the field distribution in the semiconductor for some arbitrary applied bias voltage. A depletion zone extends into the material a distance  $x$ . Consider now the application of an incremental change in bias voltage  $\Delta V$ . From Fig. 11.12 we have

$$\Delta V = \Delta E \cdot x + \frac{\Delta E}{2} \cdot \Delta x \quad (11.1)$$

where  $\Delta E$  is the field increment and  $\Delta x$  the incremental depletion distance.

Considering a diode of unit area, we have for the increment in charge at the metal contact

$$\Delta Q = \epsilon \epsilon_0 \Delta E. \quad (11.2)$$

Similarly for the incremental charge stored in the semiconductor

$$\Delta Q = en(x)\Delta x \quad (11.3)$$

where  $n(x)$  is the doping density at the edge of the depletion zone. Combining (11.1)–(11.3) gives

$$\Delta V = \frac{x}{\epsilon \epsilon_0} \cdot \Delta Q + \frac{1}{2\epsilon \epsilon_0 en(x)} \cdot \Delta Q^2. \quad (11.4)$$

This equation forms the basis for one of the two methods used to measure  $n(x)$ .

Ignoring the second order term in Eqn (11.4) we have

$$\Delta V = \frac{x}{\epsilon \epsilon_0} \Delta Q. \quad (11.5)$$

Now the small signal capacitance of the depletion layer is defined as

$$C = \frac{\Delta Q}{\Delta V} = \frac{\epsilon \epsilon_0}{x}. \quad (11.6)$$

Whence

$$\frac{dC}{dV} = -\frac{\epsilon \epsilon_0}{x^2} \frac{dx}{dV}. \quad (11.7)$$

From (11.3) and (11.6)

$$en(x)\Delta x = C\Delta V$$

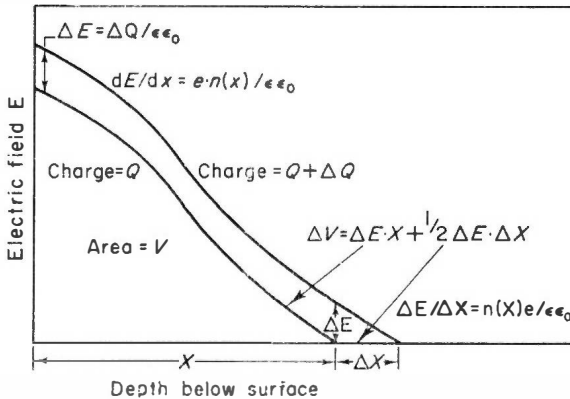


FIG. 11.12. The electric field versus depth below the surface of a semi-conductor with surface charge  $Q$  per unit area.<sup>(17)</sup>

therefore

$$\frac{dx}{dV} = \frac{C}{en(x)}. \quad (11.8)$$

Thus, from (11.6)–(11.8)

$$\frac{dC}{dV} = -\frac{\epsilon^2 \epsilon_0^2}{ex^3 n(x)}.$$

So that

$$n(x) = \frac{\epsilon^2 \epsilon_0^2}{ex^3 (-dC/dV)}. \quad (11.9)$$

This equation forms the basis for the second method.

#### *Sinusoidal Current Method*<sup>(16, 17)</sup>

In this method a current  $I \sin \omega t$  is pumped into the Schottky barrier. The corresponding charge being injected into the junction is

$$\Delta Q = \frac{I \cos \omega t}{\omega}. \quad (11.10)$$

Equation (11.4) thus becomes

$$\Delta V = \frac{I \cos \omega t}{\omega \epsilon \epsilon_0} \cdot x + \frac{I^2 (\cos 2\omega t + 1)}{4\omega^2 \epsilon \epsilon_0 e} \cdot \frac{1}{n(x)}. \quad (11.11)$$

We recognise here two components in the alternating voltage appearing across the junction. Firstly a component at the same frequency as the driving current, this having an amplitude proportional to the width of the depletion zone,  $x$ , and secondly a component at twice the driving frequency which has an amplitude inversely proportional to the carrier concentration at the edge of the depletion zone. Thus by measuring the amplitudes of the fundamental and second harmonic voltages we have the carrier concentration  $n$  and the distance,  $x$ , from the surface at which it applies. Variation of bias then leads to a continuous plot of  $n(x)$ .

#### *Capacitance Method*<sup>(18, 19, 20)</sup>

For this approach the requirement is simply to measure the small signal capacitance  $C$  at different bias voltages.  $x$  is then deduced directly from the measured capacitance, according to Eqn (11.6), and  $n(x)$  determined from the rate of change of capacitance with voltage, according to Eqn (11.9).

The measurements can be performed using a bridge to obtain values of depletion capacitance at discrete levels of bias, and the rate of change of capacitance can be interpolated to yield  $n(x)$  which is proportional to  $C^3 (-dC/dV)^{-1}$ . The accuracy of the measurement is limited by the need for interpolation to obtain  $dC/dV$ . Analogue techniques overcome this disad-

vantage and an instrument is available<sup>(20)</sup> which offers high incremental accuracy.

The range of  $x$  over which the carrier concentration can be measured is set on the one hand by the depletion which already exists at zero bias, and on the other by the avalanche breakdown of the junction which eventually occurs as the bias voltage is increased. The width of the zero depletion region increases with resistivity, and at carrier concentrations of  $10^{14} \text{ cm}^{-3}$  ( $10 \Omega \text{ cm}$ ) it amounts to a few microns or more. The dependences of the avalanche breakdown voltage of the junction, the maximum penetration, and the depth resolution, on the carrier concentration in the layer are approximately as indicated by the Table below.<sup>(17)</sup> At a given carrier level, the profiling of a layer thicker than the maximum depth indicated above, will require a sequence of profile, etch, profile, etc. stages to build up piecewise a plot of the profile through the whole layer (as Fig. 11.11 for example).

Doping density ( $\text{cm}^{-3}$ )	Maximum depth ( $\mu\text{m}$ )	Maximum d.c. volts	Depth resolution (Debye length) ( $\mu\text{m}$ )
$10^{14}$	80	500	0.50
$10^{15}$	12	100	0.15
$10^{16}$	2	20	0.05
$10^{17}$	0.3	4	0.015

The measurement of doping profiles is of considerable value, giving not only accurate values for thickness and carrier concentration, but also the detailed variation of the doping level through the bulk of the material and at the interfaces with the substrate. The profile at the surface can also be measured by lapping off the substrate, depositing barriers on the reverse side, and profiling through to the surface.

The metal evaporated to form a barrier has a diameter, typically, of a few hundred microns, so that the material parameters are being measured over a localised region. The deposition of an array of barriers over the surface, as is customary, allows the layer parameters to be mapped out, giving information on the uniformity of the grown epitaxial layer. Such information is vital to the crystal grower in enabling him to establish the correct conditions for uniform growth, and also to the device manufacturer who can select layers which can be processed to give a high yield of closely similar devices.

### 11.5.3 MOBILITY AND RESISTIVITY

The method used to evaluate the mobility and resistivity of an epitaxial-layer depends upon the conductivity of the substrate.



*Semi-Insulating (S.I.) Substrate*

When the epitaxial layer is grown on an S.I. substrate, Hall effect measurements can be used to determine the resistivity and mobility.<sup>(21,22)</sup> This can be best understood by referring to the test bar shown in the classical Hall geometry in Fig. 11.13a. When a known current  $I$  is flowing from  $a$

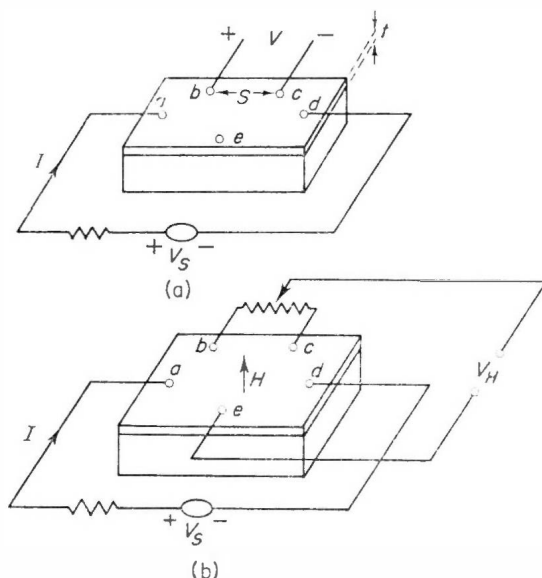


FIG. 11.13. Resistivity and Hall measurements on an epitaxial layer supported by a semi-insulating (S.I.) substrate.

to  $d$ , the resistivity can be found by measuring the voltage  $V$  between ohmic contacts at  $b$  and  $c$ . If  $S$  is in cm, and  $A$  is the cross-sectional area of the bar in  $\text{cm}^2$ , then we have

$$\rho = \frac{VA}{IS} \Omega \text{ cm.} \quad (11.13)$$

The Hall coefficient,  $R_H$ , is determined by applying a magnetic field  $H$  at right angles to the current and the top surface of the bar as shown in Fig. 11.13b. The adjustment is first made that  $V_H = 0$  for  $H = 0$ . Then, when the magnetic field is applied, a voltage  $V_H$  will be observed which is caused by the Lorentz force exerted by the magnetic field on the moving charges and the consequent separation of charge. The Hall voltage is related to the Hall coefficient by <sup>(22)</sup>

$$R_H = \frac{V_H t}{IH} \cdot r \quad (11.14)$$

where  $t$  is the epitaxial layer thickness and  $r = \langle \tau^2 \rangle / \langle \tau \rangle^2$  where  $\tau$  is the carrier relaxation time.  $\tau$  has different values for different scattering mechanisms, but all are close to unity. From this, the Hall mobility  $\mu_H$  can be calculated. Assuming  $n \gg p$ , as is true in our cases of interest, then

$$\mu_H = \frac{R_H}{\rho}. \quad (11.15)$$

This is not the same as the drift mobility, as the drift mobility is independent of the scattering dependence  $r$ . A value for the doping level in the epitaxial layer can also be deduced from the Hall measurement.<sup>(23)</sup>

$$n = \frac{1}{R_H e}. \quad (11.16)$$

The values of  $\rho$ ,  $\mu_H$  and  $n$  thus determined are of course macroscopic values, averaged over the thickness of the epitaxial layer and over a large area of the slice. Furthermore the accuracy of the Hall mobility and carrier concentration measured depends upon a previous accurate measurement of layer thickness  $t$ .

#### Conductive ( $n^+$ ) Substrate

The techniques described above can not be used with layers on  $n^+$  substrates because current can now flow through the substrate, which effectively reduces or shorts out  $V$  and  $V_H$ . In this case by alloying in an ohmic contact of area  $A$  on the surface and making the substrate the other contact (Fig. 11.14)

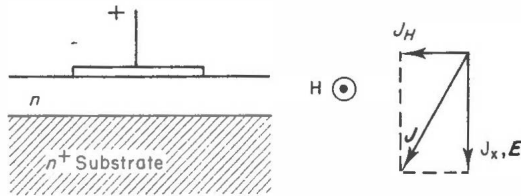


FIG. 11.14. Resistivity and geometric magnetoresistance measurements on an epitaxial layer supported by a conducting substrate.

we measure the resistance of the piece of material,  $\rho t/A$ , from which resistivity is directly calculable. Inaccuracies may arise due to fringing current flow if the aspect ratio of the element of semiconductor is not sufficiently large. Corrections can be made for this however, as can also be made for any resistance due to the substrate, and for the penetration of the alloy contact into the layer (if the layer is thin enough to warrant such a correction).

The mobility of the material can be determined by measuring the increase in the resistance of the element which occurs when a magnetic field is supplied

at right angles to the direction of current flow between the contacts. The effect is known as geometric magnetoresistance (GMR). If the dimensions of the element are much larger than the thickness, then the Hall voltage set up by the magnetic field is effectively shorted out by the metal contact and substrate. The Lorentz force acting on the carriers is not now compensated by any Hall voltage and the carriers move at an angle with respect to the applied field. As shown in Fig. 11.14 the electric field is directed across the sample and the current flows at the Hall angle. The consequence of the change in current flow is a change in the resistance,  $\Delta R$ . It is readily shown that<sup>(23)</sup>

$$\frac{\Delta R}{R} = (\mu_m B)^2 \quad (11.17)$$

provided that  $\mu_m B \ll 1$ .  $B$  is the magnetic flux density and  $\mu_m$  is the magnetoresistance mobility, which is related to the Hall mobility by a constant of proportionality  $\xi (= \mu_m / \mu_H)$ . The constant takes values which depend upon the exact scattering mechanism in the semiconductor but all are close to unity.

## 11.6 CONTACTS

Although the transferred electron effect is essentially a bulk effect, nevertheless the boundary conditions imposed by the contacts can have a considerable effect on the operation of  $t-e$  devices. Ideally the requirements to be fulfilled by a "good" contact are:

- (1) It should be non-injecting, and have a low resistance.
- (2) The contact semiconductor interface should be planar to ensure uniformity of field and current density.
- (3) It should be electrically and thermally stable under the desired operating conditions.

A number of contacts have been developed which can satisfy the first two conditions and the third condition can also be met, subject to reasonable operating conditions being specified. Many of the contacts in use are metal or metal alloy contacts and it will be instructive before describing the particular contacts to first briefly outline the nature of the general metal-semiconductor contact.

### 11.6.1 THE METAL SEMICONDUCTOR CONTACT<sup>(24)</sup>

If any semiconductor is brought into intimate contact with any metal conductor (e.g. by evaporating the metal in a vacuum) in most cases a rectifying contact results. This is certainly the case with GaAs, particularly if the carrier

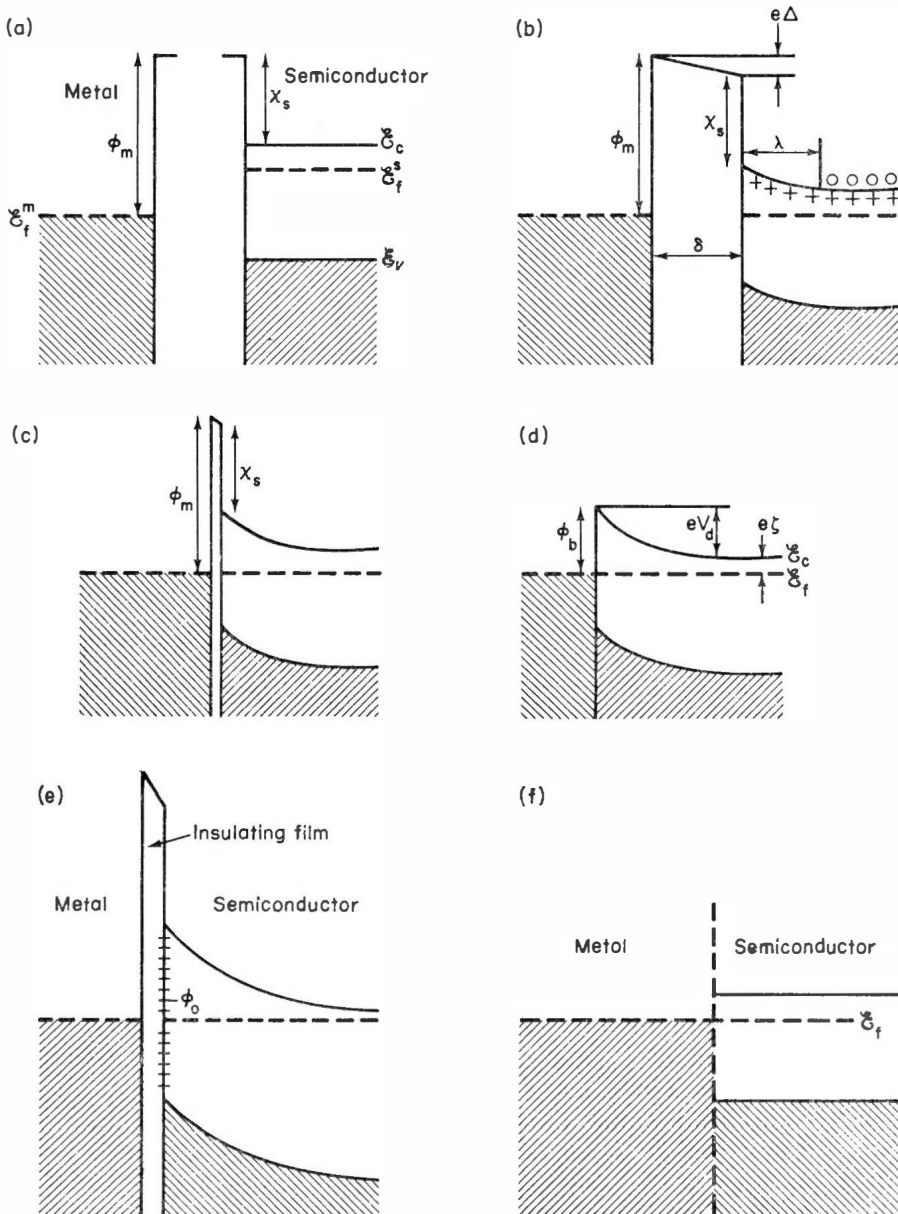


FIG. 11.15. Formation of a metal-semiconductor (Schottky) barrier.<sup>(24)</sup> Metal and semiconductor (a) neutral and isolated; (b) electrically connected; (c) in close proximity; (d) in perfect contact; (e) in contact, but in presence of an insulating film and surface states; (f) a special type of non-rectifying metal semiconductor contact.  $\circ$  denotes electron in conduction band;  $+$  denotes positive donor ion. (Reproduced by permission of the Institute of Physics.)

concentration is low. The reason for this may be appreciated from the following. Consider a metal and a semiconductor in isolation. For definiteness we take the semiconductor to be  $n$ -type. The energy band diagrams will be as shown in Fig. 11.15a, where  $\mathcal{E}_F^m$ ,  $\mathcal{E}_F^s$  are the Fermi levels in the metal and semiconductor respectively.  $\phi_m$  is the work function of the metal and  $\chi_s$  the electron affinity of the semiconductor. If we connect the two electrically, electrons will flow from the semiconductor to the metal, and a positive charge builds up on the surface of the semiconductor. A corresponding negative charge is built upon the surface of the metal. The electron flow stops when the two Fermi levels are in equilibrium, the energy level diagram then being as shown in Fig. 11.15b.

The electric field which is set up between the positive charge on the metal and the negative charge on the semiconductor has a magnitude of  $\Delta/\delta$ . To provide the positive charge at the semiconductor surface conduction electrons have receded from the surface, leaving a region of uncompensated donor ions with positive charges. Thus the energy bands are bent upwards to the surface as shown.

As the gap is reduced, the potential drop  $\Delta$  across it tends to zero if the field in the gap is to remain finite, as shown in Fig. 11.15c. Finally when intimate contact is made, the potential drop has disappeared altogether and we are left with the situation shown in Fig. 11.15d where the barrier remaining is simply due to the band-bending.

Such an interface will have rectifying properties for the electrons in the conduction band have to overcome the barrier potential before they can penetrate into the metal. In the general case of a metal in contact with a semiconductor there will also be insulating layers (oxide films, for example) and surface states at the interface and these will prevent the ideal situation depicted in Fig. 11.15d from occurring. The energy diagram will then resemble that shown in Fig. 11.15e where the potential differences are dependent on the width of insulating film and on the density of surface states.

Figure 11.15f shows a particular type of metal semiconductor boundary across which electrons can pass with ease in either direction. To realise such a junction the band-bending and surface levels must be reduced and any insulating layers removed, all of which can only be achieved with difficulty.

Another and more common type of boundary which does not present any obstruction to the flow of electrons in either direction is obtained when the semiconductor and metal are intimately mixed over a narrow region at the boundary. A gradual transition is thereby achieved between the semiconductor and metal with a corresponding gradation in conductivity.

The contacts and contact procedures to be outlined below succeed in avoiding junctions of the type in Fig. 11.15e and produce non-rectifying contacts, at least to GaAs whose carrier concentration is not too low. All of

the processes for contacting attempt to achieve this by a thermal procedure in which a molten metal etches the GaAs surfaces, breaks down the surface levels and removes any insulating layers. These processes only take place above a minimum temperature which is necessary for the etching of the GaAs surface.

It will in general be easier to make low resistance contacts to high conductivity material. This is because when the carrier concentration in the semiconductor is very high the depth depleted to supply the positive charge is very small and the barrier in Fig. 11.15d very thin. In this case electrons can tunnel very easily through the barrier. Even if a high barrier is present at the interface, as in Fig. 11.15e, if this is thin enough it will not constitute an obstruction to the passage of electrons.

### 11.6.2 THE METAL BEAD AND THE METAL LAYER CONTACTS

It is appropriate first of all to distinguish two different types of contact. Contact can be made by placing a small bead of appropriate metal (e.g. Sn) or alloy (e.g. AuGe) on to the semiconductor surface, melting it, and alloying it to the GaAs at an elevated temperature in a stream of HCl gas. Contact can also be made by evaporating a thin layer of contact metal on to the GaAs surface in a vacuum, and subjecting it to a selected temperature-time cycle. In the latter case care must be taken if the evaporated metal is easily melted, for then during the alloy temperature cycle, the metal layer will break up into a multitude of single droplets unless steps are taken to prevent this. The step usually taken is to evaporate in addition a thin layer of nickel or silver, which covers the contact layer and prevents the formation of droplets. In the alloy process a definite temperature time cycle must be adhered to. If the contacts are annealed for too long or at too high an alloying temperature, the metals are completely dissolved into the GaAs and dislocations may develop in its surface. Equally if the cycle is too short or if the temperature is too low, a proper alloyed contact will not be formed.

The metal bead type of contact does not lend itself to a mass production approach to oscillator fabrication. It therefore tends to be used only when devices are fabricated individually or in small numbers, as for example in preliminary assessments of material quality for the production of devices. We will therefore not concern ourselves further with the bead type of contact.

Three of the contacts most commonly used with GaAs devices are outlined below.

### 11.6.3 THE GOLD GERMANIUM (AuGe) CONTACT<sup>(25)</sup>

It has been found that the eutectic alloy of Au and Ge (88% Au, 12% Ge by weight) can be used to form excellent ohmic contacts to GaAs. A small

amount of Ni (2–11 % by weight) is also necessary to prevent droplet formation as noted earlier.

A sphere of AuGe eutectic and a small amount of Ni are placed in a source boat mounted on a tungsten heater, at a distance of a few cms from the GaAs surface. The chamber is evacuated and the temperature of the source boat raised until all the constituents of the boat have been evaporated. The Ge evaporates first, followed by Au and then the Ni.

With the metals evaporated on to the GaAs surface, the alloying cycle is commenced. When the semiconductor is heated the Au and Ge recombine at the eutectic temperature (356°C) and owing to the low solubility of Ni in AuGe at the alloying temperature (approx. 450°C), the Ni layer remains intact and covers the liquid AuGe on the surface, preventing droplet formation and promoting a uniform planar contact. The contacts thus formed are hard, and stable up to a temperature of over 300°C. A particular advantage of this contact is the ease with which it can be soldered, which is due to the high gold content.

#### 11.6.4 SILVER TIN (Ag/Sn) CONTACT<sup>(26)</sup>

Sn is the metal which leads most easily to non-rectifying contacts on GaAs. It effectively dopes the semiconductor surface heavily *n*-type. However experience with contacts containing a large amount of Sn indicates that when these contacts are subject to high currents and high electric field there is a tendency for the Sn to punch through or form conducting channels between anode and cathode of devices.<sup>(25,27)</sup> In the Ag/Sn contact only a small amount of Sn is used (7 % by weight).

The contact metals are evaporated on to the surface, approx. 500 Å Sn, followed by 5000 Å Ag, and the semiconductor heated. At 230°C the Sn melts but is prevented from forming droplets by the Ag layer. The contacts are alloyed by maintaining a temperature of 600°C for 1 minute. The alloy temperature is kept below the Ag–GaAs eutectic temperature (650°C) so that the Ag plays essentially a passive role as a blanket for the Sn in the contact formation.

This approach produces devices with stable reliable characteristics. To date devices operating continuously with a contact temperature of about 150°C, have logged over 30,000 hours without sign of degradation. No melting of the contact is to be expected up to the alloy temperature. of 600°C.

#### 11.6.5 THE SILVER INDIUM GERMANIUM (AgInGe) CONTACT<sup>(27)</sup>

In this contact, germanium (5 % by weight) is used to dope the GaAs and a small amount of indium (5 % by weight) is also included to reduce the liquid alloy surface tension and promote good wetting to the GaAs. Again Ag is the main constituent of the contact and the alloying (600°C for 1 minute)

takes place below the temperature at which the Ag forms a eutectic with GaAs. The contacts are stable up to temperatures near 600°C.

The contacts described above are probably the most widely used. However other alloys such as AuInGe, SnNi, InAu, and InNi have also been successfully employed. For high conductivity GaAs, ohmic contacts are much easier to achieve and the metals Ag and Au for example, are then able to make good contacts without any dopant additives.

Of the three contacts described, the high temperature contacts (Ag/Sn and AgInGe) offer several advantages. Firstly they clearly enable devices to work at high temperatures. Secondly they offer flexibility in processing—thus a contact can be fabricated and then additional high temperature processing steps carried out without interfering with the contact formed (provided that the temperature does not exceed the contact alloying temperature). Examples of the latter are the fabrication of an additional, lower temperature contact (e.g. AuGeNi) and the deposition of SiO<sub>2</sub> layers on the epitaxial surface by the oxidative decomposition of TEOS (tetraethylorthosilicate) at 475°C.

#### 11.6.6 INTERFACE LAYER

It is a common observation that devices with a metal contact can not be operated with that contact as the anode. This leads to a breakdown of the device above threshold which can be irreversible. Such behaviour has been attributed to avalanching when the high field domain enters a high resistivity layer just under the metal contact.<sup>(28)</sup> The computer simulation indicating this behaviour also indicated that such a high resistivity layer at the cathode results in a stationary high field region at the cathode which reduces oscillator efficiency.

A region of high dislocation density has been shown to occur just under the metal contact,<sup>(29)</sup> and in view of the observed behaviour of the devices it is believed that this damaged zone has a higher resistivity than the rest of the layer. This view is encouraged by the fact that high resistivity layers are not uncommon under alloy contacts, having been observed in *p*-type GaAs<sup>(30)</sup> as well as in Ge and Si.<sup>(31,32)</sup> The increased resistance may be produced by compensation due to acceptor levels associated with the dislocation or by mobility degradation in the damaged zone.<sup>(33)</sup>

#### 11.6.7 CONTACT RESISTANCE

A measure of the quality of the contact is the resistance which it introduces. This is usually expressed in terms of the specific contact resistance  $R_c \Omega \text{ cm}^2$ . Thus for a device of area  $A$  the contact resistance is  $R_c/A \Omega$ , and for metal contacts the values quoted in the Table below are typical. It is however very easy to get metal contacts with much higher resistances if the proper contact schedule is not adhered to.<sup>(34)</sup> The ratio of contact resistance to active device



resistance is given by

$$\frac{R_c/A}{\rho L/A} = \frac{R_c}{\rho L} = R_c \frac{ne\mu}{L} \propto \frac{nR_c}{L}$$

Material resistivity $\rho, \Omega \text{ cm}$	Contact	Measured $R_c$ $\Omega \text{ cm}^2$
0.6–2.6	AgInGe (ref. 27)	$10^{-3}$
0.3	AgInGe (ref. 27)	$6 \times 10^{-4}$
$\leq 0.15$	AgInGe (ref. 27)	$< 1 \times 10^{-4}$
0.1–0.3	Ag/Sn (ref. 35)	$3 \times 10^{-5}$

since mobility has only a small dependence on  $n$ . Since, furthermore, efficient transferred electron oscillators require  $nL$  to be in the region  $1\text{--}2 \times 10^{12} \text{ cm}^{-2}$ , it is evident that the above ratio is closely proportional to  $n^2 R_c$ . The experimental dependence of  $R_c$  on resistivity is very approximately such that

$$R_c \propto \rho \propto \frac{1}{n}$$

so that  $n^2 R_c \propto n$  and the ratio, contact resistance to active device resistance, varies roughly as  $n$ . This explains why for metal contacts, the effects of contact resistance become more pronounced on thin, heavily doped devices. For example, good metal contacts to a epitaxial layer with parameters  $0.1 \Omega \text{ cm}$ ,  $2 \mu\text{m}$  will produce a value  $3 \times 10^{-5} \Omega \text{ cm}^2$  approx. for  $R_c$ . For this device then the ratio of contact resistance to active resistance will be 1.5:1! By way of comparison, contact to a thick, high resistivity layer  $10 \Omega \text{ cm}$   $200 \mu\text{m}$  may result in an  $R_c$  of  $3 \times 10^{-3} \Omega \text{ cm}^2$  and the contact resistance in this case will be only 1.5% of the active device resistance.

The specific contact resistances quoted here probably represent in each case typical values for the resistivity obtained in the damaged interface layer referred to previously. When it is significant, the contact resistance produces a number of undesirable effects. Firstly it leads to a reduction of oscillator efficiency,<sup>(28)</sup> and we can expect that this reduction will be the greater if the resistance is due to mobility degradation and therefore non-linear rather than simply due to reduced carrier concentration. Secondly it results in a slow build up of oscillations after application of a bias pulse to a device.<sup>(36)</sup> Many nanoseconds may be required to build up to full amplitude in cases of high contact resistance. Thirdly, the temperature dependence of the contact resistance<sup>(37)</sup> results in devices having a poor stability of frequency against changes in temperature.<sup>(38)</sup> Finally variability in the contact fabrication

leads to wide variations in the performance of devices. These problems are always present to a greater or lesser extent depending on the magnitude of the contact resistance.

#### 11.6.8 GROWN CONTACTS

The damage which can occur in the fabrication of metal contacts can be completely eliminated if contact is made instead by growing a heavily conducting layer epitaxially on to the surface of the active layer. This produces a contact which is actually part of the crystal lattice of the active layer and which provides a smooth transition between the lower doped GaAs of the active layer and the more heavily doped GaAs of the contact layer.

The contact layer can be epitaxially grown either from the vapour phase or from the liquid phase. It can be grown immediately after the growth of the active layer by increasing the flow of dopant gas in the vapour case or by immersing it in a more heavily doped melt in the liquid case, as noted in Sections 11.3.6 and 11.3.5. This approach is clearly to be preferred over that where the contact layers are grown as a separate operation at a later time since, unlike the latter, it does not provide an opportunity for surface contamination to occur prior to growth of the contact layer. A separate contact growth procedure does however offer more flexibility in that, for example, the contacts can be grown from the vapour on to an active layer which is grown from solution. This is desirable when very thin contacts are required for these may be more readily achieved by vapour growth.

The carrier concentration levels attainable in the contact layers are typically of order  $10^{18} \text{ cm}^{-3}$ , corresponding to  $0.001 \Omega \text{ cm}$  material, and by vapour techniques the layers can be grown with thickness down to 1–2 microns without much difficulty.

The growth of  $n^+$  contact layers however is not without problems of its own, and high resistivity layers have often been observed at the interface between the grown  $n^+$  contact layer and the active layer. In a particular case where  $n^+$  contacts were formed separately by liquid growth the occurrence of the high resistivity layer was thought to be due to the loss of Arsenic from the GaAs at the high temperature involved.<sup>(33)</sup> The problem was overcome in this case by maintaining a small As overpressure to prevent As loss from the GaAs and also by etching back to remove the high resistance layer from the surface immediately prior to growing the contact layer.

In view of the problems which can arise with metal contacts it will on many occasions be preferable to employ  $n^+$  contacts, if these can be satisfactorily produced.

#### 11.6.9 OTHER CONTACTING TECHNIQUES

Two further methods of making contact are worthy of mention. These are

diffused contacts and ion implanted contacts. Little work has been carried out so far on either technique but both offer the capability of achieving the very thin contacts which are essential when devices of high mean power are to be fabricated.

Contact diffusion is achieved by heating the slice with its epitaxial layer in a reactor containing the dopant gas which can then diffuse into the epitaxial surface, doping it heavily *n*-type. The problem here is to achieve good control of the diffusion profile to give a sharp carrier concentration profile at the surface, while avoiding any undesirable diffusion of other impurities in the epitaxial layer, leading for example to a reduction in the active layer thickness. A number of elements have been used successfully to dope GaAs *n*-type, among them S, Sn, Se and Te. Details of the sites in the GaAs occupied by these and other dopants, together with other diffusion data are to be found in Ref. 39.

For ion implanted regions the desired dopant atoms are ionised and accelerated to high velocity in an electrostatic accelerator. The penetration depth will depend upon the energy given to the ions and the main advantage of the method is the precise control of penetration which can be achieved, and hence also control of the spatial distribution of the dopant. The inevitable lattice damage which arises from the bombardment must be annealed out afterwards. Implantation has not been applied much so far to contact fabrication, but it has been shown, for example, that Te can be implanted at 20 keV to form an *n*-type region, the major part of which is contained within 0.1  $\mu\text{m}$  of the surface.<sup>(40)</sup> For the implantation the GaAs was heated to 400°C and it was subsequently annealed at 600°C for 10 min in  $\text{N}_2$ .

### 11.7 DEVICE CONSTRUCTION

A number of different approaches are in use for the fabrication of transferred electron devices. The essential features which are required of any approach are:

- (1) The method of construction must be compatible with integrated circuit techniques to give a high yield of identical devices from a given slice of material.
- (2) The structure must allow for the efficient removal of heat from the small active region of the device where it is generated.
- (3) The completed devices must be reliable (electrically and mechanically) and in a form which is robust and which allows easy handling.

The first of the features is satisfied by performing as many common operations as possible while the devices are still part of the GaAs slice, and then dividing the slice up into a large number of devices for the remaining individual operations of packaging etc.

The efficient removal of heat from the active region of a device allows it to operate nearer to the ambient temperature and this means not only reduced thermal stress but also more efficient generation of microwaves.

The reliability of a device calls in question every process and every metal or alloy used in its fabrication. For example at high operating temperatures, excess Sn in the contact may spike through the active layer; or effects may occur due to strain at the metal-semiconductor interface owing to differences in the thermal expansion coefficient of metal and semiconductor. The properties of the GaAs itself are not without relevance to device reliability, for diffusion of impurities within the material will also lead to degradation of the operating characteristics.

For robustness and ease of handling, the small GaAs chips are usually mounted in suitable metal/ceramic encapsulations.

One of the most important quantities which determines the actual device construction used is the power level to be dissipated. If this is low, 1W or less, say, then a very simple device construction can be employed, which is outlined in Section 11.7.1 and shown in Fig. 11.16. For higher dissipation

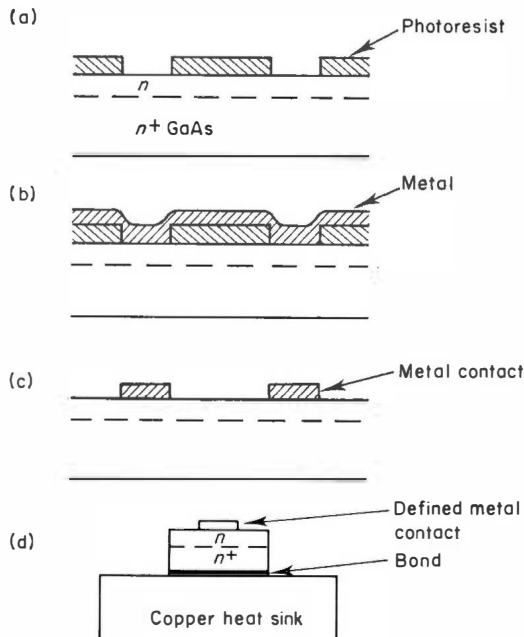


FIG. 11.16. Fabrication procedure for simple device configuration; (a) expose holes in photoresist; (b) deposit metal; (c) float off resist and fire in contacts; (d) saw up processed slice and mount individual devices on heat sinks.

the active region must be mounted as close as possible to the heat sink and this calls for the technique outlined in Section 11.7.2. For reliable devices,

a good bond of the active chip to the heat sink is essential, and a brief discussion is included of the methods available for bonding.

The bonding operation is a very critical one and is an individual operation for each device. This tends to result in an undesirable spread in device characteristics, due for example to the occurrence of voids in the bond made with some devices—this will lead to high thermal resistances for such devices and therefore to a high operating temperature which degrades operating performance. In Section 11.7.4 an outline is presented of techniques for device fabrication with *integral* heat sinks. For these devices the critical bond can be produced with near ideal characteristics and reproducibly for all devices from a slice, giving a high yield of good devices.

### 11.7.1 CONSTRUCTION OF LOW POWER DEVICES

Photoresist is applied to the surface of a slice of  $n$  on  $n^+$  GaAs. A chromium on glass mask bearing the desired pattern of metallisation is brought into contact with the epitaxial surface and the pattern is exposed through the mask. (Fig. 11.16a). The contact metals are evaporated on to the surface (as described for example in Section 11.6.3.) and the excess metal floated off using a suitable solvent for the photoresist. This leaves metal only in areas defined by the mask pattern. The metal (usually Ag/Sn) is fired in to form an array of low resistance ohmic contacts. The contact areas employed typically range from  $50\text{ }\mu\text{m} \times 50\text{ }\mu\text{m}$  to  $100\text{ }\mu\text{m} \times 100\text{ }\mu\text{m}$ .

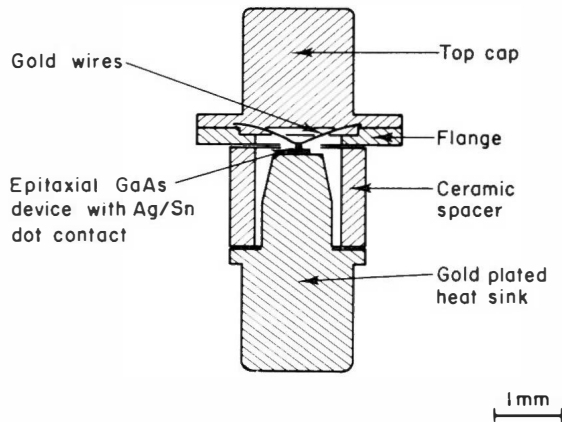


FIG. 11.17. Sectional view of device mounted in a typical encapsulation.

Having defined an array of contacts to the epitaxial layer the layer is inverted and a lower temperature contact, for example AuGe, applied to the substrate (as described in Section 11.6.3). The slice is sawn or scribed and cleaved to produce a considerable number of GaAs chips each approx.

0.25 mm  $\times$  0.25 mm, which are bonded on to a copper heat sink, as shown in Fig. 11.16d. The heat sink will usually be the pedestal of an encapsulation, as shown in Fig. 11.17. A Au wire or tape is thermocompression bonded to the defined top contact and to the flange of the package. The encapsulated device is sealed off hermetically in the package when the top cap is welded on to the flange.

The advantages of this construction are its simplicity, the control of power dissipation in the device by the choice of mask used, and the long path which can be obtained between the two electrodes, preventing electrical breakdown along the exposed surface and edge. The simplicity of manufacture makes this the cheapest microwave oscillator to produce, and its construction makes it very reliable. The long path for heat flow from the active region through the thick (approx. 100  $\mu$ m) GaAs substrate of low thermal conductivity to the heat sink, results in a limit of about 1W being set on the allowable power input to this structure. The microwave output powers range up to about 30–50 mW and devices with this structure have found wide application as local oscillators and transmitters in mini-radar equipments (Chapter 10).

### 11.7.2 FLIP-CHIP CONSTRUCTIONS

Where powers much in excess of 1W have to be dissipated, the high thermal resistance of the GaAs substrate in the previous construction can not be tolerated. This leads naturally to the configuration where the active zone on which the heat is generated is adjacent to the heat sink. For such a configuration a thermal resistance of around 15°C/W is typical, as compared with about 100°C/W for the low power device structure. Clearly it is not sufficient merely to invert the low power structure since a large area of uncontacted GaAs would then be in intimate contact with the heat sink. This would form some sort of metal semiconductor barrier which would be as non uniform as the interface itself and which would lead to current flow in the GaAs outside the desired active region as defined by the Ag/Sn contact.

Two techniques are widely used to fabricate flip-chip devices. In the first of these, the *whole* epitaxial surface is contacted with metal (i.e. no mask) and the slice diced up as before. The individual dice can now be bonded to a heat sink as shown in Fig. 11.18a, and a Au wire or tape thermocompression bonded to the substrate metallisation. With devices having this construction, treatment of the edge is critical to prevent breakdown. In addition it is difficult to maintain uniformity in device area by this technique, and devices of much less than 100  $\mu$ m side are very difficult to produce.

In the second technique, a contact pattern is defined on the epitaxial surface as for the low power device. The unmetallised areas between the

contacts are then etched away to a depth greater than the active layer thickness. This leaves the active devices as an array of mesas, raised above the  $n^+$  substrate. The slice is diced up as usual by scribing and cleaving, and the individual devices mounted, active layer down, on to a heat sink as in Fig. 11.18b.

With the latter approach devices of uniform area can be achieved, and areas down to  $50\text{ }\mu\text{m} \times 50\text{ }\mu\text{m}$  can be realised. Small diameter mesas offer the best heat sinking configuration since a large amount of heat spreads away laterally into the sink. It is therefore often desirable, instead of fabricating a single large mesa, to fabricate a number of small mesas of the same total area. The most common configuration is a three legged structure as shown in Fig. 11.18c, since this is mechanically stable.

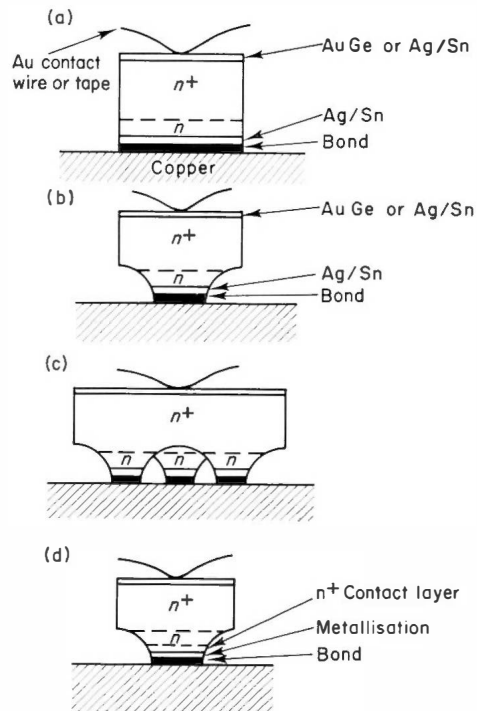


FIG. 11.18. Four flip-chip device configurations.

It will be evident that, for GaAs slices with planar grown contacts, the approach of the previous section is not applicable. However those of the present Section are, and the devices thus produced would resemble those in Fig. 11.18, except for an  $n^+$  region between active layer and metallisation. For example, the equivalent of Fig. 11.18b with a grown contact would be

as shown in Fig. 11.18d. Although desirable for the formation of a good contact to the active region, the low thermal conductivity of this additional layer of GaAs can add significantly to the thermal resistance of the structure. Hence it is desirable to make this  $n^+$  region as thin as possible, and a value of  $2\text{ }\mu\text{m}$  represents about the limit. The effect of such an  $n^+$  region on the thermal properties has been indicated previously in Section 10.1.

Having minimised all other contributions to the thermal resistance of a flip chip device (thinning the  $n^+$  region, for example) we are left with the thermal resistance due to the bond between the chip and the heat sink. The magnitude of this sets the ultimate limit.

### 11.7.3 BONDING

Three methods are commonly employed to obtain a bond between the GaAs chip and the heat sink which is satisfactory both electrically and mechanically. These are the soldered bond, the ultrasonic bond and the thermocompression bond. In practice any combination of these may be employed at will to realise the most satisfactory bond.

The first method is the simplest and is a straight forward soldering of the chip to the heat sink using a solder preform. The main disadvantage is that the large amount of solder used leads to a bond which is typically  $4\text{--}8\text{ }\mu\text{m}$  thick, which in view of the poor thermal conductivity of the known solders leads to a substantial thermal resistance.

The ultrasonic bond involves scrubbing the two surfaces to be bonded together, with the heat sink at a temperature up to  $300^\circ\text{C}$ . In this way intimate contact can be achieved between the surface molecular layers leading to excellent adhesion of the chip to the heat sink. This approach may not be desirable if small mesas are being bonded, because of the lateral stress which is applied to the mesas.

For the thermocompression bond the surfaces to be bonded are brought together, raised in temperature, and subjected to a high pressure. For successful bonding the right conditions of pressure and temperature must be established. A bond formed at high temperature requires less pressure, but if too high a temperature is used, appreciable strain will be set up in the device due to the mismatch in thermal expansion of GaAs and the metal heat sink (copper). A bond formed at low temperature however requires very high pressures and there is the danger of damaging the GaAs chip. The compromise usually employed is a temperature of  $300\text{--}350^\circ\text{C}$  and a pressure of around  $15,000\text{--}30,000\text{ lbs/in}^2$  ( $1\text{--}2$  kilobars).

For both ultrasonic and T.C. bonds it is common practice to evaporate or plate a Au layer ( $0.5\text{--}5\text{ }\mu\text{m}$ ) on to the metal contact and also to plate the heat sink with a few microns of Au, in order to facilitate the formation of the bonds. Both lead to bonds which can be less than  $2\text{ }\mu\text{m}$  thick and which,



because of the high thermal conductivity of the Au, possess low thermal resistance.

Flip chip devices, thermocompression bonded on to a Copper heat sink have been able to dissipate up to 40W of continuous power input. Microwave power outputs from these devices have reached 1W.<sup>(41)</sup>

#### 11.7.4 INTEGRAL HEAT SINK CONSTRUCTION

Formation of the bond between chip and heat sink is a critical operation which must be performed separately with each and every device. The integral heat sink approach seeks to overcome this disadvantage by careful formation of this bond at a processing stage where the whole of the slice is being handled. Having successfully formed the crucial bond, the later operation of bonding or soldering each unit into an encapsulation becomes much less important since the heat will be well spread out when it reaches the second bond. The technique thus potentially offers greater ease in the packaging of devices and greater reproducibility in the performance of packaged devices.

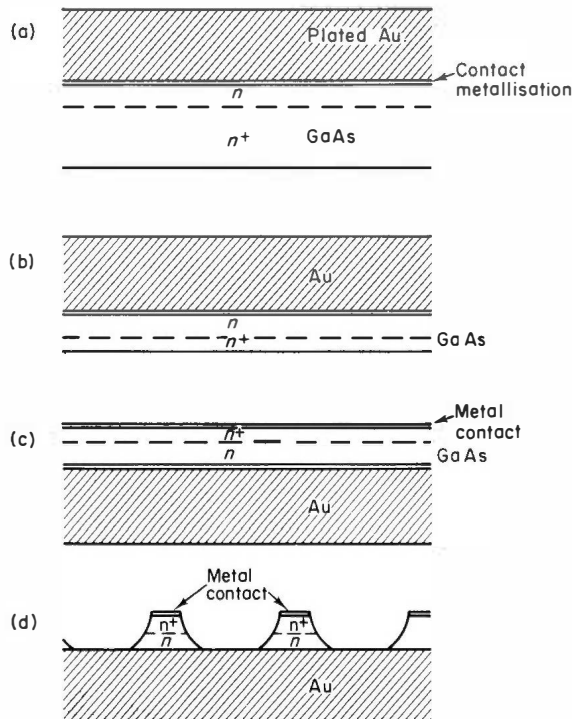


FIG. 11.19. The integral heat sink construction; (a) metallize epitaxial layer and plate with Au; (b) lap off most of substrate; (c) metallize substrate; (d) define a pattern on substrate and etch away unwanted metal and GaAs.

The slice is metallised on the epitaxial surface only and the contact fired in. Au is plated on top of the contact to a thickness of 50–100  $\mu\text{m}$  (Fig. 11.19a). The substrate is lapped and etched to reduce slice thickness (Fig. 11.19b) and the thick plated Au acts as a support for the thin GaAs slice for the rest of the process. Metallisation is then applied to the substrate and this contact fired in (Fig. 11.19c). Photoresist is deposited on to the substrate metal and exposed through a mask to define the desired pattern. The selected regions of metal and GaAs are etched away to leave the structure shown in Fig. 11.19d. The Au base is finally diced up to yield individual flip chip mesas with integral heat sinks. These can then be mounted into microwave encapsulations by soldering or thermocompression bonding.

### 11.7.5 ENCAPSULATIONS

Some of the most commonly used encapsulations are shown in Fig. 11.20. They all comprise a metal base (heat sink) and top hat or cap to which the Au bonding wires are connected (Fig. 11.17). The two parts are separated by an annular section of ceramic, usually alumina ( $\epsilon \approx 9$ ).

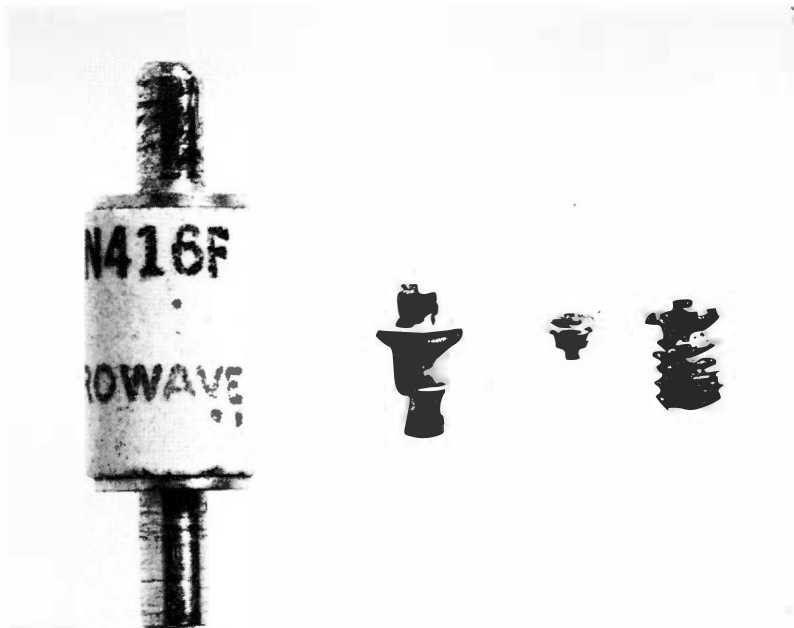


FIG. 11.20. Encapsulations commonly used with microwave solid state oscillators. (Crown Copyright, published by permission of the Controller of Her Majesty's Stationery Office).

The function of the encapsulation is to provide the small GaAs chip with a housing which is readily handled, robust, and flexible (in that it can be incorporated into a variety of microwave circuits), without detracting in any way from the microwave performance of the chip itself. In practice the latter consideration means that the maximum allowable size of the encapsulation falls with increasing operating frequency, since otherwise the parasitics of the encapsulation become important elements of the microwave circuit, which is not usually desirable.<sup>(42)</sup> This effect becomes so pronounced at the highest frequencies (over 50 GHz say) that the preferred approach is to integrate the semiconductor chip with the circuit in which it is to operate without employing any encapsulation.<sup>(43)</sup> Flexibility is inevitably lost, but the microwave performance is much improved.

The size of the highest frequency package shown is very small indeed (0.030 in diam. ceramic). To ensure good heat sinking as well as convenience in handling, this miniature encapsulation has been fabricated on the end of a large copper screw.

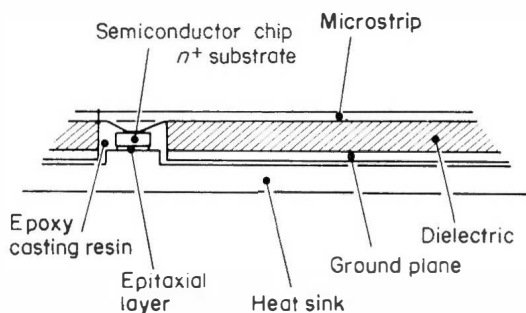


FIG. 11.21. A transferred electron device mounted directly into microstrip.

A major limitation to the usefulness of any encapsulation occurs when a resonance occurs between it and the diode it contains. The resonant frequency depends on diode impedance, of course, but one can nevertheless set down an approximate guide as to the maximum frequency at which the packages shown are useful. In order of decreasing package size, these frequencies would very approximately be 10, 25, 35 and 50 GHz.

On some occasions it is desirable to operate diodes in microstrip circuits and this is often done without any encapsulation. A typical mounting configuration for the diode will then be as shown in Fig. 11.21, where it is bonded directly on the ground plane of the microstrip and the Au tapes attached to the microstrip conductor. For reliable operation the diode is sealed by potting in an epoxy resin.

### 11.7.6 PLANAR DEVICE CONFIGURATIONS

The device configurations dealt with so far have all had the general feature that the direction of heat flow is the same as that of current flow. This is a consequence of the active layers all being grown on to  $n^+$  substrates. There are advantages to be gained by employing a different device configuration which results from growing the active layer on to a semi-insulating (S.I.) substrate. Here *both* contacts must be made to the surface of the epitaxial layer. The first attempts to construct such a device followed the simple approach of depositing metal contacts on to the surface to form both electrodes, as shown in Fig. 11.22e. This configuration proved to be prone to electrical breakdown, largely due to current crowding at the leading edge of the anode metallisation.<sup>(44)</sup> To avoid this problem the anode contact was made a sunk-in  $n^+$  region (Fig. 11.22f). Although such devices are reliable they suffer from the fact that for high frequency operation their design is a compromise since the diode parameters must be chosen to optimise geometry (minimise  $t/L$ ) as well as satisfying the  $nL$  and  $nt$  space charge criteria discussed in Chapter 4.<sup>(45)</sup>

A more optimum design can be realised by making the cathode contact a sunk-in  $n^+$  region just like the anode. If the epitaxial layers are not too thick the  $n^+$  contacts can be made to extend right through the layer and the uniform device cross-section then removes the need for any criterion on the device geometry.

The fabrication of planar devices follows the course now to be outlined. After the deposition of an  $\text{SiO}_2$  layer on to the epitaxial surface, windows are opened up as shown in Fig. 11.22a, using the standard photolithographic techniques, and GaAs etched out as shown in Fig. 11.22b. The slice is then mounted in a reactor and  $n^+$  GaAs grown into the holes. Another photolithographic process is required to apply the contact metallisation to the  $n^+$  GaAs and to remove the oxide. The result is an epitaxial layer with an array of sunk-in  $n^+$  pockets. The pockets are typically 1–2  $\mu\text{m}$  deep and of line geometry, the length being dictated by the desired value of device resistance.

For devices having a surface metal contact, a set of  $n^+$  contacts are produced followed by the evaporation of metal stripes on to the surface, each stripe being adjacent and parallel to a line of sunk-in  $n^+$  contact, and at the required separation from it (Fig. 11.22f). For a double  $n^+$  contact device, pairs of sunk-in  $n^+$  pockets are arranged to have the separation appropriate to the desired operating frequency.

The planar form of transferred electron device is of interest for several reasons.

- (1) Heat flow is transverse to the direction of current flow so that devices with large contact separations can be constructed while maintaining

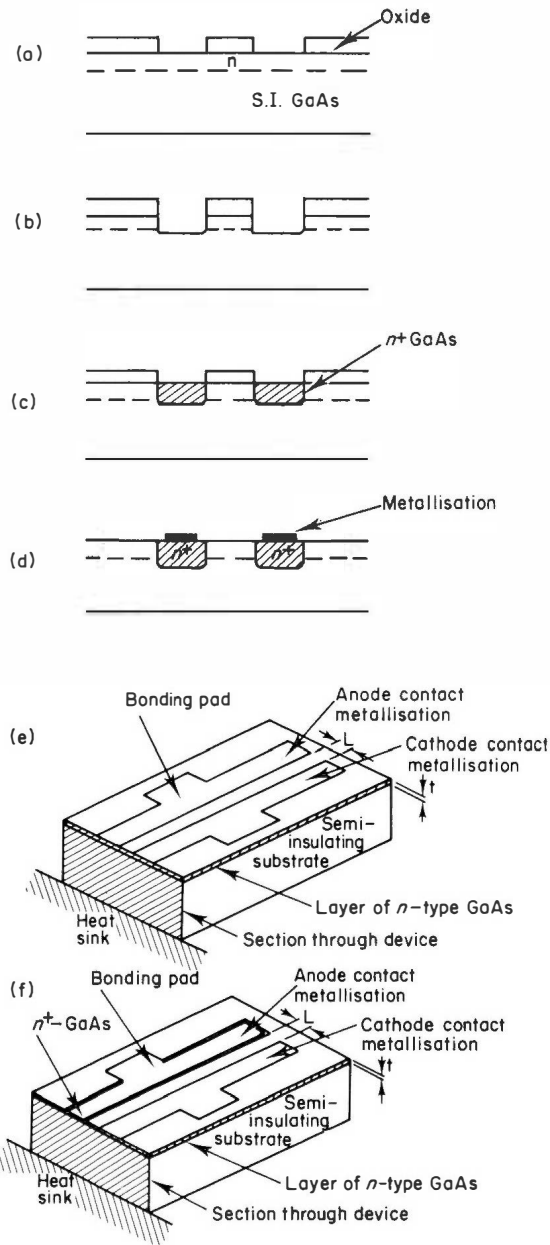


FIG. 11.22. Fabrication process for planar transferred electron devices: (a) deposit oxide and open up holes photo-lithographically; (b) etch holes in the GaAs; (c) grow  $n^+$  GaAs in these holes; (d) metallize the  $n^+$  contact region and remove oxide; (e) planar device with two surface metal contacts; (f) planar device with one surface metal contact and one sunk-in  $n^+$  contact.

close proximity of all regions of the device to the heat sink. For  $n$  on  $n^+$  devices a large thermal gradient would be set up across the layer. The large contact separation is for example required for domain mode operation at low frequencies, or for LSA operation.

- (2) Access is more readily obtained to the active region for control of domain propagation etc. This is desirable in logic applications and functional devices.<sup>(46)</sup>
- (3) Compatibility with microwave integrated circuits, in particular monolithic circuits using S.I. GaAs as the substrate material.
- (4) It is suitable for the fabrication of space charge wave amplifiers.

However, interest in these features has not so far been sufficient to stimulate much work on these devices. As far as the usual transferred electron oscillation applications are concerned, these are mostly at X-band and above, and utilise domain modes of operation. At these frequencies the planar structure is at a distinct disadvantage on thermal grounds because of the thickness of the S.I. support substrate.

#### REFERENCES

1. Richman, D. (1963). *J. Phys. Chem. Solids* **24**, 1131.
2. Mullin, J. B. *et al.* *J. Phys. Chem. Solids* **26**, 782-4.
3. Allen, J. W. (1960). *Nature*, July 30, 403-5.
4. Knight, J. R. *et al.* (1965). *Solid State Electronics* **8**, 178-80.
5. Tietjen, J. J., Amick, J. A. (1966). *J. Electrochem. Soc.* **113**, 724-8.
6. Enstrom, R. E., Peterson, C. C. (1967). *Trans. Metallurgical Soc. of A.I.M.E.* **239**, 413-8.
7. "Proceedings of the International Symposium on Gallium Arsenide". I.P.P.S. Reading, Sept. 1966.
8. Wolfe, C. M. (1969). M.I.T. Lincoln Lab. Report on Semiconductor Research.
9. Nelson, H. (1963). *R.C.A. Review* **24**, 603-15.
10. Goodwin, A. R. *et al.* (1968). *Brit. J. Appl. Phys. Ser. 2* **1**, 115-6.
11. Madelung, O. (1964). "Physics of III-V, Compounds". p. 236. John Wiley, London.
12. S.T.L. Annual Report 1969, Research Project RP7-43 and Private Communication from J. S. Heeks.
13. Kang, C. S., Greene, P. E. (1967). *Appl. Phys. Lett.* **11**, No. 5, 171-3.
14. Groves, W. O. (1962). *Semiconductor Products*, 25-28.
15. Henisch, H. K. (1957). "Rectifying Semiconductor Contacts". Oxford University Press.
16. Meyer, N. I., Guldbransen, T. (1963). *Proc. I.E.E.E.* **51**, 1631-7.
17. Copeland, J. A. (1969). *I.E.E.E. Trans.* ED-16, 445-9.
18. Thomas, C. O. *et al.* (1962). *J. Electrochem. Soc.* **109**, 1055-61.
19. Amron, I. (1964). *Electrochem. Tech.* **12**, 327-9.
20. Baxandall, P. J. *et al.* (1971). *J. Sci. Inst.* **4**, 213-221.
21. Ziman, J. M. (1964). "Principles of the Theory of Solids". p. 211. Cambridge University Press.

22. Reid, F. (1962). *Compound Semiconductors 1*, (Willardson and Goering, Eds.) Holt Reinhold, New York.
23. Smith, R. A. (1964). "Semiconductors". Cambridge University Press.
24. Salow, H. and Grobe (1967). Technical Report on Non-Rectifying Contacts to GaAs, published by the Central Office for Technical Information of the German Post Office, and Rhoderick, E. H., *J. Phys. D.* **3**, 1153, 1970.
25. Braslau, N. *et al.* (1967). *Solid State Electronics* **10**, 5, 381-3.
26. Bott, I. B. *et al.* (1966). "Proc. Int. Symposium on Gallium Arsenide". I.P.P.S. Reading.
27. Cox, R. H. and Strack, H. (1967). *Solid State Electronics* **10**, 12, 1213-8.
28. Hasty, T. *et al.* (1968). *J. Appl. Phys.* **39**, 4623.
29. Cox, R. H., Hasty, T. E. (1968). Abstract No. 496, Electro. Chem. Soc. Meeting, Montreal, 1968.
30. Weiser, K. and Woods, J. F. (1965). *Appl. Phys. Lett.* **7**, 225.
31. Park, J. N. *et al.* (1967). *J. Appl. Phys.* **38**, 5343.
32. Chynoweth, A. G. and Pearson, G. L. (1958). *J. Appl. Phys.* **29**, 1103.
33. Harris, J. S. *et al.* (1969). *J. Appl. Phys.* **40**, 4585.
34. Paola, C. R. (1970). *Solid State Electronics* **13**, 1189.
35. Colliver, D. J. *et al.* (1970). *Electron. Lett.* **6**, 11, 353.
36. Myers, F. A. (1970). Paper No. 6.4, MOGA Conf. Kluwer-Deventer, Amsterdam.
37. Bolton, R. M. G. and James, B. F. (1969). *Electron. Lett.* **5**, No. 25, 662.
38. Bird, J. *et al.* (1971). *Electron. Lett.* **7**, 300.
39. Yarbough, D. W. (1968). *Solid State Tech.* p. 23,
40. Mayer, J. W. *et al.* (1967). *J. Appl. Phys.* **38**, 1975.
41. Narayan, S. Y. *et al.* (1971). *Electron. Lett.* **7**, No. 2, 31.
42. Taylor, B. C. *et al.* (1970). *I.E.E.E. Trans. MTT-18*, 11, 799.
43. Toyama, Y. *et al.* (1970). "Proc. 2nd Conf. on Solid State Devices". Tokyo, pp. 234-40, Supplement to *J. of Jap. Soc. of Appl. Phys.* **40**, 1971.
44. Colliver, D. J. and Fray, A. F. (1969). *Solid State Electronics* **12**, 671.
45. Parkes, E. P. *et al.* (1971). *I.E.E.E. Trans. ED-18*, 10
46. Shoji, M. (1967). *I.E.E.E. Trans. ED-14*, 9, 535,

## Chapter 12

# Further Developments in Bulk Negative Conductivity

### 12.1 INTRODUCTION

Since the discovery of bulk negative differential mobility effects in GaAs and InP, similar effects have been shown to occur in a number of other semiconductors. Table 1 tabulates those semiconductors which exhibit effects at room temperature, while Table 2 records those in which the effect can be observed by going to low temperatures and/or by applying pressure to suitably modify the band structure. Negative differential mobility effects have even been observed in *p*-type Ge<sup>(11)</sup> by the application of uniaxial stress, as first suggested by Ridley and Watkins.<sup>(12)</sup> The applied stress splits the degeneracy in the valence band of Ge and a negative resistance arises due to the transfer of holes between the high and low mobility subbands.

The long list of materials presented in Tables 1 and 2 underlines the fact that bulk negative resistance can no longer be regarded as peculiar to GaAs and a few other less common semiconductors. It has become an accepted feature arising out of the complexity of the band structure of semiconductors. Negative resistance effects have been observed in the familiar semiconductors Ge<sup>(7)</sup> and InSb<sup>(8)</sup> although it only occurs at low temperatures, and in the case of InSb short pulses are also required to avoid avalanching. These facts, together with the fact that the negative resistance effect is small in the much examined semiconductor Ge, help to explain why bulk negative resistance was not discovered earlier during experiments on Ge and InSb. Figure 12.1a shows the current waveform of a Ge sample at 27°K with the characteristic Gunn effect spikes,<sup>(13)</sup> while Fig. 12.1b shows measured velocity field curves for electrons in Ge at temperatures up to 130°K in a  $\langle 100 \rangle$  orientation.<sup>(14)</sup>

We now know that electron transfer is not an essential requirement for bulk negative resistance and negative resistances occurring within a single valley are discussed in Section 12.2.



In Section 12.3 we discuss how the other binary III–V compounds compare in performance with GaAs and how new transferred electron materials can be produced by suitably alloying binary compounds.

The significance of the magnitude of the deformation potential coupling the central and satellite valleys is discussed in Section 12.4 and for weak intervalley coupling it is pointed out that we have to include higher energy sets of conduction band minima in our considerations. Semiconductors which may have a low value of intervalley coupling and which may therefore require a three energy level description are described in Section 12.4.1. Velocity field curves are presented for these three level oscillators and used to deduce operating efficiencies for the oscillators and the dependence on bias field.

In the final section we discuss what we look for in new transferred electron materials if they are to provide devices with efficiencies significantly better than those obtainable from GaAs.

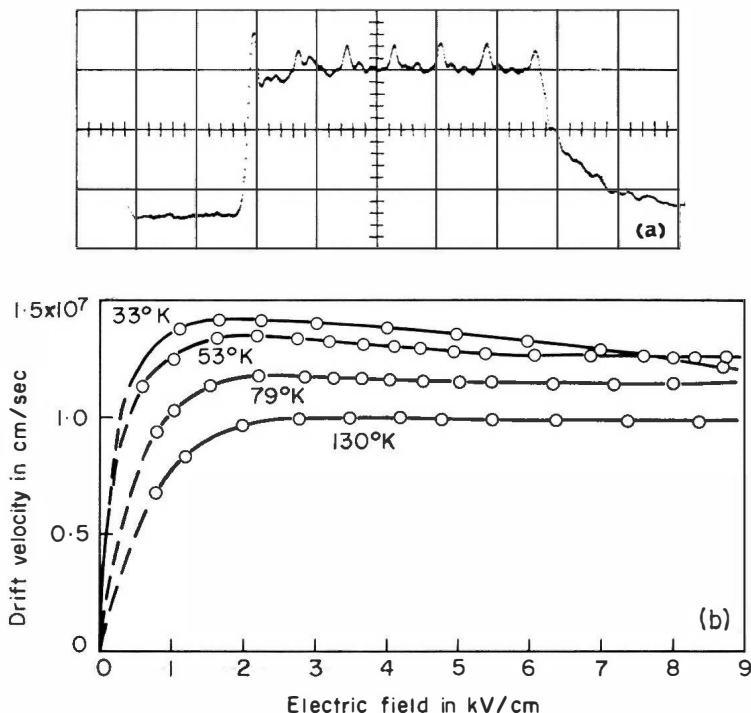


FIG. 12.1(a). Current waveform, showing spikes associated with travelling domains for a sample of  $n$ -Ge at 27°K. Bias 52 V, sample length 190  $\mu$ m, horizontal scale 2 nsec/div.<sup>(13)</sup>  
 (b) Velocity field characteristic of electrons in Ge at various temperatures determined by transit time measurements on reverse biased  $i-n^+$  diodes.<sup>(14)</sup>

## 12.2 NEGATIVE MOBILITY DUE TO INTRA-BAND SCATTERING

Hilsum<sup>(15)</sup> has calculated the velocity field characteristic for electrons in the  $\langle 111 \rangle$  minimum of GaSb which are subject to three scattering mechanisms polar optical, non-polar optical and acoustic phonon scattering. Deducing values of 3450, 7300 and 2400  $\text{cm}^2/\text{Vsec}$  for the respective low field mobility limits due to the three scattering mechanisms, he calculates the curve shown in Fig. 12.2.

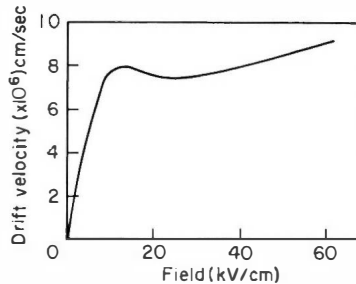


FIG. 12.2. The field dependence of the electron drift velocity in the  $\langle 111 \rangle$  conduction band minimum of GaSb.<sup>(15)</sup>

The negative resistance in this case arises from polar optical phonon scattering dominating the electron energy loss, even though acoustic modes are most important in determining the momentum loss, as is evident from the mobility values above. Polar optical phonon scattering has the characteristic that it rapidly becomes ineffective in removing energy from the electrons as the field is increased, with the result that the electron temperature can rise rapidly. This rapid rise in electron energy reflects in an increase in the rate of loss of momentum which can be so marked as to lead to a reduction in the electron drift velocity as the field increases.

Intra band scattering has been suggested as the origin of negative resistance effects observed in unstressed InSb at low temperatures.<sup>(8)</sup> It is postulated that the negative resistance is due to non-parabolicity in the central minimum.<sup>(16, 17)</sup> The non-parabolicity means a much enhanced increase of density of states with increasing energy. The electron scattering rate is therefore enhanced at high energy and the rate of increase with applied field is sufficient to lead to a reduction in the drift velocity. A more accurate calculation of the velocity field curve<sup>(18)</sup> confirms that negative resistance may arise due to non-parabolicity in the central minimum but indicates that this effect is overshadowed by electron transfer to upper minima. The curves calculated are shown in Fig. 12.3.

Calculations of the  $v$ - $E$  curve of  $n$ -Ge at low temperatures also indicate that the oscillations observed<sup>(7)</sup> are due to negative mobility induced by non-parabolicity in the lowest minimum.<sup>(19)</sup> More detailed calculations by Fawcett and Paige<sup>(20)</sup> on the other hand suggest that the more important effect is again that of transfer to upper minima.

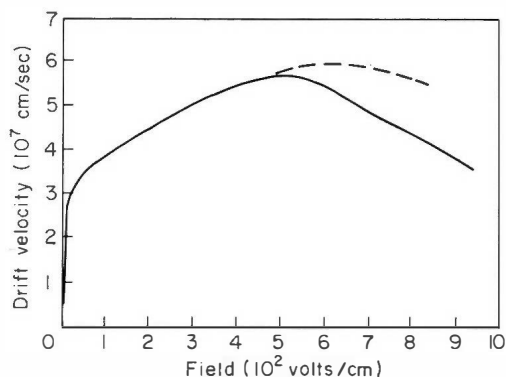


FIG. 12.3. The field dependence of the electron drift velocity in InSb at 77°K. (a) Neglecting the  $\langle 111 \rangle$  minima (broken curve); (b) Including the  $\langle 111 \rangle$  minima (full curve).<sup>(18)</sup>

### 12.3 OTHER SUITABLE III-V COMPOUNDS

From Table 1 we see that InP, CdTe and ZnSe are other binary compounds capable of being developed to produce transferred electron devices. ZnSe however looks very unattractive on account of the high threshold field required for transfer. Little is known about the band structure of CdTe but the rather high threshold field together with the comparatively low

TABLE 12.1. Materials in which effects due to negative differential mobility have been observed.

Material	Threshold field kV/cm	Peak velocity (approx) cm/sec	Reference
GaAs	3.3	$2 \times 10^7$	1
InP	7-10		1
			2
CdTe	13	$1.3 \times 10^7$	3
ZnSe	38	$1.5 \times 10^7$	4
$\text{GaAs}_x\text{P}_{1-x}$ ( $x > 0.6$ )	2.3		5
$\text{In}_{1-x}\text{Ga}_x\text{Sb}$ ( $x > 0.3$ )	0.6	$1 \times 10^7$	6

peak electron velocity suggest that it too would be unlikely to yield devices with a performance which could compete with, let alone improve on, that which can be obtained with GaAs devices.

TABLE 12.2. Materials which have been made to exhibit effects by operation at reduced temperature and/or by application of pressure.

Material	Threshold	Peak velocity cm/sec	Comments	Reference
Ge	2.3(77°K)	$1.4 \times 10^7$ (77°K)	Temperature below 120°K $\langle 100 \rangle$ or $\langle 110 \rangle$	7
InSb	0.6(77°K)		Low temperature Short pulse measurement	8
InAs	1.4	$> 2 \times 10^7$	Room temperature Uniaxial stress along $\langle 111 \rangle$	9
InSb	0.2	$3 \times 10^7$ (77°K)	Low temperature Hydrostatic pressure	10
p-type Ge	0.3		Temperature below 160°K Uniaxial stress along $\langle 111 \rangle$ or $\langle 100 \rangle$	11

The third material however, InP does warrant further consideration in view of the fairly low threshold field and the promising peak to valley velocity ratio which it offers. Taking the nearest satellite valleys in InP to be the  $\langle 100 \rangle$  and an inter-valley separation of 0.8 eV, Fawcett *et al.*<sup>(21)</sup> have calculated the  $v$ - $E$  characteristic shown in Fig. 12.4. A peak velocity of  $2.8 \times 10^7$  cm/sec is indicated and since it is believed that the  $\langle 100 \rangle$  minimum in InP is similar to that in GaAs, a saturated velocity of around  $9 \times 10^6$  cm/sec is expected at high fields. This gives InP a peak/valley

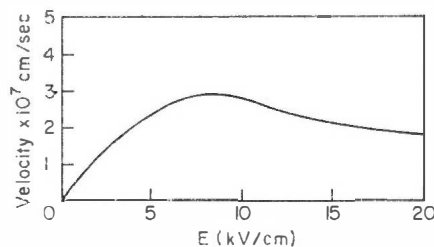


FIG. 12.4. The velocity-field characteristic for InP, assuming transfer to the  $\langle 100 \rangle$  valleys at an intervalley separation of 0.8 eV. Deformation potential  $1 \times 10^9$  eV/cm.<sup>(21)</sup>

ratio of 3.1 which is to be compared with the value of approximately 2.2 for GaAs. From the square wave model discussed in Section 5.5, we therefore predict a maximum fundamental efficiency of over 40% for InP as compared with 30% for GaAs. More important, whereas this comparison is made at room temperature, the more appropriate comparison would be at high temperatures corresponding to the operating temperature of practical devices. The much larger value for the separation of the energy minima in InP (0.8 eV) should mean a lesser degradation of efficiency as temperature is increased, thereby making the advantage to be gained over GaAs still more attractive.

Recent ideas on the band structure of InP however suggest that it may not be as assumed here and that both the  $\langle 100 \rangle$  and the  $\langle 111 \rangle$  satellite minima are involved in the transfer process. This model of InP as a three energy level system is discussed further in Section 12.4.1.

### 12.3.1 MIXED CRYSTALS

In some cases a new transferred electron material can be produced by suitably alloying two binary compounds, neither of which satisfies all the criteria for electron transfer. Furthermore we can often expect to improve the performance of an established transferred electron material by alloying to it a small amount of another material so as to modify the band structure in a desired way, for example to increase the intervalley energy separation. An example of the former would be a suitably composed alloy of InSb and GaSb, and of the latter an alloy of InAs and GaAs. Such III-V mixed crystals have the general form  $(A_x^{III} B_{1-x}^{III})C^V$  or  $A^{III}(C_x^V D_{1-x}^V)$  i.e. a group III or a group V element is common to the two binary compounds forming the alloy, and the substitution in the lattice is between atoms of the same group.

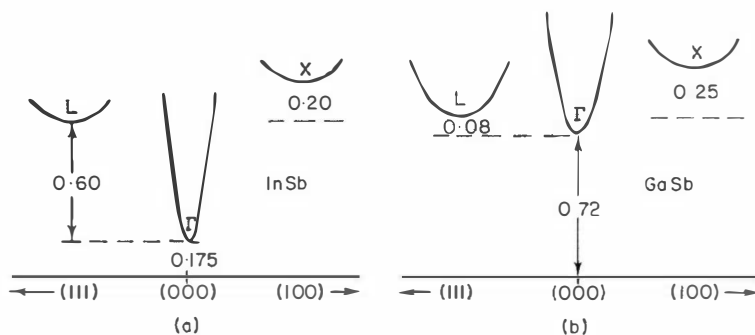


FIG. 12.5. The conduction band of (a) InSb and (b) GaSb. Energy separations as given in ref. 25.

The band structures of InSb and GaSb are shown in Fig. 12.5. Electron transfer in InSb can only be obtained with difficulty because of avalanching due to the large intervalley separation and the small energy gap. GaSb does not exhibit electron transfer because the intervalley separation is so low that the satellite minima are well populated at room temperature and with zero applied field. However, by suitably alloying the two compounds an  $\text{In}_{1-x}\text{Ga}_x\text{Sb}$  alloy can be formed (Fig. 12.6) where the intervalley separation is large enough to prohibit thermal transfer and the energy gap large enough to allow transfer to occur before ionisation energies are reached.

We might expect to improve GaAs as a transferred electron material by alloying to it a small amount of InAs so as to reduce the electron mass and increase the intervalley separation, both of which will tend to increase the

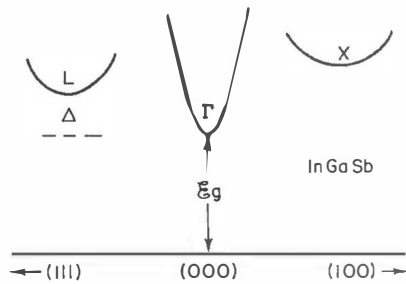


FIG. 12.6. The band structure of the mixed crystal  $\text{In}_{1-x}\text{Ga}_x\text{Sb}$ . For a suitable composition  $\Delta < E_g$  and is sufficiently large to avoid thermal transfer. The requirements for electron transfer are then satisfied.

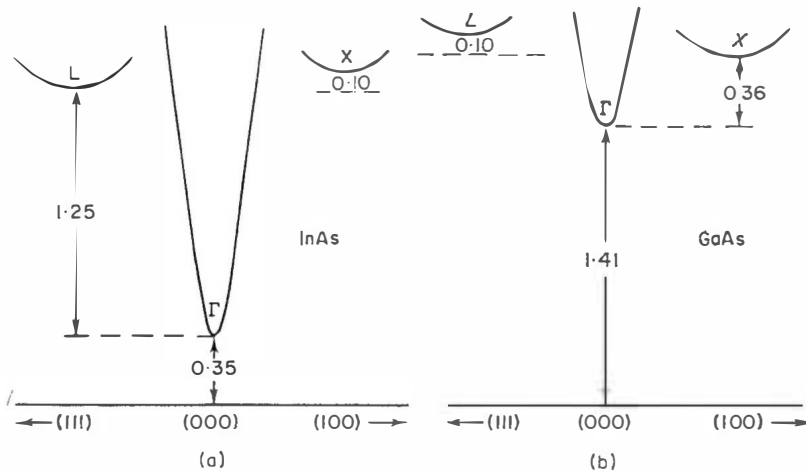


FIG. 12.7. The conduction bands of (a) InAs and (b) GaAs. Energy separations as given in refs 25 and 22. Values apply at 300°K.

peak electron drift velocity. The band structures of InAs and GaAs are shown in Fig. 12.7 and alloying InAs to GaAs will lead to an increase of the intervalley separation  $\Delta$  as shown in Fig. 12.8. Up to 50% InAs can be tolerated in the alloy before the intervalley separation becomes greater than the band gap and electron transfer is no longer obtained. For this range of composition the alloy should have an electron mass intermediate between that of GaAs ( $0.067 m_0$ ) and the very low value of InAs ( $0.022 m_0$ ). This fact and the increased separation should mean higher peak velocities in the alloy than in GaAs itself which, if the satellite velocity is essentially unchanged, will lead to a higher maximum operating efficiency.

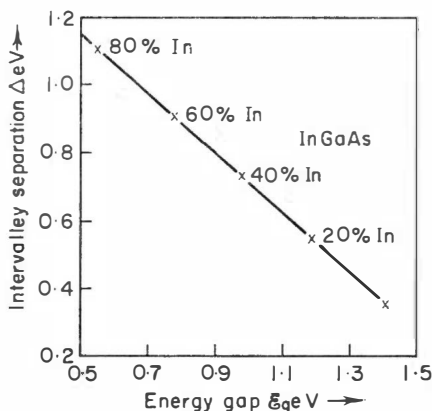


FIG. 12.8. Inter-valley energy separation  $\Delta$  versus energy gap  $E_g$  for the mixed crystal InGaAs. Data from ref. 21.

A practical transferred electron material should desirably have a large enough energy gap (1 eV, say) in order to remain extrinsic at the high temperatures often encountered in device operation. This would rule out InGaSb completely and restricts the allowable InAs content in InGaAs to less than 30%.

#### 12.4 THE IMPORTANCE OF THE INTERVALLEY COUPLING CONSTANT

Although it is generally assumed that the magnitude of the deformation potential coupling the central ( $\Gamma$ ) and  $\langle 100 \rangle$  (X) minima in GaAs is around  $1 \times 10^9$  eV/cm, this is by no means certain. Fawcett *et al.*<sup>(22)</sup> have taken values ranging from  $2 \times 10^8$  eV/cm to  $2 \times 10^9$  eV/cm and have examined how the velocity field curve varies with the magnitude of this potential. Their results are shown in Fig. 12.9 and these results and their implications will now be discussed.

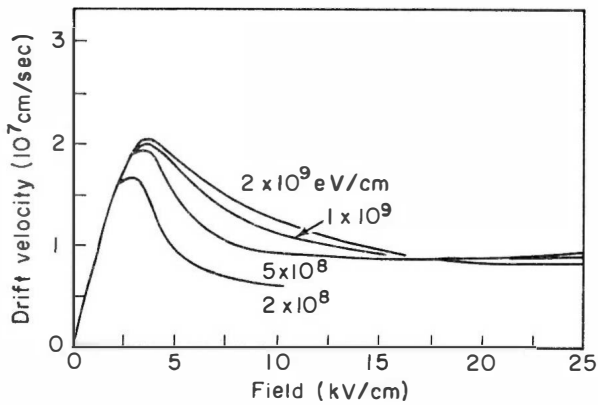


FIG. 12.9. The velocity-field curve for electrons in GaAs, assuming values of  $2 \times 10^8$ ,  $5 \times 10^8$ ,  $1 \times 10^9$ ,  $2 \times 10^9$  eV/cm for the deformation potential  $\Xi$  coupling the  $\Gamma$  and  $X$  minima.<sup>(22)</sup>

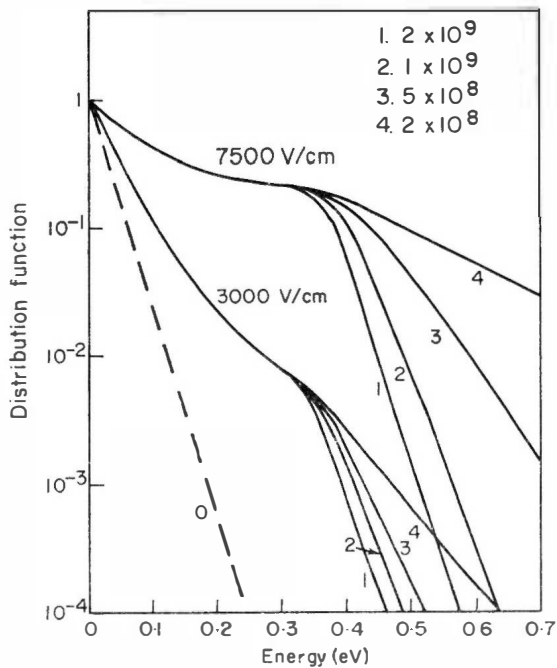


FIG. 12.10. The electron distribution function in the central ( $\Gamma$ ) minimum in GaAs at applied fields of 0, 3000 V/cm and 7500 V/cm and for values of the intervalley deformation potential  $\Xi$  from  $2 \times 10^8$  to  $2 \times 10^9$  eV/cm.<sup>(22)</sup>



The electron distribution function in the central valley is shown in Fig. 12.10 for the range of deformation potentials considered. The distribution functions are plotted for values of applied field 0, 3 kV/cm and 7.5 kV/cm. It is evident from these that for strong coupling between the central and satellite valleys (high deformation potentials), there is a rapid fall-off in the electron distribution function at high energy. The "tail" of the distribution function sets in at around 0.36 eV, the intervalley energy separation. The temperature of the electrons in the tail (indicated by the slope of the distribution function) is dependent on the deformation potential and is close to the lattice temperature (indicated by the slope at zero field) when the deformation potential is  $2 \times 10^9$  eV/cm. Further increase in deformation potential will scarcely alter the distribution function.

On the other hand, small values of the potential (weak coupling) allow electrons in the central valley to reach very high energies. Consequently at a given value of applied field there will be more electrons at high energy for weak than for strong coupling, and correspondingly there will also be more electrons in the satellite valleys in this case. This is confirmed by the data presented in Fig. 12.11.

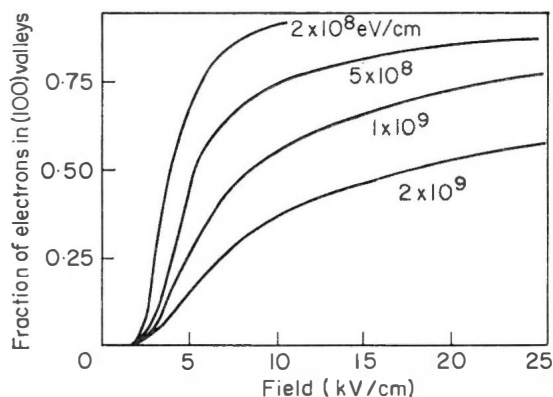


FIG. 12.11. Fraction of electrons in the  $\langle 100 \rangle$  valleys for various intervalley deformation potentials.<sup>(22)</sup>

Thus for weak intervalley coupling most of the transfer from central to satellite valleys takes place over a very narrow range of electric field and the drift velocity drops sharply as shown in Fig. 12.9. The peak-valley ratio increases to about 2.8. A disadvantage of the rapid transfer however will accrue from the fact that electrons in the satellite valleys are travelling with drift velocities below their saturated value when transfer is almost complete, and hence the drift velocity will tend to increase slowly with increasing field beyond the valley velocity.

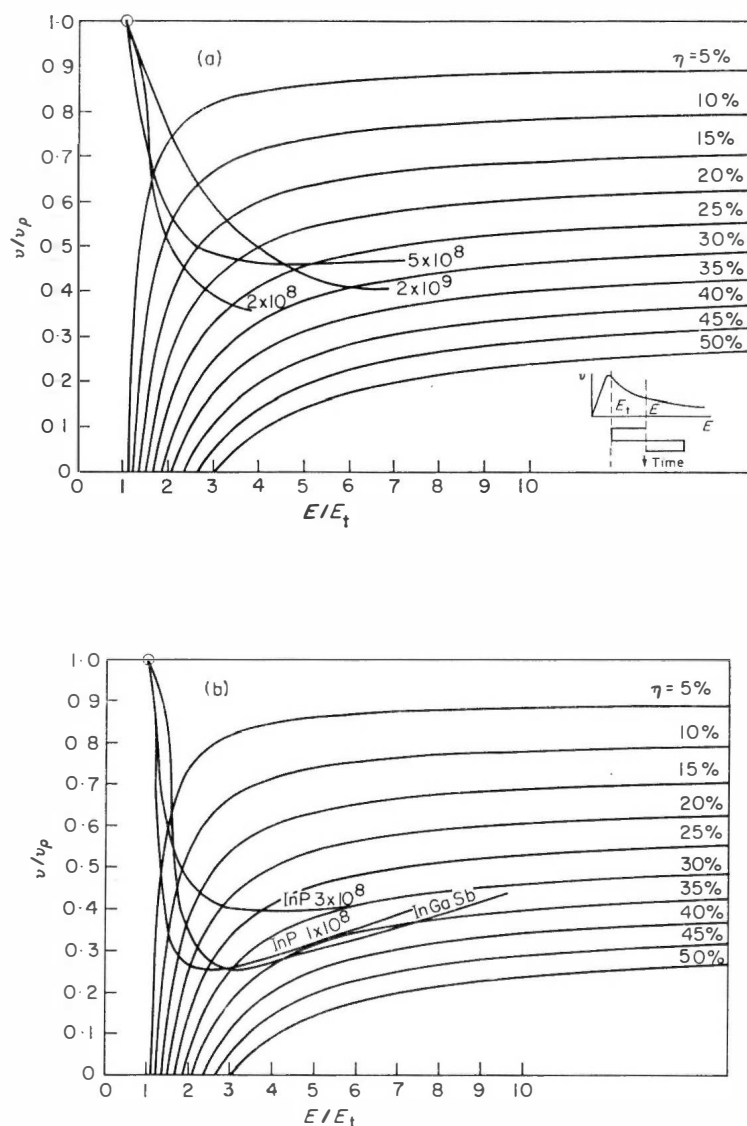


FIG. 12.12. Efficiency curves based on an assumed square wave model for the oscillation, as indicated in the insert. A normalized velocity field characteristic plotted on these curves enables fundamental operating efficiency to be read off directly for any bias field  $E^{(23)}$ . Shown plotted in normalized form in (a) are the  $v$ - $E$  characteristics for different intervalley couplings in GaAs (from Fig. 12.9) and in (b) the  $v$ - $E$  characteristics for InGaSb and InP on three level models, the two characteristics presented for InP being for two possible values of the  $\Gamma$ - $L$  deformation potential (from Fig. 12.13).

In Fig. 12.12a we plot the  $v$ - $E$  curves estimated for GaAs for  $\Xi = 2 \times 10^8$ ,  $5 \times 10^8$ ,  $2 \times 10^9$  eV/cm on the efficiency curves deduced by Hilsum.<sup>(23)</sup> For the strongest coupling efficiency continues to increase with bias towards a maximum value of 35%, while for weak coupling efficiency is higher at low bias. Weak intervalley coupling in GaAs would offer the advantage of high efficiency operation at lower bias fields. A disadvantage would be that the time constants for transfer would be slow with the result that high efficiencies would only be obtained at low microwave frequencies.

An additional complication arises with weak coupling since the very high electron energies which occur (see Fig. 12.10) would mean that the next highest set of conduction band minima also play a role. In GaAs these, the  $\langle 111 \rangle$  minima, are believed to be only 0.2 eV above the  $\langle 100 \rangle$  minima. It was in recognition of this fact that the calculation for  $\Xi = 2 \times 10^8$  V/cm was not carried out for fields above 10 kV/cm.

#### 12.4.1 THREE LEVEL SYSTEMS

While weak intervalley coupling is only a possibility in GaAs, there are reasons to believe that it does occur in other transferred electron materials, those whose lowest satellite minima lie along  $\langle 111 \rangle$  directions. This belief arises because it is known that the  $\langle 111 \rangle$  minima in Ge are weakly coupled to the central ( $\Gamma$ ) minimum and it seems reasonable to expect that this will also be the case in other zinc blende semiconductors. In Ge  $\Xi$  has been estimated as  $1.3 \times 10^8$  eV/cm.<sup>(24)</sup>

As evidenced by Fig. 12.6  $\text{In}_{1-x}\text{Ga}_x\text{Sb}$  is one transferred electron material with a band structure appropriate for weak coupling. The  $v$ - $F$  curve of this material has been calculated for  $x = 0.8$  by Hilsum and Rees,<sup>(25)</sup> taking a value of  $1 \times 10^8$  eV/cm for the deformation potential coupling the central and  $\langle 111 \rangle$  minima. The low coupling between the two lowest minima necessarily means that the third set of minima (the  $X$ -minima in this case) are also important, so that we are dealing with a three energy level system. For the  $\Gamma$ - $X$  deformation potential a value of  $1 \times 10^9$  eV/cm was taken, with a similar value for  $X$ - $L$  potential. The  $v$ - $E$  curve calculated is plotted in Fig. 12.13a. The initial transfer is to the  $\langle 111 \rangle$  minima and occurs very rapidly with increasing field as discussed in the GaAs case. Hence, the negative slope mobility is very high and the drift velocity of the transferred electrons is low since the applied field is only around 1 kV/cm when most of the electrons have transferred. As the field is increased above threshold the electrons begin to see the third set of states, the  $X$ -minima, and it is transfer of electrons from the  $L$ -minima to the  $X$ -minima (strong coupling) and thence back to  $\Gamma$ -minimum (strong coupling) which mainly causes the drift velocity to rise steadily beyond the valley velocity.

The velocity-field relation for  $\text{In}_{0.2}\text{Ga}_{0.8}\text{Sb}$  is plotted in normalized form on Fig. 12.12b. The rapid transfer to the  $L$ -minima enables a maximum efficiency of 36% to be obtained at 3–3.5 kV/cm (5–6 thresholds). The rising part of the characteristic at high fields prevents even higher efficiencies from being obtained. The  $\Gamma$ - $L$  deformation potential used to calculate this  $v$ - $E$  characteristic however was probably too low since an additional coupling mechanism is present in  $\text{InGaSb}$ , via polar phonons, which is absent in  $\text{Ge}$ .

In a previous calculation of the  $v$ - $E$  curve for  $\text{InP}$  (Fig. 12.4) transfer was assumed to take place from the  $\Gamma$  minimum to the  $X$ -minima. In the

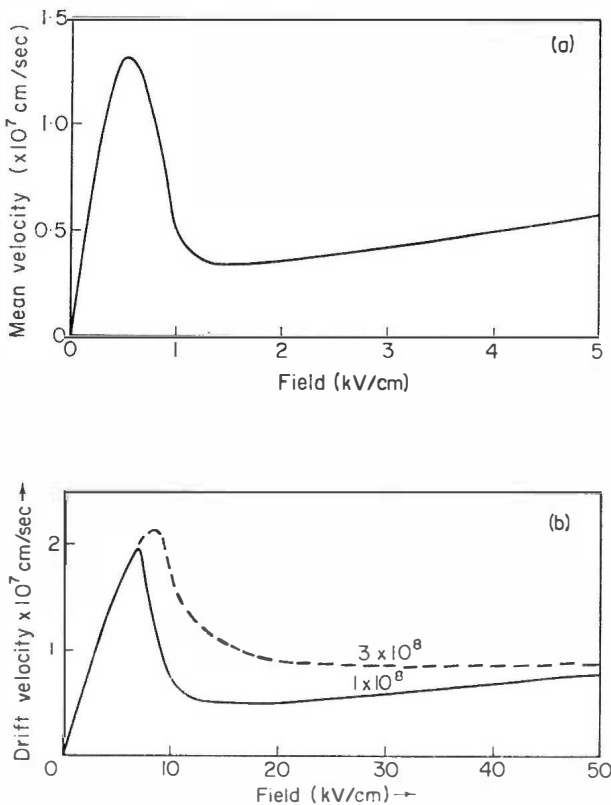


FIG. 12.13(a). Velocity field characteristics for  $\text{In}_{0.2}\text{Ga}_{0.8}\text{Sb}$  on a three level model with weak coupling between  $\Gamma$  and  $L$  minima ( $\Xi_{\Gamma-L} = 1 \times 10^8$  eV/cm), and strong coupling between the other minima ( $\Xi_{L-X}, \Xi_{X-\Gamma} = 1 \times 10^9$  eV/cm); (b) Velocity field characteristics for  $\text{InP}$  on a three level model and for two values of the  $\Gamma$ - $L$  deformation potential ( $\Xi_{\Gamma-L} = 1 \times 10^8, 3 \times 10^8$  eV/cm).  $\Xi_{L-X}, \Xi_{X-\Gamma} = 5 \times 10^8, 1 \times 10^9$  eV/cm respectively. The effective masses in the  $\Gamma$  and  $L$  minima are 0.08 and 0.4 respectively.<sup>(26)</sup>

light of recent experimental evidence Hilsum and Rees<sup>(25,26)</sup> suggest that the  $X$ -minima are not the lowest satellite valleys in InP but that the  $L$ -minima are the lowest at an energy of 0.6 eV above the central valley. This places them 0.2 eV below the  $X$ -minima. On this model of its band structure InP qualifies as a possible three energy level system. With the energy separations noted above and values of  $1 \times 10^8$  and  $3 \times 10^8$  eV/cm for the  $\Gamma$ - $L$  deformation potential, they calculate the  $v$ - $E$  characteristics shown in Fig. 12.13.<sup>(26)</sup>

These characteristics are plotted in normalized form on the efficiency curves of Fig. 12.12b. Because of the positive slope on the  $v$ - $E$  characteristic at high fields, the efficiency will pass through a maximum as the bias field is increased. For  $\Xi_{\Gamma-L} = 1 \times 10^8$  eV/cm this maximum occurs at around 40 kV/cm and the maximum efficiency is around 34%. For the higher value of  $\Xi_{\Gamma-L}$  the peak occurs at higher fields but has substantially the same value. By way of comparison, the simple two valley GaAs model with  $\Xi = 1 \times 10^9$  eV/cm predicts an efficiency of 30% at this field strength. The three level model of InP in fact leads to a lower predicted maximum efficiency than the 40% which we deduced in Section 12.3 for the two level model.

It has been suggested<sup>(25,27)</sup> that domain formation will tend to be inhibited in 3-level oscillators. This is because for fields lower than the valley field, the slow transfer from  $\Gamma$ - $L$  due to the weak coupling will result in the electrons not being able to follow rapid fluctuations in the field. In addition the diffusion rate will be greatly increased. Both these effects will tend to inhibit the formation of a domain and thus operation in non-domain modes is favoured.

Whereas in a 2-level system, weak coupling and therefore slow transfer must mean a limitation on the maximum frequency of operation, in the 3-level system the presence of the third level with strong coupling to the other minima may avoid this limitation.

## 12.5 FUTURE DEVELOPMENTS

The present position in the transferred electron field is that there is one semiconductor, GaAs, whose technology has been highly developed. The maximum efficiency predicted for the material depends somewhat on our estimate of the important material constants but generally the value is in the range 30–35%. This compares very favourably with experimental measurements of up to 32.2%.<sup>(28)</sup> For a new material to be worth developing we would require it to be capable of providing an efficiency of around 50% at room temperature. We now examine the potential of the three negative mobility systems (one, two and three level) in providing such high efficiency devices.

### One Level

Intra band negative resistances have thus far only been predicted in semiconductors where transfer to upper minima appears to be the more significant effect. However, the effect may exist on its own in semiconducting materials yet to be investigated, and if the energy separation of the two lowest minima is sufficiently large, it is conceivable that a significant fall in drift velocity may be obtained at high fields. This effect though is not likely to be as large as one which arises from transfer to a minimum where carriers have much lower mobility even when unheated by the field.

### Two Level

To obtain the high efficiency specified we are looking for peak to valley velocity ratios of over 4 : 1, which means high peak velocities and low valley velocities. It is not easy to see how a peak electron drift velocity above  $2-3 \times 10^7$  cm/sec can be obtained. High peak velocity requires high mobility and high threshold field. The mobility in polar materials varies approximately as  $m^{*-3/2}$  (Section 2.5.2). The threshold field for transfer is approximately given by the polar mode breakdown field<sup>(29)</sup> and thus varies as  $m^*$ . Consequently in maximizing the peak velocity we want to maximize this product, namely  $m^{*-1/2}$ . Hence low effective mass is required, but we are prevented from going to very low mass by the fact that the mass is related to the energy gap.

For small values of  $k$ , the conduction band is described by

$$\mathcal{E} = \mathcal{E}_g + \frac{\hbar^2 k^2}{2m_0} + \frac{P^2 k^2}{3} \left( \frac{2}{\mathcal{E}_g} + \frac{1}{\mathcal{E}_g + \Delta_{so}} \right)$$

where  $\mathcal{E}$  is the electron energy,  $\mathcal{E}_g$  the energy gap,  $\Delta_{so}$  the valence band spin-orbit splitting at the centre of the zone and  $P$  the momentum matrix element connecting the three bands which are the solution of this equation.<sup>(30)</sup> Since  $\Delta_{so}$  is small we can approximately write

$$\mathcal{E} = \mathcal{E}_g + \frac{\hbar^2 k^2}{2m_0} + \frac{P^2 k^2}{\mathcal{E}_g}.$$

Thus

$$\frac{1}{\hbar^2} \frac{\partial^2 \mathcal{E}}{\partial k^2} = \frac{1}{m_0} + \frac{2P^2}{\mathcal{E}_g}$$

so that the effective mass of the band is given by

$$\frac{1}{m^*} = \frac{1}{m_0} + \frac{2P^2}{\mathcal{E}_g}.$$

Since the effective masses of interest are small and much less than the free electron mass,  $m_0$ , we have

$$m^* = \frac{\mathcal{E}_g}{2P^2}.$$

The momentum matrix element  $P$  does not alter much from one material to the next and we can replace the term  $1/(2P^2)$  by a constant value  $0.044 \text{ eV}^{-1}$ . Hence  $m^* = 0.044 \mathcal{E}_g$  where  $\mathcal{E}_g$  is in eV.

The effective mass is thus directly proportional to the energy gap. Since any useful material must remain extrinsic at typical device operating temperatures, we can not tolerate a value of  $\mathcal{E}_g$  which is less than about 1 eV and hence we are restricted to a minimum effective mass of around 0.044. Consequently we are restricted to a maximum attainable peak velocity which is not appreciably above that for GaAs (for which  $m^* = 0.066$ ).

While the above argument is very qualitative and ignores details such as scattering mechanisms other than polar optical scattering and their field dependence, it does confirm what appears to be the case in practice, namely that peak velocities cannot be obtained which are much greater than that for GaAs ( $2 \times 10^7 \text{ cm/sec}$ ). The maximum peak velocity predicted for a semiconductor satisfying the band gap criterion is just over  $3 \times 10^7 \text{ cm/sec}$  for  $\text{In}_{0.2}\text{As}_{0.8}\text{P}^{(21)}$

If no significant improvement in peak velocity is likely, what is the prospect of a reduction in the satellite valley velocity below that in GaAs? Assuming that the velocity of interest is the saturated drift velocity and further that it is determined by optical phonon emission, then its value will be proportional to  $m^{*-1/2}$ , as calculated for Ge in Ref. 7. Thus we look for an increase in the effective mass of the satellite bands. The band gaps at the edge of the zone (where the satellite valleys often lie) tend not to vary appreciably from one semiconductor to the next among the III-V compounds. Consequently the effective mass in the bands at the zone edge, being related to the zone edge band gap, does not vary much. However in some materials the satellite minima do not lie exactly at the zone edge, and the enhancement of the density of states which this gives will lower the saturated velocity by an amount dependent upon the strength of the scattering between the satellite valleys. Strong inter-valley scattering will lead to a significant reduction. In a similar way, close proximity in energy of a third set of conduction band minima to the second lowest set will also yield a reduction in the saturated drift velocity.

Thus, although little improvement is anticipated in the peak electron drift velocity, new semiconducting materials may emerge having saturated drift velocities lower than in GaAs, and such materials might then be able to offer efficiencies of 50% or more.

### Three Level

The possibility that in some transferred electron materials, coupling to the lowest satellite valleys is weak, offers very high peak/valley ratios at comparatively low fields. In the cases examined so far, however, the increase of drift velocity beyond the valley means that we can not properly exploit the effect to get high efficiency. Somewhat better results are expected from InAsP alloys.<sup>(27)</sup>

With the same reasoning as for the two level case, little improvement is expected in peak drift velocity. The peak velocity obtainable will be limited to a value slightly less than would be available for a strongly coupled satellite valley (see Fig. 12.9) and the peak/valley velocity ratio will have to be considerably larger than 4 : 1 in order to offset the disadvantage of a  $v$ - $E$  characteristic which increases at high fields. Higher effective masses in the satellite valleys however will also tend to lower the valley velocity in the three level system, as well as to limit the rate at which the velocity rises with field beyond the valley<sup>(26)</sup> and an increase in the efficiencies predicted for three level oscillators will follow.

Introduction of the third set of levels in the electron transfer process gives an additional complexity to the transfer process. It may however also provide us with new and useful modes of operation of transferred electron devices of which we are as yet unaware. The concept of the three level oscillator is one which has arisen from a close examination of the band structures of semiconductors and from a detailed understanding of the transfer process. It is to a better knowledge of the available band structures and to a better appreciation of the consequences of particular band structures that we look for the significant improvements in transferred electron devices. Who knows, in seeking improved transferred electron materials we may succeed in discovering something entirely new and useful, just as J. B. Gunn did in 1963 when he set out to examine the mobility of the semiconductor GaAs at high electric fields.

### REFERENCES

1. Gunn, J. B. (1963). *Solid State Commun.* **1**, 89, and *I.B.M. J. Res. Develop* **8**, 141, 1964.
2. Taylor, B. C. and Colliver, D. J. (1971). *I.E.E.E. Trans.* ED-18, No. 10; Paxman, D. H. and Tree, R. J. (1971). *Electron. Lett.* **7**, No. 10, 240; Boers, P. M. (1971). *Phys. Lett.* **34A**, 329.
3. Foyt, A. G. and McWhorter, A. L. (1966). *I.E.E.E. Trans.* ED-13, 79.
4. Ludwig, G. W. and Aven, M. (1967). *J. Appl. Phys.* **38**, 5326.
5. Allen, J. W. *et al.* (1965). *Appl. Phys. Lett.* **7**, 78.
6. McGroddy, J. C. *et al.* (1969). *Solid State Commun.* **7**, 13, 901.
7. McGroddy, J. C. and Nathan, M. I. (1967). *I.B.M.J. Res. Develop*, **11**, 337; also McGroddy, J. C. *et al.* (1969). *I.B.M. J. Res. Develop.* **13**, 543.



8. Smith, J. E. *et al.* (1969). Semi. Dev. Res. Conf. Rochester N. Y.
9. Allen, J. W. *et al.* (1966). *Appl. Phys. Lett.* **9**, 39.
10. Porowski, S. *et al.* (1969). *Solid State Comm.* **7**, 13, 905
11. Kastal'skii, A. A. and Ryvkin, S. M. (1967). *Sov. Phys. Semiconductors*, **1**, 523.
12. Ridley, B. K. and Watkins, T. B. (1961). *Proc. Phys. Soc.* **78**, 293
13. Elliott, J. B. *et al.* (1967). *Appl. Phys. Lett.* **11**, 253.
14. Chang, D. M. and Ruch, J. G. (1968). *Appl. Phys. Lett.* **12**, 111.
15. Hilsum, C. (1966). *Phys. Lett.* **20**, No. 6, 576.
16. Hammar, C. and Weissglas, P. (1967). *Phys. Stat. Soc.* **24**, 531.
17. Persky, G. and Bartelink, D. J. (1969). *Bull. Am. Phys. Soc.* **14**, 748.
18. Fawcett, W. F. and Ruch, J. G. (1969). *Appl. Phys. Lett.* **15**, 368.
19. Dumke, W. P. (1970). *Phys. Rev.* **B2**, 4, 987.
20. Fawcett, W. F. and Paige, E. G. S. (1971). *J. Phys. C*. to be published.
21. Fawcett, W. F. (1969). *et al. Electron. Lett.* **5**, No. 14.
22. Fawcett, W. F. *et al.* (1970). *J. Phys. Chem. Solids*. **31**, 1963.
23. Hilsum, C. (1970). *Electron. Lett.* **6**, No.14. 448.
24. McLean, T. P. (1960). The absorption edge of semiconductors, *Prog. Semiconductors*. (A. F. Gibson and R. E. Burgess, Eds.). Vol. 5, p. 85, Heywood, London.
25. Hilsum, C. and Rees, H. D. (1970). *Electron Lett.* **6**, No. 9, 277.
26. Hilsum, C. and Rees, H. D. (1971). *Electron Lett.* **7**, 437.
27. Hilsum, C. (1971). "Cornell Conf. on High Frequency Generation and Amplification", Cornell University.
28. Reynolds, J. F. *et al.* (1969). *Proc. I.E.E.E.* 1692.
29. Butcher, P. N. (1967). "The Gunn Effect", *Progress in Physics*, **30**, 97.
30. Hilsum, C. (1965). Gallium Arsenide, *Progress in Semiconductors*, (A. F. Gibson and R. E. Burgess, Eds.), **9**, 137. Heywood, London.

## Chapter 13

# Circuit Functions

### 13.1 INTRODUCTION

Some circuit functions which limit the performance of transferred electron oscillators are discussed in this chapter. No attempt is made to review circuit theory which is adequately covered in the texts generally referenced at the end of the chapter. Some effects have been covered elsewhere. For example, ideas of  $Q$  factor and circuit stabilization of frequency are discussed in Chapter 9 and basic cavity design at other appropriate points.

### 13.2 LOCAL RESONANCES IN WAVEGUIDE MOUNTS<sup>(1)</sup>

In many cases the circuits in which transferred electron oscillators are operated are required to provide a range of mechanical tuning. This is normally achieved by the provision of a movable short-circuit plunger to alter the resonant frequency of the circuit in which the oscillator is placed. Normally the device performance is controlled by the cavity and operation of devices in high-impedance circuits can lead to good f.m. noise performance and high-frequency stability.<sup>(2)</sup> The form of mounting most commonly used for waveguide oscillators is that shown in Fig. 13.1. In normal operation in this circuit, the frequency of oscillation of the device is approximately determined by the condition that the cavity length be an integral number of half-wavelengths long. By altering the cavity length we can tune the oscillator to any frequency in the band of interest if we remain in this mode of

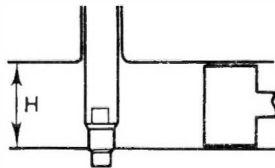


FIG. 13.1. Simple post in waveguide mounting.

the cavity, and assume that the diode negative resistance is always adequate to match the load resistance presented to it by the circuit. When these conditions are met, oscillators can be made to have wide mechanical tuning ranges and good frequency stability.

This simple waveguide circuit can also support modes of oscillation other than the waveguide modes described above. These modes are essentially resonances in the local region of the diode mount. They have lower  $Q$  than the waveguide mode and, in consequence, oscillator performance is degraded

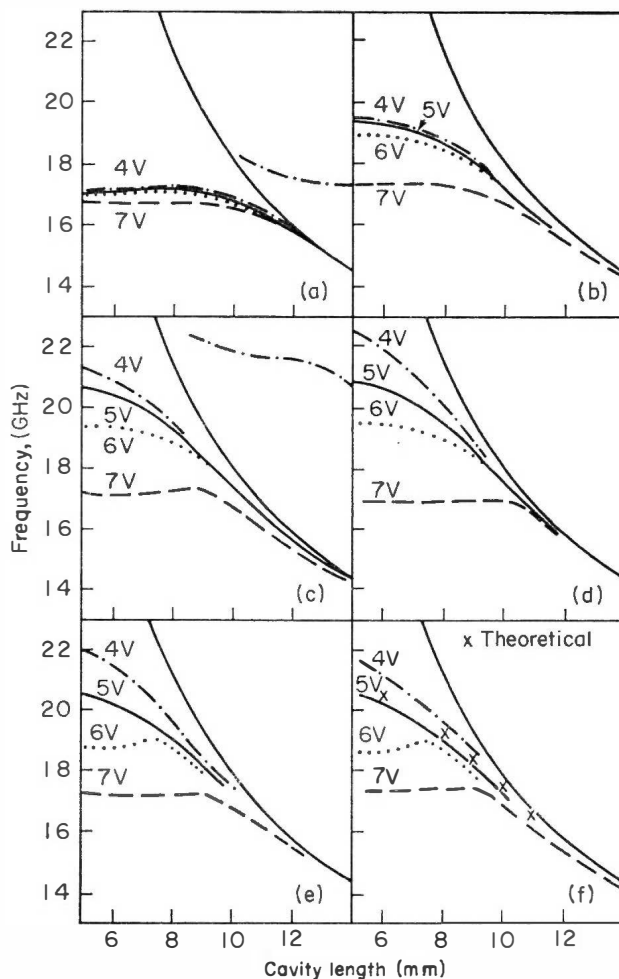


FIG. 13.2. Tuning characteristics for cavities of various heights  $H$  ranging from full height [Fig. 4(a)] to fully reduced height [Fig. 4(f)]. Operation is at bias levels of 4–7 volts. Crosses on 4(f) represent theoretical tuning curve for assumed device capacitance of 0.04 pF.

In (a)–(f),  $H = 7.9, 6.6, 5.3, 4.0, 2.7, 1.6$  mm, respectively.

when their influence is felt; in some cases the performance is severely degraded. Furthermore their existence leads to a restriction in the mechanical-tuning range and encourages frequency switching and hysteresis effects.

The effect of these modes or "local" resonances is illustrated in Fig. 13.2. This shows the variation of frequency with short circuit position in the waveguide circuit illustrated in Fig. 13.1 for various waveguide heights. In all cases it is clearly seen that the tuning "saturates" in short cavities and the saturation frequency increases with a decrease of waveguide height. Insight of these effects was gained by comparing the results with the operation in a coaxial cavity. It was found that a coaxial cavity whose length was equal to the waveguide height supported oscillations at the corresponding saturation frequency.

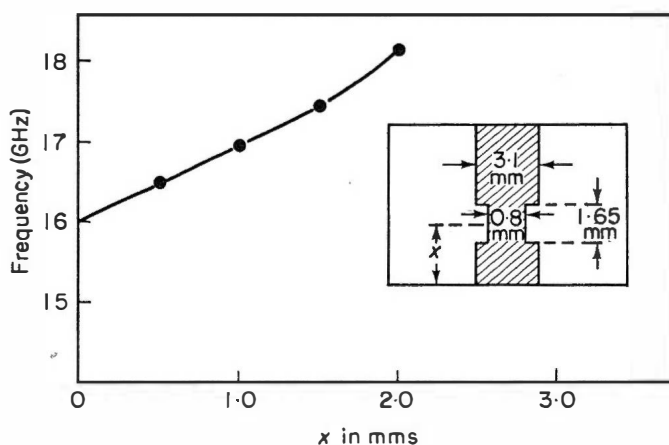


FIG. 13.3. Frequency of transverse resonance as function of position of a package along the mounting post. Package is a local reduction in diameter of mounting post, as shown in inset.

There are a number of possible local modes that could be excited around the diode mount and provide a separate resonance independent of the position of the short circuit plunger in the waveguide. However, the above mentioned observations indicate that the most likely one is a T.E.M. mode along the transmission line which has the mounting post as the centre conductor and the top and bottom waveguide walls as short circuit end planes. For this mode the resonance frequency will be a sensitive function of the waveguide height as has been observed practically.

If the frequency saturation exists within a required frequency band the above considerations show that it can be moved out of the band by a reduction in waveguide height, providing the diode encapsulation resonance is at a high enough frequency. However, since the saturation effect is determined by the resonance of a T.E.M. mode, the same objective can be achieved by

altering the position of the encapsulation in the mounting post. By moving the diode off the bottom of the waveguide, the frequency at which the coaxial circuit resonates increases. Figure 13.3 shows a typical variation of resonant frequency with mounting position.

### 13.3 OSCILLATOR DESTABILIZATION BY TRANSMISSION LINE DEFECTS

Discontinuities in the output transmission line of cavity controlled microwave oscillators are well known to affect the stability of the oscillator and cause discontinuous jumps in frequency (the "long line" effect). A quantitative estimation of the effect of discontinuities which are not large enough to cause frequency jumping but could affect the oscillator frequency stability is given here.<sup>(4)</sup>

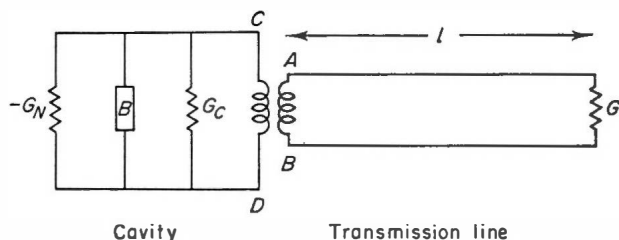


FIG. 13.4. The equivalent circuit of a cavity and external discontinuity.

A simple equivalent circuit was taken for the oscillator, cavity and output coupling as shown in Fig. 13.4.  $-G_N$  is the Gunn diode negative conductance which must be equal in magnitude to the sum of the cavity wall loss conductance  $G_c$  and the load conductance reflected into the cavity through the transformer  $ABCD$  of turns ratio  $n$ , for steady state operation. Similarly the resonance condition is set by the sum of the diode and cavity susceptance  $B$  plus the susceptance reflected into the cavity from the external discontinuity. The matched load and discontinuity are assumed to be conductive and susceptive respectively. The simplest way of representing this combination is by a pure conductance terminating the transmission line at the minimum of the standing wave pattern with a magnitude to give the correct standing wave ratio. There will be a modification of less than quarter of a wavelength in the distance of the discontinuity from the cavity compared with the position of the equivalent conductance.

The analysis is similar to that given for  $Q$ -measurements by a frequency pulling technique.<sup>(2)</sup>

If the output transmission line is perfectly matched ( $G = Y_0$ ) any change of diode susceptance,  $\Delta B$ , from an unspecified fluctuation, causes a frequency

change  $\Delta\omega$  where:

$$\Delta\omega = \left( \frac{\Delta B}{\partial B / \partial \omega} \right). \quad (13.1)$$

Any circuit defect which decreases  $\partial B / \partial \omega$  will increase the frequency fluctuation.

Where  $G \neq Y_0$  the normalised admittance at  $AB$  looking to the right is:

$$\frac{G' + jB'}{Y_0} = \frac{s[1 + \tan^2(2\pi l/\lambda)] + j(1 - s^2)\tan(2\pi l/\lambda)}{[1 + s^2 \cdot \tan^2(2\pi l/\lambda)]} \quad (13.2)$$

$\lambda$  is the wavelength in the output line and  $s(>1)$  is the standing wave ratio of the discontinuity. The total rate of change of susceptance with frequency is given by:

$$\left( \frac{\partial B}{\partial \omega} \right)_{\text{total}} = \left( \frac{\partial B}{\partial \omega} \right)_0 + \frac{1}{n^2} \left( \frac{\partial B'}{\partial \omega} \right) \quad (13.3)$$

where the subscript 0 refers to the ideally matched case. By definition<sup>(2,3)</sup>:

$$\left( \frac{\partial B}{\partial \omega} \right)_0 = \frac{2Y_0}{\omega_0 n^2} \cdot Q_E \quad (13.4)$$

where  $Q_E$  is the external  $Q$  factor ( $1/Q_E$  is equal to  $1/Q_L - 1/Q_0$  in ref. 13.2). Substituting from Eqn (13.2) into Eqn (13.3) and eliminating  $Y_0/n^2$  with Eqn (13.4) gives:

$$\left( \frac{\partial B}{\partial \omega} \right)_{\text{total}} = \left( \frac{\partial B}{\partial \omega} \right)_0 \left( 1 - \frac{\pi l}{Q_E \lambda} \cdot \frac{(s^2 - 1)[1 + \tan^2(2\pi l/\lambda)][1 - s^2 \tan^2(2\pi l/\lambda)]}{[1 + s^2 \tan^2(2\pi l/\lambda)]^2} \right)$$

which has extreme values given by:

$$\left( \frac{\partial B}{\partial \omega} \right)_{\text{max}}^{\text{min}} = \left( \frac{\partial B}{\partial \omega} \right)_0 \left\{ 1 + \frac{\pi l}{Q_E \lambda} (s^2 - 1) \left[ \begin{matrix} +1/s^2 \\ -1 \end{matrix} \right] \right\}. \quad (13.5)$$

From  $(\partial B / \partial \omega)_{\text{min}}$  it is possible to define a circuit destabilization factor  $D$  given by:

$$D = 1 - \frac{\pi l}{Q_E \lambda} (s^2 - 1). \quad (13.6)$$

### *Practical examples of stabilization and destabilization*

For a practical example, in the measurement of frequency-temperature relations or f.m. noise of Gunn oscillators the output line is often padded with an attenuator or isolator with  $s \approx 1.3$ . A typical X-band oscillator in

an approximately half wavelength coaxial cavity has  $Q_E \approx 50$  at full power output ( $Q_0 \approx 1000$ ). If the measured characteristics are to be accurate to 10% then  $l/\lambda$  must be less than 2.3.

A second example is shown in Fig. 13.5 of a variation of f.m. noise with temperature. The cyclic behaviour recurred at approximately 140 MHz intervals of the centre frequency and was traced to the reflection from a PIN diode leveller at a distance of about 33 wavelengths from the oscillator. The line between the oscillator and PIN diode contained an isolator close to the oscillator but it had a poor isolation of approximately  $-15$  dB and the reflected power from the PIN diode was  $-15$  dB corresponding to an effective standing wave ratio in the above analysis of 1.05. These values substituted in Eqn (13.5) give  $(\partial B/\partial \omega)_{\max} = 1.16 (\partial B/\partial \omega)_0$  and  $(\partial B/\partial \omega)_{\min} = 0.8 (\partial B/\partial \omega)_0$  so that the cyclic f.m. noise variation from Eqn (13.1) should be 36% discounting any other mechanisms. This is in good agreement with the variation in Fig. 13.5.

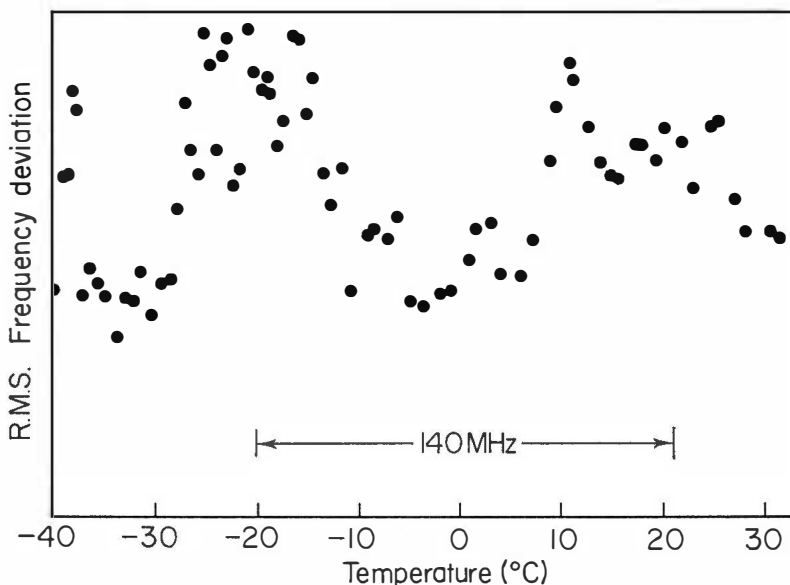


FIG. 13.5. Variation of f.m. noise caused by external discontinuities.

#### REFERENCES

1. Taylor, B. C., Fray, S. J. and Gibbs, S. E. (1970). *I.E.E.E. Trans. on Microwave Theory and Techniques* MTT-18, 799-807.
2. Warner, F. L. and Hobson, G. S. (1970). *Microwave Journal* 13, 46-52.
3. Montgomery, C. G., Dicke, R. H., and Purcell, E. M. (1948). "Principles of Microwave Circuits", p. 230, McGraw-Hill, New York.
4. Patel, B. and Hobson, G. S. Private communication.

## GENERAL REFERENCES

- Montgomery, C. G., Dicke, R. H. and Purcell, E. M. (1948). "Principles of Microwave Circuits," p. 230, McGraw-Hill, New York.
- Barlow, H. E. M., and Cullen A. L. (1950). "Microwave Measurements", Constable, London.
- Slater, J. C. (1950). "Microwave Electronics", Van Nostrand, New York.
- Ginzton, E. L. (1957). "Microwave Measurements", McGraw-Hill, New York



## Appendix 1

### Scattering Term for the One Phonon Process

Equation (3.12) may be developed to a more convenient form for one phonon scattering processes. In thermal equilibrium in the absence of fields  $\left(\frac{\partial f(\mathbf{k})}{\partial t}\right)_{\text{scatt}} = 0$  and the number of carriers scattered from  $\mathbf{k}'$  to  $\mathbf{k}$  is equal to the number scattered from  $\mathbf{k}$  to  $\mathbf{k}'$ .

In this case Eqn (3.12):

$$\left(\frac{\partial f(\mathbf{k})}{\partial t}\right)_{\text{scatt}} = \sum_{\mathbf{k}'} \{S(\mathbf{k}', \mathbf{k})f(\mathbf{k}') - S(\mathbf{k}, \mathbf{k}')f(\mathbf{k})\} \quad (3.12)$$

becomes:

$$S(\mathbf{k}', \mathbf{k})f_0(\mathbf{k}') = S(\mathbf{k}, \mathbf{k}')f_0(\mathbf{k}) \quad (\text{A1.1})$$

where  $f_0(\mathbf{k})$  is the thermal equilibrium distribution function. (A1.1) is an example of the principal of detailed balancing. For the electron concentrations to be dealt with  $f_0(\mathbf{k})$  is known from the Maxwellian classical limit of the Fermi–Dirac distribution function:

$$f_0[\mathcal{E}(\mathbf{k})] = \exp(\mathcal{E}_F/kT) \exp(-\mathcal{E}(\mathbf{k})/k_B T). \quad (\text{A1.2})$$

The above form for  $f_0$  is chosen to indicate that it only depends on  $\mathbf{k}$  through the energy  $\mathcal{E}(\mathbf{k})$ . Substituting (A1.2) in (A1.1):

$$S(\mathbf{k}', \mathbf{k}) = S(\mathbf{k}, \mathbf{k}') \exp[(\mathcal{E}(\mathbf{k}') - \mathcal{E}(\mathbf{k}))/k_B T] \quad (\text{A1.3})$$

so that  $S(\mathbf{k}', \mathbf{k})$  is only equal to  $S(\mathbf{k}, \mathbf{k}')$  if the scattering process involves no energy loss or gain by the electron.

The one phonon scattering processes affecting the distribution function at  $\mathbf{k}$  involves scattering either to or from the state  $\mathbf{k}$  with absorption or emission of a phonon in each case. If the phonon energy is  $\hbar\omega(\mathbf{q})$  ( $\mathbf{q}$  is the phonon wave vector) then the state  $\mathbf{k}$  (with energy  $\mathcal{E}(\mathbf{k})$ ) is coupled to two

other states with energy  $\mathcal{E}(\mathbf{k}) \pm \hbar\omega(\mathbf{q})$  by conservation of energy. Conservation of wave vector also requires that:

$$\mathbf{k}' - \mathbf{k} = \mathbf{q} \quad (\text{A1.4})$$

Using the above considerations it can be shown (see ref. 3.39) that the scattering probability may be written in terms of a coupling coefficient  $P(\mathbf{k}', \mathbf{k})$  and a phonon population term:

$$S(\mathbf{k}', \mathbf{k}) = P(\mathbf{k}', \mathbf{k}) \times \begin{cases} N(\mathbf{q}) \delta(\mathcal{E}(\mathbf{k}) - \mathcal{E}(\mathbf{k}') + \hbar\omega(\mathbf{q})) & \left. \begin{array}{l} \text{phonon} \\ \text{absorption} \end{array} \right\} \\ (N(\mathbf{q}) + 1) \delta(\mathcal{E}(\mathbf{k}) - \mathcal{E}(\mathbf{k}') - \hbar\omega(\mathbf{q})) & \left. \begin{array}{l} \text{phonon} \\ \text{emission} \end{array} \right\} \end{cases} \quad (\text{A1.5})$$

$N(\mathbf{q})$  is the number of phonons with wave vector  $(\mathbf{q})$  and the  $\delta$ -function is included to indicate that the scattering probability is only non-zero if the overall energy is conserved.  $\delta = 1$  if its bracketed term is zero otherwise it is zero. Equation (A1.5) is plausible for the "weak" scattering events such as concern us here in that it indicates the proportionality of the total scattering probability to the number of phonons present.

By substituting the thermal equilibrium distribution per unit volume of the phonons:

$$N(\mathbf{q}) = \{\exp(\hbar\omega(\mathbf{q})/k_B T) - 1\}^{-1} \quad (\text{A1.6})$$

in (A1.5) and then substituting the result in (A1.3) noting that the transition  $\mathbf{k}'$  to  $\mathbf{k}$  involves phonon emission and  $\mathbf{k}$  to  $\mathbf{k}'$  involves phonon absorption or vice versa:

$$P(\mathbf{k}', \mathbf{k}) = P(\mathbf{k}, \mathbf{k}'). \quad (\text{A1.7})$$

Calculation of the scattering probabilities has been reduced to the calculation of one coupling coefficient. Equation (3.12) may now be written in simpler form with all scattering possibilities explicitly included:

$$\left( \frac{\partial f(\mathbf{k})}{\partial t} \right)_{\text{scatt}} = \sum_{\mathbf{k}'} P(\mathbf{k}, \mathbf{k}') [ \{ N(\mathbf{q}) f(\mathbf{k}') - (N(\mathbf{q}) + 1) \} \delta(\mathcal{E}(\mathbf{k}) - \mathcal{E}(\mathbf{k}') - \hbar\omega(\mathbf{q})) - \{ N(\mathbf{q}) f(\mathbf{k}) - (N(\mathbf{q}) + 1) f(\mathbf{k}') \} \delta(\mathcal{E}(\mathbf{k}') - \mathcal{E}(\mathbf{k}) - \hbar\omega(\mathbf{q})) ] \quad (\text{A1.8})$$

## Appendix 2

### The Relaxation Time Approximation

The Boltzmann equation is an integro-differential equation whose solution is generally exceedingly difficult. In this appendix we consider some simplifying conditions under which the equation may be converted to a linear differential equation for the distribution function whose solution is, in principle, simple. The objective is to find, at each point of  $\mathbf{k}$ -space, conditions under which the non-spherically symmetric part of the distribution function caused by external fields relaxes to its equilibrium condition at a rate determined only by the deviation from spherical symmetry at that point of  $\mathbf{k}$ -space.

$$\text{i.e. } \frac{\partial(f(\mathbf{k}) - f(\mathcal{E}))}{\partial t} \propto - (f(\mathbf{k}) - f(\mathcal{E}))$$

$f(\mathbf{k})$  is the distribution function and  $f(\mathcal{E})$  is its spherical symmetrical part. Under the above circumstances the relaxation is exponential after removal of the perturbing field.

The solution will only be considered in a band structure with spherical constant energy surfaces which are not necessarily parabolic. The extension to non-spherical constant energy surfaces has been considered by Herring and Vogt (see ch. 3, ref. 25). In addition to this first condition the distribution function is assumed to be approximately spherically symmetric in  $\mathbf{k}$ -space. This second condition will apply at low electric fields when the disturbance of the distribution function from its thermal equilibrium value is small and also for high electric fields when the electron scattering mechanisms are approximately elastic. In the latter case the momentum randomizing collisions experienced by the electron do not appreciably alter its energy and the electrons are redistributed around a constant energy surface in  $\mathbf{k}$ -space, so preserving the spherical symmetry if the scattering is not predominantly forward or backward. Customarily, in the above two cases, the distribution function is expanded in a Legendre polynomial series in  $\mathbf{k}$ -space which is truncated

after the first two terms i.e.

$$f(\mathbf{k}) = f(\mathcal{E}) + g(\mathcal{E}) \cdot \cos \theta + (0) \cdot (3 \cos^2 \theta - 1) \quad (\text{A2.1})$$

The functional dependence of the first two terms  $f(\mathcal{E})$  and  $g(\mathcal{E})$  on the electron energy  $\mathcal{E}$  indicates the essential spherically symmetric form of these terms.  $\theta$  is the angle between  $\mathbf{k}$  and the electric field. The condition of approximate spherical symmetry overall also implies that  $g(\mathcal{E}) \ll f(\mathcal{E})$ ; a necessary condition for truncating the series.

The justification for the Legendre polynomial expansion is principally expediency. The individual terms are conveniently orthogonal and Yamashita and Inoue (see ref. 3.35) have shown that the third term of the series is much smaller than  $g(\mathcal{E})$  when  $g(\mathcal{E}) \ll f(\mathcal{E})$ . Hopefully this indicates the convergence of the series.

When the above conditions on the distribution function are satisfied the scattering term, (3.12) in the Boltzmann equation has a trivial simplification if either of the two following conditions on the scattering mechanisms are met.

(a) *Random scattering.*

When the electron velocity is randomized upon collision, the scattering term is of the following form:

$$S(\mathbf{k}, \mathbf{k}') = S(\mathbf{k}, \mathbf{k}^*) \quad (\text{A2.2})$$

where  $\mathbf{k}^*$  has the same magnitude as  $\mathbf{k}'$  but the opposite direction with respect to the position of the energy minimum in  $\mathbf{k}$ -space. Under this condition Eqn (3.12) simplifies easily by substituting (A2.1). The relative position of the states in  $\mathbf{k}$ -space are illustrated in Fig. A2.1.

$$\begin{aligned} \left( \frac{\partial f(\mathbf{k})}{\partial t} \right)_{\text{scatt}} &= \left( \frac{\partial f(\mathcal{E})}{\partial t} \right)_{\text{scatt}} + \left( \frac{\partial g(\mathcal{E})}{\partial t} \right)_{\text{scatt}} \cdot \cos \theta \\ &= \sum_{\mathbf{k}'} [f(\mathcal{E}') S(\mathbf{k}', \mathbf{k}) - f(\mathcal{E}) S(\mathbf{k}, \mathbf{k}')] \\ &\quad + g(\mathcal{E}') S(\mathbf{k}', \mathbf{k}) \cos \theta' - g(\mathcal{E}) S(\mathbf{k}, \mathbf{k}') \cos \theta] \quad (\text{A2.3}) \end{aligned}$$

where the prime refers to state  $\mathbf{k}'$ .

Application of the thermal equilibrium conditions to the scattering Eqn (3.12) gives:

$$f_0(\mathcal{E}') S(\mathbf{k}', \mathbf{k}) = f_0(\mathcal{E}) S(\mathbf{k}, \mathbf{k}') \quad (\text{A2.4})$$

so that (A2.2) may be rewritten as

$$S(\mathbf{k}', \mathbf{k}) = S(\mathbf{k}^*, \mathbf{k}). \quad (\text{A2.5})$$

For the summation of Eqn (A2.3)  $\mathbf{k}$ -space is conveniently divided in two halves in which  $\cos \theta'$  is respectively positive and negative. Now the third term on the right-hand side of (A2.3) is seen with the aid of (A2.5) to contribute two parts which are equal in magnitude but opposite in sign.

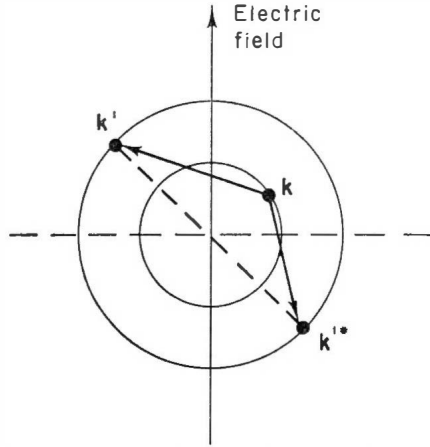


FIG. A2.1. Representation of  $\mathbf{k}$  states in  $\mathbf{k}$  space between which the scattering probability is the same ( $\mathbf{k}$  to  $\mathbf{k}'$  or  $\mathbf{k}'^*$ ) for velocity randomizing scattering events. Circles are cross-sections of constant energy surfaces.

Equating separately the coefficients of the spherically symmetric and angular terms we have the following two relationships:

$$\left( \frac{\partial f(\mathcal{E})}{\partial t} \right)_{\text{scatt}} = \sum_{\mathbf{k}'} [f(\mathcal{E}') S(\mathbf{k}', \mathbf{k}) - f(\mathcal{E}) S(\mathbf{k}, \mathbf{k}')] \quad (\text{A2.6})$$

$$\begin{aligned} \left( \frac{\partial g(\mathcal{E})}{\partial t} \right)_{\text{scatt}} &= -g(\mathcal{E}) \sum_{\mathbf{k}'} S(\mathbf{k}, \mathbf{k}') \\ &\equiv -\frac{g(\mathcal{E})}{\tau(\mathbf{k})}. \end{aligned} \quad (\text{A2.7})$$

The scattering term of (A2.6) is non-zero if  $f(\mathcal{E})$  is perturbed from its thermal equilibrium value, i.e.

$$\frac{f(\mathcal{E}')}{f(\mathcal{E})} \neq \frac{f_0(\mathcal{E}')}{f_0(\mathcal{E})}$$

The drift term of the scattering term has the relaxation time form.

(b) *Elastic Scattering.*

In this case electrons are scattered between states on the same constant energy surface and a relaxation time can be defined when the scattering

depends only on the angle between the initial and final  $\mathbf{k}$ -states and not on their absolute orientation in  $\mathbf{k}$ -space. The principle of detailed balancing applied for thermal equilibrium ( $f_0(\mathbf{k}') = f_0(\mathbf{k})$  for elastic scattering) shows that:

$$S(\mathbf{k}', \mathbf{k}) = S(\mathbf{k}, \mathbf{k}'). \quad (\text{A2.8})$$

Introducing the approximation of (A2.2), the Boltzmann scattering term

$$\left( \frac{\partial f(\mathbf{k})}{\partial t} \right)_{\text{scatt}} = \sum_{\mathbf{k}'} [f(\mathbf{k}') S(\mathbf{k}', \mathbf{k}) - f(\mathbf{k}) S(\mathbf{k}, \mathbf{k}')] \quad (3.12)$$

becomes:

$$\left( \frac{\partial f(\mathcal{E})}{\partial t} \right)_{\text{scatt}} + \left( \frac{\partial g(\mathcal{E})}{\partial t} \right)_{\text{scatt}} \cos \theta = \sum_{\mathbf{k}'} g(\mathcal{E}) \cdot S(\mathbf{k}, \mathbf{k}') (\cos \theta' - \cos \theta) \quad (\text{A2.9})$$

where  $\theta'$  and  $\theta$  are respectively the angles corresponding to  $\mathbf{k}'$  and  $\mathbf{k}$ . The first part of this summation is carried out with the aid of Figs A2.2 and A2.3. The latter is a view of the former down the axis CD.  $\mathbf{k}$  states are uniformly distributed over the spherical constant energy surface of Fig. A2.2, and we will consider the summation for all states with the same angle  $\gamma = \theta - \theta'$  between  $\mathbf{k}$  and  $\mathbf{k}'$ .  $S(\mathbf{k}, \mathbf{k}')$  is now written as  $S(\gamma)$  and noting that

$$\cos \theta' = \frac{\text{projection of } \mathbf{k}' \text{ on electric field axis}}{|\mathbf{k}'|}$$

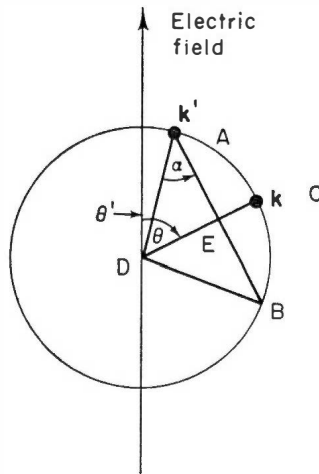


FIG. A2.2.  $\mathbf{k}$  space representation of states in an equatorial plane between which elastic scattering occurs. The circle is a cross-section of a constant energy surface.

we have

$$\cos \theta' = \frac{|\mathbf{k}'| \cos \alpha \cdot \cos \beta \cdot \sin \theta + |\mathbf{k}'| \sin \alpha \cos \theta}{|\mathbf{k}'|},$$

but

$$\alpha = \frac{\pi}{2} - \gamma.$$

Therefore

$$\cos \theta' = \sin \gamma \cos \beta \sin \theta + \cos \gamma \cos \theta \quad (\text{A2.10})$$

and (A2.9) becomes:-

$$\begin{aligned} \left( \frac{\partial f(\mathcal{E})}{\partial t} \right)_{\text{scatt}} + \left( \frac{\partial g(\mathcal{E})}{\partial t} \right)_{\text{scatt}} \cos \theta &= \sum_{\gamma} g(\mathcal{E}) S(\gamma) \sum_{\beta} (\cos \theta' - \cos \theta) \\ &= g(\mathcal{E}) \cos \theta \sum_{\gamma} S(\gamma) (\cos \gamma - 1). \end{aligned}$$

The summation over  $\beta$  caused the first term on the right-hand side of (A2.10) to disappear.

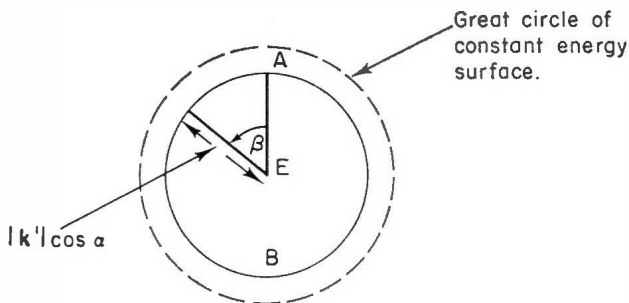


FIG. A2.3. View of A2.2 down axis  $CD$ .

Now we have

$$\left( \frac{\partial f(\mathcal{E})}{\partial t} \right)_{\text{scatt}} = 0 \quad \text{as expected}$$

and

$$\begin{aligned} \left( \frac{\partial g(\mathcal{E})}{\partial t} \right)_{\text{scatt}} &= g(\mathcal{E}) \sum_{\gamma} S(\gamma) (\cos \gamma - 1) \\ &\equiv \frac{g(\mathcal{E})}{\tau(\mathcal{E})}. \end{aligned} \quad (\text{A2.11})$$

### Appendix 3

## Finite Difference Computation of Transferred Electron Problems in One Dimension

The operation of transferred electron devices is dictated by the following equations:

*Poissons equation*

$$\epsilon\epsilon_0 \frac{\partial E}{\partial x} = e[n - N]. \quad (\text{A3.1})$$

*Continuity equation*

$$e \frac{\partial n}{\partial t} = \frac{\partial j}{\partial x} \quad (\text{A3.2})$$

where  $j$  is the particle current density given by:

$$j = nev - \frac{e\partial}{\partial x}(nD). \quad (\text{A3.3})$$

The electronic charge,  $e$ , is regarded as positive for convenience to avoid negative fields, following an often used convention.  $E$  is the electric field,  $n$  is the electron density,  $N$  is the donor density,  $t$  is the time coordinate and  $x$  is the one-dimensional space coordinate.  $v$  and  $D$  are the drift velocity and diffusion coefficients which are assumed to be instantaneous known functions of the electric field so that no account is taken of relaxation effects in the electron momentum distribution function.

The above equations are non-linear owing to the dependence of  $v$  and  $D$  on the electric field and their analytical solution is only possible in circumstances limited by approximation. Their solution under more general circumstances is possible with a finite difference numerical method and a digital computer. The treatment here is only for illustration and the reader with detailed requirements should consult the references.



The device under consideration is divided into cells of finite width in space. The charge and field quantities are regarded as constant in each of these cells and are evaluated at regular time intervals. If the cells in time and space are small enough the solution will be a good approximation to the exact solution. In the following notation the index  $i$  will identify a space cell and  $k$  will identify a time cell. A simple central difference version of a first order differential of a quantity  $f$ , could be:

$$\left(\frac{df}{dx}\right)_{i,j} = \frac{f[i+1, k] - f[i-1, k]}{2\Delta x} \quad (\text{A3.4})$$

where  $\Delta x$  is the width of the space cell and  $f[i+1, k]$  is the value of  $f$  in cell  $i+1$  at time  $k$ .

One loop of the computed evolution of  $E$  and  $n$  will now be described. Let us assume the  $n[i, k]$  are all known at the time  $k$ , either because these are input parameters at the start of the calculation or because the appropriate part of the program has been reached. From Eqn (A3.1)

$$\frac{\epsilon\epsilon_0}{e} \cdot \frac{E[i+1, k] - E[i-1, k]}{2\Delta x} = n[i, k] - N[i] \quad (\text{A3.5})$$

$N[i]$  is the known doping profile peculiar to each calculation. Providing the value of  $E$  is known in the two cells at one end of the device it is possible to evaluate the electric field profile by recurrent use of Eqn (A3.5). The end values of  $E$  are then dictated by the boundary conditions which may, for example, require that the device contacts are ohmic and relate  $E$  there to the total current density which is

$$\frac{1}{m} \sum_{i=1}^m \left\{ j[i, k] + \epsilon\epsilon_0 \cdot \frac{E[i, k] - E[i, k-1]}{\Delta t} \right\} \quad (\text{A3.6})$$

and must be continuous throughout the device. The averaging procedure in (A3.6) is necessary to reduce finite difference errors. There are  $m$  space cells in the device. Note that the difference form of  $\partial E/\partial t$  is not that given in Eqn (A3.4). Further comment on this point is made later.

After evaluation of all the  $E[i, k]$  the terminal voltage,  $V[k]$ , may be evaluated:

$$V[k] = \Delta x \sum_{i=1}^m E[i, k] \quad (\text{A3.7})$$

$V[k]$  is compared with the voltage,  $VC[k]$ , demanded by the circuit boundary condition and all the  $E[i, k]$  are corrected to give equality of  $V[k]$

and  $VC[k]$ .

$$\text{i.e. } E[i, k] \rightarrow E[i, k] + \left\{ \frac{VC[k] - V[k]}{m \cdot \Delta x} \right\} \quad (\text{A3.8})$$

$VC[k]$  is either a known function of time (i.e. of  $k$ ) or if a known circuit is connected across the device terminals it is equal to  $VC[k-1]$  plus the transient response of the circuit to the change of total current from time  $k-1$  to  $k$ .

The corrected values of  $E[i, k]$  may now be used to evaluate  $v[i, k]$  and  $D[i, k]$  and  $n[i, k+1]$  is evaluated from Eqns (A3.2) and (A3.3) as follows:

$$\begin{aligned} \frac{n[i, k+1] - n[i, k]}{\Delta t} = & \frac{n[i+1, k] \cdot v[i+1, k] - n[i-1, k] \cdot v[i-1, k]}{2\Delta x} \\ & - \frac{n[i+1, k] \cdot D[i+1, k] - 2n[i, k] \cdot D[i, k] + n[i-1, k] \cdot D[i-1, k]}{\Delta x^2}. \quad (\text{A3.9}) \end{aligned}$$

The entire process may then be repeated for time step  $k+1$  to  $k+2$ .

The limits on the dimensions of  $\Delta x$  and  $\Delta t$  may be derived from simple physical considerations. For example the electron velocity should not change too much between neighbouring space cells, i.e.

$$\Delta v \ll v.$$

But

$$\Delta v = \frac{dv}{dE} \Delta E$$

and from Eqn (A3.1) it is seen that:

$$|\Delta E| < \frac{ne}{\epsilon\epsilon_0} \Delta x$$

$$\therefore \frac{ne}{\epsilon\epsilon_0} \frac{dv}{dE} \Delta x \ll v.$$

$$\text{i.e. } \Delta x \ll v\tau \quad (\text{A3.10})$$

$\tau$  is the dielectric relaxation time and this condition is simply that  $\Delta x$  must be less than the dielectric relaxation length.

A similar diffusion limit may be derived by considering a narrow depletion layer (usually occurring at the anode contact) in a device with a stable electric field configuration ( $\partial n / \partial t = 0$ ). It is necessary that the electron

density cannot become negative. Three neighbouring cells are chosen with equal  $n$  in the outer ones. From Eqns (A3.2) and (A3.3) we have:

$$n \frac{dv}{dE} \frac{\partial E}{\partial x} = \frac{D \partial^2 n}{\partial x^2}.$$

The variation of  $D$  with  $E$  has been neglected here and  $\partial n / \partial x$  is zero when taken between the outer two cells. If the depletion is  $\Delta n (= N - n)$  then:

$$\frac{\partial^2 n}{\partial x^2} = \frac{2 \Delta n}{(\Delta x)^2}$$

and

$$\left| \frac{\partial E}{\partial x} \right|_{\max} = \frac{e}{\epsilon \epsilon_0} N.$$

Physically  $\Delta n \ll n$

$$\therefore \frac{(\Delta x)^2}{2} \frac{n}{D} \frac{\partial v}{\partial E} \frac{e}{\epsilon \epsilon_0} N \ll n$$

$$\text{i.e. } \Delta x \ll \sqrt{D\tau}. \quad (\text{A3.11})$$

The factor of  $\sqrt{2}$  has been omitted.  $\sqrt{D\tau}$  is the debye screening length.

Limitations on the time step are obtained in a similar way. In Eqn (A3.9) we must have:

$$\frac{n[i, k+1] - n[i, k]}{n[i, k]} \ll 1,$$

For this to be true the velocity term and the diffusion term must both be small.

$$\text{i.e. } \frac{\Delta x}{\Delta t} \gg v. \quad (\text{A3.12})$$

and

$$\frac{(\Delta x)^2}{\Delta t} \gg D. \quad (\text{A3.13})$$

Typical values of  $\Delta x$  and  $\Delta t$  that have been used in practice are:

$$\Delta x = 10^{-5} \text{ cm}$$

$$\Delta t = 10^{-13} \text{ sec}$$

$$N = 10^{15} \text{ cm}^{-3}$$

$v$  and  $D$  are approximately  $10^7$  cm/sec and  $200$  cm<sup>2</sup>/sec respectively. The dielectric relaxation time is greater than  $10^{-12}$  sec so that the dielectric relaxation length is greater than  $10^{-5}$  cm and the debye screening length is greater than  $1.4 \times 10^{-5}$  cm.

The computational technique described above causes the space charge and electric field details to evolve steadily in time. It is an *explicit* technique because parameters at time  $k + 1$  are explicitly related to those at time  $k$ . In order to achieve this it was necessary in Eqn (A3.6) to write the finite difference form of  $\partial E/\partial t$  as a forward difference and not as the more accurate central differences used for the space steps. Accuracy is obtained by reducing the step length until the solution is not dependent on it. This is both time consuming on the computer and somewhat unsatisfactory mathematically. It is possible to use *implicit* techniques which involve correction of the field dependent parameters and electron density at the forward time step by relating their values to neighbouring values forward in time. Such an approach allows much larger time steps than the explicit approach but requires an approximation of some quantities. As a result an interactive calculation at each time step is required until all values have converged and are self consistent. The extra computing time for the iterations can annul the advantage of longer time steps. Even though the technique can be shown to have better stability than the explicit techniques, the additional complexity with little time advantage has hindered its use.

Once a computer simulation has been programmed checks of its validity are required. These can be carried out by using operating parameters that will allow the achievement of modes close to the analytical approximations described elsewhere. The stable domain parameters of Butcher and Fawcett discussed in Chapter 4 give a check of detailed space charge evaluations. The L.S.A. mode and instantaneous domain calculations of cavity controlled modes allow a further check for a dynamic terminal voltage, even though the latter may be prohibitively long when suitable parameters are used to allow a good approximation to instantaneous domain formation.

#### REFERENCES FOR COMPUTER SIMULATION

- Copeland, J. A. (1967). *I.E.E.E. Trans. Electron Devices*, ED-14, 55-58.  
 Thim, H. W. (1968). *J. Appl. Phys.* 39, 3897-3904.  
 Fawcett, W. (1968). *Electronic Components*.  
 Ward, A. L. (1964). *J. Appl. Phys.* 35, 469-474.  
 Camp, W. O. (1969). *Proc. I.E.E.E.* 57, 220-221.  
 Jeppsson, B. I. and Jeppesen, P. (1971). *I.E.E.E. Trans. on Electron Devices* ED-18, 432-449.  
 Smith, G. D. (1965). "Numerical solution of partial differential equations", Oxford University Press.



## Author Index

The numbers in brackets are the reference numbers and those in *italic* refer to the Reference pages where the references are listed in full. Absence of page number indicates a general reference.

### A

Acket, G. A., 96 (48), 101 (67), *106*, *107*  
 Aitchison, 229 (19), *230*  
 Allen, J. W., 9 (19), *12*, 61 (2), 67 (2), 72  
 (27), 101 (58), 102 (56), 103 (58), 104  
 (2), *105*, *106*, 120 (13), *135*, 316 (3),  
 353, 358 (5), 359 (9), *371*, *372*.  
 Amick, J. A., 318 (5), *353*  
 Amron, I., 330 (19), *353*  
 Aic, H. K., 146 (7), 168  
 Aven, M., 104 (61), *106*, 358 (4), *371*

### B

Baraff, G., 84 (34), *106*  
 Barber, M. R., 186 (5), 202, 246 (13),  
 245 (13), *248*  
 Bardeen, J., 68 (39), 104 (39), *106*  
 Barlow, H. E. M., *379*  
 Bartelink, D. J., 357 (17), *372*  
 Bass, J. C., 303 (19), *312*  
 Baughan, K. M., 302 (12), *312*  
 Baxandall, P. J., 330 (20), 331 (20), *353*  
 Beck, A. H. W., 9 (15), *12*  
 Bell, D. A., 85 (36), *106*, 234 (5), 247  
 Berenz, J., 231 (29), *248*  
 Bergstresse, T. K., 63 (5), *105*  
 Bharat, R., 92 (41), *106*  
 Bird, J., 340 (38), *354*  
 Birman, J. L., 71 (22), *105*  
 Boardman, A. D., 85 (38, 72), *106*, *107*  
 Boer, K. W., 94 (44), *106*  
 Boers, P. M., 358 (2), *371*  
 Bolton, R. M. G., 340 (37), *354*

Bott, I. B., 73 (29), 75 (29), 76 (29), 77  
 (29), *106*, 113 (7), *135*, 164 (16), 165  
 (16), *168*, 178 (3), 202, 231 (1), 247, 338  
 354, (26)  
 Brady, D. P., 94 (45), 95 (45), *106*  
 Braslau, N., 96 (50), 101 (73), *106*, *107*,  
 337 (25), 338 (25), *354*  
 Brooks, H., 70 (19), *105*  
 Bulman, P. J., 162 (15), 166 (19), *168*,  
 301 (11), 304 (11), *312*  
 Butcher, P. N., 73 (28), 75 (28, 30, 31),  
 76 (30, 31), 77 (30, 31), 103 (59), 104  
 (30), *106*, 110 (15), 118 (11, 12), 119  
 (12), 121 (12), 122 (11, 12, 14, 15), *135*,  
 139 (2), 155 (12), *168*, 199 (17), 200  
 (17), 202, 369 (29), *372*

### C

Califano, F. P., 166 (18), *168*  
 Camp, W. O., *391*  
 Cardona, M., 63 (6), *105*  
 Carlson, R. O., 277 (2), 278 (2), *312*  
 Carroll, J. E., 11 (27), *12*, 151 (9), 152 (9),  
 153 (9), *168*, 271 (23), *275*  
 Chang, D. M., 97 (52), *106*, 355 (14),  
 356 (14), *372*  
 Chang, K. K. N., 11 (29), *12*  
 Chawla, B. R., 197 (19), *202*  
 Chen, Y. S., 72 (27), 101 (58), 103 (58),  
*106*  
 Chilton, R. A. 190 (12), *202*  
 Chynoweth, A. G., 61 (3), 101 (3), *105*,  
 112 (3), 113 (3), 128 (3), *135*, 154 (11),  
*168*, 204 (2), 210 (2), 211 (2), 212 (2),

- 213 (2), 214 (2), 215 (2), 230, 339 (32), 354  
 Cohen, M. G., 274 (26), 275  
 Cohen, M. L., 63 (5), 105  
 Coleman, D. J., 197 (19), 202  
 Colliver, D. J., 319 (35), 351 (44), 354, 358 (2), 371  
 Conwell, E. M., 46 (7), 56, 63 (4), 67 (10), 69 (10), 70 (18), 71 (4), 72 (4), 73 (4), 78 (4), 80 (4), 81 (4), 83 (4), 91 (4), 94 (4), 105  
 Copeland, J. A., 11 (28), 12, 72 (23), 105, 118 (10), 122 (10), 128 (17, 18), 132 (19), 135, 146 (6), 153 (10), 154 (10), 155 (10), 156 (10), 157 (10), 162 (6), 168, 171 (1), 172 (1), 174 (1), 175 (1, 8), 176 (1), 178 (1), 188 (8), 190 (1), 193 (13), 197 (8), 201 (8), 202, 246 (15), 248, 268 (21), 271 (21), 275, 329 (17), 330 (17), 331 (17), 353, 391  
 Coriell, A. S., 61 (3), 101 (3), 103 (57), 105, 106  
 Court, W. P. N., 231 (1), 239 (8), 241 (9), 242 (9), 247, 299 (9), 300 (9), 312  
 Cox, R. H., 338 (27), 339 (29), 354  
 Cullen, A. L., 379  
 Curtice, W. R., 200 (24), 202
- D**
- Dalman, G. C., 231 (29), 248  
 Das, P., 92 (41), 106  
 Day, G. F., 144 (4), 164 (4), 168  
 Dennison, E., 310 (231), 312  
 De Sa, B. A. E., 237 (28), 248  
 Dicke, R. H., 241 (21), 247, 377 (3), 378, 379  
 Dow, D. G., 10 (21), 12  
 Draysey, D. W., 231 (1), 247, 305 (20), 306 (20), 312  
 Dumke, W. P., 358 (19), 372  
 Dykman I. M., 68 (14), 105
- E**
- Early, J. M., 133 (20), 135  
 Eastman, L. F., 192 (14), 198 (16), 202  
 Edridge, A. L., 166 (17), 168  
 Edward, J. P., 274 (26), 275  
 Edwards, J. A., 312  
 Ehrenreich, H., 67 (9), 101 (55), 105, 106  
 Elliot, B., 95 (47), 106  
 Elliot, B. J., 104 (62), 107  
 Elliot, J. B., 355 (13), 356 (13), 372  
 Enstrom, R. E., 318 (6), 353  
 Esaki, L., 3 (8), 11
- F**
- Fairhurst, J. G., 312  
 Faulkner, E. A., 234 (3), 236 (3) 237 (3, 6), 238 (6), 247  
 Fawcett, W. F., 73 (29), 75 (29, 30, 31), 76 (29, 30, 31), 77 (29, 30, 31), 85 (38, 72), 87 (68), 88 (68), 89 (68), 100 (70), 103 (59), 104 (30), 106, 107, 110 (15), 113 (7), 122 (14, 15), 135, 155 (12), 164 (16), 165 (16), 168, 198 (23), 202, 224 (13), 230, 357 (18), 358 (18, 20), 359 (21), 362 (21, 22), 363 (22), 364 (22), 370 (21), 372, 391  
 Fay, B., 101 (74), 107, 246 (16), 248  
 Feldman, W. L., 61 (3), 101 (3), 105  
 Fisher, R. E., 257 (15), 260 (15), 274 (28), 275  
 Foyt, A. G., 9 (20), 12, 61 (1), 104 (1), 105, 212 (5), 230, 358 (3), 371  
 Fray, A. F., 351 (44), 354  
 Fray, S. J., 373 (1), 378  
 Frohlich, H., 67 (11, 12), 69 (17), 73 (17), 105
- G**
- Gibbons, J. F., 50 (10), 56  
 Gibbs, S. E., 193 (21), 202, 373 (1), 378  
 Ginzton, E. L., 379  
 Goldwasser, R. E., 231 (29), 248  
 Goodwin, A. R., 323 (10), 353  
 Grande, V. J., 190 (11), 191 (11), 202  
 Greene, P. E., 326 (13), 353  
 Grobe, 334 (24), 335 (24), 354  
 Groves, W. O., 328 (14), 353  
 Guetin, P., 253 (6), 275  
 Gueldbransen, T., 330 (16), 353  
 Gunn, J. B., 1 (1), 3 (7), 8 (1, 13), 9 (1,

13, 17), 11, 12, 81 (33), 94 (43), 95 (47),  
104 (60, 62), 106, 107, 113 (4), 135,  
358 (1), 371

## H

Hakki, B. W., 10 (22), 12, 212 (6), 220  
(9), 230, 246 (14), 248  
Halsted, R. E., 104 (61), 106  
Hamaguchi, C., 96 (49), 106  
Hammar, C., 357 (16), 372  
Harris, J. S., 339 (33), 341 (33), 354  
Hartnagel, H. L., 256 (10, 17), 257 (14),  
259 (14), 262 (17), 267 (10, 17), 268  
(17), 270 (22), 274 (17, 27), 275  
Hartnett, J. P., 280 (25), 312  
Hasty, T., 339 (28), 340 (28), 354  
Hasty, T. E., 339 (29), 354  
Hauge, P. S., 101 (73), 107  
Hayashi, T., 268 (21), 271 (21), 272 (25),  
275  
Hayes, R. E., 221 (10), 230  
Hearn, C. J., 199 (17), 200 (17), 202  
Heeks, J. S., 112 (5), 113 (5), 120 (5),  
126 (5), 135, 252 (4), 254 (7), 257 (12),  
275, 302 (16), 303 (17), 312  
Henisch, H. K., 328 (15), 353  
Herman, F., 6 (31), 25 (4), 26 (4), 12, 56  
Herman, P., 235 (22), 240 (22), 241 (9),  
242 (9, 22), 247, 248, 286 (4, 5), 287  
(5), 288 (5), 289 (4, 5), 291 (5), 292  
(5), 294 (5), 295 (5), 296 (5), 297 (5),  
300 (5), 312  
Herring, C., 72 (25), 106  
Hewitt, S. J., 302 (15), 312  
Higginbotham, C. W., 63 (6), 105  
Higgins, J. A., 190 (11), 191 (11), 202  
Hilsum, C., 4 (11), 5 (11), 9 (11), 10 (23),  
12, 25 (3), 26 (3), 47 (3), 56, 63 (8), 67  
(8), 103 (59), 105, 106, 178 (3), 202,  
241 (9), 242 (9), 247, 357 (15), 365 (23),  
366 (23, 25), 367 (26), 368 (25, 26, 27),  
369 (30), 371 (26, 27), 372  
Hobson, G. S., 159 (13, 14), 160 (14),  
168, 175 (2), 178 (10), 186 (4), 189 (2,  
10), 202, 234 (4), 235 (4), 236 (4, 20),  
237 (27, 28), 240 (4), 243 (4, 11), 244  
(4), 247 (11, 19), 247, 248, 373 (2),  
376 (2, 4), 377 (2), 378  
Hodgart, M. S., 298 (7), 312

Hofmann, K. R., 273 (33, 34, 36), 274  
(36), 275  
Holliday, H. R., 241 (9), 242 (9), 247,  
302 (14), 312  
Holmstrom, D., 203 (1), 216 (1), 217 (1),  
218 (1), 230  
Howes, M. J., 201 (18), 202  
Huang, H. C., 165 (5), 168, 187 (6), 202  
Hutson, A. R., 9 (14, 18), 12, 61 (3),  
101 (3), 103 (57), 105, 106

## I

Imishi, Y., 96 (49), 106  
Inoue, K., 106  
Irvin, J. C., 10 (22), 12  
Irvine, T. F., 280 (25), 312  
Izadpanah, S. H., 247 (19), 248, 256 (10,  
13, 17), 257 (14), 259 (14), 262 (13,  
17), 265 (13), 267 (10, 13, 17), 268 (17),  
269 (13), 270 (12, 22), 271 (13), 274  
(13), 275

## J

Jackets, A. E., 280 (26), 312  
James, B. F., 340 (37), 354  
James, R. P., 246 (15), 248  
Jayaraman, A., 61 (3), 101 (3), 103 (57),  
105, 106  
Jeppesen, P., 192 (25), 194 (25), 195  
(25), 202, 261 (16, 29), 275, 391  
Jeppsson, B. I., 192 (25), 194 (25), 195  
(25), 202, 261 (16, 29), 275, 391  
Johnson, E. O., 133 (21), 135  
Johnston, R. L., 10 (25), 12  
Josenhans, J., 231 (2), 241 (2), 247  
Judd, 302 (15), 312

## K

Kalashnikov, S. G., 97 (51), 106  
Kang, C. S., 326 (13), 353  
Kastal'skii, A. A., 355 (11), 359 (11), 372  
Kataoka, 116 (24, 25), 136  
Kataoka, S., 273 (35), 275



- Kawashina, M., 273 (35), 275  
 Kennedy, W. K., 134 (22), 136, 190 (12), 193 (22), 198 (16), 202  
 King, G., 72 (26), 101 (26), 106, 138 (21), 168  
 Kino, G. S., 90 (64), 98 (53), 99 (64), 101 (74), 106, 107, 145 (20), 168, 181 (7), 185 (7), 202, 246 (16), 248, 251 (18), 252 (5), 262 (18), 266 (18), 273 (32), 275  
 Knight, 276 (1), 312  
 Knight, J. R., 316 (4), 353  
 Knight, S., 72 (24), 94 (45), 95 (45), 106, 220 (9), 230, 274 (26), 275  
 Kono, T., 96 (49), 106  
 Kozdon, P., 246 (17), 248  
 Kroemer, H., 2 (3), 4 (9), 9 (16), 11, 12, 110 (2), 113 (9), 126 (9), 128 (16), 133 (9), 135, 212 (3), 213 (3), 215 (3), 230  
 Kuhn, P., 236 (25), 247  
 Kuno, H. J., 229 (18), 230  
 Kurokawa, K., 264 (19), 275  
 Kurosawa, T., 85 (37), 87 (37), 106  
 Kuru, I., 141 (3), 145 (20), 168, 181 (7), 185 (7), 202, 251 (18), 262 (18), 266 (18), 275
- L**
- Ladbrooke, P. H., 151 (9), 152 (9), 153 (9), 168, 271 (23), 275  
 Latham, C. B., 237 (27), 248  
 Lawley K. L., 94 (45), 95 (45), 106  
 Lax, M., 71 (22), 105  
 Lee, B. K., 298 (7), 312  
 Lee, C. A., 231 (29), 248  
 Lees, J., 72 (26), 101 (26), 106  
 Levy, M., 312  
 Lewin, L., 197 (15), 202  
 Loudon, R., 71 (22), 105  
 Ludwig, G. W., 47 (8), 48 (8), 56, 104 (61), 106, 358 (4), 371  
 Lyubchenko, V. E., 97 (51), 106 (2), 211 (2), 213 (2), 214 (2), 215 (2), 230  
 McGroddy, J. C., 104 (62), 107, 355 (7), 358 (6, 7), 359 (7), 370 (7), 371  
 McKelvey, J. P., 14 (1), 56, 65 (7), 105  
 MacKenzie, L. A., 165 (5), 168, 187 (6), 202  
 McLean, T. P., 366 (24), 372  
 McStay, J., 272 (31), 275  
 McWhorter, A. L., 61 (1), 104 (1), 105, 212 (5), 230, 358 (3), 371  
 Madelung, O., 325 (11), 353  
 Magarshack, J., 222 (12), 230  
 Mahrous, S., 212 (4), 230  
 Marks, R. C., 307 (22), 312  
 Mason, W. P., 2 (4), 11  
 Matsuno, K., 243 (10), 244 (12), 248  
 Matz, D., 68 (13), 105  
 Mayer, J. W., 342 (40), 354  
 Meade, M. L., 234 (3), 236 (3, 26), 237 (3, 6), 238 (6, 7), 239 (7), 247  
 Meyer, N. I., 330 (16), 353  
 Microwave, 225 (16), 230  
 Mircea, A., 222 (12), 230  
 Moll, J. L., 97 (52), 106  
 Montgomery, C. G., 377 (3), 378, 379  
 Montgomery, C. S., 241 (21), 247  
 Morin, F. J., 47 (9), 48 (9), 56  
 Mullin, J. B., 315 (2), 353  
 Myers, F. A., 272 (31), 275, 302 (12), 312, 340 (36), 354
- N**
- Narayan, S. Y., 348 (41), 354  
 Nathan, M. I., 355 (7), 358 (7), 359 (7), 370 (7), 371  
 Nelson, H., 321 (9), 353  
 Newton, C. O., 138 (1), 168, 251 (1), 254 (1, 8), 256 (8), 257 (8), 273 (8), 275  
 Nishimaki, M., 266 (20), 267 (20), 275  
 Nordbotten, A., 256 (11), 257 (11), 275  
 Norris, C. B., 50 (10), 56
- O**
- Ohmi, T., 266 (20), 267 (20), 275  
 Omori, M., 298 (8), 299 (8), 312  
 Owens, J. M., 252 (5), 275
- M**
- McCumber, D. E., 112 (3), 113 (3), 128 (3), 135, 154 (11), 168, 204 (2), 210

## P

- Paige, E. G. S., 68 (15), 70 (15), 102 (15), 105, 107, 358 (20), 372  
 Paola, C. R., 339 (34), 354  
 Paranjape, B. V., 69 (17), 73 (17), 105  
 Park, J., N., 339 (31), 354  
 Parkes, E. P., 351 (45), 354  
 Patel, B., 376 (41), 378  
 Paxman, D. H., 358 (2), 371  
 Pearson, A., 298 (6), 312  
 Pearson, G. L., 61 (2), 67 (2), 72 (27), 101 (58), 102 (56), 103 (58), 104 (2), 105, 106, 190 (11), 191 (11), 202, 339 (32), 354  
 Perlman, B. S., 222 (11), 223 (11), 230  
 Persky, G., 357 (17), 372  
 Peterson, C. C., 318 (6), 353  
 Pollak, F. H., 63 (6), 105  
 Porowski, S., 359 (10), 372  
 Prager, H. J., 11 (29), 12  
 "Proceedings of the International Symposium on Gallium Arsenide" Reading, Sept. 1966, 319 (7), 353  
 Purcell, E. M., 241 (21), 247, 377 (3), 378, 379  
 Purcell, J. J., 200 (24), 202

## R

- Rathbone, R., 312  
 Read, W. T., 10 (26), 11 (26), 12, 71 (21), 105  
 Rees, H. D., 85 (38), 92 (42, 69, 71), 100 (70), 106, 107, 135 (23), 136, 366 (25), 367 (26), 368 (25, 26), 371 (26), 372  
 Reid, F., 332 (22), 353  
 Reynolds, J. F., 368 (28), 372  
 Richman, D., 313 (1), 353  
 Ridley, B. K., 4 (10), 7 (12), 9 (10, 12), 12, 113 (8), 115 (8), 135, 355 (12), 372  
 Robson, P. N., 45 (5), 56, 116 (26), 136, 181 (7), 185 (7), 202, 212 (4), 224 (15), 230, 246 (16, 17), 248, 251 (18), 262 (18), 263 (30), 273 (32), 275  
 Ruch, J. G., 87 (68), 88 (68), 89 (68), 90 (64), 98 (53), 99 (64), 106, 107, 198 (23), 202, 224 (13), 230, 355 (14), 356 (14), 357 (18), 358 (18), 372

- Ryder, E. J., 2 (5, 6), 11  
 Ryvkin, S. M., 355 (11), 359 (11), 372

## S

- S. T. L. Annual Report 1969, 326 (12), 353  
 Salow, H., 334 (24), 335 (24), 354  
 Sandbank, C. P., 251 (3), 252 (3), 254 (7), 269 (3), 275  
 Schiff, L. I., 14 (2), 56  
 Shaw, M. P., 190 (20), 202  
 Sher, A., 71 (65), 107  
 Shockley, W., 2 (2, 4, 5), 11, 68 (39), 104 (39), 106, 110 (1), 135, 246 (15), 248  
 Shoji, M., 251 (2), 252 (2), 254 (2), 255 (2), 256 (9), 269 (2), 272 (2), 273 (2), 275, 353 (46), 354  
 Shuskas, A. J., 190 (20), 202  
 Shyam, M., 61 (2), 67 (2), 72 (27), 101 (58), 102 (56), 103 (58), 104 (2), 105, 106  
 Skinner, J. M., 308 (24), 311 (24), 312  
 Skvortsova, N. E., 97 (51), 106  
 Slater, J. C., 379  
 Smith, G. D., 391  
 Smith, J. E., 104 (63), 107, 355 (8), 357 (8), 359 (8), 372  
 Smith, R. A., 333 (23), 334 (23), 354  
 Southgate, P. D., 272 (24), 273 (24), 275  
 Special Issue (1966, 1967, 1970), 11 (30), 12  
 Spiwak, R. R., 193 (13), 202, 244 (23), 248  
 Stenflo, L., 78 (32), 83 (32), 106  
 Stertzer, F., 224 (14), 230, 303 (18), 312  
 Stover, H. L., 302 (13), 312  
 Strack, H., 338 (27), 354  
 Stratton, R., 69 (16), 91 (40), 105, 106  
 Swain, S., 85 (72), 107  
 Swan, C. B., 280 (3), 312

## T

- Takeoka, Y., 266 (20), 267 (20), 275  
 Talbot, J. A. A., 162 (15), 168  
 Taylor, B. C., 201 (18), 202, 272 (31),

- 275, 350 (42), 354, 358 (2), 371, 373 (1), 378  
 Thim, H. W., 10 (24), 12, 72 (24), 100 (54), 106, 113 (6), 135, 189 (9), 190 (9), 202, 220 (78), 221 (8), 226 (17), 227 (17), 228 (17), 230, 246 (13), 245 (13), 247 (18, 30), 248, 391  
 Thomas, C. O., 330 (18), 353  
 Thornber, K. K., 71 (65), 107  
 Tietjen, J. J., 318 (5), 353  
 Tomchuk, P. M., 68 (14), 105  
 Tomizawa, K., 273 (35), 275  
 Toyama, Y., 350 (43), 354  
 Tree, R. J., 358 (2), 371  
 Tsu, R., 3 (8), 11
- U
- Uenohara, M., 94 (45), 95 (45), 106, 268 (21), 271 (21), 275
- V
- Vassell, M. O., 63 (4), 67 (10), 69 (10), 71 (4), 72 (4), 73 (4), 78 (4), 80 (4), 81 (4), 83 (4), 91 (4), 93 (4), 105  
 Vogt, E., 72 (25), 106
- W
- Ward, A. L., 391  
 Warner, F. L., 147 (8), 150 (8), 168, 235
- (22), 240 (22), 242, (22), 248, 241 (9), 242 (9), 247, 286 (4, 5), 287 (5), 288 (5), 289 (4, 5), 291 (5), 292 (5), 294 (5), 295 (5), 296 (5), 297 (5), 300 (5), 301 (10), 312, 373 (2), 376 (2), 377 (2), 378  
 Wasse, M. P., 72 (26, 101 (26), 106  
 Watkins, T. B., 4 (10), 9 (10), 12, 355 (12), 372  
 Watters, R. L., 47 (8), 48 (8), 56  
 Weisberg, L. R., 70 (20), 105  
 Weiser, K., 339 (30), 354  
 Weissglas, P., 357 (16), 372  
 Weisskopf, V. F., 46 (7), 56, 70 (18), 105  
 Wilson, K., 232 (24), 247  
 Withers, M. J., 312  
 Wolfe, C. M., 319 (8), 353  
 Woode, A. D., 252 (4), 254 (7), 275  
 Woods, J. F., 339 (30), 354
- Y
- Yamashita, J., 106  
 Yarbough, D. W., 342 (39), 354
- Z
- Ziman, J. M., 332 (21), 353  
 Zylbersztejn, A., 81 (33), 106

## Subject Index

### A

Accumulation layer, 127, 176–181  
 Acoustic scattering, 68, 72  
 Amplification, 221–230  
     parametric, 228–230  
     travelling domain, 225–228  
     travelling wave, 224–225  
 Amplitude modulation noise, 231  
 Analogue to digital conversion, 259, 269  
 “and” gate, 262, 268  
 Annular device, 256  
 Arsenic trichloride vapour epitaxy, 316  
 Arsine vapour epitaxy, 318  
 Avalanche breakdown, 139, 162, 189, 192, 252  
 Avalanche diode, 10

### B

Band structure, 5, 20, 25, 58, 63  
 Bias voltage  $\times$  frequency product, 159  
 Bloch’s theorem, 19  
 Boltzmann equation, 63–86, 382  
 Bonding, 347  
 Bose–Einstein distribution, 40, 65  
 Bouncing ball pulse generator, 95  
 Bridgman technique, 314  
 Brillouin zone, 63  
 Butcher and Fawcett, 73–78, 87

### C

Cadmium telluride, 9, 104, 358.  
 Cavity design, 193, 196, 242, 286  
 Central valley, 59, 63  
 Clock, 271

Comparator, 256, 262  
 Computer simulation, 154, 387–391  
 Conduction band, 58, 63, 82  
 Conduction process, 32  
 Contact resistance, 339  
 Contacts, 334–342  
 C. W. operation, 157, 198  
 Conwell and Vassell, 78–83, 87  
 Coupling loop, 287  
 Crystal momentum, 15, 22  
 Current noise, 235, 236  
 Current–voltage characteristic, 139  
 Czochralski technique, 314

### D

Debye length, 51, 390  
 Deformation potential, 68, 72, 73, 81  
 Delay mode, 147, 261  
 Density of states, 28  
 Destabilization, 376–378  
 Device construction, 342–349  
 Dielectric breakdown, 60, 67, 70, 104  
 Dielectric relaxation time, 53, 95, 389  
 Dielectric surface loading, 273–274  
 Dielectric washer, 289  
 Differential negative mobility, 60, 75, 87, 92  
 Diffusion, 50, 64, 77, 98, 99, 211, 390  
 Distribution function, 62, 85  
 Dofic, 126, 269  
 Domain capacity, 139, 160, 254  
 Domain extinction, 142, 253, 272  
 Domain modulation, 272  
 Domain nucleation, 138, 253  
 Domain potential, 121, 124, 250, 265  
 Domain propagation, 113  
 Domain shape, 118, 121, 135  
 Domain transient response, 7, 263, 265, 266

Domain triggering, 257, 267  
 Domain triggering jitter, 243  
 Domain velocity, 120, 123, 253  
 Domain velocity fluctuations, 243  
 Doping, 27, 320  
 Doping inhomogeneity, 176, 188, 250  
 Doping profile, 114, 153, 328  
 Doppler radar, 305  
 Drifted Maxwellian distribution, 69, 73  
 Drift velocity, 62  
 Dynamic characteristic, 119  
 Dynamic susceptance, 131, 185, 201

## E

Effective mass, 23, 59, 63  
 Efficiency, 143, 144, 150, 172, 184  
 Elastic scattering, 384  
 Electric field probe, 100  
 Electron-electron scattering, 68  
 Electronic conduction, 62  
 Electronic tuning, 292-299  
 Electron momentum, 15, 22  
 Electron temperature, 58, 73, 76  
 Electron transfer, energy dependence, 6, 67, 104  
 Electro-optic modulation, 274  
 Encapsulations, 350  
 Energy relaxation, 90-93, 135, 199, 205, 211  
 Envelope feedback, 301  
 Equal areas rule, 120  
 Equivalent intervalley scattering, 73  
 Exclusive 'or' gate, 256, 262

## F

Fermi-Dirac distribution, 29, 380  
 Finite difference, 387-391  
 Flicker noise, 234, 236  
 Flip chips, 345  
 Frequency deviation, 232  
 Frequency locking, 257, 302  
 Frequency modulation, 238, 255-257  
 Frequency modulation noise, 231

## G

Gain-bandwidth product, 223, 229

Gallium antimonide, 357  
 Gallium arsenide phosphide, 9, 103  
 Gallium phosphide, 72  
 Germanium, 3, 34, 47, 104, 356, 358, 359  
 Gold-germanium contact, 337  
 Gunn effect, 8

## H

Hall measurement, 332  
 Heat sink, 158  
 Hole conduction, 26  
 Hot electrons, 2, 48, 58, 59, 76  
 Hybrid mode, 186  
 Hysteresis, 239

## I

Impact ionization, 139, 162, 189, 192, 252  
 Impurity scattering, 69  
 Inclusive "or" gate, 268  
 Indium antimonide, 357, 359  
 Indium arsenide, 61, 104, 359  
 Indium gallium antimonide, 366  
 Indium phosphide, 9, 104, 358, 367, 368  
 Inhibitor, 268  
 Insulators, semiconductors and metals, 22  
 Integral heat sink, 348  
 Internal scattering, 86  
 Intervalley scattering, 71-73, 91, 100, 362  
 Intravalley scattering, 66-72  
 Inverter, 269

## K

Kronig-Penny model, 19  
 $k$ -space, 62  
 $k$ -states, 17, 28

## L

Lateral non-uniformity, 249-257

Lattice vibrations, 35  
 Legendre polynomial, 78, 383  
 Limited space-charge accumulation  
   (L.S.A.), 128, 130, 169  
 Liquid encapsulation, 315  
 Liquid phase epitaxy, 321–327  
 Load line, 121, 253  
 “Local” resonances, 373–376  
 Logic 249–274

## M

McCumber and Chynoweth model,  
   204–206  
 Magnetoresistance, 333  
 Maxwell–Boltzmann distribution, 29,  
   73, 380  
 Mechanical tuning, 288  
 Memories, 270  
 Metal contact, 138, 337  
 Microstrip, 350  
 Microwave “heating” experiment, 96  
 Mini Radar, 305, 306  
 Mobility, 33, 34, 72, 76, 83, 331  
 Mobility, longitudinal and transverse,  
   54–56  
 Mobility, temperature dependence, 46,  
   87  
 Mode diagram, 132  
 Modulation, 300  
 Modulators, 272–274  
 Momentum relaxation time, 91  
 Monte-Carlo calculation, 85  
 Multi-frequency tuning, 144, 151  
 Multiple domains, 186, 190

## N

“nand” gate, 269  
 $n^+$  contact, 138  
 Nd product, 116, 273  
 Negative effective mass, 3  
 Negative resistance, 171–184  
 Negative resistance, static, 109–112  
 $n/f$  ratio, 174  
 NI product, 94, 114, 203, 209  
 $NI^2$  product, 115  
 noise/carrier power ratio, 233

Noise figure, 244  
 Noise, surface, 236  
 Noise, “white”, 233, 234  
 Non-parabolicity, 63, 68, 83  
 Non-uniform device, 249  
 “nor” gate, 269  
 Nyquist diagram, 216–218

## O

One-electron approximation, 18  
 Optical generation, 272  
 Optical phonon, 39, 67, 71  
 Oscillation starting, 165, 166, 190

## P

Periodic potential, 19  
 Phonon, 65, 67, 381  
 Piezoelectric amplification, 9  
 Planar devices, 351–353  
 Polar breakdown, 6, 67, 104, 369  
 Polar scattering, 60, 67, 72, 78  
 Power limitation, 145, 197  
 Power output, 143, 161, 167, 200  
 Power supply, 303, 304  
 Pressure experiments, 9, 61, 73, 101  
 Pulsed operation, 161–167  
 Pulse generator, 270  
 Pulse radar, 307–309  
 Pulse regenerators, 257  
 $PZf^2$  limit, 134, 145, 222

## Q

$Q$ -factor, 241  
 Quench mode, 181, 261

## R

Random scattering, 383  
 Reflection amplifier, 220  
 Regenerators, 257, 270, 274  
 Relaxation mode, 192, 260  
 Relaxation time, 34, 35, 66, 70, 71, 79,  
   382  
 Resonant scattering, 71

## S

Satellite valley, 59, 63, 72  
 Saturated drift velocity, 49  
 Scattering, 33, 41–46, 58, 63, 64, 66–73, 82, 380–386  
 Scattering probability, 65, 380, 381  
 Schrödinger wave equation, 13  
 Semi-insulating GaAs, 316  
 Series inductance, 163  
 Silicon, 26, 34, 47  
 Silver–indium–germanium contact, 338  
 Silver–tin contact, 338  
 Skin depth, 146, 197  
 Small signal impedance, 207, 209–211, 214, 226  
 Small signal transport equation, 114, 207  
 Space charge growth, 7, 173–181, 188  
 Space charge masking, 109–112, 203  
 Space-charge scattering, 70, 83  
 Space charge waves, 101, 207  
 SPRAT, 311  
 Square wave, 144  
 Stability, 206–209, 216, 299  
 Stability of steady state, 93  
 Standing wave, 197  
 “Supercritical” amplifier, 222–224

## T

Temperature effects, 299  
 Ternary compounds, 360  
 Thermal conductivity, 278  
 Thermal constants, 283  
 Thermal design, 276–284  
 Thermal gradient, 256

Thickness measurement, 327  
 Three level mechanism, 366–368, 371  
 Threshold field, 87, 94  
 Threshold oscillator, 271  
 Time of flight, 98, 99  
 Transient response of domain, 263  
 Transit frequency, 8  
 Transferred-electron effect, 4, 57  
 Transport coefficients, 83  
 Travelling-domain amplifier, 225  
 Travelling-wave amplifier, 224  
 Truth table, 257, 262, 268  
 Tuning, 200, 256  
 Two-stream instability, 9

## U

Unequal areas rule, 264, 265

## V

Valley population, 76  
 Vapour epitaxy, 316–321  
 Velocity-field characteristic, 5, 6, 57, 75, 87, 93–101  
 Velocity saturation, 49  
 Voltage tuning, 255, 256

## W

Water vapour epitaxy, 318  
 Wave function, 14

## Z

Zinc selenide, 104, 358